GEWEX Radiative Flux Assessment (RFA) Volume 1: Assessment

A Project of the World Climate Research Programme Global Energy and Water Cycle Experiment (GEWEX) Radiation Panel

Lead Authors:

Ehrhard Raschke
Max-Planck-Institute for Meteorology, Hamburg, and Institute for Meteorology of University of Hamburg, Germany

Stefan Kinne
Max-Planck-Institute for Meteorology, Hamburg, Germany

Paul W. Stackhouse
NASA, Langley Research Center, Hampton, Virginia, USA

December 2012

WCRP Report No. 19/2012

This report consists of two parts:

Volume 1 contains results, recommendations and conclusions.
Volume 2 contains various details and supplementary information.

GEWEX Radiative Flux Assessment (RFA)
Volume 1: Assessment

Table of Contents

Chapters of the Report

Chapter 3 – Radiation Budget at the TOA 23-90

Foreword

Christian Kummerow, Chair, GEWEX Data and Assessments Panel

The charge given by the GEWEX Radiation Panel (GRP) to the Radiation Flux Assessment Group was to evaluate the overall quality of available, global, long-term radiative flux data products at the top-of-atmosphere and surface. Special emphasis was to be placed on evaluating the overall fidelity with which the GEWEX Surface Radiation Budget (SRB) dataset captures seasonal to interannual variability as well as longer term trends. This dataset is approaching 28 years and has established itself as one of the benchmarks against which other products are measuring themselves. The objectives of this assessment are twofold. The first is to characterize the uncertainties in the SRB and similar products from both a quantitative as well as qualitative perspective. The quantitative portion is accomplished by comparisons among the products at various space and time scales. The qualitative portion consists of added insight provided by a group of experts who have participated in this assessment and who are acknowledged in the "author" section. The second objective of this assessment is to better understand the strengths, weaknesses and assumption that define the SRB product and its uncertainties. These parameters will become increasingly important as the GEWEX Data and Assessments panel undertakes the next step of evaluating the "observed" global water and energy budgets of which SRB is an important component.

Christian Kummerow, Chair of GRP
Colorado State University,
Fort Collins, Colorado

William Rossow, Former Chair of GRP
NOAA/CUNY
New York, New York

Assessment Co-Chairs:
Ehrhard Raschke, William Rossow, Paul Stackhouse

Disclaimer

Subchapter- and Chapter-Authors are primarily responsible for the scientific content. The Lead-Authors are responsible for the combination of all sections in their chapter. The Lead-Authors for the entire report are responsible for the final formatting, here and there some shortening of the report and in particular also cross-referencing in it.

Executive Summary

1. Key findings and recommendations covering the entire report:

The most basic components of Earth's climate are the radiation exchanges that comprise the forcing and response of the planet, so the magnitude and controlling influences on these radiation fluxes have long been a key concern of climate research. The earliest quantitative estimates of these fluxes, starting more than a century ago, focused on the global planetary radiation budget (top-of-atmosphere up- and down-welling solar and terrestrial fluxes, TOA SW and LW fluxes), even though it was already realized that a "greenhouse effect" on surface radiation was required to explain the moderate surface temperatures. These estimates were continued into the latter half of the 20th century and employed conventional (i.e., mostly surface) measurements that resulted in very sparsely and incompletely sampled measurements in space and time. Consequently, quantitative uncertainties were large and details of variability were poor. Direct measurements of TOA fluxes did not begin until the advent of Earth-observing satellites and only became comprehensive and detailed in the 1980s: the series of Earth Radiation satellite missions (chronologically, Nimbus-7, ERBE, ScaRab, CERES, GERB) and several spaceborne solar irradiance instruments have progressively increased the coverage, space and time resolution and accuracy of the TOA flux measurements. In parallel, networks such as the Baseline Surface Radiation Network, BSRN, were expanded, improved in their quality and began to include LW flux measurements. Due to accessibility requirements, most measurement sites remained concentrated on land in the northern hemisphere and did not cover all climate regimes.

Developments in the past two decades have (1) seen an increase in the space-time resolution of satellite TOA flux measurements sufficient to separate cloudy and clear conditions, (2) the advent of surface flux measurements at high time resolution with accompanying atmospheric property information and (3) the first global surface radiative flux estimates based upon data of surface and atmospheric properties coupled to radiative transfer models. In particular, in 1985 the World Climate Research Program launched the Surface Radiation Budget (SRB) project supported by the Baseline Surface Radiation Network (BSRN) to foster progress on understanding the factors controlling the radiation exchanges. As a result we now have several global, multi-decadal data products that estimate the TOA and surface SW and LW fluxes with sufficient detail and resolution to quantify weather-to-climate variations, particularly the effects of clouds. This report describes the results of a thorough assessment of these new products that focuses on determining their accuracy and flaws, as well as suggesting possible improvements of them. A key result that becomes evident in this text is that fluxes at the top of the atmosphere show remarkable consensus among products. The consensus is not quite as good at the surface due to issues primarily with ancillary data but still good enough to significantly narrow the spread among today's climate models.

Based on this assessment of all the flux products, we can report consensus values for the global annual mean fluxes at TOA and the surface (the magnitudes of flux variations on regional and seasonal scales are presented in the chapter summaries). For Global Annual Means at TOA: SWd = 340 to 342 Wm^{-2}, with the newer measurements favoring 340 Wm^{-2}, SWu = 98 to 107 Wm^{-2}, and LWu = 236 to241 Wm^{-2}.

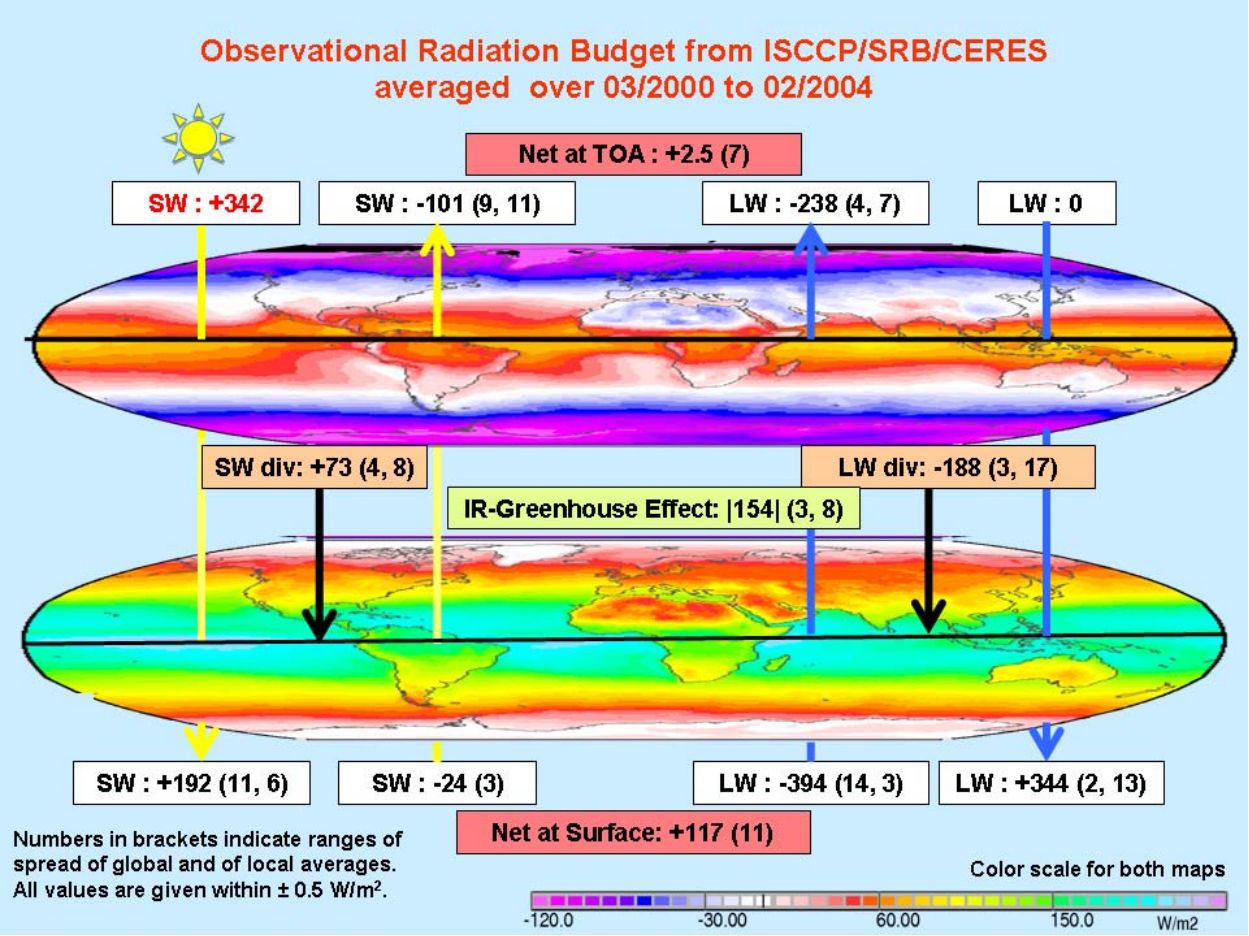

Figure 1: *Observational Annual Radiation Budget from ISCCP, SRB and CERES data sets, averaged over the period March 2000 to February 2004. The maps show mean annual distributions of net fluxes at the TOA and at the surface. Numbers in brackets indicate the ranges of spread between global and local multi-annual averages of the three data sets.*

The inferred Cloud Radiative Effects on upwelling fluxes are 46 to 51 Wm^{-2} for SW and -25 to -28 Wm^{-2} for LW. For Global Annual Means at the Surface: net 112 to 123 Wm^{-2}, SWd = 188 to 197 Wm^{-2}, SWu = 23-26 Wm^{-2}, LWd = 343-348 Wm^{-2} and LWu = 391-399 Wm^{-2}. The inferred Cloud Radiative Effects (CRE) on downwelling fluxes at the surface are -50 to -60 Wm^{-2} for SW and 31-36 Wm^{-2} for LW. The flux products that calculate physically consistent TOA and Surface fluxes provide estimates of the atmospheric divergence and the greenhouse effect; the Global Annual mean Total Divergence is - 113 to -117 Wm^{-2} with SW contributions at 71 to 75 Wm^{-2} and LW contributions at -183 to -189 Wm^{-2}. The inferred Cloud Radiative Effects (CRE) is 0 to - 9 Wm^{-2} for total divergence and 4 to -5 Wm^{-2} for SW divergence and -3 to -8 Wm^{-2} for LW divergence. The global Annual mean Greenhouse effect is 156 to 160 Wm^{-2} with a CRE of 26 to 29 Wm^{-2}.

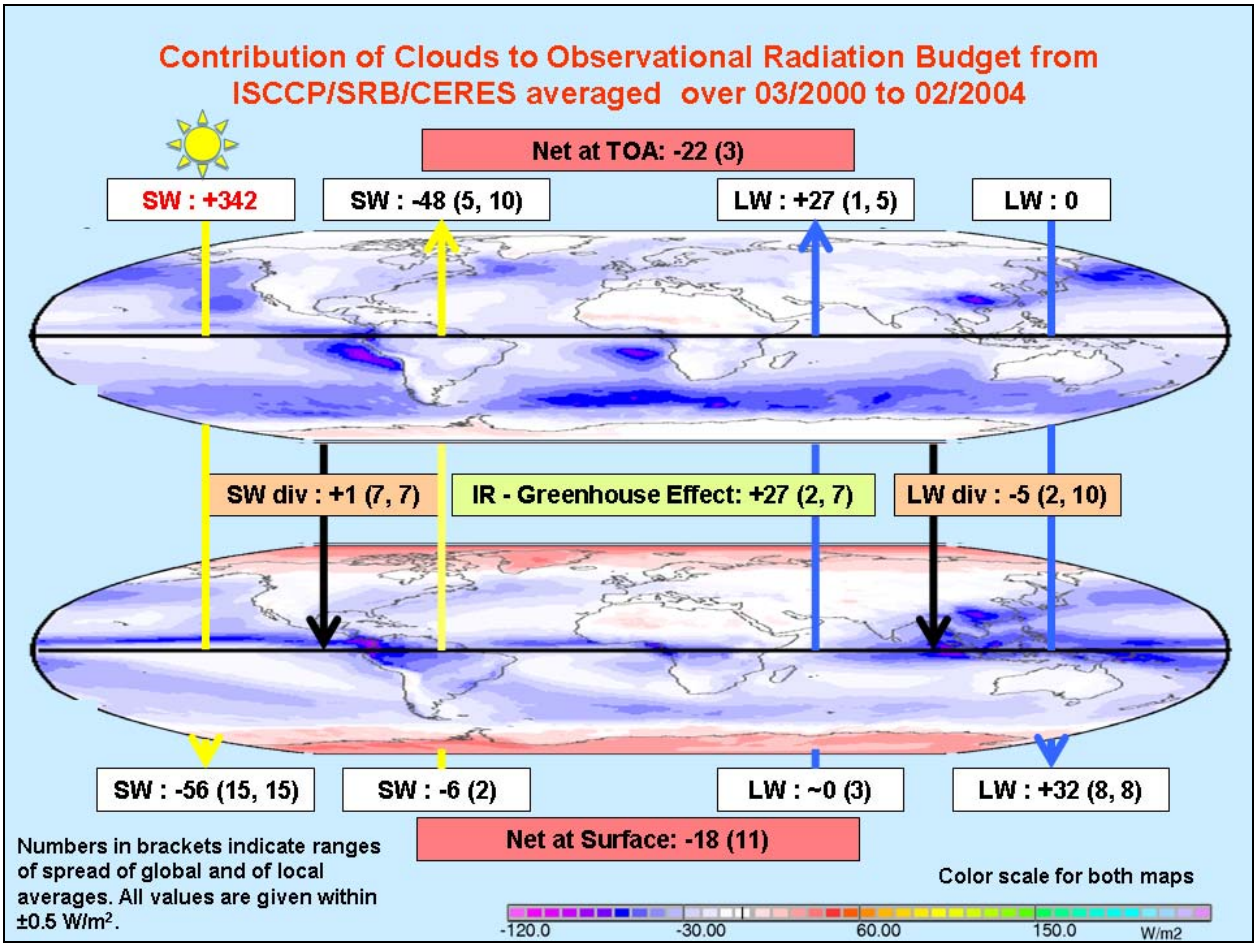

Figure 2: *Cloud Contributions to the Observational Annual Radiation Budget from ISCCP, SRB and CERES data sets, averaged over the period March 2000 to February 2004. The maps show mean annual distributions of the CRE at the TOA and at the surface. Numbers in brackets indicate the ranges of spread between global and local multi-annual averages of the three data sets.*

Comparing the direct satellite determinations of TOA fluxes indicates some differences that still need to be explained and suggest overall uncertainties of global annual mean fluxes of up to 3-5 Wm^{-2} for upwelling SW and up to 2-3 Wm^{-2} for upwelling LW. The uncertainties of the BSRN fluxes are estimated to be about 10 Wm^{-2} for SW and 3 Wm^{-2} for LW for hourly fluxes. When compared with satellite products, the BSRN uncertainties are somewhat larger because of area-representativeness issues; nevertheless, the products evaluated here had biases of downwelling fluxes of only 0-13 Wm^{-2} for SW and 1-6 Wm^{-2} for LW.

The patterns of disagreement among the flux products suggest that the current uncertainties (limitations on accuracy) come largely from the ancillary products used to produce them. Most notably these problems appear to be associated with differences in atmospheric temperature-humidity and surface temperature for the LW fluxes (especially in the upper troposphere and near the land surface), and aerosols and surface albedo for the SW fluxes. Nevertheless, there are still patterns of disagreement that are related to clouds, particularly their vertical distribution, which can change the downwelling LW flux at the surface and the pattern of upwelling LW fluxes at TOA and alter the sign of the net cloud effect on the atmospheric solar flux divergence. Further work still needs to be done to evaluate how well these products represent the diurnal-to-synoptic flux variations.

Despite the disagreements among these radiative flux products, the range of these differences is smaller than the range of differences among climate model fluxes, so that the current versions of these products can already provide useful constraints on these models. This is particularly true for regional and seasonal variations that tend to be robustly represented in all the products. More effort to improve the quality of the ancillary surface and atmospheric data, together with refined treatment of clouds using newer measurements, seems likely to pay off in much more accurate representations of the TOA and surface radiation budgets and their longer term variations.

2. Important Findings and Recommendations by Chapter

Chapter 2: Incoming Solar Radiation at TOA

The uninterrupted 34-yr total solar irradiance (TSI) record obtained from satellites is sufficiently stable to determine the solar cycle variation of TSI as well as significant long-term trends. New instrument calibrations have explained the offsets between the different instruments comprising this record and have reduced the absolute uncertainty. The favored value of TSI is 1360.8 Wm^{-2} at solar minimum, with daily and solar cycle variations of a few Wm^{-2}. Newer instruments are now documenting the spectral dependence of solar variation, drawing attention to much larger changes at UV wavelengths. Climate model calculations of TOA solar flux exhibit regional-seasonal differences that are sometimes a few Wm^{-2} in magnitude and related to how precisely the Sun-Earth geometry is determined; these computational errors can and should be eliminated.

Recommendations

- Measurements of TSI and its spectral components must be continued to support our understanding of variations of the climate

- Computations of incoming solar radiation at TOA should converge to the favored value of TSI, including if warranted its measured variation with sunspot cycle and employ astronomically accurate calculations of the solar ephemeris and Sun-Earth geometry.

Chapter 3: Radiation Budget at the Top of the Atmosphere (TOA)

Comparison of the ERBE and CERES TOA upwelling fluxes show quantitatively very similar temporal and spatial variability, but there are systematic differences in the global, annual mean fluxes and the deseasonalized time series that suggest remaining calibration differences. Some of the difference may also be caused by the different sampling of diurnal variations, particularly for the SW flux. Overall, regional monthly mean upwelling LW flux differences between ERBE and CERES are only about 1% and about 3-5% between them and the various satellite products evaluated here, relative to a consensus global annual mean value of 240±3 Wm^{-2}. Upwelling SW flux differences are about 3% between ERBE and CERES, somewhat larger than for LW, and about 5-7% between them and the other data products , relative to a consensus global annual mean value of 100±4 Wm^{-2}. Clear-sky flux differences among all these products are larger than for all-sky conditions, highlighting the importance of ancillary inputs, especially

for the calculated products but even in the EREBE and CERES products. All the products agree to within about 1-2 Wm^{-2} on the amplitude of seasonal LW and SW flux deviations from their annual means, although there are larger differences for clear-sky fluxes, especially SW fluxes over snow and ice-covered locations. The long-term records of flux anomalies exhibit flaws that prevent use of these products for monitoring the slow variations of the TOA radiance budget; but, since in many cases the causes of these flaws have been identified, improvements in these products are still possible. The state-of-the-art uncertainty in the global, annual mean flux budget is about 2-3 Wm^{-2} for each flux component and about 3-5 Wm^{-2} for regional monthly mean values, which translates into an uncertainty in the poleward heat transports by the atmosphere and ocean of less than 5%.

Recommendations

- More work is needed to reconcile the difference of upwelling SW fluxes, including further investigations of instrument calibrations and the effects of poor sampling of the rapid time variations induced by Earth's rotation and cloud variations.

- Further investigations are needed of the role and quality of ancillary inputs in all of these products, most notably surface albedo and temperature and atmospheric temperature-humidity.

- Re-processing of these products is warranted to reduce specific issues uncovered in chapter 3 of this assessment (and other evaluation studies). In particular some of the larger differences between ERBE and CERES, as well as ScaRab and GERB, need explanation to improve these datasets as reference standards.

Chapter 4: Radiation Budget at the Surface

All of the global surface radiation flux products are calculated from observed or assumed properties of the atmosphere, clouds and surface with different sources of this information and different constraints applied. The regional, annual mean surface upwelling and downwelling SW and LW fluxes from these products agree to within about 20 Wm^{-2}, with agreement being somewhat better over ice-free oceans than over land and somewhat worse in the polar regions. The regional clear-sky downwelling SW flux differences implicate significant differences in the input or assumed aerosol optical properties. The regional downwelling and upwelling LW flux differences implicate differences in the ancillary inputs for atmospheric and surface temperatures. Global annual mean values agree to within about 1% for LW, relative to consensus values of 345±3 Wm^{-2} for downwelling and 395±4 Wm^{-2} for upwelling, and to within about 3-4% for SW, relative to consensus values of about 190±10 Wm^{-2} for downwelling and about 25±2 Wm^{-2} for upwelling. The seasonal deviations of the global mean surface fluxes from their respective annual mean values exhibit agreement to within 1-2 Wm^{-2}, but agreement on long-term trends among these products is poor and seems to depend more on problems with ancillary inputs.

Recommendations

- More work is needed to improve the accuracy of the data products quantifying the properties of the surface and atmosphere, especially in polar regions and deserts.

- More work is required to improve ancillary inputs, notably surface albedo and aerosols for the SW and surface and atmospheric temperatures for the LW.

- Trend monitoring is not yet possible with these products because of flaws in ancillary inputs.

Chapter 5: Long-Term In Situ Surface Flux Data

Direct measurements of the radiative fluxes at the surface, especially for downwelling SW, have been made at a variety of sites over long periods of time; some of these records are long enough to evaluate climate-scale variations. The organization of the BSRN expanded the surface measurement activity in four crucial ways: developing network-wide calibration standards and standardizing operating procedures, adding downwelling LW flux measurements, adding upwelling SW and LW flux measurements, collecting or making measurements of relevant atmospheric properties, in particular cloud and aerosol properties as well as air temperature and humidity. The in situ flux measurement uncertainty is now estimated to be ± 10 Wm^{-2} for SW and ± 3 Wm^{-2} for LW at hourly time scale and ± 4 Wm^{-2} for SW and ± 2 Wm^{-2} for LW at monthly time scales. The main difficulties in using these data to evaluate the satellite derived products involve the differences in time resolution, the spatial representativeness of the surface measurements and the differences between site and area atmospheric and surface conditions. The BSRN data collection has nonetheless been shown to be useful for validation, despite the incomplete coverage of different climate regimes, because of the network-wide calibration and the availability of simultaneous and coincident measurements of atmospheric properties.

Recommendations

- The BSRN network inter-calibration system must be maintained so that BSRN can serve as the anchor for the monitoring of the surface radiation budget in the Global Climate Observing System. Further studies of the spatial representativeness, specific to the individual sites, are needed to reduce the uncertainties associated with this aspect.

- More effort is needed to maintain existing networks for radiation and ancillary data, interlink these networks and expand them into un-sampled climate regimes. In particular, efforts should continue to find practical ways to make these measurements in oceanic regions.

Chapter 6: Surface Satellite-Based Fluxes vs. In Situ Measurements

Comparison of the global calculated surface flux products with matched BSRN, GEBA, UOR and ASRB surface flux measurements shows systematic (rms) differences of −13 to +8 (20-28) Wm^{-2} for downwelling SW and −1 to 6 (13-21) Wm^{-2} for downwelling LW. There are notable seasonal variations in these differences, with winter exhibiting the largest values. Differences are also larger over the polar regions, deserts and mountainous regions. All of the

products had significant negative biases of their downwelling SW flux relative surface measurements in the Alps by up to 30 Wm^{-2}.

Recommendations

- Comparisons of satellite-based products (area averages) to individual sites suffer from representativeness problems with the surface measurements.

- Network density should be increased in mountainous areas to investigate the causes of the large systematic surface flux differences between satellite products and in situ measurements.

- A few quality sites that can represent the open ocean and covering a wide latitude range are needed.

Chapter 7: Vertical Radiative Flux Divergence

The advent of physically consistent calculations of TOA and surface radiative fluxes makes possible a global, detailed estimation of the atmospheric heating/cooling by radiation. The GEWEX SRB and ISCCP-FD products show that clouds slightly increase the SW heating of the atmosphere, whereas the CERES product shows a significant decrease. Differences among these products in their zonal, monthly mean divergences can be as large as 20% of the total divergence, which is about −111-116 Wm^{-2}. Nevertheless, there is consensus that clouds reduce cooling at low latitudes and enhance it at higher latitudes. Clear-sky divergences reveal more clearly the differences in ancillary inputs to these calculations that affect, in particular, the surface fluxes, namely, surface albedo and temperature; however, there are also some patterns that suggest more important differences associated with aerosols and atmospheric temperature-humidity. These effects appear to explain much of the all-sky flux divergence as well.

Recommendations:

- More work is needed to improve the quality of the ancillary data products that characterize the surface and atmospheric properties.

Chapter 8: Global Mean Radiation Budget

This summary of the status of quantifying the global mean radiation budget is based on the comparisons of these products as well as sensitivity studies to identify the leading causes of uncertainty. Generally LW fluxes at TOA, surface and in atmosphere appear to be less uncertain than SW fluxes. Nevertheless, with the exception of upwelling SW at TOA, the differences of all of these products lie within one standard deviation of the CERES uncertainties estimated from the sensitivity studies.

Recommendation:

- Narrowing the uncertainties of the surface radiation budget requires improvement in the ancillary datasets characterizing surface properties and the near-surface atmosphere's temperature and aerosols.

- SW fluxes in general would benefit from better time sampling.

Chapter 9: Radiative Energy Fluxes in Global Modeling

The range of IPCC model TOA and surface fluxes is generally larger than the range of values in the satellite flux data products being evaluated in this report. Aside from the larger model diversity there are also clear differences or biases relative to satellite data: different spatial patterns and a 10 to 20 W/m^2 smaller surface net-flux imbalance. The different spatial patterns can be traced to cloud radiative effects that, at the TOA, can be directly observed by satellites. The smaller surface flux imbalance is being investigated but may be linked to both clouds and ancillary data issues. Surface (and atmospheric) flux products, compared to the satellite flux products, exhibit notable differences associated with limitations related to characterizing of the surface (albedo, temperature) and atmosphere (aerosols, temperature, humidity). These

Recommendations

- **U**nderstanding of biases between modeled and satellite data

- TOA radiative flux patterns biased strongly suggested the need for improved representation of (low altitude) clouds in global modeling (e.g. current optical depth of coastal stratocumulus cloud optical depths is underestimated, while cloud optical depth of sub- and tropical oceans is strongly overestimated)

- Improved quality of ancillary data and ancillary data consistency to each other will establish more reliable products, especially for surface and atmosphere

List of Contributors

Name	Institution	Address
Richard Bantges	Imperial College, London, UK	r.bantges@imperial.ac.uk
Thomas B. Charlock	NASA, Langley R.C., Hampton, USA	t.p.charlock@larc.nasa.gov
Stephen J. Cox	NASA, Langley R.C., Hampton, USA	stephen.j.cox@nasa.gov
David Doelling	NASA, Langley R.C., Hampton, USA	david.doelling@nasa.gov
Ellsworth G Dutton	NOAA Res. Lab., Boulder, USA	ellsworth.g.dutton@noaa.gov
Stuart Freidenreich	NOAA Res. Lab, Princeton, USA	stuart.freidenreich@noaa.gov
J. Gröbner	PMOD/WRC, Davos-Dorf, CH	julian.groebner@pmodwrc.ch
Martial Haffelin	LMD, Polytechnique, Paris, Fr	martial.haffelin@ipsl.polytechnique.fr
Laura Hinkelman	Joint Inst. Atm. Oc. Sci., Seattle, USA	laurahin@uw.edu
Stefan Kinne	MPI Meteor., Hamburg, Ger	stefan.kinne@zmaw.de
Greg Kopp	LASP, U. Colorado, Boulder, USA	greg.kopp@lasp.colorado.edu
Norman G. Loeb	NASA, Langley R.C., Hampton, USA	norman.g.loreb@nasa.gov
Chuck Long	Pac. NW Lab, Richland, USA	chuck.long@pnl.gov
J. C. Mikovitz	NASA, Langley R.C., Hampton, USA	j.c.mikovitz@nasa.gov
Atsumu Ohmura	ETH Zürich, Ch	atsumu.ohmura@env.ehz.ch
Rachel Pinker	Atm. Sci., Univ. Md, USA	pinker@atmos.umd.edu
Ehrhard Raschke	MPI Meteor., Hamburg, Ger	ehrhard.raschke@zmaw.de
Remy Roca	LMD, Jussieu, Fr.	roca@lmd.jussieu.fr
David Rutan	NASA, Langley R.C., Hampton, US	david.a.rutan@nasa.gov
William B. Rossow	CREST at CCNY, New York, USA	wbrossow@ccny.cuny.edu
Jacqui Russell	GERB proj., Imperial Coll., London, UK	jacqi@imperial.ac.uk
George L. Smith	NASA, Langley R.C., Hampton, USA	george.l.smith@nasa.gov
Paul W. Stackhouse	NASA, Langley R.C., Hampton, USA	paul.w.stackhouse@nasa.gov
W. Su	NASA, Langley R.C., Hampton, USA	wenying.su-1@nasa.gov
B. A. Wielicki	NASA, Langley R.C., Hampton, USA	bruce.a.wielicki@nasa.gov
Martin Wild	ETH Zürich, Ch	martin.wild@ethz.ch
Takmeng Wong	NASA, Langley R.C., Hampton, USA	takmeng.wong@nasa.gov
Taiping Zhang	SSAI, NASA, La. R.C., Hampton, USA	taiping.zhang@nasa.gov
Yuan-Chong Zhang	Columbia U., New York, USA	yz7@columbia.edu

List of Various Acronyms

ASRB – Alpine Surface Radiation Budget network
ARM – Atmospheric Radiation Measurement program
BSRN – Baseline Surface Radiation Network
CERES – Clouds and Earth's Radiant Energy System
ERBE – Earth Radiation Budget Experiment
ERBS - Earth Radiation Budget Satellite
GEBA – Global Energy Balance Archive
GEOS – Goddard Earth Observing System
GEWEX – Global Energy and Water Cycle Experiment
HIRS – High-resolution Infrared Sounder
IPCC – Intergovernmental Panel Climate Change
ISCCP – International Satellite Cloud Climatology Project
LW – Long-wave radiation
NASA – National Aeronautics and Space Administration in the US
NOAA – National Oceanic and Atmospheric Administration in the US
RFA – Radiation Flux Assessment
ScaRaB – Scanner for Radiation Budget
SORCE - SOlar Radiation and Climate Experiment
SRB – Surface Radiation Budget
SW – Short-wave radiation
TSI – Total Solar Irradiance
WCRP – World Climate Research Programme

List of Various Acronyms

ASRB – Alpine Surface Radiation Budget network
ARM – Atmospheric Radiation Measurement program
BSRN – Baseline Surface Radiation Network
CERES – Clouds and Earth's Radiant Energy System
ERBE – Earth Radiation Budget Experiment
ERBS - Earth Radiation Budget Satellite
GEBA – Global Energy Balance Archive
GEOS – Goddard Earth Observing System
GEWEX – Global Energy and Water Cycle Experiment
HIRS – High-resolution Infrared Sounder
IPCC – Intergovernmental Panel Climate Change
ISCCP – International Satellite Cloud Climatology Project
LW – Long-wave radiation
NASA – National Aeronautics and Space Administration in the US
NOAA – National Oceanic and Atmospheric Administration in the US
RFA – Radiation Flux Assessment
ScaRaB – Scanner for Radiation Budget
SORCE - SOlar Radiation and Climate Experiment
SRB – Surface Radiation Budget
SW – Short-wave radiation
TSI – Total Solar Irradiance
WCRP – World Climate Research Programme

Chapter 1:

Introduction

E. Raschke, S. Kinne, P. W. Stackhouse

1.1: Purpose of the Assessment

The overarching goal of the GEWEX (Global Energy and Water Cycle Experiment) global data analysis projects is to obtain observations of the elements of the global energy and water cycles with sufficient detail and accuracy to detect and diagnose recent climate variations in terms of the energy and water exchanges within and amongst the main climate system components (atmosphere, ocean, land, cryosphere, biosphere). Various radiative flux products have been generated in Europe and in the US during the past four decades, primarily concerning the radiative fluxes at the top-of-the-atmosphere (TOA), at the surface, and also of the radiative effect of cloud fields (CRE) on these fluxes. The need to assess the remaining uncertainties of the radiative fluxes is crucial to the next step of integrating the observational understanding of the radiative and hydrological cycles. The complexity of the climate system requires modeling studies as well as observational studies, so another general use is for the development and evaluation of climate models. Thus, serious questions are being asked about the quality and reliability of current radiative flux data sets, especially when used to monitor the small and slow changes of climate. These questions must be answered quantitatively with a systematic determination of possible improvements and uncertainty limitations. To this end, the GEWEX Radiation Panel, called for a baseline assessment of the available long-term radiative flux data sets at the TOA and surface.

Several basic uncertainties are encountered in computations of the radiative energy fluxes within the climate system using relevant satellite measurements as basic input. These are related to the measurements themselves, the sampling of these measurements in time and space, the techniques for analyses of measurements with instruments of different design and all required input or ancillary data (see: Wielicki et al., 1995). All of these are potential sources for uncertainties for the derivation of the radiative fluxes at the top-of-atmosphere. Since the surface radiative fluxes cannot directly observed from space, the estimates of these fluxes depend even more heavily on the ancillary sources of information. In the solar wavelengths or shortwave (0.2 μm to 4 μm), the inference of the surface fluxes are related to the TOA reflected energy and many algorithms take advantage of those relationships. Thus, these methods include the uncertainties of the TOA plus assumptions regarding the intervening atmosphere and surface reflectance whether parameterized or specified through radiative transfer methods. In the thermal infrared wavelengths, the constituents of the atmosphere, e.g. water vapor, essentially decouple between the TOA emission and the surface fluxes and thus methods of inferring these fluxes are highly dependent upon the specification of the atmospheric temperature, specific humidity, clouds and aerosols. A parameterization or specific radiative transfer method is then needed to infer these fluxes.

Thus, the derivation of the TOA and surface radiative fluxes are related but have different sources of errors or uncertainties depending upon the observing system and the provision of ancillary information regarding the atmosphere and surface. All of these uses call for radiation

flux datasets that separate shortwave and longwave fluxes, upward and downward (the difference of which provides the net flux, the vertical derivative of which provides the radiative heating of the atmosphere), for all-sky and clear-sky conditions over the whole globe. The required accuracy depends on the space-time scales of variability and ranges from 15 to less than 1 Wm^{-2} for weather-scales to climate scales (e.g. *Ohring et al., 2005*). A complete error assessment over the whole range of scales from weather to global-decadal is needed to better characterize the scientific usefulness of the currently available long-term data sets and identify the key areas where improvements can be made. The report focuses upon data sets submitted to a central archive, but references to new versions or newly released data sets are provided particularly where these data address major uncertainties. This data set covers the period 1984 to about the end of the year 2004. More details about these data sets are found in the Appendix A.

This report represents the efforts of researchers to characterize the current data quality and usefulness of currently released data sets to establish a baseline against which future improved data sets can be compared. Toward this end, the following activities were performed:

(1) Collection, documentation, and characterization (with error indications) for the main long-term datasets and post at least the monthly mean datasets online for further evaluation and analysis and identify various error sources.
(2) Evaluation of the monthly mean, large-scale (regional) variability of radiative fluxes by comparing various products and investigating causes for differences. This variability is also compare with model variability.
(3) Evaluation of the systematic variations of radiative fluxes (diurnal, seasonal) compared with model variations.
(4) Evaluation of the instantaneous accuracy of the radiative fluxes.

1.2: Radiative Flux Assessment Archive, Data Sets and Parameters

To facilitate the analysis of the TOA and surface radiative flux data sets, several planning workshops were held beginning in 2004. Participants agreed to provide versions of their data sets at the resolution 2.5^o latitude x 2.5^o longitude (280 km x 280 km at the equator) within the time period spanning from January 1984 through December 2004. Subsequently, a Website homepage of the project was developed and hosted by the NASA Langley Research Center (LaRC) (http://gewex-rfa.larc.nasa.gov). This web site contains: (1) statement of goals & requirements statement, (2) the assessment plan, (3) sample data sets and (4) assessment participants and author resources.

Additionally, this homepage was linked to web site and data archive that was developed and hosted at the NASA LaRC Atmospheric Science Data Center (ASDC or LaRC DAAC). The web site is: http://eosweb.larc.nasa.gov/GEWEX-RFA . This web site contains (1) archive access to all the monthly mean datasets to be compared/assessed (with ftp access to full time resolution versions) and (2) data provider and read information (3) surface measurement data sets and derived data sets providing tools for analysis of the radiative flux differences cloud and aerosol information.

For this first radiative flux assessment, the participants decided to focus primarily on the essential top-of-atmosphere and surface boundary fluxes for all-sky and clear-sky conditions. A listing of the main parameters, their definitions and abbreviations are given in *Table 1.1*. This assessment will focus upon these fluxes and quantities, such as cloud radiative effect, that can be derived immediately from those data parameters.

Table 1.1: *Radiative flux values considered in this assessment: The fundamental boundary fluxes are in bold letters. Most methods considered compute these fluxes and derive the remaining quantities. However some methods estimate net fluxes directly. Note that there are two types of cloud fraction computed, one where clear-sky fluxes are estimated only in clear conditions and the other where a clear flux is computed without cloud properties.*

Parameter Level	Sky Conditions	Parameter Definition	Abbreviations used in various sections
Top-of-Atmosphere (TOA)	**All-sky Conditions**	**Shortwave downward flux (or Total Solar Irradiance – TSI)**	**ASWDN-TOA**
		Shortwave upward flux (reflected)	**ASWUP-TOA**
		Net shortwave flux (Down – Up)	ASWNET-TOA
		Albedo (Up/TSA)	AALB-TOA
		Longwave upward flux (or Outgoing Longwave Radiation – OLR)	**ALWUP-TOA**
		Total Net Flux (SW + LW)	ATOTNET-TOA
	Clear-sky Conditions	**Shortwave upward flux**	**CSWUP-TOA**
		Net shortwave flux (TSI Down – Clear Up)	CSWNET-TOA
		Albedo (Clear Up/TSI)	CALB-TOA
		Longwave upward flux	**CLWUP-TOA**
		Total Net Flux (SW + LW)	CTOTNET-TOA
Surface (SFC)	**All-sky Conditions**	**Shortwave downward flux**	**ASWDN-SFC**
		Shortwave upward flux	**ASWUP-SFC**
		Shortwave Net flux (Down – Up)	ASWNET-SFC
		Albedo (Up/Down)	AALB-SFC
		Longwave downward flux	**ALWDN-SFC**
		Longwave upward flux	**ALWUP-SFC**
		Net longwave flux (Down – Up)	ALWDN-SFC
		Total Net Flux (SW + LW)	ATOTNET-SFC
	Clear-sky Conditions	**Shortwave downward flux**	**ASWDN-SFC**
		Shortwave upward flux	**ASWUP-SFC**
		Shortwave Net flux (Down – Up)	ASWNET-SFC
		Albedo (Up/Down)	AALB-SFC
		Longwave downward flux	**ALWDN-SFC**
		Longwave upward flux	**ALWUP-SFC**
		Net longwave flux (Down – Up)	ALWDN-SFC
		Total Net Flux (SW + LW)	ATOTNET-SFC

All participants were given the opportunity to use TOA and surface radiative flux data products to provide data products at the selected grid resolution and within the time frame. The main focus of this report is flux data products estimated from passive satellite measurements. *Tables 1.2 and 1.3* present the major data set names and time periods for the TOA and surface flux data products respectively.

Table 1.2: *The* ***TOA flux data products*** *submitted to the GEWEX-RFA archive by participants. GEO means: geostationary data included.*

Type of Flux Product	Name of Research Group or Project	Name of Radiative Flux Products or Measurement	Dates Spanned	Data Set Notes
Broadband Satellite-Based TOA	CERES	TRMM: ERBE-like (Ed2), SRBAVG GEO and nonGEO (Ed2B)	1/98 - 8/98, 3/2000	CERES Measurements; VIRS scene-ID; All-sky, Clear-sky (type 1)
		Terra: FM1 ERBE-like (Ed 2_Rev1), SRBAVG GEO and non-GEO (Ed2D_Rev1)	3/2000-12/2005	CERES Measurements; MODIS scene-ID; All-sky, clear-sky (type 1)
		Aqua: FM3 ERBE-like (Ed2_Rev1)	7/2002-12/2005	CERES Measurements; MODIS scene-ID; All-sky, clear-sky (type 1)
		EBAF (Ed1a, Loeb et al., 2008)	3/2000-10/2005	Loeb et al., 2008; normalized using ocean heat estimates
	ERBE	ERBS+NOAA9, ERBS+NOAA10, ERBS+NOAA9+10, ERBS Scanner	1/1985-12/1989 (or subset)	ERBE measurement; Only ERBS Scanner spans entire period
		ERBS Non-scanner (Ed3_Rev1)	1/1985-9/1999	60 N to 60 S only; 72-day precession cycle
	ScaRaB	ScaRaB v2	3/94-2/95, 12/98-3/99	ScaRaB measurements
Satellite Direct Retrieval Based	U.Md.	HIRS OLR v2.0	1/1979-9/2003	HIRS multi-spectral channel algorithm
Satellite Ancillary Retrieval Based	FORTH	ESRB	1/1984 – 12/2004	ISCCP D2 clouds and TOVS meteorology; All-sky fluxes only; Hatzianast-assiou et al., 2005abc
	GEWEX SRB	GSW 2.0 and 2.81; GLW 2.1 and 2.5	7/1983-6/2005 (v2, 2.1 end 12/95)	ISCCP DX and GEOS; Stackhouse et al., 2002; Cox et al., 2006
	ISCCP (GISS)	FD	7/1983-12/2004	ISCCP D1 and TOVS (Zhang et al., 2004)
	U.Md. SRB	v3.1 and v3.3	7/1983-12/2004	ISCCP D1 and TOVS; SW all-sky only
Model/Re-analysis TOA	ECMWF	ERA-40	07/1983-08/2002	Reanalysis
	NOAA NCEP	NCEP-DOE R2	7/1983-6/2006	Reanalysis
	IPCC	AR4 Median, Mean and Standard Dev	01/1980-12/1999	Various climate models

Noted in the table for the TOA fluxes is the general type of satellite measurement used. TOA flux data products are derived from broadband radiance measurements (e.g., ERBE, CERES and ScaRaB), inferred directly from spectral measurements (e.g., HIRS OLR), inferred

from satellite retrievals of atmospheric quantities such as clouds (e.g., GEWEX SRB, ISCCP FD, etc.) or from model and assimilation data products (e.g., ERA-40, IPCC). The available CERES (Clouds and Earth's Radiant Energy System) data covers the period March 2000 to February 2004 (4 years) and ERBE (Earth Radiation Budget Experiment) scanner data covers a period from 1984 to 1987 (4 years). Other broadband radiometer based products have also been produced from satellite measurements with the instruments ScaRaB and GERB at the TOA. The remaining satellite based methods determine fluxes using satellite retrieved ancillary data products such as cloud properties and meteorological profiles (e.g., ISCCP-FD and FORTH). Some data products are generated using meteorological products that are output from assimilation systems (e.g., CERES SRBAVG and GEWEX SRB). The only flux data products spanning the entire time period are inferred from the International Satellite Cloud Climatology project (ISCCP) and from specific computations using ISCCP from other groups at both TOA and the surface (e.g.: ISIS, FORTH).

Table 1.3: *The surface radiative flux products and surface radiation network measurements and derived products submitted to the GEWEX-RFA archive by participants*.

Type of Flux Product	Name of Research Group or Project	Name of Radiative Flux Products or Measurement	Dates Spanned	Data Set Notes
Satellite Direct Retrieval	U.Md.	ERBE SRB	2/1985-12/1988	ERBE measurements; SW net only
Satellite-Based Surface	DLR	ISIS v1	1/1984 - 12/2004	ISCCP D1 and TOVS; SW and all-sky only (total, diffuse and direct normal)
	CERES	TRMM: SRBAVG Geo (Ed2B)	1/98-8/98, 3/2000	CERES and GEOS
		Terra: SRBAVG Geo (Ed2D_Rev1)	3/2000-10/2005	CERES and GEOS
	FORTH	ESRB	1/1984-12/2004	ISCCP D2 and TOVS
	GEWEX SRB	GSW 2.0 and 2.81; GLW 2.1 and 2.5	7/1983-6/2005 (v2, 2.1 end 12/95)	ISCCP DX and GEOS
		QCSW 2.5; QCLW 2.0 and 2.5	7/1983-6/2005 (v2, 2.1 end 12/95)	ISCCP DX and GEOS
	ISCCP (GISS)	FD	7/1983-12/2004	ISCCP D1 and TOVS
	U.Md. SRB	v3.1 and v3.3	7/1983-12/2004	ISCCP D1 and TOVS; SW all-sky only
Model/Re-anal TOA	ECMWF	ERA-40	07/1983-08/2002	Reanalysis; Clear-sky fluxes limited LW and SW net
	GFDL	GFDLCM2.1 v. 1	1/1983-12/2003	Climate Model
	NOAA NCEP	NCEP-DOE R2	7/1983-6/2006	Reanalysis; All-sky only
	IPCC	AR4 Median, Mean and Standard Dev	01/1980-12/1999	Various climate models

In order to provide a surface standard, measurements from well calibrated networks of surface radiation are included in this assessment. Measurement networks and resulting time averaged fluxes included in this assessment are given in *Table 1.4*. Monthly averages from all the networks and measurement sites are provided as available for this assessment. Monthly average diurnal cycles are also provided for all BSRN sites. Additionally, 15 minute averaged

data is provided for all BSRN, ARM and ASRB sites for the year 2004 to enable more detailed analysis. Finally, derived flux products are available for an independent estimate all-sky and clear-sky radiative fluxes over the surface sites.

Table 1.4: *The surface radiation network measurements and derived flux products submitted to the GEWEX-RFA archive by participants.*

Type of Flux Product	Name of Research Group or Project	Name of Radiative Flux Products or Measurement	Dates Spanned	Data Set Notes
Surface Measurement	MeteoSwiss	Alpine Surface Radiation Budget network	1/1/04-12/31/04	5 sites in Alps; 15 minute data
	CERES	BSRN, ARM, Buoy	1/1/04-12/31/04	Various sites; 15 minute data
	NOAA CMDL	BSRN	As available (15-minute only for 2004)	Various sites; 15 minute, monthly diurnal and monthly
	Univ. of Oregon	UOSRML v.1	As available	3 sites
	ETH Zurich	GEBA	As available	Monthly only
Derived Flux Products	PNNL	From BSRN and ARM measurement sites	As available (15-minute only for 2004)	Various sites; 15 minute, monthly diurnal and monthly

More details on each data set and on ancillary data as well are described in the Appendices A, B, and C. A shortened version of Appendix A, describing very briefly the various data sets of this assessment, is added to the print version of this report. The most recent results from various data assimilation projects (e.g. MERRA; Saha et al., 2010), could not be included into this assessment. Additionally, new versions of TOA and Surface flux data sets have been released during the course of the compilation of this report. Some of the teams have written appendix sections describing these products and comparing these to data sets in the archive. These new data sets should be evaluated as part of a separate study or a future assessment.

1.3: Initial workshops towards assessment

Workshop 1: Initial meeting was held at the ETH in Zürich, Switzerland, from 4 to 6 October 2004.

Workshop 2: Interim results were reviewed from 22 to 24 February 2006 in Williamsburg (VA)

Workshop 3: Continued the review of results and organized report outline in a meeting from 25 to 27 June 2007 in New York (NY).

Author Workshop: In December 2010, a chapter author workshop was held to further collect results and review report structure

1.4: Report Overview

The history of space-borne radiation budget measurements covers now a period from 1959 (Explorer VII) to now. Since about 1967 the early non-scanning instruments have been complemented by scanning radiometers with increasing complexity and quality. This history is summarized in *Figure 1.1*, which also shows that the derivation of longer time series of radiation budget values must be based on measurements with different instruments. There is a gap of about 13 years between measurements of scanners of the ERBE and CERES families, which can only be bridged by the results of ISCCP and SRB and/or the non-scanner measurements despite their various sampling differences. Several basic problems are encountered in computations of the radiative energy fluxes within the climate system using relevant satellite measurements as basic input. These are related to the measurements themselves, to the techniques for analyses of measurements with instruments of different design and to all required **input** or **ancillary** data. All of them are potential sources for uncertainties of the final results as also the characteristics of the different instruments onboard of satellites with different orbital pattern.

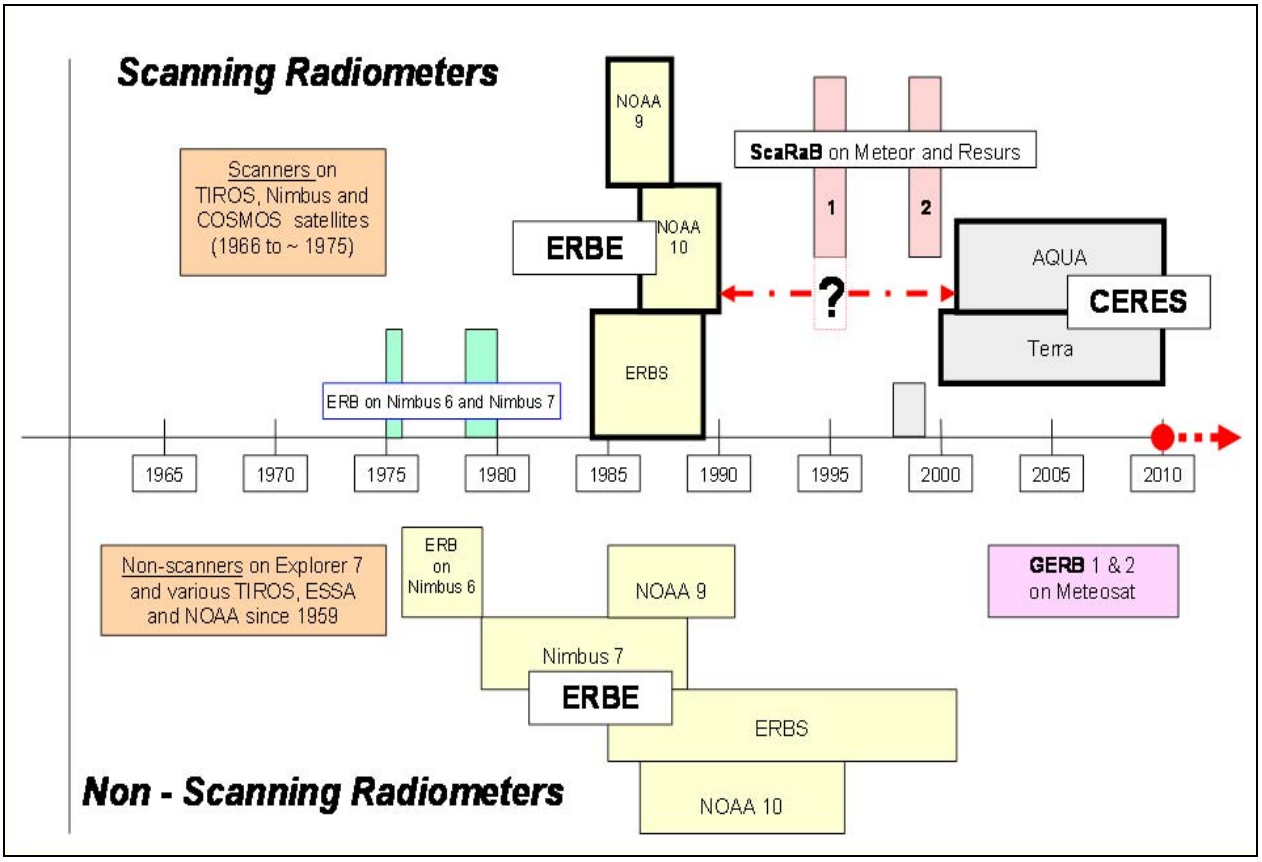

Figure 1.1: Scanning (top) and non-scanning (bottom) radiometers for radiation budget, *flown onboard various satellites. The position and horizontal extent of each colored box coincides approximately with the period of operation. A gap between scanner measurements from 1990 to 2000 could only be bridged over by non-scanner data of the ERBE or by the computed radiation products of the projects ISCCP and SRB.*

This report highlights the following issues:

(1) The Sun's electromagnetic radiation is the only energy source for processes within our climate system. Different instruments for measurements of the **solar radiation incident at the TOA** provide different answers. In ***Chapter 2*** the recent results of the SORCE mission (Kopp & Lean, 2010) are reported which explain the different levels of measurements to be corrected by corresponding calibration procedures. Furthermore, the computation of its distribution over the entire illuminated disc is reported with quite different representations of the geometry and time variations over Earths orbit.

(2) ***Chapters 3 and 4*** concentrate on the radiation fluxes and the estimated cloud radiative effects at the top of the atmosphere (TOA) and at the ground. Various **"ancillary" data** describing the radiative properties of the atmosphere and the Earth's surface are required to analyze the satellite based broadband measurements and to compute the radiative energy fluxes at the TOA (e.g. Smith et al., 1986) within the atmosphere and at ground. ***(Notify: The radiation within the atmosphere and at ground cannot be measured from satellites.)*** Some of these datasets and also from other narrow-band instruments enter into the derivation of clouds, which are the most important modifiers of radiation fluxes. The present accuracy and temporal stability does not suffice for monitoring long-term changes but are still useful for process studies and investigations of shorter-term variations.

(4) The results require careful validation and control against data from other sources. The products computed from the observed properties of the atmosphere and surface can be compared to more direct inferences of TOA fluxes from satellites, such as those from ERBE and CERES. Of the fluxes at ground direct measurements are now available from specifically designed worldwide networks ***(Chapter 5)***, such as the BSRN (Ohmura et al., 1998), and other national and international networks and data archives. ***Chapter 6*** concentrates on various problems which need to be solved when comparing the various radiation fluxes, which are computed for spatial scales of about 250X250 km^2 with single point measurements.

(5) Computations of the vertical divergence of the shortwave and longwave radiation within the atmosphere are described in ***Chapter 7***. They allow for estimates of the solar "heating" and longwave "cooling" of the atmosphere and the influence of the clouds fields on these processes.

(6) In ***Chapter 8*** are summarized statistical studies of the sensitivity of the fluxes at TOA and at the surface with respect to possible errors in input data.

(7) A very important problem concerns the reproduction of the various computed radiative energy transports in present-days climate models. In ***Chapter 9*** are discussed several comparisons for the climate models participating in the 4^{th} assessment of IPCC. Here are made also direct comparisons of model results with ground-based network results.

(8) **Appendix A** provides short descriptions of the data sets and their origin.

Chapter 2:

Incoming Solar Radiation

G. Kopp & E. Raschke

Abstract:
Chapter 2 provides an overview of solar irradiances, the dominant energy input driving Earth's climate. The uninterrupted 33-year long total solar irradiance (TSI) record from space-borne instruments requires sufficient stability for climate-quality studies, helping determine the global and regional sensitivities of Earth's climate to solar variability. New instrument calibration capabilities have helped explain the offsets between on-orbit TSI measurements and are improving instrument absolute accuracies, favoring a TSI value of 1360.8 $W\,m^{-2}$ at solar minimum. Space-borne spectral solar irradiances currently demonstrate stability only over shorter (solar rotation to year-long) time scales, providing insights into the spectral response of the Earth's atmosphere to solar fluctuations. Empirical proxy models help extend the solar irradiance measurement records back in time for historical climate comparisons, while physics-based solar models help explain the causes of irradiance fluctuations. Discrepancies between solar insolation computations, which are based on TSI measurements and provide direct inputs for Earth climate studies, are large for different regions of the Earth and are often comparable to the solar variability itself, indicating computational consistency improvements are critically needed.

2.1: Solar Irradiance Measurements

The main driver of Earth's climate, providing 2500 times the amount of energy of all other input sources combined (update of table in Sellers, 1965), is the Sun. Fortunately the Sun's energy input to the Earth is fairly stable, but even small fluctuations in this energy can affect global and regional climate (Lean and Rind 2008, Gray *et al.* 2010). Solar variability and other natural influences have historically been the Earth's primary climate drivers. Even today, when these natural influences are overshadowed by human-caused climate forcings, in order to understand climate and set appropriate regulatory policies, determining the contributions to climate change attributable to solar influences remains a key international priority and requires accurate records of solar radiation incident on the Earth (IPCC 2007).

2.1.1: Total Solar Irradiances

Both the total solar irradiance (TSI) and its spectral distribution are measured from space, as small solar fluctuations cannot be accurately measured through the Earth's highly variable atmosphere over climate-relevant time scales. The TSI is the spatially- and spectrally-integrated radiant solar energy at 1 Astronomical Unit (1-AU) from the Sun, providing a measure of the incident energy at the top of the Earth's atmosphere (TOA, usually defined as a spherical shell around the Earth about 50 km above the surface) and thus of the dominant driver of the Earth's climate system. The TSI determines the incoming portion of the Earth's radiative energy balance (described by Trenberth and Fasullo, 2010).

The 34-year space-borne record of TSI measurements is shown in **Error! Reference source not found.** and covers nearly three solar cycles. Overlap between successive TSI instruments enables corrections for measurement offsets, which are due to instrument calibration

differences, and allows the creation of a TSI composite spanning the duration of the measurements, as shown in **Error! Reference source not found.**.

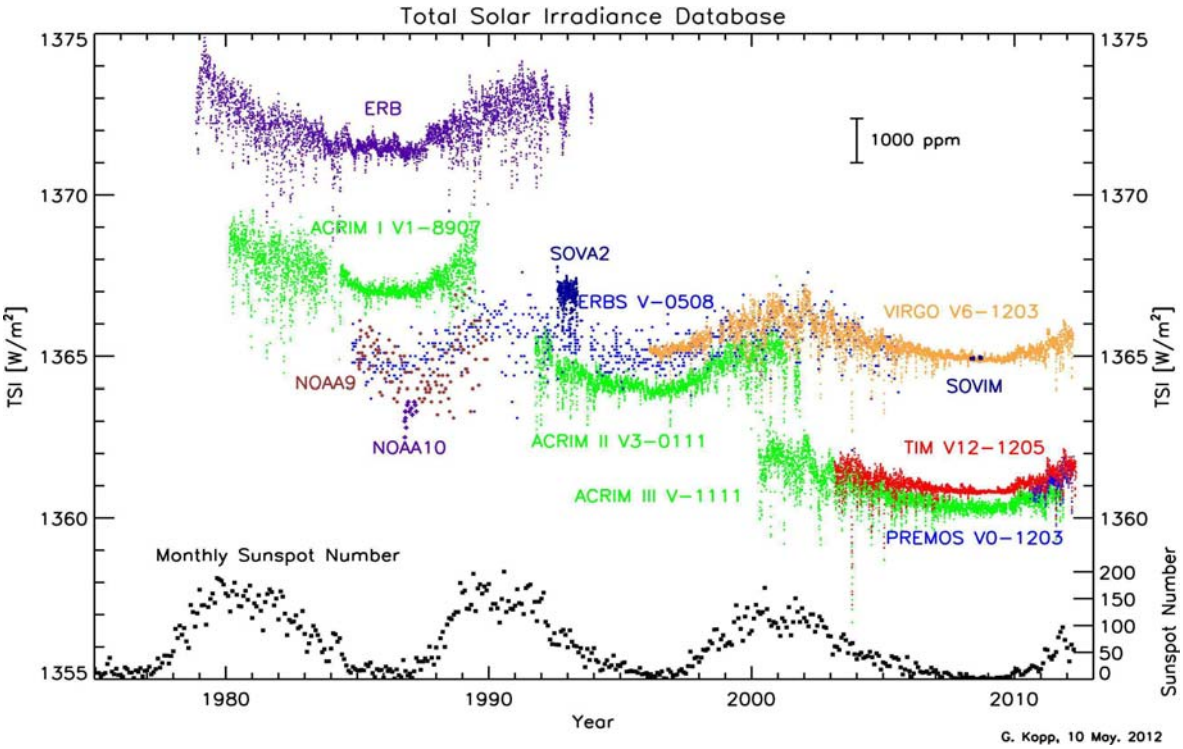

Figure 2.1: *The space-borne TSI record began in 1978 with successive instruments overlapping, which helps correct for the sizeable measurement offsets due to instrument calibration differences. These offsets have required continuity in measurements, as absolute accuracy at the needed levels has not yet been demonstrated by any flight instrument.*

The TSI increases markedly during times of greater overall solar activity, indicated in the figures by higher monthly sunspot numbers. **Error! Reference source not found.** shows that the amplitude of the 11-year solar cycle amounts to a change of about 0.12% (or 1.6 W m-^{2}) in TSI between recent solar minima and maxima values. Larger short-term deviations of ~0.3% due to the growth and decay of active regions and their rotation across the solar disk occur with periods as short as a few days. Solar variability estimates over durations longer than the satellite data record – and highly relevant for long-term climate studies – rely on extensions via empirical models, which allow historical reconstructions of the TSI back thousands of years (Usoskin *et al.* 2003, Steinhilber *et al.* 2009). Even over the last 400 years, such reconstructions differ markedly (Wang *et al.* 2005, Shrijver *et al.* 2011, Tapping *et al.* 2007, Shapiro *et al.* 2011), leading to large changes in estimated climate sensitivity to solar forcing. Since all such historical reconstructions are underpinned by modern spacecraft TSI measurements, this measurement record's accuracy and stability are critical.

While solar variability can be monitored long-term despite large relative offsets between TSI instruments by having continuous and overlapping instrument coverage, measuring the absolute value of the TSI accurately is important for two reasons: 1) Mitigating a potential data gap to maintain continuity with the existing 33-year TSI climate record of **Error! Reference source not found.** will rely on instrument absolute accuracy to discriminate a possible change in solar irradiance from differences between the instruments spanning the gap; and 2) To assess the Earth's net radiation budget, the balance between incoming solar and reflected plus thermally-

emitted outgoing radiative energy, both incoming and outgoing fluxes need to be known, with any difference being accounted for by some Earth reservoir heat sink (Trenberth and Fasullo 2010, Loeb *et al.* 2009). Absolute accuracies of nearly 0.01% are needed (Ohring *et al.* 2007) but not yet demonstrated by any flight instrument.

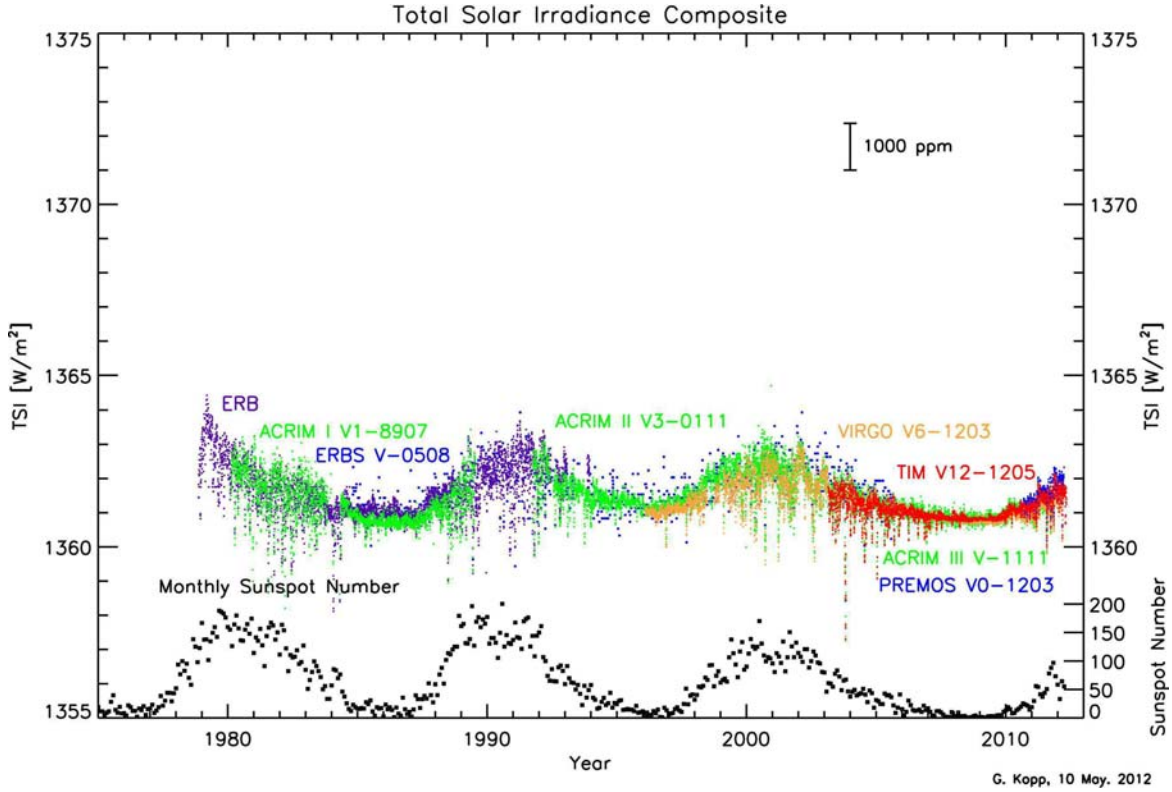

Figure 2.2: *This composite shows the spaceborne record of TSI measurements adjusted to the values from the SORCE/TIM, which established a new, lower TSI value with its improved instrument optical design. Note the increase in solar irradiance during times of higher solar activity, as indicated by the sunspot number (black), despite the short-term TSI decrease associated with these small, dark regions of the solar disk.*

Despite the seemingly large offsets in **Error! Reference source not found.**, these modern space-era measurements have higher accuracies than historical estimates, which are summarized in *Table 2.1*. Before the availability of high altitude aircraft, balloons, and rockets, these measurements were acquired from the ground using pyrheliometers and other actinometers, and attempts were made to correct for the large (~30%) atmospheric losses. These large corrections far exceed actual solar variations between measurements, which contribute only a small amount to the differences between tabulated values.

Measurements from the most modern TSI instrument, the Total Irradiance Monitor (TIM) (Kopp and Lawrence, 2005) on NASA's SOlar Radiation and Climate Experiment (SORCE) mission, indicate that the TSI level at the 2008 solar minimum is 1360.8 W m^{-2} (Kopp, Lawrence, and Rottman 2005; Kopp and Lean 2011). Measurements from earlier spaceborne instruments ranged between 1365 and 1372 W m^{-2}, with the variances likely attributable to unaccounted for scattered and diffracted light causing erroneously high readings, as suggested by Butler *et al.* (2008) and verified by Kopp and Lean (2011). The TIM is the first TSI instrument with an optical design placing the defining small primary aperture at the front of the instrument to reduce such unintended scatter, and it therefore provides the lowest and most accurate TSI values.

The new ground-based TSI Radiometer Facility (TRF) (Kopp *et al.* 2007) is improving the accuracy of future flight instruments and helping diagnose the causes of the existing instrument offsets shown in **Error! Reference source not found.**. The TRF is the world's first TSI calibration facility to directly compare instrument irradiance measurements to those of a reference NIST-calibrated cryogenic radiometer at full solar power levels under space-like vacuum conditions. Spatial patterning of the incident beam enables diagnostics such as determining internal instrument scatter.

Recent comparisons at this facility using ground-based representatives of flight TSI instruments indicate that scatter from the front surfaces or baffle sections of some TSI instruments causes erroneously high readings of the magnitude shown in ***Error! Reference source not found.*** (Kopp and Lean, 2011). To date, the flight Glory/TIM and PICARD/PREMOS instruments have been validated in this facility, along with ground-based versions of the SORCE/TIM, SoHO/VIRGO/PMO6, and ACRIMSat/ACRIM-3. Diagnostic tests in the TRF indicate high levels of scatter in all tested non-TIM radiometer designs. A recent update to the ACRIM-3 data includes these TRF corrections, reducing that instrument's reported measurements by 0.34% to the values shown in **Error! Reference source not found.**. Additionally, the PICARD/PREMOS instrument launched in 2010 is expected to have similar TSI values to the SORCE/TIM, although those data have not yet been released.

With the TSI community coming to consensus on this lower absolute TSI value, namely the 1360.8 W m^{-2} for the 2008 solar minimum reported by the TIM, the incoming radiation budget estimates based on satellite data since 1978 should be adjusted to this new value, as in **Error! Reference source not found.**, and climate models should be modified accordingly to use this value. Studies on the effects that this lower value has in global climate models are underway.

TABLE 2.1: HISTORICAL ABSOLUTE VALUES OF TSI

From the Earth's Surface	
French IPY Expedition to Tierra del Fuego (1883)	2.02 ly min-1 (1409 W m^{-2})
Smithsonian Institution mean for 1900-1950	1.96 ly min-1 (1367 W m^{-2})
Johnson (1954)	2.00 ly min-1 (1395 W m^{-2})
Various older textbooks (e.g.: Foitzik and Hinzpeter, 1958: Table 7.1 on page 173, and Table 7.4 on page 185) list earlier values determined e.g. by Angström (1890; 2017 W m-2), Langley (1884: 2051 Wm-2) and Pouillet (1837; 1230 Wm^{-2}).	
From Aircraft, Rockets, Satellites, or High Altitude Balloons	
Drummond et al. (1967)	1375 W m^{-2}
Murcray et al. (1969)	1364 W m^{-2}
Willson (1973)	1368 W m^{-2}
Thekaekara (1976)	1353 W m^{-2}
Kondratyev and Nikolskii (1980)	1373 W m^{-2}
Neckel and Labs (1981)	1368-1377 W m^{-2}
Willson et al. (1981)	1368 W m^{-2}
AB1 and WR1 during 1980 (Fröhlich, 2000)	1368 W m^{-2}
Hickey et al. (1982)	1373 W m^{-2}
Fröhlich (1983)	1367 W m^{-2}
Crommelynck et al. (1986)	1361.5 W m^{-2}
SMM (1978-1993)	1367.4 W m^{-2}
Fröhlich and Lean (1998)	1366.5 W m^{-2}
ERBS during1984-2000 (Fröhlich, 2006)	1365.3 W m^{-2}

2.1.2: Spectral Solar Irradiances

The solar irradiance is highly wavelength dependent with the spectral distribution shown in **Error! Reference source not found.**. This spectrum is nearly blackbody in character, giving a Sun-surface temperature of 5770 K indicated by the visible and near-infrared radiation emanating directly from the photospheric region. Higher regions in the solar atmosphere absorb this radiation in certain spectral regions, suppressing the continuum blackbody radiation in narrow spectral Fraunhofer lines indicative of the absorbing atoms or molecules. At shorter ultraviolet wavelengths, which emanate from higher regions of the solar atmosphere, the emissions are significantly higher than those from a 5770 K blackbody, indicative of the hotter temperatures at these higher atmospheric layers.

Similarly to being emitted from different layers in the solar atmosphere, these different spectral regions are absorbed by the Earth's atmosphere at different altitudes. The visible and near-infrared radiation transmits readily through the atmosphere to the Earth's surface, causing warming of the surface and troposphere. Ultraviolet wavelengths are absorbed by the atmosphere, causing heating and ionization at different altitudes in the stratosphere and thermosphere, as shown in **Error! Reference source not found.**.

Since solar irradiances and hence solar variability change greatly with wavelength, the effects of solar temporal fluctuations on the Earth's atmosphere, chemistry, and climate are very wavelength dependent (Gray *et al.* 2010, Woods and Lean 2010, Haigh *et al.* 2010, Merkel *et al.* 2011, Haigh 2004, Hood 2003), making spectral solar irradiance (SSI) measurements important in understanding the Earth's coupled climate responses to solar forcings.

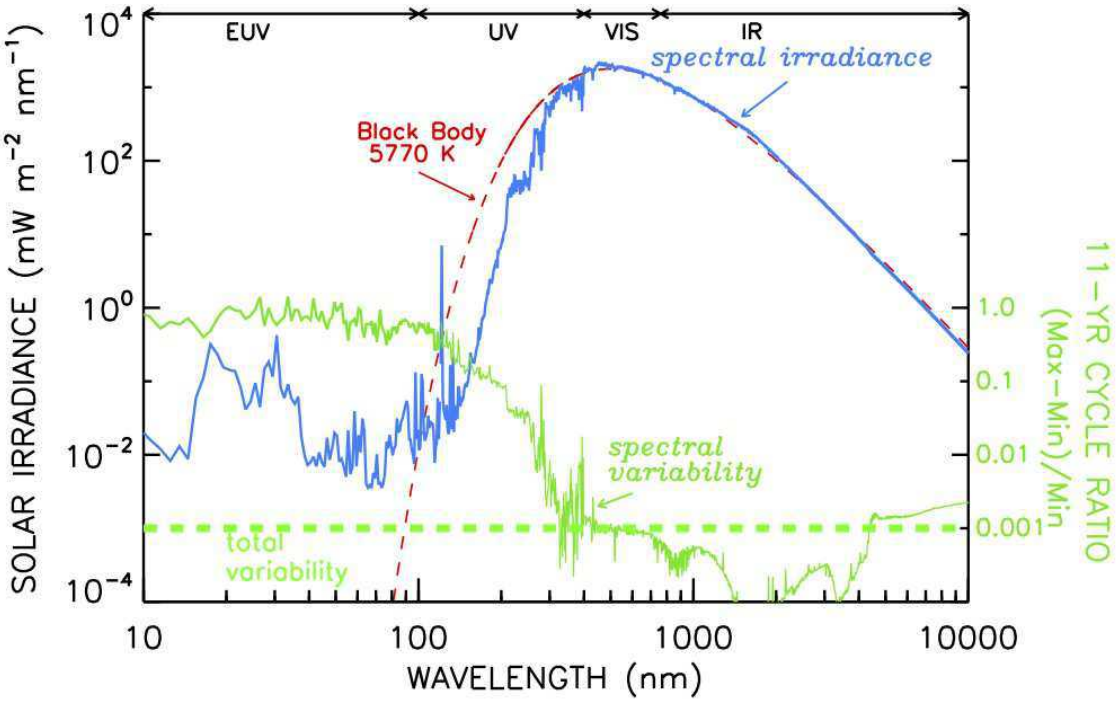

Figure 2.3: *Spectral solar irradiance measurements (blue) are characteristic of a 5770 K blackbody (red) in the visible and near-infrared spectral regions. These spectral irradiances and their variability (green) help determine the effects solar variability has on the Earth's atmosphere and climate, as absorption and scatter processes are wavelength dependent. (from Lean and Woods 2010, courtesy of J. Lean)*

Prior to recent spacecraft measurements, knowledge of the solar spectrum was derived from ground-based and airborne measurements with attempts to remove atmospheric absorption (e.g. Neckel and Labs, 1984; Thekaekara, 1976). Since the mid-1970's, various satellite instruments have provided more detailed information on the spectral distribution of solar radiation with improvements in absolute accuracies and relative stabilities, allowing measurements of solar spectral variability with time. Because of the smaller signals and the more complex instrumentation, SSI measurements are much less accurate and less stable than those of TSI, limiting long-term knowledge of solar variability. Recent measurements combining data from the TIMED (Woods *et al.*, 1998) and the SORCE (Rottman 2005) missions provide spectrally continuous coverage of the SSI from the ultraviolet into the near infrared (see **Error! Reference source not found.**), and are proving helpful for understanding atmospheric changes over the shorter time scales where these measurements have been acquired and where they remain stable.

Currently the SSI record in the visible and near-infrared, initiated in 2003 with the SORCE/SIM, has not demonstrated the needed long-term stability to definitively address variability on solar cycle and longer time scales. Harder *et al.* (2009) report SSI variations in the visible and near-infrared that are out-of-phase with the solar cycle, but it is unclear whether this result, which would predict climate results contrary to what is observed at the surface and troposphere, is due to real solar variations or uncorrected instrumental drifts. On shorter (solar rotation) time scales where the instrument is less susceptible to drifts, these SSI variations are more consistent with observed atmospheric responses (Haigh *et al.* 2010, Merkel *et al.* 2011).

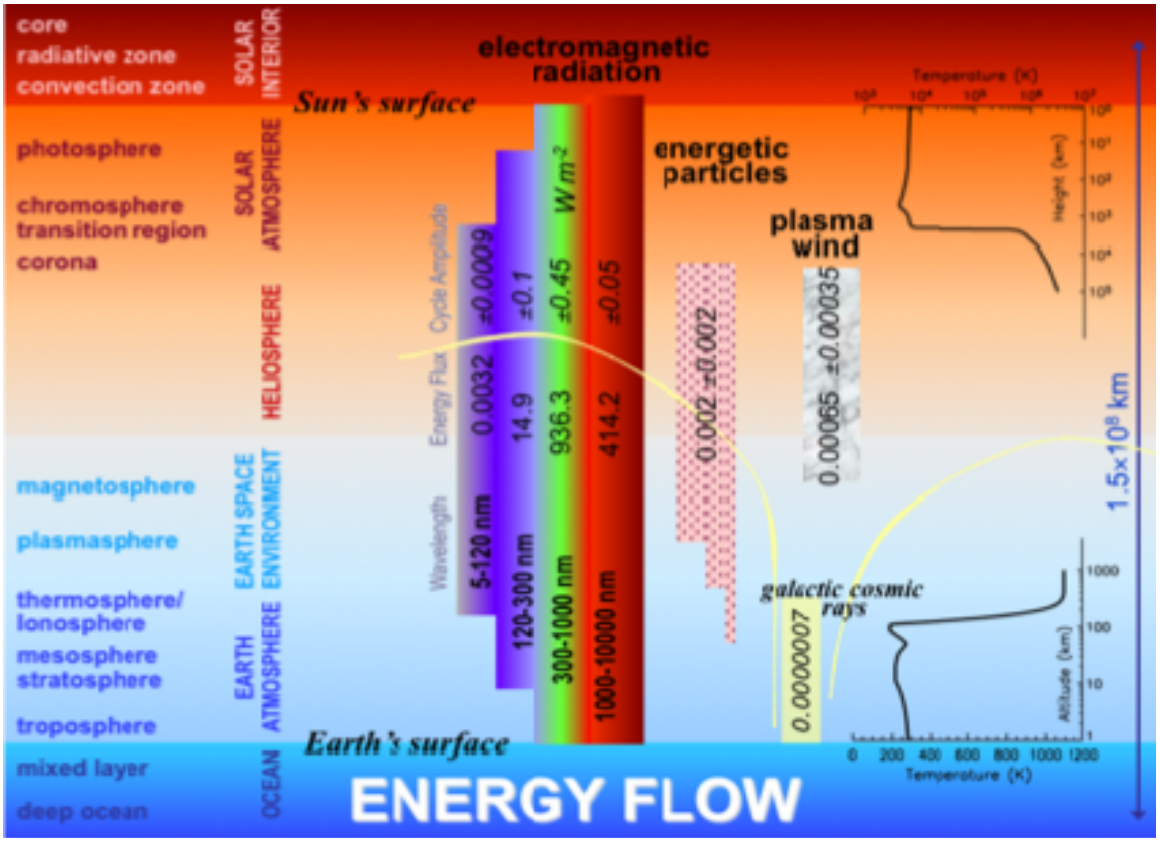

Figure 2.4: *Just as different spectral regions are emitted from different layers in the solar atmosphere, they are absorbed by different layers in the Earth's atmosphere, with shorter wavelengths emanating from higher solar regions and being absorbed by higher Earth atmospheric layers. (from Lean and Woods 2010)*

These relative short-term variations are shown in **Error! Reference source not found.** as a function of wavelength relative to TSI changes – that is, for a given relative fluctuation in TSI the spectral irradiance changes from its nominal value by the relative amount shown. For example, a typical change of 0.1% in TSI on average causes 1.5X this change at 400 nm, the same 0.1% change in the mid-visible, and slightly more than half this variation in the NIR. Note that the relative variability is greatest at the ultraviolet wavelengths, which more directly influence the Earth's upper atmosphere.

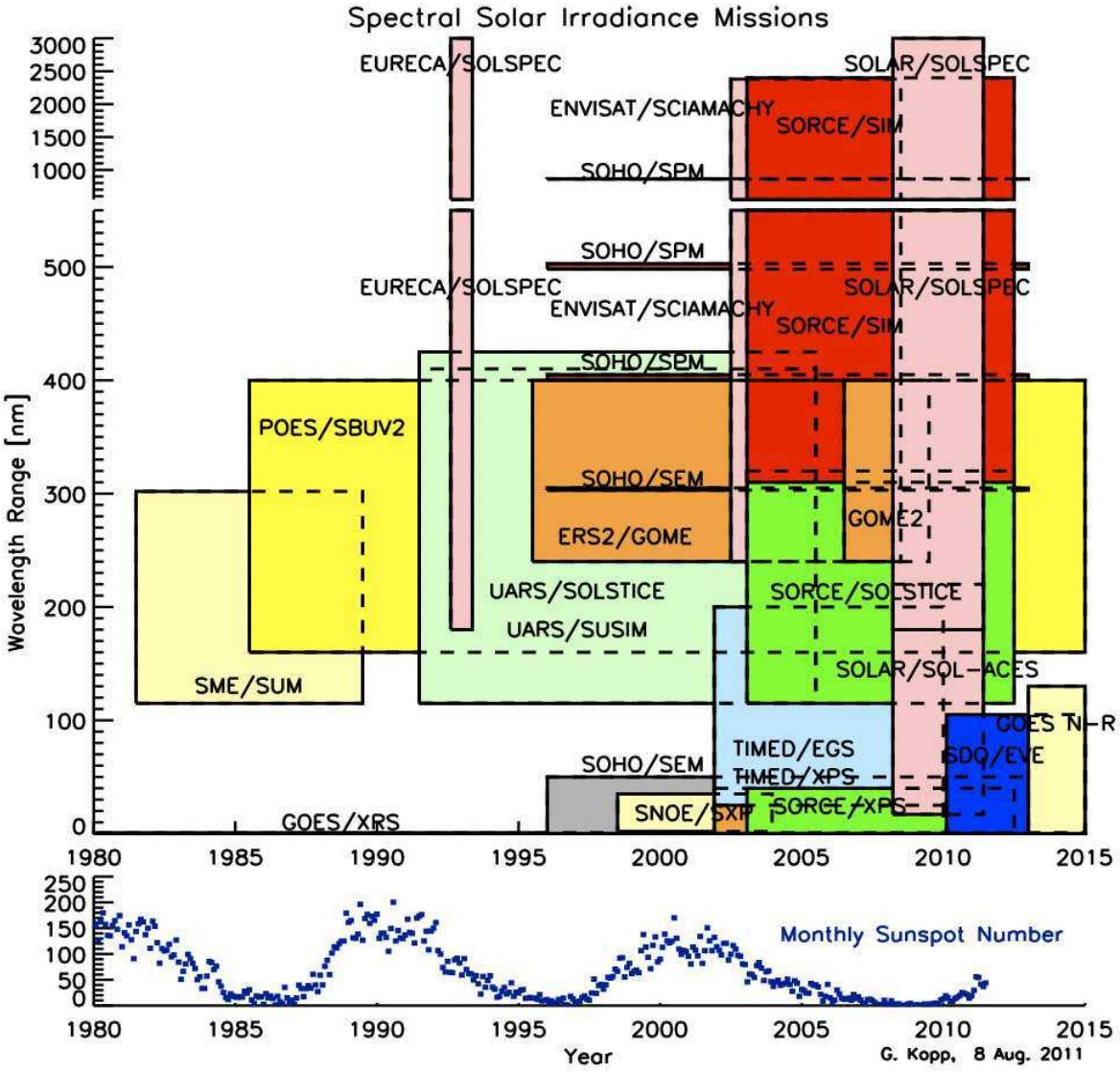

Figure 2.5: *Spectral solar irradiance (SSI) measurements are currently acquired with continuity from the ultraviolet to the near infrared. These measurements are important in understanding the response of the Earth's atmosphere and climate to solar variability.*

Even though the spectral irradiances are much lower in the ultraviolet spectral region, relative solar variations increase with decreasing wavelengths (see **Error! Reference source not found.** and **Error! Reference source not found.**). Although inherent ultraviolet instrumental stability is generally poorer than for visible and near-infrared instruments, the much larger relative solar variations in the UV are clearly apparent even over solar cycle time frames. The SOLSTICE instruments on NASA's UARS and SORCE missions employed a novel new technique to correct for on-orbit instrument degradation by monitoring several bright blue stars, the resulting ensemble average from which provides a relative reference against which instrumental degradation can be corrected (McClintock *et al.* 2005).

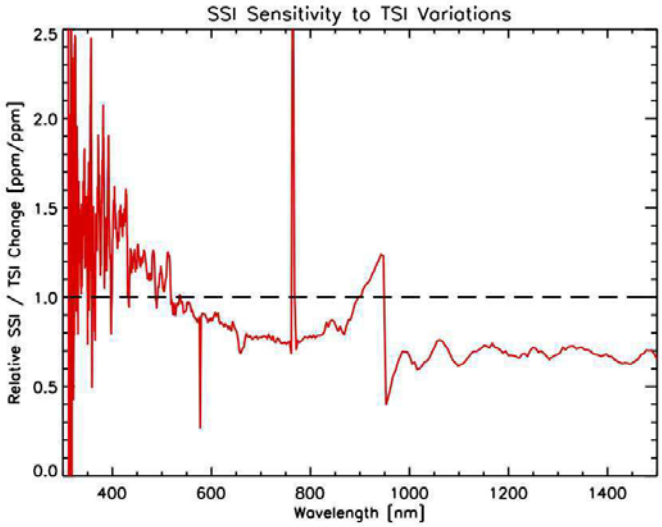

Figure 2.6: *SSI measurements show greater relative variability at shorter wavelengths based on solar activity over relatively short time periods of a few months. For a typical change in TSI of 0.1% over these short time scales, the SSI varies by ~0.07% in the near infrared, a similar 0.1% in the mid-visible, and ~0.15% in the near ultraviolet. Correlations between SSI and TSI are not unity, and the plotted sensitivities are derived from average SSI and TSI correlations. The spikes in the plot and the peak near 950 nm are due to uncorrected SSI instrument artifacts. (updated from Kopp et al., 2006)*

2.2: Solar Irradiance Models

Models estimating solar irradiances 1) extend the irradiance data records to times prior to spacecraft measurements, thus providing historical climate inputs, 2) help understand the solar causes of irradiance variations, and 3) help discern differences between solar-monitoring instruments. Such models are generally classified as either empirical proxy models or physics-based models.

Empirical proxy models are derived based on correlations between observed irradiances and some indicator, or proxy, of solar magnetic activity, with results summarized by Domingo *et al.* (2009). The sunspot record, the longest available real-time measurement indicative of solar variability, is the basis for many TSI proxy models. Correlations between TSI and sunspot number are readily apparent in **Error! Reference source not found.**, allowing solar irradiance estimates to be extended directly and indirectly to prior times using the 400-year long sunspot record, as explained by Fröhlich and Lean (2002). The 10-cm solar radio flux (F10.7) (Tapping *et al.* 2007) and Mg II provide proxies of solar faculae, albeit of more limited duration – the space-borne Mg II records only extend back to the time continuous TSI measurements began while F10.7 measurements date back to 1947 – so are useful for detailed short-term and multi-decadal

comparisons to solar irradiances, but do not match the sunspot record for the long-term historical reconstructions desired for Earth climate comparisons. Gray *et al.* (2010) give a very nice summary of these different TSI proxy-based reconstruction methods over the 400-year sunspot record (see **Error! Reference source not found.** for a reproduction of their Figure 7).

Cosmogenic isotopes allow extensions prior to the sunspot record, as the cosmic rays creating them are influenced by solar activity, particularly open magnetic fields, and thus long-term isotope records are indicative of extended historical solar variations. Most notable among these records are ^{10}Be and ^{14}C, obtained from polar ice core and tree ring samples respectively. Steinhilber *et al*. (2009) reconstruct the TSI assuming a strong relation between the TSI and the open solar magnetic field, estimated from the cosmogenic radionuclide ^{10}Be, to create a TSI time series covering the last 9500 years. It is from comparisons of such proxy-based models of solar activity to similarly created proxy-based models of Earth temperatures that both global and regional climate sensitivities to solar forcing are estimated (Lean & Rind, 2008).

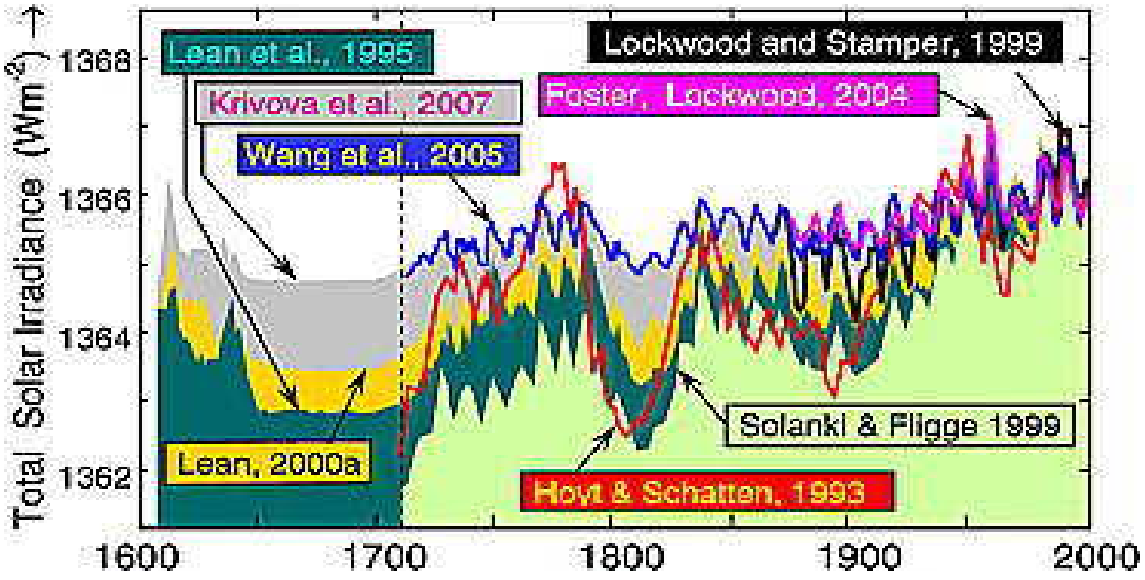

Figure 2.7: *(Figure from review by Gray et al. 2010) Historical TSI values can be estimated prior to the spacecraft era measurements using various solar proxies, such as solar cycle length (Hoyt and Schatten, 1993), annual sunspot number (Solanki & Fligge, 1999), sunspot cycle comparisons with Sun-like stars (Lean et al, 1995 and 2000), open magnetic flux (Lockwood and Stamper, 1999; Wang et al., 2005), sunspot observations (Foster, 2004; Lockwood, 2004), and group sunspot number (Krivova et al., 2007).*

Image-based empirical proxy models help identify the solar features responsible for irradiance variations. The simplest are two-component models that determine areal extent of the solar disk filled with sunspots or faculae and then correlate these with TSI variations (Fröhlich and Lean, 1997; Krivova *et al*., 2003). These authors show that while sunspots cause short-term decreases in TSI, associated faculae cause a longer duration overall increase in solar irradiance (see **Error! Reference source not found.**), explaining why the TSI is greater at times of higher sunspot number in **Error! Reference source not found.**. These two activity types explain the majority (80-90%) of the short-term TSI variations, but cannot indicate possible secular trends suggested by the sunspot record and cosmogenic isotopes.

Physics-based models, such as that by Fontenla *et al.* (1999), compute spectral irradiances based on radiative transfer in model solar atmospheres for each of several types of solar activity.

Using refinements based on current TSI and SSI measurements, these models not only reproduce relative solar irradiance variations using active regions identified from space- or ground-based images of the Sun, but also improve knowledge of the solar atmosphere and the emitted radiation causing these irradiance changes. Dedicated flight instruments, such as the Solar Bolometric Imager (Foukal and Bernasconi, 2008), show possibilities of directly measuring solar irradiance fluctuations as a function of position on the Sun and improving irradiance models by spatially identifying the sources contributing to TSI variations.

Empirical proxy models of solar irradiances provide millennia-scale historical reconstructions needed for comparisons with Earth climate and estimates of sensitivity to solar forcing, with image-based models successful at the 80-90% level for estimating short-term TSI fluctuations and identifying their solar causes. Physics-based models help understand the solar causes of irradiance variations, but are more limited in addressing potential secular fluctuations influencing climate on long time scales. Both model types offer benefits extending the space-based solar irradiance record to times when no measurements were available.

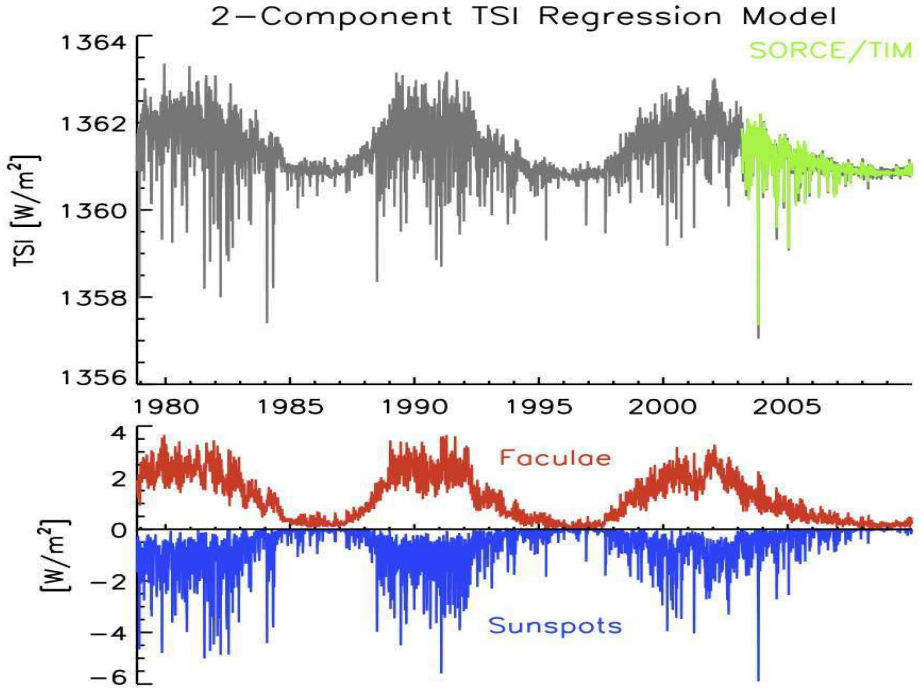

Figure 2.8: *This 2-component empirical model (top plot, grey) is based on regressions of sunspot darkening and facular brightening (bottom plot) to TSI measurements (top plot, green) and then extended to times preceding the actual measurements via the derived proxy model. (Data and model courtesy of J. Lean, 2010.)*

While these models work well over short time periods, they predict very different results over multi-century time scales depending on their relation to sunspot number. Hoyt and Schatten (1993) give estimates of the late 1600's Maunder Minimum TSI values that are 0.14% to 0.35% lower than present solar minima based on duration and mean activity level of solar cycles (interpreted from the observed sunspot number) and sunspot decay rate. This range is consistent with Lean (2000), who analyzes activity of Sun-like stars to suggest that the Sun was lower in TSI by 0.2% during the Maunder Minimum. Wang *et al.* (2005), however, model open vs. closed solar magnetic flux to estimate lower Maunder Minimum values of only 0.07%. More recently, Schrijver *et al.* (2011) argue that the Sun reaches a minimum magnetic activity level that is

underestimated by sunspot number alone, and that the Maunder Minimum TSI value was similar to that observed during the recent 2008-2009 solar minimum, or a mere 0.014% to 0.036% lower than typical minima. Contrary to this trend toward little change in TSI between the Maunder Minimum and the present Sun, Shapiro *et al.* (2011) give a value that is 0.44% lower than at present based on neutron monitor data and cosmogenic isotope proxies. Because of these large discrepancies when modeling long time scale variations, the major benefits currently from TSI models are in identifying the solar activity causes of irradiance fluctuations and in identifying differences between instrument measurements.

2.3: Computations of Solar Insolation at TOA

Being largely geometry-based calculations, computed estimates of solar insolation, the solar radiant energy incident on a specified surface, apply equally to total and spectral irradiances. These estimates provide necessary regional (primarily latitude- and altitude-dependent) solar forcing inputs for climate models throughout the year.

The globally- and temporally-averaged value of the TOA solar insolation is exactly one fourth of the (1-AU) TSI itself, this being the ratio of the Earth's cross sectional area to surface area. The annual global average of the insolation is thus 340.25 Wm^{-2} from a nominal TSI value of 1361 Wm^{-2}

Regional computations of TOA insolation must take into account Earth orbital effects, such as eccentricity, perihelion, and obliquity, as well as additional regional physical effects. Orbital quantities can be obtained from the Astronomical Almanac, which uses JPL ephemeris DE405 starting in 2003 and is based on the VSOP87 ephemeris (Bretagnon and Francou 1988), or from the fundamental work by A. Berger *et al.* (1978). The annual variation of the globally averaged insolation is largely determined by the Earth's orbital eccentricity, which causes insolation variations of ±3.3%. Extreme geographical latitudes where the Sun illuminates areas at high incidence angles may be affected by refraction through the Earth's atmosphere. Applications in stratospheric and mesospheric research may need to consider the spherical structure of atmospheric layers, which can be illuminated by scattered light from below near the terminator.

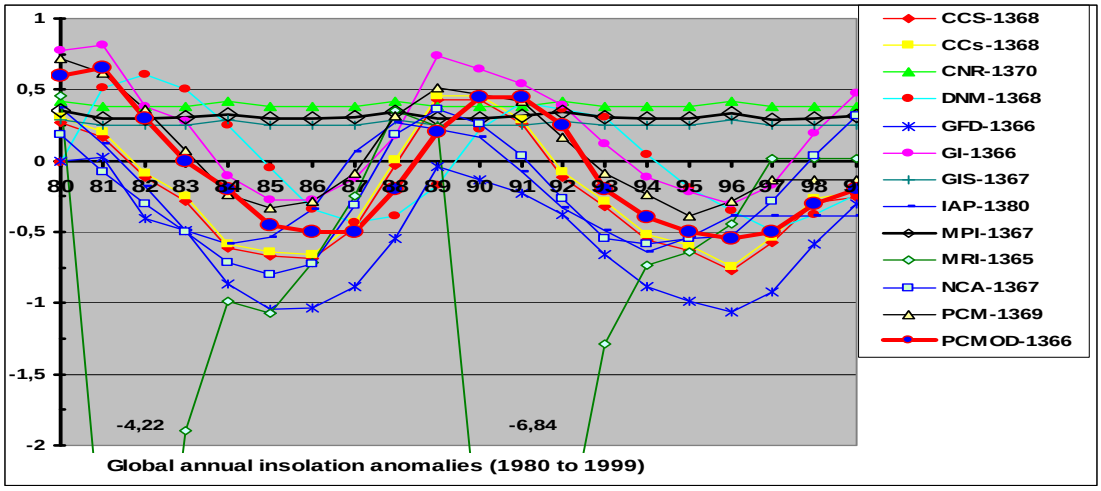

Figure 2.9: *This inter-comparison of computed insolation (in Wm^2) from several models shows large variations due to different TSI values, Sun-Earth distances, and solar variability.*

Climate modelers have inter-compared the input solar insolation used in their models for specified time periods to determine the models' sensitivities to insolation differences (see **Error! Reference source not found.**). Two such comparisons were performed for the Atmospheric Model Intercomparison Project (AMIP II; Gates *et al*., 1999) and the IPCC 4th Assessment Report (IPCC 2007). These inter-comparisons indicated that the insolation models did not follow the input requirements given by Raschke, *et al.* (2005), using different values for TSI and modeling the phase of the 11-year solar cycle differently. Since climate models and analyses often rely on calculated insolation estimates rather than direct data, it is very important to eliminate such computational errors.

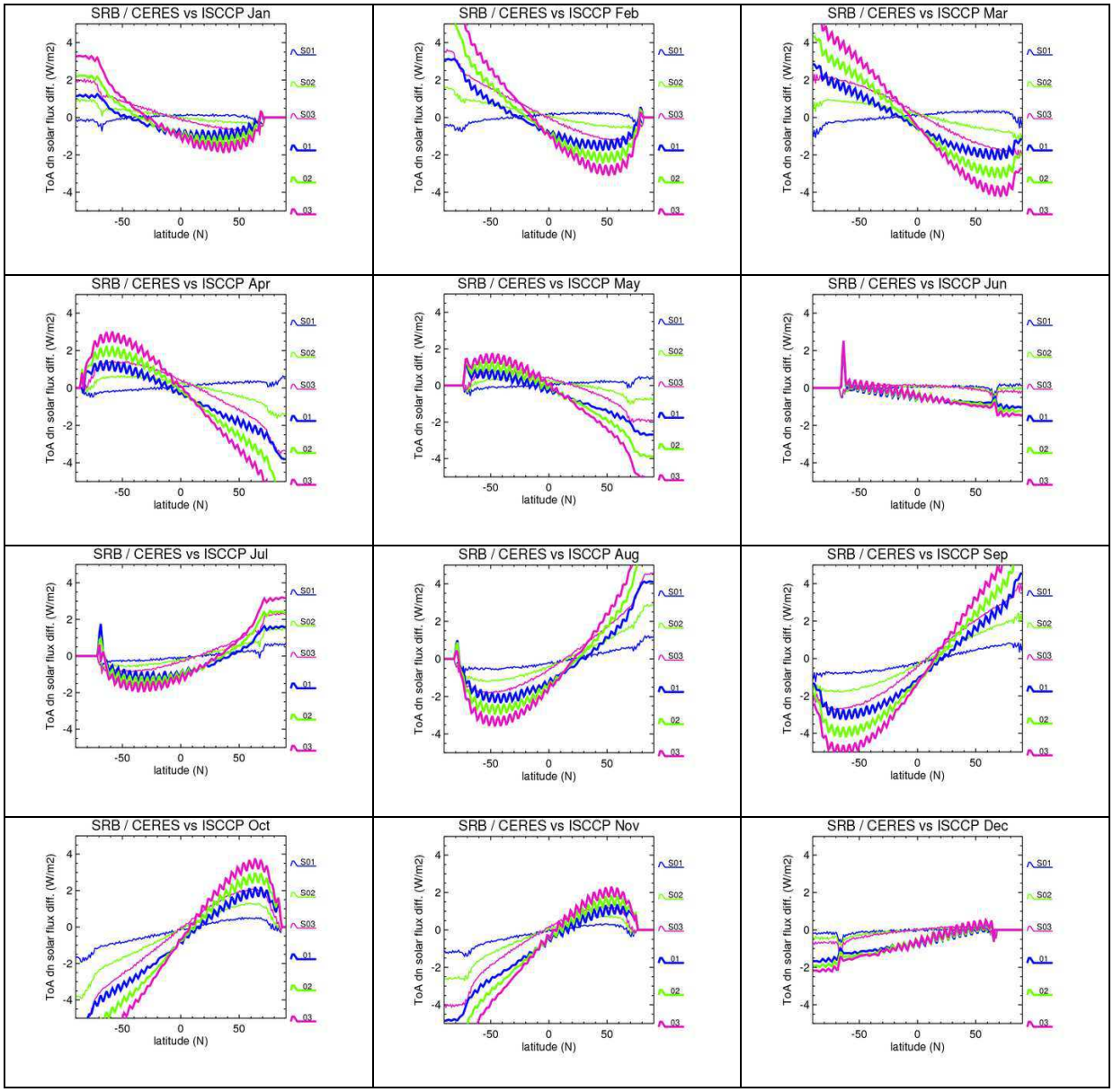

Figure 2.10: *Monthly averages of the differences to ISCCP values for zonal averages of the insolation are computed for the SRB climatology (thinner lines) and the CERES climatology (thicker lines). These differences vary with radial velocity of the Earth's orbit, indicating non-physical errors. Curves for the years 2001, 2002, and 2003 are in red, green, and blue, respectively.*

Computational methods can also affect accuracies. Algorithm implementation, such as integration step widths in space and time, can cause computed insolation differences even for identical input TSI values. Discrepancies between computations of the insolation at the TOA due to different handling of the extra day during leap years can exceed 0.2 Wm^2. Y. Tsushima *et al.* (2008, IRS-2008) find similar discrepancies when the day of the vernal equinox is changed from 21 March to 20 March, and show that such seemingly small changes cause significant fluctuations particularly over the polar and sub-polar regions. Giorgetta *et al.* (private communication, 2007) demonstrated with a simplified version of their GCM ECHAM-5 that small changes of the daylight length can perturb atmospheric circulation.

Meridional profiles for different insolation computations show non-physical effects, such as being highly correlated with the radial velocity of the Earth on its orbit and having a systematic trend between poles; such computational errors cause a dramatic change of computed seasonal meridional gradients, which seem to be related here to basic computational principles and required input astronomical information. **Error! Reference source not found.** shows example differences in computed meridional profiles of the insolation at TOA between the CERES and SRB data sets and those of ISCCP. [Documented in detail on the ISCCP website http://isccp.gis.nasa.gov (see also Rossow and Duenas, 2001), the selection of ISCCP as the reference for this comparative purpose does not imply that these results are more accurate than the other two.] These curves in **Error! Reference source not found.** indicate that differences in the regional insolation at TOA might be as high as 3 to 10 Wm^{-2} depending on the season. In a separate study, Loeb *et al*. (2009) have shown that additional uncertainties of less than ±0.5 Wm^{-2} (global average) may be due to the non-spherical shape of the Earth.

2.4: Conclusions and Recommendations

The total solar irradiance, the dominant driver of Earth's climate, has now been acquired from spacecraft instruments for nearly three solar cycles with uninterrupted measurements providing a means of correcting for offsets due to calibration differences between instruments. Recent ground-based tests using a new calibration facility have identified the likely cause of the offsets in the space-based measurements, and favor a TSI value at solar minimum of 1360.8 $W\ m^{-2}$. Spectral solar irradiance measurements have commenced with coverage from the ultraviolet to the near infrared, and are useful for atmospheric studies over short time scales but require improved measurement stabilities for long-term climate studies. Empirical proxy models help extend these solar irradiance records back in time to enable historical comparisons with global and regional temperatures from which Earth's climate sensitivity to solar forcing is estimated, while physics-based solar models help understand the causes of solar variability.

The extended TSI climate data record and the newer SSI record are being incorporated into climate models, where they provide input radiative forcings to the Earth's surface and atmosphere. Measurement uncertainties have improved such that they are now comparable to previously minor differences between insolation computation methods used by climate models, necessitating improvements in these insolation computations.

Chapter 3:

Radiative Fluxes at the Top-of-the-Atmosphere (TOA)

T. Wong and W. B. Rossow, Y. C. Zhang, L. Hinkelman, E. Raschke, S. Kinne,
J. Russell, R. Bantges, R. Roca, G. L. Smith, N. Loeb

Abstract: *(T. Wong)*

Comparisons of TOA radiative fluxes were carried out to examine the level of consistency among different radiation budget datasets submitted to the GEWEX RFA archive. In general, we found that the longwave data agree better than those of the shortwave and the net radiation. Some disagreements can be traced directly to deficiencies in the ancillary input data that were used to generate these radiation data. Reprocessing of these ancillary input data is needed to improve the quality of these radiation budget data. Geostationary satellite artifacts are also common in datasets that used ISSCP cloud products (i.e., ISCCP-FD and GEWEX SRB). Better physical treatments and time-space sampling method are needed to remove these geostationary artifacts. While most of the regional statistics between the old ERBE scanner data from the 1980s are similar to those of the new CERES scanner data from the 2000s, systematic differences remain. These systematic disagreements are caused by differences in absolute calibration, climatological period, and data processing algorithms. Overlapping satellite data, such as those from the ERBS nonscanner longwave dataset, are critical to tie these datasets together for long term climate study. Geostationary broadband radiation budget data shows great promise in understanding diurnal cycle of radiation. However, further studies are needed to improve radiance to flux conversion. We also recommend detailed data uncertainty analysis similar to those provided by the ERBE and CERES project, to be part of the data release for all future datasets. This will provide a scientific framework to understand the differences among radiation budget datasets.

3.1: Introduction (T. Wong)

There is a long history of satellite radiation budget measurements dating back to the 1960s. Over this long period of time, many methods for generating TOA radiation budget data set have been put forward and tested. Today, there are two major approaches for deriving radiation budget quantities from satellite measurements. The first approach is to derive the spatial and temporal distribution of TOA radiation budget using measurements of broadband radiance and/or hemispheric flux at satellite altitude. This is the approach used by the Nimbus-7, ERBE, ScaRaB, and CERES project. The broadband measurements from these projects are also highly stable due to their on-board calibration sources. The second approach is to use cloud, temperature, and moisture retrieved from narrowband satellite instruments or generated from atmospheric reanalysis model as inputs to broadband radiative transfer model to calculate the broadband radiation field at TOA. The broadband radiation calculations can be applied at either the footprint or the grid-box level. This second approach is used by ISCCP-FD, GEWEX SRB and FORTH project. Because the narrowband visible sensors don't have on-board calibration sources, the stability of the datasets from this approach may not be quite as good as the former. In addition, a hybrid approach may be used in some datasets which combines these two approaches to obtain TOA fluxes. There are numbers of steps one must take to move from instantaneous sensor

voltages, to instantaneous calibrated measurement, to spatially gridded observations, and finally to monthly mean fields. Ancillary data are required in these processes for both approaches.

In this chapter, we will take a closer look at our current understanding of TOA radiative fluxes by comparing datasets that have been submitted to the GEWEX-RFA archive. Detailed description of each of the TOA radiation budget datasets in the RFA archive is given in Appendix A along with the name of the data provider. The results from this chapter are provided by various GEWEX-RFA contributors who have volunteered to examine specific aspects of the GEWEX-RFA datasets. Section 3.2 examines the similarities and differences of the two standard data products; namely the ERBE multi-satellite product and the CERES/Terra SRBAVG GEO product. Section 3.3 and 3.4 show comparisons of TOA radiative fluxes from the GEWEX-RFA archives for the two classic baseline periods: the ERBE period from February 1985 to January 1989 and the CERES period from March 2000 to February 2004. This is followed in section 3.5 with a closer look at the comparison of the anomalies in ISCCP-FD, GEWEX-SRB with the ERBE and CERES baseline datasets. Section 3.6 examines the monthly mean differences found between the high-temporal GERB dataset and the standard CERES/Terra SRBAVG GEO product. Section 3.7 highlights historical comparison results for the ScaRaB project. Section 3.8 gives a literature research of the works in diurnal cycle of radiation budget. Section 3.9 gives results for the required meridional energy transports. The uncertainty of the ERBE and CERES data is discussed in Section 3.10. A summary and recommendations are given in Section 3.11.

3.2: ERBE and CERES TOA Flux Comparison (W. B. Rossow and Y. C. Zhang)

3.2.1: Introduction

This section will look closer at the ERBE scanner (2/1985 to 1/1989; global combined ERBS-NOAA9-NOAA10 product) and the CERES SRBAVG GEO (1/2001 to 12/2004; global Terra product) TOA radiation budget dataset that are in the GEWEX-RFA archive. The scientific goal of the ERBE project is to provide a better understanding of global Earth radiation budget (Barkstrom 1984). CERES project expands this scientific goal to include understanding of cloud and cloud radiative effect (Wielicki et al. 1995). While Nimbus 7 was the first project to provide stable long-term multi-year broadband earth radiation budget data using traceable on-board calibration sources, CERES provides further enhancement to the ERBE project using improved instruments and scientific algorithms. CERES data are available starting in March 2000 with a large data gap between ERBE scanner and CERES. These two stable broadband datasets have been well documented in the literature and provide a good starting point for the GEWEX-RFA project. Given the fact that there are real differences in absolute calibration, data algorithm, input data source, and background climatology (i.e., 1980s vs. 2000s) between these two datasets, it is beyond the scope of this section to trace down the specific causes of their disagreements. Rather, this section will document the similarities and differences between these two broadband datasets.

3.2.2: Climatological Annual Regional Averages

Figures 3.2.1 show the annual mean map of different radiation variables at the TOA for both ERBE and CERES period. *Table 3.2.1* gives the statistical summary for *Figure 3.2.1*. The global mean all-sky SW (shortwave radiation) is about 4.5 Wm^{-2} larger for ERBE than CERES. The range of values (corrected for the mean difference) and spatial standard deviation are about the same for both datasets. Notable differences in the geographic pattern that contribute, in part, to the larger ERBE values occur over the ocean between Svalbard and Norway, over the marine stratus regimes and over Antarctica. The global mean clear-sky SW is only about 2 Wm^{-2} larger for ERBE than CERES, but ERBE exhibits a much larger range of values with a maximum over Antarctica that is larger than the all-sky value and minima over the oceans that appear to lower than the Rayleigh reflectivity over a black surface. The CERES dataset exhibits a range of clear-sky SW values that is about 15 Wm^{-2} larger than for all-sky SW, but the range for the ERBE clear-sky SW is 75 Wm^{-2} larger than for all-sky SW. The geographic patterns of clear SW are very similar (spatial standard deviations about the same) except that the ERBE land-ocean contrasts are stronger and the effect of sea ice in the Antarctic region is missing in the ERBE results because ERBE algorithm does not include dynamic sea-ice information for the southern oceans. The global mean values of SW cloud radiative effect from ERBE and CERES agree to within about 1 Wm^{-2} but the range of values differs by nearly 20 Wm^{-2} (ERBE being larger). ERBE shows negative values of SW cloud radiative effect over the permanent ice sheets; whereas CERES generally does not (there is a small region of negative values over northern Greenland). ERBE and CERES exhibit values of SW cloud radiative effect very near zero over the Sahara and Saudi deserts.

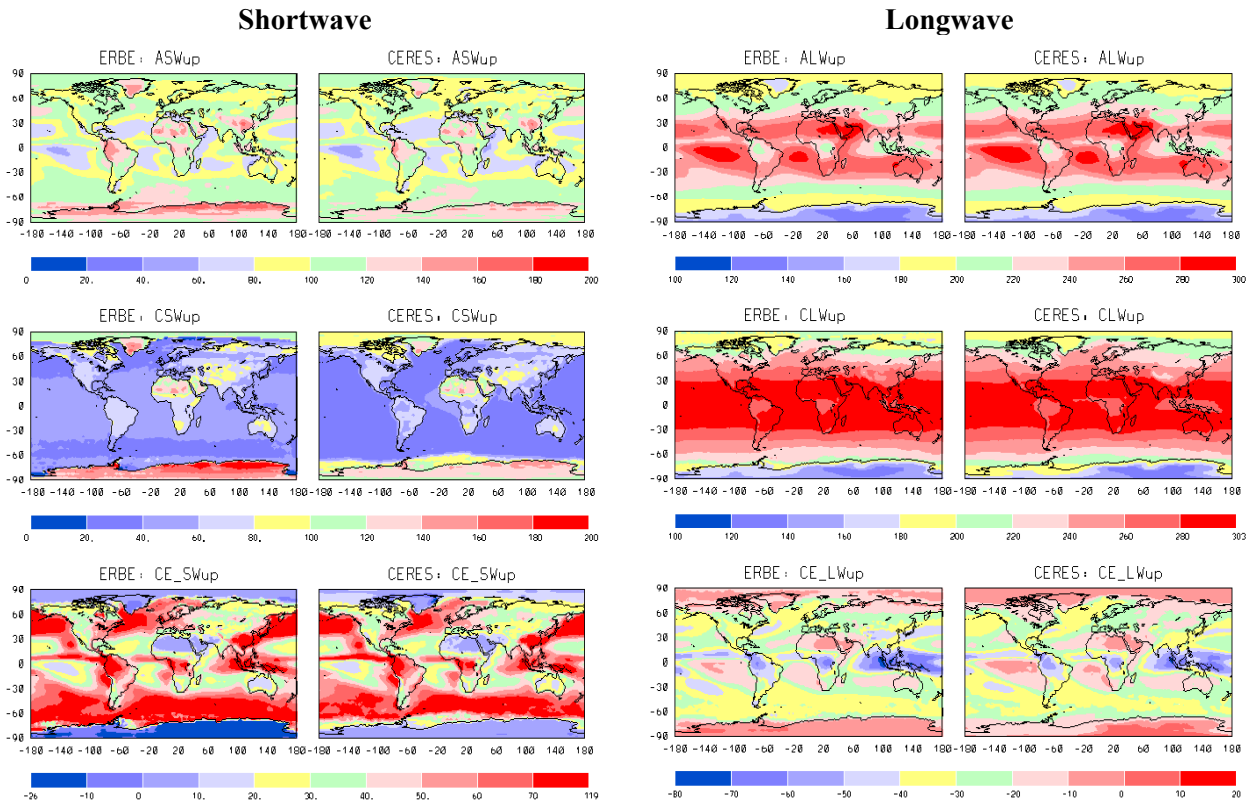

Figure 3.2.1. *Climatological mean regional comparisons of shortwave and longwave variables for ERBE based on data from 2/1985 to 1/1989 and CERES based on data from 1/2001 to 12/2004 for all-sky shortwave (ASWup), clear-sky shortwave (CSWup), shortwave cloud radiative effect (CE_SWup), all-sky longwave (ALWup), clear-sky longwave (CLWup) and longwave cloud radiative effect (CE_Lwup) in* Wm^{-2}.

The global mean values of all-sky LW (longwave radiation) are within 2 Wm^{-2} with nearly identical ranges and patterns of geographic variation. There is an even closer agreement of the global mean clear-sky LW, but the ERBE range is slightly smaller. There are subtle geographic differences, notably over Alaska, coastal Antarctica and Indonesia. LW cloud radiative effect (generally a negative value) is slightly smaller in magnitude for CERES than ERBE because of the difference in all-sky LW. Both datasets exhibit positive values of LW cloud radiative effect over Antarctica, especially CERES.

Table 3.2.1: *Statistical Summary for Figure 3.2.1 (Mean value ± 1 Sigma spatial variability)*

	Shortwave		Longwave	
	ERBE	CERES	ERBE	CERES
All-sky	102.6±19.4	98.0±18.2	235.2±29.8	237.1±29.4
Clear-sky	53.9±25.5	51.6±24.0	264.8±31.7	264.1±31.3
Cloud Effect	48.5±23.4	47.2±20.8	-29.2±13.3	-27.0±12.2

3.2.3: Temporal Variability

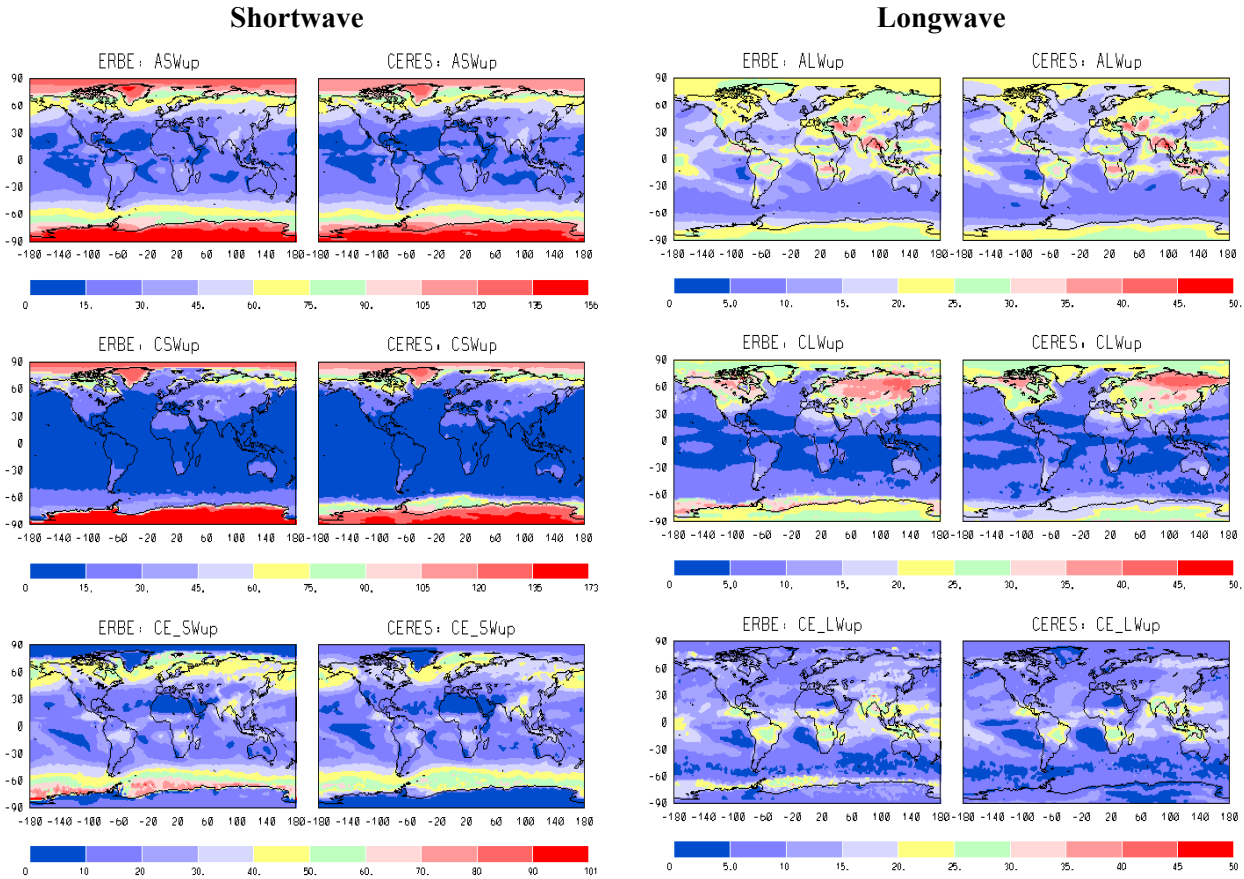

Figure 3.2.2. *Same as Figure 3.2.1 but for comparison of the temporal variability*

Figure 3.2.2 shows the temporal variability of the regional data for the ERBE and CERES baseline dataset. The variability is represented by the standard deviation of the whole 4-year time record for the ERBE and CERES periods, respectively, for each grid cell's original monthly mean to reflect seasonal and inter-annual variations mixed with possible error bars. *Table 3.2.2* summarizes the results in *Figure 3.2.2*. In general, both datasets show nearly the same magnitude of regional time variations for all SW and LW components. The ERBE data exhibits somewhat larger SW variations over Greenland, Arctic and Antarctica and much smaller variation over the Antarctic sea ice zone. The ERBE data also show larger variations of clear-sky LW and LW CRF over the coastal Antarctica and sea ice zone and smaller variation over the northern hemisphere snow zone.

Table 3.2.2: *Same as Table 3.2.1; but for Figure 3.2.2.*

	Shortwave		**Longwave**	
	ERBE	**CERES**	**ERBE**	**CERES**
All-sky	38.4±28.3	36.8±28.3	16.6±7.0	15.7±7.1
Clear-sky	17.5±26.8	18.0±27.9	10.5±9.4	10.5±8.5
Cloud Effect	25.7±14.3	23.2±12.9	11.9±5.6	10.3±5.3

3.2.4: Deseasonalized Monthly Time Series

The left portion of *Figure 3.2.3* shows the deseasonalized monthly, global mean anomaly

time series for the SW components from ERBE and CERES. The 4-yr ERBE record shows a systematic decrease of all-sky SW of about 2 Wm^{-2}, whereas the 4-yr CERES record shows no significant variation. There is a small variation of clear-sky SW for either time record suggesting cloud changes explain this increase of the global mean solar heating (the ISCCP global monthly mean cloud cover declines over the earlier but not the later period). This figure also shows that the decrease in ERBE all-sky SW occurs more strongly over land areas than over ocean areas, which is true in both hemispheres (not shown); consequently, there is a stronger decrease in the northern hemisphere than in the southern.

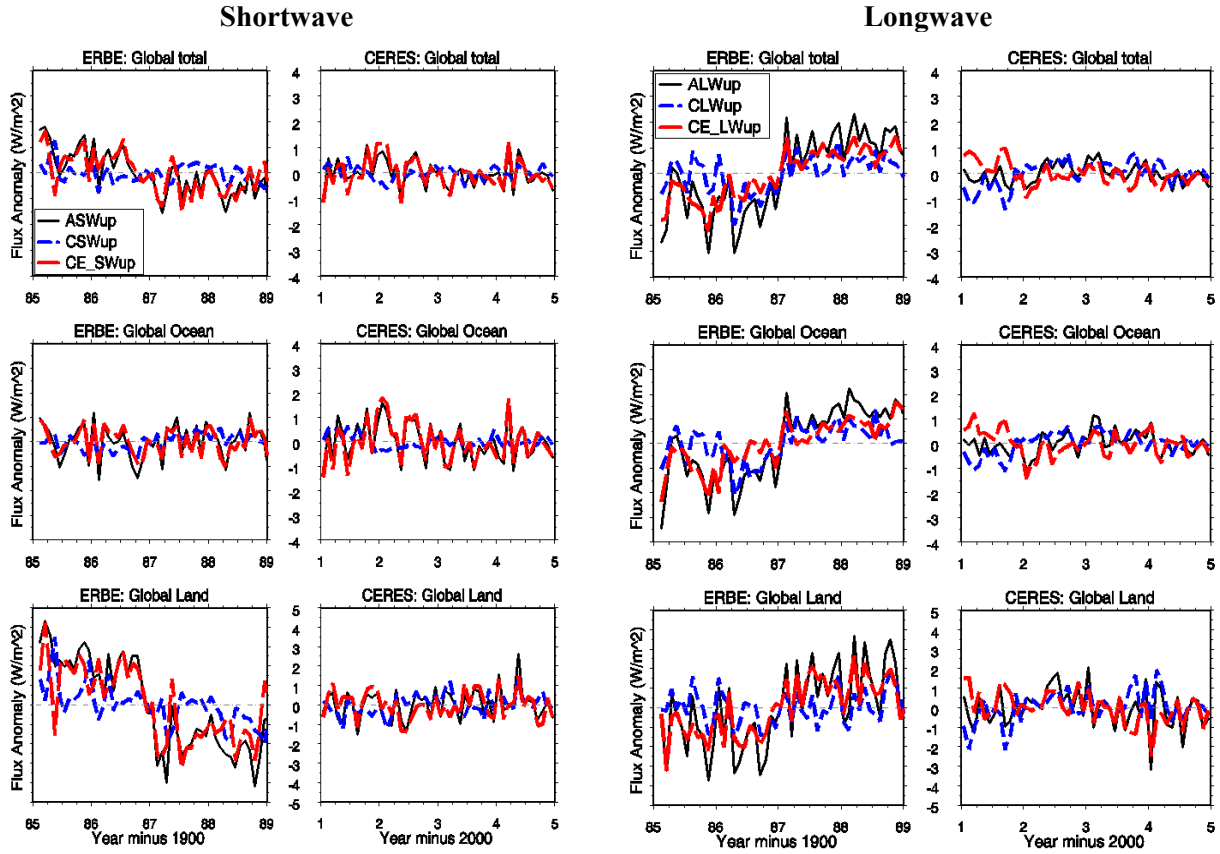

Fig. 3.2.3. *Deseasonalized monthly time series of shortwave and longwave variable for the ERBE (left panels) and CERES (right) dataset for all-sky SW (ASWup), clear-sky SW (CSWup) SW CRF (CE_SWup), all-sky LW (ALWup), clear-sky LW (CLWup) and LW CRF (CE_Lwup) in Wm^{-2} for global total, ocean and land (upper, middle, and lower panel, respectively).*

Although the CERES global time series show no significant variation, there appears to be small offsetting changes over land and ocean areas by about 1 Wm^{-2}, with all-sky SW decreasing slightly over oceans and increasing slightly over land. Given how closely the time series for SW CRE follows that for all-sky SW, this variation (if real) may be explained by a subtle change of the relative cloud properties between land and ocean.

The right portion of *Figure 3.2.3* shows the deseasonalized monthly, global mean anomaly time series for the LW components from ERBE and CERES. The 4-yr ERBE record shows a systematic increase of all-sky LW of about 3 Wm^{-2} that is about equally large over both land and ocean areas, whereas the 4-yr CERES record shows no significant variation. There

appears to be a corresponding, but smaller (about 1 Wm^{-2}), increase of the ERBE clear-sky LW, suggesting both a water vapor and/or cloud change is involved.

The CERES time series show a small increase of clear-sky LW of about 1 Wm^{-2} to the middle of the period and then a decline. This feature is clearer over ocean than land (although it appears stronger over southern hemisphere land, not shown), suggesting that water vapor and cloud changes may be acting against each other. In this case, the time series for all-sky LW and LW CRE do not follow each other as closely as for SW. The SW and LW changes during the ERBE period, if accurate, suggest a small net cooling (decreased all-sky SW offset by increased all-sky LW), where as the changes during the CERES period suggest a geographic rearrangement of net radiation without a significant change in the global average. These features deserve further investigation.

3.2.5: Zonal Annual Cycle

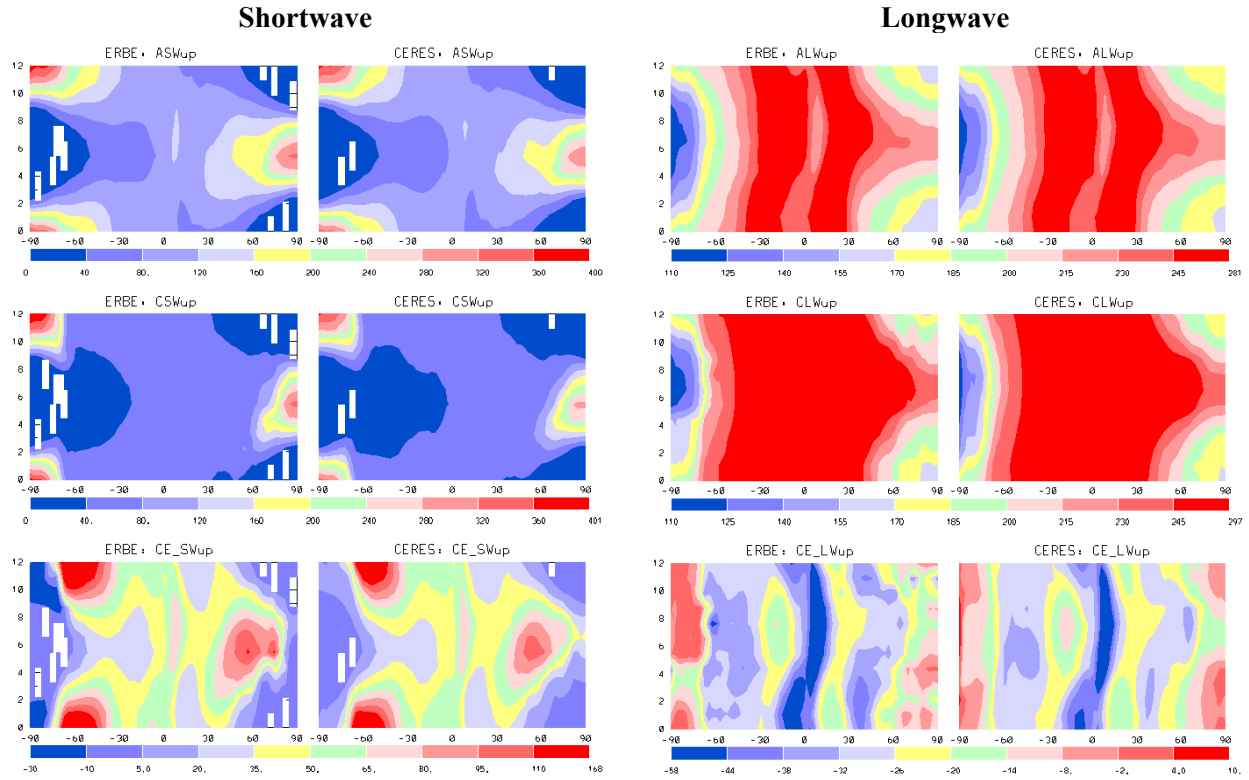

Figure 3.2.4: *Comparison of zonal-mean annual cycle of shortwave (SW) and longwave (LW) radiation for both the ERBE and CERES baseline period for all-sky flux (upper), clear-sky flux (middle) and cloud radiative effect (bottom) in* Wm^{-2}.

The left portion of *Figure 3.2.4* compares the zonal mean annual cycle of the SW components from ERBE and CERES as anomalies from the zonal annual mean. The patterns and quantitative agreement for all-sky SW are excellent with ERBE showing slightly higher polar maxima than CERES. The clear-sky SW comparison is similar. The SW CRE latitude-month distribution is also very similar for ERBE and CERES but CERES shows slightly larger northern hemisphere summertime maximum; the ERBE results also show negative values over southern hemispheric polar region.

The right portion of *Figure 3.2.4* compares the zonal mean annual cycle of the LW components from ERBE and CERES. Again the patterns and quantitative agreement are excellent

but ERBE shows a slightly smaller north polar minimum in January. The agreement for clear-sky LW is slightly worse with CERES showing a somewhat higher mid-latitude summertime maximum at latitudes greater than 50ºN and ERBE showing a lower south polar wintertime minimum but with larger south polar values in the austral spring. CERES also exhibits a slight minimum in clear-sky LW near the equator over most of the year that ERBE does not show (as clearly). The agreement for LW CRE is still poorer with ERBE showing a lower minimum in southern mid-latitudes over the whole year, a slightly lower minimum over the ITCZ in boreal summertime and lower values over Antarctica. The annual cycle of LW CRE over Antarctica shows different amplitude and phase for ERBE and CERES.

3.2.6: Seasonal Cycle

The left portion of *Figures 3.2.5* illustrates the mean seasonal cycles of the SW components by plotting the difference between the average hemispheric values for each month from all years and the time record average: a phase portrait is formed by plotting the northern hemisphere anomalies against the southern hemisphere anomalies. The left side shows the ERBE baseline results and the other datasets compared with it and the right side shows the CERES baseline results and the other datasets compared with it. The values are normalized by subtracting their respective global means and shown as fractions of their global means. The hemispheric mean seasonal variations of all-sky SW exhibit significantly larger amplitude in the southern than northern hemisphere with maxima-minima in June and December. The variations of all-sky SW are very similar for both baseline datasets and among all the other products. There is about a 5% spread of values in the ERBE set (ignoring the ERBS dataset which is not globally complete) for many months: in some cases, such as March and September, the disagreement is confined to the northern hemisphere, whereas for December the disagreement is confined to the southern hemisphere. December shows the largest spread in the CERES set. There is somewhat more disagreement of magnitude but not phase for clear-sky SW, particularly in boreal summer months. A very subtle feature of the clear-sky SW plot is a hysteresis caused by hemispheric differences in seasonal phase (in contrast to all-sky SW): during the boreal spring-summer, the northern hemisphere reaches its maximum value before the southern hemisphere reaches its minimum value, whereas the northern minimum and southern maximum both occur in December. The seasonal variations of SW CRE are also in good agreement, but the IPCC models show some difference with ERBE.

The right portion of *Figures 3.2.5* illustrates the mean seasonal cycles of the LW components by plotting the difference between the average hemispheric values for each month from all years and the time record average: a phase portrait is formed by plotting the northern hemisphere anomalies against the southern hemisphere anomalies. The left side shows the ERBE baseline results and the other datasets compared with it and the right side shows the CERES baseline results and the other datasets compared with it. The values are normalized by subtracting their respective global means and shown as fractions of their global means. Note that the magnitude of the seasonal variations for the LW components is an order of magnitude smaller than for the SW components, so the disagreements are more evident. The basic shape of the curves for all-sky LW is similar for all products, showing a five times larger seasonal amplitude in the northern hemisphere than in the southern hemisphere.

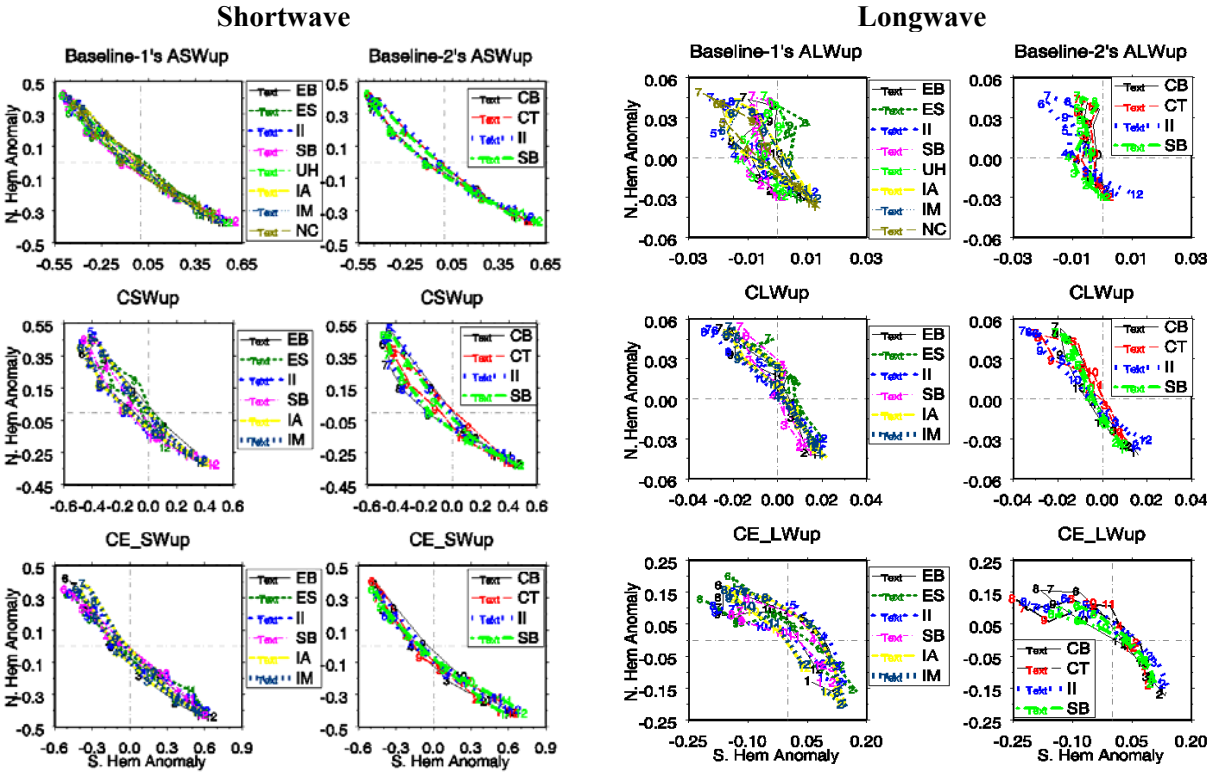

Figure 3.2.5: *Normalized hemispherical seasonal anomaly cycle for (a) SW and (b) LW for all available products over periods of baseline 1 (left panels) and baseline 2 (right) for all-sky (upper panels), Clear-sky (middle) and CRE (lower). Numbers of cycles represent months (1- 12). EB=ERBE, ES=ERBS, II=ISCCP, SB=SRB, UH=University Maryland, IA=IPCC average, IM=IPCC medium and NC=NCEP.*

The amplitude of variation is larger in the southern hemisphere for ISCCP FD and NCEP2 in the boreal spring-summer seasons; there is better agreement in boreal fall-winter seasons when compared with ERBE. GEWEX SRB all-sky LW values for December disagree more with ERBE than with CERES. ERBE shows larger seasonal amplitude of all-sky LW than CERES, whereas the ISCCP FD shows amplitude that is almost three times larger than CERES. There is better agreement among the products for clear-sky LW, but still the tendency for GEWEX SRB to have smaller seasonal amplitude than ERBE more consistent with CERES and ISCCP FD to have slightly larger seasonal amplitude than ERBE. The hemispheric asymmetry of seasonal variation amplitude of clear-sky LW is significantly smaller than for all-sky LW, indicating an important cloud (and water vapor) effect on the seasonal LW cooling. This cloud effect is better seen in the plot for LW CRE, where the seasonal variation amplitude is much larger for the southern than the northern hemisphere. It is notable that the LW CRE anomalies for the spring-fall seasons are both larger than the annual mean value, which offsets the tendency for the SW CRE anomalies in these seasons to be smaller than the annual mean value.

3.2.7: Summary

In this section, we examine the radiation budget data from the ERBE scanner and the CERES datasets that are submitted to the GEWEX-RFA archive. While these two datasets, which are based on two completely different data periods, show very similar temporal and spatial variability, differences in annual global mean and deseasonalized time series between them indicate absolute calibration differences and/or climatological differences exist between these two datasets. Without a high quality long-term dataset that spans the ERBE and CERES period,

it is difficult to assess the relative importance of absolute calibration versus climatology in producing these differences.

3.3: Comparisons of top-of-atmosphere earth radiation budget during ERBE and CERES period.

Part I: Climatological Mean and Time Series Comparisons (T. Wong)

3.3.1: Introduction

The purposes of this section are (1) to highlight the absolute radiometric differences among the different observational based top-of-atmosphere radiation budget datasets in the current GEWEX RFA archive and (2) to examine the temporal consistency between these datasets over time. We will concentrate our comparisons on datasets that have true global coverage. In particular, we will break up our analysis into two periods where we have good broadband data coverage: the ERBE period from February 1985 to January 1989 and the CERES period from March 2000 to February 2004. Section 3.3.2 will describe the datasets and the common analysis technique used for the two data periods to minimize statistical differences due to methodology. Results of these comparisons are reported separately in sections 3.3.3 for the ERBE period and 3.3.4 for the CERES period. This is followed by an assessment of ERBE and the CERES longwave flux differences in section 3.3.5. A summary is given in section 3.3.6.

3.3.2: Datasets and Analysis Methods

Tables 3.3.1 and 3.3.2 show the GEWEX-RFA TOA datasets and their corresponding variables used for the ERBE period and CERES period comparisons. The variables of interest include solar incoming radiation, all-sky and clear-sky reflected shortwave radiation, all-sky and clear-sky outgoing longwave radiation, and all-sky and clear-sky net radiation. For the ERBE period, three datasets (ISCCP-FD, and GEWEX SRB and UMD SW) are derived in different ways from input data from the ISCCP project. The two remaining datasets are the ERBE broadband scanner multi-satellite dataset and the UMD HIRS OLR dataset. For the CERES period, four sets of data (EBAF, SRBAVG-NonGEO, SRBAVG-GEO, and ERBE-like) are estimates from the CERES broadband instrument. The other two datasets (ISCCP FD and GEWEX SRB) are derived in different ways from input data from the ISCCP project.

For each of the data periods, 4-year climatological annual means (i.e., regional, zonal, and large-area average) will be used to assess the absolute differences among each GEWEX-RFA dataset. Regional climatology of radiation field is calculated for each variable and each dataset during the specific CERES and ERBE period. Climatological zonal mean, tropical and global mean are calculated directly from the GEWEX-RFA time series archive when possible or are obtained based on the calculated regional climatology above. Standard statistical analysis will be used to summarize the global and tropical mean results. For the purpose of regional and zonal mean comparisons, we used the ERBE scanner multi-satellite data as the truth field during the ERBE period and the CERES-SRBAVG-GEO as the truth field during the CERES period and compared them with other datasets in their respective period. For large area mean comparison, we utilized the multi-dataset ensemble mean as the truth since this method summarizes the results quickly (however, if one dataset has very different features than the others, these features can be projected into the differences for all datasets with the ensemble mean). Multi-dataset ensemble mean, standard deviation, and range will be reported for each variable within the two periods.

Once the absolute differences among these datasets are established, we will turn our attention to the analysis of deseasonalized monthly mean global and tropical mean time series.

This is used to examine the temporal consistency among the GEWEX-RFA datasets for both the ERBE and CERES period. Deseasonalized time series are calculated by subtracting the monthly mean data from their corresponding four-year mean calendar month climatology. Standard statistical analysis will be used again to provide a quick summary of these comparisons. Finally, we will use available GEWEX-RFA datasets (i.e., ERBS non-scanner, UMD HIRS, and GEWEX SRB SW) to bridge the data gap between the ERBE and the CERES period and to address the differences between these two data periods. This is done using tropical mean time series analysis.

Table 3.3.1: *GEWEX-RFA datasets and their variables used in the ERBE period comparisons*

TOA ERB Dataset	Solar down	All-sky Fluxes			Clear-sky Fluxes		
		SW up	LW up	Net down	SW up	LW up	Net down
ERBE Scanner	X	X	X	X	X	X	X
GEWEX SRB	X	X	X	X	X	X	X
ISCCP FD	X	X	X	X	X	X	X
UMD SW	X	X	---	---	---	---	---
UMD HIRS OLR	---	---	X	---	---	---	---

Table 3.3.2: *GEWEX-RFA datasets and their variables used in the CERES period comparisons*

TOA ERB Dataset	Solar down	All-sky Fluxes			Clear-sky Fluxes		
		SW up	LW up	Net down	SW up	LW up	Net down
CERES EBAF	X	X	X	X	X	X	X
CERES SRBAVG-NonGEO	X	X	X	X	X	X	X
CERES SRBAVG-GEO	X	X	X	X	X	X	X
CERES ERBE-like	X	X	X	X	X	X	X
ISCCP FD	X	X	X	X	X	X	X
GEWEX SRB	X	X	X	X	X	X	X

3.3.3: ERBE Period Results (February 1985 to January 1989)

a) Regional Map and Regional Difference Map

The all-sky and clear-sky climatological mean regional map of each component of Earth Radiation budget from the GEWEX-RFA datasets and the climatological mean regional difference map (relative to the ERBE multi-satellite data set) are given in the appendix D.3.3. Readers are encouraged to explore these figures. The following will provide a quick highlight of the regional findings along with selected illustrated figures.

In general, the large-scale regional patterns of all-sky longwave radiation are very similar among all datasets, indicating good agreement~~s~~ between them. Subtle regional differences between datasets do exist (i.e., subsidence regions, and areas of deep convection). Large-scale regional pattern of the all-sky shortwave radiation shows more dissimilarity among datasets (i.e., mid-latitude storm tracks, stratus regions, ITCZ). Some differences in the Polar region are artifact of the missing data, which are not filled in ERBE shortwave regional dataset. The differences in regional pattern of the all-sky net radiation are very similar to those of the shortwave radiation; indicating the dominate effects of the shortwave radiation on the quality of the net radiation.

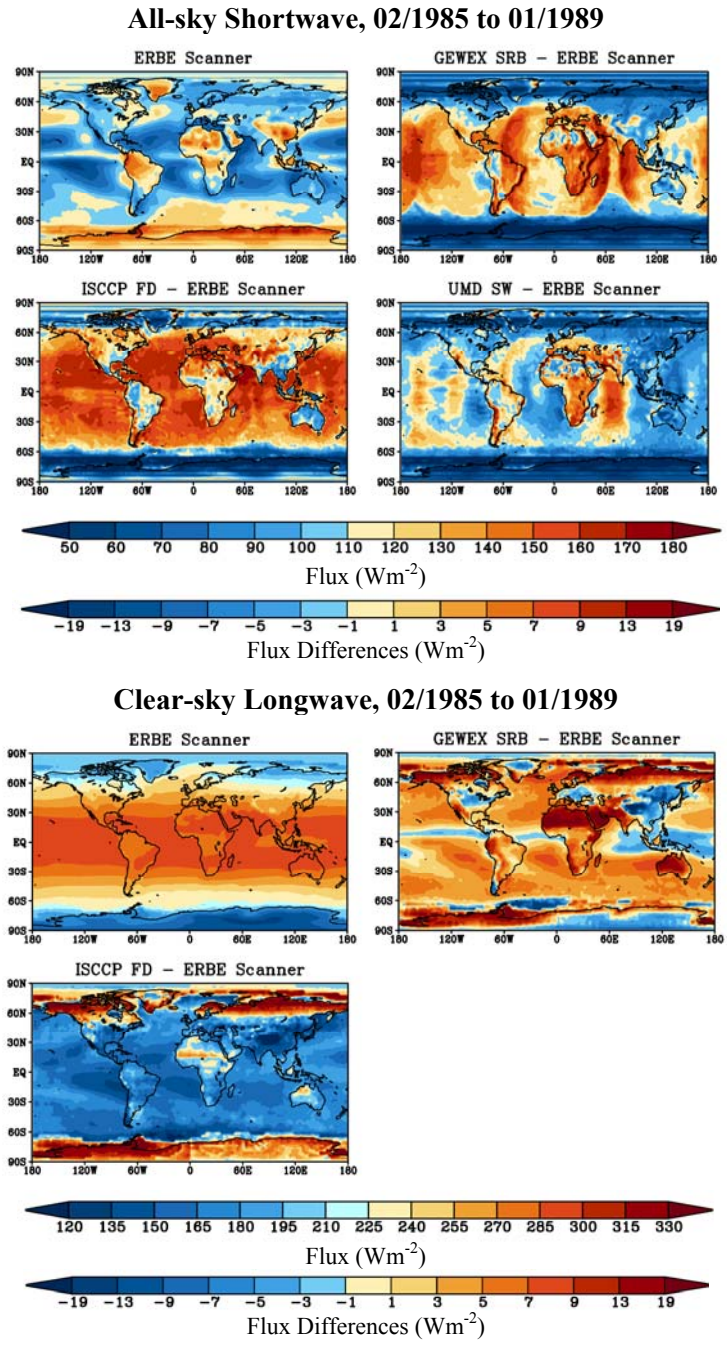

Figure 3.3.1: *ERBE scanner regional map and differences map (relative to ERBE Scanner) for all-sky shortwave (top set) and clear-sky longwave (bottom set) radiation. Top portion of the pair color scale is for regional map; bottom portion of the same pair color scale is for regional difference map.*

For the clear-sky longwave flux, significant differences are noticed over areas of desert and subsidence regions over the ocean. Excluding the polar region, the patterns of clear-sky shortwave flux are very similar between datasets. Similar to the all-sky shortwave flux, some of the regional clear-sky shortwave differences in the polar region are an artifact of missing data. The differences in clear-sky Net radiation are the product of both the differences in clear-sky longwave and clear-sky shortwave fluxes. Considerable differences are noticed over areas of deserts and subsidence regions, similar to those of the clear-sky longwave differences. Differences in clear-sky net flux are also found over the polar region, which is caused by differences in clear-sky shortwave flux.

Figure 3.3.1 shows the regional difference map (relative to ERBE scanner data) for all-sky shortwave and clear-sky longwave component of the Earth Radiation Budget from all four datasets for the ERBE period (February 1985 to January 1989). Differences in the ranges of ± 20 Wm^{-2} are visible throughout these maps. The results are very similar to those shown in the CERES period. These disagreements are due to differences in instrument, science processing algorithms, as well as input ancillary datasets used in the construction of these datasets. These large disagreements can make regional assessments difficult to perform. More works are needed in the future to map the physical causes of these differences. This is the only way to improve regional comparisons in the future.

b) Climatological Zonal Mean

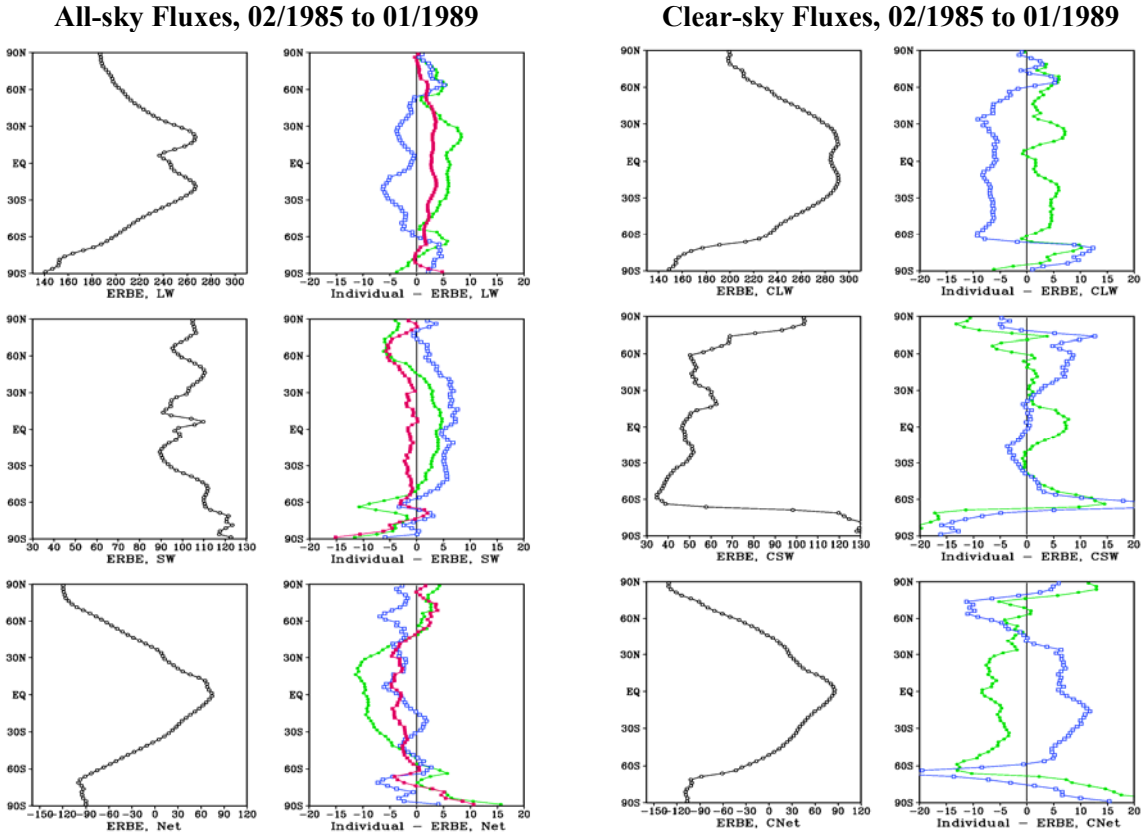

Figure 3.3.2: *ERBE zonal mean all-sky (first column) and clear-sky profile (third column) and the individual dataset minus ERBE mean (second column: all-sky, fourth column: clear-sky) for longwave (top), shortwave (middle), and net flux (bottom), for GEWEX SRB (green), ISCCP FD (blue), UMD SW & UMD HIRS OLR (light red) dataset.*

Figure 3.3.2 (first and second column) shows the ERBE scanner climatological zonal average profiles of all-sky longwave, shortwave and net radiation along with the absolute differences between the individual dataset and the ERBE scanner mean for the ERBE period. These results are similar to those of the CERES period. For all-sky longwave flux, the ERBE zonal mean profile shows a typical feature with double maxima in the subtropics and minima in the tropics and the two poles. The lowest all-sky longwave flux occurs at the South Pole. Most of the GEWEX-RFA datasets are within ± 7 Wm^{-2} of the ERBE scanner mean. The agreements among datasets are the best for zonal mean regions poleward of 45°N latitude. The largest differences between datasets occur in regions along the tropics and the subtropics. For all-sky shortwave flux, the ERBE zonal mean profile has a complicated shape reflecting the distribution of clouds and surface features. The highest shortwave value occurs at around 75° S latitude. The lowest shortwave value locates at about 20°S latitude. Most of the GEWEX-RFA datasets are again within ± 7 Wm^{-2} of the ERBE scanner mean. The ISCCP based products tend to cluster on one side while the UMD HIRS OLR data tends to located on the others side of the zero line. There are also larger disparities between datasets than those of the all-sky longwave cases. The differences are also larger over the southern polar region than their northern counterpart. For the all-sky net flux, the ERBE scanner zonal mean profile shows a single maximum near the equator and two minima in the Polar Regions. Most of the datasets are within ± 7.5 Wm^{-2} of the ERBE

mean. The zonal profile of the net flux differences reflected the combined differences of both all-sky shortwave and all-sky longwave flux. Similar to the shortwave flux, there are larger disparities between datasets. These disparities among datasets also seem to be uniform with latitude between 60° N and 60° S. The largest difference between a pair of dataset occurs at the South Pole. *Figure 3.3.2* (third and fourth column) shows the corresponding comparisons for clear-sky fluxes. Overall, the differences among clear-sky fluxes are as large as or larger than those of the all-sky fluxes, reflecting the different approaches used in each of the clear-sky datasets. For example, the clear-sky shortwave and clear-sky net flux, there are very large differences over the southern Polar region.

c) Global and Tropical (20°N-20°S) Average

Table 3.3.3 shows the multi-dataset ensemble mean constructed from the five datasets along with their corresponding absolute and relative standard deviation (1-sigma) and actual ranges for the period between February 1985 and January 1989. The multi-dataset ensemble mean for solar incoming radiation is 341.2 Wm^{-2} with a 1-sigma standard deviation of 0.9 Wm^{-2} or 0.3% relative to its mean value. The use of different values for the solar constant in the various datasets causes a small difference in the annual global average solar incoming radiation, which ranges between 339.9 and 341.8 Wm^{-2}. The multi-dataset ensemble mean for outgoing longwave radiation is 236.6 Wm^{-2} (slightly lower than their corresponding CERES period value) with a 1-sigma of 2.9 Wm^{-2} or 1.2% relative to its mean value (slightly larger than their corresponding CERES period value). The range of outgoing longwave radiation among datasets is between 233.3 and 240.0 Wm^{-2}. The multi-dataset ensemble mean for reflected shortwave radiation is 102.2 Wm^{-2} (slightly larger than their corresponding CERES period value) with a 1-sigma of 2.7 Wm^{-2} or 2.6% relative to its mean value (slightly less than their corresponding CERES period value). While the shortwave absolute standard deviation is almost the same as those in the longwave, its relative standard deviation is two times larger than that of the longwave. The range of reflected shortwave radiation is between 99.5 and 105.9 Wm^{-2}. The larger relative shortwave flux disagreement among the various datasets again reflects the need for further improvement of this variable in the future. The multi-dataset ensemble mean for net downward radiation is 2.4 Wm^{-2} with a 1-sigma of 2.3 Wm^{-2} or 95.8% relative to its mean value. The very large relative standard deviation in net downward radiation is the artifact of the small mean value. The range of net radiation among datasets is between –0.6 to 4.9 Wm^{-2}. The large absolute standard deviation in net flux is driven by both longwave and shortwave flux.

Table 3.3.3*: Multi-dataset ensemble mean global average summary (February 1985 to January 1989)*

Parameter	Multi-dataset ensemble Mean	Absolute Standard Deviation (1-σ)	Relative Standard Deviation (1-σ)	Range (Min, Max)
Solar Incoming	341.2	0.9	0.3%	(339.9, 341.8)
Longwave	236.6	2.9	1.2%	(233.3, 240.0)
Shortwave	102.2	2.7	2.6%	(99.5, 105.9)
Net	2.4	2.3	95.8%	(-0.6, 4.9)
Clear Longwave	264.3	4.5	1.7%	(259.5, 268.4)
Clear Shortwave	54.8	1.1	2.0%	(53.6, 55.5)
Clear Net	22.6	4.4	19.5%	(18.1, 26.8)

The results for the clear-sky variables are similar to those of the all-sky variables. The multi-dataset ensemble mean clear-sky longwave radiation is 264.3 Wm^{-2} with a 1-sigma of 4.5 Wm^{-2} or 1.7% relative to its mean value. The range of clear-sky longwave datasets is between

259.5 and 268.4 Wm^{-2}. The multi-dataset ensemble mean for clear-sky shortwave radiation is 54.8 Wm^{-2} with a 1-sigma of 1.1 Wm^{-2} or 2% relative to its mean value. The range of clear-sky shortwave dataset is between 53.6 and 55.5 Wm^{-2}. The multi-dataset ensemble mean for clear-sky net downward radiation is 22.6 Wm^{-2} with a 1-sigma of 4.4 Wm^{-2} or 19.5% relative to its mean value. The range of the clear-sky net dataset is between 18.1 and 26.8 Wm^{-2}.

Table 3.3.4 shows the tropical (20°N to 20°S) average results for the multi-dataset ensemble mean along with absolute and relative standard deviation (1-sigma) and the actual ranges from all six datasets for the all-sky and clear-sky comparison. The multi-dataset ensemble mean for solar incoming radiation is 409.2 Wm^{-2} with a 1-sigma standard deviation of 1.1 Wm^{-2} or 0.3% relative to the ensemble mean. Both the standard and relative standard deviation is similar to those of the global mean. The range of tropical mean solar incoming radiation is between 407.6 and 410.0 Wm^{-2}. The ensemble mean for outgoing longwave radiation is 254.4 Wm^{-2} with a 1-sigma of 3.8 Wm^{-2} or 1.5% relative to the ensemble mean. The relative standard deviation is similar to those of the global mean. The range of outgoing longwave radiation among datasets is between 250.1 and 258.9 Wm^{-2}. The ensemble mean for reflected shortwave radiation is 99.0 Wm^{-2} with a 1-sigma of 3.4 Wm^{-2} or 3.4% relative to the ensemble mean. The relative standard deviation is larger than those of the global mean, indicating more differences between datasets in the tropics. The range of reflected shortwave radiation is between 95.7 and 102.8 Wm^{-2}. The absolute standard deviation in the shortwave is more than 2 times as larger as those in the longwave. The ensemble mean for net downward radiation is 55.8 Wm^{-2} with a 1-sigma of 4.1 Wm^{-2} or 7.3% relative to the ensemble mean. The range of net radiation among datasets is between 50.2 and 59.9 Wm^{-2}. This large standard deviation in net flux is driven equally by both outgoing longwave and reflected shortwave flux.

Table 3.3.4: *Same as Table 3.3.3; but for tropical mean (20°N to 20°S) climatology*

Parameter	Multi-Dataset Ensemble Mean	Absolute Standard Deviation (1-σ)	Relative Standard Deviation (1-σ)	Range (Min, Max)
Solar Incoming	409.2	1.1	0.3%	(407.6, 410.0)
Longwave	254.4	3.8	1.5%	(250.1, 258.9)
Shortwave	99.0	3.4	3.4%	(95.7, 102.8)
Net	55.8	4.1	7.3%	(50.2, 59.9)
Clear Longwave	286.9	4.6	1.6%	(281.7, 290.6)
Clear Shortwave	51.9	3.0	5.8%	(49.8, 55.3)
Clear Net	71.1	7.2	10.1%	(64.1, 78.5)

The results for the clear-sky variable are similar to those of the all-sky variables. The ensemble mean clear-sky longwave radiation is 286.9 Wm^{-2} with a 1-sigma of 4.6 Wm^{-2} or 1.6 % relative to the ensemble mean. The relative standard deviation is slightly better than those of the global mean. The range of clear-sky longwave datasets is between 281.7 and 290.6 Wm^{-2}. The ensemble mean for clear-sky shortwave is 51.9 Wm^{-2} with a 1-sigma of 3.0 Wm^{-2} or 5.8% relative to the ensemble mean. The relative standard deviation is 3 times larger than the global mean; indicating significantly more differences between datasets. The range of clear-sky shortwave dataset is between 49.8 and 55.3 Wm^{-2}. The ensemble mean for clear-sky net radiation is 71.1 Wm^{-2} with a 1-sigma of 7.2 Wm^{-2} or 10.1% relative to the ensemble mean. The range of the clear-sky net datasets is between 64.1 and 78.5 Wm^{-2}. Majority of the differences are driven by the differences in both clear-sky longwave and clear-sky shortwave flux.

d) Deseasonalized Time Series Analysis

Figure 3.3.3 shows deseasonalized monthly mean global average and tropical average time series of earth radiation budget component during the 4-year ERBE period. The temporal features in the two figures are very similar with tropical averages showing larger variability than the global average. For this period, all five datasets seem to have similar variability over time.

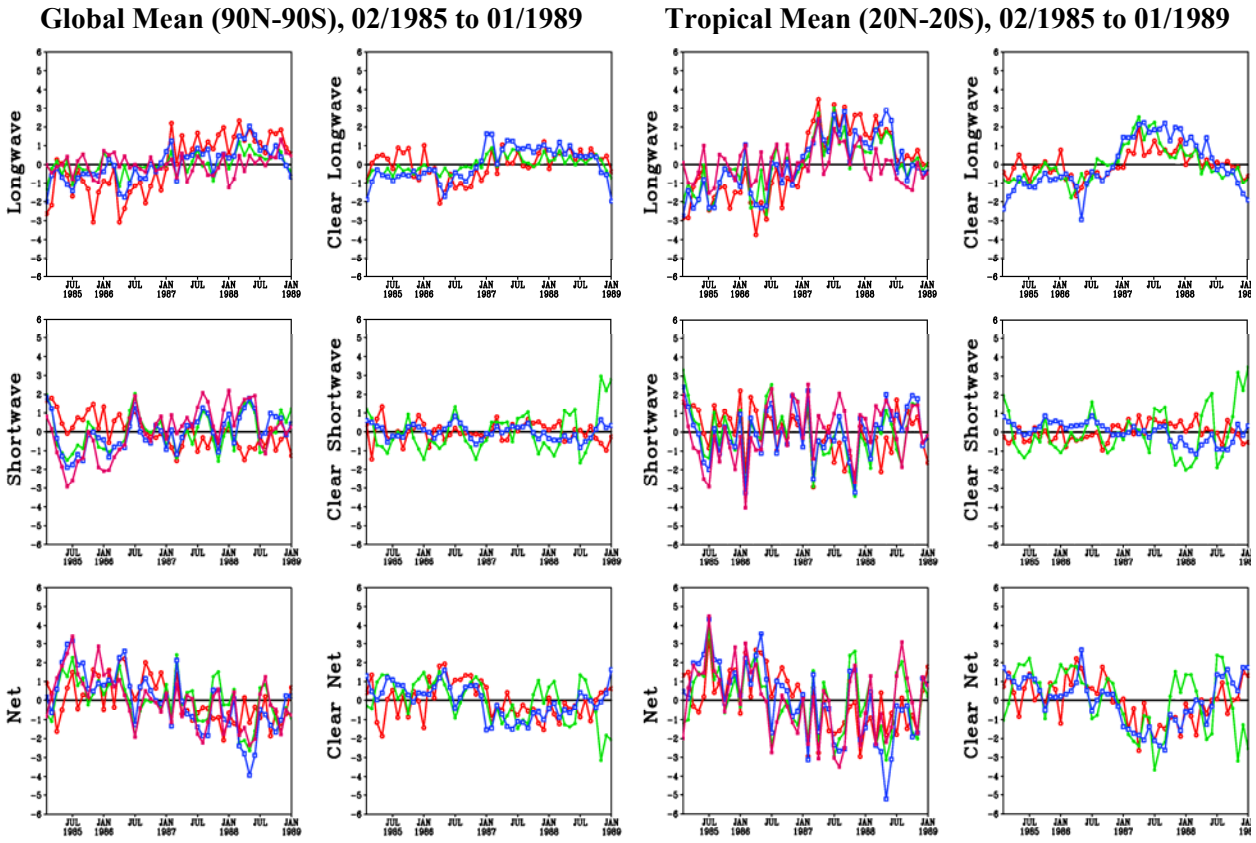

Figure 3.3.3: *Deseasonalized time series of global mean (90N to 90S, left set of six figures) and tropical mean (20N to 20S, right set of six figures) of TOA fluxes during the ERBE period (February 1985 to January 1989) for ERBE Scanner (dark red), GEWEX SRB (green), ISCCP FD (blue), and UMD (light red) dataset.*

3.3.4: CERES Period Results (March 2000 to February 2004)

a) Climatological Regional Map and Regional Difference Map

The all-sky and clear-sky climatological mean regional map of each component of Earth Radiation budget from six datasets and the climatological mean regional difference map (relative to the CERES SRBAVG-Geo data set) are given in the appendix C.3.3. Readers are encouraged to explore these figures. The following will provide a quick highlight of the regional findings along with selected illustrated figures.

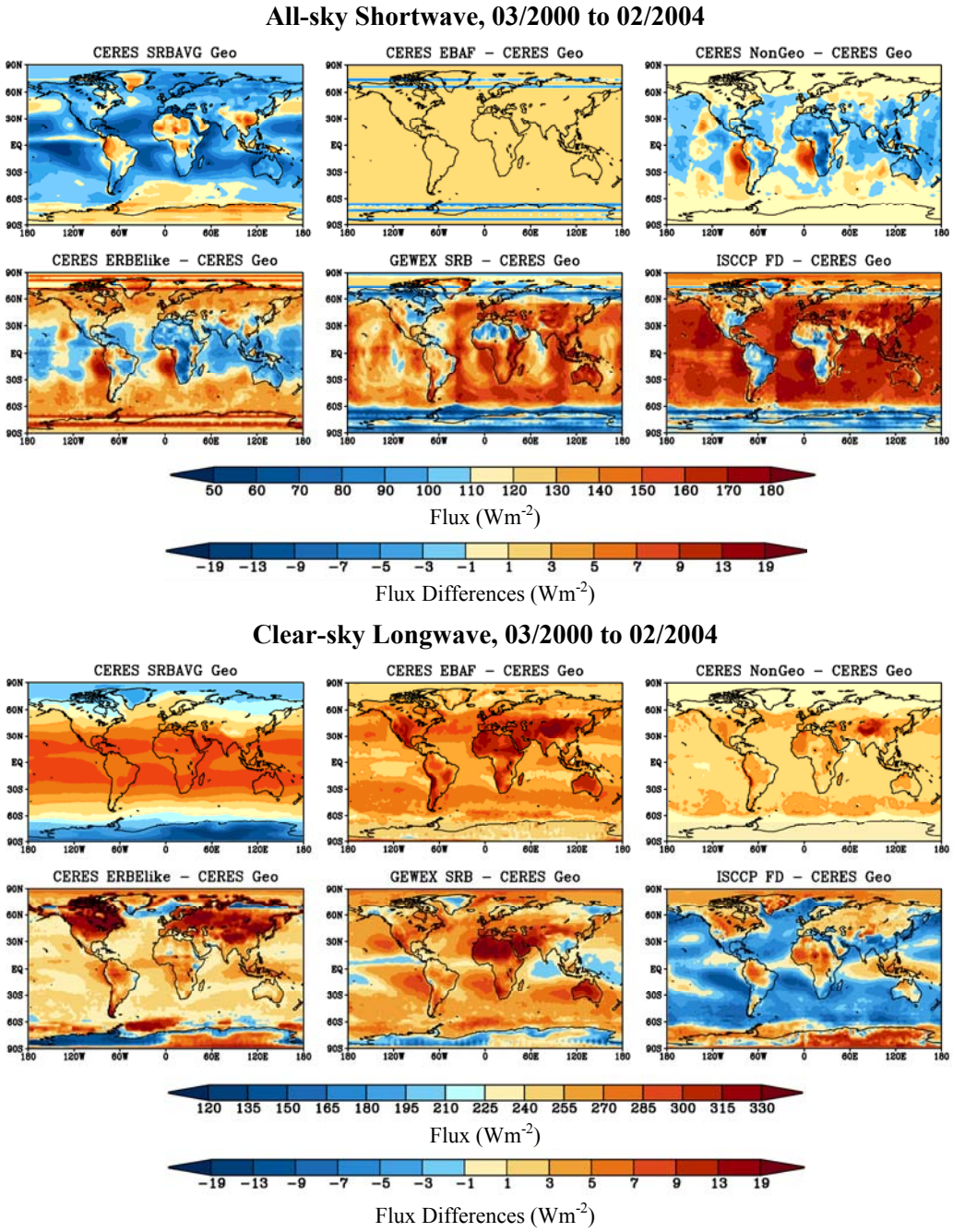

Figure 3.3.4: *Regional differences (relative to CERES SRBAVG GEO) for all-sky shortwave (top set) and clear-sky longwave (bottom set) radiation.*

The large-scale regional patterns of all-sky longwave radiation are very similar among all six datasets, indicating good agreement between them. Subtle regional differences between datasets do exist. Specifically, noticeable longwave differences are found in the subsidence regions over the open ocean and over desert, as well as in the deep convective regions over land and over ocean. Large-scale regional pattern of the all-sky shortwave radiation shows more dissimilarity among datasets. For example, major differences are found in the mid-latitude storm

track regions of both hemispheres and in the Stratus regions off the west coast of the major continents. There are also considerable differences in the shortwave patterns over the ITCZ and in the tropical western Pacific regions. Some differences in the Polar region are artifact of the missing data, which are not filled in CERES shortwave regional dataset. The differences in regional patterns of the all-sky net radiation are very similar to those of the shortwave radiation; indicating the dominating effects of the shortwave radiation on the quality of the net radiation.

For the clear-sky longwave flux, significant differences are noticed over areas of dessert and subsidence regions over the ocean. GEWEX SRB tends to have the warmest desserts and subsidence regions. Excluding the polar region, the patterns of clear-sky shortwave flux are very similar between datasets. Similar to the all-sky shortwave flux, some of the regional clear-sky shortwave differences in the polar region are the artifact of missing data. The differences in clear-sky net radiation are the product of both the differences in clear-sky longwave and clear-sky shortwave fluxes. For example, considerable differences are noticed over areas of deserts and subsidence regions, similar to those of the clear-sky longwave differences. Differences in clear-sky net flux are also found over the polar region, which is caused by differences in clear-sky shortwave flux.

Regional difference maps are used to investigate possible biases associated with each dataset. *Figure 3.3.4* show the corresponding all-sky shortwave and clear-sky longwave regional climatological difference map (relative to CERES SRBAVG-GEO data), respectively, from all five common GEWEX-RFA datasets during the CERES period. Differences of ± 20 Wm^{-2} and larger in radiative fluxes are visible throughout these maps. These distinct disagreement patterns are related to differences in instruments (broadband vs. narrowband), data sampling patterns, science processing algorithms, as well as input ancillary datasets used in the construction of these datasets. For examples, geostationary satellite artifacts, missing data stripping, and absolute calibration differences are clearly evident in these comparisons. These dataset specific issues can make regional assessments difficult to perform since they add large uncertainty to the regional results. Additional works are needed to trace the exact physical causes of these regional differences in order to minimize the disagreement among them in the future.

b) Zonal Mean

Figure 3.3.5 (right panels) shows the CERES SRBAVG-Geo climatological zonal average profiles of all-sky longwave, shortwave and net radiation along with the absolute differences between the individual dataset and CERES SRBAVG-Geo dataset. For the all-sky longwave flux, the zonal profile shows a typical feature with double maxima in the subtropics and minima in the tropics and the two poles. The lowest all-sky longwave flux occurs at the South Pole. Most of the GEWEX-RFA datasets are within ± 5 Wm^{-2} of the CERES SRBAVG-GEO data. The CERES derived products look very similar to each other and have a smaller deviation from SRBAVG GEO mean profile than the ISCCP-based products. The agreement among datasets is the best for zonal mean regions polewards of 45N latitude. The largest differences between datasets occur in regions along the tropics and the subtropics. For all-sky shortwave flux, the CERES SRBAVG GEO zonal mean profile has a complicated shape reflecting the distribution of clouds and surface features. The highest shortwave value occurs at around 75N latitude. The lowest shortwave value locates at about 20S latitude. Most of the GEWEX-RFA datasets are within ± 7.5 Wm^{-2} of the CERES SRBAVG GEO data. Similar to the all-sky longwave, the ISCCP based products have a larger derivation from the CERES SRBAVG GEO mean profile than the CERES based products. There are also larger disparities between clear-sky longwave fluxes than those of the all-sky longwave cases. These disparities seem to be uniform with latitude between 60N and 60S with

CERES based data clustered closer together with smaller difference values while ISCCP based products also stayed together but having much larger difference values. The differences are also larger over the southern polar region than their northern counterpart. For the all-sky net flux, the CERES SRBAVG GEO zonal mean profile shows a single maximum near the equator and two minima in the Polar Regions. Most of the datasets are within ± 7.5 Wm^{-2} of the CERES SRBAVG GEO mean. The zonal profile of the net flux differences reflected the combined differences of both all-sky shortwave and all-sky longwave flux. Similar to the shortwave flux, there are larger disparities between datasets. These disparities among datasets also seem to be uniform with latitude between 60N and 60S. The largest difference between a pair of dataset occurs at the South Pole.

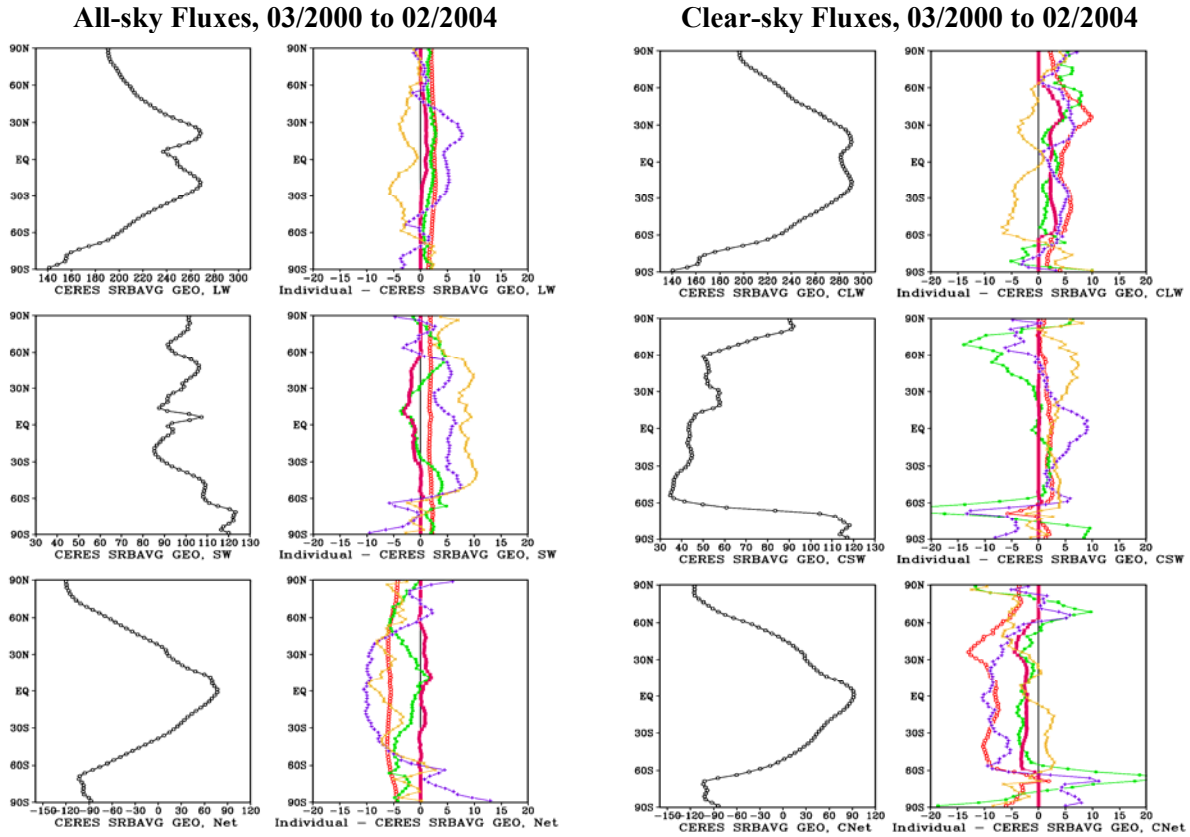

Figure 3.3.5: *CERES SRBAVG GEO zonal mean all sky (first column) and clear-sky (third column) profiles and the individual dataset minus CERES SRBAVG-GEO mean (second column: all-sky and fourth column: clear-sky) for longwave (top), shortwave (middle), and net flux (bottom), for CERES EBAF (dark red), CERES ERBE-like (green), CERES SRBAVG-NonGEO (light red), GEWEX SRB (purple), and ISCCP FD (yellow) dataset.*

Figure 3.3.5 (left panels) shows the corresponding comparisons for clear-sky fluxes. The CERES SRBAVG GEO zonal mean clear-sky longwave flux profile increases equatorward with a small dip just north of the equator. The value of the clear-sky flux are larger than it all-sky components. For the clear-sky shortwave flux, the zonal ensemble mean profiles show a lower value than their all-sky component for most area, expect those over the polar region. Overall, the differences among datasets are as large as or larger than those of the all-sky fluxes, reflecting the different algorithm approaches used in deriving each of the clear-sky datasets. For example, the differences in the clear-sky longwave fluxes among datasets are large even for the Polar region in the Northern Hemisphere. Previously, this region has the smallest disagreement among all-sky

longwave datasets. For the clear-sky shortwave and clear-sky net flux, there are very large zonal average differences, 15 to 20 Wm^{-2}, over the northern and southern Polar regions. Specifically, the CERES ERBE-like data set appears to have large differences, relative to the CERES SRBAVG GEO mean, over the Southern polar ocean. This fact points to the deficiency of the CERES ERBE-like clear-sky scene ID algorithm over these regions.

c) Global and Tropical (20°N-20°S) Average

Table 3.3.5 shows the multi-dataset ensemble mean constructed from six of the datasets along with their corresponding absolute and relative standard deviation (1-sigma) and actual data ranges for the period between March 2000 and February 2004. The individual climatological global mean values of all-sky and clear-sky TOA radiation budget variables from all six datasets are given in the appendix. The multi-dataset ensemble mean for solar incoming radiation is 341.3 Wm^{-2} with a 1-sigma standard deviation of 0.7 Wm^{-2} or 0.2% relative to its mean value. The use of different solar constant in the various datasets causes a small difference in the annual global average solar incoming radiation, which ranges between 340.0 and 341.8 Wm^{-2}. The multi-dataset ensemble mean for outgoing longwave radiation is 238.3 Wm^{-2} with a 1-sigma of 1.8 Wm^{-2} or 0.8% relative to its mean value. The range of outgoing longwave radiation among datasets is between 235.6 and 240.5 Wm^{-2}. The multi-dataset ensemble mean for reflected shortwave radiation is 99.9 Wm^{-2} with a 1-sigma of 3.2 Wm^{-2} or 3.2% relative to its mean value. While the shortwave absolute standard deviation is almost twice as large as those in the longwave, its relative standard deviation is four times that of the longwave. The range of reflected shortwave radiation is between 96.6 and 105.2 Wm^{-2}. The larger shortwave flux disagreement among the various datasets again reflects the need for further improvement of this variable in the future. The multi-dataset ensemble mean for net downward radiation is 3.2 Wm^{-2} with a 1-sigma of 3.2 Wm^{-2} or 100% relative to its mean value. The very large relative standard deviation in net downward radiation is the artifact of the small mean value. The range of net radiation among datasets is between –0.4 to 7.0 Wm^{-2}. The large absolute standard deviation in net flux is driven mostly by the large standard deviation in reflected shortwave flux.

Table 3.3.5: *Multi-dataset ensemble mean global average summary (March 2000 to February 2004)*

Parameter	Multi-dataset ensemble Mean	Absolute Standard Deviation (1-σ)	Relative Standard Deviation (1-σ)	Range (Min, Max)
Solar Incoming	341.3	0.7	0.2%	(340.0, 341.8)
Longwave	238.3	1.8	0.8%	(235.6, 240.5)
Shortwave	99.9	3.2	3.2%	(96.6, 105.2)
Net	3.2	3.2	100%	(-0.4, 7.0)
Clear Longwave	266.1	2.7	1.0%	(262.0, 268.0)
Clear Shortwave	52.0	1.9	3.6%	(49.2, 54.5)
Clear Net	23.1	3.3	14.3%	(18.1, 26.2)

The results for the clear-sky variables are similar to those of the all-sky variables. The multi-dataset ensemble mean clear-sky longwave radiation is 266.1 Wm^{-2} with a 1-sigma of 2.7 Wm^{-2} or 1% relative to its mean value. The range of clear-sky longwave datasets is between 262 and 268 Wm^{-2}. The multi-dataset ensemble mean for clear-sky shortwave radiation is 52 Wm^{-2} with a 1-sigma of 1.9 Wm^{-2} or 3.6% relative to its mean value. The range of clear-sky shortwave dataset is between 49.2 and 54.5 Wm^{-2}. The multi-dataset ensemble mean for clear-sky net downward radiation is 23.1 Wm^{-2} with a 1-sigma of 3.3 Wm^{-2} or 14.3% relative to its mean value. The range of the clear-sky net dataset is between 18.1 and 26.2 Wm^{-2}.

Table 3.3.6 shows the tropical average results for the multi-dataset ensemble mean along with absolute and relative standard deviation (1-sigma) and the actual ranges from all six datasets for the all-sky and clear-sky comparison for the same 4-year period. The individual tropical (20 N to 20S) mean values of all-sky and clear-sky TOA radiation budget variables from all six datasets is given in the appendix for references. In general, the relative differences as measured by the relative standard deviation for the tropical results (i.e., solar incoming, longwave, shortwave, all-sky and clear-sky) are similar to or slightly larger than those of the global mean results even thought the absolute deviation may be higher. This is because the tropical averages usually have higher fluxes than their corresponding global average values. For example, the multi-dataset ensemble mean for outgoing longwave radiation is 255.7 Wm^{-2} with a 1-sigma of 2.2 Wm^{-2} or 0.8% relative to the ensemble mean. The relative standard deviation is the same as the global mean even though the absolute standard deviation is higher. The ensemble mean for reflected shortwave radiation is 94.8 Wm^{-2} with a 1-sigma of 4.1 Wm^{-2} or 4.3% relative to the ensemble mean. The relative standard deviation is slightly larger than those of the global mean, indicating more differences between datasets in the tropics. The absolute standard deviation in the shortwave is more than 5 times as larger as those in the longwave. The relative net flux differences among datasets are actually smaller for the tropical mean due to the large tropical mean fluxes. The ensemble mean for net downward radiation is 58.9 Wm^{-2} with a 1-sigma of 4.4 Wm^{-2} or 7.5% relative to the ensemble mean. This large absolute standard deviation in net flux is driven mostly by the large standard deviation in reflected shortwave flux. The results for the clear-sky cases are very similar to the all-sky results with the majority of the differences driven by the differences in clear-sky shortwave flux. These tropical mean results are very consistent with the findings from the global mean analysis.

Table 3.3.6: *Same as Table 3.3.5; but for tropical mean (20°N to 20°S) climatology.*

Parameter	Multi-dataset ensemble Mean	Absolute Standard Deviation (1-σ)	Relative Standard Deviation (1-σ)	Range (Min, Max)
Solar Incoming	409.4	0.7	0.2%	(408.1, 410.0)
Longwave	255.7	2.2	0.8%	(253.3, 259.3)
Shortwave	94.8	4.1	4.3%	(91.0, 101.1)
Net	58.9	4.4	7.5%	(52.7, 63.4)
Clear Longwave	287.9	2.1	0.7%	(284.8, 290.6)
Clear Shortwave	47.8	2.7	5.6%	(45.7, 52.8)
Clear Net	73.5	3.7	5.1%	(68.4, 76.8)

d) Deseasonalized monthly mean time series analysis

Figure 3.3.6 shows deseasonalized monthly mean global average and tropical average time series of earth radiation budget component during the 4-year CERES period. The CERES-based time series tends to have less variability over time than the ISCCP-based time series. In addition, these figures also indicate a calibration shift in the ISCCP time series around 2001 due to changes in TOVS sounder analysis method. *Table 3.3.7* summarizes these results in term of 1-sigma variability of the time series. It can be seen from the table that ISCCP-based datasets for this period is 1.2 to 4 times more variability than the CERES-based datasets.

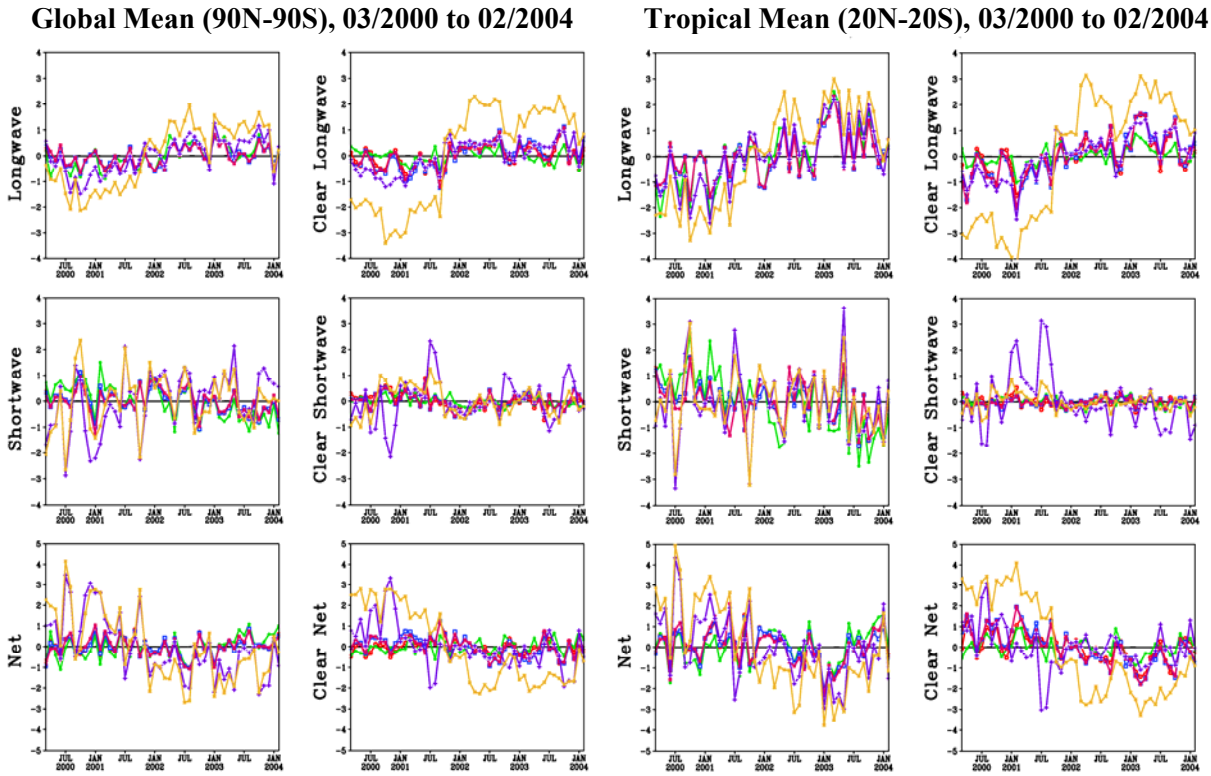

Figure 3.3.6: *Deseasonalized time series of global mean (90N - 90S, left set of six figures) and tropical mean (20N - 20S, right set of six figures) of TOA fluxes for the period from March 2000 to February 2004 for CERES EBAF (dark red), CERES ERBE-like (green), CERES SRBAVG-GEO (blue), CERES SRBAVG-NonGEO (light red), GEWEX SRB (purple), and ISCCP FD (yellow) dataset.*

Table 3.3.7: *Variability (1-Sigma) of global (90N to 90S) and tropical (20N to 20S) mean deseasonalized time series (March 2000 to February 2004) from each of the six datasets*

	Global Mean (90N to 90S)					
	LW	**SW**	**Net**	**CLW**	**CSW**	**Cnet**
CERES-EBAF	0.4	0.5	0.5	0.4	0.3	0.4
CERES ERBE-like	0.5	0.7	0.6	0.3	0.2	0.4
CERES SRBAVG-GEO	0.4	0.5	0.5	0.5	0.3	0.5
CERES SRBAVG-NonGEO	0.4	0.5	0.5	0.5	0.3	0.5
GEWEX SRB	0.7	1.2	1.5	0.6	0.8	1.1
ISCCP FD	1.2	1.1	1.7	1.9	0.6	1.8
	Tropical Mean (20N to 20S)					
	LW	**SW**	**Net**	**CLW**	**CSW**	**Cnet**
CERES-EBAF	0.9	0.8	0.8	0.8	0.2	0.7
CERES ERBE-like	1.1	1.2	0.9	0.4	0.2	0.4
CERES SRBAVG-GEO	0.9	0.8	0.8	0.8	0.2	0.9
CERES SRBAVG-NonGEO	0.9	0.8	0.9	0.8	0.2	0.9
GEWEX SRB	1.2	1.3	1.6	0.9	1.1	1.1
ISCCP FD	1.8	1.2	2.1	2.4	0.3	2.4

3.3.5: ERBE and CERES differences

The left panel of *Figure 3.3.7* shows a simple tropical mean monthly mean time series analysis of all available longwave radiation data from 1979 to 2005. One thing that is striking in this figure is that there is a level jump between the older (i.e., ERBE, Nimbus-7) and newer (i.e., ScaRaB and CERES) broadband instruments records. Fortunately for all-sky longwave radiation, there were enough overlapping data records between each pair of these broadband instruments to allow cross-calibration analysis. The calibration difference between ERBE and CERES for tropical mean longwave is on the order of 4 Wm^{-2}. The right panel shows the same figure after the longwave calibration differences were removed from all broadband instruments. In addition, the new records are tied to the CERES data record on the absolute scale. It can be seen that the longwave broadband records are now consistent with the UMD/NOAA HIRS OLR. There are clearly some absolute calibration differences between the broadband records and those from the ISCCP FD and GEWEX SRB record. *Figure 3.3.7* also shows the level jump in the ISCCP-FD data record in 2001 due to change in TOVS analysis method. This will need to be addressed in the future reprocessing of the ISCCP FD dataset. We currently do not have enough overlapping shortwave data records to perform a robust cross-calibration analysis between the ERBE and the CERES data. However, some simple climatological comparisons suggest that the shortwave record is not affected by calibration issues. More analyses are needed to examine this issue in the future.

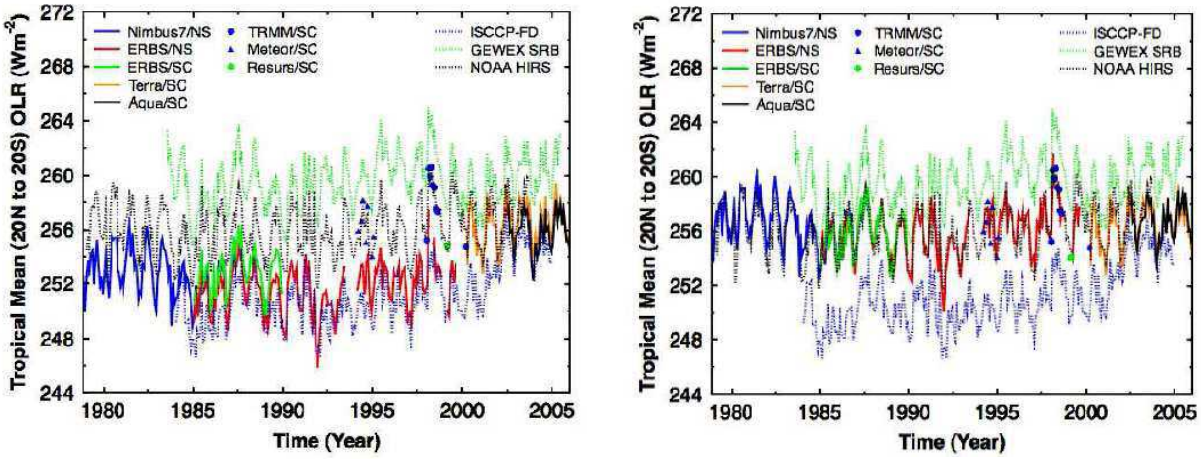

Figure 3.3.7: *Tropical mean (20N to 20S) all-sky longwave flux time series from 1978 to 2005 before (left) and after (right) moving broadband instrument calibration differences.*

3.3.6: Summary

Comparisons of the TOA radiation budget dataset in the GEWEX-RFA archive for the period from CERES period (March 2000 to February 2004) and the ERBE period (February 1985 to January 1989) were performed. Regional maps were compared. While these datasets show good agreement for the longwave flux, they have significant disagreement for both the shortwave and net flux. Comparisons of the zonal mean profile with respect to ERBE Scanner and CERES Scanner period were performed to examine the zonal mean differences among datasets. Multi-dataset ensemble means for each earth radiation budget variable were constructed for each of these periods for large area mean comparisons. Global mean and tropical mean statistics are used to summarize the final findings. These datasets seems to agree very well for incoming solar

radiation with a relative standard deviation of 0.2-0.3% (with respect to the ensemble mean) for both global and tropical mean. They also agree well for the all-sky longwave radiation with a relative standard deviation of 0.8-1.3% for both global and tropical mean. The six datasets, however, did not agree well for both the all-sky shortwave and the all-sky net radiation. In the all-sky shortwave, the relative standard deviation is 3.2% for the global mean and 4.3-5.8% for the tropical mean. The datasets disagree more in the tropics. The all-sky net flux differences between datasets are driven in a large part by the differences in the shortwave flux. The relative standard deviation is near 100% for the global mean and 7.5-10%% for the tropical mean. The differences in the clear-sky fluxes are as large as or larger than the all-sky fluxes. Since the differences in the net radiation are driven mostly by the differences in shortwave flux, it is important that future efforts be spent on refining the shortwave component (both all-sky and clear-sky) of ERB in order to decrease the differences among datasets. Tropical mean longwave time series analysis also yields interesting results in regard to older and newer broadband instrument differences. This calibration difference must be removed before meaningful time series analysis can be performed.

3.4: Comparisons of top-of-atmosphere earth radiation budget during ERBE and CERES period.

Part II: Climatological Annual Mean Cycle Comparisons (L. Hinkelman)

3.4.1: Introduction

Annual cycle of radiation is a fundamental feature of the Earth climate system. Comparisons of this radiative flux cycle will provide useful information about the state of the radiation datasets in the GEWEX-RFA archive. This section will analyze the TOA radiative flux annual cycle.

3.4.2: Data Description and analysis Method

The input to this section consisted of time series of all-sky and clear-sky monthly mean fluxes averaged over the global and tropical (20°S-20°N) latitudes. Several data providers submitted time series data directly to the Flux Assessment archive (EBAF, ERBE-like, SRBAVG-GEO, and SRBAVG-nonGEO from CERES, GEWEX SRB, and ERBS910). For the remaining data sets (ISCCP-FD, FORTH, U. Maryland, and ERBE scanner), monthly TOA flux data at 2.5º resolution was supplied. For these data sets, global and tropical mean time series were computed from the global map data using equal area weighting. In constructing these time series, we required a minimum of 98% of the area in the averaging region to be available in a given month in order to produce a valid data sample. Time series were created for the ten variables listed in *Tables 3.4.1* for both all-sky and clear-sky fluxes. If a given variable was not included in the archive for a particular data set, the corresponding time series was produced from the related variables, if possible (e.g., ASWNET from ASWUP and ASWDN). The time series available for each data set at the conclusion of this process are listed in *Tables 3.4.1*. Note that many of these data sets provide values for every grid box regardless of whether a corresponding measurement was available (i.e., a clear-sky value even when the grid box was overcast and vice versa). However, the CERES products (EBAF, ERBE-like, SRBAVG-GEO, and SRBAVG-nonGEO) only include actual measured values, so the regional means from these products include filled data. The FORTH data product includes shortwave variables for only 60°S-60°N, so only tropical means were included for this data set in the analysis. Only tropical averages were available for all ERBE scanner variables. Note that the product referred to as "ERBE scanner" here consists of data from the ERBE instrument on the Earth Radiation Budget Satellite (ERBS) alone while the product "ERBS910" is derived from a combination of the data collected by the ERBE scanners that flew on ERBS, NOAA-9, and NOAA-10.

Mean annual cycles were computed for each data set, parameter, and region over two time periods, the "ERBE period" (defined as February 1985 – January 1989) and the "CERES period" (March 2000 – February 2004.) At least three valid monthly mean values from the four-year period were available in every case. The mean and standard deviation for each month over all available data sets was then computed. The mean over all data sets is termed the composite annual cycle in this study. Annual cycles in terms of monthly deviations from the overall mean value of the parameter for a given data set, region, and time period, termed anomaly annual cycles, were then computed. The annual cycles for each data set and their mean (composite) were compared on a monthly basis. Statistics describing the variability of the monthly cycles

were also computed. The complete set of annual cycle results (plots and tables) is given in the appendix at the end of this report. A short summary of the major results is given below.

Table 3.4.1. *Data sets and their variables (all-sky and clear-sky fluxes) used in this study. G = global, T = tropical (20°S-20°N).*

Data Set	All-sky Fluxes					Clear-sky Fluxes				
	ASW DN	**ASW UP**	**ASW NET**	**ALW UP**	**ATOT NET**	**CSW DN**	**CSW UP**	**CSW NET**	**CLW UP**	**CTOT NET**
ISCCP	G,T	G,T	G,T	G,T	G,T	G,T	G,T	G,T	G,T	G,T
CERES EBAF*	G,T	G,T	G,T	G,T	G,T	G,T	G,T	G,T	G,T	G,T
GEWEX SRB	G,T	G,T	G,T	G,T	G,T	G,T	G,T	G,T	G,T	G,T
ERBE-LIKE*	G,T	G,T	G,T	G,T	G,T	G,T	G,T	G,T	G,T	G,T
ERBS910**	G,T	G,T	G,T	G,T	G,T	G,T	G,T	G,T	G,T	G,T
FORTH	G,T	T	T	G,T	T					
ERBE Scanner**	T	T	T	T	T	T	T	T		
HIRS				G,T						
U. Maryland	G,T	G,T	G,T							
SRBAVG-GEO*	G,T	G,T	G,T	G,T	G,T	G,T	G,T	G,T	G,T	G,T
SRBAVG-nonGEO*	G,T	G,T	G,T	G,T	G,T	G,T	G,T	G,T	G,T	G,T

* CERES time period (3/2000-2/2004) only. ** ERBE time period (1/1985-12/1989) only.

3.4.3: Statistical Results

The overall variability among the annual cycles from different satellite TOA products can be summarized most easily using the statistics of Tables. The most important variable for this assessment is the range of values provided by the different satellite flux products. Agreement is best for the global mean shortwave downwelling flux (given in *Table 3.4.2*) – the maximum standard deviation over all conditions and time periods for this variable is 0.2 Wm^{-2}. This is to be expected, since TOA downwelling shortwave is always assumed based on earlier, separate measurements. Nearly all of the other variables, the standard deviations of the monthly anomalies range between 0.2 and 1.0 Wm^{-2}. For a few individual variables and months, the standard deviations are greater, but still only as high as 1.6 Wm^{-2}. The only exception is the clear-sky total net flux during the ERBE time period with a standard deviation of 2.2 Wm^{-2}.

Other generalizations can be made from the statistical results. The first is that, during every time period and sky condition, the variable for which the data products differ most is the total net flux (shown in *Table 3.4.3*). This indicates that, like the annual cycles themselves, the deviations for the net shortwave flux and the outgoing longwave flux are opposite in sign, so that they augment rather than cancel each other. It is also of note that the global mean clear-sky fluxes during the ERBE time period have the greatest standard deviations of all the time, space, and sky condition groupings. Each of the ERBE period global mean clear-sky flux variables (except the shortwave down) has a maximum monthly standard deviation greater than 1.0 Wm^{-2}. This is surprising, given that clear-sky fluxes are typically thought to be easier to estimate than all-sky fluxes; in fact, the clear sky fluxes are usually more dependent on ancillary information than the all-sky fluxes, even for the directly measured products.

Relative standard deviations among the satellite data products depend on the mean magnitude of each variable as well as the size of the standard deviation. Nevertheless, most of the relative standard deviation results are similar to those described above. Overall, relative standard deviations are generally less than 1%. The worst relative values occur for the total net fluxes. Values up to 3% occur for the tropical all-sky (ERBE and CERES time periods) and clear-sky (ERBE period alone) total net fluxes. Maximum values over 10%, and as high as 41%, are found

for the global mean all-sky and clear-sky total net fluxes (given in *Table 3.4.3 and 3.4.4)* for both the ERBE and CERES periods. The other variable with atypical relative standard deviation values is the global mean clear-sky upwelling shortwave flux. For both the ERBE and CERES time periods, most monthly standard deviations are between 1% and 2%.

Table 3.4.2: *Global mean annual cycle of ASWDN over all data sets, ERBE and CERES time periods.*

Mon	ERBE period (ASWDN annual means = 341.2 Wm^{-2})						CERES period (ASWDN annual means = 341.2 Wm^{-2})					
	Mean	Anom	Std Dev	Rel StD	Range	N	Mean	Anom	Std Dev	Rel StD	Range	N
1	352.5	11.2	0.0	0.0%	11.1, 11.2	5	352.4	11.2	0.1	0.0%	11.1, 11.4	8
2	349.7	8.4	0.1	0.0%	8.3, 8.5	5	349.6	8.4	0.1	0.0%	8.3, 8.6	8
3	344.8	3.4	0.1	0.0%	3.3, 3.6	5	344.6	3.4	0.1	0.0%	3.3, 3.6	8
4	338.9	-2.4	0.1	0.0%	-2.5, -2.3	5	338.7	-2.4	0.1	0.0%	-2.5, -2.3	8
5	333.9	-7.5	0.1	0.0%	-7.6, -7.4	5	333.6	-7.5	0.1	0.0%	-7.7, -7.4	8
6	330.8	-10.5	0.1	0.0%	-10.6, -10.4	5	330.6	-10.6	0.2	0.1%	-10.8, -10.4	8
7	330.4	-10.9	0.1	0.0%	-11.0, -10.8	5	330.2	-10.9	0.1	0.0%	-11.1, -10.8	8
8	332.9	-8.4	0.1	0.0%	-8.5, -8.3	5	332.7	-8.4	0.1	0.0%	-8.6, -8.3	8
9	337.6	-3.7	0.1	0.0%	-3.9, -3.6	5	337.4	-3.7	0.1	0.0%	-3.8, -3.6	8
10	343.4	2.1	0.1	0.0%	1.9, 2.2	5	343.3	2.1	0.1	0.0%	2.0, 2.2	8
11	348.8	7.5	0.1	0.0%	7.4, 7.6	5	348.7	7.5	0.1	0.0%	7.4, 7.7	8
12	352.1	10.8	0.1	0.0%	10.6, 10.9	5	352.1	10.9	0.2	0.1%	10.6, 11.1	8

Note: All values are for monthly mean anomalies from the overall annual average except for the overall monthly means listed in the first column. Relative standard deviations are computed with respect to the corresponding monthly mean. N is number of GEWEX-RFA dataset used in the analysis.

Table 3.4.3: *Same as Table 3.4.2 but for global mean annual cycle of ATOTNET.*

Mon	ERBE period (ATOTNET annual means = 2.3 Wm^{-2})						CERES period (ATOTNET annual means = 3.1 Wm^{-2})					
	Mean	Anom	Std Dev	Rel StD	Range	N	Mean	Anom	Std Dev	Rel StD	Range	N
1	9.6	7.3	0.3	3.2%	6.9, 7.5	3	10.8	7.6	0.8	7.8%	6.1, 8.6	6
2	11.2	8.9	0.9	8.4%	7.9, 9.7	3	11.5	8.4	0.5	4.7%	7.7, 9.2	6
3	8.7	6.4	0.9	9.8%	5.5, 7.2	3	9.8	6.6	0.7	7.3%	6.0, 8.0	6
4	3.0	0.7	0.5	16.6%	0.2, 1.2	3	4.1	0.9	0.5	11.6%	0.4, 1.8	6
5	-3.6	-5.9	0.4	-9.9%	-6.3, -5.7	3	-3.1	-6.3	0.4	-12.5%	-6.9, -5.8	6
6	-8.4	-10.7	1.0	-12.3%	-11.8, -9.8	3	-7.2	-10.4	0.6	-8.4%	-11.3, -9.6	6
7	-7.0	-9.3	1.6	-22.4%	-10.4, -7.5	3	-6.1	-9.2	0.8	-12.6%	-9.8, -7.7	6
8	-4.5	-6.8	1.0	-22.3%	-7.8, -5.8	3	-2.6	-5.8	0.6	-23.4%	-6.2, -4.5	6
9	0.6	-1.7	0.3	41.7%	-1.9, -1.4	3	1.8	-1.3	0.3	17.7%	-1.7, -0.8	6
10	4.6	2.2	0.3	6.1%	2.0, 2.5	3	4.7	1.6	0.5	9.9%	1.1, 2.2	6
11	5.7	3.4	0.7	12.0%	2.8, 4.1	3	6.2	3.1	0.8	12.1%	2.1 3.9	6
12	7.8	5.4	0.7	9.0%	4.6, 5.9	3	7.8	4.7	1.2	15.1%	2.8, 5.7	6

Table 3.4.4. *Same as Table 3.4.2 but for global mean annual cycle of CTOTNET.*

Mon	ERBE period (CTOTNET annual means = 22.6 Wm^{-2})						CERES period (CTOTNET annual means = 23.1 Wm^{-2})					
	Mean	Anom	Std Dev	Rel StD	Range	N	Mean	Anom	Std Dev	Rel StD	Range	N
1	34.5	12.0	0.4	1.1%	11.8, 12.4	3	35.6	12.5	0.6	1.8%	11.6, 13.1	6
2	33.9	11.3	1.2	3.7%	10.3, 12.7	3	33.9	10.7	0.6	1.8%	9.9, 11.7	6
3	27.7	5.2	2.0	7.3%	3.9, 7.5	3	28.2	5.1	0.9	3.3%	4.4, 7.0	6
4	19.1	-3.5	1.2	6.3%	-4.6, -2.2	3	20.1	-3.0	0.8	4.0%	-4.0, -1.7	6
5	11.5	-11.1	0.6	5.3%	-11.6, -10.4	3	12.2	-10.9	0.9	7.4%	-11.7, -9.2	6
6	9.0	-13.6	2.1	23.9%	-15.8, -11.5	3	9.7	-13.5	0.7	7.2%	-14.7, -12.6	6
7	11.3	-11.3	2.2	19.3%	-13.8, -9.8	3	11.8	-11.3	1.1	9.7%	-12.8, -9.3	6
8	15.1	-7.5	1.6	10.5%	-8.9, -5.8	3	15.9	-7.3	0.9	5.9%	-8.7, -5.8	6
9	20.6	-2.0	0.7	3.4%	-2.7, -1.4	3	20.9	-2.2	0.5	2.6%	-3.0, -1.3	6
10	26.4	3.8	1.2	4.4%	2.0, 5.0	3	25.9	2.8	0.5	1.9%	2.3, 3.6	6
11	29.2	6.7	0.6	2.2%	6.2, 7.4	3	29.8	6.6	0.4	1.3%	6.1, 6.9	6
12	32.5	10.0	1.0	3.0%	9.4, 11.1	3	33.6	10.4	0.8	2.3%	9.1, 11.1	6

3.4.4: Qualitative Results

Inspection of the comparison plots reveals further information about the level of agreement among the satellite TOA flux products. The ERBE period global mean clear-sky fluxes which, taken together, have the highest standard deviations of all the time, space, and sky condition groupings, are strongly influenced by the limited number of data sets that include these fluxes. As indicated in *Table 3.4.1,* only the ERBS910, ISCCP-FD, and GEWEX SRB products provide these variables. Thus any difference in even one of these products greatly affects the standard deviation. Plots for these variables are shown with the global clear-sky data for the CERES time period in *Figures 3.4.1*. Here we see that the full range of monthly mean values is quite similar for the two time periods. However, in most cases, at least three of the five CERES time period products cluster together, lowering the overall standard deviation. This is to be expected, given that three of the CERES period products (SRBAVG-GEO, SRBAVG-nonGEO, and EBAF) are based on similar algorithms. ERBS910, ISCCP-FD, and GEWEX SRB are also the only products to provide all of the variables needed to compute the global mean all-sky total net flux for the ERBE time period, thus this variable has the largest standard deviations of all the global mean fluxes for this period. In this particular case, the GEWEX SRB and ISCCP-FD values fall on opposite sides of the composite while the ERBS910 follows this line closely. This is surprising, since the ISCCP-FD and GEWEX SRB products are both based on ISCCP cloud and radiance data. This spread arises because the magnitude of the ISCCP-FD outgoing longwave flux annual cycle is smaller than that of all the other available data products while the magnitude of the net shortwave flux from the SRB is large.

Several other differences among the satellite records are worth noting. One is that the ISCCP-FD outgoing longwave flux (OLR) deviates from the others in nearly all instances. The ISCCP-FD OLR annual cycle has a lower magnitude for both the all-sky and clear-sky global mean fluxes, while its magnitude is larger for the topical mean clear-sky fluxes. For the all-sky tropical mean fluxes, it is low only during the Northern Hemisphere summer. The global mean clear-sky outward longwave fluxes from the Terra-based CERES ERBELIKE product are also smaller than average during the Northern Hemisphere summer, while the magnitude of the all-sky annual cycles from FORTH, and to some extent HIRS, are slightly high. Thus a number of discrepancies are noted among the outward longwave fluxes from the various satellite products. Finally, the annual cycles of both the GEWEX SRB and CERES ERBELIKE global mean clear-

sky upward shortwave fluxes during the CERES period differ significantly from the rest of the products.

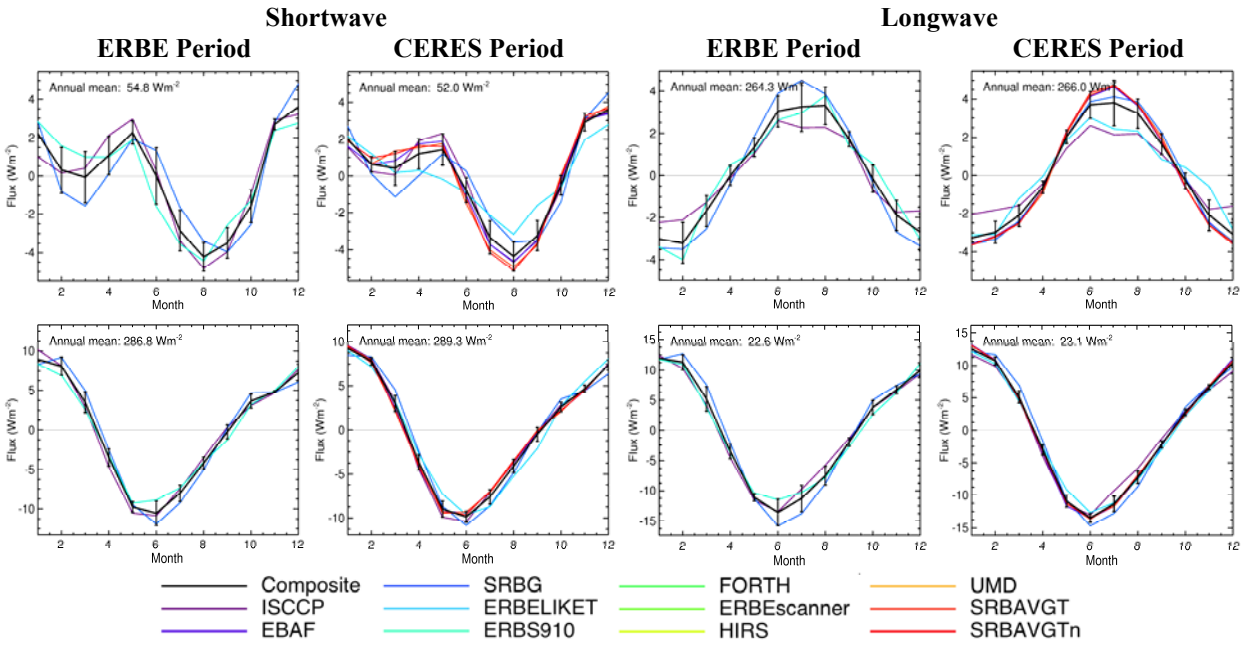

Figure 3.4.1. *Global mean annual cycles for clear-sky shortwave (CSWUP: top Left, CSWNET: bottom left) and clear-sky longwave (CLWUP: top right, CLWNET: bottom right) parameters over the ERBE and CERES time periods shown as deviations from the corresponding annual means. Error bars indicate +/- one standard deviation.*

3.4.5: Summary

This section describes an analysis of top-of-atmosphere radiative flux annual cycle data from a number of satellite data products. The analysis examined global and tropical (20°S-20°N) mean annual cycles averaged over the ERBE (February 1985 – January 1989) and CERES (March 2000 – February 2004) time periods. In general, the annual cycles *from the different data* products are quite similar, but several exceptions were noted. The typical level of agreement among the participating data sets for individual months fell in the range of 0.2 to 1.0 Wm^{-2}. The worst agreement was found for global mean clear-sky fluxes during the ERBE period. This was likely due to the fact that only three satellite products included values for these parameters. While differences among the outgoing longwave fluxes from the various products were noted, on average, the standard deviations of the monthly means for this term were not significantly larger than those from the other basic flux variables (upward and downward shortwave fluxes). Since the largest differences were found among the total net (shortwave + longwave) fluxes, we can only recommend that data providers attempt to improve the accuracy of estimates for all three basic flux components.

3.5: Anomalies in data sets of ISCCP FD, GEWEX SRB, ERBE/ERBS & CERES (E. Raschke and S. Kinne)

3.5.1: Introduction

Even though the components of the radiation budget at the top of the atmosphere (TOA) can be derived readily from direct satellite-based measurements, errors sources introduced during the data construction phase can still affect the final quality of these data product. For example, the measurements of the broadband radiances leaving the earth to space can be made with very high accuracy and stability. However, the conversion from radiances to hemispheric radiant flux densities, leaving a finite and defined area of the Earth to space, still requires several computational steps with inclusion of ancillary data which describe the complete 3-D radiative states of the atmosphere from the surface to TOA (e.g., clouds, gaseous concentrations, and aerosols). Errors in these ancillary data, in additions to errors caused by insufficient time-space sampling and orography of continents, can find their ways into radiation data product.

In this section, we compare the radiative fluxes from the CERES-SRBAVG-GEO (March 2000 to February 2004) and the ERBE/ERBS scanner product (January 1985 to December 1988) which are based on TOA measurements with those calculated from the ISCCP FD and GEWEX SRB project (January 1984 to December 2004) from climate (ancillary) data only. These projects and their data sets are briefly described in *Appendix A*. Comparisons of ISCCP FD and GEWEX SRB TOA fluxes and their Cloud Radiative Effect (CRE) with the same quantities of ERBE/ERBS and CERES are done here assuming that the latter ones, basing directly on satellite measurements, could be used as a baseline. Details on "clear-sky" fluxes are shown in *Appendix D.3.5* for supplementary data to Chapter 3.5.

3.5.2: Errors in ancillary data used in ISCCP cloud retrievals and radiation computations

Ancillary data are used in the ISCCP project to extract cloud properties from narrowband radiances. The same ancillary data and the ISCCP retrieved clouds properties are used again in ISCCP-FD project to compute radiation fields. The GEWEX SRB project uses different ancillary information for the atmospheric and surface properties but incorporates some ISCCP clouds properties and/or radiances into its radiation computations. Thus, errors in ancillary data can directly affects the radiation computations of these two data products. The documentations on the ISCCP website (*http://isccp.giss.nasa.gov*) has identified various sources of systematic uncertainties in ancillary data used to extract information on clouds and surface properties from satellite data. We show here four such examples.

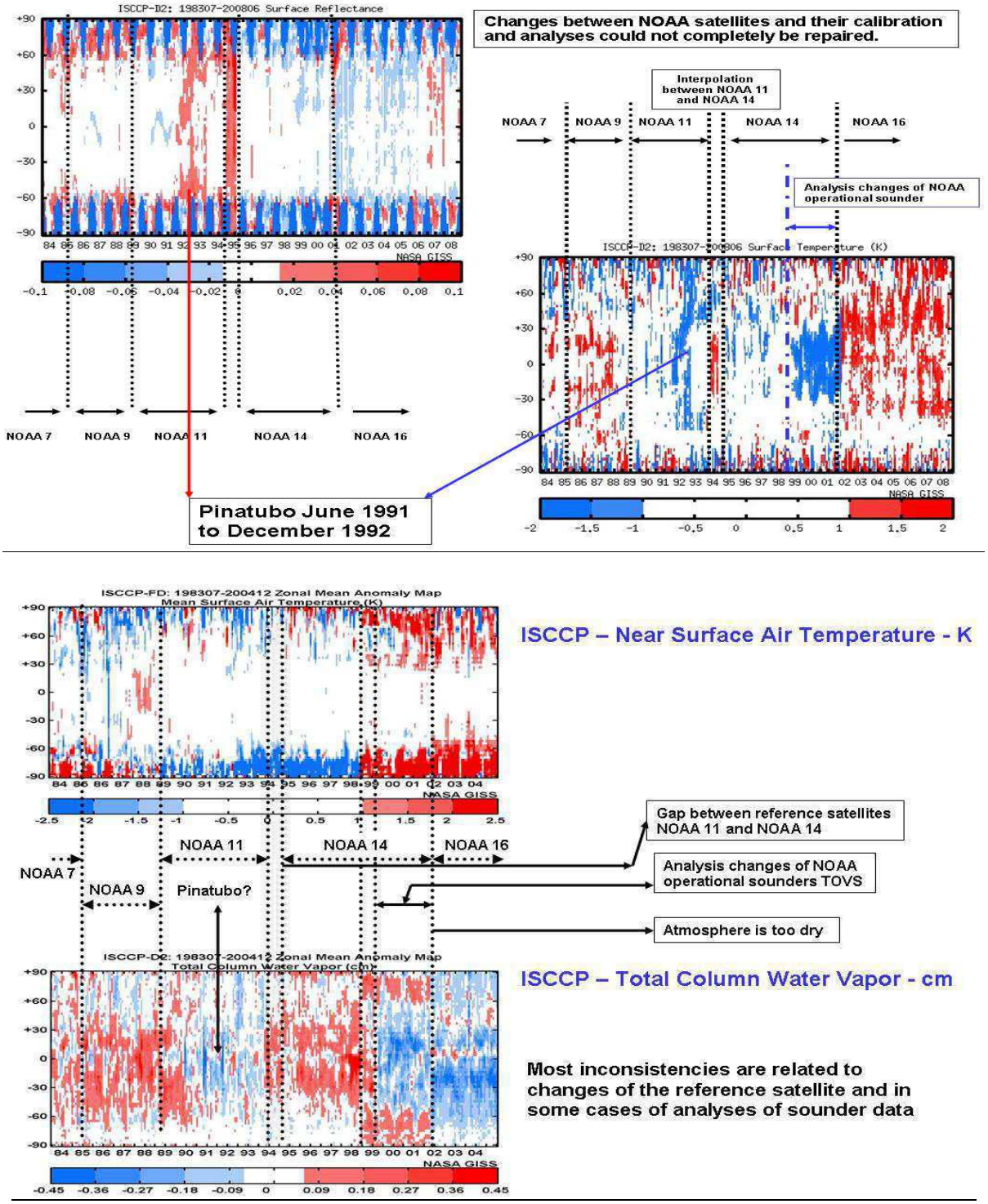

Figure 3.5.1: *Deseasonalised (with respect to the period 1984-2008) anomalies of zonal averages of the surface reflectance (upper left), the surface skin temperature (lower left), near surface air temperature (upper right), and total atmospheric column water vapor (lower right). Diagrams are from* [*http://isccp.giss.nasa.gov*](http://isccp.giss.nasa.gov)*.*

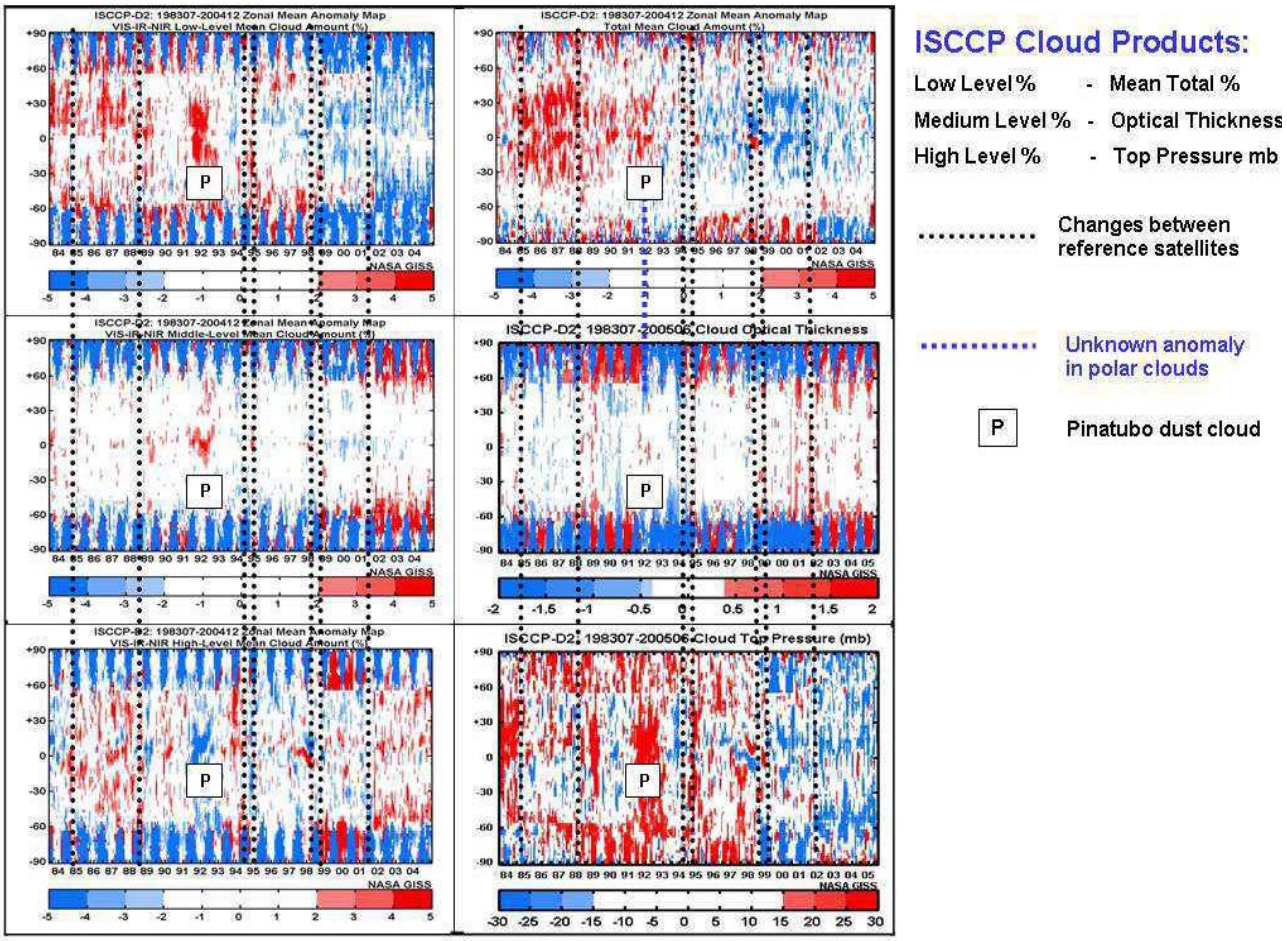

Figure 3.5.2: *Deseasonalised anomalies of the ISCCP cloud amounts: Left, from top downward: low, medium and high level; right, from top downward: total cloud amount, cloud optical thickness and cloud top pressure (diagrams from http://isccp.giss.nasa.gov). Note, that ISCCP identifies the Pinatubo aerosols as a contribution to low level clouds and reduces the amount of high clouds accordingly.*

Figures 3.5.1 and 3.5.2 show the deseasonalised monthly zonal average anomalies of surface reflectance, surface (skin) temperature, lower tropospheric air temperature and total column water vapor content of the atmosphere. These anomalies show structures which can be related to changes in both the "reference" satellite and the operational analyses of satellite retrieval of atmospheric properties. The amplitudes of these systematic errors are often very small; but are large enough to affect the interpretation of the final results. In addition to these artifacts, natural anomalies are also visible in the figures (e.g. the influence of the Pinatubo aerosols from 1992 to 1994 and the shift in cloud patterns during 1998 El-Nino event). For example, visible artifacts can be seen as a sudden rise in surface temperature during the fall 2001 preceded by a systematic drop in surface temperature in 1998 while air temperatures continued to rise. Over the Polar Regions a sharp rise of the air temperature and water vapor occurs in 1998, where the latter quantity suddenly decreases at all latitudes during fall 2001. Because these four ancillary data sets are used in the ISCCP algorithms to estimates cloud parameters, the ISCCP cloud fields (shown in *Figure 3.5.2*) also exhibit similar systematic patterns. Since the ISCCP cloud properties are used in both the ISCCP-FD and GEWEX SRB algorithm to compute TOA radiative fluxes, these systematic anomalies in ancillary data can enter directly into the radiation

products of both projects. The occurrences of these systematic errors encourage a new end-to-end analysis of all datasets.

3.5.2.1: Regional anomalies in fields of incoming solar radiation at TOA

As we have already mentioned in *Chapter 2*, the computational procedures for distributing the incoming parallel beams of solar irradiance over the spherical Earth can act as a basic error source if these procedures are not handled carefully. As an example we show here seasonal averages of the incoming radiation computed for both January 1985 to December 1988 and March 2000 to February 2004. *Figure 3.5.3* shows small differences between regional values of the TOA insolation between ISCCP FD ~~&~~ and GEWEX SRB to ERBE/ERBS and CERES. The ERBE and CERES data in the GEWEX-RFA archive use a solar constant of 1365 Wm^{-2}, while ISCCP FD and GEWEX SRB utilize a slightly higher value of 1367. The differences of ISCCP-FD and GEWEX SRB regional seasonal values to CERES or ERBE/ERBS are large, ranging between about -3.0 (-4.0) and +3.0 (+4.0) Wm^{-2}. They are apparently caused by different increments in space and time for the integration over each segment. These differences can introduce errors in the meridional gradients of TOA solar insolation. In order to make better comparison, we also suggest using the "new" solar constant of 1361 Wm^{-2}, as discussed in *Chapter 2*, for all future computations of TOA insolation.

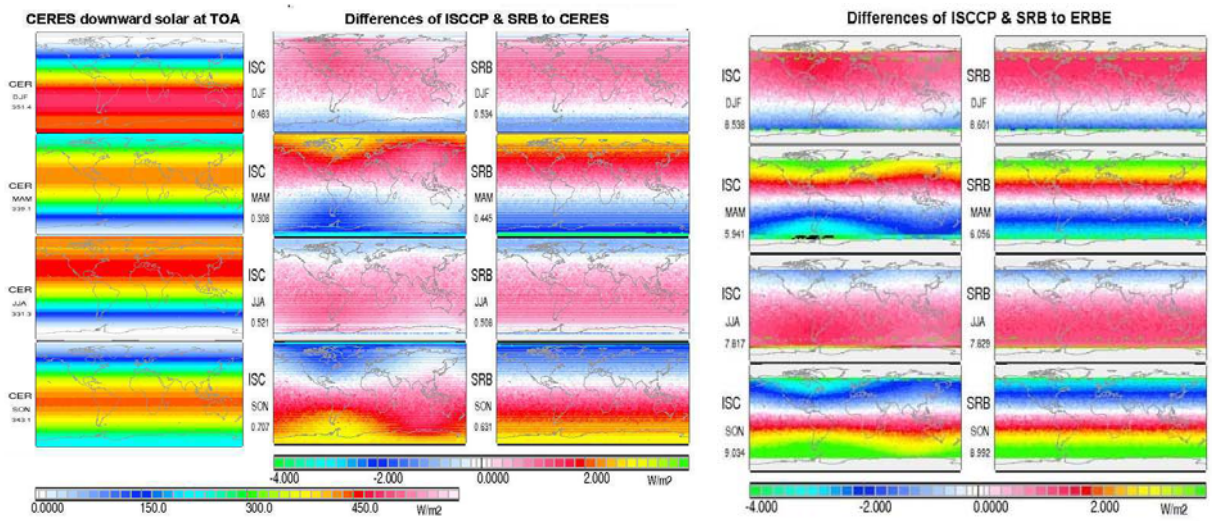

Figure 3.5.3: *Regional seasonal averages of downward solar radiation at TOA. Left – CERES (March 2000 to February 2004); right – ERBE (January 1985 to December 1988). Corresponding values of the "solar constant" are 1367, 1367 and 1365 Wm^{-2} and for ERBE 1365 Wm^{-2}, respectively.*

3.5.3: Time series of upward solar and terrestrial radiation (ISCCP FD vs. GEWEX SRB)

Time series of unique data sets are required to identify and even interpret low-frequency changes in the climate. Can we readily rely on such time series from ISCCP FD and GEWEX SRB? To answer this question, we use deseasonalised zonal anomalies of various radiation fluxes (in Hovmoeller diagrams) to demonstrate the source of time series perturbation by both errors and natural disturbances in the ancillary data. The reproduction of the fluxes and their differences to those of other data sets should help to identify further error sources.

3.5.3.1: All-sky and clear-sky anomalies

Figure 3.5.4 shows deseasonalized all-sky anomalies of TOA albedo and OLR from both ISSCP FD and the GEWEX SRB project. The large systematic patterns found in this figure are similar to those shown in *Figure 3.5.1* and *3.5.2* and support our suspicion that various uncertainties in the ancillary data (see diagrams above) have penetrated into final TOA radiation results. This is in contrast to the CERES anomalies (not shown here) which appear to be distributed randomly with small amplitudes. The ISCCP FD and GEWEX SRB anomalies caused by the effect of both 1998 El-Nino (near the equator) and a sudden rise of temperatures in the middle of 1998 and in October 2001 are very noticeable in *Figure 3.5.4*. In additions, lower albedo anomalies during the 1998 to 2001 period are also found in both the ISCCP FD and GEWEX SRB data. Are these anomalies real and what causes them?

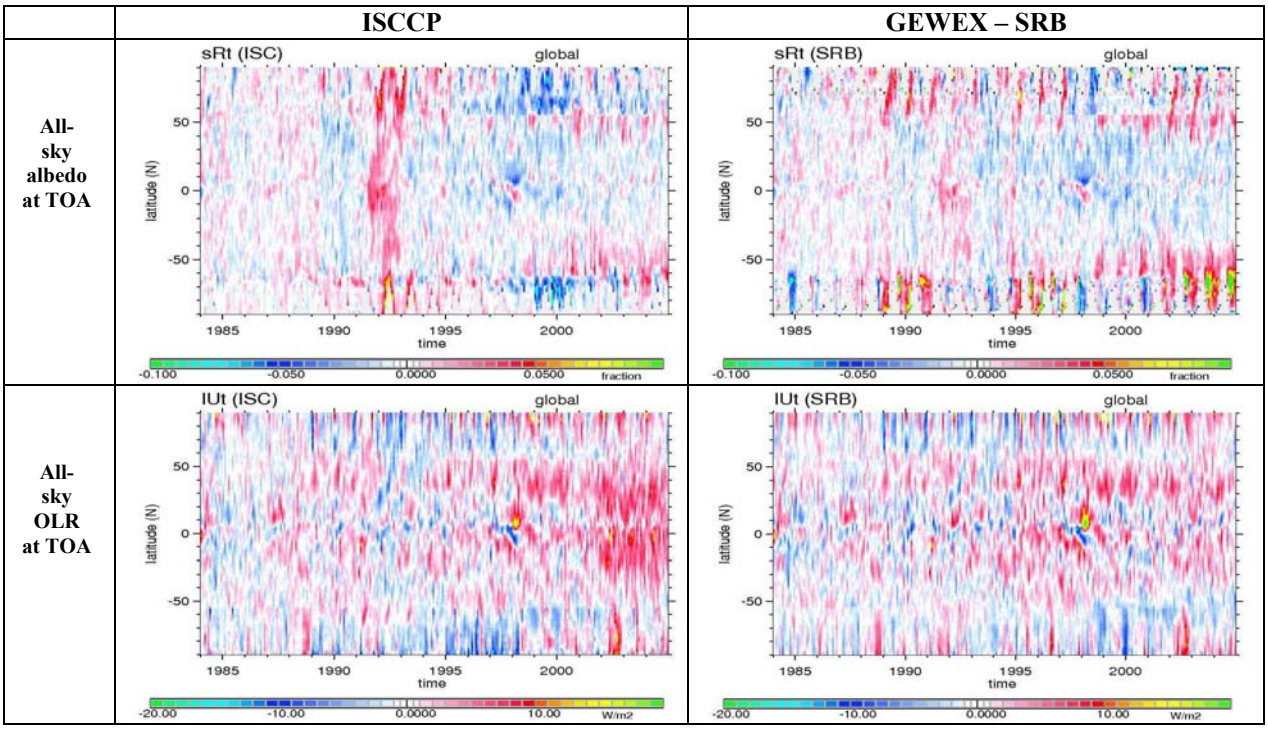

Figure 3.5.4: *Monthly zonal deseasonalised all-sky anomalies of TOA planetary albedo (top panels) and outgoing longwave radiation (OLR: bottom panels) from January 1984 to December 2004 for ISCCP-FD and GEWEX SRB. The reference period covers 4 years from January 1985 to December 1988. ISCCP-FD and GEWEX SRB anomalies show patterns which are due to uncertainties in various ancillary data. Major events occurred in 1985, 1989, 1994-95, 1998 and 2001and affect the pattern in the figure.*

The upward clear-sky solar radiation anomalies (shown *Figure 1 in Appendix D.3.5*) are primarily affected by the surface albedo anomalies. In addition, aerosol anomalies in the atmosphere also modified this quantity by changing the amount of the solar radiation reaching the surface and reflecting back to space. The effect of Pinatubo dust tended to cause a larger clear-sky albedo anomalies in the ISCCP FD data than in the GEWEX SRB data. In addition, the changes in ISCCP FD clear-sky albedo anomalies after 1995 are also smaller than those from the GEWEX SRB data. The upward clear-sky longwave radiation anomalies are dominated by the surface temperature anomalies with some modifications by dust and atmospheric temperature and

water vapor anomalies. In the ISCCP FD results the Pinatubo dust reduces clear-sky OLR anomalies. This is followed by a sudden rise in clear-sky OLR emission in September 2001 due to increase in TOVS temperatures. These patterns also occurred with smaller amplitude in the GEWEX SRB all-sky and clear-sky data. These diagrams show clearly anomalies which are related to those discussed in the previous section. The pattern in GEWEX SRB clear sky diagrams also indicates the influence of Pinatubo aerosols, but it is entirely different during the years after 1995 (even with opposite sign). This is again in contrast to the CERES data which show (1) no clear-sky albedo anomalies between 50° N and 50° S and (2) a small positive clear-sky OLR anomaly after October 2001.

3.5.3.2: Anomalies of the Cloud Radiative Effects (CRE)

Figure 3.5.5 shows deseasonalized anomalies of cloud radiative effect (CRE) on planetary albedo and outgoing longwave radiation (OLR) for both ISCCP FD and GEWEX SRB dataset. The pattern of anomalies for the planetary albedo CRE is quite similar in both data sets, even though they use the ISCCP information about clouds in different ways (ISCCP FD uses both cloud amount and optical thickness whereas GEWEX SRB uses cloud amount but retrieves its own cloud optical thickness from the visible radiances). However the ISCCP FD results for longwave CRE anomalies show a stronger response to the temperature rise after September 2001 than those from the GEWEX SRB data, where the latter uses the same cloud information from ISCCP but different atmospheric temperature data. Most CRE anomalies range between ± 0.10 (or 10%) for planetary albedo and between ± 5 Wm^{-2} for OLR. Systematic patterns in this figure can be traced to events relating to the 1991-1994 Pinatubo aerosols, the 1998 El-Nino and a sudden increase of surface temperatures in October 2001 (see also *Chapter 4.4*).

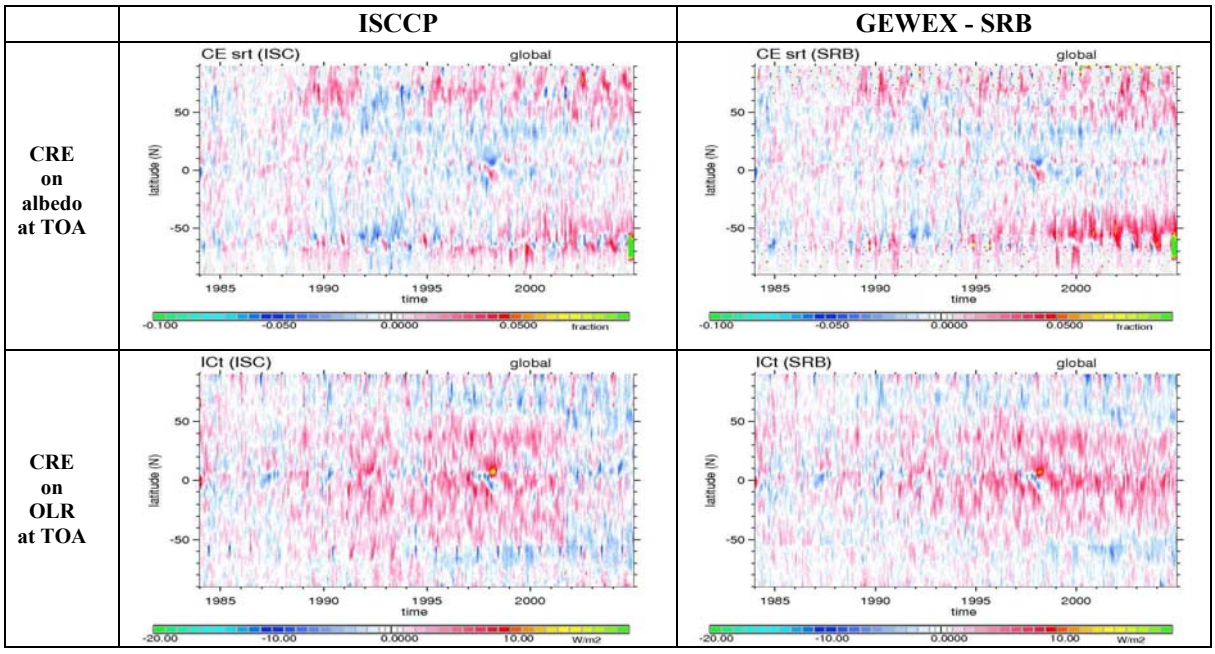

Figure 3.5.5: *Monthly zonal deseasonalised anomalies of the TOA cloud radiative effect (CRE) on the planetary albedo and outgoing longwave radiation (OLR) from January 1984 to December 2004 for ISCCP-FD and GEWEX-SRB. The reference period covers 4 years from January 1985 to December 1988. Changes of satellites occurred in 1985, 1989, 1994-95, 1998 and 2001 and affect the pattern in the figure.*

3.5.3.3: Interannual variability of annual averages (ISCCP FD and GEWEX SRB)

Longer time series of the interannual variability of TOA radiation quantities allow for regional climate change studies. *Figure 3.5.6* show the interannual variations of annual averaged planetary albedo and outgoing longwave radiation from 1984 to 2004. Complementary maps for the clear-sky fluxes and CRE are given in *Figures 2 to 5* in *Appendix D.3.5*. We should keep in mind that most of the structures in the figure are natural in origin, but with large artifacts due to insufficient angular correction of the geostationary data. The changes of patterns with time are dominated by the Pinatubo aerosols (1992 to 1994) and various inconsistencies in ancillary data including those of the surface (see Chapter 4.4 for more discussions).

Clear sky radiation fluxes (given in *Figures 2 & 3* in *Appendix S.3.5*):

While the clear-sky fluxes of ERBE and CERES data are based on a "satellite footprint clear-sky selection technique", those from the ISCCP-FD and GEWEX SRB are computed by removing clouds from the atmosphere while keeping the temperature and moisture fields unaltered. We must distinguish these two types of cloud-free data sets. Type 1 is obtained by formal replacement of all "cloudy" cells in the calculations by no-cloud conditions and Type 2 is obtained ~~with~~ by identifying clear scenes in the satellite data, where all cloud-free elements are sought using statistical technique (i.e., histogram). In most regions this latter technique produces a dryer atmosphere with lower aerosol optical depth than average (e.g. Sohn et al. 2006). Maps of upward and downward solar radiation at clear skies also confirm that "Type 2" clouds are not completely removed.

Interannual deviations of ISCCP FD and GEWEX SRB global averages of the clear-sky planetary albedo from the reference means are extremely small over the oceans (less than 1%). However systematic deviations in regional values can be seen over continents. While Africa and South America become darker by up to 5% after 1995, the Eastern portion of Asia is brightening by a similar magnitude. The Pinatubo aerosols cause a systematic brightening of more than 3%. Since the land surface reflectance retrieved is retrieved by ISCCP ignoring aerosol and corrected in ISCCP FD using a reconstructed aerosol dataset, some of this variability could reflect errors in accounting for aerosols over land.

Cloud radiative effects (see also *Figures 4 & 5* in Appendix S.3.5):

The interannual variability of global averages CRE is very small with ranges of less than 0.7%. However regional anomalies can reach values between about –5% and +7% with a small increase after the year 1995 in both ISCCP-FD and GEWEX SRB data. Regional maps of both datasets also show spurious geostationary artifacts due to the incomplete angular sampling (especially in the shortwave – this feature is smaller in ISCCP FD than in GEWEX SRB).

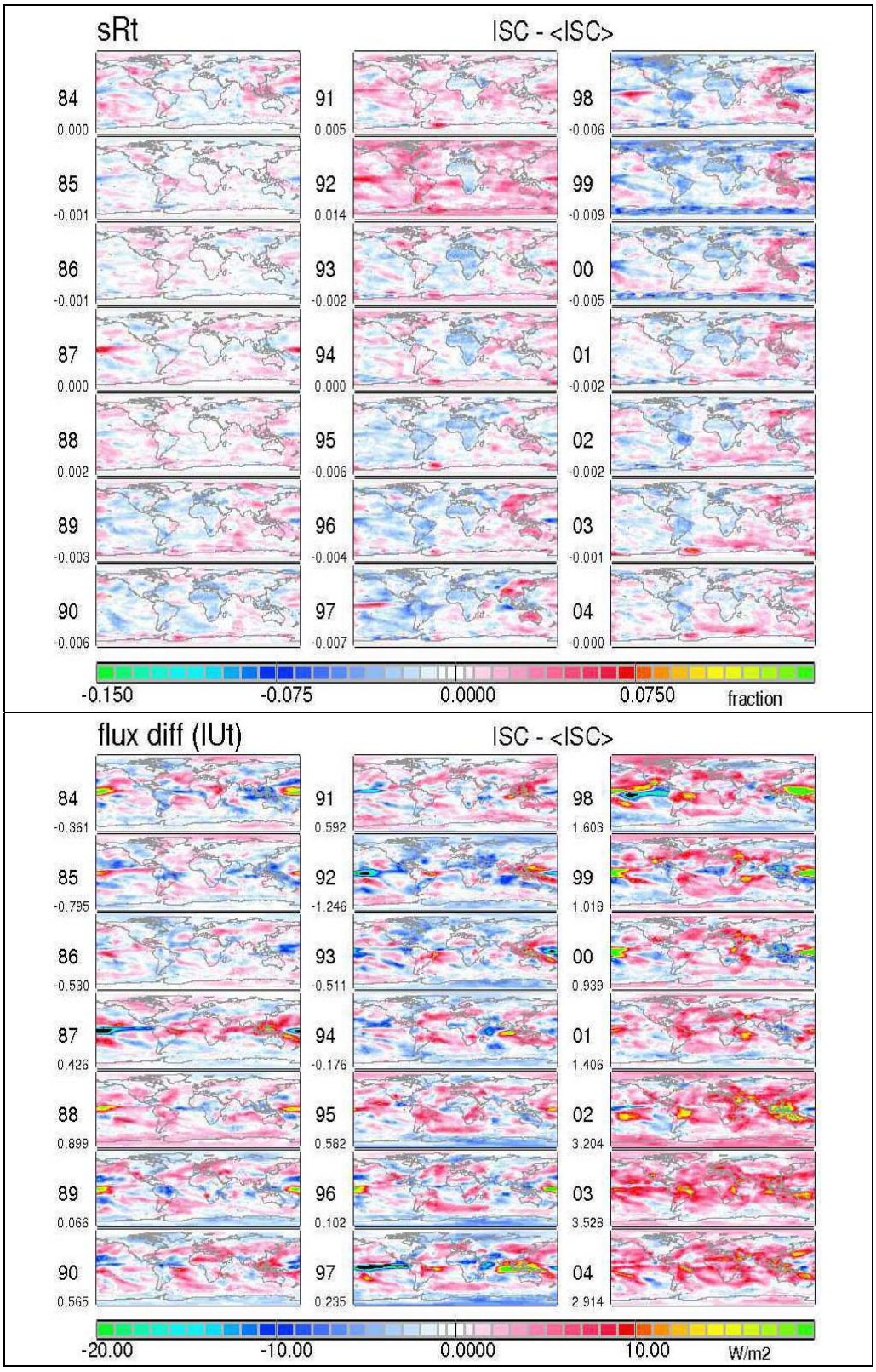

Figure 3.5.6: *Inter-annual variability of annual averages of differences to averages of the reference period 1985 to 1988 of the* ***all-sky planetary albedo*** *(top) and* ***outgoing longwave radiation*** *(bottom) at the TOA.*

3.5.4: Seasonal average comparisons of ISCCP FD and GEWEX SRB data with CERES data

In this section the results for ISCCP FD and GEWEX SRB based entirely or mostly on computations using ancillary data are compared with those of CERES data which are based primarily on direct measurements. Seasonal anomalies of all-sky fluxes and their corresponding CRE from 4-year period (March 2000 to February 2004) are used. Clear-sky results are shown in Appendix D.3.5.

3.5.4.1: All-sky Planetary albedo

In general the ISCCP FD and GEWEX SRB albedo and its corresponding CRE are slightly higher than those of the CERES data (shown in *Figures 3.5.7 and 3.5.8*). The cloud albedoes increase the planetary albedo considerably from about 17 to 32%. Note that over most areas the ISCCP FD albedo is 3 to 6% higher than in those of the CERES and GEWEX SRB data. GEWEX SRB and CERES data are somewhat uncertain over sub-polar areas, where they are affected by snow/ice detection issues or missing shortwave data. ISCCP FD and GEWEX SRB albedo are generally higher than CERES albedo over the ocean. Both products show geostationary satellite artifacts with different magnitudes. Over most continental areas, the albedo values from these datasets are pretty close to each other except for regions over Northern Eurasia. The geostationary satellite artifacts are also visible in the CRE comparisons.

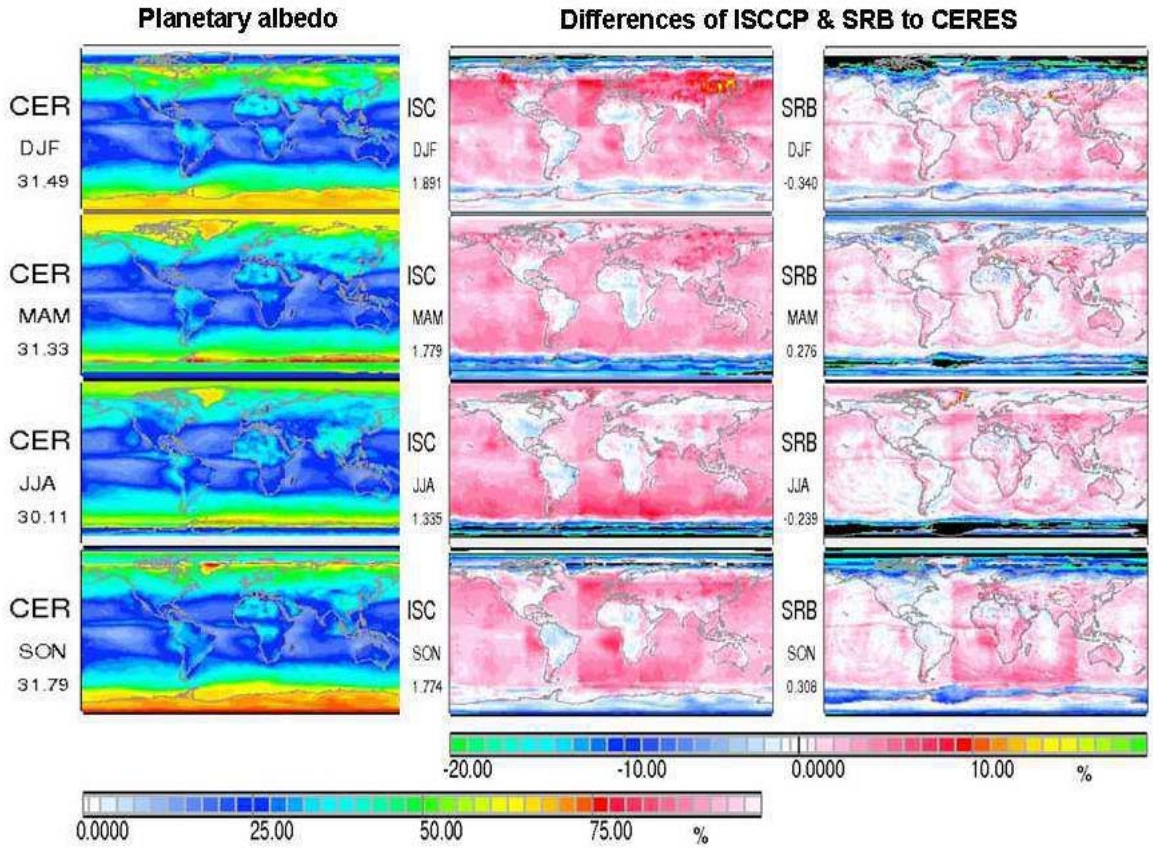

Figure 3.5.7: *Mean seasonal all-sky CERES TOA planetary albedo and their corresponding differences with ISCCP FD & GEWEX SRB data (right) from March 2000 to February 2004. Artifacts are visible in the difference figures.*

Results for clear-sky albedo (shown in *Figure 7* in *Appendix D.3.5*):

While the seasonal global averages of CERES clear-sky albedo data range from 16 to 17.5%, those from the GEWEX SRB and ISCCP FD are systematic higher by 0.9 to 1.8% and 1.4 to 2.7%, respectively. Regional differences between ISCCP FD and CERES, and GEWEX SRB and CERES can be as large as 3 to 5 % over oceans. The regional differences over most continental areas (except central and southern portions of Africa in GEWEX SRB data), however, show ISCCP FD and GEWEX SRB have slightly darker value than the CERES albedo. Larger differences over the sub-polar zones are possibly caused by errors in ice/snow cover and/or missing data issues. ISCCP FD clear sky albedo values are systematically higher than the others.

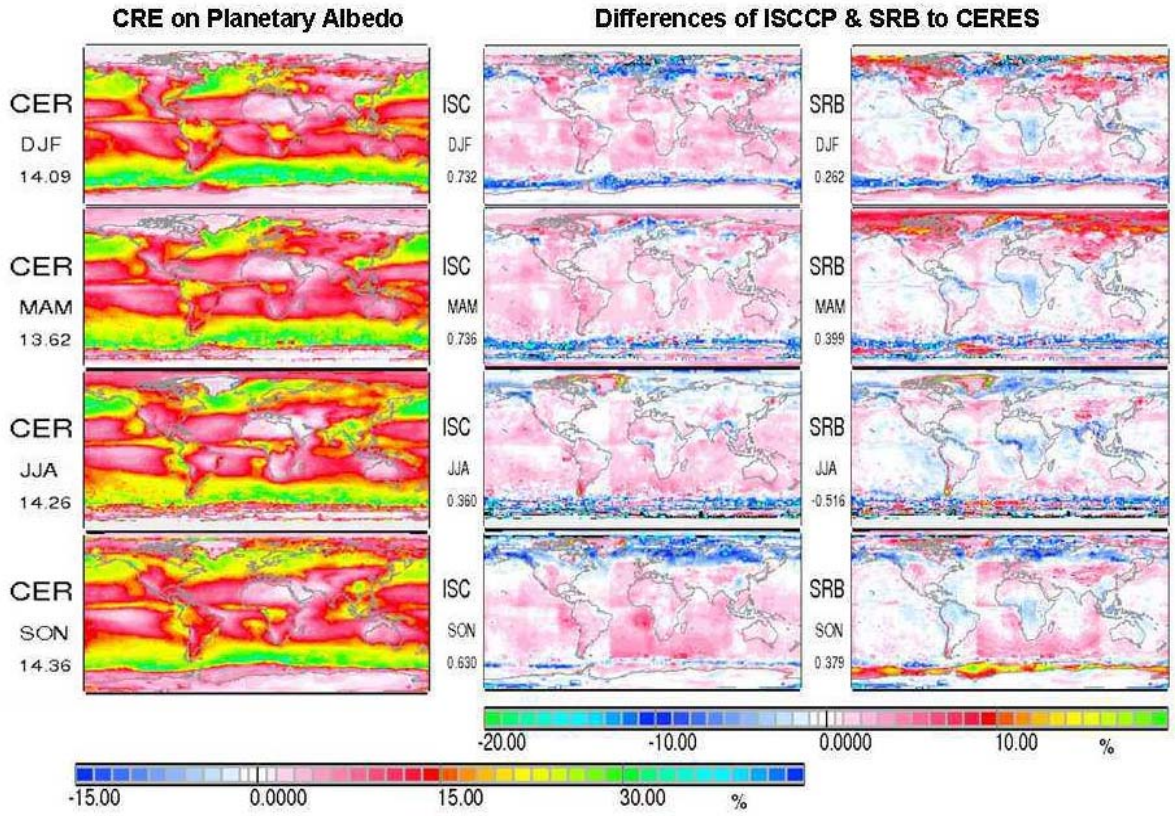

Figure 3.5.8: *Mean Seasonal all-sky CERES TOA CRE on planetary albedo (left) and their corresponding differences (middle and right) with ISCCP FD & GEWEX SRB data from March 2000 to February 2004. CERES-CRE is based on statistically selected cloud-free areas while the CRE from both ISCCP FD and GEWEX SRB is based on radiative transfer computations without clouds.*

3.5.4.2: All-sky outgoing longwave radiation (OLR)

The regional patterns of OLR are dominated by cloud and atmospheric temperatures and to a lesser extent by surface temperature except over dry and partly cloudy regions. Relative to the CERES data, there are significant differences between ISCCP FD and GEWEX SRB values

(shown in *Figure 3.5.9*). For most areas the ISCCP FD OLR are lower than the CERES values indicating issues with lower cloud heights and/or lower cloud temperatures. Largest differences between ISCCP FD and CERES vs. GEWEX SRB and CERES are found over subtropical cloud fields. The flux differences between ISCCP FD/GEWEX SRB and CERES data over the oceans can be related mostly to differing atmospheric temperature-humidity profiles. While ISCCP FD OLR over the oceans is 10 Wm^{-2} colder than the corresponding CERES value, the GEWEX SRB OLR over most areas is warmer than those in the CERES data. In the latter case the differences can reach +20 Wm^{-2} over African deserts and South America. Clouds generally reduce the emission to space. Largest reductions of OLR are found in convective regions with values as high as 80 Wm^{-2}. Relative to the CERES data, this reduction is somewhat smaller in ISCCP FD OLR. In addition, the GEWEX SRB data at higher latitudes are again dominated by geostationary artifacts. The clouds in CERES data and to a larger extent in GEWEX SRB data are exhibiting a smaller CRE (*given in Figure 3.5.10*). Since most cloud fields in ISCCP FD data over the oceans are colder than CERES, this translates to a negative 10-15 Wm^{-2} CRE differences in the figure. This is in contrast to the GEWEX SRB data which has a higher emission (~15-20 Wm^{-2}) in most areas.

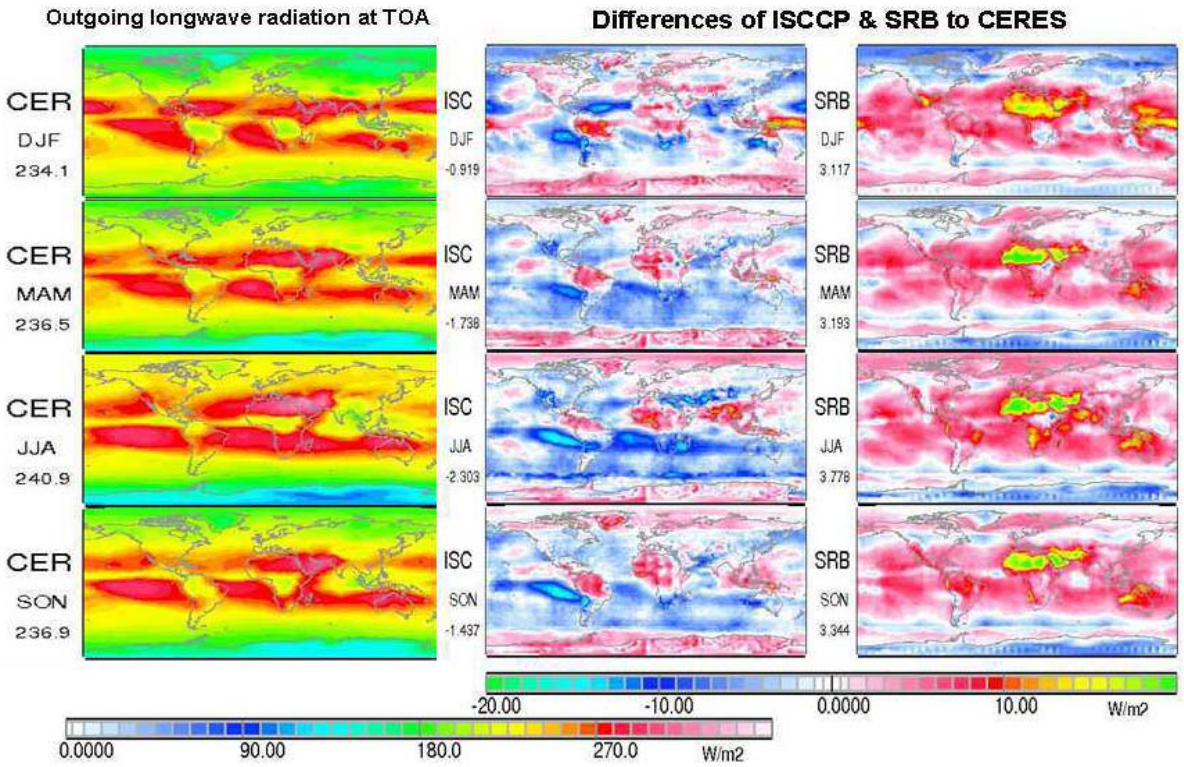

Figure 3.5.9: *Same as Figure 3.5.7 but for all-sky outgoing longwave radiation.*

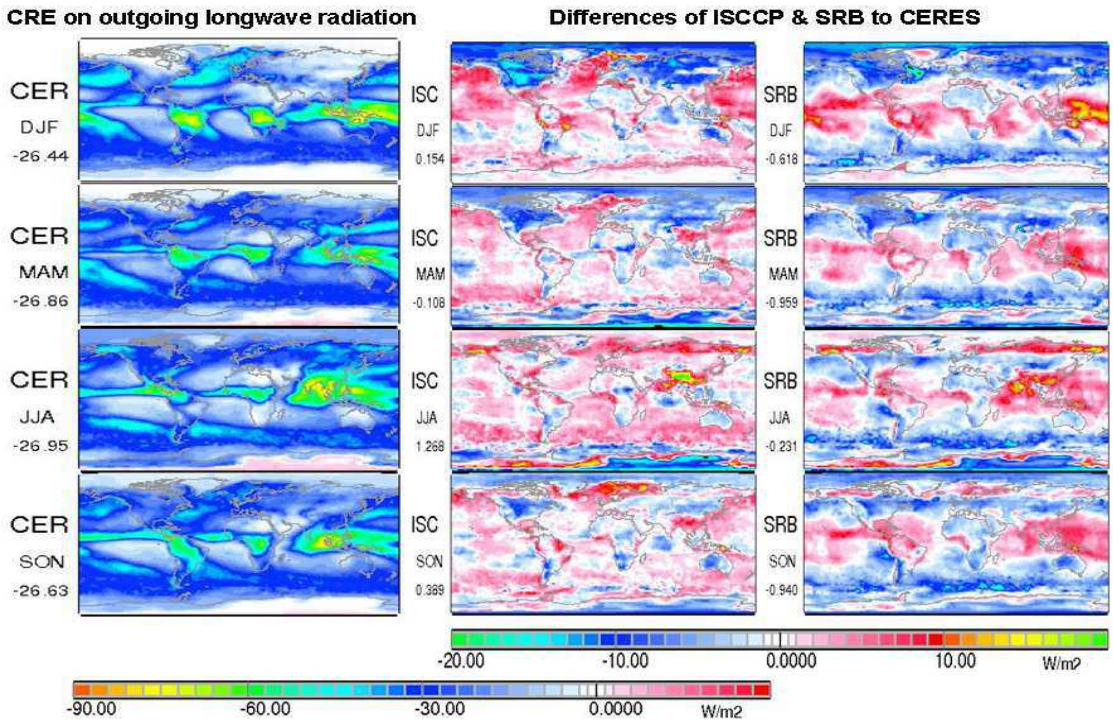

Figure 3.5.10: *Same as Figure 3.5.8 but for longwave cloud radiative effects.*

Clear-sky outgoing longwave radiation (see Figure 8 in Appendix S.3.5)

The clear-sky OLR is dominated by surface skin temperatures and the properties of the gas components in the atmosphere. The fields of differences between ISCCP FD and GEWEX SRB to CERES show patterns which are related to cloud fields indicating that clouds are not completely removed. ISCCP FD values over most low level clouds are smaller by 10 to 15 Wm^{-2}. On the other side those of GEWEX SRB are higher over the same areas and over some continental surfaces by 15 to 20 Wm^{-2}. Small traces of geostationary data artifacts are also visible in the figure which further complicates the interpretation of the results.

3.5.4.3: All-sky total net radiation

During the 4-year period from March 2000 to February 2004, CERES data has an annual average net radiation imbalance of about +6 Wm^{-2} while the same quantity from ISCCP FD and GEWEX SRB data are closer to balance. The difference maps however indicate, that parts of this balance are related to data artifacts (e.g. over the Atlantic and Indian Oceans). Cloud fields tend to reduce the radiative energy gain of our planet as shown in the left column in *Figure 3.5.11*. There are significant large differences between ISCCP FD/GEWEX SRB and CERES values. Their patterns however are dominated by geostationary data artifacts.

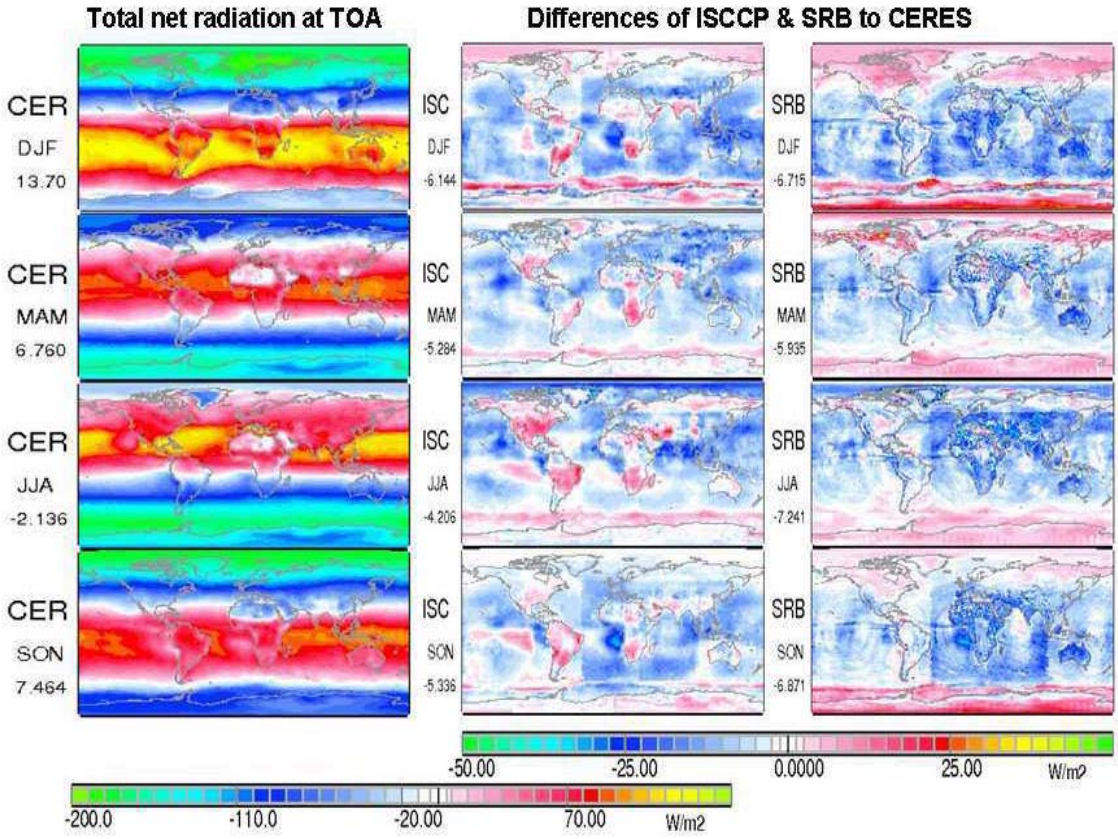

Figure 3.5.11: *Same as Figure 3.5.7 but for all-sky total net radiation.*

Results for clear-sky and the CRE (see *Figure 9 and 10* in *Appendix S.3.5*)

Table 3.5.1: *Summary of all global seasonal (DJF, MAM, JJA, SON) averages. Note there are a few smaller rounding errors.*

	Planetary albedo			Upward longwave			Total net radiation		
	CERES	ISC-CER	SRB-CER	CERES	ISC-CER	SRB-CER	CERES	ISC-CER	SRB-CER
Cloud-Free	17.2	1.87	0.17	259.2	0.30	5.11	40.5	-4.05	-6.72
	17.1	1.76	0.51	262.3	-0.49	5.27	25.3	-3.51	-7.01
	15.7	2.67	1.79	266.2	-1.92	5.66	16.8	-2.58	-10.43
	17.2	1.39	0.09	262.6	-0.88	5.37	30.1	-2.19	-7.34
CRE	14.1	0.85	0.24	-26.4	0.15	-0.62	-26.8	-2.09	2.01
	13.6	0.78	0.42	-26.9	-0.11	-0.96	-18.7	-1.78	1.07
	14.3	0.56	0.39	-27.6	1.27	-0.23	-20.7	-1.63	3.19
	14.4	0.66	0.37	-26.6	0.37	-0.94	-22.7	-3.14	0.47
All-sky (cloudy)	31.5	2.53	0.26	234.1	-0.92	3.12	13.7	-6.14	-6.71
	31.3	1.14	0.34	236.5	-1.74	3.19	6.76	-5.28	-5.31
	30.1	2.15	0.25	240.9	-2.30	3.78	-2.14	-4.21	-7.24
	31.8	1.86	0.28	236.9	-1.44	3.34	7.96	-5.34	-5.87

The pattern in almost all clear-sky difference figures is dominated by geostationary data artifacts. ISCCP FD values over most areas are higher than those of the CERES, which might be explained in part by the different definition of clear sky in these two products. *Table 3.5.1* provides a summary of the global seasonal averages of all three parameters in the CERES dataset along with their differences with respect to ISCCP-FD and GEWEX SRB data. In general, these differences

are small due to compensation of positive and negative deviations over different regions. Such regional differences can be as large as 5 to 10% of the albedo and up to 10 to 30 Wm^{-2} for various flux quantities, respectively. These are often a high percentage (up to 15%) of the fluxes themselves. Large uncertainties are found over both polar zones. Some of the patterns in difference maps are probably related to low level clouds and to convective clouds. We speculate here, that the CERES clear sky data may be contaminated by optically thin clouds. The cloud radiative effect (given in *Figure 10 in Appendix D.3.5*) in ISCCP FD data is generally lower than in CERES data, while more positive areas can be found in the differences of GEWEX SRB to CERES data.

3.5.5: Comparison with results of ERBE/ERBS scanner data

This section summarized the TOA radiation budget components from January 1985 to December 1988 using ERBE measurements from the ERBS spacecraft. They are further compared to radiative transfer model computed results from the ISCCP FD and GEWEX SRB project. We use here again seasonal averages which are averaged over this 4-year period. Only a few results are shown here. Complementary information is contained in Appendix C.3.5.

3.5.5.1: All-sky planetary albedo

Figure 3.5.12 summarized the mean seasonal patterns of ERBE/ERBS planetary albedo and their differences to both the ISCCP FD and the GEWEX SRB data. First of all we must recognize that the ERBE/ERBS data set did not provide complete global coverage. Records stopped polewards of about 70° latitude North and South.

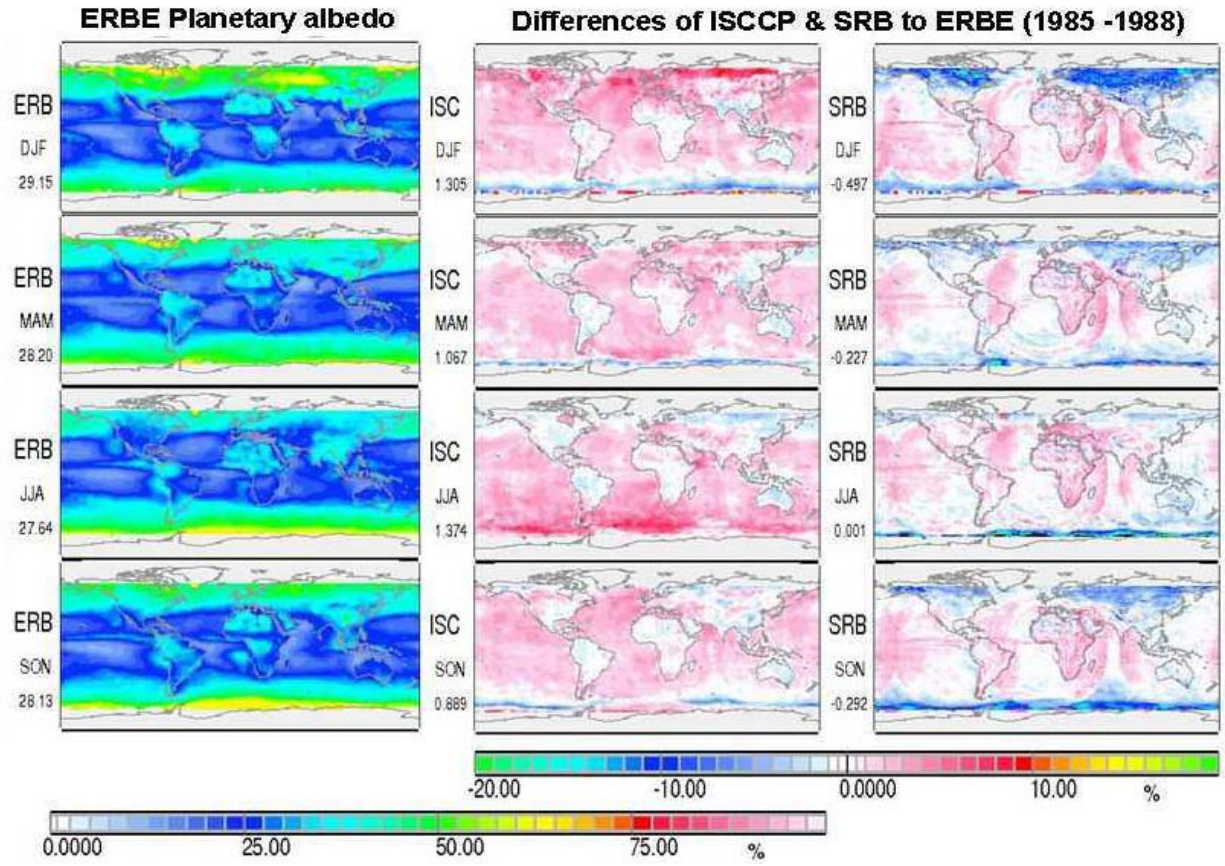

Figure 3.5.12: *Mean seasonal averages of the ERBE/ERBS TOA planetary albedo (left) from January 1985 to December 1988 and their respective differences to ISCCP FD and GEWEX SRB values. Note: ERBE/ERBS data do not cover both Polar Regions.*

The results of ISCCP FD appear to be about 4 to 8 % higher than those of the ERBE/ERBS over almost all ocean areas and they are almost equal over most continents. There are small perturbations due to the incomplete inclusion of geostationary data, which unfortunately dominate the pattern of the differences of GEWEX SRB and the ERBE/ERBS data.

3.5.5.2: All-sky outgoing longwave radiation

Figure 3.5.13 shows the mean seasonal averages of the ERBE/ERBS OLR along with their differences to ISCCP FD and GEWEX SRB OLR. Differences of simultaneous and co-located GEWEX SRB to ERBE/ERBS data are entirely dominated by geostationary data artifact. Note that this means that other differences between these results are smaller than these artifacts, which are only a few percent in magnitude. Such structures are less dominant but still visible in ISCCP FD minus ERBE/ERBS results. Largest deviations of ISCCP-FD to ERBE/ERBS OLR occur over areas of lower level clouds, which apparently are higher and colder in the ISCCP FD than in the ERBE/ERBS dataset. The ISCCP FD CRE appears to be higher over most areas in *Figure 11 in Appendix C.3.5* and the many structure are due to missing data in the ERBE/ERBS clear-sky OLR. ISCCP FD clouds are higher (and colder) than those of GEWEX SRB and ERBE/ERBS. ISCCP FD albedo is also higher. However, this relation is opposite in three areas along the equator. The ERBE/ERBS clear-sky dataset contain large data gaps. Thus only crude comparison with others is possible. We find similar differences of ISCCP FD and GEWEX SRB to ERBE/ERBS as for all-sky results. The same holds for their corresponding CRE results.

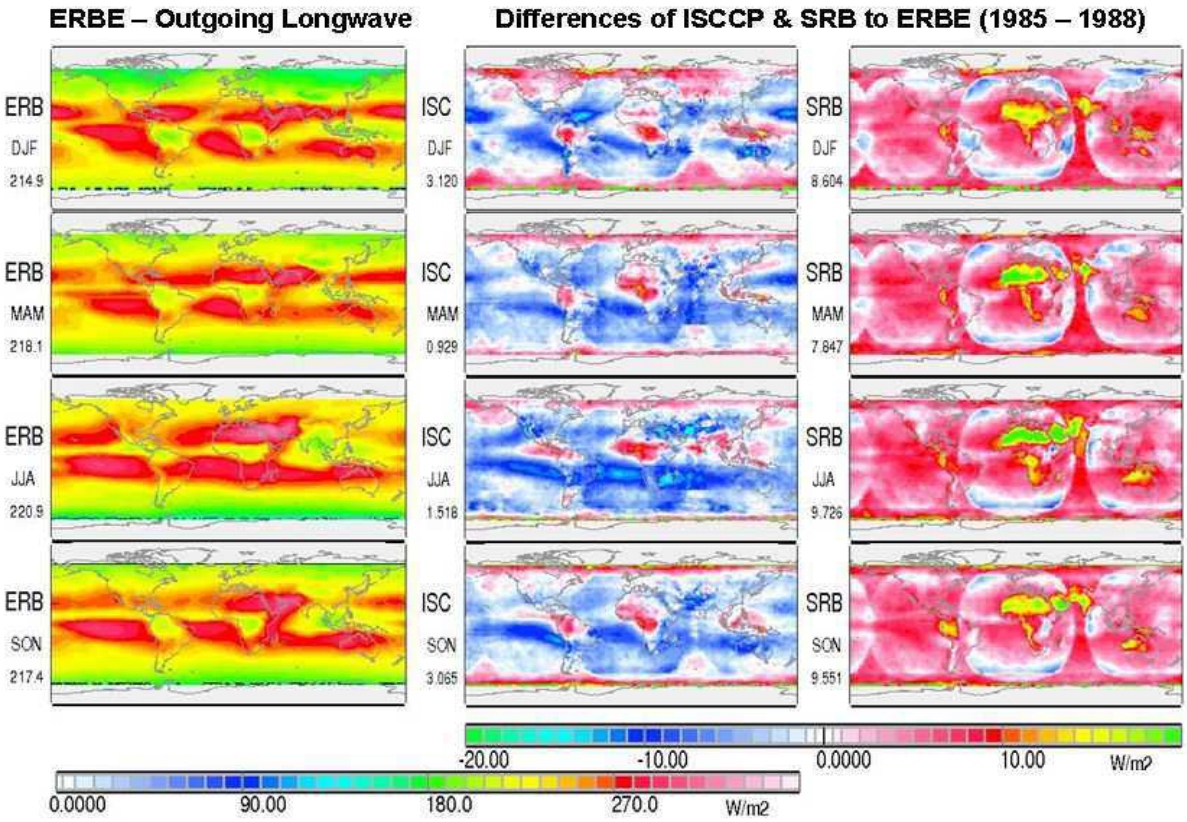

Figure 3.5.13: *Sane as Figure 3.5.12 but for outgoing longwave radiation.*

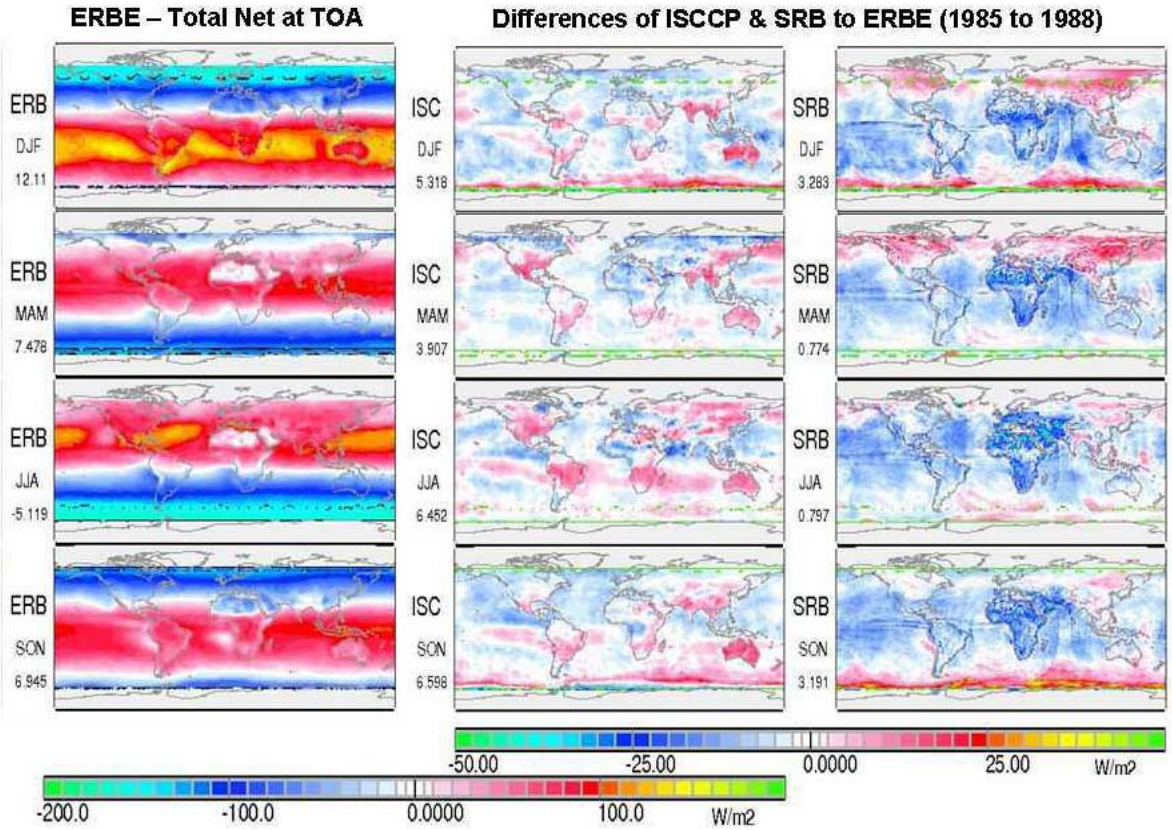

Figure 3.5.14: *Same as Figure 3.5.12 but for total net radiatio.*

3.5.5.3: All-sky TOA Total net radiation

The ISCCP FD TOA net radiation (given in *Figure 3.5.14*) over many areas is smaller than that of the ERBE/ERBS value. But there are slightly positive areas over low level cloud regions. GEWEX SRB budget values are considerably lower (by up to -25 Wm^{-2}) over the Meteosat satellite area.

3.5.6: Comparison of ERBE/ERBS and CERES flux fields

Although ERBE/ERBS and CERES measurements are from two different climatological data periods, simple analysis of their TOA deviations can provide useful information. *Figure 3.5.15* show the difference maps of the planetary albedo and of the outgoing longwave radiation between these two datasets. While the ERBE/ERBS reflection values over most areas are higher by up to 15 Wm^{-2} than those of the CERES, those for the OLR are lower by 10 Wm^{-2}. The patterns in both maps show only little correlation to each other and to the known mean cloud field distribution. These differences are encouraging and point to the possible use of both datasets to "calibrate" ISCCP FD and GEWEX SRB values for longer time series study. The maps of the CRE on both field quantities indicate that CERES values are higher than those of ERBE/ERBS. But this pattern is dominated by the green color, which indicates clear-sky identification issues in many of the ERBE/ERBS regions.

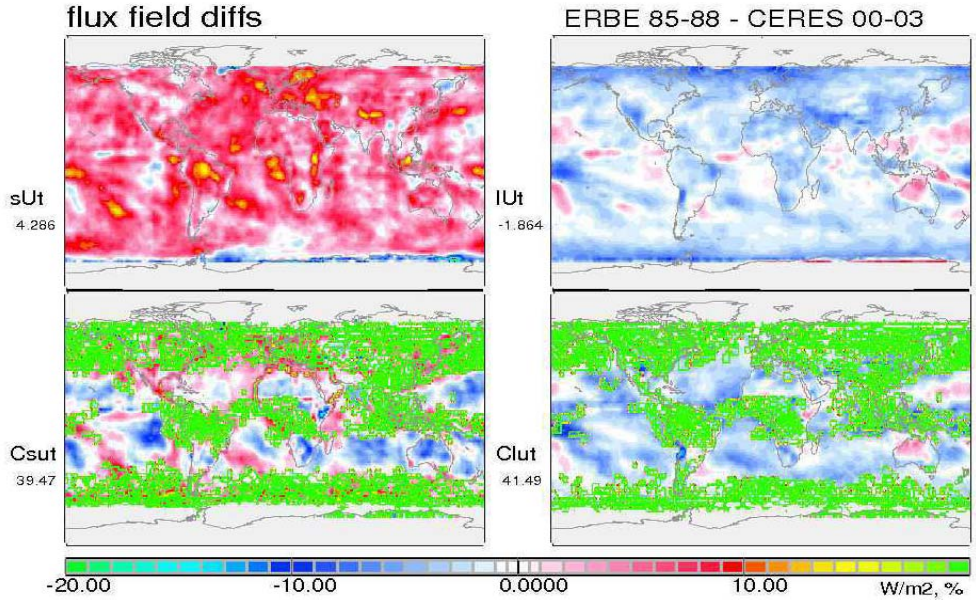

Figure 3.5.15: *Differences between TOA flux fields derived from ERBE/ERBS (1985 to 1988) and from CERES (2000 to 2004) data for all-sky outgoing short-wave and longwave radiation in* Wm^{-2} *(top row) and of the corresponding cloud radiative effects (bottom row). Green areas in the bottom row mark regions without data points in fields of cloud-free areas.*

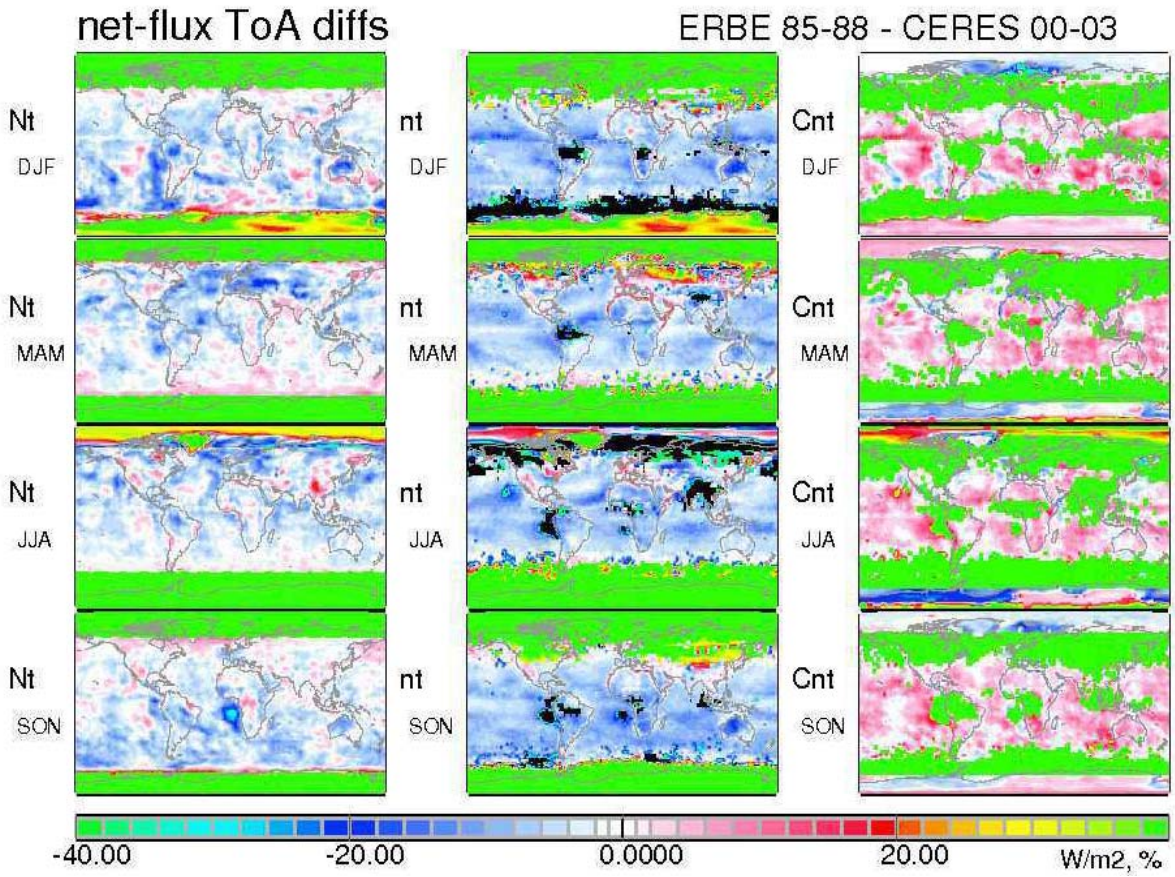

Figure 3.5.16: *Differences between all-sky (left column: Nt) and clear- sky (middle column: nt) total seasonal net flux fields and of the related CRE (right column: Cnt) derived from ERBE/ERBS (1985 to 1988) and from CERES (2000 to 2004) data.*

Relevant differences of the TOA all-sky and clear-sky total net radiation and of the related CRE between ERBE/ERBS and CERES data are shown in *Figure 3.5.16*. Most green areas in this figure contain missing data and all other shaded color areas polewards of 60° latitude in both hemispheres should not be considered. In general the ERBE all-sky net budget values are slightly smaller than those of CERES. Maximum deviations reach -20 Wm^{-2} and in a single case of more than -30 Wm^{-2}. The pattern in the all-sky budget values is only weakly related to cloud field structures. The contribution of clouds to the net budget seems to be larger in ERBE/ERBS than in the CERES results (red areas in the right column). The green and black areas in the clear-sky fluxes and the CRE maps contain no data.

3.5.7: Some conclusions and recommendations

TOA all-sky radiation fields computed from ISCCP FD and GEWEX SRB project should be considered less accurate than those of the ERBE/ERBS and CERES mission since the latter are based primarily on direct broadband measurements from different polar satellite orbits. In this section we used limited datasets from the ERBE and CERES projects which only cover two short periods of time: ERBE/ERBS from 1/1985 to 12/1988 and CERES from 3/2000 to 2/2004. The comparisons of these two datasets with ISCCP FD and GEWEX SRB should provide basic systematic deviations among them. This information is needed to understand changes in long term climate during the interim period between the ERBE/ERBS and the CERES mission. The CERES clouds are based on narrowband MODIS imager data. The CERES-clouds do not completely agree with the ISCCP cloud properties due to differences in narrowband imager spectral coverage, scientific retrieval algorithm, ancillary data and other factors. Therefore we often find large differences between these dataset over regions of dominant cloud cover.

The basic inconsistencies in the radiation fields among these datasets stem from various ancillary data used to determine TOA fluxes from broadband measurements (ERBE, CERES) and to compute the radiation fields in ISCCP FD and GEWEX SRB project. Specifically, anomalies in clouds, aerosols, temperature, water vapor and surface properties have made their way into the flux statistics of the ISCCP FD and GEWEX SRB. Artifacts in these ancillary data can therefore affects the radiation budget data. Particular large anomalies in ISCCP-FD and GEWEX SRB radiation budget occur due to (1) the Pinatubo aerosols clouds with larger impact on ISCCP FD results than on GEWEX SRB results, (2) a smaller but sudden increase of temperatures in middle of 1998, (3) a very strong temperature increase of 3K from September to October 2001 and (4) artifacts relating to geostationary measurements, and of other unknown origin.

For the TOA incoming solar radiation we find significant anomalies of ±3 Wm^{-2} during the main seasons (*Figure 3.5.3*). Therefore, we strongly recommend that modelers and climate analysists should use the same solar constant value (see also *Chapter 2*) and the same increments in space and time for the computations of daily TOA insolation over each area of the earth. Also a common agreement has to be found and accepted for the consideration of the leap year.

Maps of the interannual variability of annual averages of the albedo, OLR and their CRE values show that the zonal monthly averaged anomalies occur with different strength over various regions of the earth and often with different signs. Regional fields of TOA radiation budget for seasonal averages ISSCP FD and GEWEX SRB data during the 4-year ERBE/ERBS or CERES period and their difference to the ERBE/ERBS and CERES results are shown. The pattern of all-

sky planetary albedo is dominated by the cloud fields and to a smaller extent by continents. While the CERES and ERBE/ERBS albedo values are slightly lower (~5%) over all oceans than ISCCP FD values, they are higher over the continents. GEWEX SRB results are too "contaminated" by systematic errors in angular correction from geostationary satellites. They seem to be closer to ERBE/ERBS and ISCCP FD values. In the infrared ERBE/ERBS, CERES and GEWEX SRB have systematically higher values of the emission to space than ISCCP FD, possibly due to choices of lower cloud tops. There are major discrepancies over areas of both low clouds and high convective cloud fields. The GEWEX SRB emission to space appears to be systematically higher by up to 20 Wm^{-2}. The CRE in ISCCP FD and GEWEX SRB data is slightly higher than those in the ERBE/ERBS and CERES data. The TOA total net radiation in CERES/GEWEX SRB data is significantly higher/lower than others, respectively Model computed results are dominated by many regional anomalies between ±30 Wm^{-2}. CREs are evident in all components of radiation budget with large regional variations.

While these results provide an excellent view into the different components of the TOA radiation budget and their corresponding CRE, the deviations between the different data sets are, however, so large that we can only recommend a complete reanalysis of ISCCP FD and GEWEX SRB radiation budget data which should be preceded by a reanalysis of all ancillary data. Note that these products were not designed or intended for monitoring long-term changes. While there seems to be better agreement between ERBE/ERBS and ISCCP FD, the ISCCP CRE seems to be generally higher than those in ERBE/ERBS data, which may depend in part on the different definitions of clear sky. The earlier data in the 1980s from ERBE/ERBS agree well with those of the ISCCP FD and GEWEX SRB. There are preferences of larger deviations over areas covered by high convective clouds and low maritime cumulus. However the data of the ISCCP FD and GEWEX SRB projects are perturbed by geostationary satellite artifacts.

Finally a comparison of all-sky planetary albedo and OLR is made of annual averages between ERBE/ERBS and CERES fluxes (unfortunately not measured during the same time period). The results shows that (1) ERBE/ERBS produces regional upward solar radiation that are up to 15 Wm^{-2} higher than those of CERES everywhere and the CRE in ERBE/ERBS data is slightly lower than that in CERES data with a strong regional variability, (2) The ERBE/ERBS emission to space is almost everywhere lower by about 5 to 8 Wm^{-2} than those of the CERES data and the CRE of CERES is higher than those in ERBE data, and (3) The ERBE/ERBS net radiation budget is slightly smaller (up to -20 Wm^{-2}) than that of CERES, without significant preference of known cloud fields or continental areas. We can only speculate about the causes of those disagreements.

3.6: GERB and CERES Monthly Average Comparison for July 2004

(J. Russell and R. Bantges)

3.6.1: Background

The Geostationary Earth Radiation Budget (GERB) radiometers on Meteosat-8 and Meteosat-9 are the first instruments to provide broadband radiation budget measurements from geostationary orbit (Harries et al, 2005). The geostationary viewpoint enables high temporal resolution observations to be made, with measurements of both the longwave (LW) and shortwave (SW) components every 15 minutes.

In principle, this excellent temporal sampling of the broadband radiances makes the production of monthly mean and monthly mean diurnal cycle products straightforward, at least for all all-sky conditions (see Futyan and Russell, (2005) for discussion of clear-sky sampling and interpolation issues for the GERB mission). However, for the observed radiances to be converted to flux requires knowledge of the scene and the anisotropy of the radiation field which can be difficult under certain viewing geometries, specifically for glint angles over ocean and for twilight conditions (solar zenith angles between 80° and 105°). Combined with the fact that the geostationary orbit results in a fixed viewing geometry for each location results in flux estimates being systematically absent for certain regions and times, and thus special treatment of these conditions are required. The fixed viewing geometry also means that errors in the radiance to flux conversion specific to particular viewing angles do not reduce so readily in averages as would be the case if the scenes were observed from a variety of angles.

3.6.2: Processing overview

At the time of writing an official GERB monthly mean product is still in development. Here we follow the expected procedure for the production of the all-sky monthly average products. All initial processing is done on the GERB HR products which are 15 minute snapshot resolution enhanced fluxes produced as part of the standard GERB processing and the scale at which the GERB radiance to flux conversion is made. Here we use the fluxes present in the GERB 2 HR V003 which are produced as part of the production of the GERB Edition 1 products, for July 2004. However we apply additional treatment in the shortwave for ocean points within 25° of the glint angle and observations with solar zenith angles between 80° and 104.5°. In addition we reinstate the shortwave land fluxes for which the 'glint' angle is less than 15° as these were erroneously removed in the processing based on the glint angle formula without consideration of the underlying surface. These procedures deal with the majority of missing flux points resulting in almost complete coverage. The data are averaged to the 2.5 by 2.5 longitude latitude grid defined for the GEWEX radiative flux assessment, each 15 minute UTC timeslot is then averaged over all the days of the month and then all 96 timeslots of the monthly diurnal average are averaged to form the overall monthly average.

a) Treatment for glint region

Sun glint occurs when the instrument viewing angle is close to the specular reflection direction, resulting in calm ocean surfaces appearing as bright mirrors. This causes two problems in the retrieval of shortwave flux data: firstly, for a visible channel cloud detection the bright

ocean surface is difficult to distinguish from overlying clouds and secondly, the angular models used to convert the observed radiances to fluxes for clear sky conditions are less reliable for glint conditions.

The glint angle is defined as the angle between the reflected ray and the specular ray for a flat ocean surface. Here, when the glint angle is less than 25° with and underlying ocean, in clear conditions the observed radiance is not used to determine the shortwave flux, instead a climatological ocean flux, based on the CERES/TRMM angular model adjusted to mean GERB ocean flux level for that month is used. For this study in July 2004 the multiplication factor used is 1.074 (note this adjustment factor is to the GERB product SW flux level and must then be scaled along with all the GERB SW fluxes by the SW calibration update multiplier 0.976). The standard visible channel based GERB scene ID is used for glint angles greater than 15°, but for glint angles less than this the GERB cloud identification has been shown to be unreliable thus in addition to the special treatment for clear scenes the scene identification itself needs first to be determined by alternative means. Here we use the pre or post-glint scene ID (whichever is closest valid value) for the glint region as long as this is not more than 3 hours removed. Based on this ID the flux is determined either using TRMM ADMs if the scene is cloudy or based on an adjusted TRMM angular model for clear ocean.

b) Treatment for solar zenith angles between 80° and 104.5°

For solar zenith angles greater than 80° the standard GERB scene ID of the cloud conditions (percentage cover, optical depth and phase) which is based on the visible SEVIRI channels becomes unavailable. For solar zenith angles between 80° and 88° here we fill the flux field using the processing of the GERB-like products which bases cloud cover on the SEVIRI MPEF cloud flag which uses IR channels, and assumes a fixed water cloud phase and the fixed cloud optical depth of 4.0. For solar zenith angles between 88° and 104.5° fluxes are filled based on the CERES twilight model values (Kato and Loeb 2003).

c) Averaging

Having treated the missing data as fully as possible remaining gaps of one or two time steps (15 – 30 minutes) are filled by linear interpolation and the data are averaged to a 2.5 degree fixed grid for the GEWEX radiative flux assessment comparison. Each GERB HR point is assigned to a given 2.5° by 2.5° longitude-latitude region if its pixel center falls within the region; an area weighted average is then made of all HR points within each lon-lat region, boxes at the edge or beyond the valid GERB observing region which include observations for HR pixels with viewing zenith angles greater than 70° are set as invalid. In the shortwave filling is sometimes incomplete and thus some HR points within a lon-lat box inside the valid region are missing. In these cases as long as 60% of the points are present the average albedo of these points is applied to the missing points and multiplied by the incoming solar to fill the missing values before forming the average of the 2.5° by 2.5° region. In the longwave very little data is missing so most 2.5° by 2.5° region has the full coverage, however even in event of missing longwave points an area weighted average is made for a lon-lat box as long as 90% of the required HR points are valid. The resulting 15 minute resolution 2.5° data is then averaged for each 15 minute UTC time slot over all the days of the month to produce a monthly average diurnal product, a straight average of which is then made to produce the overall monthly average. No valid average is produced for points which have any single timeslot missing on more than 4 days in the month or

less than the 95% of the total possible timeslots (96 x number of days in the month) present, for a 30 day month this 95% criteria means that less than a total of a day and half of missing data in the month is permitted.

3.6.3: Result and Comparison

The resulting average on a 2.5° by 2.5° longitude/latitude grid is presented in *Figure* ***Error! Reference source not found.*** below for the GERB viewing region, also shown is the CERES SRBAVG GEO TERRA Ed 2d 2.5° by 2.5° data submitted to the GEWEX radiative flux assessment for the region 60 E to 60 W, 60 N to 60 S.

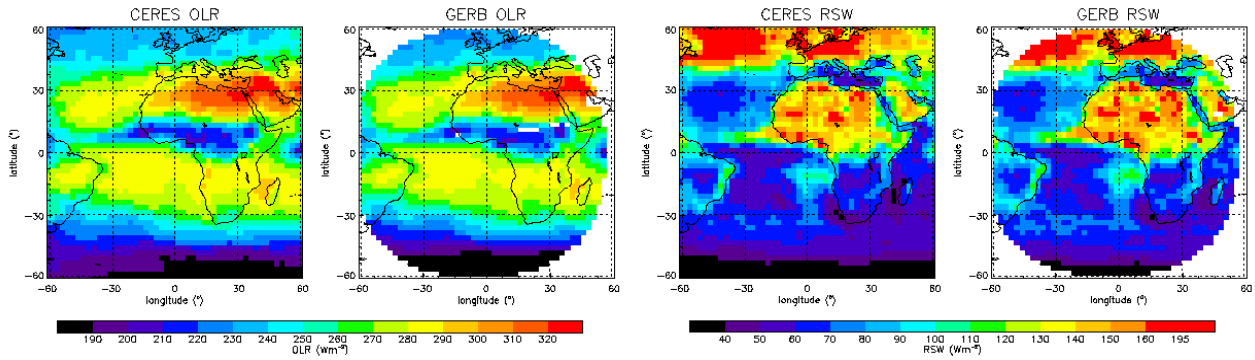

Figure 3.6.1: *Monthly average top of atmosphere outgoing longwave (left set) and reflected solar (right set) shown for the GERB region on the GEWEX radiative flux assessment 2.5 by 2.5 degree longitude latitude grid for July 2004. GERB average shown on the right hand side of the set with the CERES SRBAVG GEO TERRA average shown for comparison on the left. Missing data is indicated by white.*

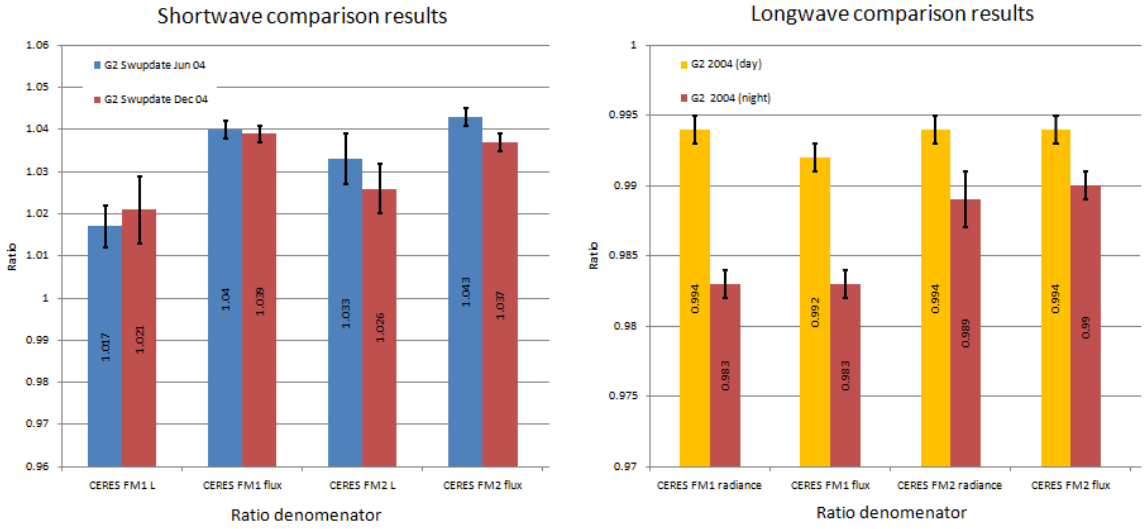

Figure 3.6.2: *GERB 2 Ed 1 / CERES SSF Ed 2 Rev 1 shortwave (left) and longwave (right) ratios for matched points in June and December 2004, see Clerbaux et al., 2009 for details of the comparison methodology.*

Before considering the difference between the GERB and CERES monthly averages, the difference between the GERB and CERES measurements should be considered. As part of the GERB validation, studies have been made of the difference between matched GERB and CERES

observations. This has been performed for temporally spatially and angularly matched radiances and for temporally and spatially matched fluxes. Results have been reported for comparisons made in June and December 2004 between GERB 2 and CERES FM1, FM2, FM3 and FM4 SSF Ed 2 rev 1 products (see Clerbaux et al., 2009), selected results adjusted here to account for the GERB 2 SW calibration update issued subsequent to this paper are reproduced here for the two CERES instruments on the TERRA satellite. The matched point comparison results shown in *Figure* ***Error! Reference source not found.*** indicate the GERB shortwave fluxes, after application of the SW calibration update, are around 4% higher than the FM1 and FM2 values, whilst the GERB longwave fluxes are around 1% lower with around a half to one and half day-night variation in the ratio.

Bearing the results of the matched point comparison in mind we plot the CERES – GERB monthly average differences in *Figure* ***Error! Reference source not found.****2*, showing both the actual difference in the left hand panels of each set and a difference after adjusting for the average GERB/CERES calibration offset (right hand panels of each set). The longwave average flux difference shows increasing positive differences at points corresponding to higher GERB viewing angles and a central area of negative differences. In the shortwave there are larger positive differences in northern hemisphere towards the edge of the GERB region and in several regions over land in Africa and Europe. There are also large negative differences off the West coast of Africa and in East Africa in the region of Ethiopia / Sudan and Mozambique.

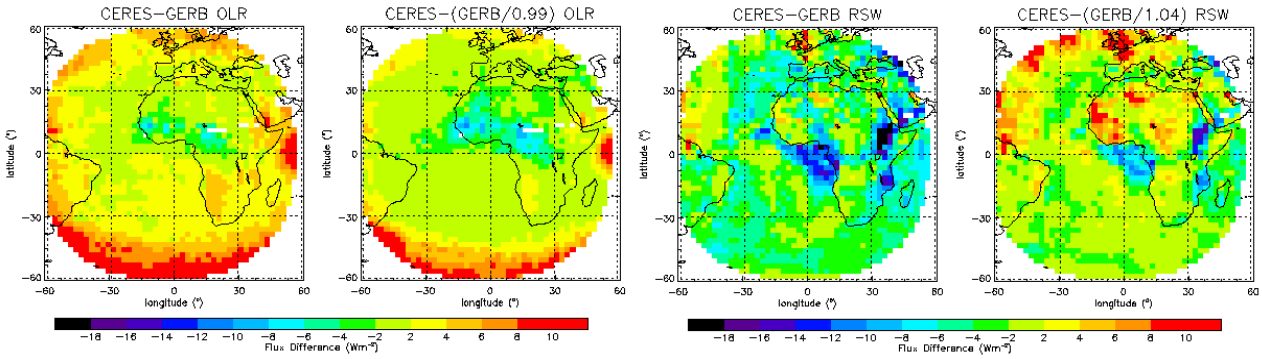

Figure 3.6.2: *Differences of CERES – GERB outgoing longwave (left set) and reflected shortwave (right set) flux differences for July 2004 monthly average 2.5 degree gridded data, shown for actual fluxes on the right side of the set and after scaling for the mean offset between the instruments on the left.*

Comparing the monthly average differences to the differences found in GERB / CERES co-located and temporally matched fluxes can help determine which are due to the different observation points and processing of the instantaneous fluxes and which to the different temporal coverage and averaging treatment. *Figures* ***Error! Reference source not found.*** *and* ***Error! Reference source not found.*** show the monthly average GERB/CERES ratio for July 2004 (left) and a map of the average GERB/CERES ratio for matched flux points from June and December 2004, the latter figures are taken from Clerbaux et al 2009, but the shortwave ratio scale has been adjusted here to account for the GERB 2 SW calibration update. For the matched points the average is specific to the time of the CERES overpass (~10:30 LST), but some features in the monthly average differences are also observed in these plots.

In the longwave a similar pattern of higher GERB 1 fluxes in the central region corresponding the low GERB viewing angles and lower values towards the edge of the GERB region corresponding to high viewing angles are a result of deficiencies in the GERB longwave radiance to flux conversion for higher viewing angles and in the presence of thin high cloud, which coupled with the fixed GERB viewing geometry result in as persistent feature in the monthly

average. This effect explains much of the difference seen in the average although the differences in the central region slightly exceed those observed in the matched comparison. The only additional feature observed in the monthly average comparison is the very low ratio close to the equator at the eastern edge of the GERB region.

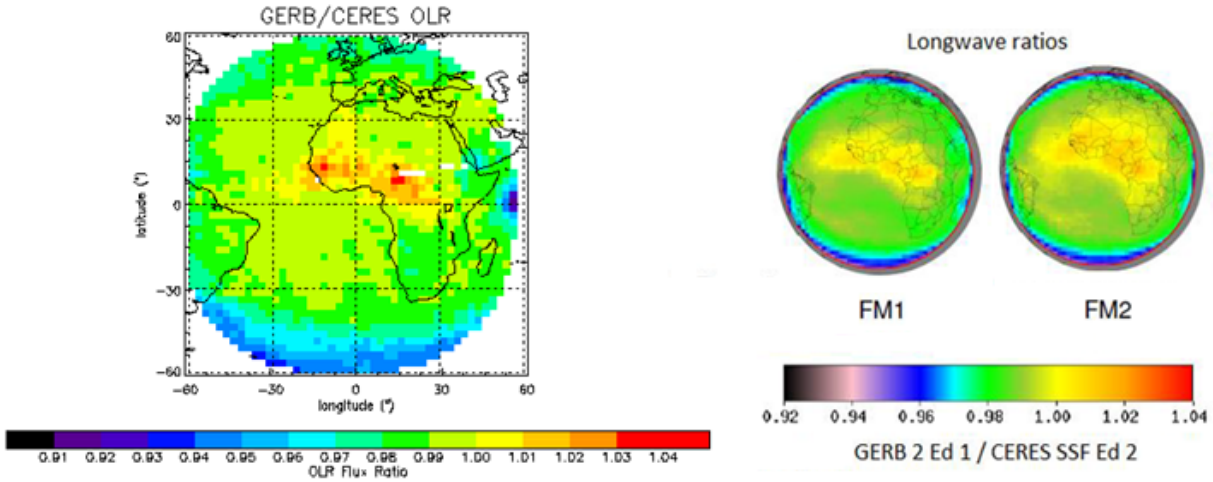

Figure 3.6.3: *GERB / CERES ratio for July 2004 monthly average OLR (left) and for comparison the average ratio obtained from instantaneous GERB 2 and CERES FM1 and FM2 SSF Ed 2 matched outgoing longwave data for June and December 2004.*

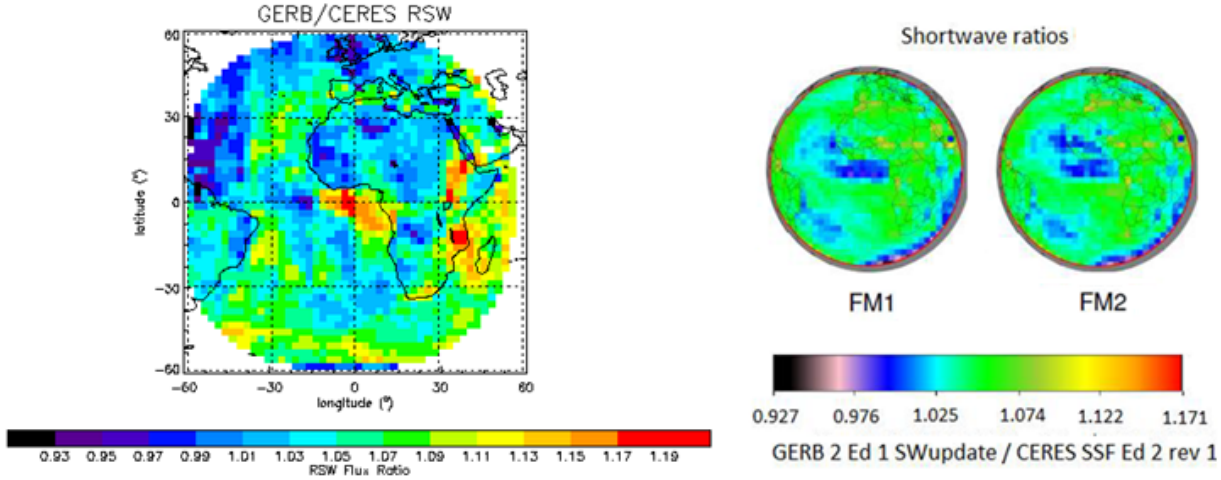

Figure 3.6.4: *GERB / CERES ratio of July 2004 monthly average reflected shortwave (left) and for comparison the average ratio obtained from instantaneous GERB 2 and CERES FM1 and FM2 SSF Ed 2 matched reflected solar data for June and December 2004.*

For the shortwave whilst some low ratios over West Africa are observed for the FM2 / GERB matched point comparison the monthly average displays a much larger region of lowered ratios over the African land as well as to the Eastern and North-Eastern edges of the GERB region which are not observed in the matched point comparison. In addition the shortwave monthly average ratio shows very high values off the West of Africa around and to the South of the equator as well as in East Africa in Ethiopia / Sudan and Mozambique, off the West Coast of Madagascar and in South Africa which again are not obvious in the matched point comparison. Some differences over ocean are expected due to the fact that the GERB edition 1 products, in

contrast to CERES, do not have an aerosol amount dependent treatment of the radiance to flux conversion over ocean (note: neither instrument has an aerosol amount dependent treatment of the conversion over land). In addition GERB employs a climatologically wind speed to choose the clear ocean ADM in the shortwave rather than making an explicit wind speed determination. Some differences may also arise from differences in scene identification that only manifest at times of day not covered by the matched point comparisons. However the differences in the Sahara region are unlikely to be due to such factors.

3.6.4: Summary

A monthly average flux based on the GERB 15 minute resolution enhanced HR data product has been produced for July 2004 and averaged to a 2.5 by 2.5 longitude latitude grid. Missing data in the GERB HR products is dealt will according to the currently recommended practice of the GERB project, in particular special treatment is given to solar zenith angles between 80° and 104.5° and for ocean surface when the glint angle is less than 25° including the use of an alternative scene ID for glint angles less than 15°. Compared to the similarly gridded CERES SRBAVG GEO TERRA Edition 2d data submitted to the GEWEX radiative flux assessment, the differences in the longwave are similar to those seen in instantaneous matched GERB CERES comparisons and are dominated by the inability of the GERB Edition 1 longwave radiance to flux conversion to fully capture the angular dependency of the radiation field particularly at high viewing zenith angles and in the presence of thin high cloud. In the shortwave the range of differences is slightly larger for the monthly average than observed in the matched comparisons and includes high ratios off the West Coast of Africa and in Eastern Africa as well as low ratios in Northern Africa and towards the Eastern and North Eastern Edges of the GERB region which are not observed in the matched comparisons. Nor were such features observed in the matched comparisons with the CERES AQUA instruments which have an afternoon overpass. Whether they are a result of differences in the temporal coverage of the instruments or differences in the processing of the instantaneous fluxes, for example scene identification differences, that only manifest themselves at times other than the CERES overpass remains to be determined.

3.7: Selected ScaRaB Results

(O. Chomette, R. Kandel, P. Raberanto, R. Roca and M. Viollier)

3.7.1: Introduction

ScaRaB (Scanner for Radiation Budget) is an instrument for the determination of Earth Radiation Budget parameters from space, which has been embarked in the 90s on two Russian satellites: Scarab-1 on Meteor in 1994 and ScaRaB-2 on Resurs in 1998. We describe in this section the methods of on board and ground calibration of this instrument and the methods to derive the top-of-the-atmosphere instantaneous and averaged fluxes from radiances measurements. A summary of data comparison found in scientific literature is also given to highlight the similarity and differences between ScaRaB-1/ScaRaB-2 with older version of data from others instruments like ERBE/ERBS and CERES/TRMM.

3.7.2: Description of ScaRaB Instrument

Two models of the ScaRaB radiometer (Scanner for Radiation Budget) have operated in space aboard the Russian satellites Meteor-3-7 (February 1994 to March 1995, Kandel et al., 1998) and Resurs 1-4 (August 1998 to April 1999, Duvel et al., 2001). Preparation of these missions began in the mid-1980s in the framework of the Franco-Soviet Space Cooperation, following encouragement by P. Morel, director of the World Climate Research Program. This later became a cooperative project of France, the Federation of Russia and the Federal Republic of Germany, with constitution of a broader International ScaRaB Scientific Working Group (Kandel et al., 1998). The satellite orbits were polar, sun synchronous (10:30) for Resurs, and with a slow precession (24 hours in roughly 200 days) for Meteor. ScaRaB is a 4-channel cross-track scanning radiometer (Monge et al., 1991, Kandel et al., 1998, Golovko et al., 2003). The earth scanning angle is 100°. Scanning is obtained by rotation of a cylinder carrying the optics, filters, detector, choppers and analog-digital conversion electronics about an axis parallel to the direction of motion of the spacecraft. Four channels (*Table 3.7.1*) include two broad spectral bands from which the reflected SW and emitted LW radiances are derived, and two narrower bands, one corresponding to the infrared atmospheric window, the other to the visible (green to red) portion of the solar spectrum. Both auxiliary channels have been used to study the narrow-to-broad band conversions (Trishchenko and Li, 1998, Li and Trishchenko, 1999, Duvel et al., 2000, Chang and Trishchenko, 2000). The window infrared channel is also particularly useful for the geophysical cross-calibration of the broadband channels (Duvel and Raberanto, 2000).

Table 3.7.1: *ScaRaB channels*

Channel	Description	Spectral Interval	Filter Type
1	VIS (visible)	0.55 – 0.65 μm	Interferential
2	SW (or solar)	0.2 – 4 μm	Silica filter
3	T (total)	0.2 – 100 μm	No filter
4	IR (infrared)	10.5 – 12.5 μm	Interferential

General designs of the ERBE/CERES and ScaRaB scanners are quite different: DC thermistor bolometer for ERBE/CERES, AC pyro-electric detector with 16 Hz frequency chopping against an internal blackbody for ScaRaB; telescope with two mirrors for ERBE/CERES and one for ScaRaB.

3.7.3: The ScaRaB flux products

a) Calibration

Radiometric performances were first estimated on the ground (Sirou et al., 2000). In a vacuum chamber, ScaRaB was tested with an actively-controlled-temperature blackbody. These operations established the linearity of response and provided radiometric calibration of the temperature and emissivity of the on-board calibration blackbodies, and calibration of the temperature dependence of detector gains. For the solar ground calibration, the calibration standard was a reference diffuser, illuminated by the Sun. Simultaneously; the incoming solar irradiance was measured by a calibrated pyrheliometer (Mueller et al, 1997). In laboratory, additional tests were carried out with a calibrated integrating sphere. The accuracy of the onboard lamp sources was then estimated to be better than 1.5%. In flight, the temperature of the reference blackbody (emissivity = 0.993) for channel 3 is measured by a platinum resistance thermometric sonde and included in the scientific telemetry.

For the SW domain, the calibration system was designed with 3 sets of pre-aged incandescent lamp source (Tremas et al., 1997). The thermal leak corresponds to the Earth emitted radiation captured by the SW channel (beyond 3.5 μm). Owing to inter-channel comparisons, it was found to be lower than 0.8 Wm^{-2} sr^{-1} and corrected as function of the window IR measurements. Daytime radiation in the LW band (nominally 4 to 50 μm) is determined by appropriately weighted subtraction of the SW signal from the TW signal. Possible differences or variations in SW spectral response of the SW and TW channels can lead to errors in filtered and unfiltered daytime LW radiances, but analysis have indicated that these LW daytime errors are smaller than 0.3 %. Because of the channel stability (0.1% stability was measured in flight on channel 3), the inter-channel consistency was also evaluated by complementary cross-checking operations. Analysis of very cold bright daytime cloud scenes over tropical convective regimes, for which the TW signal is dominated by SW reflection and the LW component can be estimated independently from the IRW radiance, yields agreement at the 1% level (Duvel and Raberanto, 2000).

b) Conversion to Fluxes and time integration

In order to minimize biases between ERBE and ScaRaB time series, the data processing is based on ERBE algorithms according to published descriptions: Smith et al. (1986), Wielicki and Green (1989) for Inversion, and Brooks et al. (1986) for the Monthly Time Space Averaging. However, the LW day-time calculation and the spectral corrections have been adjusted to the ScaRaB spectral characteristics (Viollier et al., 1995).

However, several ways to improve the ERBE-type processing have been studied. Instead of using the LW anisotropic emission factor tabulated for different viewing zenith angles, seasons, latitude band, and scene type, the angular LW correction is parameterized (Stubenrauch et al., 1993) as a function of the atmospheric pseudo-absorptance defined as the normalized difference between the broadband LW radiance (from ScaRaB channels 3 and 2) and the integrated Planck emission at the 11.5 μm brightness temperature derived from the ScaRaB window channel 4. Applications to CERES estimates have shown that this method is efficient at least for the clear-sky scene. New SW angular corrections have been computed for desert scenes

using Meteosat data (Capderou 1998). The two ScaRaB narrow-band radiances have also been used to refine cloud scenes taking into account cloud phase and spatial heterogeneity. This is done by applying the ISCCP algorithms to the ScaRaB narrow-band radiances. General assessment is obtained by comparing ScaRaB data, ScaRaB ISCCP-reprocessed data and real ISCCP data (Stubenrauch et al., 2002). For the diurnal interpolation, Standfuss et al., (2001) have proposed to use a diurnal climatology of the planetary albedo to improve the reflected solar flux monthly means estimates. The regional diurnal (hourly) albedo climatology is derived for each month from the 5-year data record of ERBS.

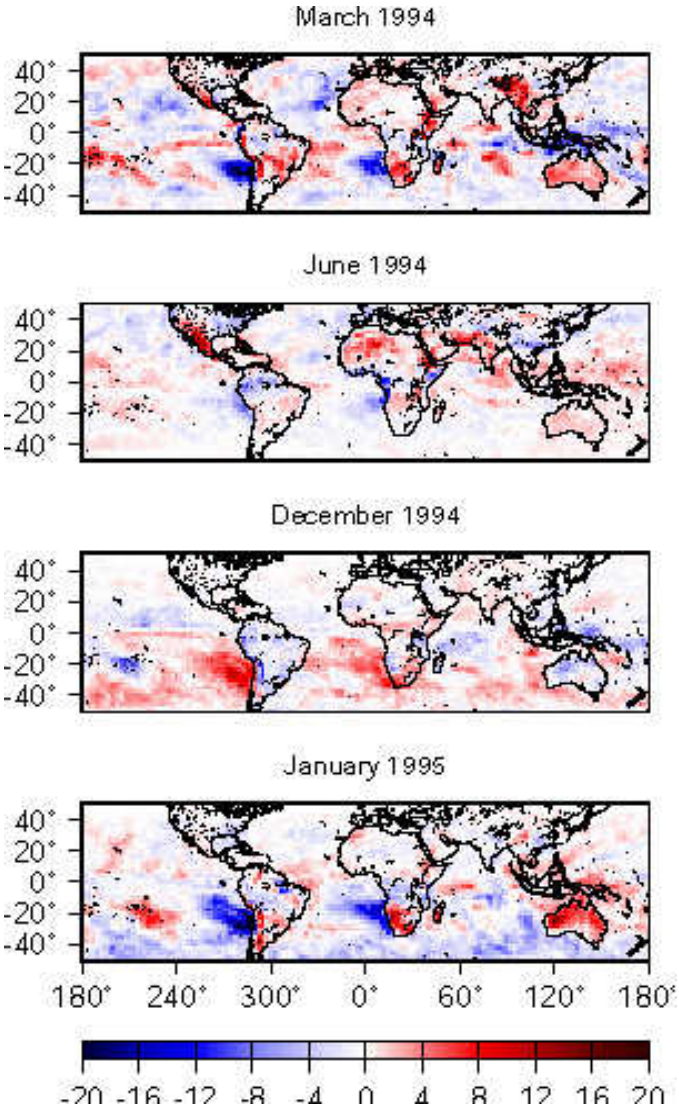

Figure 3.7.11: *Application to ScaRaB1: Difference of ScaRaB monthly mean SW fluxes calculated by CDIEP and EDIEP in [Wm-2]. From Standfuss et al., 2001.*

Figure 3.7.1 shows the differences between the new interpolation (CDIEP – Climatological Diurnal Interpolation Extrapolation Procedure) and the ERBE-like approach (EDIEP – ERBE DIEP) SW monthly means for four months to illustrate the variability of the time sampling error from one month to the next. For March 1994 and January 1995, CDIEP introduces negative correction up to 10-20 Wm^{-2} on marine stratocumulus regions and on the western Pacific area. These negative differences are due to the decreased cloud cover in the afternoon. But the more frequent presence of convective clouds in the afternoon on subtropical land (southern Africa, Australia and parts of South America) gets a positive impact of about +8 Wm^{-2}. For June 1994, the corrections over marine stratocumulus in Southern Hemisphere are smaller than in March due to weaker insulation. For December 1994, corrections are of opposite signs as for the other months: positive over stratocumulus regions and negative over subtropical land. The data provided to the GEWEX-RFA group correspond to the ERBE-like results. The other versions do not change values of the global means by more than one percent.

3.7.4: Intercomparison to other data

Inter-comparisons of ScaRaB and ERBE WFOV were carried out by Bess et al. (1997). They are also discussed by Smith et al. (2006) who show significant agreements (deviations <

1%). More precisely, Haeffelin et al. (2001) have worked with CERES (Clouds and the Earth's Radiant Energy System). They have used unfiltered radiances from ScaRaB FM2 (Radiometer on board the satellite Resurs) and CERES PFM data (Proto-flight model) on board on TRMM (Tropical Rainfall Measuring Mission). These 2 radiometers scan parallel to each other to align the scan plane of ScaRaB with the scan plane of CERES to enhance the number of co-located pixels especially for the SW radiances (the LW radiances are independent of the relative azimuth angle). To do that, they use the capability of CERES to rotate its scanning azimuth. Data on January and March 1999 have been selected on 14 days (52 daytime and 47 nighttime orbital crossing between the 2 radiometers). After the co-located step of these data (in space, time and also in an angular point of view because the radiances have to be measured from the same scene in the same direction), they compute differences (ScaRaB – CERES radiances on 1° grid) and RMS. The results are shown on *Table 3.7.2* for the SW, the LW during daytime and nighttimes.

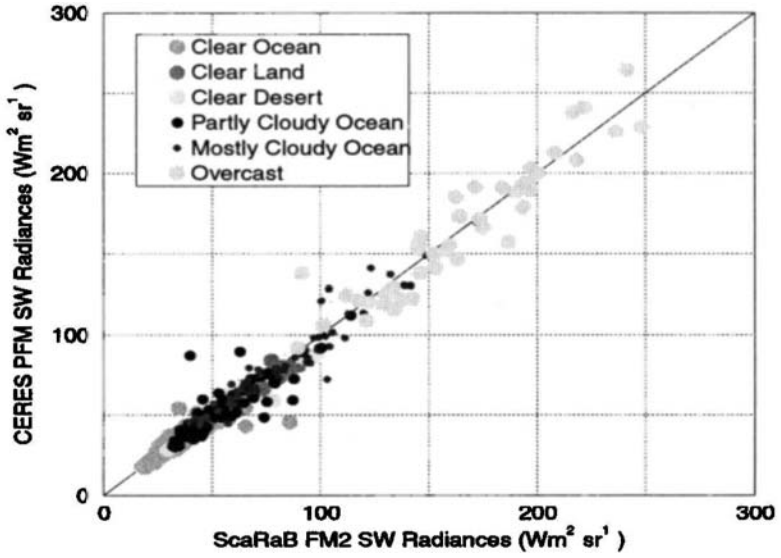

Figure 3.7.2: *Scatter plot of ScaRaB FM2 and CERES PFM unfiltered SW radiances. From Haeffelin et al., 2001.*

In the SW domain (see *Figure 3.7.2*), the ScaRaB and CERES SW radiances difference is 1.0 Wm^{-2} sr^{-1} for these 14 days. In *Figure 3.7.2*, we can see that a significant scatter exists in this domain, in particular for scenes identified as mostly cloudy and overcast. The RMS for this case is 8.3 $Wm^{-2}sr^{-1}$. On the other side, the scatter (not shown) for the LW domain is much less pronounced. In this case, the difference is -0.7 $Wm^{-2}sr^{-1}$ during daytime and -0.5 $Wm^{-2}sr^{-1}$ during nighttimes with a RMS between 2 and 3. As the differences shown in *Table 3.7.2* are not scene types dependent, they can be attributed to uncertainties in the absolute calibrations of the instruments. These results are very encouraging and give confidence to interpret differences between the two datasets as real geophysical signals rather than as calibration discrepancies.

Table 3.7.2: *Comparisons of 1° averaged ScaRaB FM2 and CERES PFM radiances matched in viewing and illumination geometry. From Haeffelin et al., 2001*

	ScaRaB – CERES $Wm^{-2}sr^{-1}$	**RMS** $Wm^{-2}sr^{-1}$
SW	1.0	8.3
LW Day	-0.7	2.3
LW Night	-0.5	3.1

Duvel et al., (2001) extended the comparison to monthly means fluxes at the top of the atmosphere by focusing on the tropical zone (20°N-20°S) and compared the inter-annual variations of ERBE, ScaRaB and the CERES on TRMM dataset. Figure 3.7.3 displays comparisons for the OLR (Outgoing Longwave Radiation), together with the continuous

evolution of the National Oceanic and Atmospheric Administration (NOAA) which underestimates the OLR by approximately 8.5 Wm^{-2} compared to measurements from instruments. Apart from this constant underestimate of 8.5 Wm^{-2}, there is a very good agreement between all the values. The gap between ScaRaB and CERES (approximately 5 Wm^{-2}) is fully consistent with the variation of the NOAA OLR.

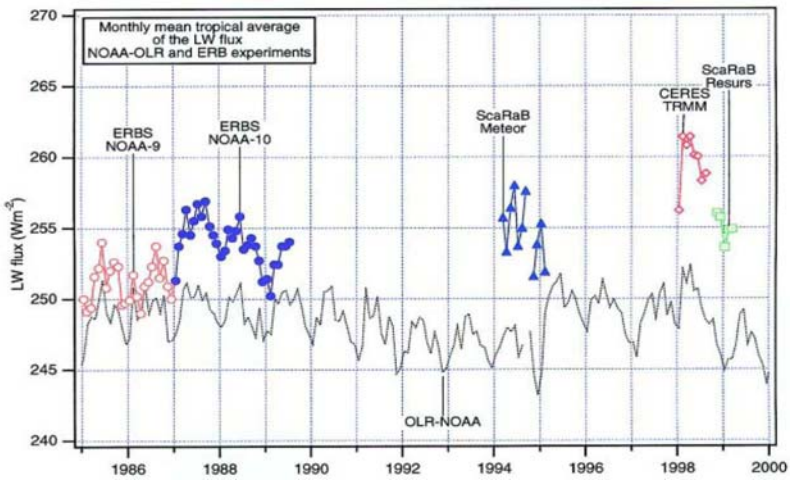

Figure 3.7.3: *Monthly mean tropical (20°N, 20°S) average of the outgoing LW fluxes for ERBE, CERES and ScaRaB experiments, and for the NOAA OLR time series*

3.7.5: Summary

In summary, the ScaRaB-1 and -2 flux products at both instantaneous and monthly time scale have been intercompared with other similar measurements and have shown remarkable consistency, within the flux retrieval uncertainty, in support of the good calibration results obtained for these instruments (Kandel and Viollier 2010). The third version of this instrument will soon be flying on board the Megha-Tropiques mission (Desbois et al., 2007). This third instrument has been improved through the simplification of the internal calibration module. The solar filter can now be switched from the solar to the total channel, that which allows checking calibration and balance of the shortwave responses of both channels. ScaRaB-3 will also benefit from an updated data processing (Viollier et al., 2009) in order to make the flux computation consistent with CERES. Anticipated intercomparisons for this new flight model include systematic comparison with the CERES and GERB radiances and flux products.

3.8: Diurnal Cycle of TOA Radiation

(G. Louis Smith and T. Wong)

3.8.1: Introduction

Diurnal cycle of radiation is a fundamental feature of the climate system. Better knowledge of the observed diurnal cycle of radiation is critical to our understanding of both climate processes and climate variability. This section will examine the observed features of diurnal cycle of TOA radiation based on works found in the scientific literature. This information will serve as baseline knowledge for future radiative flux assessment activities.

3.8.2: Outgoing Longwave Radiation

While diurnal cycle of longwave radiation has long been recognized to be an important component of the surface energy budget, diurnal cycle studies of the TOA outgoing longwave radiation have only been feasible in the last few decades due to limited availability of global satellite measurements. Some of the earliest satellite studies of diurnal cycle of OLR are based on hourly narrowband window channel radiance measurements from operational geostationary weather satellite (e.g.: Schmetz and Liu, 1988). Using one day of METEOSAT hourly data, Saunders and Hunt (1980) gave preliminary estimates of OLR over the METEOSAT regions. They found that diurnal cycle of OLR is strong function of surface scene type and cloud type with OLR being constant over sea surfaces and low cloud regions, but significantly altered over the desert regions during the day, due to strong diurnal cycle of surface heating. Minnis et al (1984) further examined the diurnal cycle of OLR using one full month of GOES narrowband window channel radiance data over the western hemisphere. They found that the mean clear-sky OLR varied diurnally by as much as 100 Wm^{-2} over high elevation desert area in the Andes to as little as 2 Wm^{-2} over some ocean areas. In additions, large diurnal range (as high as 50 Wm^{-2}) was also observed over area with regular deep convective diurnal cycle. These diurnal OLR cycle features were also found in other geographical regions around the globe (Hartmann and Recker, 1986) using composited data from both NASA and NOAA polar satellites with different local crossing time for the period from 1974 to 1983. The observed large diurnal cycle of OLR over land can be problematic issue for satellite mission with limited temporal sampling (i.e., those on sun-synchronous polar orbit). This temporal sampling issue must be dealt with in order to minimize their effects on daily and monthly mean radiation fields. Using hourly GOES data, Brooks and Minnis (1984) showed that the diurnal variation of OLR over land was very nearly a half-sine during the day and nearly constant at night. This information is used to develop the ERBE temporal interpolation method of OLR in order to extend OLR measurements from time of observation to every hour throughout the day.

Harrison et al. (1988) studied the diurnal cycle of OLR for April 1985 using broadband measurements from the multiple ERBE scanning radiometers aboard the Earth Radiation Budget Satellite (ERBS) and the NOAA-9 satellite. While the ERBS spacecraft precessed through all local times every 72 days, or five times per year, the NOAA-9 satellite was in a sun-sync polar orbit with a 2:30 pm equatorial crossing time. Because ERBS was in an orbit with 57° inclination so as to precess, the measurements were limited to 60° latitude, north and south. NOAA-9 provided global measurements from North Pole to South Pole. The combination of these two satellite measurements provided the best global and diurnal coverage of OLR. Harrison et al. (1988) found the largest diurnal OLR range over the clear-sky desert (up to about 70 Wm^{-2}) and

the smaller diurnal OLR range over the clear ocean (less than 5 Wm^{-2}). They also noted that the local time of maximum OLR occurs at a wide range of times throughout the day and night over oceans, but generally occurs from noon to early afternoon over land and desert regions.

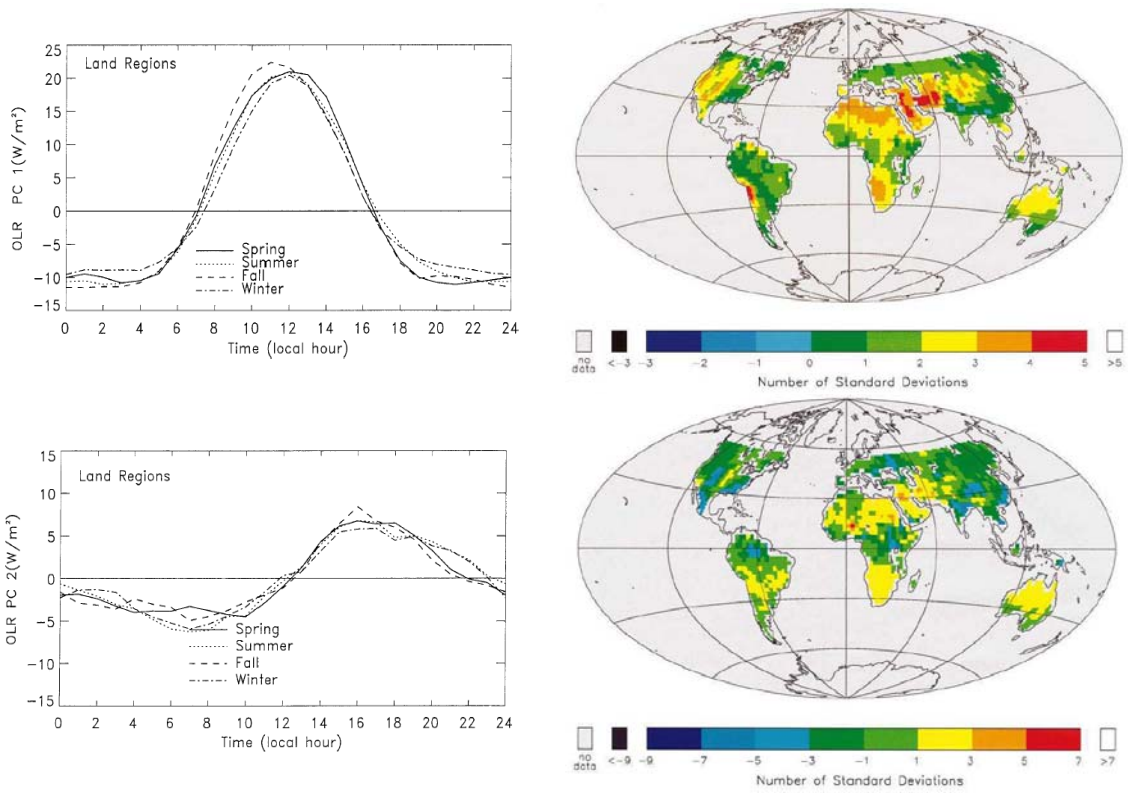

Figure 3.8.1. *First (top) and second (bottom) principle component (left) of diurnal cycle of OLR for the land regions for each season and their associated maps of EOF (right) for the summer season (Smith and Rutan, 2003).*

Recently Smith and Rutan (2003) used five years of ERBE/ERBS instantaneous regional data to describe the diurnal cycle of OLR. Due to data constraints they used seasonal averaging periods and results were limited to 60° from the Equator as for Harrison et al. (1983). They described the diurnal cycles of OLR of each grid in terms of principal components. The diurnal cycle for land and ocean differ considerably with the first EOF for land accounting for 73 to 85% of the variance, whereas the first EOF for ocean accounts for only 16 to 20% of the variance, depending on season. For the land regions (shown in *Fig. 3.8.1*), the first term was very close to the half-sine of Minnis et al. (1984) and the corresponding map showed the magnitude. The second term was approximately a sine wave with zero near noon. This term gives the phase of the cycle, moving the maximum to the morning for regions with afternoon cloudiness and the maximum to the afternoon for regions with morning cloudiness. The first EOF for land has a daytime peak of about 20 Wm^{-2} between 11 and 13 LST and a nighttime minimum of about -10 Wm^{-2}. For the ocean, the first EOF and second EOF are similar to those of land, except for spring, when the first ocean EOF is a semidiurnal cycle and the second ocean EOF is the half-sine. The first EOF for ocean has a daytime maximum of about 5 Wm^{-2} near noon, a second maximum of 1 Wm^{-2} near midnight, and minima of -3 Wm^{-2} near sunrise and sunset. Comer et al. (2007) performed similar EOF analysis using data from the Geostationary Earth Radiation Budget (GERB) broadband instrument aboard the Meteosat-8 satellite. The GERB instrument

scans the Meteosat sector every 15 minutes to provide excellent temporal sampling and data are processed to give the OLR and reflected shortwave radiation on a 1°x1° grid. The results from their study are very similar to those of Smith and Rutan (2003).

The lack of observations at latitudes greater than 60° over the course of a day has hindered describing the diurnal cycles of OLR at high latitudes. The ERBS did not measure beyond 60° latitude, nor does the GERB. ScaRaB-1 was in a near-polar orbit and precessed in a posigrade direction so that it covered a range of local times, but the diurnal cycle is entangled with the annual cycle such that it is problematic as to whether it is possible to extract the diurnal cycles. Improved satellite observation over the polar region is required to improve diurnal cycle of OLR in this region of the Earth.

3.8.3: Reflected Shortwave Radiation

In contrast to OLR, very limited research has been done regarding the diurnal cycles of TOA reflected shortwave radiation (RSR) or TOA albedo. Some of the earliest satellite studies of diurnal cycle of RSR are again based on hourly narrowband visible channel radiance measurements from operational geostationary weather satellite (i.e., Saunders and Hunt, 1980; Minnis et al., 1984). Using one day of Meteosat hourly data, Saunders and Hunt (1980) gave preliminary estimates of albedo over the Meteosat regions. They found the albedo over desert and both high and low clouds remained constant, but altered over sea surface. Minnis et al. (1984), however, found a large diurnal cycle of albedo over stratus region and a moderate diurnal cycle of albedo over deep convection region and desert region using one month of GOES narrowband data. These diurnal changes in albedo also matched well with diurnal cycle of cloudiness over these regions (shown in *Figure 3.8.2*). The diurnal range of albedo is about 30% for the desert and land deep convection region and 50% for the south Pacific stratus region.

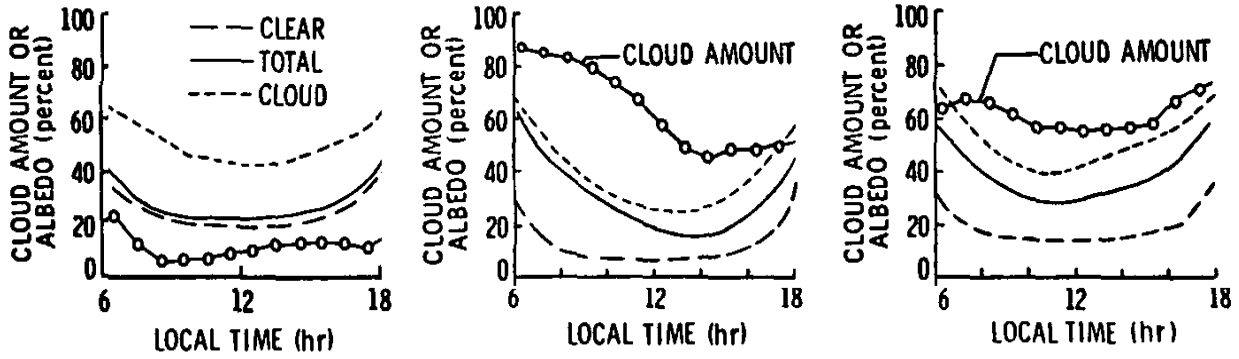

Figure 3.8.2: *November 1978 monthly hourly, daytime regional cloud amount and albedo for a desert region center at 25.9S, 68.7W (left), a south Pacific stratus region centered at 21.4S, 86.3W (center), and a Amazon deep convection region centered at 10.1S, 55.1W (right) extracted from Minnus et al. (1984).*

Hartmann et al (1991) examines the diurnal cycle of albedo over five different climate regimes between 60N and 60S using ERBE broadband scanner data. They found that diurnal cycle of albedo is a function of changes in both cloudiness (cloud type and cloud amount) and solar zenith angle. Rutan and Smith (1998) presented a preliminary study of the variation of albedo similar to their study of the diurnal cycle of OLR. These results showed that globally about 91% of the variation of albedo with time of day over ocean is the increase of albedo with

solar zenith angle. Over land the variation due to solar zenith angle accounts for 84 to 89% of the variance. However, it is not clear from their study how changes in cloudiness during the day have affected their results since there are strong correlation between changes in solar zenith angle and cloudiness over many regions on Earth.

3.8.4: Summary

In conclusion, diurnal cycle of OLR and albedo are affected by changes in surface temperature/heating, cloudiness, and solar zenith angle. The range of diurnal changes is strongly affected by underlying climate regime and surface condition (land or ocean). More works are required to understand the regional patterns of diurnal cycle of TOA radiation (longwave, shortwave, and Net) from observations. The advent of several global products that resolve the diurnal variations of TOA fluxes makes possible more detailed studies of the causes of these variations, but comparisons of the observed diurnal cycle of radiation from different TOA radiation budget datasets are needed in future assessment activities.

3.9: Required Meridional Energy Transports in the Earth-Atmosphere System

(Y.-C. Zhang)

The required total (northward) mean meridional energy transport of the Earth-system (atmosphere and ocean) may be taken as a kind of overall assessment of the total TOA net fluxes, especially its mean meridional distribution and gradient. The transport can be derived from the annual mean, total net flux at TOA. Similar to the averaging method in Chapter 3 used for the two 4-year baseline periods, ERBE (Feb. 1985 to Jan. 1989) and CERES (2001 to 2004), the monthly-averaged, total net flux at TOA (with minimum requirement of at least a month having data for a grid cell) over four years is calculated for each map grid and then averaged over the 12 months of the year (requiring at least three months of data available) for the two periods, respectively. This is done for all the available GEWEX-RFA data products: ERBE, ISCCP-FD, GEWEX-SRB, IPCC-average, IPCC-median and NCEP for ERBE period, and CERES, CERES-ERBElike, ISCCP-FD and GEWEX-SRB for CERES period.

Table 3.9.1: *Global-mean TOA Total Net Flux for Two Baseline Periods*

	ERBE Period (Feb. 1985 – Jan. 1989)						**CERES Period (2001 – 2004)**			
Product	ERBE	FD	SRB	IPCC-a	IPCC-m	NCEP	CERES	CERES-ERBElike	FD	SRB
Net (Wm^{-2})	5.34	2.63	-0.60	1.52	0.54	-7.52	6.77	4.54	0.33	-0.95
Cross-equatorial transport S-N	0.25	0.58	0.36	0.36	0.38	0.53	0.22	0.37	0.19	0.09

As the required energy transport is really the thermodynamic response of the system to a geographically un-balanced radiative flux distribution, the global mean of which is assumed to be near zero, but, because the data products have bias errors, we must remove the global mean values before calculating transports. *Table 3.9.1* lists the global-mean values of the products.

Following Zhang and Rossow (1997), the meridional energy transports to balance the net total radiative fluxes at TOA are determined for all the products. The comparisons for the two periods are shown in *Fig 3.9.1a* and *3.9.1b*, respectively, but NCEP is not shown because its transport has about four times larger bias with ERBE than all the other products; such a pronouncedly large bias is caused by its ~30 Wm^{-2} smaller polar-to-tropical gradient than all the others in zonal averages of total TOA net flux (not shown, but implied in Chapter 3), suggesting that reanalysis products may not have reasonable energy balance, especially on TOA upwelling SW flux as NCEP appears (not shown).

In both the *Figures 3.9.1a and 3.9.1b,* the reference transport for each baseline (ERBE or CERES) is shown with ± 1 standard deviation of the product differences (excluding NCEP); also the transport differences with the ERBE and CERES references are shown (with respect to the right Y axes). In addition, the difference of transport for ERBE minus CERES is shown in *Figure 3.9.1b* (not included in the standard deviation).

In *Figure 3.9.1a,* all of the products exhibit differences < 0.4 pW but the SRB difference reaches ~0.5 pW bias at ~±35° latitude, where transports reach their peak. In *Figure 3.9.1b,* ISCCP-FD and GEWEX-SRB have differences ≤ 0.3 − 0.4 pW bias around the peak values, comparable with either ERBE or CERES-ERBE-like differences with CERES. Both *Figures 3.9.1a and 3.9.1b* suggest that the uncertainty ranges of GEWEX_SRB, ISCCP-FD, as well as the IPCC model median and average are comparable to ERBE or the combination of ERBE and CERES in terms of their transports. The cross-equator values of all the transports are positive with the smallest of ~0.1 pW by CERES-ERBElike and the largest of ~0.6 pW by ISCCP-FD for

ERBE period. All the transports (except NCEP) are consistent with other published results, e.g. ERBE-CERES mean transport by Fasullo and Trenberth (2008).

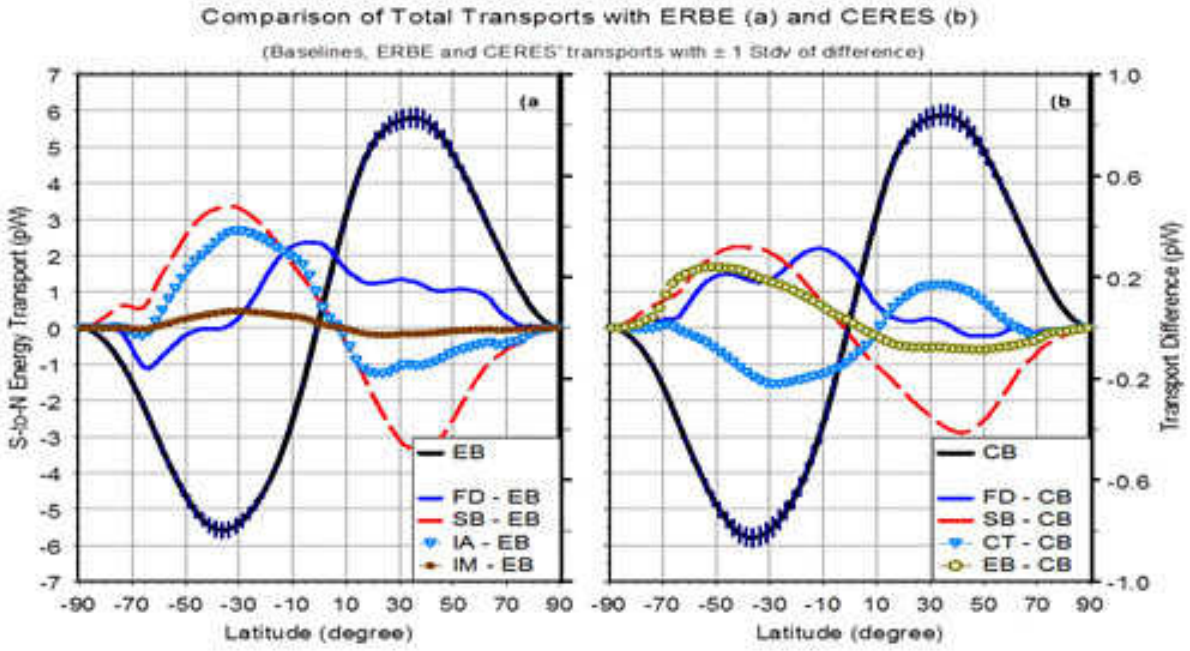

Figure 3.9.1: *The total meridional energy transports of the Atmosphere-Earth system (**in pW = 10^{15} Watts**) required to balance net flux imbalance at TOA for ERBE (EB) and CERES (CB) with ± 1 standard deviation in vertical bars from transport differences with the reference (see text). The differences in transports are also shown with respect to the right Y axes, where FD, SB, IA and IM represent ISCCP-FD, GEWES-SRB, IPCC-average and IPCC-median, respectively while CT is for CERES-ERBE-like. The differences for ERBE minus CERES transport is also shown in (b), but not taken into account in the Stdv calculation.*

3.10: ERBE and CERES Data Uncertainty (N. Loeb and T. Wong)

3.10.1: Introduction

All man-made measurements contain uncertainties and TOA radiation budget datasets are no exception to this universal fact. A full documentation of the factors that cause these measurement uncertainties can be used to better understand the limitation of these satellite datasets, which should lead to more robust scientific assessments about them. Estimating satellite measurement uncertainties are a complex undertaking and a complete end-to-end error analysis is not always available for most satellite data products. This section will highlight uncertainty in ERBE and CERES data based on information from scientific literatures.

3.10.2: ERBE Scanner Data Uncertainty

Uncertainty of ERBE scanner data can be broken down in four sources: calibration, angle sampling, time sampling, and space sampling. Wielicki et al. (1995) had provided estimate of ERBE scanner data errors for each of these four sources. *Table 3.10.1* summarized their published uncertainty for the ERBE Dataset at various space and time scale for both 5-year trend of monthly average regional data and 1-standard deviation of monthly average regional data. For climate monitoring (i.e., 5-year trend), the total error in 2.5° monthly regional data for SW, LW, and Net are 2.0, 2.4, and 3.1 Wm^{-2}, respectively. These total errors are dominated largely by calibration uncertainty.

Table 3.10.1: *ERBE scanner data errors in top-of-atmosphere radiative fluxes given in unit of Wm-2 based on estimates from Suttles et al. 1992; Harrison et al. 1990, 1992; Green et al. 1990; Barkstrom et al. 1989; Suttles et al. 1988)*

ERBE Error Source	2.5° monthly regional 5-yr trend, So=348 Wm^{-2}	2.5° monthly regional 1std dev, So=348 Wm^{-2}	Instantaneous pixel 1 std dev, So=1000Wm^{-2}
SW			
Calibration	2.0	2.1	6.0
Angle Sampling	0.0	3.3	37.5
Time Sampling	0.0	3.9	0.0
Space Sampling	0.3	0.3	0.0
Total SW error	**2.0**	**5.5**	**38.0**
LW			
Calibration	2.4	2.4	2.4
Angle Sampling	0.0	1.6	12.5
Time Sampling	0.0	1.3	0.0
Space Sampling	0.2	0.2	0.0
Total LW error	**2.4**	**3.2**	**12.7**
Net			
Calibration	3.1	3.2	6.5
Angle Sampling	0.0	3.7	39.5
Time Sampling	0.0	4.1	0.0
Space Sampling	0.4	0.4	0.0
Total Net error	**3.1**	**6.4**	**40.1**

For individual monthly average (i.e., 1-sigma), the total errors in 2.5° monthly regional data for SW, LW, and Net are 5.5, 3.2, and 6.4 Wm^{-2}, respectively. All four error sources contribute to the total error at this time/space scale. For instantaneous pixel data, total errors are very large for SW, LW and Net and are dominated by angular sampling error.

3.10.3: CERES Data Uncertainty

Recently the CERES project has produced one of the most complete uncertainty estimates of TOA fluxes at varying time and space scales available (Loeb et al. 2009). *Table 3.10.2* summaries these uncertainties in annual averaged global mean TOA fluxes from 5-year of CERES/Terra SRBAVG GEO product. The CERES/Terra SRBAVG GEO climatological mean value for TOA incoming solar, outgoing SW, outgoing LW, and Net incoming during this period are 341.3, 237.1, 97.7, and 6.5 Wm^{-2}, respectively. The sources of uncertainty are divided into two categories: bias errors of known sign and bias errors of unknown sign. Bias errors of known sign include those from total solar irradiance, spherical earth assumption, near-termination flux, and heat storage. Bias errors of unknown sign include those from total solar irradiance, filtered radiance, unfiltered radiance, radiance-to-flux conversion, flux reference level, and time and space sampling. Detail discussions of the individual error terms in this table are given in Loeb et al. (2009). The combined global averaged annual mean TOA flux uncertainty is 2 Wm^{-2} (2% of the global mean at 95% significance level) in the SW and 3.7 Wm^{-2} (1.5% of the global mean at 95% significance level) in the LW. The expected overall range in global mean net TOA flux is –2.1 Wm^{-2} to 6.7 Wm^{-2}. *Table 3.10.3* summarizes the uncertainties for the various time and space scales, ranging from instantaneous footprint scale to monthly 1-degree regional scale to 5-year global mean scale. Instantaneous TOA flux uncertainties for CERES Terra and Aqua were determined by comparing nadir and oblique view TOA fluxes for days when CERES is in along-track mode (Loeb et al., 2007). TOA flux uncertainty is 5% (1σ) in SW and 3% (1σ) in the LW. At the 1σ confidence level, this corresponds to 15 Wm^{-2} in the SW and 7.5 Wm^{-2} in the LW (for 1000 Wm^{-2} incident solar flux, 0.3 albedo, and instantaneous mean LW flux of 250 Wm^{-2}).

Regional monthly mean TOA flux uncertainties are mainly due to uncertainties in absolute calibration, radiance-to-flux conversion, and time-space averaging. Radiance-to-flux conversion uncertainties are 1.4 Wm^{-2} in the SW and 0.7 Wm^{-2} in the LW (1σ) (Loeb et al., 2007). Time-space averaging uncertainties are derived by comparing 1° regional monthly mean SRBAVG-GEO fluxes from Terra and Aqua. Recall that Terra and Aqua time sampling difference can be as little as one hour at 60°N and 6 hours at 60°S. RMS differences in monthly mean regional fluxes from Terra and Aqua are 4.1 Wm^{-2} (4.4%) (1σ) for SW and 2.3 Wm^{-2} (1%) (1σ) for LW. When Terra-Aqua fluxes are compared directly without using geostationary data (non-GEO), differences are 60% larger in the SW and 30% larger in the LW. Combining calibration, radiance-to-flux and time-space averaging uncertainties, the overall SW uncertainty (1σ) is $(1^2+1.4^2+4.1^2)^{1/2}$ = 4.5 Wm^{-2}, and the overall LW uncertainty (1σ) is $((0.5x3.7)^2+0.7^2+2.3^2)^{1/2}$ = 3 Wm^{-2}. The 1σ uncertainties for 5-year global mean fluxes are 1 Wm^{-2} for SW and 1.8 Wm^{-2} for LW.

3.10.4: Summary

In summary, a thoughtful analysis and understanding of the factors that affects the accuracy and stability of the TOA radiation datasets, such as those discuss above, should be required for all future TOA radiation budget datasets. This information is critical to establishing creditability and limitations of scientific results deduced from analysis of these datasets. For ERBE data, the 1-sigma monthly regional uncertainty for SW and LW flux is on the order of 5.5 and 3.2 Wm^{-2}, respectively. For CERES data on an equivalent ERBE 2.5° grid, the 1-sigma

monthly regional uncertainty for SW and LW is on the order of 3 and 2 Wm^{-2}, respectively. The 1-sigma uncertainty in 5-year ERBE global mean SW and LW flux is 2.0 and 2.4 Wm^{-2}, respectively. The corresponding 1-sigma uncertainty in 5-year CERES global mean SW and LW flux is 1.0 and 1.8 Wm^{-2}, respectively.

Table 3.10.2. *Bias error (2σ) for CERES SRBAVG-GEO global mean fluxes. Numbers in parentheses correspond to clear-sky.*

	Bias Errors of Known Sign (Wm^{-2})				
Error Source	Incoming Solar	Outgoing SW	Outgoing LW	Net Incoming	Comment
Total Solar Irradiance	+1	0	0	+1	Recent solar irradiance measurement vs. assumed solar irradiance in CERES
Spherical Earth Assumption	+0.29	+0.18 (+0.11)	-0.05 (-0.06)	+0.16 (+0.24)	Weighting latitude zones in geocentric vs. geodetic coordinates.
Near-Terminator Flux	0	-0.3	0	+0.3 (+0.15)	Discretization uncertainty in time-space averaging algorithm at $\mu_o > 85°$
Heat Storage	n/a	n/a	n/a	+0.85	Hansen et al. (2005)
	Bias Errors of Unknown Sign (Wm^{-2})				
Source	Incoming Solar	Outgoing SW	Outgoing LW	Net Incoming	Comment
Total Solar Irradiance	±0.2	0	0	±0.2	Absolute Calibration (95% confidence)
Filtered Radiance	0	±2.0	±2.4(N) ±5.0(D)	±4.2	Absolute Calibration (95% confidence)
Unfiltered Radiance	0	±0.5	±0.25(N) ±0.45(D)	±1.0	Instrument spectral response function + unfiltering algorithm
Radiance-to-Flux Conversion	0	±0.2	±0.3	±0.4	Angular distribution model error
Flux Reference Level	0	±0.1	±0.2	±0.2	Uncertainty in assuming a 20-km reference level
Time and Space Averaging	0	±0.3	±0.3	±0.4	Geostationary instrument normalization with CERES
Heat Storage	n/a	n/a	n/a	±0.15	Hansen et al. (2005)
	Expected Range in Net TOA Flux: -2.1 Wm^{-2} to 6.7 Wm^{-2}				

Table 3.10.3. *Uncertainty (1σ) in SW and LW flux from CERES. (Units in Wm^{-2}).*

Spatial/Temporal Resolution	**SW**	**LW**
Instantaneous	15	7.5
1° Monthly Regional	4.5	3
5-year Global Mean	1	1.8

3.11: Summary and Recommendations (T. Wong):

The components of the TOA ERB are fundamental to our understanding of climate and climate variability. In order to better understand our current observational knowledge of the TOA radiation fields, number of different TOA ERB datasets from various projects were collected and analyzed for the GEWEX RFA. In general, these datasets can be separated into two classes: data from direct broadband measurements constructed with ancillary information (i.e., ERBE, ScaRaB, CERES, and GERB) or data from broadband radiative transfer computation based solely on ancillary information of clouds, aerosols, atmospheric profiles of temperature and gaseous, surface emissivity and albedo (i.e., ISCCP FD, FORTH, and GEWEX SRB).

While the majority of the large scale regional features are similar among these TOA ERB datasets, subtle but important regional differences do occur. Shortwave regional differences are larger than their longwave counterpart. These disagreements are the products of the differences in instruments (broadband vs. narrowband), science processing algorithms, as well as ancillary input dataset used in the construction of these datasets. For global and tropical tropical average climatological mean (CERES or ERBE period), the differences among datasets are small for incoming solar radiation (global mean 1-sigma relative differences of 0.2 to 0.3%), larger for TOA longwave (i.e., all-sky global mean 1-sigma relative differences of 0.8 to 1.2%), and much larger for TOA shortwave (all-sky global mean 1-sigma relative differences of 2.6 to 3.2%) and net radiation (all-sky global mean 1-sigma absolute differences of 2.3 to 3.2 Wm^{-2}).

While all GEWEX-RFA datasets can produce the overall feature of the annual cycle of radiation budget, the differences among datasets are significant for all three components of the radiation budget. Improvements in all three components are required to bring these datasets in better agreement with each other.

Deseasonalized time series analysis shows good agreement for the GEWEX-RFA datasets during the ERBE period; but only fair agreement for the CERES period. Note that these products were not designed to monitor the much smaller interannual variations of fluxes. The largest change is associated with a sudden increase of skin temperatures in the ISCCP-based dataset due to a change in the TOVS sounding profile during the CERES period. Other artifacts in ancillary data (i.e., cloud, temperature, moisture, surface scene type) have been identified that strongly affect the quality of the long term TOA radiation budget datasets (especially for those based on radiative transfer computations). Reprocessing of these ancillary input datasets should lead to improvements in the overall quality of the GEWEX-RFA datasets. In additions, the integration of satellite measurements from polar and geostationary orbits (i.e., those in ISCCP FD and GEWEX SRB) is far from perfect. Additional works are needed to remove regional artifacts relating to data from these different orbits.

Differences between monthly mean GERB data and CERES/Terra SRBAVG GEO data relate to errors in GERB LW radiance to flux conversion algorithm. Monthly mean shortwave differences are complicated and more work is required to understand them. While the current datasets in the GEWEX-RFA archive lack information about the diurnal cycle of radiation, selected peer-reviewed publications on this topic did show very interesting diurnal signatures relating to surface scene type. Since diurnal cycle of radiation is a fundamental feature of the climate system, comparisons between the GERB products and the reconstructions in some of the calculated products, especially GEWEX SRB and ISCCP FD which resolve the diurnal variations, are strongly recommended for future GEWEX-RFA activity.

Error analysis of ERBE and CERES data shows the largest source of uncertainty coming from absolute instrument calibration. These systematic calibration differences must be removed

when piecing the long term record together using these combined scanner datasets. While the long-term ERBE/ERBS non-scanner data can be used to bridge these two scanner datasets in the longwave with some successes, current data gaps in the shortwave must be filled before these two datasets can be combined together. Additional ERBE/ERBS non-scanner data during the data gaps period must be processed to enable this task. In addition, future improvements in instrument design are highly desirable to reduce absolute calibration uncertainty. We also recommend that all future ERB projects to provide detailed end-to-end error analysis as part of their data products. This will further enhance our scientific understanding of the findings from these datasets.

Chapter 4:

Surface Radiation Budget

P. W. Stackhouse with S. Cox, J. C. Mikovitz, W. B. Rossow, Y. C. Zhang, L. Hinkelman, R. Pinker, E. Raschke, S. Kinne

Abstract

This chapter contains an analysis and assessment of global surface radiation budget datasets submitted to the GEWEX-RFA archive. The analysis here is focused upon comparing the annual average surface fluxes from 3 central periods (1) ERBE Period (Jan 1985 – Feb. 1989), (2) the CERES Period (Mar. 2000 – Feb. 2004) and the 21 year entire period length (Jan 1984 – Dec. 2004). The chapter evaluates the differences between surface flux data products for the shorter periods relative to the long period. Then the variability of the long-term annual average time series between the data products is assessed. The seasonal cycles between the data sets are assessed and lastly the long-term changes for the main and derived data products (e.g., implied cloud effects, transmission, etc.) are assessed both in long-term variability and in spatial differences. Lastly, a section of the various sensitivities of the flux products is presented relative to the temporal and spatial differences found between the data products.

4.1. Introduction and Overview (P. Stackhouse)

Improving the estimate of global surface fluxes is paramount to understanding and closing global energy and water cycle budgets. This need has been recognized for some time (workshop report by Suttles and Ohring, 1986). This document became the impetus for the establishment of the Surface Radiation Budget project, then under the World Climate Research Program, but later was moved under the umbrella of the GEWEX project. A key result of the workshop was to define uncertainty goals for the surface radiation fluxes. These goals are reproduced in *Table 4.1.1*. These requirements have now been updated at the global annual average scale to include long-term stability besides the general accuracy by Ohring et al. (2005). The relevant surface flux requirements are given in *Table 4.1.2*.

This *Chapter 4* serves to compare the surface radiative fluxes for the available satellite-derived products in the GEWEX RFA archive, as *Chapter 3* examined the top-of-atmosphere fluxes. Critical to the estimation of the surface fluxes is the uncertainties and assumptions regarding the input cloud, meteorological and surface properties. Of the data sets compared here, only the early versions of the CERES surface radiation data sets do not use the ISCCP cloud properties as inputs. Thus, the assessment of the differences is largely based upon assumptions made in other input properties that data developers used in the methods to estimate the surface radiation. The focus of this chapter is on the basic surface radiation parameters as identified in *Table 4.1.1*. All analyses presented here were performed on monthly to multiyear average fields of SRB parameters and the time series of the zonal and global averages of those parameters. Appendix A.3 provides an overview of all the various algorithms used to estimate surface fluxes assess some of the uncertainties in the ISCCP cloud properties. Inferences from those materials are used in the course of this chapter.

Table 4.1.1: *Original surface net flux accuracy goals from the Suttles and Ohring (1986) report. Here accuracy is taken to be a measure of bias or systematic error.*

Region	Resolution		Accuracy			
	Space ($W\ m^{-2}$)	Time ($W\ m^{-2}$)	Net SW ($W\ m^{-2}$)	Albedo	Net LW ($W\ m^{-2}$)	Total Net ($W\ m^{-2}$)
Ocean						
Tropical	2 x 10°	Month				10
Extratropical	5 x 5°	Month				10
Land	250 km	Month	10	0.05	10	
Cryosphere	250 km	Month		<0.05		<10
Atmosphere	250 km	Month				<25

Table 4.1.2: *Updated requirements for the observation of key surface radiative flux properties based upon Ohring et al., (2005). The recommended accuracies are on the global annual averaged scale or as noted*

Climate Variables	Signal	Accuracy	Stability (per decade)
Surface albedo	Forcing	0.01	0.002 $decade^{-1}$
Downward LW flux	Feedback	1 Wm^{-2}	0.2 Wm^{-2} $decade^{-1}$
Downward SW flux	Feedback	1 Wm^{-2}	0.3 Wm^{-2} $decade^{-1}$

In *section 4.2*, an analysis of the entire 20-year period over which the surface radiation data sets overlap is reviewed for differences in global and regional means and temporal variability. In *section 4.3*, an analysis is presented of the two separate time periods corresponding to two 48-month time periods: the CERES time period from March 2000 through February 2004, and the ERBE time period from February 1985 through January 1989. This analysis is also completed over global and regional means, but the map differences are also presented. Zonal mean comparisons and time series anomalies are assessed for two periods directly. In *section 4.4* an assessment of the seasonal cycles for the various surface radiation data sets is discussed. In *section 4.5*, a more comprehensive assessment of the ERBE, CERES, ISCCP-FD and GEWEX SRB data sets is made for a number of parameters and over the length of the records.

4.2: Surface Radiation Budget Comparisons with GEWEX-SRB Products

(P. Stackhouse, S. Cox, J. C. Mikovitz)

Abstract

Eight surface radiation budget datasets in the GEWEX-RFA archive are compared for the March 2000-February 2004 time period. Ensemble means are computed from these datasets and the product differences from the ensembles are analyzed. While agreement is generally good among the datasets, some areas of large difference are noted. The shortwave agreement is generally worse than the longwave. For both shortwave and longwave, the poles and deserts are the areas of strongest disagreement. These results show where future efforts may be most productive in improving knowledge of the total Earth surface radiation budget.

4.2.1: Overview and Data Set Description

Intercomparison and analysis of archived datasets reported in this section was performed for two different periods: 1) March 2000 - February 2004, called the CERES period; and 2) February 1985 - January 1989, called the ERBE period. A longer period containing most of these two periods and the intervening years is described in section 4.3. Since all archived datasets are not available all periods, datasets analyzed for the three periods are not the same. Also, since ground-based measurements of SRB parameters that can be used as reference for evaluating satellite-derived products are not available, especially on global and long-term basis, one among the satellite-based datasets, namely, the GEWEX-SRB was chosen as the reference by participant consensus. Note that the GEWEX-SRB team has submitted a second set of products known as GEWEX-SRB (Parameterized). This latter dataset is a product of SW and LW models known as the Langley Parameterized Shortwave Algorithm (LPSA) and the Langley Parameterized Longwave Algorithm (LPLA) respectively (Gupta *et al*., 2010). Analysis in this section is limited to the all-sky fluxes as shown in *Table 4.2.1,* the surface albedo and total net radiation at the surface (ATOTNET).

Table 4.2.1: Datasets available for GEWEX-RFA surface flux analysis for the three periods.

SRB Dataset	All-sky SW Down (ASWDN)	All-sky SW Up (ASWUP)	All-sky SW Net (ASWNET)	All-sky LW Down (ALWDN)	All-sky LW Up (ALWUP)	All-sky LW Net (ALWNET)	ERBE Period (2/85-1/89)	CERES Period (3/00-2/04)	21-year Period (1/84-12/04)
CERES/SRBAVG-GEO	X	X	X	X	X	X		X	
DLR-ISIS	X						X	X	X
ERBEsrb-Li			X				X		
FORTH	X	X	X	X	X	X	X	X	X
GEWEX-SRB	X	X	X	X	X	X	X	X	X
SRB QC (Paramet.)	X	X	X	X	X	X	X	X	X
ISCCP-FD	X	X	X	X	X	X	X	X	X
UMD-SRB	X	X	X				X	X	X

All datasets were submitted as monthly averages on a 2.5°x2.5° grid as per RFA agreements. Comparisons of multi-year average gridded fields and zonal averages as well as deseasonalized time-series of monthly, global and tropical (20°S-20°N) averages were carried out relative to the GEWEX-SRB products for the three periods mentioned above. Graphical presentations of comparisons contain results of GEWEX-SRB and differences between each of the models and GEWEX-SRB.

4.2.2: Multi-year Regional Comparisons

Comparisons of regional climatological averages are presented below, separately for the two periods. Geographical distributions of the same parameter from different contributors showed general agreement as to the broad features but some regional differences are also apparent. Shortwave differences are most pronounced over major deserts, polar regions, and the

Intertropical Convergence Zone (ITCZ). Longwave differences are largest over deserts and tropical oceans, including the marine continent. These differences were generally attributable to identifiable specific causes. Results for the other period are discussed, where feasible, causes for differences are identified.

a) The CERES Period (March 2000 - February 2004)

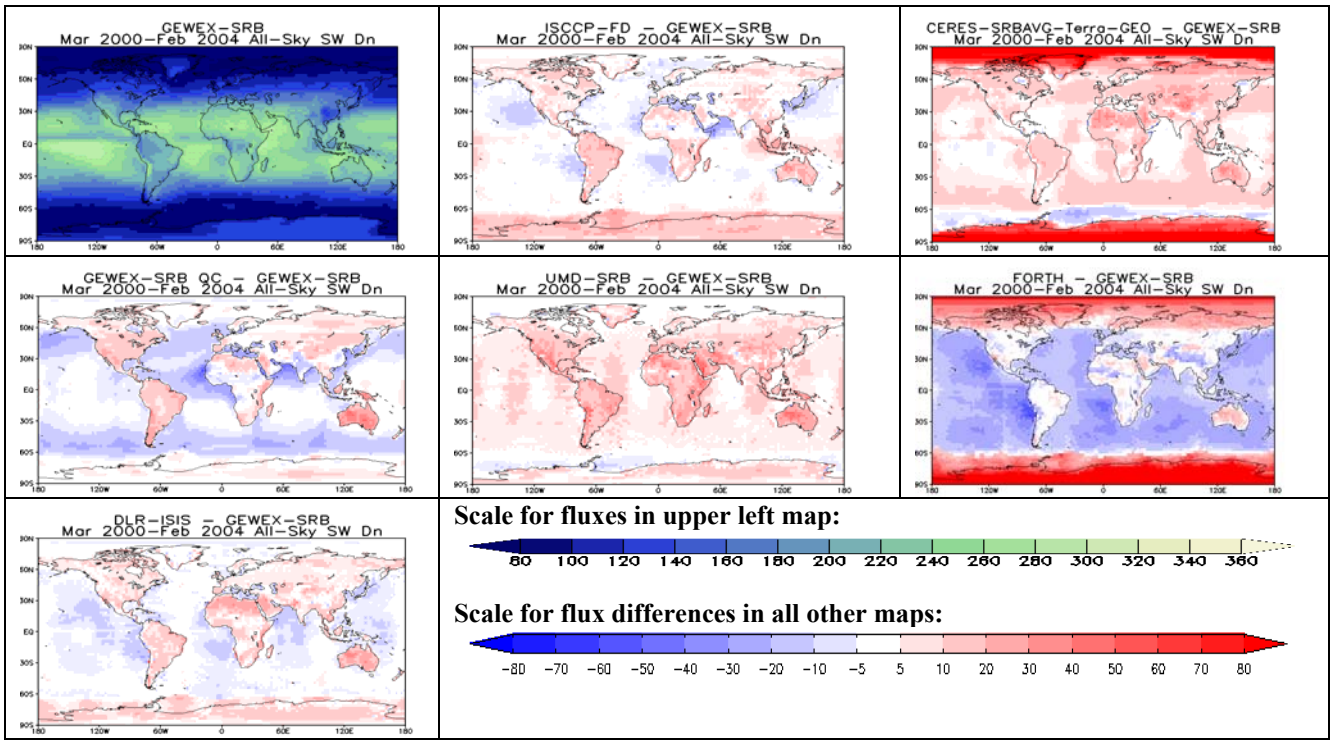

Figure 4.2.1: *Maps of* ***ASWDN*** *(in Wm^{-2}) for available GEWEX-RFA products averaged over the CERES period. The field of GEWEX-SRB flux is shown at upper left. The other maps are differences of the other six products and GEWEX-SRB. The upper color bar applies to the GEWEX-SRB map and the lower one applies to the difference maps.*

Examples of comparisons of geographical distributions of the means for ASWDN, ASWNET, ALWDN and ALWNET (all-sky sort- and longwave downward and net radiation) for this period are presented in *Figures. 4.2.1, 4.2.2, 4.2.3 and 4.2.4* respectively. The figure for each of the flux shows the field of GEWEX-SRB and the differences of other available fields of that flux. The top color bar in each figure refers to the GEWEX-SRB field and the bottom color bar to the difference fields.

For ASWDN, the inter-product regional agreement is generally within 20 Wm^{-2}. UMD-SRB, ISCCP-FD and DLR-ISIS are in closest agreement with GEWEX-SRB. Each is generally within 5 Wm^{-2} over oceans, but more than 10 Wm^{-2} higher over land, in line with a known sharp land-ocean gradient in GEWEX-SRB. FORTH and CERES/SRBAVG GEO are more than 60 Wm^{-2} higher polewards of 60°. For the ASWNET (*Figure 4.2.2)*, the differences overall are less than those in the ASWDN. Polar differences are likely directly related to downward flux differences, but continental differences speak to likely aerosol and surface albedo differences. ASWNET from GEWEX SRB, ISCCP FD, UMd SW and CERES agree over ice free oceans to within about ± 10 Wm^{-2}, but larger differences are seen with the SRB QC and FORTH products.

A feature of the SW fluxes tends to be differences that appear to be following contours of geosynchronous satellite boundaries.

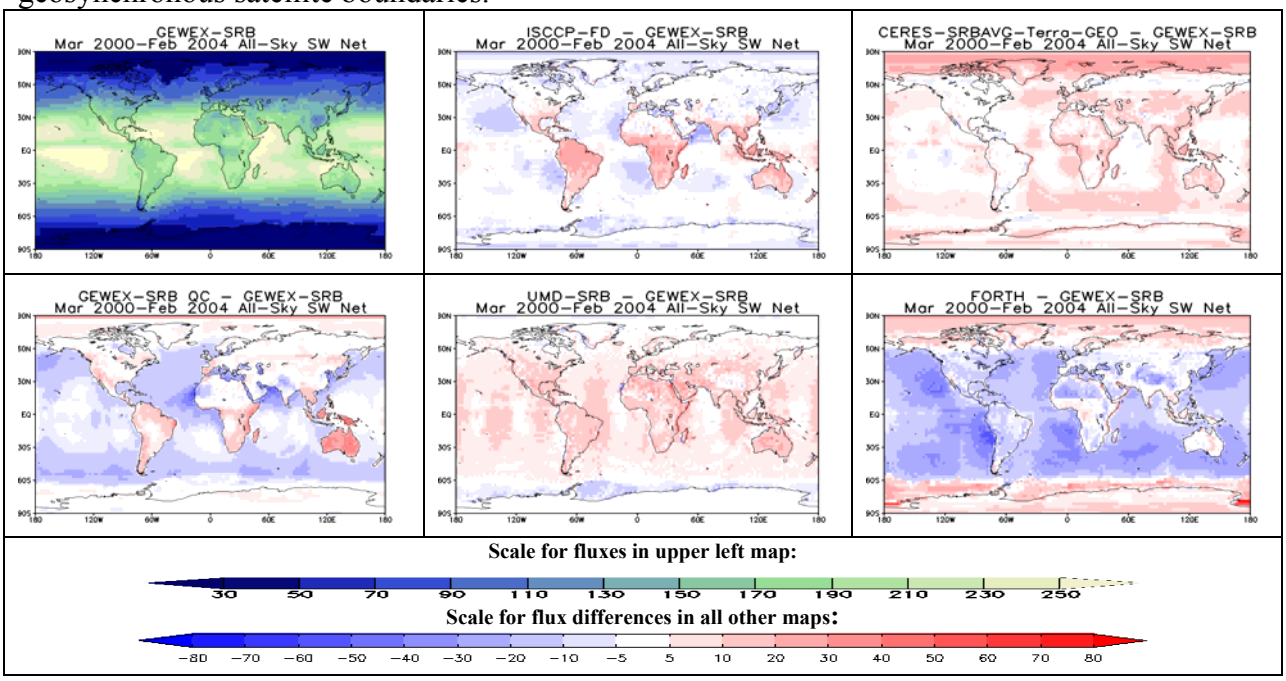

Figure 4.2.2: *Maps of* ***ASWNET*** *(in Wm^{-2}) for available GEWEX-RFA products averaged over the CERES period. The field of GEWEX-SRB flux is shown at upper left. The other maps are differences of the other six products and GEWEX-SRB. The upper color bar applies to the GEWEX-SRB map and the lower one applies to the difference maps.*

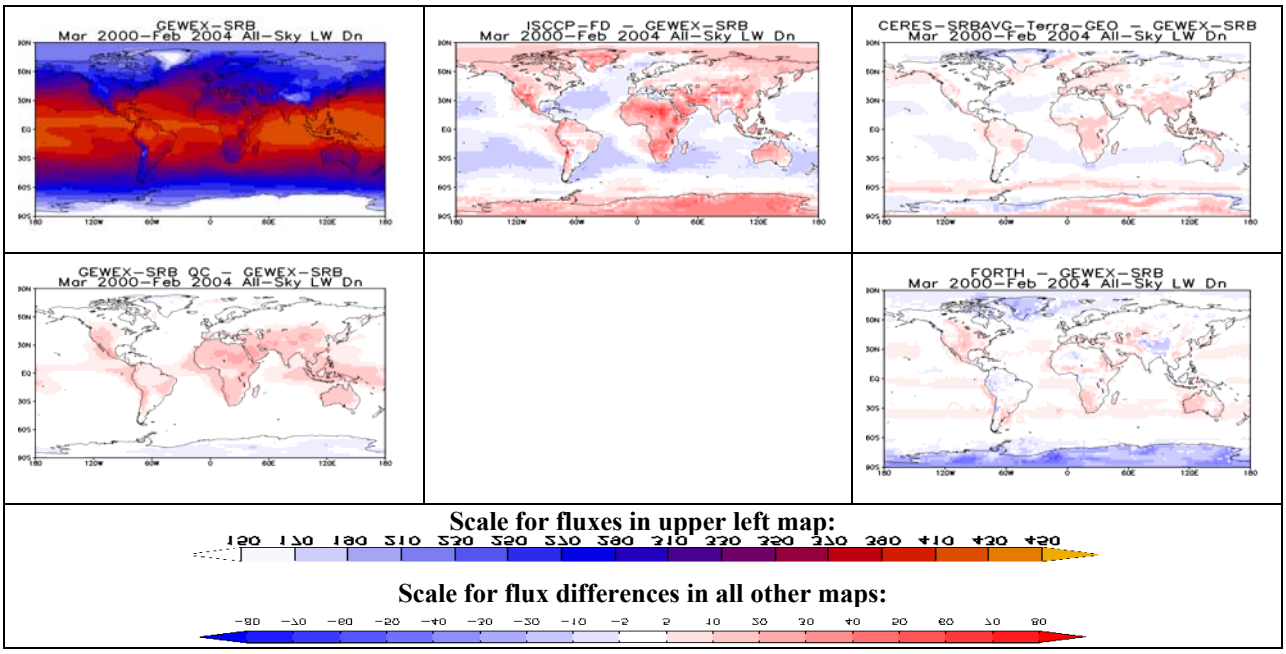

Figure 4.2.3: *Maps of* ***ALWDN*** *(in Wm^{-2}) for available GEWEX-RFA products averaged over the CERES period. The field of GEWEX-SRB flux is shown at upper left. The other maps are differences of the other six products and GEWEX-SRB. The upper color bar applies to the GEWEX-SRB map and the lower one applies to the difference maps.*

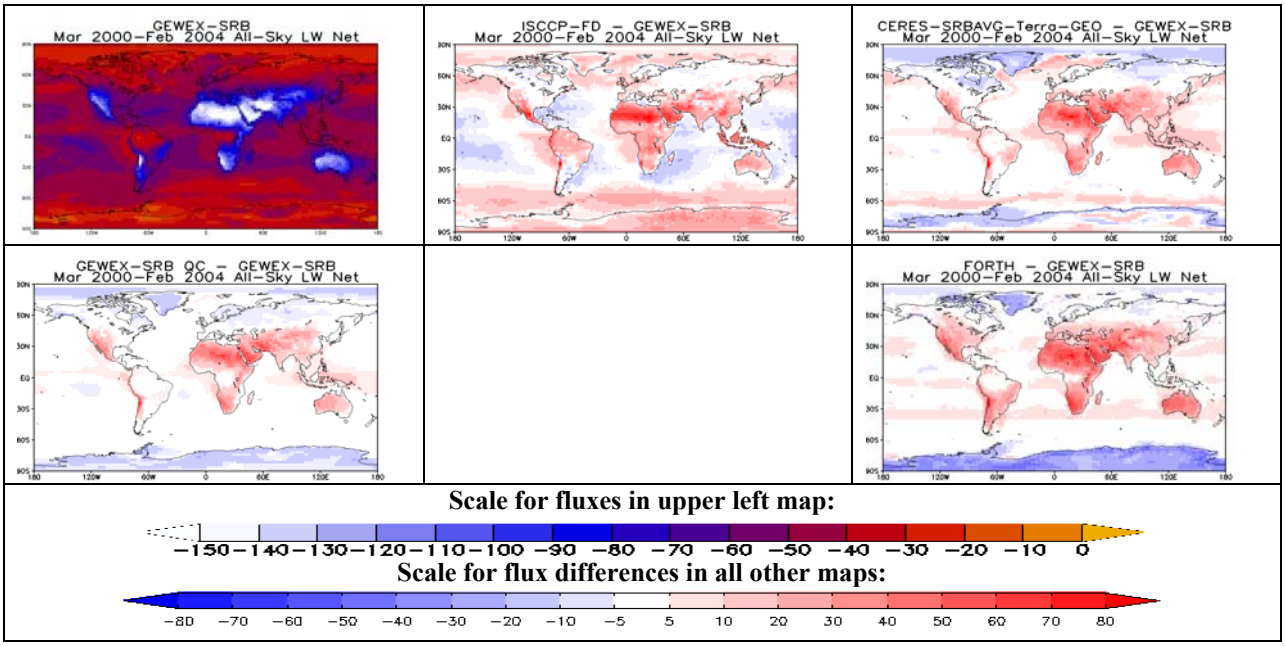

Figure 4.2.4: *Maps of* ***ALWNET*** *(in Wm^{-2}) for available GEWEX-RFA products averaged over the CERES period. The field of GEWEX-SRB flux is shown at upper left. The other maps are differences of the other six products and GEWEX-SRB. The upper color bar applies to the GEWEX-SRB map and the lower one applies to the difference maps.*

The ALWDN and ALWNET shown in *Figures 4.2.3 and 4.2.4* respectively show small differences in general, but the largest differences over continental land areas, particularly Africa. Relative to GEWEX SRB all the data products tend to be producing more net LW flux over arid land areas. This is likely due to issues concerning the skin and near-surface temperatures. Results show significant departures from GEWEX-SRB and from one another, indicating that the SW and LW net surface radiation budget is not yet constrained within the 10 Wm^{-2} target noted in *Table 4.1.1*, except in limited regions.

b) The ERBE Period (February 1985-January 1989)

Most results from this period, especially in the shortwave, show an artifact in the central Indian Ocean stemming from a lack of geostationary satellite coverage in the ISCCP dataset for much of this period, a gap that is filled in the CERES time period. ISCCP cloud amounts are spuriously higher at the edges of geostationary coverage, so the area between the two satellites shows markedly lower cloud amounts. The GEWEX-SRB shortwave algorithm is particularly sensitive to this discontinuity, more so even than is the ISCCP-FD product, which tends to compensate for view angle effects more smoothly. Products which cover both the CERES and ERBE periods (GEWEX-SRB, GEWEX-SRB QC, ISCCP-FD, FORTH, UMD-SRB, and DLR-ISIS) are quite similar in both periods.

4.2.3: Multi-year Zonal Averages

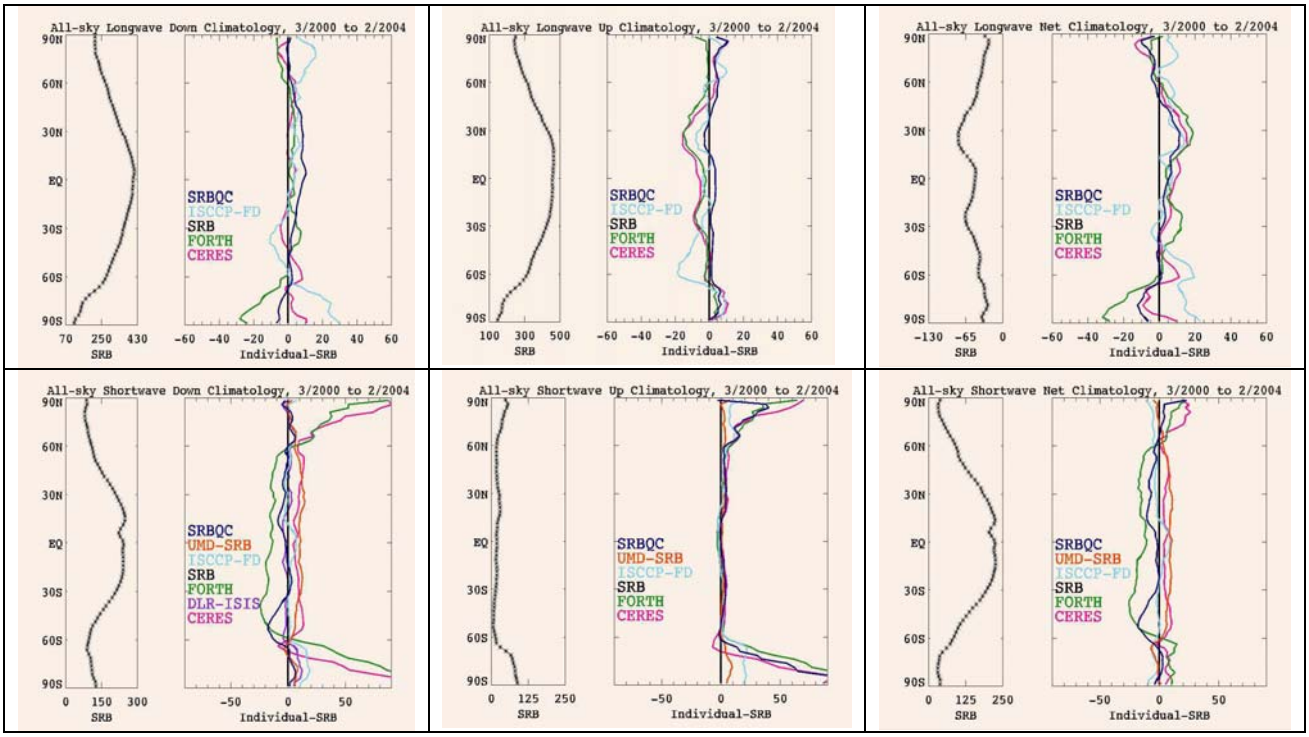

Figure 4.2.5: *Climatological zonally-averaged values the six fluxes for the CERES period. Left panel for each flux shows the GEWEX-SRB profile while the right panel shows the anomalies of available fluxes relative to GEWEX-SRB. The other models are: GEWEX-SRB (Parameterized; dark blue), ISCCP-FD (light blue), FORTH (green), and CERES SRBAVG GEO (pink). All values in* Wm^{-2}.

Zonally averaged fluxes, which are valuable for analyzing implied meridional heat transport are shown in *Figure 4.2.5* for the CERES period. The left panel for each flux shows the GEWEX-SRB profile while the right panel shows the anomalies of other available fluxes relative to GEWEX-SRB. The ASWDN and ASWNET profiles for GEWEX-SRB show the expected strong tropical maximum with the ITCZ providing a dip near the equator. The products are within 20 Wm^{-2} of GEWEX-SRB over the tropics and midlatitudes but show substantial disagreement over polar areas. ALWDN and ALWUP profiles show maxima over the Equator, and minima over Antarctica. Again tropical and midlatitude agreement is within 10 Wm^{-2}, but polar differences approach 40 Wm^{-2}. The products agree on the total net surface flux to within 20 Wm^{-2} at all latitudes. The strong exception is IPCC-AVERAGE, which is 40-60 Wm^{-2} lower than GEWEX-SRB at nearly all latitudes. Zonal profiles for the ERBE and the 20-Year periods are not significantly different and are not shown in view of the space limitation.

4.2.2.1: Global Averages

Climatological global averages for the CERES period for all-sky surface flux components are shown in *Tables 4.2.2. Table 4.2.3* reproduces corresponding ensemble means, absolute and relative standard deviations, and range of values for all fluxes. The ASWDN ensemble mean is 188.0 Wm^{-2}, with a standard deviation of 6.3 (3.3%) and a range of 178.4 to 197.6. Standard deviation for ASWUP, only 2.9 Wm^{-2} in magnitude, is large (9.3%) relative to the ensemble mean

of 23.9 Wm^{-2}, indicating wide disagreement among modeled surface albedoes in the various products. The ALWDN ensemble mean is 344.9 Wm^{-2}, with a small standard deviation of 2.5 Wm^{-2} (0.7%) and a range of 342.9 to 347.9, indicating strong inter-product agreement. Similarly, ALWUP ensemble mean is 394.8 Wm^{-2} with a small standard deviation of 3.1 Wm^{-2} (0.8%) and a range of 391.9 to 399.1. The ALWNET, with an ensemble mean of -49.8 Wm^{-2} and a standard deviation of 3.9 Wm^{-2} shows a larger range of -57.0 to -47.6 Wm^{-2} and large relative standard deviation (7.8%). Combining ASWNET and ALWNET into ATOTNET yields an ensemble mean of 115.1 Wm^{-2}, a range of 104.2 to 123.7, and a standard deviation of 7.5 Wm^{-2} (6.5%).

Table 4.2.2: 4-Year Global Annual Averages for the CERES Period.

SRB Dataset	All-sky SW Down	All-sky SW Up	All-sky SW Net	All-sky LW Down	All-sky LW Up	All-sky LW Net	All-sky Total Net
CERES/SRBAVG GEO	197.6	6.25	171.7	344.0	392.0	-47.9	123.7
DLR-ISIS	186.0						
FORTH	178.4	25.5	152.9	344.4	391.9	-47.6	105.3
GEWEX-SRB	186.3	20.6	165.7	342.9	397.1	-54.2	111.6
GEWEX-SRB	183.2	25.5	160.5	347.9	399.1	-51.1	109.4
ISCCP-FD	188.7	22.9	165.8	345.4	393.7	-48.3	117.5
UMD-SRB	195.7	22.7	173.0				

Table 4.2.3: Ensemble Statistics of Global Average Fluxes for the CERES Period.

Parameter	Multi-Dataset Ensemble mean	Absolute Standard Deviation (1-sigma)	Relative Standard Deviation (1-sigma)	Range (Min, Max)
All-sky SW Down	188.0	6.3	3.3%	(178.4, 197.6)
All-sky SW Up	23.9	2.9	9.3%	(20.6, 26.8)
All-sky Net SW	164.9	6.9	4.2%	(152.9, 173.0)
All-sky LW Down	344.9	2.5	0.7%	(342.9, 347.9)
All-sky LW Up	394.8	3.1	0.8%	(391.9, 399.1)
All-sky Net LW	-49.8	3.9	7.8%	(-57.0, -47.6)
All-sky Total Net	115.1	7.5	6.5%	(104.2, 123.7)

4.2.2.2: Tropical Averages (20°S - 20°N)

Table 4.2.4: *Climatological Tropical (20°S - 20°N) Averages for the CERES Period.*

SRB Dataset	All-sky SW Down	All-sky SW Up	All-sky Net SW	All-sky LW Down	All-sky LW Up	All-sky Net LW	All-sky Total Net
CERES/SRBAVG GEO	245.5	2.15	224.0	404.2	450.5	-46.2	177.8
DLR-ISIS	235.9						
FORTH	223.1	18.0	205.1	404.5	453.1	-48.6	156.5
GEWEX-SRB	238.9	19.6	219.3	402.5	457.8	-55.4	163.9
GEWEX-SRB (Parameterized)	235.8	20.6	215.2	410.3	460.4	-50.1	165.1
ISCCP-FD	242.0	18.1	223.8	405.0	456.2	-51.2	172.6
UMD-SRB	249.4	20.8	228.6				

Table 4.2.5: *Ensemble Statistics of Tropical Average Fluxes for the CERES Period.*

Parameter	Multi-dataset Ensemble mean	Absolute Standard Deviation (1-sigma)	Relative Standard Deviation (1-sigma)	Range (Min, Max)
All-sky SW Down	238.6	11.3	4.7%	(215.6,249.4)
All-sky SW Up	19.8	1.4	7.3%	(18.0,21.5)
All-sky Net SW	219.4	11.3	5.1%	(197.3, 228.6)
All-sky LW Down	405.3	2.8	0.7%	(402.5, 407.5)
All-sky LW Up	455.6	3.6	0.8%	(450.5,460.4)
All-sky Net LW	-50.3	3.1	6.1%	(-55.4, -46.2)
All-sky Total Net	169.0	11.1	6.6%	(146.8,177.8)

Tropical averages of all fluxes for the CERES period are shown in *Table 4.2.4. Table 4.2.5* shows corresponding ensemble averages, absolute and relative standard deviations, and range of values for all fluxes. Compared to global ensemble averages, ASWDN, ASWNET, ALWDN, and ALWUP are much higher, ASWUP is lower and ALWNET is about the same. All these combine to give a much larger ATOTNET in a totally expected manner. Relative standard deviation for ASWDN is higher (4.7%) than for global average, but lower (7.3%) for ASWUP.

4.2.2.3: Deseasonalized Monthly Mean Time Series Analysis

Table 4.2.6: *Variability (1-Sigma) of global (90°S to 90°N) mean deseasonalized time series (March 2000 to February 2004) from each dataset.*

	ALWDN	ALWUP	ALWNET	ASWDN	ASWUP	ASWNET
CERES SRBAVG GEO	1.3	1.1	0.8	1.1	0.5	0.9
DLR-ISIS				1.8		
FORTH	1.7	1.1	0.9	2.1	0.6	1.7
GEWEX SRB	1.5	4.7	3.8	1.5	1.0	1.9
GEWEX SRB (Paramet.)	1.5	1.2	1.0	1.2	0.3	1.0
ISCCP FD	4.2	7.9	4.6	1.5	1.4	1.8
UMD-SRB				1.9	1.0	2.1

Global and tropical deseasonalized time series for the CERES (not shown) with 1-sigma variabilities are shown in *Tables 4.2.6 and 4.2.7.* Agreement in longwave fluxes among the products is generally within a few Wm^{-2}, with the striking exception of the ISCCP-FD product, which shows a step change in October 2001 of 10-15 Wm^{-2}. This is known to result from a change in the TOVS operational algorithm at that point instantly raising surface temperatures by 3 to 5 K (see also chapter 3.5). GEWEX-SRB is affected by this anomaly as well, but to a lesser degree. LW products are not affected by this, they show similar variabilities.

Table 4.2.7: *Variability (1-Sigma) of tropical (20°S to 20°N) mean deseasonalized time series (March 2000 to February 2004) from each dataset. All values in* Wm^{-2}.

	ALWDN	ALWUP	ALWNET	ASWDN	ASWUP	ASWNET
CERES SRBAVG GEO	2.0	1.3	1.4	1.6	0.6	1.3
DLR-ISIS				2.6		
FORTH	2.5	1.5	1.3	2.6	0.5	2.1
GEWEX SRB	2.2	5.9	4.9	2.3	1.5	2.6
GEWEX SRB (Paramet.)	2.4	1.5	1.6	1.7	0.3	1.4
ISCCP FD	5.4	10.4	7.3	2.2	1.4	2.4
UMD-SRB				2.8	1.3	3.0

4.2.4: Summary

Eight datasets of surface radiative fluxes submitted to the GEWEX-RFA archive were analyzed and intercompared over two time intervals: 1) the CERES period (Mar2000-Feb2004) and 2) the ERBE period (Feb1985-Jan1989). Datasets in comparisons for the two periods are not the same because all datasets are not available for all periods. All datasets were compared with GEWEX-SRB by participant consensus. Thus, six other datasets were compared for the CERES period and six others for the ERBE period. Ensemble averages, their absolute and relative standard deviations, and ranges were also examined. Results for all periods are found to be quite similar and the differences, where they exist, are attributable to explainable causes. Graphical results and tables are presented only for the CERES period, but those plots for the ERBE period are available in the on-line supplemental appendix. Global averages of ALWDN and ALWUP agree to within a 1% relative standard deviation. SW flux agreement was not as good. Relative standard deviation for ASWDN is about 3.3% while those for ASWUP and ATOTNET are 9.3% and 6.5% respectively. Improving agreement in the SW fluxes is the most necessary step towards improving knowledge of ATOTNET. Similar results hold for the tropics. On a regional basis, areas of strongest disagreement for both SW and LW fluxes are the poles (especially the ice covered areas) and the deserts. Some polar differences likely result from satellite difficulty in recognizing clouds over ice. Over the deserts and other continental areas, skin temperature, temperature and humidity profiles, and surface albedo models are likely candidates for improvement, leading to improved agreement in the radiative fluxes.

4.3: Surface Radiation Budget Data Product Comparison

Y.-C. Zhang and W. B. Rossow

Abstract

Annual global averages and also monthly global averages on the surface radiation budget components, as computed with several data sets are used to estimate their possibly linear trends and other statistical measures during the period January 1984 to December 2003. Quite controversial results were found possibly due to the influence of various ancillary data on the radiative state of the atmosphere and surface.

4.3.1: Datasets and Time Period Covered

For a comparison of the long-term records of Surface Radiation Budget products in this section, we select all products that have global coverage (with one exception) and monthly-averaged results covering a period of 20 years from January 1984 to December 2003 with spatial resolution of 2.5°, available from GEWEX-RFA collection. There are seven such products: (1) GEWEX-SRB Ed281 and Ed025 for SW and LW, respectively (SRB, Stackhouse, et al., 2004), (2) ISCCP-FD Ed000 (FD, Zhang et al., 2004), (3) GFDLCM2.1_Ed001 (GFDL, Delworth et al., 2006), (4) FORTH_Ed01a (FRTH, Pavlakis et al., 2003), (5) NCEP-DOE-R2_Ed002 (NCEP, Kanamitsu et al., 2002), (6) UMD-SRB_Ed033 (UMD, based on Pinker and Laszlo, 1992) and (7) DLR-ISIS_Ed001 (ISIS, Lohmann et al., 2006). The seven products and their available flux

components are listed in *Table 4.3.1*. The detailed descriptions for these products can be found at http://eosweb.larc.nasa.gov/GEWEX-RFA/.

Since there are no high-quality, direct surface-flux measurements with global and 20-yr coverage (other than measurements from a sparse, very limited number of surface stations, mostly with records < 20-yr, such as the BSRN data), we do not have a direct-observation-based product that can serve as a standard baseline for the long-term comparison for evaluating satellite-based or model-based flux values. Because the primary goal of the product comparison is to evaluate the SRB product, we use it as the reference and focus on differences between SRB and the other products. We study 12 surface flux components as numbered in *Table 4.3.1* (column one): ASWDN, ASWNET, ALWDN, ALWNET, ATOTNET, CALB2, CSWDN, CLWDN, SWCE, LWCE, ASWUP and ALWUP. There are only three products (SRB, FD and GFDL) that are complete, having all the components available over the whole globe. We focus on global mean results, but also mention regional averages when there are notable features. The regions are defined as: tropical-subtropical (30° S – 30° N), southern- (60°S – 30°S) and northern-hemispheric mid-latitude (30°N – 60°N), all low-to-mid-latitudes (60°S – 60°N), the South (90°S – 60°S) and North (60°N – 90°N) Polar regions, the Tropical Pacific Ocean (20°S – 20°N and 130°E – 270°E) and the North Atlantic Ocean (0°N – 60°N and 285°E – 355°E), a total of eight regions.

The uncertainties of the baseline product, SRB Release 2, are described in Stackhouse et al. (2004), based on their comparison with BSRN; they give estimates of bias (RMS) for monthly-mean SRB surface fluxes collocated with the BSRN sites as: -3.4 (23.0) Wm^{-2} and -5.2 (15.5) Wm^{-2} for ASWDN and ALWDN, respectively. Uncertainties for the other products vary or are not available; for further information, see other sections of the Chapter 4.

Table 4.3.1: *Availability of Flux Components for the Seven Data Products ('av' = available)*

Flux Component♦	Products						
	1	2	3	4	5	6	7
	SRB	FD	GFDL	FRTH	NCEP	UMD	ISIS
1. ASWDN	av	av	av	av†	av	av	av
2. ASWNET	av	av	av	av†	av	av	
3. ALWDN	av	av	av	av	av		
4. ALWNET	av	av	av	av*	av		
5. ATOTNET	av	av	av	av†	av		
6. CALB2	av	av	av				
7. CSWDN	av	av	av				
8. CLWDN	av	av	av				
9. SWCE	av	av	av				
10. LWCE	av	av	av				
11. ASWUP	av	av	av	av†	av	av	
12. ALWUP	av	av	av	av	av		

♦This study mainly focuses on the twelve numbered flux components as shown in column one.
†Only cover ±60º latitudinal zones;

4.3.2: Annual Mean Time Series

a) Global Means

Table 4.3.1 provides an overview of the twelve flux components by showing the 20-yr, global average values from the seven products. The twelve components are organized in six sub-tables, (a) through (f), based on the order of their series numbers in *Table 4.3.1*. For each flux

component, the table shows each product's time mean (over 20 years) as well as temporal standard deviation (stdv) of annual means, the linear trend per decade (in Wm^{-2} $decade^{-1}$ for fluxes or % $decade^{-1}$ for albedo) and the relative trend per decade (in % $decade^{-1}$ as the ratio of the trend to the stdv). The trends are based on the slope of linear least-squares fit to the annual anomaly time series. *Figures 4.3.1 (a to f)* shows the annual anomaly time series for SRB and the linear fits for the twelve flux components. As shown by *Table 4.3.2(a)* (representing sub-table a, similarly throughout Section 4.3.2), the time averages differ over a range ~10 Wm^{-2} (or > 5% relative to the average of all the products) for both ASWDN and ASWNET. UMD has the largest values: 194.7 and 171.5 Wm^{-2} for ASWDN and ASWNET, respectively, while GFDL and NCEP have the smallest values, 185.3 and 160.2 Wm^{-2}, respectively, for these two flux components. All the standard deviations are ~1-2 Wm^{-2}. The magnitude of the relative trends is generally > 10% $decade^{-1}$ (except FD = -3.1 % $decade^{-1}$ for ASWDN) with the largest being ~100% $decade^{-1}$ for both ASWDN and ASWNET for UMD and NCEP. All relative trends are positive for both ASWDN and ASWNET, except for GFDL. The trend of ASWDN for FD is near zero (-0.04 $Wm^{-2}decade^{-1}$). In other words, there is no agreement on the sign of trends from the available products and the trend magnitudes differ by as much as 1.5 (ASWDN) and 2.5 Wm^{-2} $decade^{-1}$ (ASWNET). *Figure 4.3.1(a)* shows that SRB trend for ASWNET is larger than for ASWDN because of a negative trend of ASWUP (*Panel f*). All of the products agree on this feature as can be seen in *Table 4.3.2(a) and (f)*. The negative trend for ASWUP is primarily caused by the negative trend of CALB2 (see *Figure 4.3.1(c)* for SRB and *Table 4.3.2(c)* for all available products).

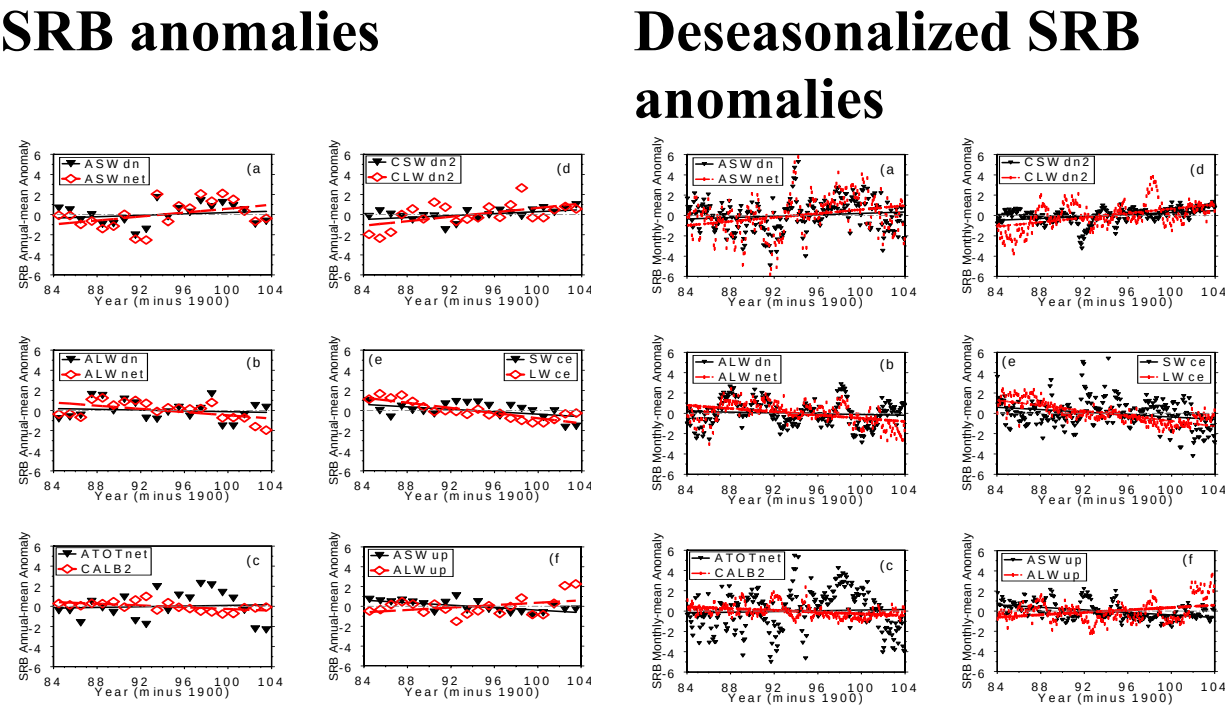

Figure 4.3.2 : *SRB anomaly (left) and deseasonalized SRB anomaly (right) time series from global, annul mean for twelve flux components in six panels (two for each panel) for 1984 to 2003 period (all in Wm^{-2} except CALB2 in %). The corresponding linear least-square regression line is also shown. See text for the meaning of all the acronyms.*

In other words, all five available products exhibit an increase of the ASWNET trend

compared with the ASWDN trend, primarily caused by a negative trend of ASWUP. Therefore, there appears a qualitative agreement on negative trend for ASWUP and CALB2. *Table 4.3.2(f)* gives a range of trends for ASWUP from -127 (FD) to -41 % decade^{-1} (NCEP) and for CALB2 (*Table 4.3.2(c)*) from -0.13 % decade^{-1} (GFDL) to -1.5% decade^{-1} (FD).

Although all the five available products have different signs for the trend of ALWNET, the relationship between ALWNET and ALWDN is the opposite of the one between ASWNET and ASWDN. As shown in *Table 4.3.2(b)*, except for FD, all ALWNET trends decrease with respect to the trends of ALWDN, because ALWUP has positive trends (*Table 4.3.2(f)*), except for FD). This result seems to reflect a positive trend of surface skin temperature (TS), which is consistent with other analyses.

The negative trend in the FD value of ALWUP is understood to be caused by artifacts introduced into the TOVS atmospheric temperature profile dataset by analysis procedure changes; since this dataset is used by ISCCP to retrieve TS and to produce FD, the trends are dominated by these artifacts (Zhang et al., 2006). The ALWNET trends range from -1.04 (FRTH) to 1.76 (FD) Wm^{-2} decade^{-1}, or from -130 (FRTH) to 124 (GFDL) % decade^{-1} relative, making it difficult to judge whether there is any significant trend. The all-sky SW and LW net fluxes, however, add to a positive ATOTNET for all four available products (*Table 4.2.2(c)*), ranging from 0.18 (SRB) to 2.62 (FD) Wm^{-2} decade^{-1}, or 12 (SRB) to 115% decade^{-1} (NCEP) relative.

For all twelve flux components, the average differences range from ~3 Wm^{-2} (SWCE) to ~13 Wm^{-2} (ATOTNET), or ~1% (ALWDN and ALWUP) to 32% (LWCE) relative, and 1.7 % (~12% relative) for CALB2 *(Table 4.3.2, above)*. The average differences are generally larger than their TOA counterparts (if any) compared with ERBE and CERES by up to a factor of ~2 – 3 (see Chapter 3), indicating that there are much larger uncertainties for surface flux products than the TOA ones.

Overall, the available products generally exhibit agreement on the sign of the long-term trends for seven out of twelve components: ATOTNET, CSWDN and CLWDN with a positive sign and CALB2, SWCE, LWCE, and ASWUP with a negative sign (*Table 4.3.2*). The decadal trend magnitudes are generally comparable with their inter-annual values of the standard deviation with a few exceptions, especially for CSWDN, for which, FD and GFD exhibit much smaller decadal trends below 0.1 of their standard deviation. SRB is consistent with these results: *Figure 4.3.1* shows the SRB results. Such agreement may indicate some true trends for the seven flux components (plus TS as mentioned above), at least qualitatively, because some of the products are largely independent except for their cloud information. Although we have only qualitative agreement at best, the range of magnitudes is still significant compared the median value. Nevertheless, these results suggest that we are close to sufficient accuracy to determine true trends in a quantitative way for all the components.

We also compared the global, annual-mean anomaly time series of all other products with SRB in terms of the standard deviation of differences, correlation coefficient, and slope and intercept values from linear least-square regression with SRB (as the abscissa). For ASWDN, ASWUP and ASWNET, all satellite-based products (FD, UMD and ISIS) have larger correlations with SRB (which is also satellite-based) with the largest being for FD = 0.86 and the smallest UMD = 0.54 for ASWDN. The correlations are even larger for ASWNET (> 0.80) and ASWUP (> 0.81). In contrast, the reanalysis- (NCEP) and model-based results (GFDL) exhibit correlations of only ~0.4, ~0.2 and ~0.3 for ASWDN, ASWNET and ASWUP, respectively. The reason is likely that the former all have satellite-based cloud information from ISCCP, while the latter are dependent on model-generated clouds.

Table 4.3.2: *Absolute Time Mean ('mean') of 20-yr (1984 to 2003) Annual-mean Time Series in Global Average, Standard Deviation ('stdv'), and Absolute Trend ('trend' in absolute value per decade) and Relative Trend ('rel trend', in % per decade for the ratio of absolute trend to stdv) from Least-square Regression for Anomaly Time Series for the Twelve Flux Components in Six Pairs (all fluxes in Wm^{-2}, but albedo in % without unit.*

(a)

Data Product	ASWDN				ASWNET			
	mean	stdv	trend	rel trend	mean	stdv	trend	rel trend
SRB	186.5	0.994	0.34	35	165.7	1.380	0.98	71
FD	189.3	1.280	-0.04	-3	165.9	1.475	0.85	58
GFDL	185.3	0.731	-0.26	-35	162.1	0.619	-0.07	-12
NCEP	187.2	0.676	0.67	100	160.2	0.690	0.76	110
UMD	194.7	1.423	1.56	110	171.5	2.170	2.62	121
ISIS	185.9	1.459	0.81	55	NA	NA	NA	NA

(b)

Data Product	ALWDN				ALWNET			
	mean	stdv	trend	rel trend	mean	stdv	trend	rel trend
SRB	343.2	0.966	-0.20	-21	-52.9	0.886	-0.80	-90
FD	343.8	1.777	0.22	12	-49.4	3.125	1.76	56
GFDL	338.2	1.417	1.79	126	-57.9	0.400	0.50	124
FRTH	344.2	0.989	-0.10	-10	-46.9	0.794	-1.04	-131
NCEP	339.5	1.060	1.03	97	-56.9	0.340	-0.10	-30

(c)

Data Product	ATOTNET				CALB2			
	mean	stdv	trend	rel trend	mean	stdv	trend	rel trend
SRB	112.8	1.423	0.18	12	13.0	0.452	-0.44	-96
FD	116.5	3.390	2.62	77	13.5	1.092	-1.50	-138
GFDL	104.2	0.676	0.43	63	14.7	0.088	-0.13	-150
NCEP	103.3	0.569	0.66	115	NA	NA	NA	NA

(d)

Data Product	CSWDN				CLWDN			
	mean	stdv	trend	rel trend	mean	stdv	trend	rel trend
SRB	242.6	0.581	0.49	84	307.9	1.165	1.10	95
FD	247.7	1.259	0.05	4	312.9	1.523	0.49	32
GFDL	244.5	1.063	0.10	9	312.9	1.490	1.94	130

(e)

Data Product	SWCE				LWCE			
	mean	stdv	trend	rel trend	mean	stdv	trend	rel trend
SRB	-50.0	0.754	-0.61	-81	34.7	0.888	-1.28	-144
FD	-52.9	0.827	-0.17	-20	29.4	0.852	-0.25	-29
GFDL	-52.4	0.531	-0.36	-67	25.2	0.125	-0.15	-121

(f)

Data Product	ASWUP				ALWUP			
	mean	stdv	trend	rel trend	mean	stdv	trend	rel trend
SRB	20.8	0.565	-0.63	-112	396.1	0.929	0.60	65
FD	23.4	0.639	-0.89	-127	393.2	3.445	-1.54	-45
GFDL	23.2	0.155	-0.19	-119	396.1	1.031	1.29	125
NCEP	26.9	0.208	-0.09	-41	396.4	0.887	1.13	128
UMD	23.2	0.852	-1.05	-128	NA	NA	NA	NA

This situation is also true for ALWDN: FD and FRTH have correlations with SRB > 0.65, while GFDL has a correlation of only 0.12. Note, however, that NCEP also has a correlation of 0.65, which may be because its atmospheric temperature/humidity profiles are based on a reanalysis, somewhat similar to the GEOS4 assimilation product used by SRB as input (cf. Zhang

et al. 2006). *Table 4.3.3(f)* shows that the four products (FD, GFDL, FRTH and NCEP) are all well correlated with SRB for ALWUP with smallest correlation of 0.52 for GFDL. The combination of ALWDN and ALWUP, however, produces much smaller correlations < 0.43 for ALWNET for all four products, implying that the relationship between the atmospheric and surface temperatures is different among the products. All the differences of the SW or LW flux determinations lead to smaller correlations for ATOTNET (< 0.5). Only FD and GFDL report values for CSWDN and CLWDN; the correlations of FD with SRB are 0.60 and 0.47, respectively, smaller than the all-sky counterparts (0.86 and 0.65), but GFDL shows the opposite relationship, correlations of 0.57 for both CSWDN and CLWDN but 0.42 and 0.12 for ASWDN and ALWDN, respectively. A possible explanation is that FD clear-sky properties differ more from SRB than the cloudy-sky properties, both based on ISCCP, whereas the GFDL clear-sky properties are more similar to the SRB properties than their clouds are. The similarities between satellite-based fluxes (FD, FRTH, UMD and ISIS) and SRB are also reflected in the difference standard deviation and slope values. The difference stdv (with SRB) of the satellite-products are generally smaller than their own inter-annual variability *(Table 4.3.2),* indicating some agreement on the inter-annual variations, while the model-based results have difference stdv larger than their own inter-annual variations, indicating little agreement on inter-annual variations. The slope values for the satellite-based flux components are closer to 1 with a few exceptions than the model-based components that can be explained by the same factors as above.

2) Regional Means

We have also examined all the same types of results for the regional statistics for the eight regions as defined in Section 4.3.1, but these are not shown here for brevity. None of the products shows consistency of trend sign agreement between global and regional results for the same flux components. The number of flux components with trend-sign agreement varies from region to region: varying from eight components in the North Polar Region to only two components in the 60°S – 30°S and Tropical Pacific Ocean regions. More interestingly, the net trend increase (decrease) of ASWNET (ALWNET) with respect to ASWDN (ALWDN) still holds for most of the regions for most of the products with only minor exceptions (mostly by NCEP and FRTH for ASWNET and by FD for ALWNET). In addition, although CALB2 in FD has a positive trend for some regions, its ASWUP still has a negative trend sign. The stdv and trend magnitudes for all the regional cases are generally up to twice to three times larger for the Polar Regions compared with the global mean values.

The corresponding stdv of differences with SRB for the regional time series are generally much larger, with the largest increases in the Polar Regions, indicating that all the products disagree most in these difficult areas. The satellite-based fluxes are more similar to SRB than the model- or assimilation-based products as in the global case (with a few exceptions). However, UMD ASWDN exhibits a much smaller correlation of 0.34 and 0.18 for the North Polar and 60°S – 30°S regions, respectively, despite being very similar to SRB in treatments of clouds, suggesting an important difference in the treatments of surface albedo and aerosol.

4.3.3: Monthly Mean Time Series

We found also that all the time-mean and absolute trend values are essentially identical to those of annual-mean time series (except a few cases); but the standard deviation are generally larger by ~50% or so (up to > 100% for polar regions), so the relative trend values are generally decreased to maintain the same absolute values. Therefore, the above discussion of the annual-

mean time series holds true for the monthly-mean time series. This gives us some confidence for the stability of the trend values. For the regional time series, the same tendencies appear as discussed for the annual-mean time series.

4.3.4: Conclusions

Because we will not likely ever have a direct-measurement-based global, long-term surface flux dataset, the products like the ones compared here must be made accurate enough for monitoring climate changes. These products are all produced based on two fundamental parts that determine their quality and characteristics: a radiative transfer model and the input datasets. Although there are differences among the models, the differences of the products are dominated by the differences of their input datasets. Therefore, the degree of closeness to truth for a flux product components is highly dependent on the degree of approximation to the actual physical properties of the atmosphere and surface for its input datasets; likewise the similarity between two flux products are also more dependent on the similarity of their input datasets. Because our baseline for comparison is SRB, which has cloud properties from ISCCP and other input datasets that are more or less related to satellite observations, all the other satellite-based products are more similar to it than the model-based (GFDL) or assimilation-based (NCEP) products. However, the NCEP results exhibit similar agreement with SRB for the LW flux components because the assimilated temperature-humidity results are similar to those used by SRB. In other words, further improvement will have to come more from improving the input datasets than improving the radiative modeling.

Based on relative independence of these products and their own uncertainties (if available), the 20-yr trend values for the different flux components may have captured some indication of true climatological tendencies over these two decades, especially for ASWUP (CALB2) and ALWUP (TS). All the products agree that global (and most regional) trends of ASWNET are larger than for ASWDN and that of ALWNET are smaller than for ALWDN. The combination of the trends of ASWNET and ALWNET produces a positive trend for global mean ATOTNET. The trend of ALWUP and TS are consistent with the observations from other independent sources (e.g., Hansen et al., 2010), while the negative trend of ASWUP and CALB2 needs some further investigation. Although the sign of these trends may be robust, the uncertainty of magnitude is still very large, ranging from ~10% decade^{-1} to >100% decade^{-1} relative. For the other flux components, the situation is more mixed among these products. The largest discrepancies among all the products appear in the South and North Polar regions as might be expected.

In conclusion, while the agreement about decadal trends is still very poor, these results encourage the belief that more work on the quality of the input datasets can achieve more useful accuracy, possibly enough to quantify the decadal trends in the fluxes and the cloud effects on them.

4.4: Annual cycle variability of surface radiative fluxes

L. Hinkelman

Abstract:

In his section are studied annual cycles of all radiation budget components at the surface. Small differences occur between the different data sets.

4.4.1: Data Description

The analysis of surface radiative flux annual cycle data is described in this report chapter. The input to this analysis consisted of time series of monthly mean fluxes averaged over the global and tropical (20°S-20°N) latitudes. Several data providers submitted time series data directly to the Flux Assessment archive (SRBAVG-GEO, GEWEX-SRB, and GEWEX-SRB (Parameterized)). For the remaining data sets (ISCCP, FORTH, DLR ISIS, U. Maryland, and ERBEsrb-Li), only monthly surface flux data at 2.5º resolution was supplied. For these data sets, global and tropical mean time series were computed from the global map data using equal area weighting. In constructing these time series, we required a minimum of 98% of the surface area in the averaging region to be available in a given month in order to produce a valid data sample. Time series were created for the fourteen variables listed in *Tables 4.4.1 and 4.4.2*.

If a given variable was not included in the archive for a particular data set, the corresponding time series was produced from the related variables, if possible (e.g., ASWNET from ASWUP and ASWDN.) The time series available for each data set at the conclusion of this process are listed in *Tables 4.4.1 and 4.4.2*. Note that the majority of these data sets provide values for every grid box regardless of whether a corresponding measurement was available (e.g., a clear-sky value even when the grid box was overcast.) However, the CERES products only include actual measured values, so the SRBAVG-GEO regional means include filled data. The SRBAVG-GEO time series analyzed here were produced by the CERES team using their preferred filling techniques. For the SRBAVG-GEO version analyzed here, these produced erroneous values in the global mean shortwave variables during the northern hemisphere summer traceable to deficiencies in filling of the Polar Regions. These issues have since been corrected in a later version of the product. The FORTH data product includes shortwave variables for 60°S-60°N only, so only tropical means were included for this data set in the analysis.

Table 4.4.1*: Data sets and their variables used in this study, all-sky fluxes. G = global, T = tropical (20°S-20°N).*

Data set	ASWDN	ASWUP	ASWNET	ALWDN	ALWUP	ALWNET	ATOTNET
ISCCP	G, T	G, T	G, T	G, T	G, T	G, T	G, T
FORTH	T	T	T	G, T	G, T	G, T	T
ISIS*	G, T						
SRBAVG-GEO*	G, T	G, T	G, T	G, T	G, T	G,T	G, T
GEWEX SRB	G, T	G, T	G, T	G, T	G, T	G, T	G, T
GEWEX SRB-QC	G, T	G, T	G, T	G, T	G, T	G, T	G, T
U. Maryland	G, T	G, T	G, T				
ERBEsrb-Li**			G, T				

* CERES time period (3/2000-2/2004) only. ** ERBE time period (1/1985-12/1989) only.

Table 4.4.2: *Data sets and their variables used in this study, clear-sky fluxes. G = global, T = tropical (20°S-20°N).*

Data set	CSWDN	CSWUP	CSWNET	CLWDN	CLWUP	CLWNET	CTOTNET
ISCCP	G, T	G, T	G, T	G, T	G, T	G, T	G, T
SRBAVG-GEO*	G, T	G, T	G, T	G, T	G, T	G, T	G, T
GEWEX SRB	G, T	G, T	G, T	G, T	G,T	G, T	G, T
GEWEX SRB-QC	G, T			G, T			

* CERES time period (3/2000-2/2004) only. ** ERBE time period (2/1985-1/1989) only.

4.4.2: Analysis Method

Mean annual cycles were computed for each data set, parameter, and region over two time periods, the "ERBE period" (defined as February 1985 – January 1989) and the "CERES period" (March 2000 – February 2004). At least one valid monthly mean value from the four-year period was required to be available when computing the four-year averages. However, at least three values were available in every case. The mean and standard deviation for each month over all available data sets was then computed. The mean over all data sets is termed the composite annual cycle in this study. Annual cycles in terms of monthly deviations from the overall mean value of the parameter for a given data set, region, and time period, termed anomaly annual cycles, were then computed.

The annual cycles for each data set and their mean (composite) were compared on a monthly basis, as shown in the figures below. Statistics describing the variability of the monthly cycles, given in the tables, were also computed.

4.4.3: Qualitative Results

a) Global Mean Annual Cycles

A qualitative picture of the variability of the annual cycles of the included flux variables over the various data sets can be gained from *Figures 4.4.1 and 4.4.2*. For nearly all variables, the global mean cycles from all data products track together well. The first obvious exception to this is the deviation of the SRBAVG-GEO all-sky and clear-sky shortwave downward and net fluxes from the other data sets during May through July. These differences, which were discussed in the Data Description section above, can reach 5 Wm^{-2} and are passed through to the corresponding total fluxes. Since these obviously incorrect values were included in the composite cycles, the standard deviations for these months are inflated.

Only the all-sky longwave net flux annual cycles differ significantly in phase. This may be due in part to the magnitude of the monthly anomalies being quite small, with a total range of less than 4 Wm^{-2}. Nevertheless, while the ISCCP data exhibits a strong cycle with peaks in July and January (minima in April and September) during the ERBE time period, only the GEWEX SRB-QC shows a similar pattern (with smaller magnitudes). The GEWEX SRB global mean net longwave data has a single broad minimum in the northern hemisphere summer and a strong peak in December, while the variations in the FORTH data are very small and oppose the phase of the ISCCP data. During the CERES time period, the patterns are similar, but the SRBAVG-GEO product is added. Its annual cycle is of moderate amplitude with a minimum in May and maximum in August. Therefore, this variable would seem to be the least consistent over the various data sets. However, we will see that the standard deviations of the set of flux values at

each month are no larger for ALWNET than for the other flux variables. For the clear-sky longwave net fluxes, there are fewer data products available, but all are reasonably in phase.

A few other features stand out in the other global mean annual cycles. For example, the ISCCP data tend to have a greater range in amplitude for the upward shortwave fluxes. In particular, the August lows are around 2 Wm^{-2} deeper than for the other data sets. These dips also occur slightly earlier for the ISCCP data. While the annual cycles of upwelling longwave flux peak in July for all other data sets, ISCCP shows a slight dip in July for the clear-sky and all-sky data in both the ERBE and CERES time frames. The cause of this difference is unclear.

b) Tropical Mean Annual Cycles

As to be expected, the shape of the annual cycles of several variables are quite different for the tropical versus the global means (e.g., solar fluxes going through two cycles per year.) However, the areas of disagreement are similar to those for the global fluxes. Except for the clear-sky LWNET during the ERBE time period, all longwave net variables show significant differences in phase and magnitude among the data sets. A best agreement is among SRBAVG-GEO, GEWEX SRB, and GEWEX SRB-QC for all-sky values during the CERES time period.

The magnitude of the monthly anomalies in shortwave upward fluxes is much smaller for the tropical than the global means. The magnitude of the ISCCP SW upward flux annual cycles is still greater than that from the other products, but the differences are less noticeable than before. Indeed, the September peak in the SW upward flux from the GEWEX SRB in the CERES time period differs from the composite mean as much as the ISCCP values do. Finally, it should be pointed out that the tropical means of the shortwave fluxes for the SRBAVG-GEO data do not show the problems associated with the global means.

4.4.4: Statistical Results

The variability among the annual cycles from different satellite surface products is presented quantitatively in the statistics of *Tables 4.4.3 and 4.4.4*. These statistics have been computed for the same variables and time periods as shown in the accompanying figures and are provided for the reader desiring information in greater detail. However, the patterns in these statistics can be described in just a few sentences.

The most important variable for this assessment is the range of values provided by the different satellite flux products. For nearly all of the variables, the standard deviations of the monthly anomalies over all available products range between 0.1 and 1.8 Wm^{-2}. For a few individual variables and months, the standard deviations are higher, from 3 Wm^{-2} to as high as 5.9 Wm^{-2} in two cases. Most of these outliers can be attributed to the bad SRBAVG-GEO shortwave fluxes while a few (3) are occur when only a limited number of data sets are included in the analysis. The one exception is a value of 3.6 Wm^{-2} for March in the CERES time period. This can be traced to the FORTH data set, which exhibits an out of phase cycle of all-sky net longwave fluxes and a relatively high all-sky shortwave downwelling flux during this month. Since the monthly standard deviation values all fall within a small range, relative standard deviations mainly depend on the overall magnitude of the individual variable. For most variables, magnitudes are greater than 100 Wm^{-2}, so that the relative standard deviations are less than 1%. The upwelling shortwave fluxes (both clear- and all-sky) and all-sky longwave net fluxes have absolute values of ~30 Wm^{-2} or less and their relative standard deviations can be as high as 10%.

As noted above, very data products are available for certain variables, particularly the clear-sky fluxes (only two for most clear-sky variables in the ERBE time frame), making the

computed statistics less meaningful. The agreement between these two or three data sets is in most cases no different than agreement for the variables that include many data products.

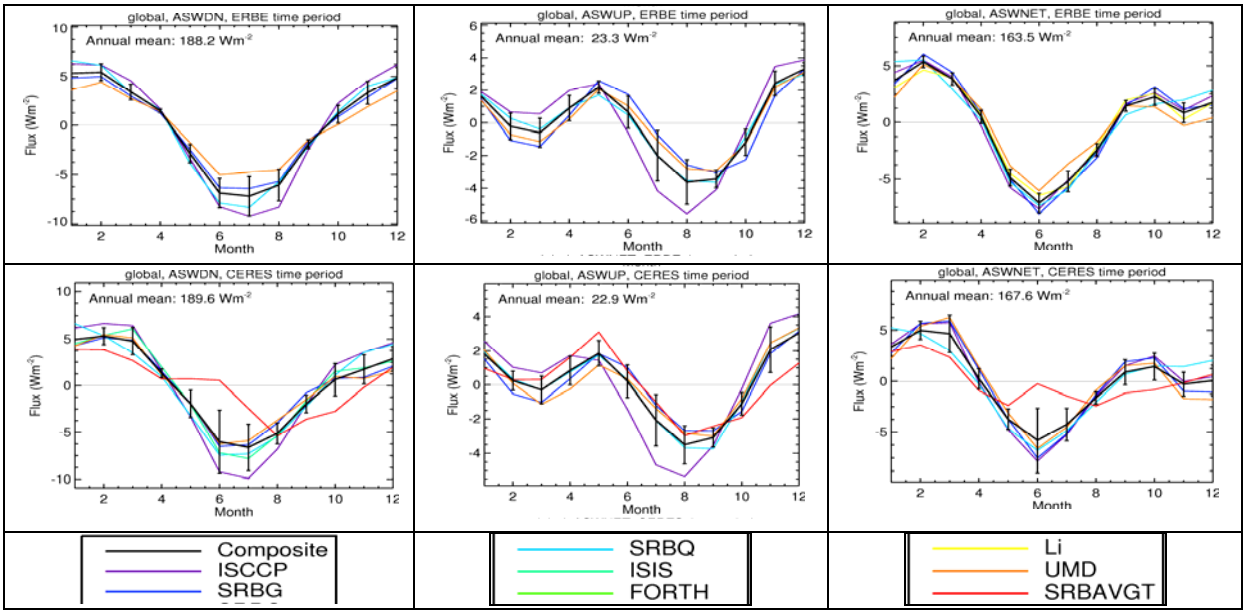

Figure 4.4.1: *Global mean annual cycles for all-sky shortwave parameters over the ERBE and CERES time periods shown as deviations from the corresponding annual mean. Error bars indicate +/- one standard deviation.*

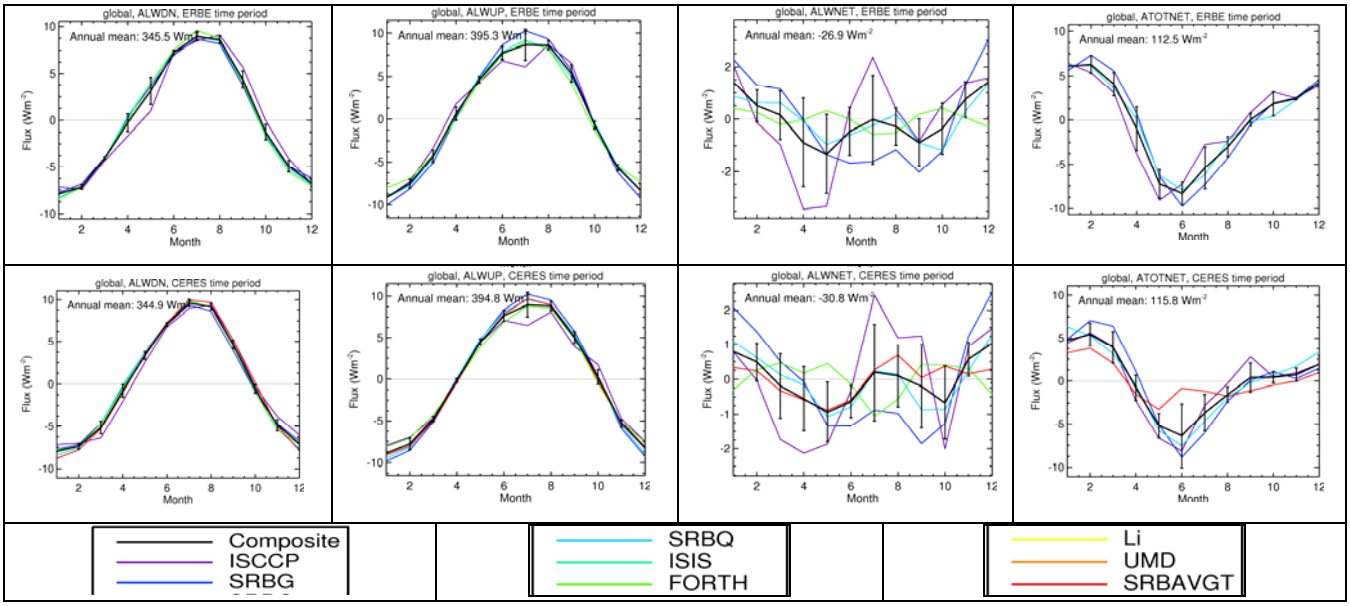

Figure 4.4.2: *Global mean annual cycles for all-sky longwave parameters and total net flux over the ERBE and CERES time periods shown here as deviations from the corresponding annual mean. Error bars indicate +/- one standard deviation.*

Table 4.4.3: *Global mean annual cycle data for ASWDN over all data sets, ERBE and CERES time periods. All values are for monthly mean anomalies from the overall annual average except for the overall monthly means listed in the first column. Relative standard deviations are computed with respect to the corresponding monthly mean. Annual means: ERBE = 188.2 Wm^{-2}, CERES = 189.6 Wm^{-2}.*

	ERBE period						CERES period					
Month	**Mean**	**Anom**	**St Dev**	**Rel StD**	**Range**	**N**	**Mean**	**Anom**	**St Dev**	**Rel StD**	**Range**	**N**
1	**193.6**	**5.3**	**1.4**	**0.7%**	**3.6, 6.6**	**4**	**194.5**	**5.0**	**1.1**	**0.6%**	**3.9, 6.7**	**6**
2	**193.7**	**5.4**	**0.9**	**0.5%**	**4.4, 6.2**	**4**	**194.9**	**5.3**	**0.9**	**0.5%**	**3.9, 6.7**	**6**
3	**191.6**	**3.4**	**0.8**	**0.4%**	**2.7, 4.6**	**4**	**194.4**	**4.8**	**1.5**	**0.8%**	**2.7, 6.5**	**6**
4	**189.7**	**1.5**	**0.2**	**0.1%**	**1.2, 1.6**	**4**	**190.9**	**1.3**	**0.5**	**0.2%**	**0.7, 2.0**	**6**
5	**185.4**	**-2.9**	**0.9**	**0.5%**	**-3.9, -1.8**	**4**	**187.6**	**-1.9**	**1.5**	**0.8%**	**-3.3, 0.7**	**6**
6	**181.4**	**-6.9**	**1.5**	**0.8%**	**-8.3, -5.0**	**4**	**183.6**	**-6.0**	**3.4**	**1.8%**	**-9.2, 0.6**	**6**
7	**181.1**	**-7.2**	**2.0**	**1.1%**	**-9.2, -4.8**	**4**	**183.0**	**-6.6**	**2.5**	**1.4%**	**-9.9, -2.4**	**6**
8	**182.2**	**-6.1**	**1.6**	**0.9%**	**-8.3, -4.5**	**4**	**184.5**	**-5.1**	**1.1**	**0.6%**	**-6.8, -3.7**	**6**
9	**186.3**	**-1.9**	**0.5**	**0.2%**	**-2.4, -1.5**	**4**	**187.6**	**-2.0**	**0.9**	**0.5%**	**-3.6, -0.8**	**6**
10	**189.4**	**1.1**	**0.9**	**0.5%**	**0.1, 2.2**	**4**	**190.2**	**0.6**	**1.7**	**0.9%**	**-2.7, 2.2**	**6**
11	**191.6**	**3.3**	**1.2**	**0.6%**	**1.9, 4.5**	**4**	**191.3**	**1.7**	**1.6**	**0.8%**	**-0.2, 3.6**	**6**
12	**193.1**	**4.9**	**1.1**	**0.6%**	**3.5, 6.2**	**4**	**192.5**	**2.9**	**1.3**	**0.7%**	**1.6, 4.6**	**6**

Table 4.4.4*: Global mean annual cycle data for ASWUP over all data sets, ERBE and CERES time periods. All values are for monthly mean anomalies from the overall annual average except for the overall monthly means listed in the first column. Relative standard deviations are computed with respect to the corresponding monthly mean. Annual means: ERBE period = 23.3 Wm^{-2}, CERES period = 22.9 Wm^{-2}.*

	ERBE period						CERES period					
Month	**Mean**	**Anom**	**St Dev**	**Rel StD**	**Range**	**N**	**Mean**	**Anom**	**St Dev**	**Rel StD**	**Range**	**N**
1	**24.9**	**1.6**	**0.2**	**1.0%**	**1.4, 1.9**	**4**	**24.7**	**1.8**	**0.6**	**2.4%**	**1.0, 2.6**	**5**
2	**23.1**	**-0.2**	**0.8**	**3.5%**	**-1.1, 0.7**	**4**	**23.1**	**0.2**	**0.6**	**2.4%**	**-0.5, 1.0**	**5**
3	**22.7**	**-0.6**	**0.9**	**3.9%**	**-1.5, 0.5**	**4**	**22.6**	**-0.3**	**0.8**	**3.6%**	**-1.1, 0.7**	**5**
4	**24.2**	**0.9**	**0.8**	**3.2%**	**0.2, 2.0**	**4**	**23.7**	**0.8**	**0.8**	**3.5%**	**-0.3, 1.7**	**5**
5	**25.5**	**2.2**	**0.4**	**1.5%**	**1.7, 2.6**	**4**	**24.7**	**1.9**	**0.7**	**3.0%**	**1.2, 3.1**	**5**
6	**24.0**	**0.7**	**1.0**	**4.1%**	**-0.6, 1.7**	**4**	**23.1**	**0.2**	**1.0**	**4.2%**	**-1.4, 1.0**	**5**
7	**21.3**	**-2.0**	**1.5**	**7.2%**	**-4.2, -0.7**	**4**	**20.8**	**-2.1**	**1.5**	**7.3%**	**-4.7, -1.0**	**5**
8	**19.7**	**-3.6**	**1.4**	**6.9%**	**-5.6, -2.6**	**4**	**19.4**	**-3.5**	**1.1**	**5.7%**	**-5.3, -2.7**	**5**
9	**19.9**	**-3.4**	**0.5**	**2.7%**	**-4.1, -2.9**	**4**	**19.8**	**-3.1**	**0.6**	**2.8%**	**-3.7, -2.4**	**5**
10	**22.1**	**-1.2**	**0.8**	**3.6%**	**-2.3, -0.4**	**4**	**21.8**	**-1.1**	**0.7**	**3.0%**	**-1.9, -0.2**	**5**
11	**25.7**	**2.4**	**0.8**	**2.9%**	**1.7, 3.5**	**4**	**24.9**	**2.1**	**1.3**	**5.4%**	**-0.0, 3.6**	**5**
12	**26.6**	**3.3**	**0.4**	**1.5%**	**3.0, 3.9**	**4**	**25.9**	**3.0**	**1.1**	**4.1%**	**1.3, 4.2**	**5**

4.4.5: Summary

This report section describes an analysis of surface radiative flux annual cycle data from a number of satellite data products. The analysis examined global and tropical (20°S-20°N) mean annual cycles averaged over the ERBE (February 1985 – January 1989) and CERES ((March 2000 – February 2004) time periods. At least four data sets were available for most variables and averaging combinations, except for the clear-sky values, which were included in only two or three data sets. In general, the annual cycles from the different data products track each other well, but several exceptions were noted. The CERES SRBAVG-GEO v. 2D globally averaged SW data provided for this study contain errors related to filling near the poles. This has been corrected in a later version of the data set. Only the global and tropical average all-sky longwave net flux annual cycles for the various products differ significantly in phase. The standard deviations among the products for individual months fell in the rage of 0.1 and 1.8 Wm^{-2} for variables where no specific problems were noted, so we conclude that this is the typical level of agreement among the participating data sets.

4.5: Zonal and Regional Radiation Flux Anomalies at the Surface

E. Raschke, S. Kinne

Abstract:

Data diversity associated with surface radiation budgets is explored in time series and in seasonal and regional comparisons. Climatological data of the projects ISCCP, SRB and CERES (SRBAVG-Terra-GEO-MOD_Ed02) are compared. Investigated ISCCP and SRB data cover 21 years with a focus on 1984-1995 seasonal averages. Investigated CERES data cover the Mar2000 - Feb2004 time-period. De-seasonalized anomalies of zonal monthly averages of ISCCP and SRB explore data consistency and reproductions of natural impacts (e.g. Mt.Pinatubo, ENSO events). In addition seasonal averages maps of CERES for relevant radiative fluxes are presented and regional anomalies of ISCCP and SRB with respect to CERES are analyzed. Hereby, contributing solar and infrared radiative surface fluxes are examined and with respect to their clear-sky and cloud-effect components.

Significant data-set diversity is caused by deficiencies in applied ancillary data in terms of accuracy and consistency. In particular, the treatment of aerosol and surface properties (albedo and skin temperatures) shows strong variations. For most surface radiative flux properties data-set diversity by (non-cloud) ancillary data is at least at the level of the diversity introduced by differences in the representation of clouds. However, the large diversity by (non-cloud) ancillary data often goes unnoticed in comparisons of all-sky surface radiative fluxes due to choices in the representation of clouds, which at least in part compensate (non-cloud) ancillary errors. Other minor complications of current satellite data-sets are differences in the definition for clear-sky conditions and circular artifacts in global maps from cloud retrievals at the edges of geostationary coverage.

4.5.1: Introduction

Satellite sensors cannot directly measure the components of the radiation budget at the Earth's surface. Many different ancillary data need to be considered, including global maps of vertically and spectrally resolved atmospheric properties (of clouds, aerosol, trace-gases), atmospheric state (e.g. temperature and pressure) and surface properties (temperature and solar albedo). Generally, applied ancillary data-sets are derived from different data-sources. Thus, these data are often inconsistent to each other. In addition, individual data-sets often face accuracy issues and also self-consistency problems over extended time-periods. A (if not the) dominating reason for radiative flux product diversity is the representation of clouds. Hereby, cloud impacts (or 'cloud radiative effects', CRE) can be extracted from radiative flux differences between cases with clouds ('all-sky') minus cases without clouds ('clear-sky'). Still, also other ancillary data can introduce significant start-up diversity among data-sets. (More background on ancillary data impacts is given in *Chapters 2, 3, and 7,* and in the *Appendix C*). Thus, none of the satellite data for surface fluxes can be considered as a reference. Potential reference data are offered by surface-based networks (see *chapters 5 and 6*). However, currently there are only a few sites, these sites are restricted to continents and their distribution there is quite uneven. And there are additional issues with the regional representation, when site data statistics is matched with regional averages of 100km*100km and larger. Thus, most of the efforts in this sub-chapter will simply compare different data-sets and explore their diversity.

The investigated climatological data-sets are ISCCP and SRB for the 1984-2004 period and CERES *(SRBAVG-Terra-GEO-MOD_Ed02)* data for the Mar2003-Feb2004 period. Two data

aspects are explored. The first aspect explores long-term data records of ISCCP and SRB. Hovmoeller diagrams (as in *Chapter 3.5*) visualize and discriminate anomalies caused by natural events or artifacts. And inter-annual variability adds information on the regional character of these anomalies. The second aspect compares multi-annual seasonal averages between ISCCP, SRB and CERES. For each examined flux-property CERES data are selected to illustrate characteristic regional and seasonal distributions. Differences between ISCCP minus CERES and SRB minus CERES then explore data diversity on a regional seasonal basis. Hereby, additional insights to flux differences at all-sky conditions are provided by examining its two sub-components: the flux differences for clear-sky conditions and the flux differences for cloud radiative effects. The solar surface radiative flux component is examined first, then infrared (i.e. longwave) surface radiative fluxes are addressed, and finally combined (solar and infrared, up minus down) net radiation budget maps and their differences are explored.

4.5.2: Time Series of Deseasonalised Monthly Zonal Anomalies for ISCCP and SRB

Long data-sets for solar and longwave (IR) broadband radiative fluxes are provided by ISCCP and SRB climatological data. 21 years of data permit an examination of long-term anomalies for both solar and infrared fluxes at the surface. Some of these detected anomalies are due to artifacts in the representation of clouds and (non-cloud) ancillary data (such as assumed properties for aerosol or surface properties, while other anomalies are real and associated with natural events. Major natural events during the examined 1984-2004 time-period are enhanced stratospheric aerosols between 1991 and 1994 following the Mt.Pinatubo eruption, which reduced the solar downward radiative flux at the tropopause, and a strong ENSO event in 1997 which caused strong changes to the cloudiness in the eastern Pacific.

4.5.2.1: Solar radiative fluxes at the earth's surface

For the representation of the downward solar radiative flux at the surface, its relation to the incoming solar radiation at TOA was chosen: the effective solar atmospheric transmittance. Hereby, a distinction is made between all-sky (with clouds) and clear-sky (without clouds) conditions for a better separation of anomaly features associated with clouds or (non-cloud) ancillary data.

Hovmoeller diagrams address monthly zonal anomalies for three solar radiative properties: the clear-sky solar transmittance, the all-sky solar transmittance and the clear-sky solar surface albedo. The solar transmittance values is based on the ratio between surface and TOA downward solar fluxes and the solar surface albedo is based on the ratio of upward and downward fluxes at the surface. Zonal anomalies are presented with respect to the 1985-1988, because this is a time-period without any major natural anomaly. Zonal anomalies between ISCCP and SRB are compared in *Figure 4.5.1*.

The clear-sky anomalies reveal the reduced solar atmospheric transmission between 1991 and 1993. The expected impact is much more realistic reproduced by ISCCP. The SRB impact is too weak and SRB-data seem to compensate this deficiency by an increased solar surface albedo, as illustrated by solar surface albedo anomalies.

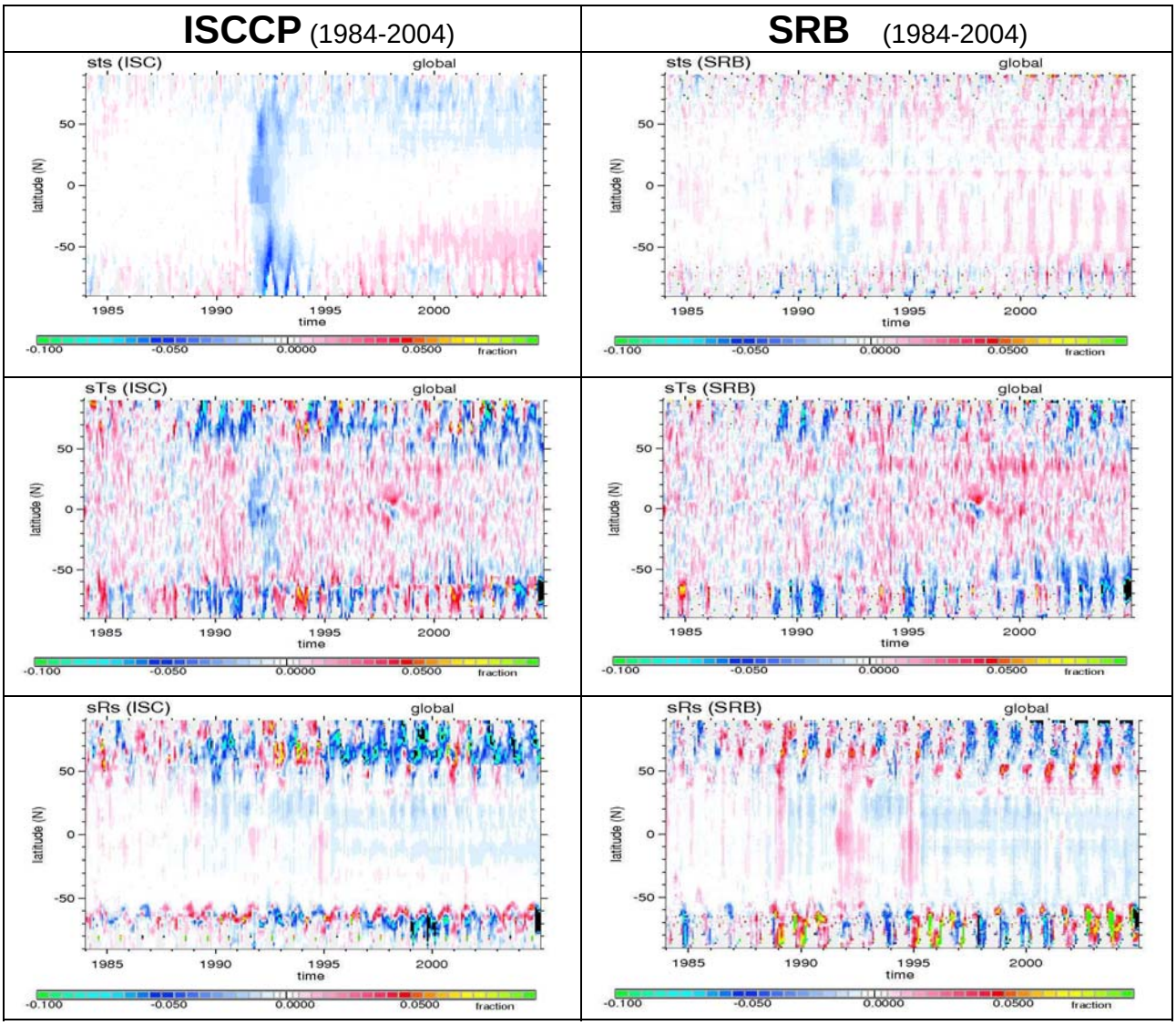

Figure 4.5.1: *Monthly zonal deseasonalised anomalies (in absolute % change) for the clear-sky solar atmospheric transmittance (top row), for the all-sky solar atmospheric transmittance (center row) and for the effective surface albedo (bottom row) for ISCCP (left) and for SRB (right) satellite climatologies. Anomalies are in reference to the 1985-1988 time-period. Note, that some abrupt changes are associated with switches to different satellites, which occurred in 1985, 1989, 1994, 1998 and 2001. (see also Figures 3.5.1, 3.5.2 and 3.5.3)*

The (noise) impact of clouds on the monthly solar transmission is on the order of ±5% at lower latitudes and even larger at polar latitudes. Thus, for the all-sky solar transmission, the distinct clear-sky Mt. Pinatubo signal (1991 to 1993) is almost lost, as cloud associated features are mixed in. Particularly strong is the ENSO associated cloud variability in 1998. On some occasions there are inconsistencies in the time-series. Some of them are associated with sensor issues, including platform switches which occurred in 1985, 1989, 1994, 1998 and 2001. The decline in Arctic sea-ice extent after 1995 seems to be captured in the surface albedo of both ISCCP and SRB. Although tempting, the displayed temporal trends (e.g. increased clear-sky solar

transmission over southern latitudes or reduced clear-sky surface albedo in the tropics) are meaningless due to instrumental noise.

4.5.2.2: Terrestrial longwave radiative fluxes at the earth's surface

Downward longwave (or IR) radiative fluxes at the surface are explored at all-sky (with clouds) and clear-sky (without clouds) conditions for a better separation of anomaly features associated with clouds or (non-cloud) ancillary data. In addition, also anomalies for (all-sky) upward fluxes from the surface are examined. For these longwave fluxes, zonal anomalies of ISCCP and SRB, with respect to their 1985-1988 data averages, are compared in *Figure 4.5.2*.

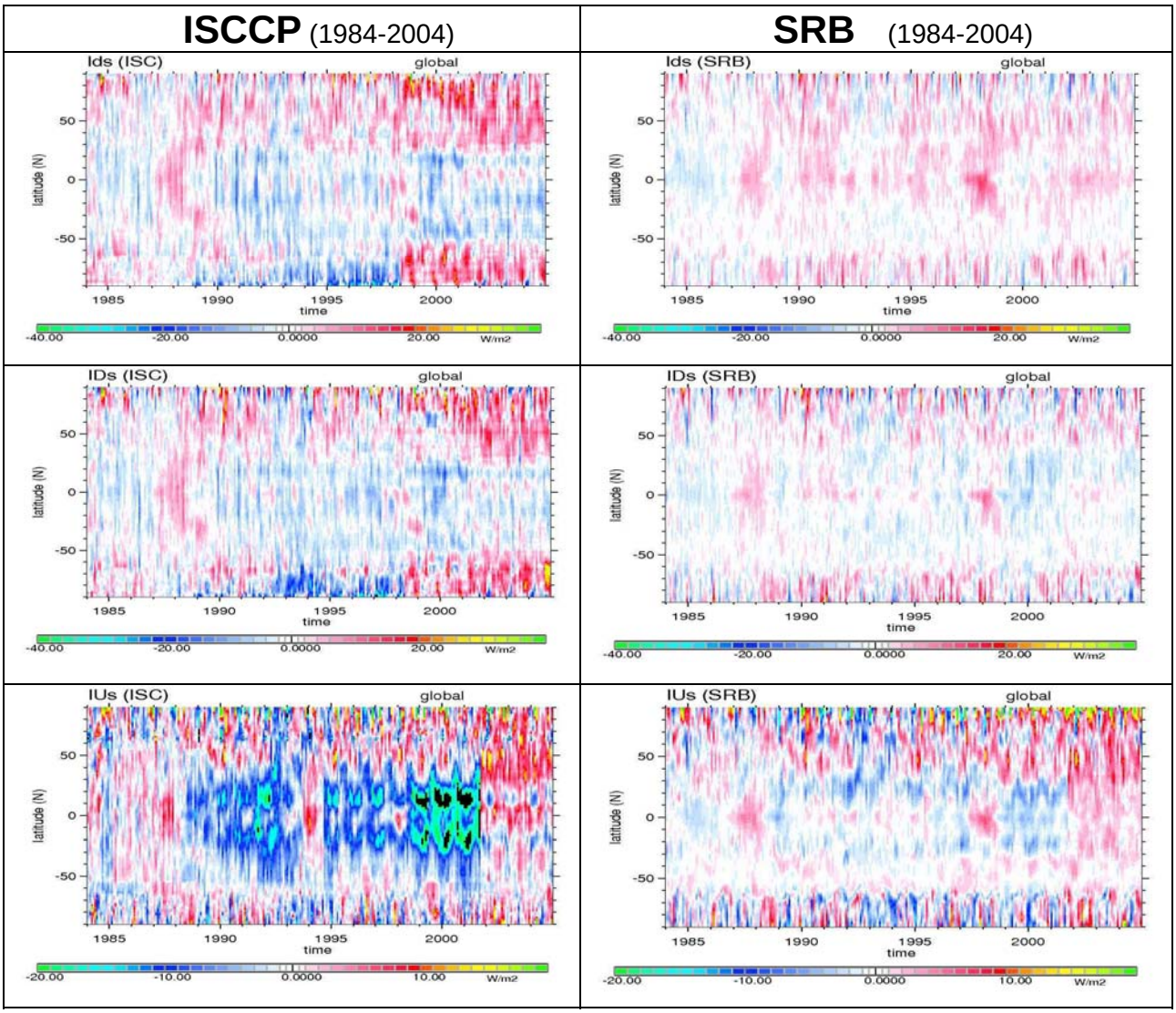

Figure 4.5.2: *Monthly zonal deseasonalised anomalies (in Wm^{-2}) for downward longwave radiative fluxes to the surface at clear-sky conditions (top row) and at all-sky conditions (center row) and of the upward (all-sky) longwave radiation fluxes from the surface (bottom row) for the satellite data climatologies of ISCCP (left) and SRB (right). Anomalies are in reference to the 1985-1988 time-period. Some abrupt changes may be linked to platform changes. A black color shows anomalies more negative than -20 Wm^{-2}. See also Figures 3.5.1 to 3.*

The longwave downward flux anomalies for clear-sky and all-sky conditions are quite similar. Significant variability at high latitudes, which was also displayed for the solar surface albedo anomalies in *Figure 4.5.1*, is at least in part related to inter-annual changes in sea-ice and snow cover. Otherwise, explanations for anomalies for the downward longwave fluxes (aside from the 1998 ENSO event) appear difficult. Also only for a few cases, the timing of abrupt anomaly changes can be attributed to platform changes. Some interpretation help, however, is offered by the anomalies for the upward longwave fluxes from the surface. These anomalies are also presented in *Figure 4.5.2*. Hereby, upward longwave fluxes from the surface are strongly linked to surface temperature data, which are ancillary in nature. These data, display significant discontinuities with time-periods of colder temperatures in the tropics especially between 1998 and 2002. Since locally changes in upward longwave fluxes from the surface are generally proportional to longwave downward fluxes to the surface, many anomaly features for downward longwave fluxes are now better understood. Some of the anomalies are not real but the consequence of poor and inconsistent ancillary data.

The most significant anomaly change for upward longwave fluxes from the surface occurred between September 2001 and October 2001. In the ISCCP data the upward flux change in the tropics is on the order of 15 Wm^{-2}. However, there is also a regional aspect to this anomaly in both ISCCP and SRB data. To demonstrate this, upward longwave flux anomalies among the three data-sets of CERES, ISCCP and SRB for the consecutive months of September 2001 and October 2001 are compared in *Figure 4.5.3*.

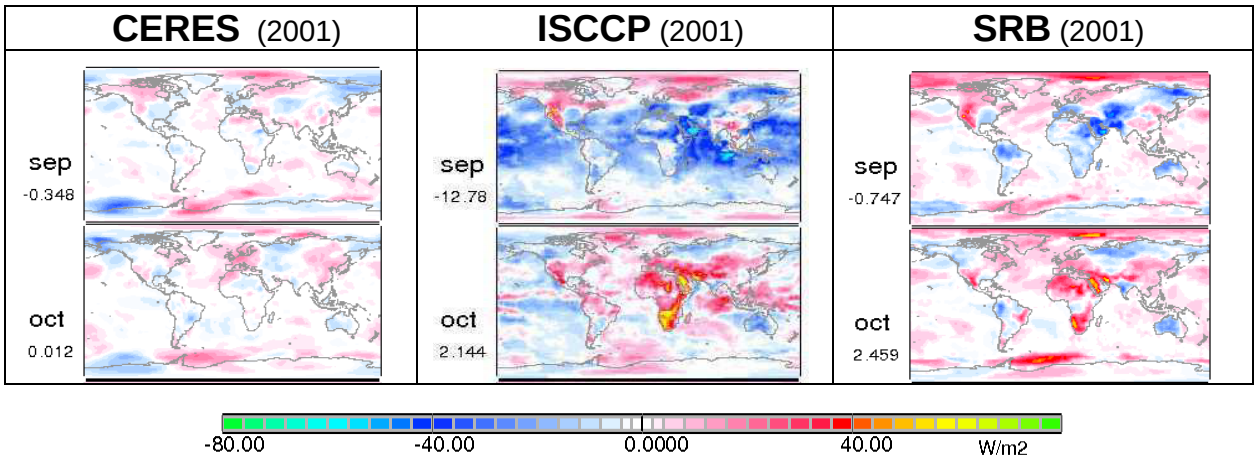

Figure 4.5.3: *Deseasonalised anomalies (in Wm^{-2}) for upward longwave radiative fluxes from the surface in data-sets of CERES (left), ISCCP (middle) and SRB (right). Anomalies are in reference to the 1985-1988 time-period. Anomalies are presented for consecutive months of September 2001 and October 2001.Values below the labels indicated global averages. See also Figures 3.5.1 to -3.*

The temperature anomaly change is observed in the ISCCP and SRB data, but not in the CERES data. Regional patterns for the temperature anomaly change are similar for ISCCP and SRB. The largest anomalies occur over Africa and the mid-East and for ISCCP only also over tropical oceans. With the added ocean anomaly the ISCCP anomaly change on a global basis is about three times larger than the SRB anomaly change.

4.5.3: Interannual Variation of Ancillary Data

Long time series are tempting to explore trends. These trends, however, will only be meaningful, if instrumental issues are understood and if applied ancillary data are accurate and consistent. This temporal consistency is here explored for two ancillary data-sets as they are applied in the ISCCP and SRB data. The two investigated ancillary data are the solar surface albedo (describing the solar reflectance at the surface) and the upward longwave fluxes from the surface (representing surface temperature and surface emissivity). Both ancillary data-sets are essential for the determination of the radiative net-fluxes at the surface in both data-sets.

Consecutive sequences of annual global maps are chosen to identify geographic areas where data inconsistencies occur. These inconsistencies could be caused by natural phenomena or could be artifacts either due to poor data handing or by applying supplementary data of poor quality. Inter-annual regional variability for the annual effective surface reflectance (i.e. solar surface albedo at all-sky conditions) for ISCCP and SRB are presented in *Figure 4.5.4*.

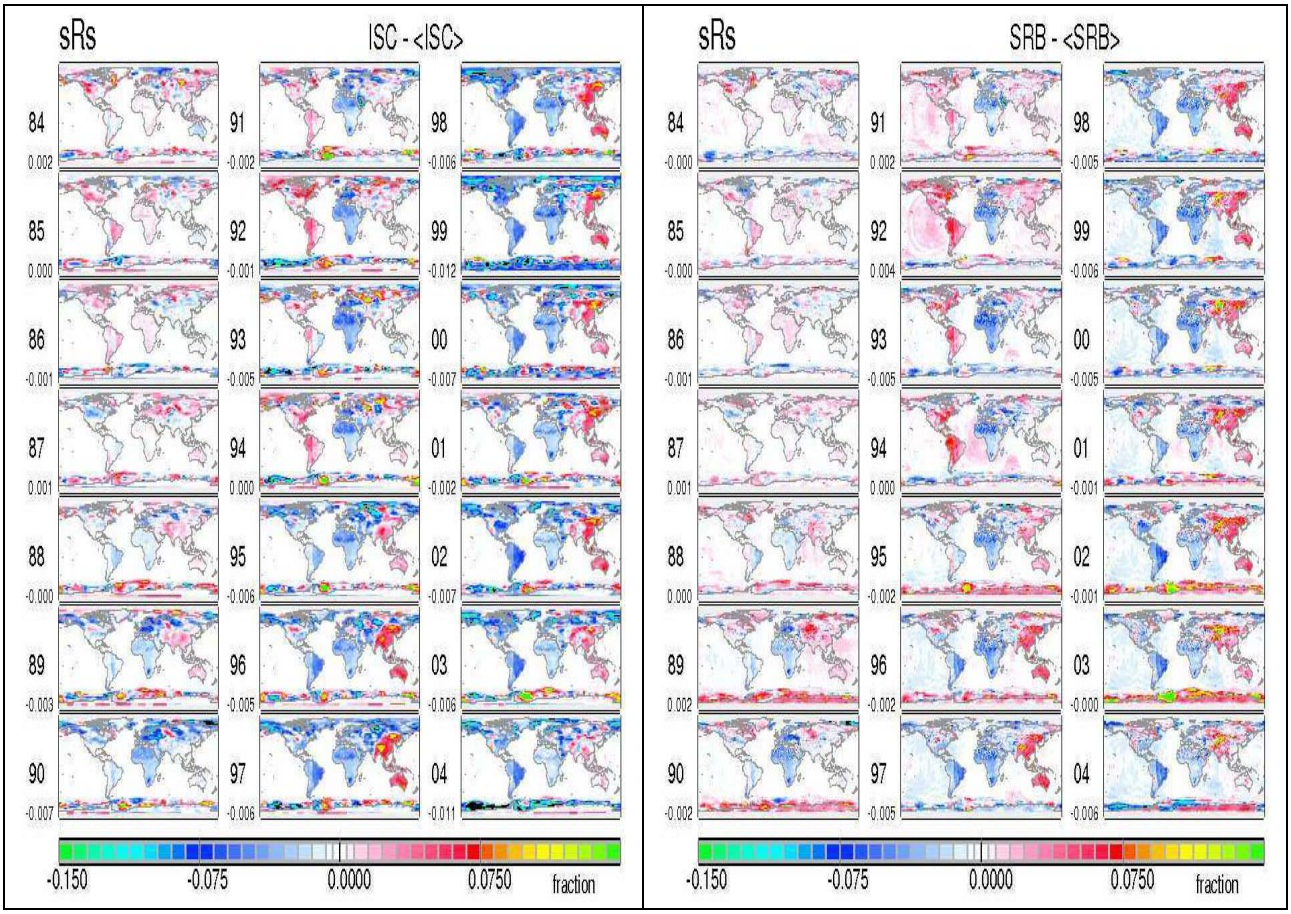

Figure 4.5.4: *Anomalies of annual averages of the effective all-sky solar surface albedo (sRs in fraction) for ISCCP (left) and SRB (right) with respect to the 1985-1988 reference period.*

Temporal trends suggest a systematic surface darkening of most continents (by up to 7 % over South America) and a surface brightening over eastern Asia and Australia (by up to 5 %). Hereby, the regional patterns for ISCCP and SRB are similar. Most of the major changes are abrupt, including also a brightening of the American continents in the 90ies. This abrupt nature is

indicative for artifacts, especially since inter-annual changes to the solar surface albedo in excess of 5% over regions not affected by snow or ice are difficult to explain by natural events.

Inter-annual regional variability for the annual upward longwave fluxes from the surface (i.e. representing assumption for surface temperature and surface emissivity) for ISCCP and SRB (at all-sky conditions) are presented in *Figure 4.5.5*.

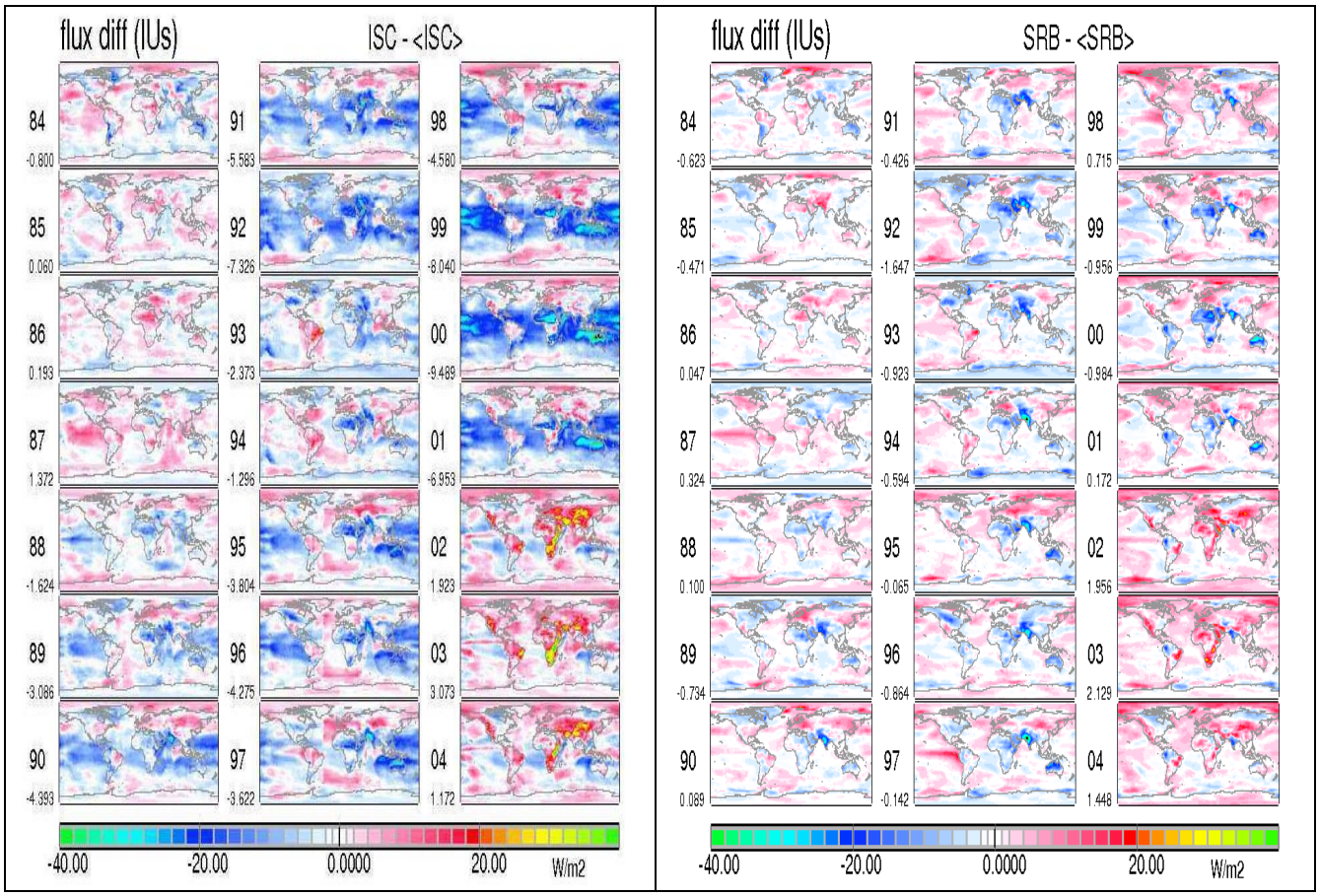

Figure 4.5.5: *Anomalies of annual averages for all-sky upward longwave fluxes from surface (lUs, Wm^{-2}) for ISCCP (left) and SRB (right) with respect to the 1985-1988 reference period.*

With climate warming, slightly warmer surface temperature could be expected. However, these increases would be so small that they would be hardly detectable by reddish color of the chosen color scale. In contrast, very large regional amplitudes are detected, especially for ISCCP. Some anomaly changes last for a few years, others are abrupt. Only one ISCCP anomaly can be linked to a natural event. Reduced upward longwave fluxes between 1991 and 1993 could be attributed to surface cooling following the Mt. Pinatubo eruption. This natural feature is much weaker in SRB data. Most other anomalies appear to be artificial, including the strong increase between 2001 and 2002, which was already discussed earlier. For ISCCP, the artificial origin of most anomalies can be demonstrated by strong temporal correlations to skin temperature anomalies, which were presented in *Chapter 3.5*.

Both investigated properties, demonstrated that ancillary data, as they are applied in currently available radiative flux products of ISCCP and SRB, have temporal inconsistencies. These inconsistencies introduce error, which propagate into many radiative flux products, especially products associated with the surface radiation budget. Unless these errors are

understood, inter-annual trend applications with ISCCP and SRB in their current state are strongly discouraged. Efforts need to be made to acquire and establish more accurate and more consistent ancillary data. Only with better ancillary data reprocessing is recommended.

4.5.4: Seasonal CERES Maps and Difference Maps of ISCCP and SRB to CERES

Presentations of this sub-chapter serve two goals: the presentation of characteristic data and the documentation of associated regional and seasonal diversity among CERES, ISCCP and SRB. Seasonal global maps of CERES multi-annual (03/2000 to 02/2004) averages are selected to illustrate characteristic radiative fluxes at the surface and to convey satellite data-set diversity for radiative fluxes at the surface, seasonal global difference maps between ISCCP minus CERES and SRB minus CERES are presented. Hereby, ISCCP and SRB multi-annual seasonal averages relate to a different but longer time-period (1984-1995), also to avoid the recognized artifact in those data due to the sudden rise of surface temperatures in 2001. Although CERES data serve as baseline in differences plots, CERES data are as much as the other two data-sets the result of model simulations and should not be considered a basic reference. Thus, the presented differences should generally be interpreted as data-set diversity.

The overall focus of this chapter is the data-set diversity for the (combined shortwave and longwave) net-flux imbalance at the surface. However, to better understand these differences, solar and infrared fluxes as well as their non-cloud ancillary and cloud radiative effects components are separately explored. First, however, the diversity in ancillary data is examined.

4.5.4.1: Ancillary information

Important ancillary data for surface fluxes are atmospheric and surface properties. The treatment of aerosol is examined by comparing the solar clear-sky transmission. Alternately, the treatment of clouds (e.g. cloud optical depth and/or cover) is explored by comparing cloud-effects on solar downward fluxes. And assumptions for surface solar and infrared properties are examined by comparing the solar surface albedo and upward infrared fluxes from the surface. Usually seasonal maps are presented, which are based on monthly data, hereby combining data of the months December, January and February for northern hemispheric winter or southern hemispheric summer and data of the months of June, July and August for northern hemispheric summer or southern hemispheric winter. Similarly the data for months of March, April and May and data for the months of September, October and November are combined for the two transitional seasons.

a.) Atmospheric aerosols

Clear-sky solar atmospheric transmittance provides information on the treatment of trace-gas absorption but mainly on the treatment of atmospheric aerosol. Solar broadband transmission data are retrieved from the ratio of solar fluxes reaching the surface to solar fluxes incident at the top of the atmosphere (TOA). Seasonal values for CERES and differences of ISCCP minus CERES and SRB minus CERES are presented in *Figure 4.5.6*.

Values for cloud-free atmospheric solar transmissions are usually between 60 and 75%. Clear-sky solar transmissions are correlated with land elevations and time-fractions for high sun-elevations and anti-correlated with aerosol loads. Higher CERES clear-sky solar transmittance data over regions usually occupied by off-coastal stratocumulus fields, are due to CERES low

bias for water vapor over cloudy regions, associated with the 'clear-sky' definition which for CERES is based on clear-sky observations, rather than modeling, as for the other two data-sets. The very low solar transmission values for CERES over Antarctic coastal waters are likely in error, as solar transmissions by ISCCP and SRB in those regions are consistently much stronger.

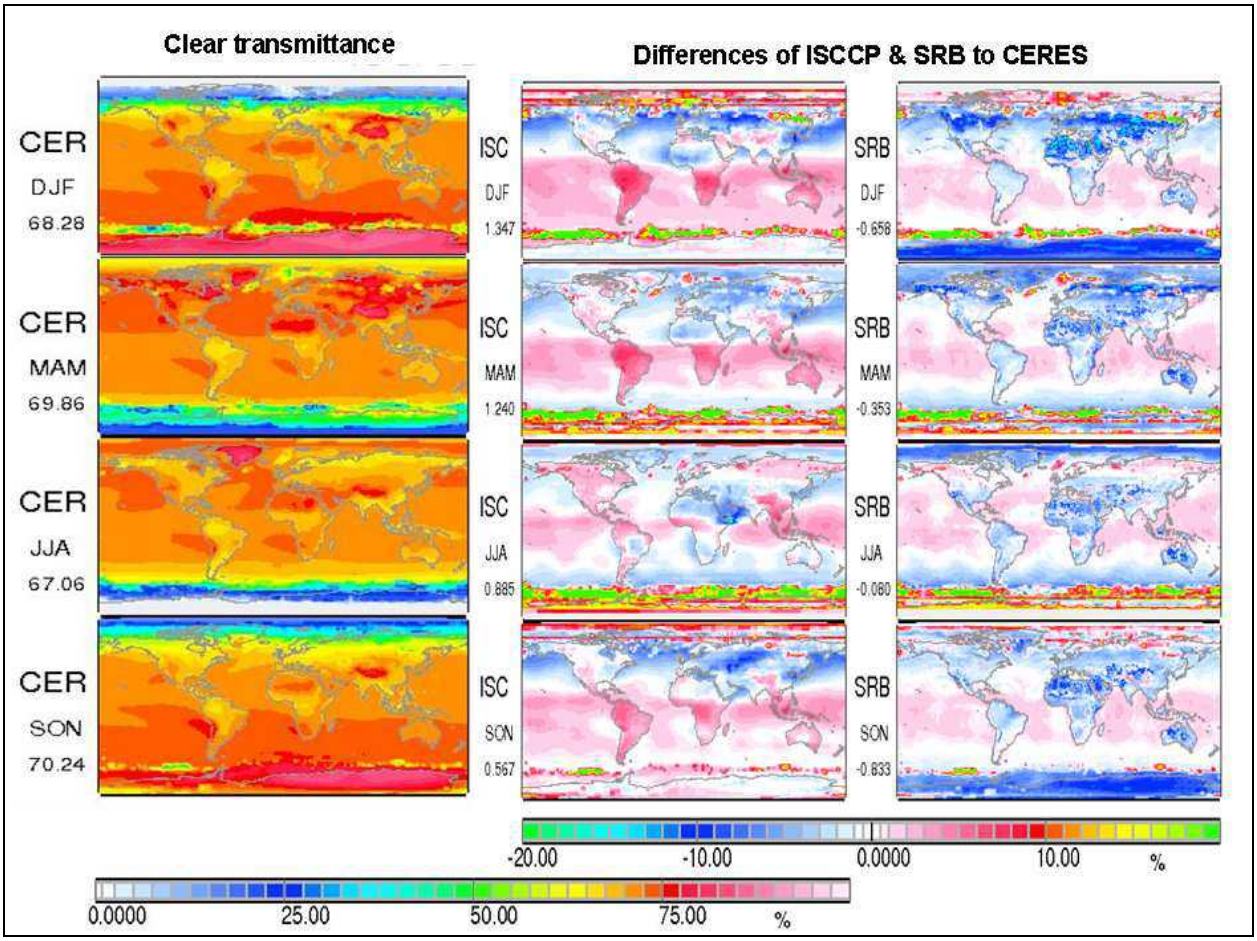

Figure 4.5.6: *Seasonal averages of the clear-sky solar atmospheric transmittance (in %) of CERES (left)**,** and (absolute %) differences of ISCCP minus CERES (center) and SRB minus CERES (right). ISCCP and SRB data refer to 1984-1995 and CERES data to Mar2000-Feb2004 time-periods. Values below labels indicate global means.*

Compared to CERES, the clear-sky solar transmission on a global average basis is higher for ISCCP and weaker for SRB. But there are significant regional and in particular latitudinal differences. CERES data apply newer advanced aerosol products from aerosol component modeling. Thus, here CERES data will be considered as a general reference. ISCCP has much lower transmissions over mid-latitude regions of the northern hemisphere. This strongly suggests ISCCP aerosol amount overestimates for urban pollution. ISCCP also has much larger transmissions over the tropics and the southern hemisphere. This indicates ISCCP underestimates to both amount and absorption of biomass burning aerosol. SRB differences to CERES display a continent-ocean contrast. The differences suggest that SRB overestimates aerosol amount over land, especially over regions with dust, and that SRB underestimates aerosol over oceans.

b.) Atmospheric Clouds

Cloud impacts on solar transmission ('all-sky' minus 'clear-sky') differ among the three satellite climatologies. These differences reveal assumptions for cloud cover and/or cloud optical depth. Seasonal cloud radiative effects (CRE) on the solar transmission by CERES and differences of ISCCP minus CERES and SRB minus CERES are presented in *Figure 4.5.7*.

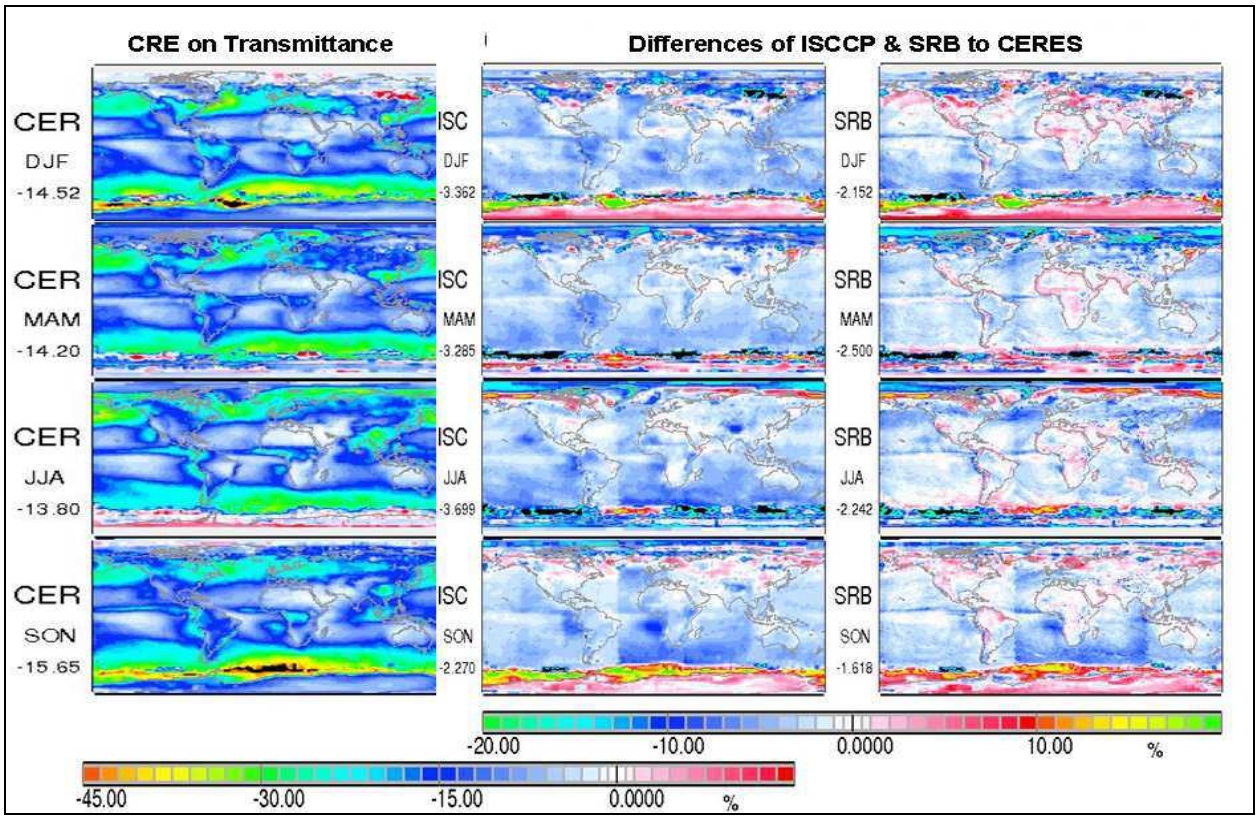

Figure 4.5.7: *Seasonal averages of cloud radiative effects (CRE) on the solar atmospheric transmittance (in %) of CERES (left) and (absolute %) differences of ISCCP minus CERES (center) and SRB minus CERES (right). ISCCP and SRB data refer to 1984-1995 and CERES data to Mar2000-Feb2004 time-periods. Bluish colors in the difference maps mark areas where CERES values are smaller (in absolute values) than others. Values below labels indicate global means. Note the rectangular structures in the differences between ISCCP and SRB to CERES, which are artifacts.*

Clouds in the CERES data-set reduce the solar atmospheric transmission on a global average basis by about 15%. However, there are strong regional and seasonal variations. Regional % reductions to the CERES solar transmissions are largest for mid-latitude cloud regimes and even exceed 45% over the southern hemispheric during spring and summer. Cloud impacts near polar latitudes are less reliable and increases to CERES solar transmissions over northern Asia during winter are difficult to explain.

Cloud induced reductions to the solar atmospheric transmission are stronger for ISCCP and SRB, at 18% and 17%, respectively, on a global average basis. This indicates that assumed cloud optical depths in CERES are relatively small. However, there are also regional differences. Against this overall trend, weaker cloud impacts occur for ISCCP and SRB at higher northern mid-latitudes and for SRB over deserts. These are just those regions, where aerosol impacts were

stronger in ISCCP and SRB (see *Figure 4.5.6*). Thus, in these regions differences will partially compensate, and larger data-differences will go unnoticed when exploring data-set differences at all-sky conditions (all-sky solar transmission comparisons are provided in Appendix S).

c.) Solar Surface Albedo

The effective solar surface albedo, the ratio of upward to downward fluxes, is the result of various assumptions on the surface state (e.g. sea-ice extent, snow cover, vegetation). The effective surface albedo in the different data-sets is extracted from the ratio of upward and downward solar fluxes at the surface. Seasonal values for CERES and differences of ISCCP minus CERES and SRB minus CERES are presented in *Figure 4.5.8*.

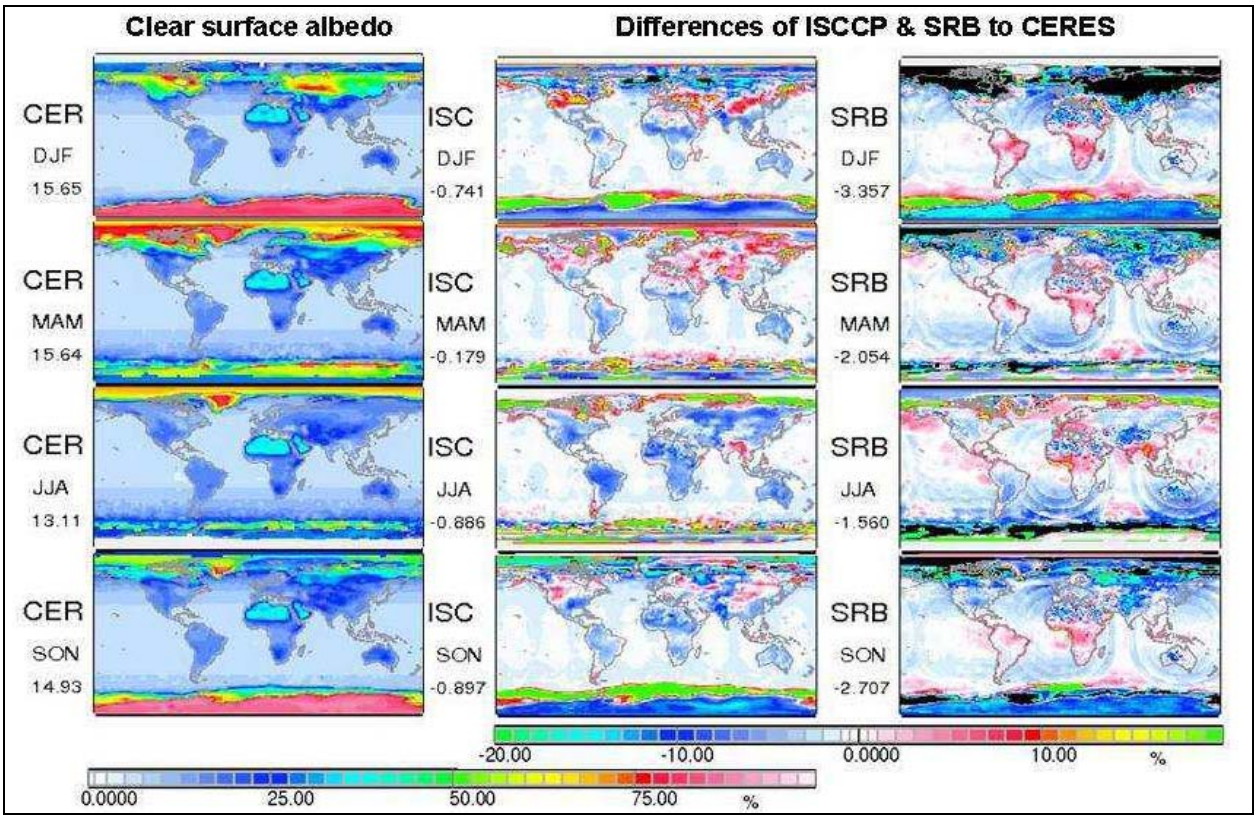

Figure 4.5.8: *Seasonal averages of the clear-sky effective solar surface albedo (in %) of CERES (left) and (absolute %) differences of ISCCP minus CERES (center) and SRB minus CERES (right). ISCCP and SRB data refer to 1984-1995 and CERES data to Mar2000-Feb2004 time-periods. Note, black colors display absolute % differences more negative than -20%, and light green colors indicate absolute % differences more positive than +15%. Values below labels indicate global means.*

CERES solar surface albedo data (at 'clear-sky' conditions) are near 15% on a global annual basis. The expected regional biases display highest solar surface albedo values over ice and snow, high values over desert regions and relatively low values over oceans.

ISCCP and SRB solar surface albedoes on a global annual basis are slightly weaker than in CERES, at 14% and 12%. Differences are better understood by regional analyses. Larger diversity occurs at high latitude regions affected by snow and sea-ice cover. In those regions SRB flux data reproduce much lower values. This strongly suggests that SRB underestimates the solar

reflection by ice and snow. In contrast, continental snow reflectance of ISCCP is stronger than for CERES. Otherwise, ISCCP surfaces are darkest over (non-snow) continents, SRB is brightest for southern continents and CERES is brightest over oceans. Circular features in the SRB solar albedo data are artifacts and related to geostationary data.

d.) Surface temperature and surface emissivity

The product of surface (or 'skin') temperature (raised to the fourth power) and surface emissivity determines the upward longwave (or IR) fluxes from the surface. Usually this upward flux is modulated by the surface temperature since the emissivity is usually close to unity. Lower emissivity usually occurs only for sand-like background as over deserts. Seasonal upward longwave fluxes for CERES and difference of ISCCP minus CERES and SRB minus CERES are presented in *Figure 4.5.9*.

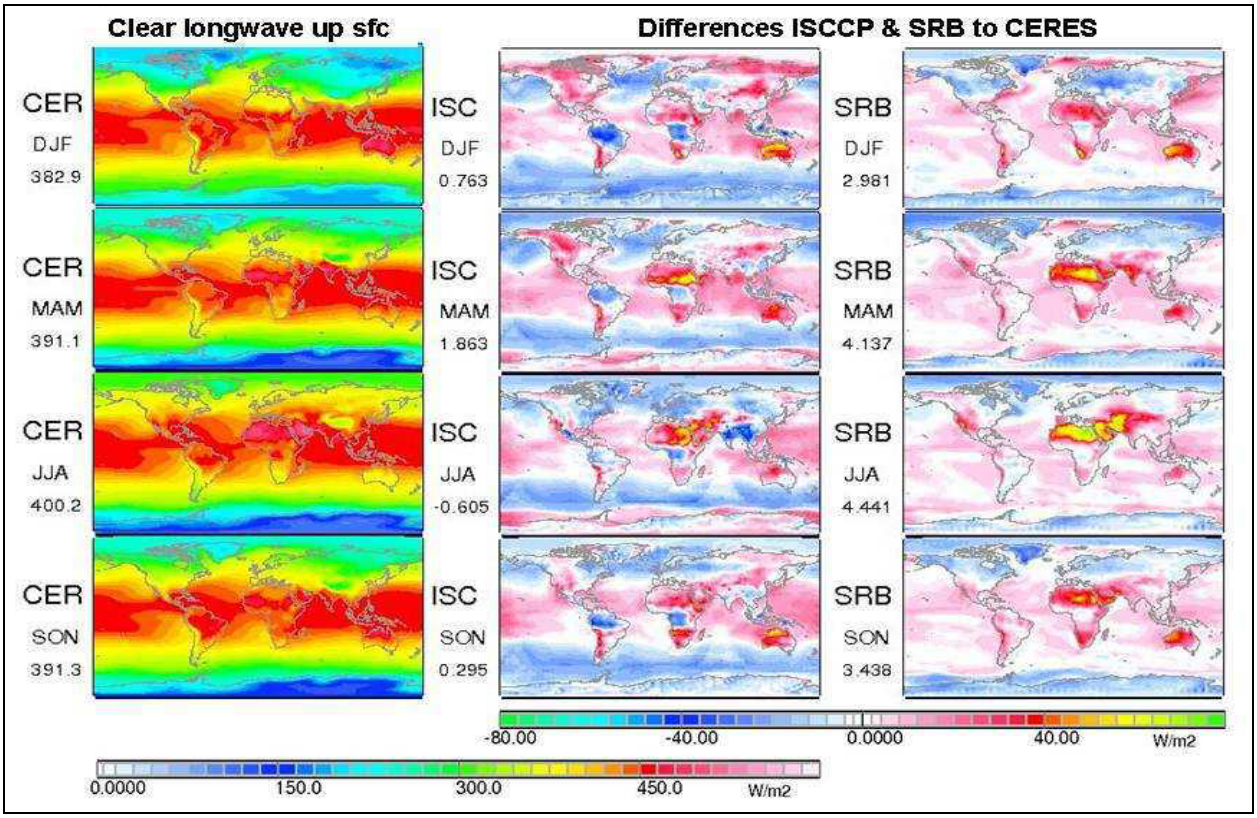

Figure 4.5.9: *Seasonal averages of clear-sky upward longwave (IR) fluxes from the surface by CERES (left) and differences of ISCCP minus CERES (center) and SRB minus and CERES (right). ISCCP and SRB data refer to 1984-1995 and CERES data to Mar2000-Feb2004 time-periods. Values below labels indicate global means. Note regional differences to CERES vary between -40 and +60 Wm^{-2}*

.

The CERES data display the expected latitudinal distribution with the larger upward longwave fluxes from the surface over the warmer tropic and smaller values towards the colder regions at higher and polar latitudes. The largest values occur over deserts.

Differences among the three data-sets indicate that SRB, on a global basis, has 4 Wm^{-2} higher upward longwave fluxes. This corresponds to a globally 1K warmer surface temperature than in CERES or ISCCP. However, this positive SRB bias is largely a desert regional effect,

because apparently the assumed surface emissivity over deserts is much closer to unity than in ISCCP or CERES. Otherwise, ISCCP has weaker upward fluxes over vegetated tropical regions and CERES has larger upward fluxes in Polar Regions and weaker upward fluxes over oceans.

4.5.4.2: Solar fluxes to the surface

To understand the data-set diversity for all-sky downward solar fluxes, the diversity of clear-sky and cloud radiative effect components are investigated first. Seasonal downward solar fluxes for CERES at clear-sky conditions and difference of ISCCP minus CERES and SRB minus CERES are presented in *Figure 4.5.10*. (This figure is closely linked to the solar transmission comparisons presented earlier in *Figure 4.5.6*.)

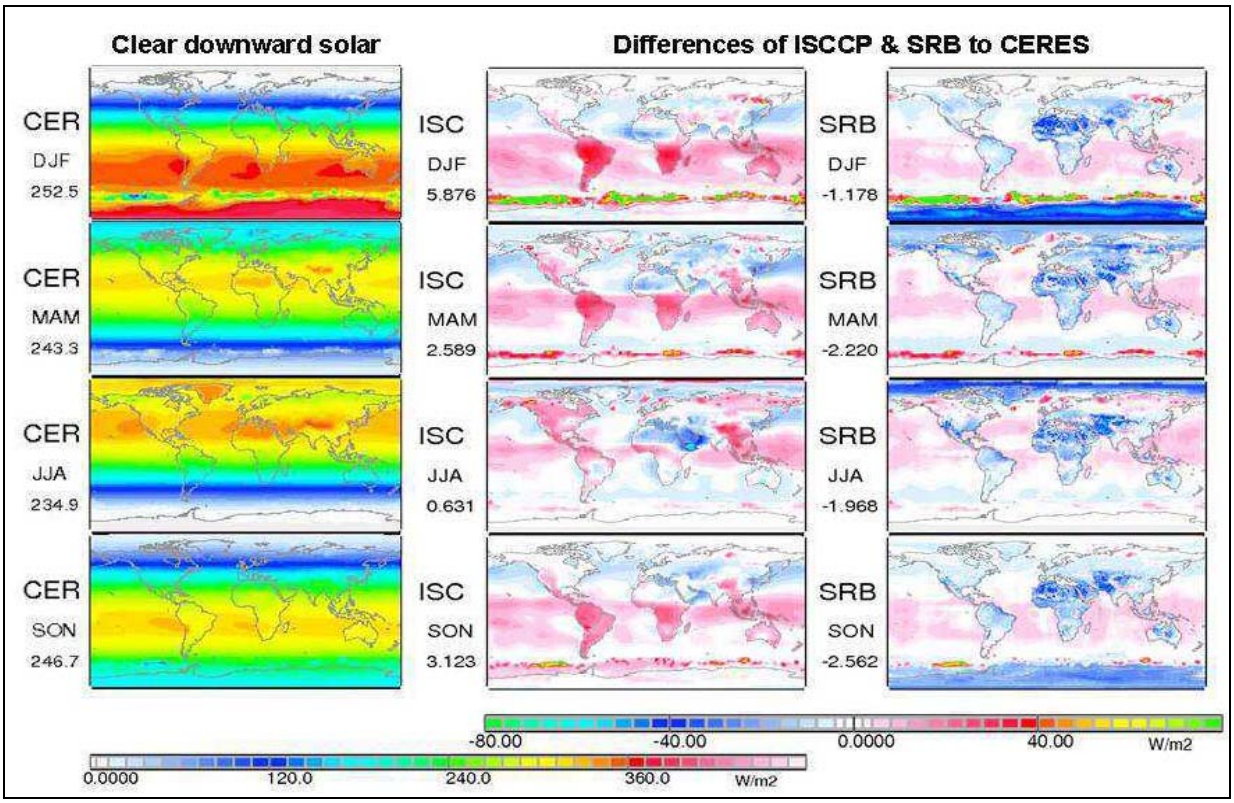

Figure 4.5.10: *Seasonal clear-sky downward solar fluxes of CERES (left) and the differences of ISCCP minus CERES (center) and SRB minus CERES (right). ISCCP and SRB data refer to 1984-1995 and CERES data to Mar2000-Feb2004 time-periods. Values below labels indicate global means.*

Global annual averages for the clear-sky solar downward fluxes are near 240 Wm^{-2}. The global distribution is largely zonal in nature. The distribution is dominated by the latitudinal distance from the seasonal varying latitude position of the sun and is also modulated by atmospheric aerosol loading.

On a global basis ISCCP has the highest and SRB the lowest downward solar fluxes at clear-sky conditions. Regionally, the ISCCP high tendency is mainly limited to the southern hemisphere while over the northern hemisphere ISCCP displays a low tendency, due to relative high urban-industrial aerosol loads. The low tendencies for SRB originate from continental

regions. Especially over dust regions, where aerosol loads are high, and SRB downward solar fluxes at clear-sky conditions are very low.

Cloud radiative effects on downward solar fluxes for CERES and difference of ISCCP minus CERES and SRB minus CERES are presented in *Figure 4.5.11*. This figure is closely linked the solar transmission comparisons presented earlier.

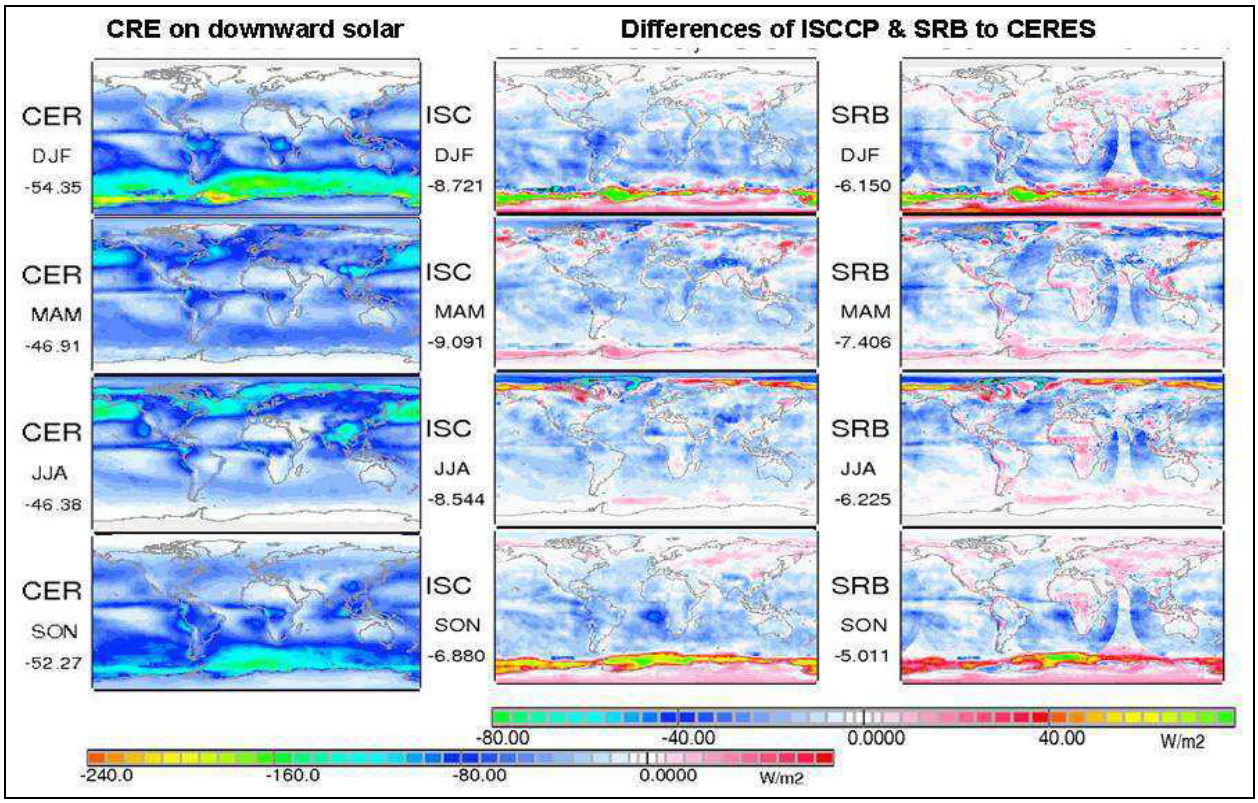

Figure 4.5.11: *Seasonal cloud radiative effects (CRE) on downward solar fluxes of CERES (left) and differences of ISCCP minus CERES (center) and SRB minus CERES (right). ISCCP and SRB data refer to 1984-1995 and CERES data to Mar2000-Feb2004 time-periods. Note, since this cloud radiative effect (CRE) is negative by definition. Thus, a negative difference (by ISCCP or SRB) means a stronger cloud radiative effect than CERES and a positive difference (by ISCCP or SRB) a weaker effect. Values below labels indicate global means. Note the circular pattern in the SRB differences which are caused by geostationary data. They cause anomalies of -40 Wm^{-2} and less.*

Clouds reduce the downward solar fluxes to the surface globally by about -50 Wm^{-2}, with values exceeding -150 Wm^{-2} over mid-latitude oceans during summer. ISCCP and SRB cloud radiative effects on solar downward fluxes are 5-10 Wm^{-2} stronger than for CERES, supporting the concept of relatively low cloud optical depths in CERES data. Differences are larger over oceans than over continents and especially over off-coastal stratocumulus fields the cloud optical depths by ISCCP and SRB are significantly larger. The differences to CERES (and especially those of SRB) reveal circular artifacts from geostationary edge data applied to ISCCP cloud retrievals (and ISCCP cloud information is used in SRB). The comparison of the last two figures demonstrates that solar differences by non-cloud ancillary data are almost as large as differences from cloud representations. When examining local seasonal differences, deviations for non-cloud ancillary data and cloud effects are not always additive. Often for the same location and the same season both component deviations have opposite signs so that all-sky deviations give the illusion

of a better agreement. Such compensating biases in terms of all-sky flux differences are most pronounced for ISCCP, where relatively strong cloud effects partially compensate weak aerosol effects, in particular over the tropics and the Southern Hemisphere. The resulting all-sky solar downward fluxes for CERES and differences of ISCCP minus CERES and SRB minus CERES are presented in *Figure 4.5.12*.

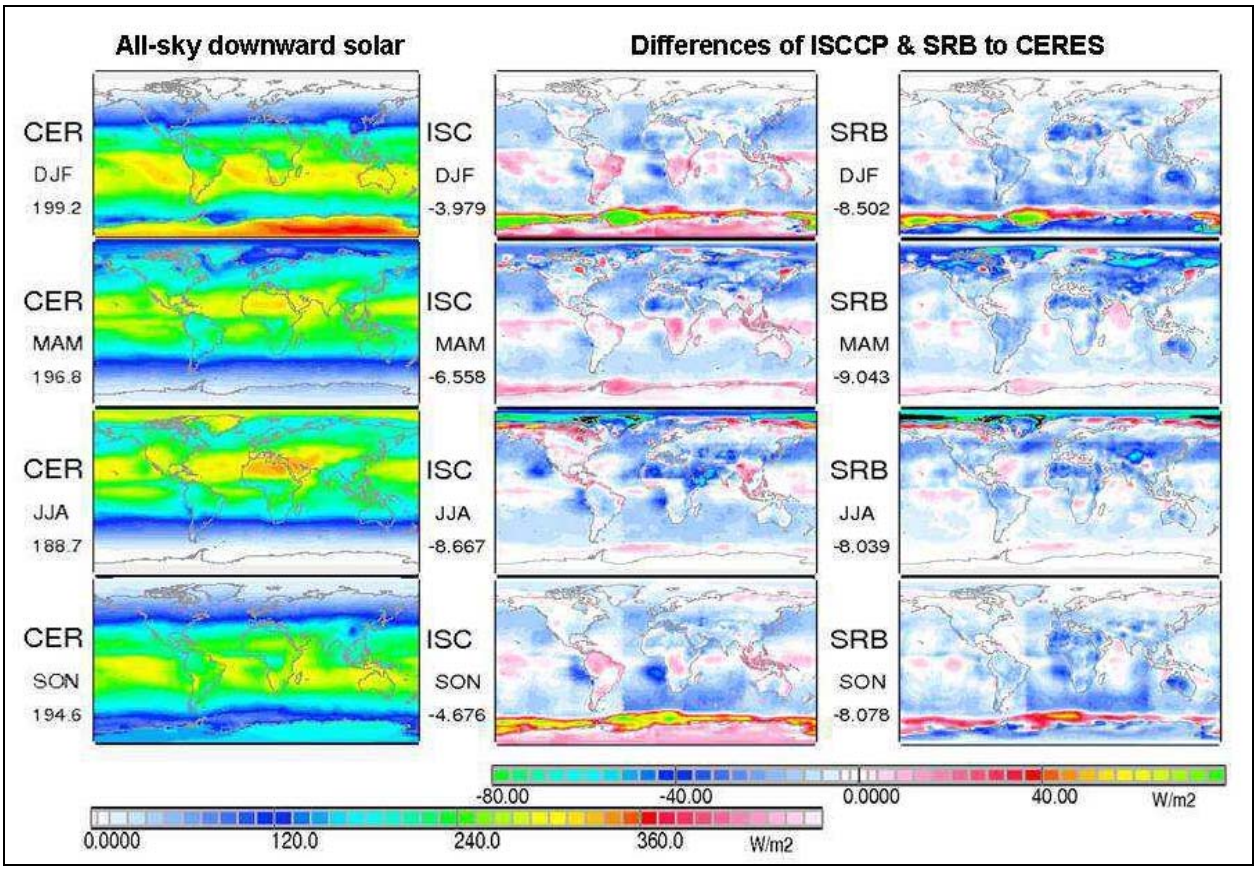

Figure 4.5.12: *Seasonal all-sky downward solar fluxes of CERES (left) and differences of ISCCP minus CERES (center) and SRB minus CERES (right). ISCCP and SRB data refer to 1984-1995 and CERES data to Mar2000-Feb2004 time-periods. Note, vertical and circular patterns are artifacts. Values below labels indicate global means.*

Globally averaged downward solar fluxes reaching the surface at all-sky conditions are near 185 Wm^{-2}. The largest values occur over Polar regions during summer and over sub-tropical regions with usually little cloud cover.

Globally, SRB has the lowest downward solar all-sky fluxes and CERES has the largest. SRB solar fluxes that reach the surface at northern hemispheric high latitudes during spring are particular low, hereby conveniently compensating the rather weak surface reflectance in SRB, so that deviations for SRB solar net-fluxes at the surface are less significant.

For most regions the disagreement for downward solar fluxes remains below ±20 Wm^{-2}. This is much lower than the diversity among global models of the IPCC 4th assessment, which is presented in *Chapter 9*.

4.5.4.3: Longwave fluxes to the surface

To understand the data-set diversity for all-sky downward longwave (or IR) fluxes, the diversity of clear-sky and cloud radiative effect components are investigated first. Seasonal downward longwave fluxes for CERES at clear-sky conditions and difference of ISCCP minus CERES and SRB minus CERES are presented in *Figure 4.5.13*.

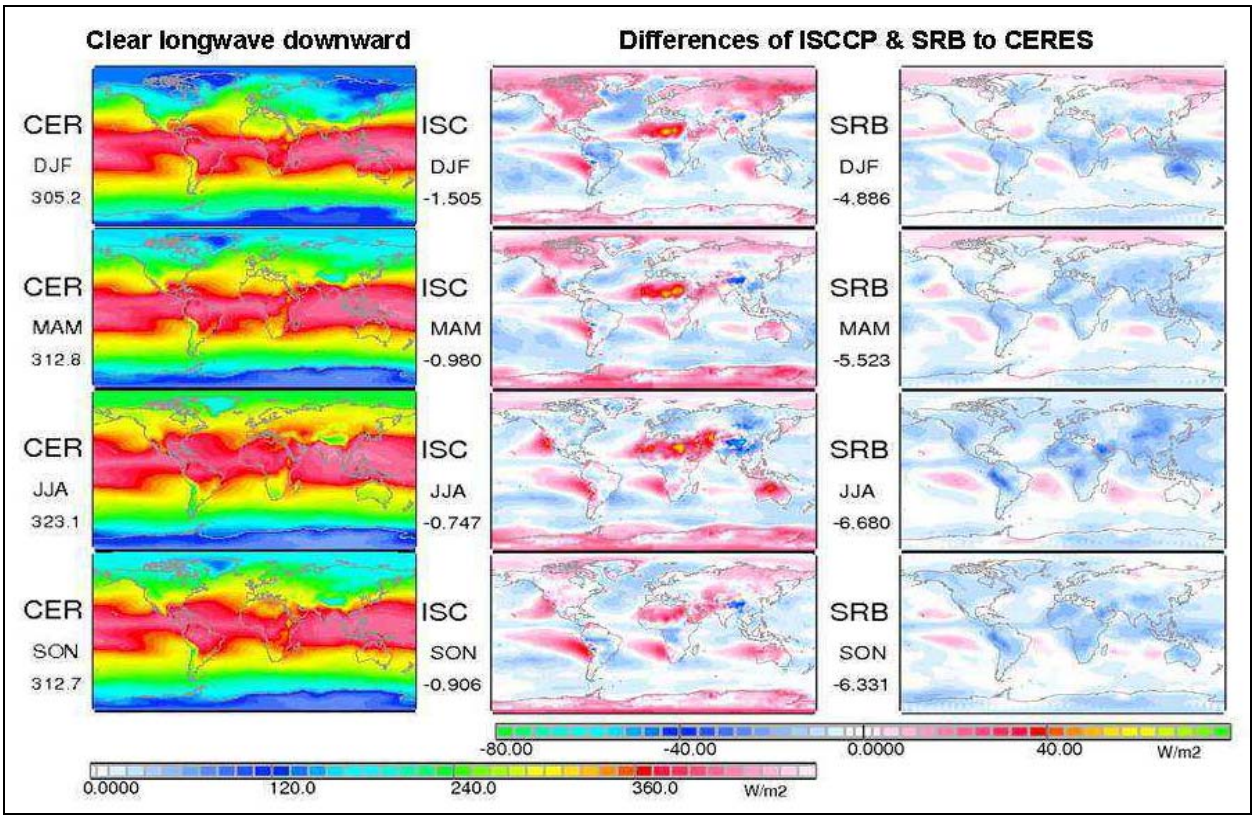

Figure 4.5.13: *Seasonal downward infrared fluxes of CERES (left) and differences of ISCCP minus CERES (center) and SRB minus CERES (right). ISCCP and SRB data refer to 1984-1995 and CERES data to Mar2000-Feb2004 time-periods. Values below labels indicate global means.*

The downward longwave flux to the surface at cloud-free conditions depends on the composition of the lower troposphere. Important factors are near surface atmospheric temperatures and near surface trace-gas absorption, mainly by water vapor. In addition, also contributions of larger size dust aerosol will contribute. Globally averaged downward longwave fluxes to the surface at clear-sky conditions are near 320 Wm^{-2}. Regional maxima occur in the tropics.

Before commenting on data-set differences it should be pointed that CERES clear-sky downward fluxes to the surface appear biased high in comparisons to ISCCP and SRB. CERES clear-sky data are based on observations, whereas clear-sky data for the other two data-sets are derived from the artificial removal of clouds. Since atmospheric water vapor is increased near clouds. CERES clear-sky water vapor is underrepresented in cloudy regions. Thus, in regions with significant cloud cover, ISCCP and SRB longwave downward clear-sky fluxes to the surface should be stronger - by 'clear-sky' definition. Such tendencies are in fact noticeable for ISCCP minus CERES and SRB minus CERES differences. The effect, however, is not too apparent for

SRB, since SRB has generally weak downward IR fluxes. In contrast, this bias is better displayed for ISCCP. ISCCP also has the strongest impact by dust aerosol, with significantly larger longwave downward fluxes over the Sahara than the other two data-sets.

Cloud radiative effects on downward longwave fluxes for CERES and difference of ISCCP minus CERES and SRB minus CERES are presented in *Figure 4.5.14*.

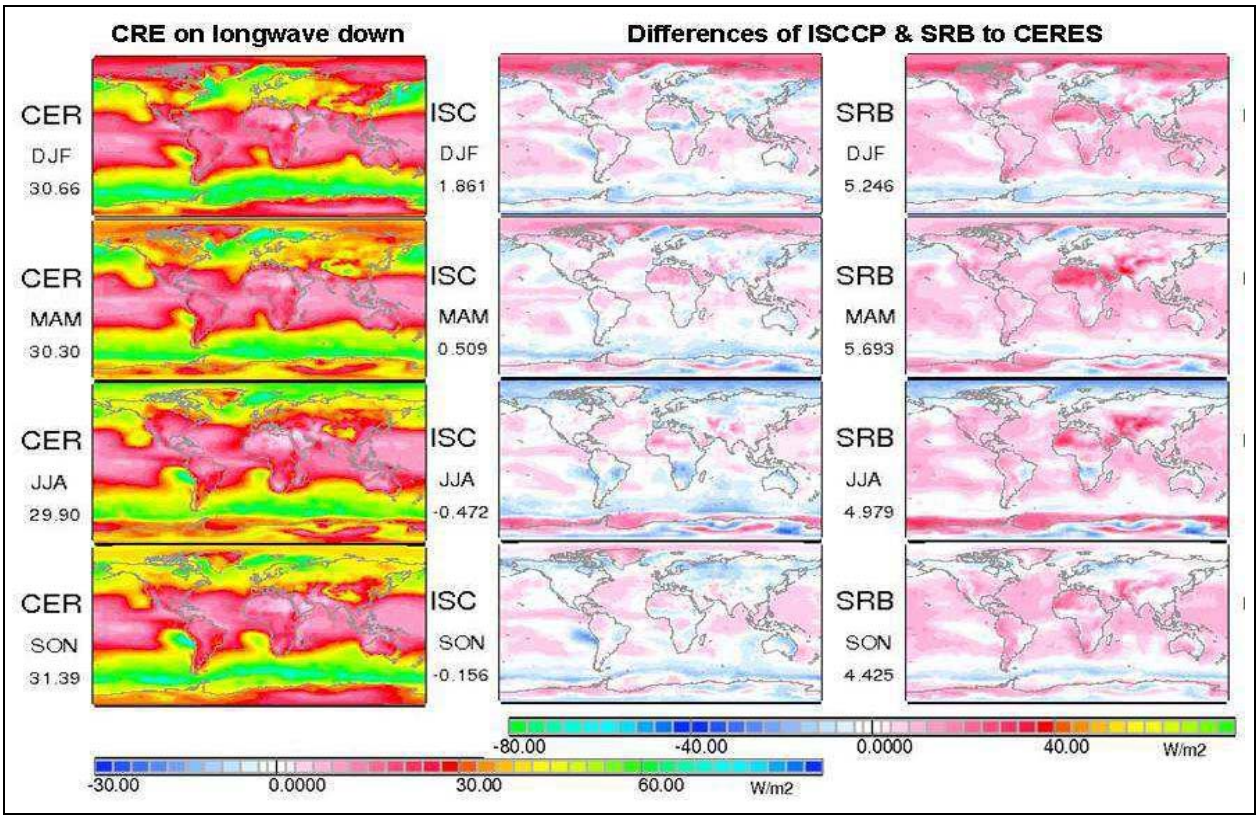

Figure 4.5.14: *Seasonal cloud effects on downward IR fluxes of CERES (left) and differences of ISCCP minus CERES (center) and SRB minus CERES (right). ISCCP and SRB data refer to 1984-1995 and CERES data to Mar2000-Feb2004 time-periods. Values below labels indicate global means.*

The strength of the cloud-effect on downward longwave flux to the surface depends on the cloud optical depth and/or cloud cover and on the atmospheric temperature at the cloud base. Clouds increase the downward longwave flux to the surface globally by about 30 Wm^{-2}, with values exceeding 60 Wm^{-2} over mid-latitude oceans.

When exploring the difference two biases in CERES data should be considered. One bias is negative, as CERES assumes relatively weak cloud optical depth (from solar flux comparisons). The other bias is positive, since in regions of clouds (due to the different 'clear-sky' definition) the CERES cloud-effect also includes a ('all-sky' minus 'clear-sky') water vapor effect. This 'clear-sky' definition impact is easily detectible in ISSCP minus CERES differences but again less apparent for SRB. SRB minus CERES difference are strongly positive as SRB have globally a 5 Wm^{-2} stronger longwave cloud effect on downward longwave fluxes to the surface. Interestingly, there are strong compensating effects between SRB minus CERES differences for clear-sky and for cloud effects (well beyond the 'clear-sky' definition issue), as another example for offsetting deviations. The resulting all-sky solar longwave fluxes for CERES and differences of ISCCP minus CERES and SRB minus CERES are presented in *Figure 4.5.15*.

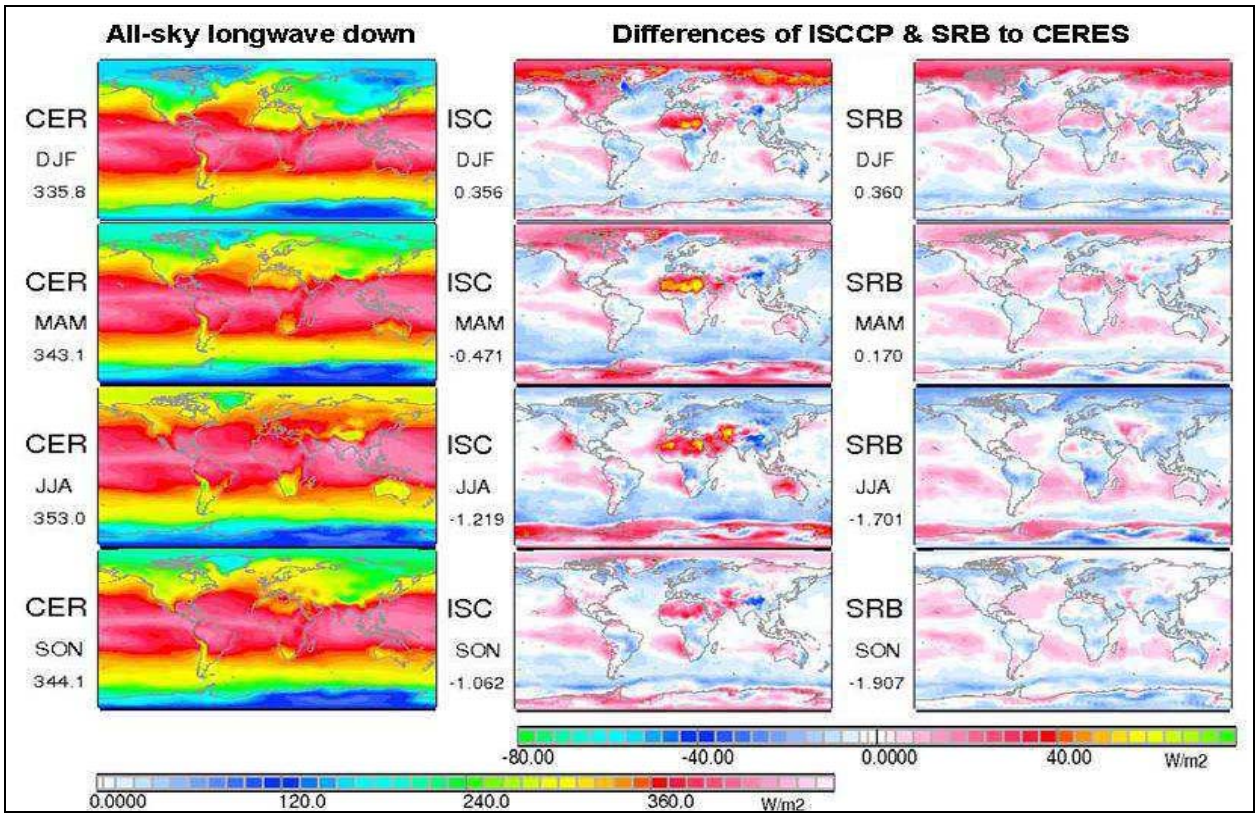

Figure 4.5.15: *Seasonal all-sky downward IR fluxes of CERES (left) and differences of ISCCP minus CERES (center) and SRB minus CERES (right). ISCCP and SRB data refer to 1984-1995 and CERES data to Mar2000-Feb2004 time-periods. Values below labels indicate global means.*

The globally averaged longwave solar fluxes reaching the surface at all-sky conditions are near 345 Wm^{-2}. The largest regional values occur over the warmer lower latitudes.

Differences among the three data-sets are rather moderate, compared to diversities at sub-component fluxes. Relative large values occur for ISCCP over off-coastal stratocumulus (larger cloud optical depth) and over desert regions (dust aerosol). Relatively low ISCCP values occur over mid-latitude oceans. During the northern winter the downward emission in ISCCP and SRB data is up to 40 Wm^{-2} higher than in the CERES data.

4.5.4.4: Net fluxes at surface

The net-fluxes at the surface combine solar and longwave (or IR) fluxes and in addition subtract the upward from downward components. Also for the surface net-flux, before examining all-sky diversity, first the clear-sky and cloud impact components are examined. Seasonal surface net-fluxes for CERES at clear-sky conditions and difference of ISCCP minus CERES and SRB minus CERES are presented in *Figure 4.5.16*.

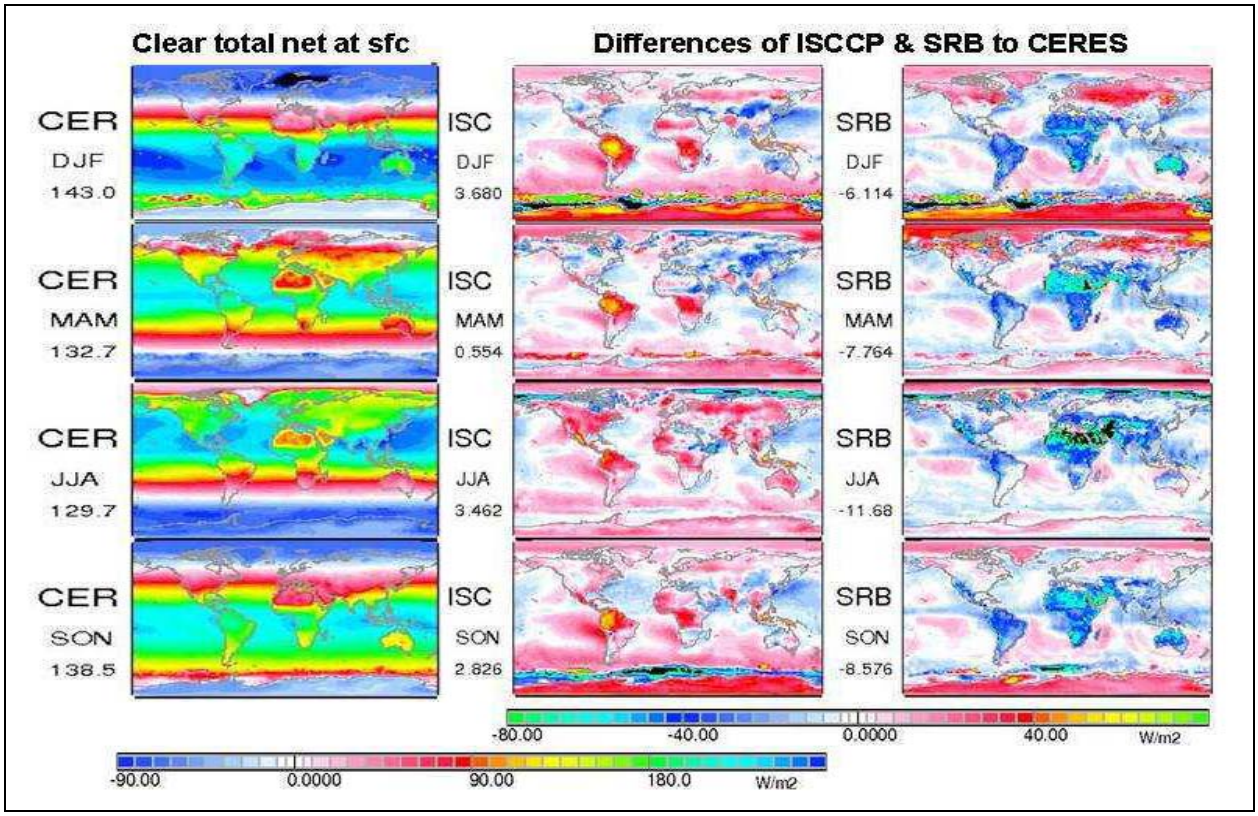

Figure 4.5.16: *Seasonal net-fluxes of CERES (left) and differences of ISCCP minus CERES (center) and SRB minus CERES (right). ISCCP and SRB data refer to 1984-1995 and CERES data to Mar2000-Feb2004 time-periods. Values below labels indicate global means.*

Globally averaged downward surface net-fluxes for clear-sky conditions are near 140 Wm^{-2}. The regional distribution shows a strong latitudinal dependence, with values well above 200 Wm^{-2} over tropical and sub-tropical waters near overhead sun latitudes. Clear-sky solar surface net-fluxes strongly decline towards high latitudes and display negative values over Polar regions. Warm, but highly solar reflecting sub-tropical deserts experience only a surplus of about 100 Wm^{-2}.

On a global basis, ISCCP has the largest and SRB the weakest solar surface fluxes at clear-sky conditions. Regionally, ISCCP has larger values over southern hemisphere continents and especially over South America where relatively weak (solar and longwave) upward fluxes cause 30% (or about 50 Wm^{-2}) larger values than CERES. The relatively low ISCCP clear-sky surface net fluxes over Asia in winter and spring are related to a relatively high surface albedo. In the same region and for the same seasons SRB has relatively high values, as solar reflectance over in SRB is relatively weak. Otherwise SRB has relatively low clear-sky surface net fluxes over all continental areas. The values are especially low over deserts and drop to almost neutral values over the Sahara, mainly due to much larger surface SRB emissivity over deserts.

The other component to the all-sky surface net-fluxes are the cloud radiative effects. Seasonal surface cloud radiative effects on net-fluxes for CERES and difference of ISCCP minus CERES and SRB minus CERES are presented in *Figure 4.5.17*.

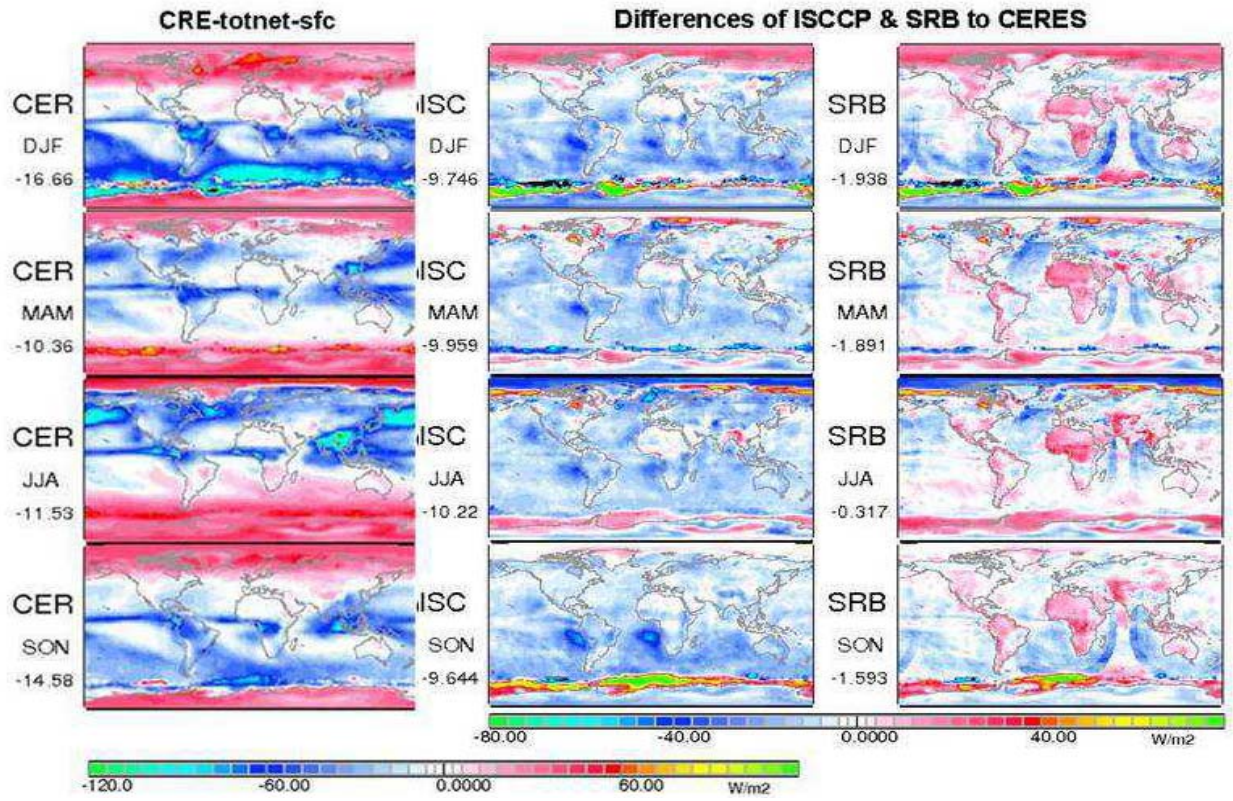

Figure 4.5.17: *Seasonal net-fluxes of CERES (left) and differences of ISCCP minus CERES (center) and SRB minus CERES (right). ISCCP and SRB data refer to 1984-1995 and CERES data to Mar2000-Feb2004 time-periods. Note, clouds cause typically a reduction to net-fluxes. Thus, a negative (ISCCP or SRB) difference (with respect to CERES) means that cloud radiative effects on surface net-fluxes are larger (and vice versa). Values below labels indicate global means.*

On a global basis clouds reduce the clear-sky surface budget by about -15 Wm^{-2}. The strongest reductions occur for mid-latitude clouds over oceans during summer. An interesting aspect is that the cloud impact changes its sign at polar latitudes, to become strongly positive.

ISCCP has a much larger cloud impact than the other two data-sets. In comparison to CERES this is mainly explained by stronger solar cloud attenuation in ISCCP. In contrast, SRB cloud impacts are globally similar to CERES, but with a different regional distribution, as cloud impacts are relatively smaller over continents and relatively larger over oceans. This is explained by the SRB interplay of relatively strong longwave re-radiation to the surface (see *Figure 4.5.14*) and larger than CERES (over oceans) and smaller (over continents) cloud optical depths for the solar spectrum (see *Figure 4.5.11*). SRB also suffers from geostationary cloud retrieval artifacts, as visualized in SRB minus CERES differences.

The combination of clear-sky net-fluxes at the surface and cloud impacts on these net-fluxes yields surface all-sky solar net-fluxes. Resulting all-sky solar net-fluxes for CERES and differences of ISCCP minus CERES and SRB minus CERES are presented in *Figure 4.5.18*.

Globally averaged downward surface net-fluxes for all-sky conditions are near 125 Wm^{-2}. Compared to clear-sky conditions clouds moderated the latitudinal gradient, reducing maxima over the tropics and minima over Polar Regions.

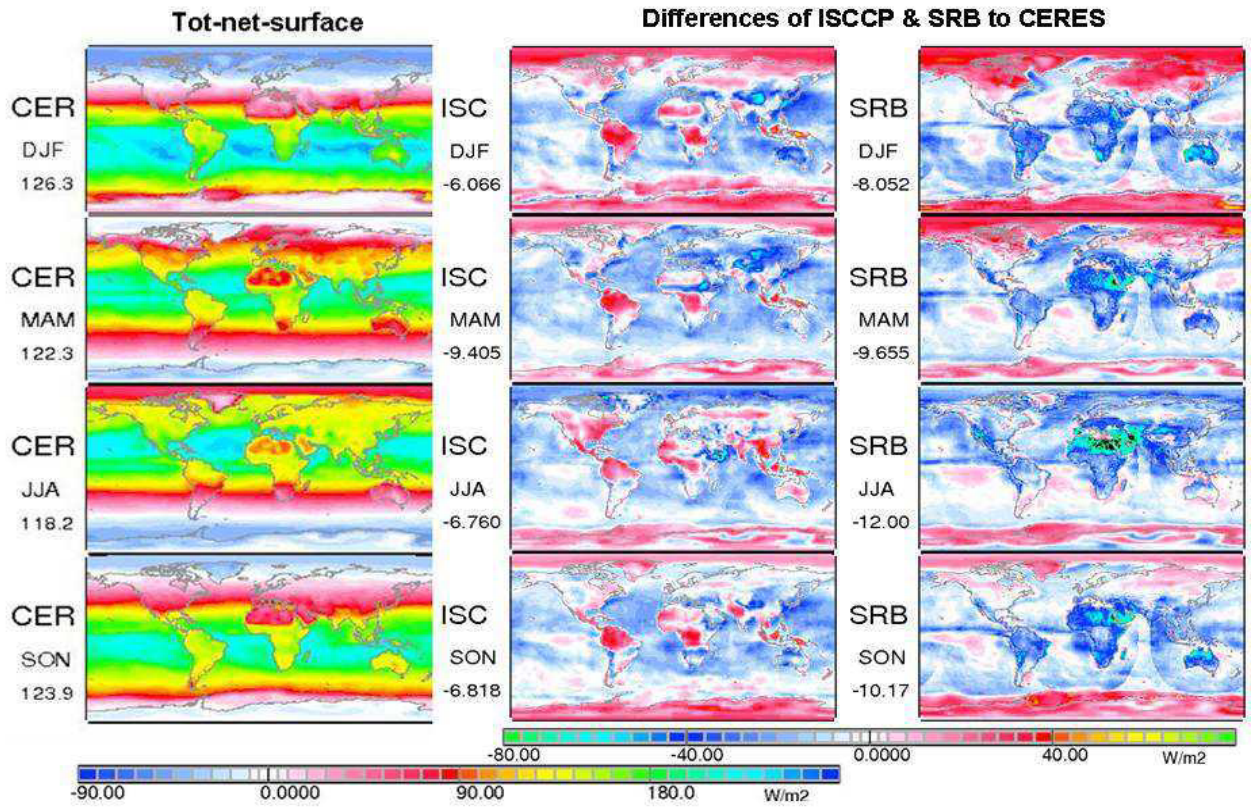

Figure 4.5.18: *Seasonal net-fluxes of CERES (left) and the differences of ISCCP minus CERES (center) and SRB minus CERES (right). ISCCP and SRB data refer to 1984-1995 and CERES data to Mar2000-Feb2004 time-periods. Values below labels indicate global means. Note the artifacts in SRB differences which dominate pattern over the oceans.*

On a global basis CERES has the strongest surface net-flux (imbalance) and SRB the weakest, SRB being overall lower by about 10 Wm^{-2} than CERES. On a regional basis the diversity is particularly larger over lower latitude continental regions. There, ISCCP displays relatively large values (especially over S.America and S.Africa), while SRB displays relatively small values (especially over the Sahara). Larger ISCCP differences to CERES at clear-sky conditions are moderated by stronger ISCCP cloud impacts. Thus, all-sky diversity between ISCCP and CERES is smaller than at a component level. The displayed patterns strongly relate to clear-sky differences. SRB all-sky differences to CERES generally reproduce the clear-sky differences. This indicates that, ancillary data (and not representations of clouds) are responsible for dominant regional differences among the satellite data-sets.

Finally, some comments are added regarding values for surface all-sky net-fluxes of satellite data-sets in comparisons to values suggested by global modeling. Except for a minor contribution (of about 1 Wm^{-2}, which is absorbed in oceans), the large majority of the all-sky surface net-flux should be balanced by the release of latent and sensible heat fluxes from the surface. Now, satellite based surface net-fluxes are significantly larger than what modeling suggests, CERES by about 20 Wm^{-2}, ISCCP by 14 Wm^{-2} and SRB 10 Wm^{-2}. Since sensible heat is well constrained by the surface temperature, satellite data suggest missing latent heat release or missing precipitation in modeling. The underestimation of precipitation in models by 20 Wm^{-2} (as CERES suggests) is highly questionable, but the matter certainly still needs further investigation.

4.5.5: Summary and Conclusions

From satellites we cannot measure directly the radiation budget components at the surface. Needed computations rely on a variety of different ancillary data. These ancillary data cover surface properties as well as the atmospheric state, including properties for aerosol and clouds. Errors and inconsistencies in these ancillary data influence the accuracy of all surface radiative flux products. Inter-comparisons of sub-components for the surface fluxes by the three climate projects CERES, ISCCP and SRB showed that currently the diversity for no-cloud ancillary data is comparable to the diversity in cloud representations. Locally, differences for cloud effects and non-cloud ancillary data often do partially offset each other. Thus, larger differences among data-sets may go unnoticed when inter-comparing all-sky data only. Many data-set accuracy problems are associated with data-handling issues (e.g. the treatment at oblique viewing and gap-filling in regions without geostationary data coverage) and temporal inconsistencies (e.g. sensor drift, platform changes). A better compensation of data-handling problems and a review of all ancillary data in terms of accuracy and consistency are essential tasks prior to any data re-processing. However, the then reprocessed data hold the promise of a more useful reference in applications such as climate modeling.

In the context of global modeling it should be mentioned that surface net-fluxes in global modeling are generally significantly smaller than those associated with satellite-data. Difference seasonal maps for surface net-fluxes of CERES, ISCCP and SRB with respect to the IPCC model median (for see chapter 9) are presented in *Figure 4.5.19*.

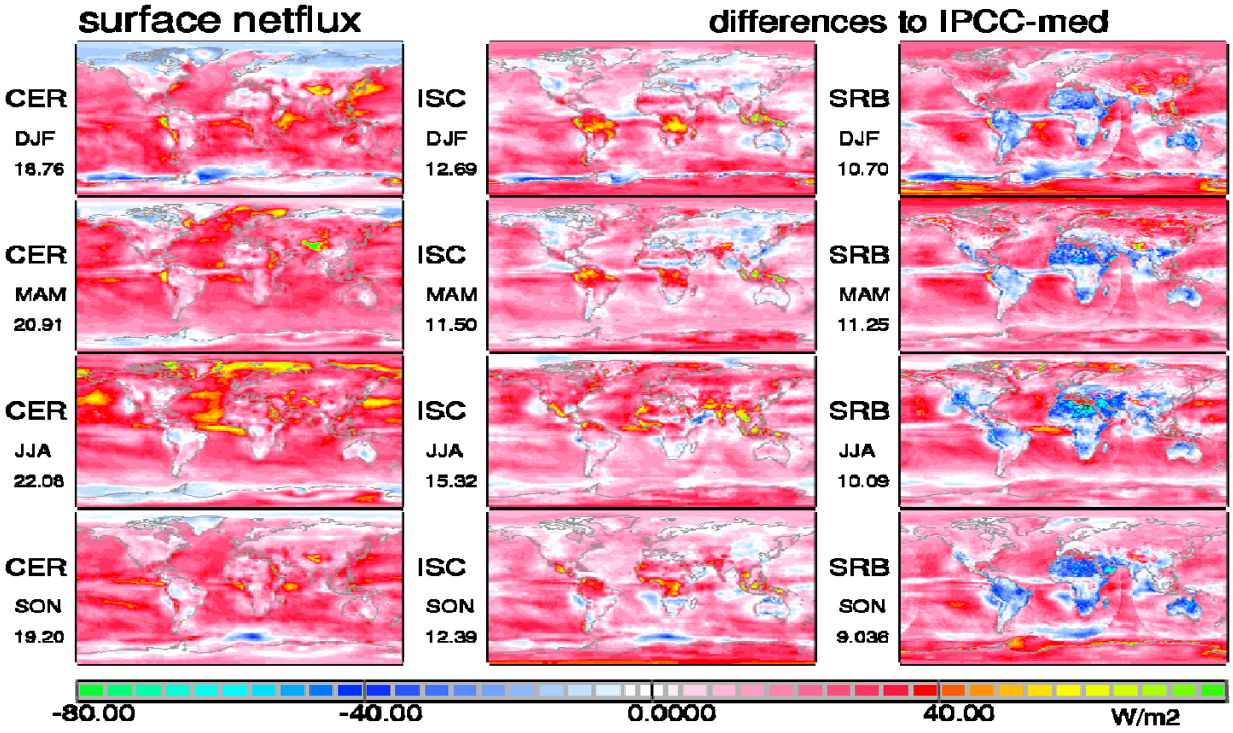

Figure 4.5.19: *Seasonal difference maps of spectrally combined (solar and IR) radiative net-flux at the surface at all-sky (with clouds) conditions between CERES (1.column, 3/2000-2/2004), ISCCP (2.column, 1984-1995), SRB (3.column, 1984-1995) with respect to median of models participating in the IPCC 4th assessment model (1984-1995). Values below labels indicate global means.*

Globally averaged, differences indicate that satellite based surface net-fluxes are significantly larger than typical values in global modeling (CERES +21Wm^{-2}, ISCCP +13Wm^{-2}, SRB +10Wm^{-2}). Surface net-fluxes of the three satellite data-sets are consistently larger over oceans, especially for summer seasons. Over continents the differences to modeling are usually weaker, but also more diverse, due to inconsistencies of current satellite surface net-fluxes over continents. The larger satellite values, if correct, would require stronger compensating losses (e.g. via latent heat and precipitation), than what is currently considered in global modeling. Clearly, these differences need further attention.

The comparisons demonstrated, that

- applied ancillary data often lack temporal consistence
- available time-series of ISCCP and SRB are unfit for studies on inter-annual trends
- all-sky diversity often hides larger (off-setting) diversity of sub-components
- lack of clear-sky definitions complicate a sub-component analysis
- flux diversity by (no-cloud) ancillary data often exceeds flux diversity by clouds data
- for surface fluxes, ancillary data dominate cloud data with respect to anomaly patterns
- surface net-fluxes of satellite data-sets are larger than usually in global modeling

This sub-chapter only explored two subcomponents for all-sky diversity, the clear-sky (non-cloud) diversity and the cloud representation diversity. The representation of clouds has many more aspects, including optical depth, altitude and overlap and microphysics. Similarly the list of non-cloud ancillary data is even longer, including different properties for aerosol, surface and atmospheric state. Not only accurate and consistent data are needed for each ancillary property but also these individual data have to be consistent to each other. To assist in the required ancillary data-consistency, assimilation techniques and assimilated data-products should be considered. Once more consistent ancillary data are available then a complete re-analysis of all three data sets is recommended.

(Additional figures and comments to subchapter 4.5 are available in Appendix C.)

Chapter 5:

Long-Term In-Situ Surface Flux Data Products

E. G. Dutton and C. Long, with contributions by M. Wild, A. Ohmura, J. Groebner, A. Roesch

Abstract:

Ground-based in situ observations of the surface radiation budget components have long been pursued and were enhanced under the encouragement of WCRP in the satellite era to permit more critical and extensive evaluations of related satellite derived products. These in-situ measurements are independent, continuous, direct measurements of the irradiance quantities of interest but are more limited in spatial representativeness than satellite products. In contrast, the satellite products are deduced from inferences constrained by the less frequent satellite observations at or near the top of the atmosphere. Therefore, the ground-based data are useful for validation and verification of the satellite products. However, such quantitative comparisons are limited by complicated spatial and temporal representativeness differences as well as persistent and complex observational error propagation in both methodologies. This Chapter addresses the primary areas of uncertainty in the in situ observations as they are utilized in other portions of this assessment, as well as some examples of results from stand-alone applications utilizing the in situ data. The assessment of the observational uncertainties, both instrumental and representativeness, is in an effort to aid in the assignment of overall uncertainty to the satellite products.

5.1: Introduction

This Chapter provides an assessment of quality and utility of certain in situ observed surface solar and thermal IR irradiance data used elsewhere in this report to aid in the assessment of related satellite-derived values and products. Covered in the quality analysis are the instantaneously acquired values along with the impact of various temporal and spatial averaging methods. This includes an evaluation of measurement accuracies and other sources of uncertainties in ground-based in situ observations. Considerable emphasis is placed on the basic measurements and their uncertainties but also included is an evaluation of several products derived from the basic measurements as well as discussion and summary of long-term temporal variations in amalgamated subsets of the data. This Chapter provides the reader with not only a reference to the measurement uncertainties in these data but also examples of some of the more fruitful and valuable standalone applications of these data. *Section 5.2* covers the measurement uncertainties including the effects of temporal averaging and spatial representativeness.

Section 5.3 gives a description of several derived products relating primarily to determination of clear-sky conditions and cloud impacts on the irradiance observations. *Section 5.4* looks at the application of surface-based irradiance to long-term variability studies and *Section 5.5* wraps up with a brief discussion of ongoing issues in the area of direct surface-based irradiance observations for climate research applications. Additional details pertaining to in situ surface irradiance data utilized in this report and their uncertainties are found in *Appendix A2*.

5.2: Measurement Uncertainty Estimates

5.2.1: Overview

The observed quantities considered here are point measurements of downwelling solar and thermal IR irradiance as measured with common, high-quality, commercially available radiometers. Although international guidelines and manufactures' specifications exist for uncertainty of individual instrument types, provided here are the results of independent determination of these instrument related uncertainties based primarily on experiences and practices within the BSRN (WCRP-Baseline Surface Radiation Network), NOAA CMDL & SURFRAD [Climate Monitoring and Diagnostics Laboratory (now Earth System Research Lab/Global Monitoring Division) and SURFace RADiation], and DOE-ARM (Atmospheric Radiation Measurements) observational networks. (Note: The terms "uncertainty(ies)" and "error(s)" are used interchangeably throughout this *Section, 5.2*)

Measurement uncertainties are defined as potential departures of a reported observation from an absolute exact quantification of the irradiance at the time and location of the measurement. Uncertainties discussed in this section do not include any contribution from interpretation of the observations' representativeness when comparing to satellite-based or other model based estimates as done elsewhere in this assessment. Unless otherwise indicated, the uncertainties reported here are the full ranges, plus and minus from the reported observation, within which the true value can be expected to occur 95% of the time under normal, non-precipitating, ambient observing conditions. Measurement uncertainties are reported in Wm^{-2} unless otherwise noted.

Irradiance measurement uncertainty includes both bias and random error sources. Temporal or spatial averaging will reduce the random errors included in the instantaneous point observations but any missing data over the averaging domain can introduce additional bias uncertainty as discussed in *Section 5.2.9*. Many potential mean bias errors not caused by missing data are removed in the instrument calibration process, although, any biases in the calibration standard reference or introduced by a specific measurement activity remain. For example, temperature and solar zenith angles dependencies can be accounted for at the time of calibration but will introduce errors if the field measurement conditions vary from those at the time of calibration. Considerable effort has gone into the design and deployment of available surface irradiance instrumentation to minimize these and similar dependencies but which become more of a concern at shorter time scales and in measurement environments far from those encountered during instrument calibration.

Values given for the measurement uncertainties are typically estimated quantities for which an additional uncertainty also exists. No explicit effort is made here to quantify this uncertainty of the uncertainties, although the method of determining the basic uncertainties (95% spread in PDFs) may infer some level of qualitative confidence in the stated uncertainty ranges. Several summaries of the assessment of related uncertainties have been given, e.g., Myers, 1989; Ohmura et al., 1998; Augustine et al., 2000; Gueymard and Myers, 2008 & 2009; and Stoffel et al., 2010. Those and other recently compiled results are utilized for this assessment of in situ surface irradiance measurement uncertainty.

The data used in this assessment have been edited for the purpose of removing the catastrophic effects of obstructions, misalignments, or precipitation when they can be detected and, therefore, do not contribute to the reported uncertainty ranges. However undetected similar errors can and do remain in the utilized data and will contribute to the stated uncertainties when

those uncertainties are determined from the total scatter in the data about mean or expected values.

5.2.2: Observations of Interest to This RFA

The in situ observed quantities of interest here are surface solar and thermal IR irradiance point measurements made at a wide variety of locations around the world, typically within a few meters of the earth's surface. The measurement instruments are continually exposed to the ambient environmental conditions and electronic signals representing the received irradiances are sampled typically once per second and averages of one to a few minutes are retained for subsequent processing. The instruments for measuring downwelling irradiances are located such as to minimize obstructions between the detector and sky, typically on elevated platforms either in open fields or on the roofs of buildings. Occasional to frequent manual inspection of the instrumentation for proper operation and cleanliness is desirable and has been encouraged at participating sites. Detailed specifications for the recommended observational methodologies are given in the BSRN operations manual (McArthur, 2005) and are practiced at most participating sites as listed in Appendix A2, which also provides more information on the different sites and programs supplying in situ data for this assessment. The downwelling solar is often redundantly measured (as recommended by BSRN) both as a single total quantity and as the sum of its two components, the vertical components of direct and diffuse measured separately, although this dual component method is subject to more data loss due to exacting solar tracking requirements.

5.2.3: Instruments Utilized

The instruments used for irradiance measurements discussed here are broadband thermal sensing radiometers with thermopile sensors. They are calibrated relative to an independent source for the purpose of converting the raw instrument signal into physical units of irradiance in Wm^{-2}.

Thermopile broadband radiometers have several features that make them prominent in the field – linearity, stability, durability, and are relatively inexpensive, although less expensive instruments without the preceding qualities do exist and care needs to be taken in the evaluation of actual instruments deployed. The instruments used for the various datasets utilized in this assessment were manufactured by a variety of commercial sources.

Observations made with the commercially available pyranometers, pyrheliometers, and pyrgeometers are under consideration. Pyranometers are used to measure separately the total downwelling and upwelling solar irradiance in the nominal spectral band of 0.3 to about 3.0 micrometers. Pyranometers are also used in a solar shaded configuration to observe diffuse sky solar radiation where the detector is blocked from the direct sun by a small disk that mechanically tracks the position of the sun.

Pyrheliometers are used to measure the irradiance in the direct solar component on a surface normal to the beam and must be attached to a mechanical solar tracker. The field-of-view of the direct component is ideally on average (over the range of solar elevation angles) nearly matched by the size of the shading disk for the diffuse measurement, thus when combined with the diffuse measurements produces a sum that is representative of the downwelling hemispheric irradiance. Pyrgeometer is used to measure separately both the upwelling and downwelling thermal infrared (IR) irradiance, nominally in the wavelength region of 3.5 to 50 μm.

5.2.4: Methodologies for Determining Measurement Uncertainty

Various methods of estimating measurement uncertainty exist. These include estimating total uncertainty by mathematically combining individual error contributions from all known sources (sometimes called formal error analysis), comparisons to reference instruments for which a detailed uncertainty has be estimated by the formal method, and by an evaluation of the spread of independent collocated simultaneous observations that provides a realistic uncertainty range that includes unanticipated and undetected operational errors. All three of these methods contribute to this assessment. One method's results can be compared to another's for mutual substantiation and extension of the confidence in the inferred uncertainty. Operational radiometer observational uncertainty can be determined by statistical analysis of departures from reference instrument observations under actual field conditions. However, maintaining a true calibration reference in the field under all conditions is not practical. In several cases, redundantly deployed field instruments have been evaluated to provide a realistic estimate to actual uncertainty of those instruments, as reported near the end of *Section 5.2.10*.

5.2.5: Uncertainties in the Measurement of Total Downward Solar Irradiance

There are two techniques commonly used for the in situ observation of downward solar irradiance. One is the use of a relatively simple, level, upward-facing, unshaded pyranometer with a clear view of the entire sky hemisphere. The other method is to combine (sum) the separately measured vertical component of direct solar beam measured with a tracking pyrheliometer with the diffuse sky irradiance observations made with an appropriately shaded pyranometer. The BSRN (Ohmura et al, 1998) and others have recommended the use of the combined measurement (summation) as the most accurate for instrumentation and methodologies available in the early 1990s and is widely applied for data provided for this assessment. In *Appendix A.2.1.1* there are uncertainty assessments for both approaches using various instrumentation available through the mid 2000's. Results from both measurement techniques have been utilized in this assessment. The relative value of a more complete data record using single unshaded pyranometer versus a sometimes (often) spotty and discontinuous but more accurate (for a single observation) summation method needs to be considered and may depend on the application of interest, e.g., instantaneous satellite or model result comparison vs monthly or annual averages.

It is important to note that through the time period for which in situ surface solar irradiance data have been supplied for the assessment, the primary calibration reference has been the World Radiation Scale as defined in the *Appendix A.2.1.1.2.2* By 2010 there were new advances in commercial instrumentation that would likely improve the uncertainty estimates reported here but were not yet available for broad deployment at the time of the data collection phase of this assessment, e.g., Michalsky et al 2011.

5.2.6: Uncertainties in the Surface Received Downwelling Thermal IR Irradiance

Downwelling thermal IR is the atmospheric emitted irradiance reaching the Earth's surface on a horizontal plane. Unlike the downwelling solar irradiance, there is not a dominant directional component and hence no dominate cosine response error that plagues solar observations, see *Appendix A.2.1.1.1*. The incident IR radiation is dependent on the local temperature and moisture (including clouds) with small contributions from certain other trace atmospheric constituents. There are no inherent wavelength boundaries on this quantity, however

nearly all relevant radiant energy falls between the spectral boundaries of about 4 μm to 50 μm, which correspond to typical spectral limits of the broadband filtered instrumentation used for this measurement, pyrgeometers.

Pyrgeometers spectral shortwave cutoff near 4.0 μm blocks most solar source irradiance (which is partially accounted for in the solar measurements, see *A.2.1.1.2.3*) and the longwave cutoff of near 50 μm is due to practical filter manufacturing limitations. The small atmospheric emission contribution outside those limits is accounted for, to the first order, in the calibration process where the instrument response is equivalenced to unfilteredreference irradiance , either blackbody or sky, for terrestrial temperature ranges. The uncertainties due to the dome spectral characteristics are discussed more in *Appendix A.2.1.2.3*.

The shortwave cutoff is a compromise between cutting off the tail of the IR spectrum and allowing some irradiance contribution originating from the sun. To minimize the solar contribution in the pyrgeometer measurement, it is recommended (BSRN, McArthur 2005) that direct sun be blocked from the pyrgeometer by a solar shading disk. Further detail on the evaluation of pyrgeometer uncertainties can be found in *Sections 5.2.8-11* below and in *Appendix A.2.1.2.*

5.2.7: Considerations for Uncertainties in Upwelling Irradiance Observations

The same instrumentation is used to measure the upwelling solar and thermal IR as is used for the downwelling irradiances, with the exception that the lack a distinct direct solar beam negates the need for mechanical solar tracking. The uncertainties are considered similar to the instruments that are measuring downwelling irradiance while in the upward facing position, but without error sources related to direct solar beam, primarily the detector cosine response error. Additionally, dome cooling due to IR emission to the sky that contributes to dome thermal offset issues is greatly reduced or eliminated when the instruments are facing the ground surface at a height of only a few meters.

One of the issues to be addressed concerns whether or not the orientation of the radiometers affects their calibration and performance. Pyrgeometers and pyranometers have similar thermal conduction and convection properties so it can be assumed that they would be similarly impacted by inverted orientation. Pyrgeometers have been calibrated in both the up- and down-facing positions with no detectable differences, as in the Philipona et al (1998) round-robin comparisons and in Dutton (1993) when comparing his to Eppley results. With those and other informal results reported by various practioners, it is concluded that orientation of thermopile radiometers have no significant effect on their performance other than altering the viewed irradiance field.

The main concern with measured upwelling irradiances is the limited representativeness relative to surrounding, especially non-homogenous, surfaces. While this does not result from an explicit error in the measurement, it does result in problematic interpretation when performing comparisons to other methods of estimating upwelling irradiances that include extended surrounding surface area. The BSRN has made an effort to solicit sites surrounded by homogenous surfaces but few sites completely satisfying that criteria have been established. The extent of the homogeneity, or lack thereof, surrounding surface measurement sites needs to be carefully considered when using in situ surface data to compare to alternately determined similar quantities influenced by a much larger surrounding area. Only a subset of surface radiation sites used in this assessment make upwelling irradiance observations, and therefore the comparison with satellite and model products in this assessment is likewise limited.

5.2.8: Time Averaging

The previous sections (and *Appendix A.2.1*) address the likely uncertainty in nearly instantaneous radiometer observations. However, in practice only observations of a nominal minimum duration (averaging or integrating) time, typically one minute, are available for analysis and are used as basic data in this assessment before being further averaged for some applications. Additional averaging can lead to improvements of the observational accuracy by reducing random error but then leads to interpretation issues as to just what portion of the atmosphere in motion has been sampled along with issues concerning the treatment of the occasional but inevitable missing data resulting in gaps over an averaging interval. As opposed to random uncertainty, cyclic uncertainties such as can be introduced by diurnal and annual solar zenith angle variations are minimized by averaging over a specific amount of time related to the respective cycle. However, it is not possible to determine the actual total accuracy improvement associated with longer averaging intervals because to date, an absolute field reference has not been maintained on other than shorter time scales. A description of the various stages of data sampling, integration and averaging that go into producing irradiance products from ground-based observations is provided in *Appendix A.2.1.3*. The potential for error reduction or enhancement that can result from further averaging of the basic one-minute data are discussed next with some examples using redundant instrumentation given in *Section 5.2.10*.

The uncertainties described in the preceding section and *Appendix A.2.1.1* and *A.2.1.2* are considered to be applicable to near instantaneous observations when obtained under near-ideal, stable, environmental conditions with temperature and cosine response errors accounted for. Longer averaging times are desirable for many applications including those in this assessment. However, additional averaging does not assure further reduction in the inherent point measurement uncertainty. Averaging is often done to simply reduce the amount of data points or to achieve better spatiotemporal consistency with independently determined quantities nominally collocated in space and/or time. Irradiances averaged for several minutes up to an hour or two are common for both reasons.

Irradiances averaged more than about one hour will begin to substantially detract from the ability to resolve diurnal variability. Averaging over the period of an entire day has an advantage of reducing some of the error introduced by any cosine response or other solar elevation or azimuth introduced errors, although seasonal bias could remain due to limited the range of solar angles in any 24-hour period at a particular location. In general, 24-hour averages completely remove the diurnal variability without adding any further uncertainty, unless there are gaps in the data, and may help reduce some semi-random instrumentally introduced uncertainty. Furthermore, the full 24-hour average (including night conditions) for solar irradiance produces a value consistent with climatologically related energy budget studies.

Further averaging of irradiance measurements to weeks, months, and seasons will have a small effect on reducing solar position induced measurement errors with continued risk of increased uncertainty resulting from missing data. Annual averages can be considered optimal for analysis of adequately long data records for four reasons. First, a large range of solar angles are observed minimizing angular dependence error of the instrumentation. Second, any introduced bias due to missing data is further reduced by the longer averaging interval where missing data is more likely to be randomly distributed. Third, any intra-annual variability and related autocorrelation that complicates certain time-series analysis is inherently removed. Fourth, remaining random errors are further minimized. For adequately long data records, annual averages therefore become the preferred, lowest uncertainty quantity other than even longer

multiple-year averaging that would further reduce uncertainty due to inter-annual variability but may be less viable for analysis due to record length.

Roesch et al. (2011) have examined how missing data and certain gap filling methodologies can affect monthly average downwelling solar and IR irradiance data supplied for this assessment. Roesch et al. examine the effects of; 1) ignoring the gaps, which effectively fills each missing value with the monthly average of the existing values, 2) filling from a table of monthly mean AM and PM zenith angle dependent averages compiled from the existing data for that month, 3) same as 2) but using existing data from the 2-week period, 4) filling from a table of monthly mean diurnal cycle compiled from existing data, and 5) forming monthly average only when a specified percentage of data for the month exist. Roesch et al. find that both the amount of missing data and the method for treating those gaps can make up to a 10 Wm^{-2} difference in direct solar monthly averages for the amount of missing data that can occasionally occur at a BSRN site, but with most months' differences being in the 1-2 Wm^{-2} range, see *Figure 5.2.1*. Obviously, larger amounts of missing data will result it potentially larger bias in monthly averages formed from the available data.

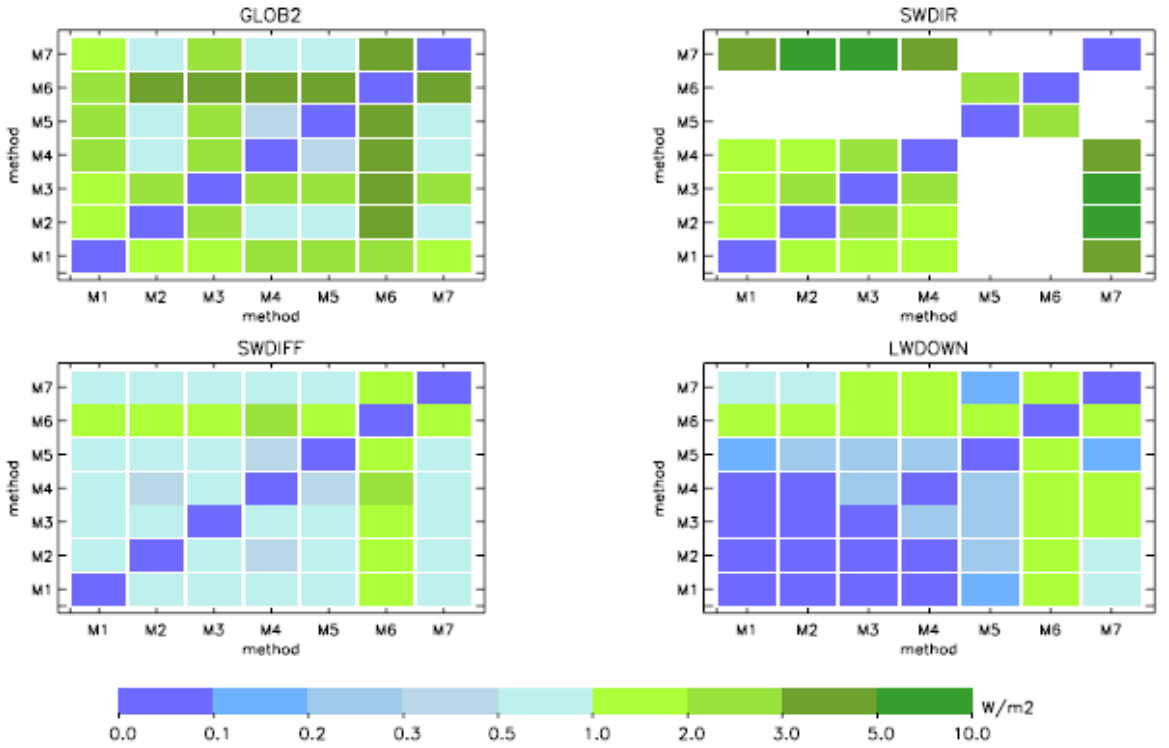

Figure 5.2.1: *Comparison matrices showing the mean differences of monthly surface irradiance averages computed by 7 different averaging methods M1-M7 described in Roesch. Quantities clockwise from the upper right panel are Global SW, Direct SW, Diffuse SW, and Downwelling IR. Approximately 5200 station-months of BSRN data were used to compile each of the above charts. Blanks in the SWDIR are because those comparisons were not possible with the data provided. (Figure from Roesch et al., 2011)*

Roesch et al. conclude that of the methods tested those that determine a mean diurnal cycle and derive fill data from that to produce monthly averages provide the best results. The averaging method defined as M7 in Roesch et al , which uses monthly mean diurnal variations to fill missing data, was used for the monthly mean BSRN data supplied to this assessment.

5.2.9: Long-term Measurement Stability

The relative variability of surface irradiance rather than absolute accuracy is of primary interest for some applications such as a record of local or regional temporal variations where those variations are predicted by, or compared to, those inferred from other sources. In such cases the temporal stability of those records should be substantiated against some further independent reference of known stability. However, this becomes difficult if the absolute accuracy of those references has not been established.

The World Radiation Center in Davos Switzerland reports that the current solar irradiance reference standard (WRR) has been maintained as the consensus of the group of characterized reference absolute cavity instruments over the past 38 years with a suggested total drift of less than 0.02%, and with the inherent assumption that all cavities of various designs and manufacture have not drifted together.

For infrared measurements there are three independent groups of reference instruments available, the internationally-maintained WISG (http://www.pmodwrc.ch/pmod.php?topic=irc, several laboratory blackbody calibration sources, and shelf reference pyrgeometers, all of which have demonstrated stability to within about 0.5% over the past 10 years. Based on long term records of the calibration of individual thermopile radiometers, yearly to triennial calibration of field instruments is generally adequate to maintain the stability of the long-term mean field observations to about the same level as the reference standard levels, although new field instruments are usually calibrated more frequently to establish their initial stability.

5.2.10: Redundant Measurements as an Uncertainty Assessment Tool

Redundant measurements provide a means to check of uncertainty estimates as well as on-going operational quality control. However, in addition to the differences revealed by the simultaneous redundant measurements, bias errors exist in the calibration references to which the field instruments were equated during calibration. With the assumption that the individual instruments operate independently but are tied to the same calibration scale, the range of differences between them over time indicate the extent of random uncertainty in the field deployed instrument after removing obviously erroneous data (e.g., from obstructions) typically identified in the data editing process. This uncertainty could be expected to be larger than from either ideal calibration conditions (as the published BSRN specifications, Ohmura et al 1998) or from idealized formal uncertainty analysis because of conditions not accounted for or anticipated in those analyses, such as obstructions, icing and etc.

For several years, redundant solar direct and diffuse measurements were made at a number of NOAA radiation field sites (Barrow, Alaska; Mauna Loa, Hawaii; South Pole; Trinidad Head, California; Boulder, Colorado; Prospect Hill, Bermuda; and Kwajalein, Marshall Islands). The field data were edited for erroneous outliers suspected of being caused by instrument failure, obstructions or other contamination. Differences between the redundant sensors on a minute-by minute basis and longer averaging intervals were computed and incorporated into relative frequency of occurrence histograms (or probability density functions, PDFs). In addition to the analysis of the redundant direct and diffuse solar measurements, the difference between the unshaded-pyranometer-measured total solar irradiance and that determined by summation method were also examined and respective PDFs were developed. The differences from the various instruments were averaged over increasing time intervals from the basic measurement one-minute of 1 Hz samples to one hour, one day, one month and out to one year. There are about 40 station-years of direct, thirty station-years of diffuse redundant

measurements available for this analysis. Additionally, nearly 90 station years of SURFRAD data were analyzed similarly for the differences between unshaded pyranometer and summation method for total incoming solar irradiance. The results for all components are shown in *Figures 5.2.2 to 5.2.5* and are summarized in *Table 5.2.11.1* where the ranges given are for the inclusion of 95% of results determined from the 2.5% and 97.5% points on the accumulative frequency of occurrence from the PDFs. It should be noted that the distributions are not normally distributed so inferences of the 95% inclusion range using normal-distribution statistics, i.e. standard deviation and error, would yield invalid results. Relatively smooth distributions were obtained in most cases except for the annual averages where too few points exist.

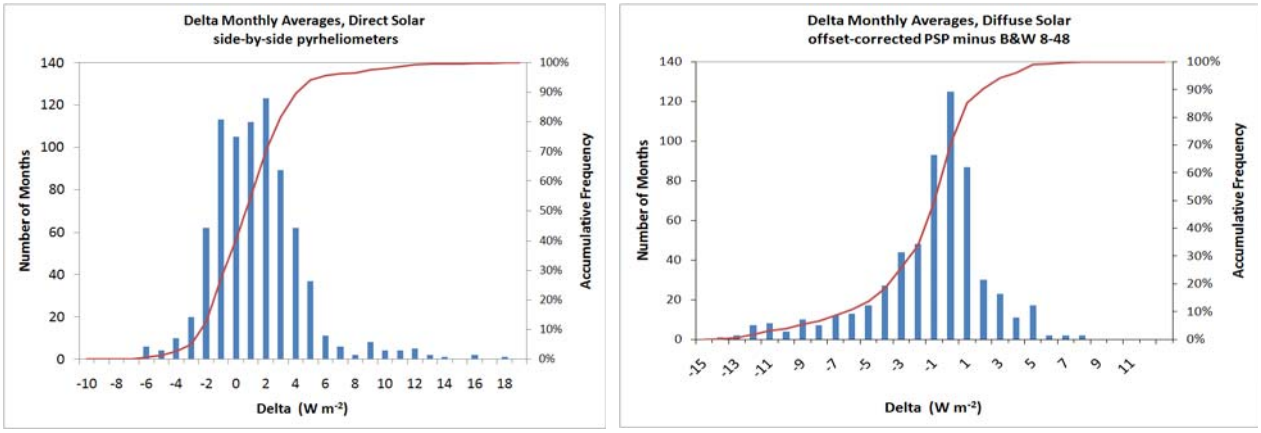

Figure 5.2.2*: Histogram and accumulative frequency of the differences (Wm^{-2}) between monthly averages of direct (left panel) and diffuse (right panel) solar radiation measured with two pyrheliometers at a single site for the several different field sites given in the text. The red line corresponds to the accumulative frequency of the histogram given on the right-hand axis. The slight negative bias results from the small deficiency in the PSP offset correction of Dutton et al., 2001.*

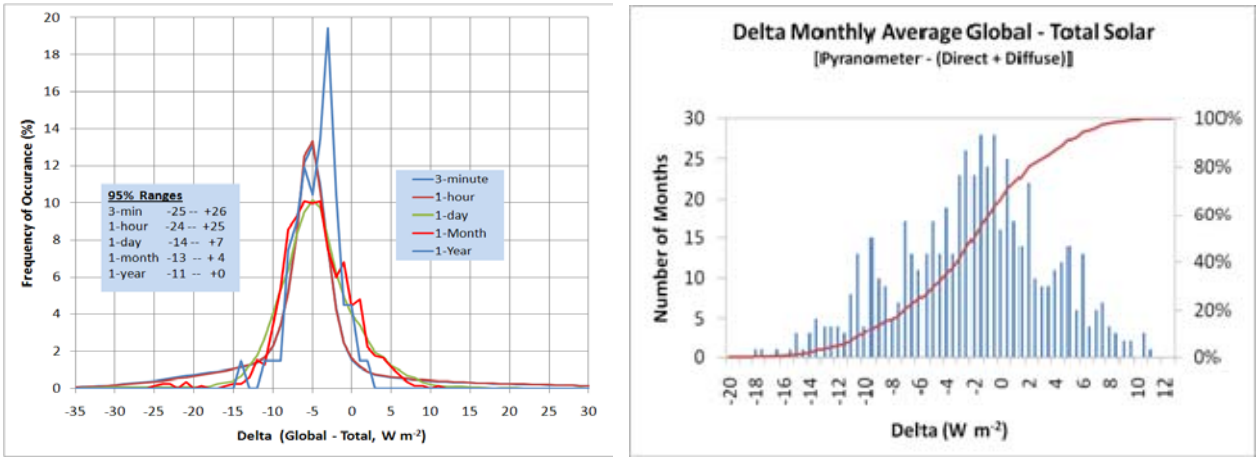

Figure 5.2.3 (Left panel): *Histograms of the differences (Wm^{-2}) between downwelling solar radiation measured by two different methods (global pyranometer minus diffuse + direct, or total) for various averaging intervals indicated in graph legend. There were 15 years of 3-minute data from 6 SURFRAD sites used to compile these curves. The small apparent negative bias of about 5 Wm^{-2} is likely due to the global pyranometers not being thermal-off-set adjusted.* ***Right panel:*** *Differences between ushaded and summation total solar) except for monthly averages only with an accumulative frequency curve (RHS) for data obtained at the NOAA/CMDL global baseline observing sites*

. Nonetheless the transition to smaller 95% ranges as the averaging times increase is evident. For the results given in *Table 5.2.11.2*, the entire range of solar zenith angles over a 24-hour day were used giving consistency with values that would be used in daily or longer term energy budget studies. Considerable narrowing of the 95% ranges is seen going from the 1-hour to 1-day interval because in day average then includes a portion of the day that has nighttime zero readings. It should be noted that in these comparisons Eppley PSP and 8-48 pyranometers and NIP pyrheliometers were used exclusively. Comparisons between virtually thermal offset-free diffuse pyranometers (see *A.2.1.1.4*) confirm a higher level of agreement at the shorter time intervals for diffuse obtained under idealized conditions, Michalsky et al., 2008.

Quantity	1-3 min	1 Hr	1 Day	1 month	1 year	Figure #
SW Direct	± 16	± 14	± 8	± 5	± 4	5.1.2
SW Diffuse	± 14	±13	± 8	± 5	± 4	5.1.3
SW Hemisph.	± 25	± 24	± 11	± 8	± 6	5.1.4a
SW Total	± 21	± 19	± 11	± 7	± 6	
LW Hemisph.	± 6			± 4*		5.1.5

Table 5.2.10.1: *The 95% inclusion ranges (Wm^{-2}) of redundant measurement differences from operational network field sites for all zenith angles including nighttime. The values for the various parameters were obtained from the indicated or similar Figures with SW Total values were computed from square root sum of squares of the SW Direct and SW Diffuse.* **** Averaging times vary between one and several weeks.***

Another similar study utilized three collocated redundant surface radiation systems at the ARM Southern Great Plains site. In this study, Shi and Long (2002) compared the three collocated measurements from the years 1997-2001 using for both the original 1-minute data and 15-minute averages of the data with the results, mean absolute differences and their standard deviations????, given in *Table 5.2.10.2* where the "best agreement" category are the differences between whatever pair of the three measurements agreed best at a given time.

Similarly the "worst" category includes whichever pair of measurements disagreed the most, and the remaining pair of measurements were included in the "typical" category. For the 1-minute data, the diffuse SW agreement ranges from an average of 4 Wm^{-2} to 12 Wm^{-2} for "best" to "worst" agreement. Similarly, the ranges for the direct normal component SW and global SW (as measured by an unshaded pyranometers) are 6 Wm^{-2} to 15 Wm^{-2}, and 9 Wm^{-2} to 18 Wm^{-2}, respectively. For the downwelling LW, the range of average agreement spans 3 Wm^{-2} to 7 Wm^{-2}.

	Best	Typical	Worst
Diffuse SW	4.0 ± 1.4	8.9 ± 2.9	11.8 ± 3.7
Direct Normal SW	6.2 ± 3.2	13.6 ± 6.4	15.0 ± 6.8
Downwelling LW	3.3 ± 0.7	5.6 ± 1.4	7.7 ± 2.2
Downwelling SW	9.2 ± 4.0	16.1 ± 7.5	17.5 ± 7.2
Upwelling SW	11.1 ± 2.8		
Upwelling LW	9.6 ± 3.0		

	Best	Typical	Worst
Diffuse SW	3.6 ± 1.5	8.8 ± 3.10	11.3 ± 3.8
Direct Normal SW	5.3 ± 2.9	13.2 ± 6.6	14.6 ± 6.9
Downwelling LW	3.2 ± 0.7	5.8 ± 2.0	8.1 ± 2.5
Downwelling SW	7.1 ± 4.2	15.6 ± 7.8	17.7 ± 7.2
Upwelling SW	10.7 ± 2.9		
Upwelling LW	9.6 ± 3.3		

Table 5.2.10.2: *Operational field results for multiple instrument comparisons from ARM SGP for 1997-2001 inclusive. Tabulated values are means of 95% inclusion points from annual accumulative frequency distributions of the absolute differences between instrument pairs and the ± values indicate the average absolute departure from those mean values over the 5 years. The "Best"category is the best agreement pair of the three measurements at any given time, "Worst" is the most disagreement pair, and "Typical" is the remaining pair at any given time. Left Panel is for 1-minute average data, the right panel is for 15-minute averages.*

Unfortunately there is only one pair of downward facing radiometers available, so only the average agreement for these quantities could be determined as 11 Wm^{-2} and 10 Wm^{-2} for the upwelling SW and LW, respectively. A similar comparison was done using 15-minute averages of the above data, which is the temporal resolution of the surface data used in this Radiative Flux Assessment document.

The 15-minute comparison results are given in the right panel of *Table 5.2.10.2,* they show only slight or no improvement in agreement compared to the 1-minute analysis. Although both downwelling and upwelling LW comparisons are included in the above study by Shi and Long (2002), fewer redundant overlap measurements exist for pyrgeometer IR field measurements than for SW measurements. Limited comparisons have been conducted at NOAA/GMD over a three-year period where 36 Eppley PIR pyrgeometers were run for a minimum of one week side-by-side with a triplet of three-thermistor reference pyrgeometers calibrated at the WRC to the world reference, WISG (see *A2.1.2*.) The mean difference of each the test instruments relative to the reference triad was determined and a histogram of those differences given in *Figure 5.2.5* along with the 95% ranges for individual 1-minute results over nominal deployment time given in *Table 5.2.10.1*. *Figure 5.2.5* also indicates about a 3.5 Wm^{-2} bias with the spread of 4 Wm^{-2}.

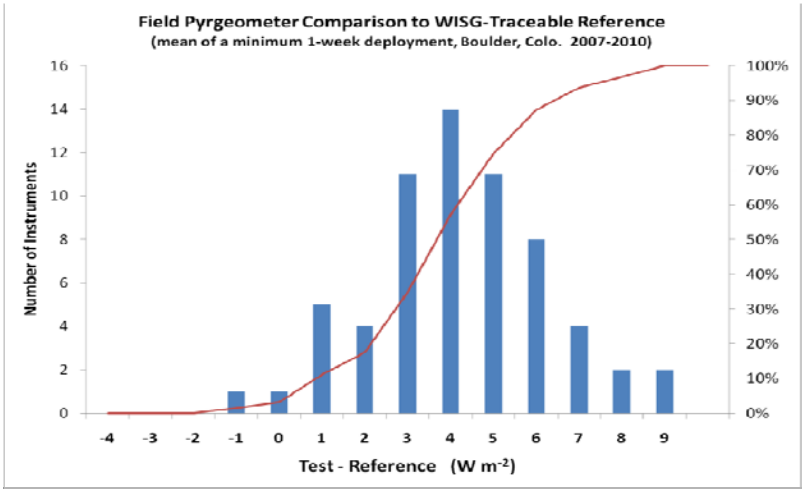

Figure 5.2.5: *Differences (Wm^{-2}) between the average of each of 63 deployments of 36 different test pyrgeometers and the mean of a simultaneously deployed fixed group of reference (WISG) pyrgeometers. Each deployment was for one to several weeks.*

The bias is partially due (about 2.2 Wm^{-2}) to an determination of the test PIRs' dome correction coefficient that is too large by about 0.5 (see *A.2.1.2.1*), and may be also partially due to an imperfectly replicated WISG reference for this comparison, or an offset in the NOAA/GMD blackbody calibration when applied to outdoor measurements.

5.2.11: Spatial Representativeness (see also Section 6.8)

Although surface irradiance observations are point measurements, they are essentially continuous in time (typically 1 Hz sampling with 1/60 (or 1/50) sec integrated samples) so that the sampled atmospheric volume is increased by advection when lengthening averaging times. The inability of satellite or model estimates to simultaneously observe or represent the identical volume has long been considered a deficiency in the surface observations because uniform grid-

or pixel-shaped spatial sampling is desirable for large scale analysis and numerical modeling. However, there is frequently a likely random relationship between the surface-sampled volume and that represented in models or satellite derived estimates. The extent of mutual agreement (difference PDFs) between the methods can be determined and the relative agreement between the two can be attributed to aspects of each method. The relationship between the surface-sampled volume and that ascribed to a model or satellite derived value is indicative of the spatial representativeness of the site, to the extent the model or satellite product properly represents the assigned area and all other uncertainties are properly considered.

An evaluation of the physical characteristics of the land surface surrounding a surface irradiance in situ measurement site is necessary to fully understand its potential spatial representativeness under clear skies, although, the spatial pattern of clouds can be the primary factor determining spatial representativeness when they exist. A close examination of the area surrounding a surface site using aerial or satellite imagery should be made in determining any positive or adverse aspects of a particular site. Failing to do this when combining a number of sites together for the purpose of comparing to either satellite or model calculations will introduce variations in the comparisons that could have been avoided and are not due to any other particular deficiency in either observing system. The extent of this representativeness issue is seen in scatter plot comparisons between in situ and satellite observations as illustrated in *Chapter 6*. To what extent a measurement at a single point can be valid is a question often encountered in all branches of the atmospheric science. The question is essential for designing observation networks, and also for interpolating between observational sites. The same question is also asked in regard to comparisons between satellite-based terrestrial information and in situ observations. Traditionally, this subject was treated by study of the spatial autocorrelation. Earlier studies using hourly global radiation showed that the correlation coefficient declined to 0.9 within 80 km over a plain, and within 20 km when the two sites are separated by mountains (Fröhlich and London, 1986). The same study and WMO (1981) indicate 120 to 200 km as the 0.9-radius for daily values. The same source indicates the decline of the autocorrelation to 0.9 over 300 km for monthly and 400 km for annual means. These values are very useful to keep in mind to assess the spatial variability of global radiation qualitatively, but offer no direct means to evaluate the difference between two quantities separated by a certain distance, or the difference between single site observations and the regional mean. The former question arises when designing observational networks. The latter problem must be faced when satellitederived surface irradiance data representing a certain area must be compared with observations made at a single site. The density of pyranometers at the earth's surface is generally not high. One of the densest pyranometer concentrations in the world is seen in Switzerland. Including pyranometers operated by non-meteorological organizations, a rough estimate of the concentration is one instrument for 400 km^2, or one instrument in a circular area with about 11 km radius, which is about twice of a pixel of geo-stationary satellites (circa 1995) for mid-latitudes.

	Kloten	**Reckenholz**	**Irchel**	**Met.Swiss**	**Birmensdorf**
Kloten	0	5	8.5	11	14
Reckenholz		0	4	6.5	10
Irchel			0	2.5	9
Met.Swiss				0	9
Birmensdorf					0

Table 5.2.11.1: *Distances (km) between the four stations with pyranometers in the vicinity of Zurich that were analyzed for their mutual representativeness of surface solar irradiance*

Within Switzerland, the region of Zurich has especially a dense observational network with 5 sites within 95 km^2 of a rectangle equivalent to 8 km (latitude) and 12 km (longitude). The inter-station distances are presented in *Table 5.2.11.1*.

The area representativeness of a single pyranometer can be measured by a deviation from the long-term mean value of the four sites (1989 to 2003). The standard error from the mean for each month of each year is calculated for each site: The mean values of the four sites are presented in *Table 5.2.11.2 below.*

	Jan	Feb	Mar	Apr	May	Jun	Jul	Aug	Sep	Oct	Nov	Dec	Annual
1989	1.08	1.30	2.82	2.38	5.06	5.31	3.88	3.05	2.09	3.52	2.47	1.42	1.65
1990	2.06	4.25	2.75	4.05	5.80	6.33	7.78	4.33	3.59	1.59	0.81	1.08	2.79
1991	1.36	4.14	1.55	5.70	5.12	5.52	7.24	5.23	2.30	2.52	1.77	1.89	2.58
1992	1.26	2.83	2.97	4.44	2.46	4.41	8.83	5.69	2.92	0.89	0.92	1.48	2.60
1993	2.53	2.59	2.70	2.28	7.39	11.65	9.21	8.86	5.81	1.86	0.93	0.50	4.00
1994	0.61	2.49	3.80	5.20	5.97	6.89	4.90	4.97	2.53	4.17	1.03	1.75	3.02
1995	1.44	2.36	4.38	3.47	6.54	4.83	7.85	9.18	4.55	7.08	1.87	0.48	3.92
1996	2.42	3.64	6.03	5.22	4.88	4.72	4.30	6.16	5.84	2.79	0.85	1.64	1.98
1997	1.91	4.08	3.87	7.55	7.35	6.05	5.71	5.58	6.82	3.52	3.00	1.57	4.47
1998	0.24	5.07	5.87	6.40	7.77	10.26	8.24	7.82	4.54	2.87	1.45	1.18	4.20
1999	1.69	5.64	6.91	9.21	9.13	7.09	11.42	7.35	4.47	1.87	1.81	0.35	2.63
2000	0.66	1.20	3.09	4.85	8.59	10.13	9.63	6.02	5.01	1.93	1.38	1.52	4.77
2001	1.71	2.20	1.91	5.07	7.19	9.42	7.64	6.35	3.97	5.25	0.99	1.42	3.94
2002	1.27	1.83	4.42	6.35	6.10	11.13	7.93	6.57	3.39	3.23	1.50	0.81	4.09
2003	1.36	2.43	4.90	4.81	8.08	11.51	11.57	8.07	5.38	2.24	1.21	0.90	4.86
Mean of STDs	1.44	3.07	3.86	5.13	6.49	7.68	7.74	6.35	4.21	3.02	1.47	1.20	3.40
Norm STDs	**0.037**	0.045	0.033	0.032	0.031	0.034	0.035	0.032	0.032	0.039	0.037	0.042	0.023

Table 5.2.11.2: *Spatial standard deviation of the monthly and annual means, that indicates the relative agreement between four surface irradiance measurements in the vicinity of Zürich.*

The average monthly standard deviations of the five sites are larger in summer, proportional to the monthly mean global radiation. The mean of the twelve months for the period of 15 years is 4.5 Wm^{-2}. Since the error of a pyranometer is proportional to global radiation, the range of uncertainty may be better expressed in percent of the mean irradiance. The normalized monthly standard deviation ranges between 3 and 4% with mean of 3.7%. The same concepts for the annual mean values are smaller than those of the monthly deviations, 3.4 Wm^{-2}, corresponding to 2.3% of the mean. Therefore, if the concerned area is about a pixel of geo-stationary satellites, the uncertainty of a monthly mean global radiation measured at a single site with respect to the regional mean is about 5 Wm^{-2}, or 4% of the mean flux. A typical deviation of the annual mean at a single site from the regional mean is 3 Wm^{-2} or 2%. This result justifies the validation of a typical satellite pixel using monthly and annual values with a single well-calibrated and maintained pyranometer.

Several additional studies have addressed the spatial representativeness of ground based total downwelling solar irradiance measurements. A thorough discussion of the results of each is beyond the scope of this work but a brief summary of one such paper follows. Hinkelman et al 2009 show significant agreement between the time series of BSRN data averaged over the network and a satellite derived global average, and further shows improved agreement for when the network size grows from 35 to 50 sites. Dutton et al., 2006 show high statistically significant spatial cross correlations between annual average time series from each of 5 globally widespread sites and gridded ISSCP (FD) data for up to several 1000 km from the surface sites and additional

teleconnected areas much further removed from the surface site. Deneke et al., 2005 show a comparison of satellite and ground based data over a relatively dense network of 45 stations spread across The Netherlands and do a detailed analysis of the contribution of a pair neighboring sites to that comparison. Barnett et al., 1998; and Long and Ackerman, 1995 look at the de-correlation distances between a group of sites in Oklahoma and Wisconsin, respectively. Long et al., (2002) used the 21 sites of the ARM SGP network and showed that for daily averages, the average distance for 0.8 - 0.9 correlation for sky cover (the primary driver of daylight downwelling SW variability) is on the order of 75 - 100 km, but with significant day-to-day spread in the correlation distance with many days representing less than 50 km. And for a final example, Li et al., 1995 show that the scatter in a comparison between GEBA (Global Energy Budget Archive, maintained by ETH, Zürich) and satellite data decreases as the number of surface sites within a satellite grid area increases.

5.2.12: Summary of Uncertainties in Ground-Based Surface Irradiance Observations

Stable and traceable calibration reference standards have been developed for the basic measurement types such that the fundamental accuracy of the standards is known to within about 0.4% for solar and 1% in the IR. Operational accuracies (95% spread) appear to be within about 20 Wm^{-2} for the solar and 6 Wm^{-2} for the infrared for near instantaneous observations reducing to about 6 Wm^{-2} and 4 Wm^{-2} respectively for annual averages. While larger instantaneous uncertainties can occur under certain adverse conditions, careful editing and adequate averaging substantially reduces the random component to levels useful (adequate) for comparison to satellite and model determined values depending, in part, of the suitability of individual site locations. Additional sources of uncertainty arise when these observations are utilized in comparison with larger spatial-mean irradiances such as the satellite derived values. This increased uncertainty results from temporal averaging for sometimes incomplete in situ data sets and from the miss match of spatial representativeness between the data types. Further discussion and quantitative error analysis detail are given in *Appendix A.2.1*.

5.2.13: Conclusions and Recommendations

- BSRN-quality long-term uncertainty estimates are tied to calibration references standards with demonstrated stability of approximately 0.01% /decade in the solar and, while the references standard for IR being more recently developed, have shown stability to better than about 1 Wm-2 per decade.
- Simultaneous redundant in situ observations provide a means to investigate the impact of varying averaging intervals. The range of agreement between simultaneous redundant observations is reduced from as much 25 Wm^{-2} to 4 Wm^{-2} when the averaging interval is extended from 1-minute to 1-year. BSRN-type surface measurements have established operational uncertainty by ± 4 to 8 Wm^{-2} for most parameters for averaging periods of a month or more.
- Differences between monthly averaging methodologies depend upon the gap-filling algorithm and the nature of the data gaps. Algorithms for computation of monthly averages show that data gaps can make differences up to about 10 Wm^{-2}. In general, the assessment team recommends that monthly means be computed from a monthly averaged diurnal cycle. Conclusions drawn from primarily from Roesch et al 2011.

5.3: In Situ Surface Flux Derived Products

The recently developed Radiative Flux Analysis is a methodology designed to analyze the time series of surface broadband shortwave (SW) and longwave (LW) irradiance to identify periods of clear (i.e. cloudless) skies. Functions are fit to the detected clear-sky data, then fit coefficients are interpolated for cloudy periods and continuous clear-sky SW and LW estimates are calculated. The measured and clear-sky values are then used to infer the cloud effects on the surface radiation, and various cloud macro-physical properties. Details of the methodology used to derive specific variables have been published in a series of papers, including Long and Ackerman (2000) for detection of daylight clear-sky periods and estimation of clear-sky downwelling SW, Long et al. (2006) for estimation of daylight fractional sky cover, Long and Turner (2008) for detection of "LW effective" clear-sky periods and estimation of clear-sky downwelling LW, and an adaptation of the Dürr and Philipona (2004) technique for continuous LW effective fractional sky cover. Daylight cloud visible optical depth for overcast (sky cover > 0.9) uses the technique first described in Barnard and Long (2004), and later improved as described in Barnard et al. (2008). The methodology for the remaining variables, as listed in *Table 5.2.1* below, have not yet undergone peer reviewed publication but are described in Long (2004, 2005), and in Appendix A.2.1.4 of this document.

5.3.1: Available Derived Products

Table 5.3.1 lists the primary variables included in the output files from the Radiative Flux Analysis processing. The output includes monthly average diurnal cycles and monthly averages, calculated as the average of 15-minute resolution monthly average diurnal cycles of all available data that passed quality assessment screening. In this way no artificially manufactured values were used to "fill in" for missing or bad data, while at the same time mitigating the influence of what part of the diurnal cycle the data were missing, especially for the solar variables. The output also includes 15-minute average data for the agreed upon years of 2004 and 2005 for more detailed comparison studies, output as daily files. More information pertaining to the variables included in the Radiative Flux Analysis output files and the processing methodology notes are included in Appendix A.2.1.4 of this document.

The sites processed include the three tropical western Pacific sites of the ARM Program, as well as the ARM Southern Great Plains site. Also included are the six longest-running continental US sites of the SURFRAD network. The remaining sites are part of the BSRN. The output data includes all data available at the time of processing, with the stipulation that at least 5 years of data were available. More information about these sites, their locations and surface/climatology characteristics are available at the following Web sites:

http://www.arm.gov/
http://www.srrb.noaa.gov/
http://www.pangaea.de/ddi?request=http://store.pangaea.de/Projects/BSRN/BSRNEvent&format=html&title=BSRN+Stations

5.3.2: Quality and Uncertainty of Derived Products

Prior to processing to infer clear-sky and cloud macro-physical properties, all measured data were first assessed for quality using the QCRad methodology described in Long and Shi

(2008). The QCRad methodology is an automated process that tests all SW and LW data for occurrences that lie outside climatologically-derived expected ranges for each particular site. *Table 5.2.1* lists estimates of the uncertainty of both the measured and inferred variables included in the output files, inferred from published reports where available. As described in *Appendix A.2.1.4* of this document, some of the included variables are still experimental to date, have not been vetted through the peer review process, and have been included as "highly preliminary" results to be used at risk in assessment activities. These "experimental" variables are noted in *Table 5.2.1* as variables with "unknown" uncertainty assessment, and specifically described and noted in *Appendix A.2.1.4* of this document.

Table 5.3.1: *Primary variables and estimated uncertainties in the Radiative Flux Analysis output*

Variable	Est. 95% Uncertainty	Information Source
Downwelling Total SW	6% or 10 Wm^{-2}	Stoffel, 2005, ARM-TR
Downwelling Diffuse SW	3% or 4 Wm^{-2}	Stoffel, 2005, ARM-TR
Downwelling Direct SW	6%or 20 Wm^{-2}	Stoffel, 2005, ARM-TR
Clear-skyTotal, Diffuse, Direct SW	RMSE(2X Meas. Uncert.)	Long and Ackerman, 2000
Upwelling SW	6% or 10 Wm^{-2}	Stoffel, 2005, ARM-TR
Clear-sky Upwelling SW	RMSE(2X Meas. Uncert.)	Long, 2005
Downwelling LW	2.5% or 4 Wm^{-2}	Stoffel, 2005, ARM-TR
Clear-sky Downwelling LW	4-5 Wm^{-2}	Long and Turner, 2008
Upwelling LW	2.5% or 4 Wm^{-2}	Stoffel, 2005, ARM-TR
Clear-sky Upwelling LW	Unknown	
Daylight Fractional Sky Cover	10%	Long et al., 2006
LW Effective Sky Cover	1-2 Oktas	Durr and Philipona, 2004
Cloud Visible Optical Depth	10%	Barnard & Long, 2004; Barnard et al., 2008
Effective Cloud Transmissivity	10%	Estimated from above Total and Clear-sky SW
Cloud Radiating Temperature	Unknown	
Cloud Radiating Height	Unknown	

In any determination of whether there are clouds present, some inherent definition of what is and is not a cloud is used. Always some amount of condensed water, either liquid or ice, is allowed under the "clear-sky" classification, otherwise the "cloud cover" would be "overcast" for every square meter of Earth because inevitably there is at least one tiny ice particle and/or liquefied aerosol somewhere in the column. As determined in DuPont et al. (2008), for the SW-based daylight total sky cover the Long and Ackerman (2000) method of clear-sky detection generally allows up to a visible optical depth of about 0.15 to be classified as "clear-sky," usually as sub-visual cirrus. This "definition" of clear-sky effectively matches that of sky imager retrievals and human sky observations, as shown in Long et al. (2006).

Because the surface broadband downwelling LW is virtually insensitive to high, cold cloud emissions through the intervening atmosphere, "LW effective" clear-sky can contain cirrus of even larger optical depths (DuPont et al., 2008). Similarly, the "LW effective" sky cover retrievals represent primarily low and mid-level cloud amounts, and rarely include high clouds.

The Radiative Flux Analysis derived products provide a powerful constraint for comparison of measurements to satellite-derived estimates, especially clear/cloudy sky scene identification. Where most traditional satellite-surface radiation flux comparisons and evaluations are limited to aggregate all-sky conditions the detection of clear-sky periods, and production of continuous clear-sky estimations and cloud amounts, for the surface site allows a far more comprehensive analysis of, for instance, the relative contributions to errors between atmospheric state (clear-sky), cloud amounts, and treatment of cloud micro-physical properties by the satellite retrieval algorithms.

The systematic and comprehensive suite of surface Radiative Flux Analysis variables allows for more comprehensive satellite-surface comparison analyses. For instance, a current study (Zhang et al, 2010) goes beyond the usual to develop a new way to make more precise, meaningful and simultaneous evaluations of both the ISCCP and Radiative Flux Analysis products included in this assessment effort. Based on the functional relationship between fluxes and their associated meteorological parameters the new approach, which has been named the Meteorological Similarity Comparison Method (MSCM), essentially matches measurements with the atmospheric and surface physical properties as close to each other as possible.

It seems conclusive that MSCM does improve such evaluations as well as reveal more information that can be used to improve both the products. The specific or optimum matching criterion varies for different statistics and for different fluxes, reflecting that multiple factors affect the flux discrepancies. These are also important sampling issues, rooted in the fundamental nature of the differences between the two products.

In short, by using MSCM to exploit the functional relationship between radiative fluxes and their associated meteorological parameters, the study extends the previous evaluation of ISCCP derived products and obtains more accurate and meaningful uncertainty estimates on both data products. Therefore, the newly emerging Radiative Flux Analysis product is useful for more accurate, simultaneous evaluations on both radiation modeling and surface observation.

5.4: Long-Term Surface In Situ Time Series Analysis

5.4.1: Available Data and Quality

Monitoring of surface radiative fluxes started in the early 20th century at selected sites, predominantly measuring the downwelling solar component (also known as "global radiation" or surface solar radiation). For example, continuous measurements of surface solar radiation began in 1923 at the Stockholm observatory (*Figure 5.2.5*). More widespread measurements of this quantity with thermopile pyranometers were initiated in the International Geophysical Year (IGY, 1957/1958). Many of these historic measurements have been compiled in the GEBA (Ohmura et al., 1989, Gilgen et al., 1998), and in the World Radiation Data Centre (WRDC) of the Main Geophysical Observatory in St. Petersburg, Russia, maintained by Dr. A. Tsvetkov. The data in GEBA underwent different quality checks to assure homogeneity in the data (Gilgen et al. 1998). Homogeneous climatological records assert that any changes and variations in the data are induced by natural phenomena and are not an artifact.

The accuracy of these historic measurements has been estimated in Gilgen et al. (1998) at 2% on an annual basis. However, the quality of the measurements, performed predominantly under the auspices of the national weather services, is highly variable and not always well established. Consequently, in the late 1980s the necessity for a reference network of surface radiation measurements with improved and defined accuracy was recognized. As a result, the BSRN was established (Ohmura et al. 1998). The first BSRN sites, equipped with instruments of the highest possible accuracy, became operational in the early 1990s. To date more than 50 anchor sites in different climate regimes provide data at high temporal resolution (minute data) for both solar (total, diffuse/direct, and reflected) and thermal (downward and upward) components. The BSRN accuracy targets are for total solar radiation (global radiation) 2% or 5 Wm^{-2} (ventilated pyranometer), for direct solar radiation 1% or 2 Wm^{-2} (normal incidence pyrheliometer), for diffuse radiation: 4 % or 5 Wm^{-2} (ventilated shaded pyranometer), for reflected SW radiation: 5% (ventilated pyranometer) and for downward and upward thermal

radiation ± 2 Wm^{-2} (pyrgeometer). Other radiation networks with comparable quality standards were established around the world in recent years: The ARM Program with a few worldwide distributed sites (Stokes and Schwarz, 1994; Ackerman and Stokes, 2003), the SURFAD network, the NOAA Earth System Research Laboratory (ESRL) Network with five worldwide distributed remote sites (Dutton et al., 2006), the Australian Network maintained by the Bureau of Meteorology, and the Alpine Surface Radiation Budget network (ASRB) with seven sites in the Swiss Alps (Philipona et al., 2004). The achieved operational accuracies of these projects are discussed elsewhere in this chapter and Appendix 2.2

5.4.2: Results of Time Series Analyses

The earliest studies analyzing extended observational records of surface solar radiation appeared in the early 1990s (e.g, Wild 2009a for a more complete overview). These pioneering studies presented the first evidence that solar radiation at the Earth's surface has not been constant over time as previously assumed, but show significant decadal variations. Specifically, they pointed to declines in surface solar radiation since the 1950s in different regions of the globe. The first analyses with comprehensive datasets of sites distributed worldwide, as available from GEBA/WRDC, were performed by Gilgen et al. 1998, Stanhill and Cohen 2001, and Liepert, 2002. These studies reported an overall decrease of solar radiation at widespread locations over land surfaces on the order of 6–9 Wm^{-2} between 1960 and 1990, corresponding to 4%-6% over 30 years. This term "global dimming" to describe this decrease was coined by Stanhill and Cohen (2001). Increasing air pollution and associated increases in aerosol concentration have been suggested as major cause of this phenomenon, although changes in cloud amount and optical properties may also contribute (see Wild 2009a for an overview). A direct assessment of the origins of solar dimming is complicated by the lack of adequate long-term observational datasets on variations of cloud and aerosol properties.

The studies on "global dimming" were all limited to data prior to 1990, since GEBA contained no data after 1990 at the time these studies were completed. More recently, ETH Zürich undertook a major effort to update the worldwide measured surface radiation data in GEBA for the period from 1990 to present (Ohmura 2006). Wild et al. (2005) evaluated the newly available surface observational records from GEBA and BSRN to investigate the trends in solar radiation in the more recent years. This analysis showed that the decline in solar radiation at land surfaces seen in earlier data is no longer visible in the 1990s at many locations. Instead, a brightening is observed since the late 1980s at the majority of the available observation sites.

This has been substantiated by numerous analyses focusing on globally distributed sites (Wild 2009a and references therein). A major exception is India, where the records show a continuation of the dimming up to present (Padma Kumari et al. 2007). The brightening during the 1990s is not just found under all sky conditions, but also seen under clear skies at various sites, pointing to aerosol as a major cause of this trend reversal (Wild et al. 2005, Norris and Wild 2007, 2009). The trend reversal is reconcilable with trends in aerosol emission, aerosol optical depth, and atmospheric transmission, which also show a distinct trend reversal during the 1980s (Russak 2009, Ohmura 2009, Ohvril et al. 2009) (*Figures 5.2.6 and 7*). The trend reversal in aerosol emission towards a reduction and the associated increasing atmospheric transmission since the mid 1980s may be related to air pollution regulations and the breakdown of the economy in the former communist countries. Changes in cloud properties also play a role in some regions and seem to be responsible for example for the dimming and brightening in New Zealand (Liley, 2009) and the recent brightening in the US (Long et al., 2009).

The longest observational SSR records, extending back to the 1920s and 1930s at a few sites in Europe, further indicate some brightening during the first half of the 20th century, known as "early brightening" (Ohmura 2006, 2009). This suggests that dimming, at least in Europe, was restricted to a period between the 1950s and 1980s.

The current generation of climate models used in the IPCC 4th assessment report is not capable of reproducing these decadal variations in surface solar radiation adequately. They substantially underestimate the decadal variation in surface solar radiation and related impacts on global warming (Wild and Schmucki, 2011). As potential explanations for this inability, the large uncertainties in the historic emission inventories and associated aerosol burdens in the atmosphere which may not contain the full extent of decadal variations, the inadequate representation of the direct and indirect aerosol forcings as well as a general underestimation of the unforced natural variability in the models have been put forward (Ruckstuhl and Norris, 2009, Wild and Schmucki, 2011).

The latest updates on solar radiation changes observed at the surface beyond the year 2000 suggest a continuation of the brightening at sites in Europe, in the US, and in parts of Asia (Korea) (Wild et al. 2009). Brightening seems to level off at sites in Japan and Antarctica after 2000, while indications for a renewed dimming are seen in China, likely associated with large emission increase in China after 2000. The compensating tendencies in various regions of the globe may tentatively indicate that the overall surface solar radiation signal inferred from the ground-based observations did not undergo dramatic changes since the year 2000 (Wild et al. 2009). This fits to the general picture provided by satellite observations, which suggest that the global mean planetary albedo as well as the background aerosol burden of the atmosphere may not have undergone substantial changes between 2000 and 2005, at least globally (Loeb et al., 2007).

Climate relevant surface radiative forcing is not only determined by surface solar variations, but also strongly governed by the reduced thermal surface cooling with enhanced greenhouse capacity of the atmosphere, manifest in increased downward thermal radiation from the atmosphere to the surface. Compared to the solar component, much less information from direct observations is available on the temporal evolution of the downward thermal component. Operational monitoring of this quantity started in the 1990s in the abovementioned networks of BSRN, ARM, SURFRAD, and ASRB. First analyses of the still very short time series of downward thermal radiation indicate an overall average increase in this quantity of 2-3 Wm^{-2}/decade since the early 1990s at the globally distributed measurement sites of BSRN (Wild and Ohmura 2004). Measurements taken in the Swiss Alps by Philipona et al. (2004) show an even larger increase of downward thermal radiation since 1995 in this particular region. An increase in the downward thermal radiation is in line with the expectations from greenhouse theory and climate model scenarios (Wild et al. 1997) and gives direct evidence for the real existence of an increasing greenhouse effect (Philipona et al. 2004).

5.4.3: Methodological Issues

There remain a number of methodological issues related to the time-series analyses based on surface observations of radiative quantities.

1) Data quality. In general, the accuracy of historic radiation measurements is not well established and often unknown as noted above. Quality assessment procedures were applied in some of the analyses, as described, for example, in Gilgen et al. (1998), Dutton et al. (2006), and Shi et al. (2008). In addition, the recent reversal of the downward tendencies in surface solar radiation at many sites adds credibility to the measured variations because most radiometers

typically lose sensitivity with time, and, unless properly recalibrated, can indicate spurious downward, but not upward, trends. The more recently established radiation networks (e.g., BSRN, ARM, SURFRAD, ESRL, and ASRB) provide high quality radiation data with known accuracy beginning in the early 1990s. Further uncertainties can be introduced by differing methods of aggregating high temporal resolution (minute, hourly) data to daily, monthly or yearly means, particularly if significant data gaps exist in the records (Roesch et al. 2011).

2) Data analysis. The establishment of significant changes at individual sites by a rigorous trend analysis is often not possible given the combination of the amount of data, scatter in the data, and autocorrelation in the data, as well as lack of statistical independence of the fit residuals. Yet, the preponderance of similar results based on a large number of records analyzed in various independent studies with different methods gives support to the existence of non-spurious decadal changes in surface solar radiation. Note also that linear regressions as used for simplicity in most analyses may not always be an appropriate statistical model to describe the temporal changes in the data. Higher order statistical models may provide a more adequate description of the temporal evolution of the observed surface fluxes. This is, for example, the case for surface solar radiation records that include both dimming and brightening phases (e.g., Gilgen et al., 1998, 2009; Dutton et al., 2006; Hinkelman et al., 2009, Makowski et al., 2009). To make optimal usage of all available station records with typically largely varying length Gilgen et al., (1998, 2009) propose to sample the station records onto a global grid. They then fit regression models allowing for station effects to the records located in the individual cells, under the assumption that the temporal trend estimated is representative for the entire grid cell. This method avoids the introduction of spurious trends induced by simple averaging over station records of differing length.

3) Data coverage and representativeness. There are large gaps in direct observations of surface solar radiation over vast areas of Africa, South America, and the Maritime Continent. And, of course, ocean surfaces are almost entirely unrepresented in the surface observations, except for a few sites on small islands. The situation is even worse for thermal radiation measurements, which are only performed operationally at a few locations worldwide (such as in the BSRN network). For the more recent decades, satellite-derived estimates may be able to close these gaps (Hinkelman et al. 2009). Further, reconstructions of surface radiation from more widely performed meteorological measurement quantities may be used to extend records spatially and temporally (e.g. surface solar radiation inferred from sunshine duration or diurnal temperature range measurements (Makowski et al. 2009) thermal radiation from temperature and humidity measurements. In any attempt to scale up information from point observation, the representativeness of the individual sites for their larger-scale settings becomes critical. Dutton et al. (2006) provided a framework to estimates a site's spatial representativeness using spatial cross correlation with satellite-derived global estimates of surface solar radiation. Li et al. (2005) performed a detailed analysis of the sampling error when using point measurement of surface solar radiation to represent larger scale grid boxes up to several hundred km width and found that sampling uncertainties decrease rapidly as the time-averaging interval increases up to 24 hours and then level off to a relatively small and stable value. They conclude that, for computing grid mean surface solar irradiance over more than 5 days, there is no need for an overly dense network of observation stations. Simulations of the BSRN network using satellite-derived fluxes by Hinkelman et al. (2009) suggest that the network is becoming more representative of the globe as it expands, but that the Southern Hemisphere and oceans remain seriously underrepresented in the surface networks. In addition, possible "urbanization effects" in the surface solar radiation data (Alpert et al., 2005) may have to be taken into account and need quantification.

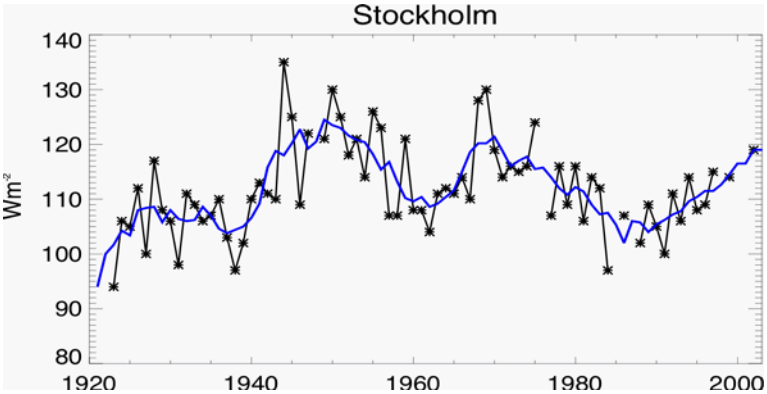

Figure 5.4.1*: Annual mean surface solar radiation (in Wm^{-2}) as observed at Stockholm, the longest observational record available from GEBA (beginning 1923). Five year moving average in blue. (From Wild 2009a).*

5.5: Outstanding Issues and Concerns

An assessment of the state and quality of in situ broadband surface irradiance observations would not be complete without a brief overview of the remaining and ongoing issues that face maintaining the observational capability as assessed above. Maintaining and extending this capability will be crucial to the observational determination of future surface radiation budget changes with expansion of the current efforts required to have measurements more representative of the extensive spatial and temporal variability both expected and potential.

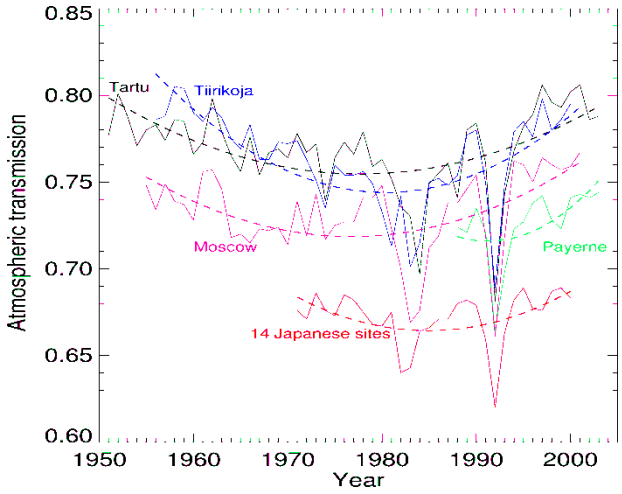

Figure 5.4.2: *Time series of annual mean atmospheric transmission under cloud free conditions determined from pyrheliometer measurements at various sites in Russia (Moscow), Estonia (Tartu-Toravere and Tiirikoja), Switzerland (Payerne), and Japan (average of 14 sites). (From Wild et al. 2005)*

5.5.1: Calibration Reference Standards

First and foremost, the calibration reference standards must be maintained to assure the future, past and present observations can be reliably intercompared and interpreted as to real

variations as separated from fundamental observational uncertainty. This work has traditionally fell on the individuals involved with making the measurements but with a slow emergence of internationally centralized World Reference Standards maintained at the WMO recognized World Radiation Center (WRC) in Davos Switzerland.

5.5.2: Spatial Gaps in Surface Measurements

Currently, the highest quality routine long-term surface observations have large gaps in certain geographically remote regions. The world's oceans are the best example but also areas of minimal population and or resources in general typically exemplify the issue. Some of these gaps could be readily addressed with current capabilities and adequate support provided to willing and capable institutions. Other more difficult or remote gap regions could be addressed by the development and deployment of autonomous automated observational installations but which could be rather costly and present security and servicing issues in many cases. The likely indefinite persistence of substantial gaps in the ground based in situ surface radiation observations reinforces the mutual cooperative reliance on satellite and ground measurements to acquire the most accurate, complete and timely observational data set possible.

5.5.3: Quality of Widely Deployed Instrumentation

Growing and expanding interests in surface radiation data for applications beyond critical climate and climate change applications have led to the relatively large scale proliferation of secondary and tertiary quality instrumentation and methods for observing surface radiation, particularly incoming solar. Continued vigilance for assuring the level of quality of radiation observations utilized in climate research is and will be required.

5.5.4: Environmental Interference, Especially in Cold Regions

Modern surface radiation observational methodologies have not completely solved issues of certain environmental conditions on the optical sensors required. Such things as condensation and contaminant collection on continuously operating radiometer inlet optics can be of particular issue where the data are either rendered useless or with uncertainties, if not captured, identified, and removed, of far greater uncertainty that assessed here. Current practices of reducing these events include the ventilation and judicious heating of the inlet optics. The extent of the success of the active methods varies but becomes most severe in regions experiencing cold temperature extremes in association with frozen condensate collecting on the surfaces beyond which the judicial artificially applied heat, if available, can compensate for. Therefore, not only are the polar regions of the earth generally underrepresented observationally but also those observations that do exist must be addressed with additional consideration for the potential of excessive icing almost year round. Work that is being pursued by various groups to optimally reduce these problems (for example the BSRN Cold Climate Issues Working Group) needs to continue.

5.5.5: Spatial and Temporal Resolution

Considering that a significant application of the in situ observed surface radiation data is used for comparison with both satellite and atmospheric model generated radiation values, ongoing deficiencies or incompatibilities in those comparisons needs to be further addressed. The primary issue resulting from the typically sparse high-time-resolution point in situ measurements

being compared with lower temporal and spatial resolution model derived values. Such comparisons comprise the basis for much of the assessment of satellite and model data presented elsewhere in this report.

While there is no specific limitation on the density of point sensors that could be deployed, again practical limitations prevent extremely dense deployments over other than relatively small areas and or time periods. As a result, much of the scatter seen in these comparisons is due to spatial and to some extent temporal miss-match. Improvements, less scatter in the comparisons, could be accomplished by the more extensive deployment of high density surface radiometers and or addressing the satellite observational and modeling limitations on higher spatial resolution in their products. As well, as discussed in *section 5.3*, expansion of the use of analysis techniques such as the Radiative Flux Analysis and subsequent application using the Meteorological Similarity Comparison Method (Zhang et al, 2010) can also greatly refine our abilities to meaningfully compare surface observations with satellite and model products.

5.5.6: Ancillary Data

In situ surface irradiance measurements are largely to completely independent of any additional information at the time of the observation (exceptions being knowledge of conditions that could lead to erroneous measurements, such as the presence of obstructions. However, modeled or satellite derived surface radiation values derived from the principles of radiative transfer are dependent not only on how those principles are computationally implemented but also on separate and independent observations of atmospheric composition, surface properties as well as constraining radiative quantities observed or assumed at the top of the atmosphere. So, it has proven beneficial in the utilization of in situ observations surface irradiance observations to have additional in situ observations of certain parameters including: vertical profiles of air temperature and humidity, surface pressure, column aerosol optical depth, cloud height and cover, surface type and condition, and spectral surface albedo. Currently only few of the surface sites provide all this information, so it would be highly desirable for measurement capabilities at the surface sites to be expanded.

Chapter 6:

Comparisons of Satellite-Estimated Radiative Fluxes Reaching the Surface to Ground Observations

Laura Hinkelman, Taiping Zhang, and Paul Stackhouse

Abstract: This chapter compares the broadband downward fluxes from the satellite data sets to local measurements at the ground. Such comparisons require consideration of both the spatial scale differences between the two types of data and the inherent uncertainties of the ground measurements. Use of monthly means in the comparisons reduces spatial scale related variability but not local biases that may be introduced at sites near coasts or mountains. Thus despite these limitations, general aspects of the satellite data can be investigated.

6.1: Introduction

Unlike TOA satellite measurements, satellite-based estimates of broadband solar (SW) and longwave (LW) radiative fluxes at the surface can be compared to in-situ measurements. These surface measurements can be quite accurate (see *Chapter 5* and *Appendix 2*). However, the local nature of surface site data can introduce discrepancies relative to averages over large areas. Thus, for the coarse-gridded (2.5°x2.5°) radiative flux data sets used in this Assessment, the evaluation potential of site data is somewhat limited. Issues related to differences in the temporal and spatial scales of these two types of data are addressed later in this chapter and in *Section 5.2.11*.

Seven broadband surface flux data sets based on satellite measurements were submitted to the GEWEX-RFA archive. This chapter focuses on comparisons of the satellite-derived downward fluxes at the Earth's surface to ground-based measurements from four different broadband radiometer networks:

- the Baseline Surface Radiation Network (BSRN)
- the Global Energy Balance Archive (GEBA)
- the University of Oregon (UOR) Solar Radiation Monitoring Laboratory, and
- the Alpine Surface Radiation Budget (ASRB) network.

Clear-sky fluxes estimated from the BSRN measurements using the Radiative Flux Analysis method are also used in the comparisons.

The BSRN began operation with a few sites in 1992 (see *Chapter 5*). Additional sites have been added progressively since then. Currently, there are about 40 globally distributed sites in operation. GEBA and UOR data is available over the entire ISCCP time period (July 1983-present), while the ASRB data in the RFA archive covers only the year 2004. Six of the seven satellite-based surface flux data sets cover the entire ISCCP period. Thus, direct comparisons of local monthly averages are possible for this full time period. In contrast, CERES data has only been produced since 2000, so that it may only be evaluated over the March 2000 to February 2004 period. In addition to site-by-site comparisons, time series are explored, and comparisons to BSRN and GUOR site ensemble averages are made.

6.2: Ground-Based Reference Data

6.2.1: The BSRN data.

The Baseline Surface Radiation Network (BSRN) data that were provided for the GEWEX-RFA archive consist of 15-minute and monthly mean values covering the time period from January 1992 to March 2006. (The time period covered and the number of data samples differs from site to site.) The BSRN data in the archive are from the 35 sites indicated in *Figure 6.1.* Additional information about the sites is listed in *Table A.2.2.2* of the Appendix. A.2.

The BSRN

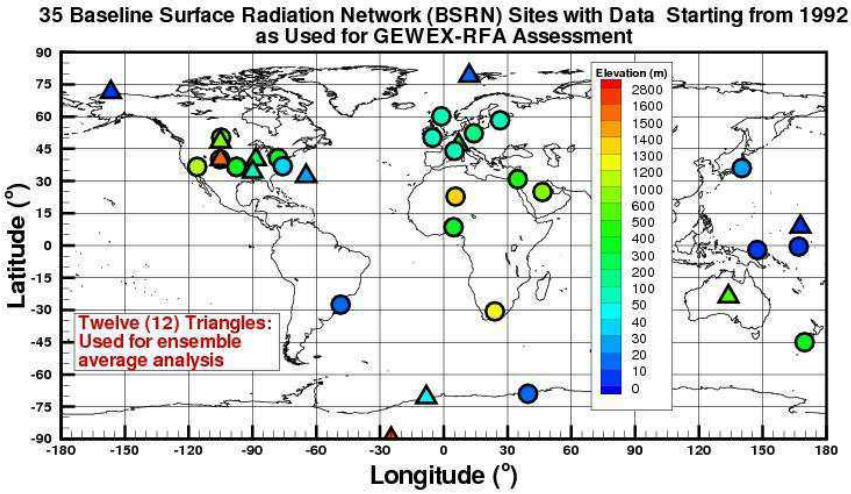

since the

Figure 6.1*: The 35 BSRN sites included in the GEWEX RFA archive. The triangles denote sites incorporated in a subsequent ensemble analysis.*

BSRN has advised that this form of the total downward solar irradiance is more accurate. (See *Chapter 5.1.6.*) Downwelling longwave flux (ALWDN) measurements from the BSRN are also used in these comparisons. Only the monthly data are analyzed.

The BSRN accuracy goals for 1-minute data are 1% or 2 Wm^{-2} for direct SW irradiance, 4% or 5 Wm^{-2} for diffuse SW irradiance, and 2 Wm^{-2} for downwelling LW irradiance (*Chapter 5.4.1.*) However, side-by-side comparisons of identical instruments on monthly time scales yielded 95% inclusion intervals of ±5 Wm^{-2} for the direct and diffuse SW downward fluxes, ±7 Wm^{-2} for the combined (direct + diffuse) SW downward flux, and ±4 Wm^{-2} for the downward LW flux (*Table 5.2.10.1*). Additional uncertainty of up to 10 Wm^{-2} (but typically 1-2 Wm^{-2}) arises from the choice of the averaging method applied when determining monthly means from the higher temporal resolution samples (*Chapter 5.2.8*). Thus, the overall uncertainty of the BSRN data used here is estimated at ±9 Wm^{-2} for monthly mean SW downward fluxes and ±6 Wm^{-2} for the corresponding downward LW fluxes. Note that the uncertainty due to the method of averaging the data (which may have missing values) applies to all of the ground-based data used in this chapter. It should also be noted that achieving the accuracy levels estimated for each data set is dependent on the level of instrument maintenance and monitoring provided by the local site operators.

Expected clear-sky fluxes have been estimated from the BSRN measurements and are available in the Radiative Flux Analysis data set. The uncertainty of these values is not well defined, but must exceed that of the flux measurements upon which they are based. Nevertheless, the Flux Analysis data enables us to compare clear-sky fluxes from the satellite

products against surface data on a monthly-mean basis, which would not otherwise be possible, providing further insight into the specific causes of any discrepancies between the all-sky measurements and satellite data. Specific information about the Radiative Flux Analysis methods and resulting data is given in Section A.2.2.4.

6.2.2: The GUOR data.

For the purposes of this assessment, the Global Energy Budget Archive (GEBA) and University of Oregon (UOR) data sets are combined and referred to as the GUOR set. Data from 30 GEBA sites (*Table A.2.2.1* in the Appendix) and three UOR sites (*Table A.2.2.8 in the Appendix*) was used in the comparisons. The locations of the 33 total GUOR sites are shown *Figure 6.2*. The UOR and GEBA data provided for the GEWEX-RFA are monthly mean shortwave total downward fluxes from individual pyranometers, i.e., ASWDHEM fluxes.

The GEBA archive includes measurements dating back as far as 1919. However, as for

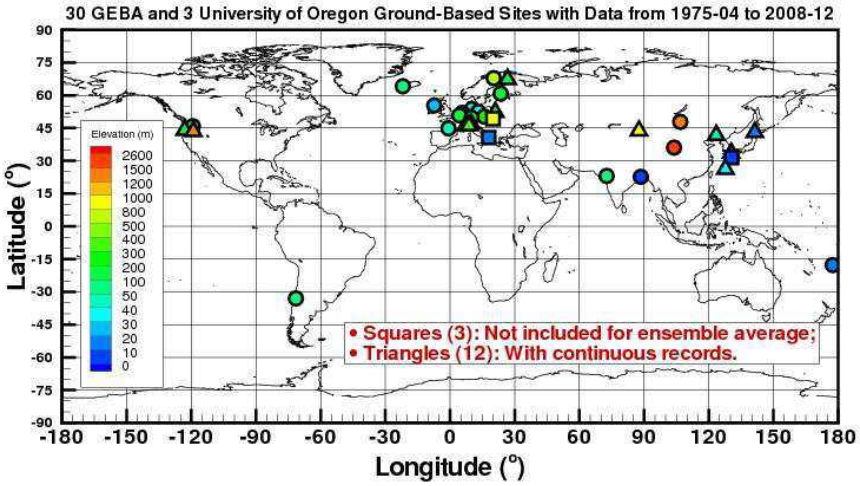

Figure 6.2*: The 33 GUOR (GEBA and University of Oregon) sites. All of the sites except for those shown as squares are used in the 30-site ensemble while only those marked with triangles are included in the 12-site ensemble.*

the BSRN data, the time coverage of individual sites is usually smaller and varies by site. The GEBA data contributed to the RFA archive was selected from those sites with the longest and most continuous records. Further details about the GEBA data set are given in *Appendix A.2.2.1*.

Data from the University of Oregon (UOR) Solar Radiation Monitoring Laboratory has been used for very few climate studies (e.g., Riihimaki et al., 2009) because it is collected primarily to serve the solar energy community. However, its high quality and long period of record (from the mid-1970s to the present) makes it a valuable asset. In particular, it compliments the GEBA data set, which contains no North American measurement series covering the entire length of the ISCCP period. Further information about the UOR data is provided in *Appendix A.2.2.6.*

The quality of the GEBA flux data is difficult to estimate because the measurements are made by individual investigators or national weather service agencies who may not apply rigorous quality control. There is also no standardization of instruments or calibration regimens. Nevertheless, the data is checked by the archive operators and the overall uncertainty for the monthly averages has been estimated at 5% (*Gilgen and Ohmura, 1999*). The maintenance and data quality check routines of the Solar Radiation Monitoring Laboratory of the University of Oregon are documented at http://solardat.uoregon.edu/PacNWSolarRadiationDataBook.html. Overall

uncertainty of UOR monthly mean hemispheric SW irradiances is estimated at ±6 Wm^{-2} (personal communication, F. Vignola.)

6.2.3: The ASRB data.

The six Alpine Surface Radiation Budget (ASRB) stations are all located in Switzerland, as shown in *Figure 6.3* and listed in *Table A.2.2.7* of Appendix A. ASRB data was provided to the Assessment only for the year 2004. It includes monthly mean shortwave total hemispheric downward fluxes (ASWDHEM) from pyranometer measurements and longwave downward fluxes (ALWDN). Missing values are rare, with well above 90% of the possible samples passing quality control checks at each station. More information about the ASRB sites is given in Appendix *A.2.2.5*.

The ASRB network uses standardized instrument clusters and quality assessment routines and is monitored by MeteoSwiss personnel. The uncertainty of daily averages for both SW and LW flux data is estimated at ±3 Wm^{-2} (personal communication, R. Philipona.)

6.3: The Satellite-Based Data Sets

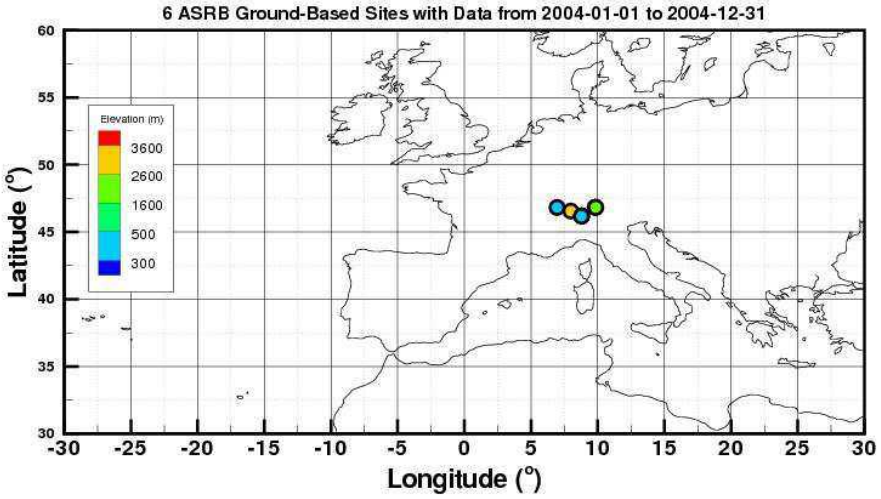

Figure 6.3: *The six ASRB sites. Note that, due to the close proximity of the sites, only four points are visible in the figure.*

The satellite-based downward flux data sets analyzed here are listed in *Table 6.1*. All of the data sets either have a native 2.5°x2.5° grid or have been converted to this grid system. Most of the data sets include both SW and LW surface fluxes except for the DLR-ISIS and UMD-SRB products, which include SW values only. We note that the monthly SW values are set to "missing" in the FORTH data set for areas experiencing polar night during that period. The impact of these missing values on the comparisons is discussed as appropriate in the following text. However, these missing values mainly affect comparisons to the BSRN data because this network includes several polar stations. The CERES-SRBAVG data set also has missing values, but only near the terminator when the solar zenith angle is between 87.5° and 90°. This affects many fewer grid cells than the FORTH polar night treatment.

Table 6.1*: Temporal availability of satellite- and ground-based data sets.* For the surface measurements, ASWDN = sum of all-sky direct and diffuse downwelling SW flux measurements; ASWDHEM = all-sky single-instrument measurement of total SW hemispheric downwelling flux; ALWDN = measured all-sky longwave downwelling flux.*

Data Set	Time Span	SW	LW
Satellite Data Sets			
CERES_SRBAVG_Terra_GEO_MOD_Ed02d	2000-03 / 2005-10	ASWDN	ALWDN
DLR-ISIS_Ed001	1984-01 / 2004-12	ASWDN	-
FORTH_Ed01a	1984-01 / 2004-12	ASWDN	ALWDN
GEWEX-SRBGSW_Ed281, GLW_Ed025	1983-07 / 2005-06	ASWDN	ALWDN
GEWEX-SRBQSW_Ed025, QLW_Ed025	1983-07 / 2005-06	ASWDN	ALWDN
ISCCP-FD_Ed000	1983-07 / 2004-12	ASWDN	ALWDN
UMD-SRB_Ed033	1983-07 / 2004-12	ASWDN	-
COMMON Satellite Time Span	**2000-03 / 2004-12**		
Ground-Based Data Sets			
BSRN	1992-01 / 2006-04	ASWDN ASWDHEM	ALWDN
GEBA+UOR	1979-04 / 2008-12	ASWDHEM	-
ASRB	2004-01 / 2004-12	ASWDHEM	ALWDN

***** Note: Some of the CERES and FORTH grid boxes are missing SW flux values

6.4: Evaluation Methods

Each satellite monthly mean flux value represents a spatial average over a 2.5°x2.5° grid box. These values are evaluated in this chapter by comparing them to monthly means of in situ measurements from a site within the grid box. For each site-grid box pair, the bias is computed as the mean difference between the satellite values and their ground-based counterparts (satellite minus in-situ values) over all available months with matches. The standard deviation and root-mean-square (RMS) difference between the satellite and surface values are also computed, as is the correlation between the two sets of fluxes. The common time span of all satellite-based data sets is from March 2000 to December 2004 ("CERES time period"), although many of the data sets extend from July 1983 through December 2004 ("ISCCP time period.") Thus the comparisons are made over either or both of these time periods, depending on the computation. Evaluation is also performed over multi-site ensembles. The BSRN ensemble includes 12 sites (marked with triangles in Figure 1). These are BSRN sites with nearly continuous records for the 1997 to 2004 time period. The first GUOR ensemble includes 30 GUOR sites with few temporal gaps. The second GUOR ensemble includes the 12 sites with complete data records over the full ISCCP time period. The 12-site ensemble is also used for investigations and comparisons of long-term solar flux trends. Use of this more limited set of sites was necessary, as prior studies (e.g., Hinkelman et al., 2009) indicate difficulties in interpreting trends computed from data with random temporal or spatial gaps. Each ensemble time series is constructed by first deseasonalizing the data for each individual site by subtracting the mean annual cycle computed over the entire time period of interest and then averaging these individual records.

6.5: Evaluation against BSRN Data

Data from the Baseline Surface Radiation Network is of very high quality because the BSRN instruments have been well characterized and are maintained according to published standards (Ohmura, et al., 1998). In addition, an attempt has been made to sample various

geographic regions and climatological areas when establishing BSRN sites. Although the full desired distribution has not yet been achieved, this network has the best distribution of locations available in any single grouping at this time. We thus begin our assessment with comparisons between the satellite data and irradiances from the BSRN.

6.5.1: All-sky Shortwave Fluxes.

The shortwave fluxes from the satellite data sets are first compared with the BSRN ASWDN (direct + diffuse) fluxes over the entire period for which both satellite and measurement data are available, that is, January 1992 to December 2004. These comparisons include all possible matches between the satellite and BSRN data sets. (Note that fewer points are used for the FORTH and CERES comparisons for the reasons explained above.) The bias, standard deviation, root-mean-square difference, and correlation are presented here.

A representative result of this comparison is shown in *Figure 6.4*. The left panel is a scatter plot of the GEWEX SRBQC-Ed025 irradiances against all available BSRN ASWDN values. While some scatter about the 1:1 line is evident, the overall bias is 0.8 W m^{-2}, with a standard deviation of 21.5 Wm^{-2}. The right panel of *Figure 6.4* shows a histogram of the SRBQC-BSRN differences. Along with the histogram, a normal curve with the same standard deviation but zero mean is plotted as a reference. Note that the bar at the center of the histogram includes 116 instances of differences less than 5 Wm^{-2} that arise because these months are dominated by the polar night. Also note the high kurtosis in this case, which implies that most of the variance is due to the few large deviations (so called "outliers") rather than many deviations of moderate amplitude.

The statistics for the GEWEX SRBQC-Ed025-BSRN comparison fall within the range of values computed for the entire group of satellite products, which are listed in *Table 6.2*. Three of the data sets have biases below 1 Wm^{-2}, and, except for FORTH, the rest are below 10 Wm^{-2}. Typical standard deviations are between 20 and 25 Wm^{-2} while correlations lie between 0.95 and 0.98, bearing in mind (here and throughout this chapter) that correlations are inflated when the annual cycle is included in the data. Because of the large number of sites included in this comparison, the missing FORTH polar night values have very little effect on the overall statistics: If zeros were substituted for the missing values, the bias and standard deviation would be -12.6 and 24.1 Wm^{-2}, respectively.

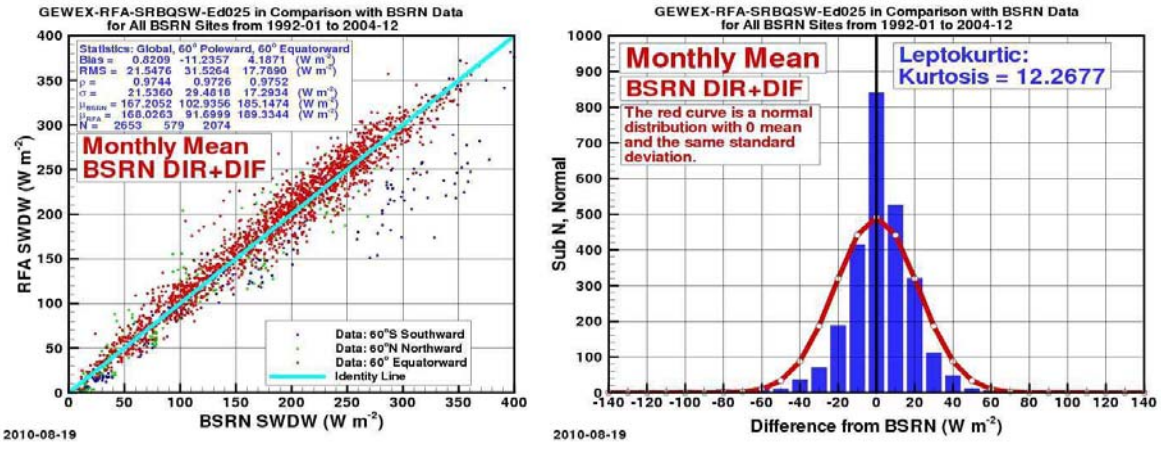

Figure 6.4:. *Comparison between the GEWEX SRBQSW-Ed025 and BSRN shortwave downward fluxes from 1992 to 2004 for all-sky conditions. The histogram for the SRBQSW minus BSRN differences is shown in blue in the right-hand panel. The superimposed red curve is the best-fit zero-mean Gaussian curve. The y-axis label "Sub N" refers to the number of points in a given bin.*

Table 6.2: *Statistics from comparisons between the satellite and BSRN shortwave downward fluxes under all-sky conditions from January 1992 to December 2004. Bias, root-mean-square difference (RMS), and standard deviation (σ) are all given in Wm^{-2}. The cross correlation is denoted by ρ and N is the number of samples used in the comparison.*

Satellite Data Set	Bias	RMS	ρ	σ	N
DLR_ISIS_Ed001	-0.4	20.1	0.978	20.1	2653
FORTH_Ed01a	-13.2	28.0	0.955	24.7	2380
GEWEX_SRBGSW_Ed281	-5.6	23.9	0.970	23.2	2653
GEWEX_SRBQSW_Ed025	0.8	21.5	0.974	21.5	2653
ISCCP_FD_Ed000_010	0.5	19.5	0.979	19.5	2653
UMD_SRB_Ed033	7.7	27.0	0.966	25.8	2653

Figure 6.5 illustrates the temporal variability of the bias and standard deviation for each satellite data set relative to all possible BSRN ASWDN values during the period 1997-2004. All of the bias and standard deviation time series move together, including the CERES-SRBAVG, which is the only product that does not make use of ISCCP data. However, the monthly bias time series are offset by the satellite products' overall mean biases, with UMD-SRB being the most positive and FORTH being the most negative. For all data sets, peak positive biases occur in the Northern Hemisphere (NH) summer and peak negative biases during the NH winter. In addition, there is an overall downward trend for the satellite SW flux values relative to the surface measurements over this time period. Standard deviations do not show the same symmetric cyclic pattern as the biases, with extreme values ranging from 30 to 60 Wm^{-2} occurring only during the NH winter. Between these peaks, biases are generally in the range of 12-18 Wm^{-2}, except for small peaks around 20 Wm^{-2} in the NH summer. Note that a shorter time range is used for this analysis to provide similar sample numbers for each individual month.

Explanations for these seasonal patterns are subject to speculation at this time. The negative biases in combination with large standard deviations during NH winter could be caused by overestimation in cloud optical depth or cloud cover due to misclassification of snow cover as cloud in the satellite data sets. High biases in summer could be caused by underestimates of aerosol loads. To separate aerosol effects from cloud effects, additional comparisons limited to clear-sky conditions are needed. (See Section 6.5.2.)

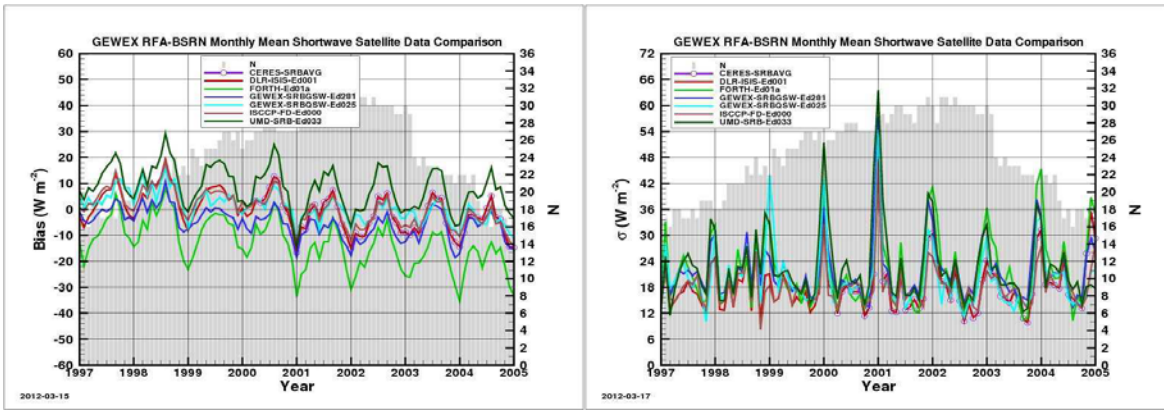

Figure 6.5*: Time series of bias and standard deviation for shortwave downward fluxes by each satellite product relative to BSRN data from January 1997 to December 2004. "N" is the number of values available from the BSRN data set; the actual number of comparisons is smaller for the FORTH and CERES-SRBAVG satellite data sets.*

The plots in *Figure 6.6* show how the bias and standard deviation between the satellite-based and surface-measured shortwave fluxes vary with location. In these plots, the latitude of the radiometer sites progresses from north to south moving left to right along the horizontal axis. (The latitudes are represented by the black diamonds in the left-hand panel.)

Excessively large (30-80 Wm^{-2}) and consistent biases between the surface measurements and satellite estimates are obvious at Ilorin, Nigeria (ILO), and Florianopolis, Brazil (FLO). In addition, the standard deviations at Florianopolis are quite large (35-45 Wm^{-2}). A cursory analysis suggests the occurrence of measurement errors, possibly due to misalignment of the shadowing elements in the diffuse flux measuring instruments (pyranometers). Further analysis is required to verify this conclusion. We note fewer than ten monthly means were available for each of these sites.

Aside from Ilorin and Florianopolis, it is evident that overall disagreement is largest for the sites on the Antarctic coast -- Syowa (SYO) and Georg von Neumeyer (GVN) – where all of the satellite products underestimate the downward solar fluxes and the standard deviations run from 25 to 65 Wm^{-2}. This may again be due to misinterpretation of bright surfaces as cloud when temporal variations in sea ice extent are not well represented in satellite surface flux computations. Smaller but consistently positive biases are found for Bermuda (BER), Nauru (NAU), Manus (MAN), and Goodwin Creek, Mississippi (GCR); all of these but GCR are islands. Consistent negative biases occur for Sede Boker, Israel (SBO), and at the South Pole. Relatively large standard deviations occur at Solar Village, Saudi Arabia (SOV), and the Arctic sites in addition to the coastal Antarctic locations. The Solar Village standard deviations are noteworthy given the unremarkable biases found there.

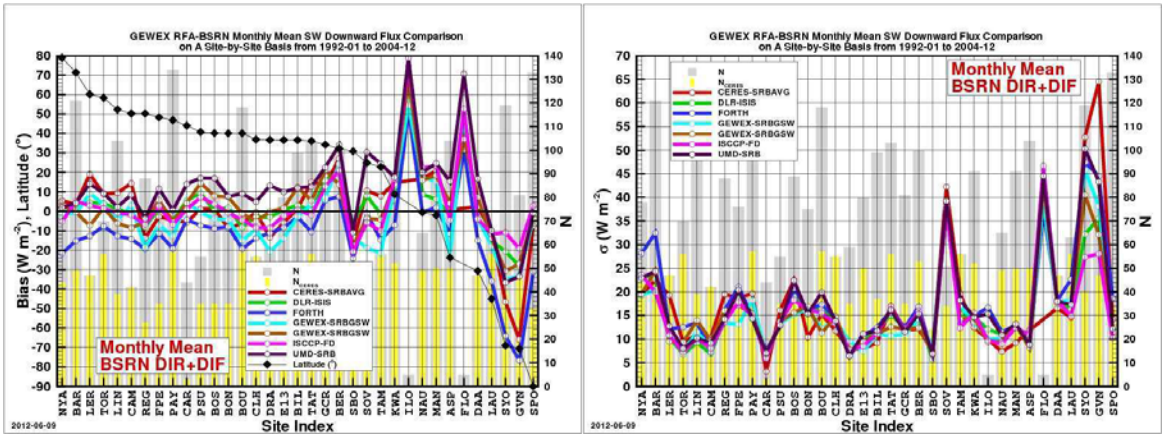

Figure 6.6: *Biases and standard deviations for downward solar fluxes at individual BSRN sites for each set of satellite-based downward fluxes relative to measurements between January 1992 and December 2004. The yellow bars indicate the number of samples included for the CERES data (due to the time period and some missing values), while the gray bars indicate the number of samples for the other satellite products.*

For a general assessment by site character, the BSRN reference sites were categorized according to surface type as indicated in *Table 6.3*. Note that the categories include different numbers of sites. Comparison results for the CERES time period are presented in *Figure 6.7*. Consistent biases relative to BSRN downward solar flux measurements occur for island sites (overestimates) and for polar sites (underestimates). The largest standard deviations are also computed for the polar sites. Desert site data are also poorly reproduced, with large and inconsistent biases among the different data sets.

Table 6.3: *BSRN sites categorized by surface type.*

Surface type	BSRN site labels (see Appendix)
Continental	**FPE, GCR, E13, PAY, BIL, BON, CAR, ILO, LIN, REG, TAT, TOR**
Coastal	**CLH, CAM, FLO**
Island	**MAN, NAU, BER, KWA, LER**
Mountain	**BOU, BOS, PSU, LAU**
Desert	**DRA, ASP, SBO, DAA, TAM, SOV**
Polar	**BAR, SPO, SYO, GVN, NYA**

The satellite grid cells including islands typically also cover large portions of the ocean. These ocean regions may be less polluted and are not affected by convective cloud formation that occurs over the heated island surface, so that the SW fluxes inferred over the grid box are greater than those measured at the island station. The polar-site bias is related to cloud cover overestimates in the satellite algorithms as well as uncertainty about the extent of the oceanic polar ice sheets over time. Since cloud cover is not a major element in desert regions, the differences in those regions are likely connected with different representations of aerosol in the various satellite products.

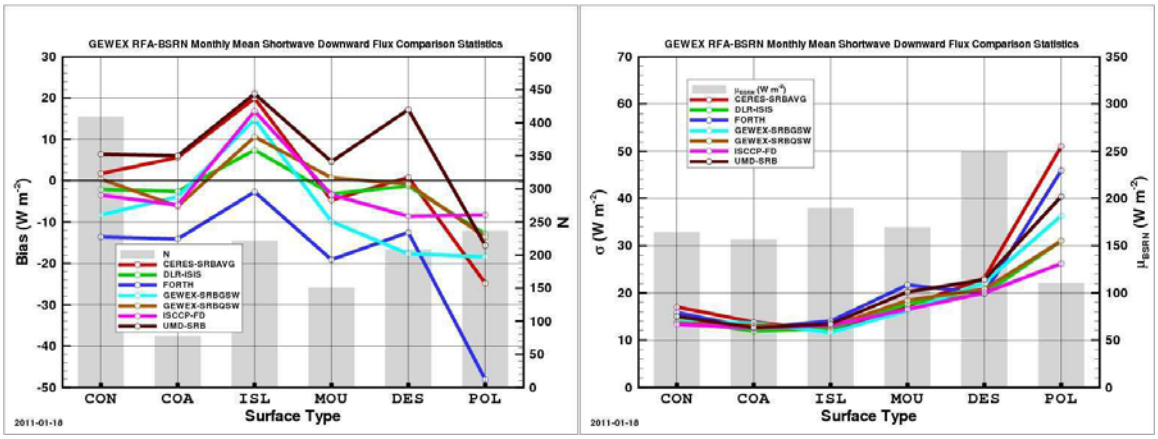

Figure 6.7: *Comparisons between the satellite and BSRN monthly mean shortwave downward fluxes from March 2000 to February 2004 sorted by surface type. "CON" stands for continental, "COA" for coastal, "ISL" for island, "MOU" for mountain, "DES" for desert, and "POL" for polar.*

Table 6.4 *Statistics of comparisons between downward solar fluxes at the surface from the satellite and BSRN data sets from March 2000 to February 2004. Bias, RMS, and standard deviation (σ) are in Wm^{-2}. Cross correlation is denoted by ρ and N is the number of samples. For each data set, the first line (black) is for the entire globe; the second line (red) is for the tropics (20°S to 20°N); the third line (green) is for mid-latitudes (20° to 60°); the fourth line (blue) is for polar latitudes (60° to 90°). Statistics with filling missing polar night values by zero are listed in parentheses.*

Data Set	Bias	RMS	ρ	σ	N
CERES_SRBAVG_Terra_GEO	0.4	28.3	0.950	28.3	1252
_MOD_Ed02d	(0.3)	(27.7)	(0.957)	(27.7)	(1306)
	18.2	20.0	0.953	8.4	140
	2.0	19.3	0.978	19.2	891
	-17.4	52.7	0.911	49.8	221
	(-14.0)	(47.2)	(0.929)	(45.2)	(275)
DLR_ISIS_Ed001	-2.6	20.3	0.977	20.2	1306
	5.0	11.2	0.952	10.1	140
	-1.3	16.8	0.980	16.7	891
	-10.7	31.5	0.972	29.7	275
FORTH_Ed01a	-15.9	29.7	0.954	25.2	1184
	(-15.4)	(29.3)	(0.965)	(24.9)	(1306)
	-3.3	11.7	0.934	11.2	140
	-13.4	22.7	0.975	18.4	886
	-41.2	60.1	0.928	49.3	158
	(-28.3)	(48.4)	(0.956)	(39.3)	(275)
GEWEX_SRBGSW_Ed281	-7.6	25.0	0.968	23.8	1306
	14.0	17.0	0.948	9.7	140
	-8.8	20.5	0.974	18.6	891
	-14.7	38.0	0.961	35.2	275
GEWEX_SRBQSW_Ed025	-1.0	20.8	0.976	20.8	1306
	14.7	17.4	0.945	9.4	140
	0.2	16.6	0.979	16.6	891
	-12.8	31.7	0.973	31.7	275
ISCCP_FD_Ed000_010	-1.9	19.8	0.978	19.7	1306
	19.6	22.1	0.937	10.3	140
	-3.7	17.1	0.979	16.7	891
	-6.8	25.8	0.979	24.9	275
UMD_SRB_Ed033	6.4	26.8	0.964	26.1	1306
	19.1	21.6	0.940	10.2	140
	10.0	21.6	0.977	19.2	891
	-11.7	40.8	0.948	39.1	275

For a general assessment by site latitude, the BSRN reference sites were grouped as indicated in *Table 6.4*. Comparison statistics for the CERES time period were then computed over these groupings. (Note that the number of sites included in the latitude bands varies.) The standard deviations indicate that the downward solar fluxes for all satellite data sets differ most from the surface measurements at polar sites and least at the tropical sites. In most cases, the

biases are negative for the polar and mid-latitudes and positive for the tropics, leading to very small average biases (mainly under 3 Wm^{-2}) over the entire ensemble of sites. However, larger than average negative biases for polar and mid-latitudes lead to an overall bias of -7.6 Wm^{-2} for the GEWEX_SRBGSW data while a significant positive mid-latitude bias contributes to an overall bias of 6.4 Wm^{-2} for UMD_SRB. As for the earlier comparisons using all available BSRN data (1992-2004, Table 2??), the overall standard deviations are generally between 20 and 25 Wm^{-2} and the correlation coefficients between 0.95 and 0.98.

Unlike the other satellite data sets, FORTH has negative biases at all latitudes. The FORTH data differs most from the surface observations in the polar regions. This strong deviation is enhanced by the fact that polar night data were marked as undefined, so that near-zero disagreement during the polar night could not enter the statistics. Re-computing the statistics after substituting zeros for the undefined values reduces the magnitude of the FORTH bias from 41 to 28 Wm^{-2} (still the most negative regional bias among all data sets) and standard deviation from 49 to 39 Wm^{-2} and increases the correlation from 0.93 to 0.96, as shown in parentheses in *Table 6.4*. The SRBAVG data was also missing 51 polar data samples. Here, substitution of zeros also improved the statistics, but not as dramatically as for FORTH.

The final form of analysis performed using the BSRN shortwave data was to create an ensemble data set using 12 sites (marked by triangles in *Figure 6.1*) with nearly continuous records for years between 1997 and 2004. For every data set, the departures from the mean annual cycle over the entire time period were computed at each location and then the resulting anomaly time series were averaged. Results of the comparisons are presented in *Figure 6.8*. The left-hand panel of this figure shows deseasonalized ensemble averages (mean anomalies) for each data set, while the right panel shows the time series of differences between each satellite data set and its BSRN counterpart. The difference statistics for the ensemble average comparisons are given in *Table 6.5*. CERES SRBAVG is omitted from these computations because of its shorter data record. The FORTH data has also been excluded from this comparison because its lack of polar night data.

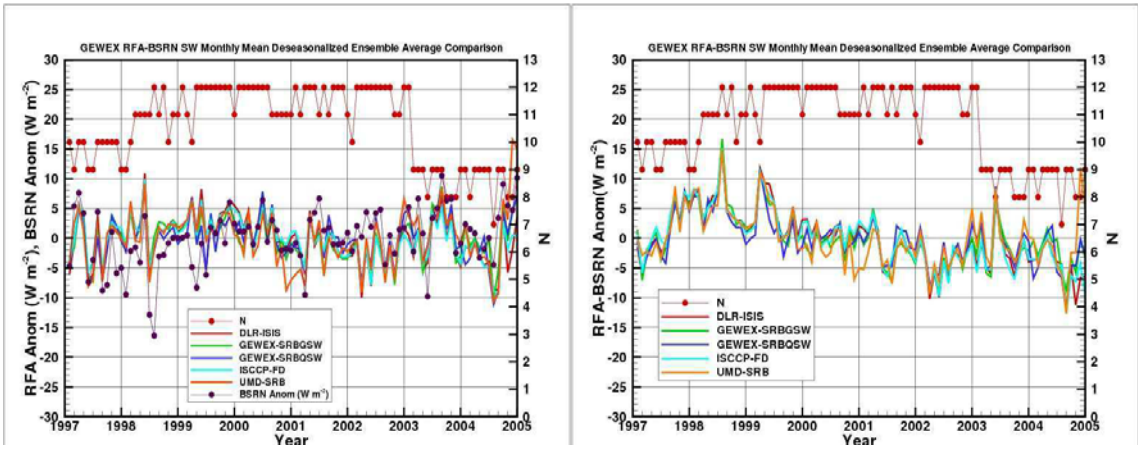

Figure 6.8: *Time series of the shortwave downward flux ensemble average over 12 BSRN sites with nearly continuous records. Shown here are the anomalies after the data from individual sites has been deseasonalized by subtracting the mean annual cycle computed over the full time period shown and then averaged to create the ensemble mean.*

Table 6.5*: Statistics of comparisons between the satellite and BSRN 12-site shortwave ensemble averages from January 1997 to December 2004. Standard deviation (σ) is in Wm^{-2}. Cross correlation is denoted by ρ and N is the number of samples.*

Satellite Data Set	ρ	σ	N
DLR_ISIS_Ed001	0.422	4.9	1015
GEWEX_SRBGSW_Ed281	0.477	4.5	1015
GEWEX_SRBQSW_Ed025	0.538	4.3	1015
ISCCP_FD_Ed000_010	0.371	4.9	1015
UMD_SRB_Ed033	0.524	4.7	1015

The left-hand panel of *Figure 6.8* is similar to the left-hand panel of *Figure 6.5*, except that the number of comparison points is more constant over time and that systematic errors in the seasonal cycle have been removed. This eliminates any overall bias in a given data set. Analyses of this data emphasize the ability of satellite-based data sets to represent deviations from the mean conditions at the selected sites. With annual cycles removed, the satellite SW fluxes track those from the surface measurements well except that the magnitudes of the variations in the surface measurements are often larger than those in the satellite data. The absolute differences among the satellite data sets and between the satellite and surface in-situ data decrease relative to those in *Figure 6.5*, as demonstrated by the lower standard deviations (all less than 5 Wm^{-2}) listed in *Table 6.4* relative to those in *Table 2* (~20-25 Wm^{-2}.) The right-hand panel presents differences between the satellite and station mean anomalies, again revealing a tendency for the satellite data sets to exceed the station measurements between 1998 and 2001 and be lower during the remainder of the period examined, as was evident in *Figure 6.5*. This may relate in part to the trends in cloudiness detected by the ISCCP sensors over this period (clouds decreasing between 1998 and 2000, then increasing through at least 2005 (*Evan et al., 2007.*)) Alternatively, aerosol loads at the BSRN sites may have increased more than considered in computations of solar flux in the satellite data processing. Note that the correlation coefficients are substantially reduced by deseasonalization.

6.5.2: Clear-sky Shortwave Fluxes.

Three of the satellite data sets included shortwave fluxes under clear-sky conditions. These are values computed for all grid cells at all times, regardless of the actual cloud conditions. We are able to evaluate them because clear-sky flux estimates at the BSRN locations were also provided for the Assessment (see Appendix A.2.2.4 for a description of this data set.) The statistical results of these comparisons are given in Table 6.6 and can be compared to the analogous results for all-sky conditions in Table 6.2. Interestingly, although the standard deviations are smaller and the correlations higher for the clear-sky data, the biases are all larger and negative (i.e., smaller than the measurements.) This implies that excess water vapor, ozone, or aerosol is included in the satellite-based estimates or that the surface albedo is not accurately accounted for in the original conversion of measured TOA satellite radiances to irradiances. The smaller deviations reflect the absence of the extreme solar flux variability associated with cloud systems.

Table 6.6*: Statistics from comparisons between the satellite and estimated BSRN shortwave downward fluxes under clear-sky conditions from January 1992 to December 2004. Bias, root-mean-square difference (RMS), and standard deviation (σ) are all given in Wm^{-2}. The cross correlation is denoted by ρ and N is the number of samples used in the comparison.*

Satellite Data Set	Bias		ρ	σ	N
GEWEX_SRBGSW_Ed281	-12.6	18.7	0.993	13.8	2974
GEWEX_SRBQSW_Ed025	-6.7	13.5	0.995	11.8	2974
ISCCP_FD_Ed000_010	-4.7	12.0	0.995	11.0	2974

6.5.2.1: All-sky Longwave Fluxes

Comparisons between the RFA satellite downward longwave fluxes and the BSRN data are performed in the same way as the shortwave comparisons. The results are shown in *Figures 6.9-6.13* and *Tables 6.6-6.9*.

Comparing the longwave results for the GEWEX_SRBGLW data in *Figure 6.9* to the corresponding solar evaluations of *Figure 6.4*, the bias and standard deviation are smaller for the longwave fluxes (*Figure 6.9*) than for solar fluxes (*Figure 6.4*). Possible explanations for this improvement are the reduced impacts of aerosol, cloud structure, and cloud microphysics. The histograms in the right-hand panels of these figures show that longwave flux differences are more normally distributed. The fact that longwave fluxes are nonzero during the polar night reduces the number of near-zero differences, eliminating the large peak at the center of the histogram.

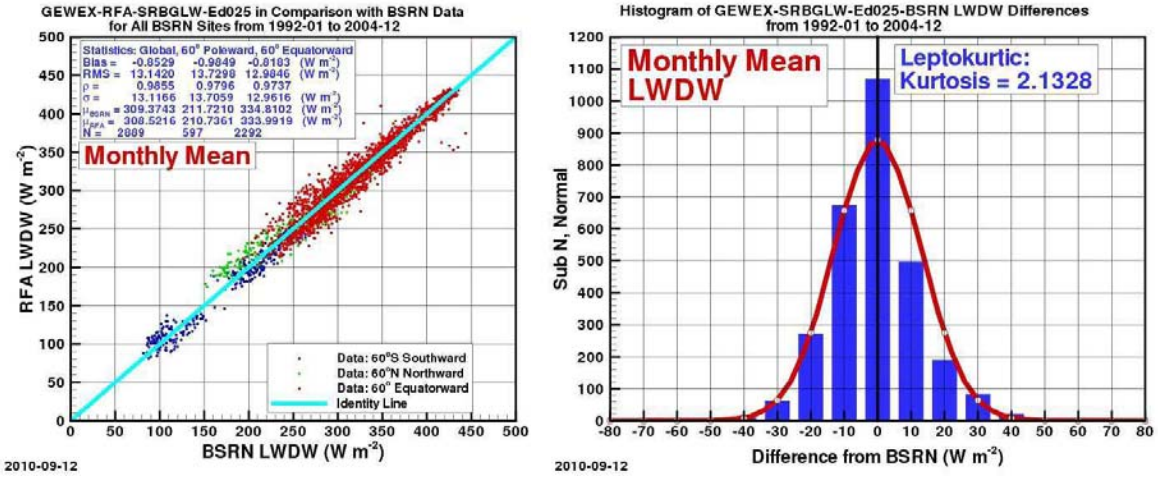

Figure 6.9: *Comparison between GEWEX-SRBGLW and BSRN longwave downward fluxes from 1992 to 2004 for all-sky conditions. The histogram for the SRBQSW-minus-BSRN differences is shown in blue in the right-hand panel. The superimposed red curve is the best-fit zero-mean Gaussian curve. The y-axis label "Sub N" refers to the number of points in a given bin.*

Statistics for all of the satellite-based surface longwave products in the RFA archive that cover the full BSRN time period are given in *Table 6.7* and those for the CERES period in *Table 6.8*. The better agreement with BSRN for longwave fluxes is demonstrated by comparing the statistics from *Table 6.7* to the corresponding solar statistics of *Table 6.2*. The bias ranges are

slightly lower for longwave fluxes (0.8 to 6 Wm^{-2}) compared to solar biases (0.5 to 13.2 Wm^{-2}), while all standard deviations are comparable to or lower than values for the solar fluxes. Longwave standard deviations are between 13 and 21 Wm^{-2}, while solar standard deviations are between 20 to 25 Wm^{-2}. The longwave correlation values are also higher (0.97-0.99) compared to the solar correlations (0.95-0.98). Still, these changes are not consistent for the four satellite data sets examined (e.g., a significant bias increase for the ISCCP_FD data set). Note that the downward longwave fluxes from the satellite-based data are consistently larger than the in-situ observations.

Table 6.7: *Statistics from comparisons between the satellite and BSRN longwave data from 1992 to 2004. Bias, root-mean-square difference (RMS), and standard deviation (σ) are in Wm^{-2}. Cross correlation is denoted by ρ and N is the number of samples.*

Data Set	Bias	RMS	ρ	σ	N
FORTH_Ed01a	2.2	16.7	0.982	16.6	2889
GEWEX_SRBGLW_Ed025	-0.8	13.1	0.986	13.1	2889
GEWEX_SRBQLW_Ed025	6.1	16.1	0.984	14.9	2889
ISCCP_FD_Ed000_010	6.1	21.0	0.966	20.1	2889

Table 6.8: *Statistics from comparisons between the satellite and BSRN longwave data from March 2000 to February 2004 (the CERES period). Bias, root-mean-square difference (RMS), and standard deviation (σ) are in Wm^{-2}. Cross correlation is denoted by ρ and N is the number of samples.*

Data Set	Bias	RMS	ρ	σ	N
CERES_SRBAVG_Terra_GEO_MOD_Ed02d	2.4	12.5	0.987	12.3	1272
FORTH_Ed01a	3.4	17.4	0.979	17.1	1272
GEWEX_SRBGLW_Ed025	0.5	13.4	0.984	13.4	1272
GEWEX_SRBQLW_Ed025	7.8	17.8	0.980	16.0	1272
ISCCP_FD_Ed000_010	10.8	24.2	0.958	21.6	1272

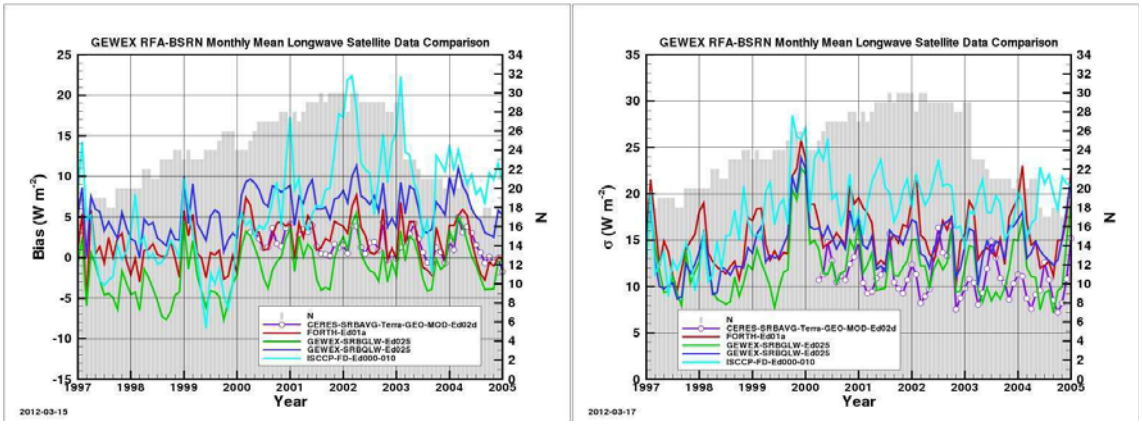

Figure 6.10: *Time series of bias and standard deviation for monthly mean downward longwave fluxes from each satellite product relative to BSRN data from 1997 to 2004.*

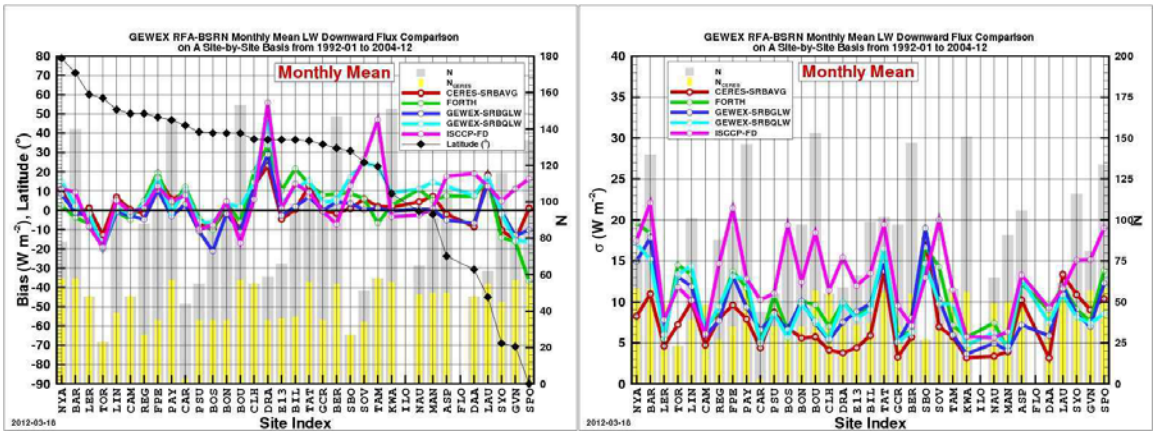

Figure 6.11: *Bias and standard deviation at individual BSRN sites for each set of satellite-based longwave downward (monthly average) fluxes relative to BSRN measurements between 1992 and 2004. Yellow bars indicate the number of samples included for the CERES data (because of the time period) while the gray bars indicate the number of samples for the other satellite products.*

The bias time series in *Figure 6.10* exhibit a clear positive shift in 2000. The largest increase occurs for the ISCCP fluxes. This corresponds to a change in the TOVS temperature retrieval algorithms (Zhang et al., 2006). It is possible that this change also affected the other ISCCP-based products, yet their response is much smaller. The standard deviations also jump at the end of 1999, but slowly return to their earlier values, except for ISCCP. The GEWEX-SRBGLW satellite product exhibits the smallest increase in standard deviation. CERES-SRBAVG, which is completely independent of ISCCP variables, cannot show a bias change in 2000 because its data record begins in this year, but it does show a parallel decrease in standard deviation from 2000 to 2005. Such a trend in standard deviation is difficult to explain on a physical basis. The biases tend to be more positive in the NH summer and more negative during the NH winter, opposite the bias pattern exhibited for the SW fluxes. For most of the five satellite data sets, higher standard deviations still occur in the NH winter, as for the SW fluxes. However, this pattern is less clear for the ISCCP data.

Locations problematic for LW flux estimation can be determined through analysis at each individual BSRN site, as shown in *Figure 6.11*. By far the largest differences (underestimates) occur at Florianopolis (FLO) in Brazil, but, given that the corresponding SW values appear to be incorrect, inaccuracy in these values cannot be ruled out. Consistently large mean differences between satellite data sets and surface measurements (satellite overestimates) occur at Desert Rock (DRA) in Nevada, and at the other desert sites of Tamanrasset (TAM) in Algeria, and Solar Village (SOV) in Saudi Arabia for ISCCP-FD and GEWEX-SRBQLW. This suggests that the data sets tend to underestimate atmospheric dust aerosol or that boundary layer heating is overestimated at those sites. Notable divergence in biases among the data sets occurs at the South Pole (SPO). This may be due to differences in the water vapor amounts used in the flux computations. Consistently large standard deviations occur at the Arctic sites (NYA and BAR), the island site Tateno, Japan (TAT), and at Sede Boqer (SBO) and the Saudi Solar Village (SOV) in the Middle East.

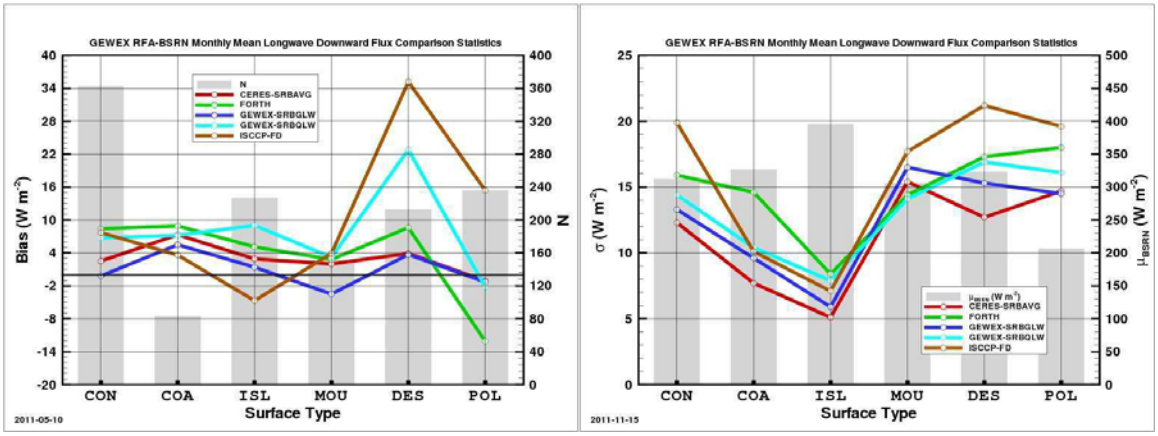

Figure 6.12: *Comparisons between the satellite and BSRN monthly mean longwave downward fluxes from March 2000 to February 2004. Site data are sorted by surface type. "CON" stands for continental, "COA" for coastal, "ISL" for island, "MOU" for mountain, "DES" for desert, and "POL" for polar.*

For a general assessment by site character, all BSRN reference sites were categorized by surface type as indicated in *Table 6.3*. Comparison results are presented in *Figure 6.12*. The results reflect the findings of the previous paragraph, with the largest biases occurring for the desert sites and a range of biases in the polar areas. In addition, the standard deviations are found to be smallest at the island and coastal sites.

Table 6.9: *Statistics of comparisons between satellite data sets and BSRN longwave downward fluxes from March 2000 to February 2004 (CERES period). Bias, root-mean-square difference (RMS), and standard deviation (σ) are all given in Wm^{-2}. The cross correlation is denoted by ρ and N is the number of samples used in the comparison.*

Data Set	Bias	RMS	ρ	σ	N
CERES_SRBAVG_Terra_GEO _MOD-Ed02d	2.4	12.5	0.987	12.3	1272
	4.4	6.1	0.854	4.2	144
	3.0	12.9	0.963	12.5	854
	-0.7	13.8	0.978	13.8	274
FORTH_Ed01a	3.4	17.4	0.979	17.1	1272
	6.8	9.6	0.197	6.8	144
	7.6	17.4	0.944	15.7	854
	-11.3	20.3	0.971	16.9	274
GEWEX_SRBGLW_Ed025	0.5	13.4	0.984	13.4	1272
	1.4	4.2	0.740	3.9	144
	1.0	14.2	0.952	14.2	854
	-1.4	13.7	0.979	13.7	274
GEWEX_SRBQLW_Ed025	7.8	17.8	0.980	16.0	1272
	12.7	13.8	0.758	5.4	144
	10.1	19.1	0.942	16.2	854
	-2.0	15.2	0.975	15.1	274
ISCCP-FD_Ed000_010	10.8	24.2	0.958	21.6	1272
	-2.5	6.5	0.675	6.0	144
	12.6	26.2	0.872	23.0	854
	12.1	23.4	0.964	20.1	274

Results of comparisons generalized by latitude bands are listed in *Table 6.9*. This analysis is limited to the CERES time period to allow comparisons among all of the satellite data sets. As

in the corresponding solar analysis of *Table 6.4*, there are different numbers of stations in each category. However, in this case, valid data are available at every grid box containing surface measurement stations for all of the satellite products. This allows consistent comparisons across the different data sets. Similar to the solar fluxes, the standard deviations are by far the smallest in the tropical latitudes. However, the tropical biases are not smaller than those for other latitude bands. In contrast to the shortwave fluxes, the statistics for the polar regions are generally similar to those for the mid-latitudes.

The final all-sky LW analysis performed using the BSRN data involves ensemble averages over 12 stations as discussed in *Section 6.1.4*. The results are presented in *Figure 6.13,* complementing the solar comparisons of *Figure 6.8*. The ensemble mean time series of the anomalies from the seasonal cycle for each data product is shown in the left hand panel of *Figure 6.13*, while the time series of differences between the ensemble anomalies from the satellite-based data products and the surface measurements are shown in the right-hand panel. The number of sample points for each month is shown using red circles in each of the plots (right vertical axis).

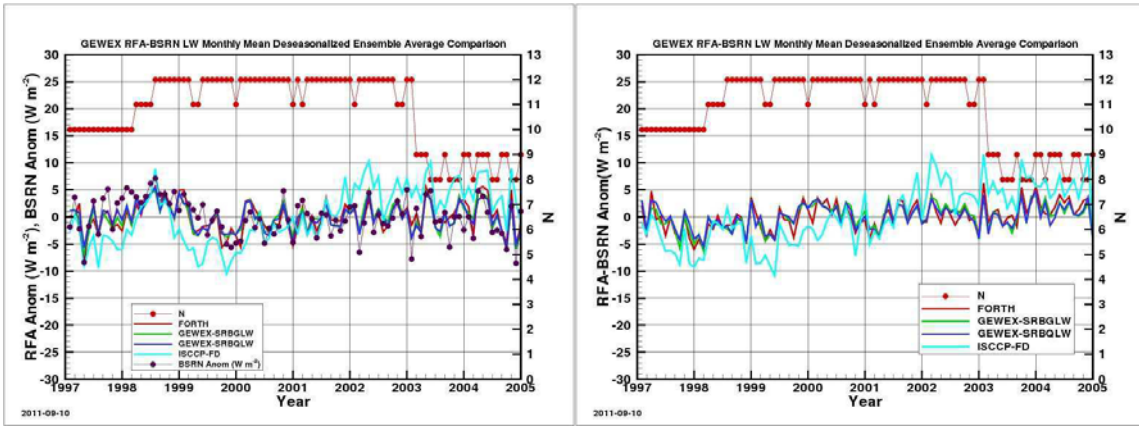

Figure 6.13: *Time series of the longwave downward flux for an ensemble average of 12 BSRN sites with nearly continuous records and the corresponding deviations for the different (satellite) data sets. Shown here are the anomalies after the data from individual sites has been deseasonalized by subtracting the mean annual cycle computed over the full time period.*

The anomaly plot shows that ensemble means from the satellite data track the BSRN values reasonably well, although the magnitudes of the variations are often smaller for the satellite products than the surface measurements, as was also the case for the solar fluxes. *Table 6.10* shows that the standard deviations of the satellite-based anomalies from the BSRN values are less than 6 Wm^{-2}. In fact, most satellite products reproduce the ensemble mean of the in-situ measurements to within 3 Wm^{-2}. As observed previously in comparisons to measurements from individual stations, the ISCCP-FD data matches the mean ensemble average surface fluxes poorly, with a standard deviation of 5.5 Wm^{-2} (vs. ~2.5 Wm^{-2} for the other three satellite products) and a lower correlation of 0.25 (vs. ~0.7). The differences between the ISCCP-FD and BSRN fluxes also increase from 1999 through 2004. Again, this is mainly related to the inconsistency of the surface temperature ancillary data over time, which affects the longwave atmospheric re-radiation to the ground.

Table 6.10: *Statistics of comparisons between the satellite and BSRN 12-site longwave ensemble averages from January 1997 to December 2004. Standard deviation (σ) are all given in Wm^{-2}. The cross correlation is denoted by ρ and N is the number of samples.*

Satellite Data Set	ρ	σ	S-M
FORTH_Ed01a	0.671	2.7	1032
GEWEX_SRBGLW_Ed025	0.727	2.4	1032
GEWEX_SRBQLW_Ed025	0.757	2.3	1032
ISCCP_FD_Ed000_010	0.254	5.5	1032

6.5.2.2: Clear-sky Longwave Fluxes

Statistics from comparisons between clear-sky longwave flux estimates from the satellite and BSRN data sets are shown in *Table 6.11*. The statistics are generally similar to the corresponding values under all-sky conditions. However, the bias is noticeably larger for the standard GEWEX SRB product. As for the shortwave data, this may be due to excess absorbers in the atmosphere. Alternatively, the near-surface temperatures used in the radiative transfer computations may be too low, although this was not apparent in the all-sky data. The changes in near-surface temperature data used by ISCCP noted previously appear to cancel each other over time leading to a near-zero bias when no clouds are present.

Table 6.11*: Statistics from comparisons between the satellite and estimated BSRN longwave downward fluxes under clear-sky conditions from January 1992 to December 2004. Bias, root-mean-square difference (RMS), and standard deviation (σ) are all given in Wm^{-2}. The cross correlation is denoted by ρ and N is the number of samples used in the comparison.*

Satellite Data Set	Bias	RMS	ρ	σ	N
GEWEX_SRBGLW_Ed025	-12.1	19.0	0.987	14.6	2216
GEWEX_SRBQLW_Ed025	-3.4	17.5	0.987	17.1	2216
ISCCP_FD_Ed000_010	1.5	20.4	0.969	20.3	2216

6.6: Evaluation against GUOR data (GEBA and UOR)

The University of Oregon's (UOR) Solar Radiation Monitoring Laboratory surface radiative flux measurements (SRML) as well as those residing in the Global Energy Balance Archive (GEBA) are extremely useful for satellite data evaluation because of their long records: some of GEBA's records extend back to the early 1900s while the University of Oregon's SRML began recording solar flux data in 1979. This makes it possible to evaluate satellite-based surface fluxes back to the beginning of the ISCCP era (July 1983). However, the locations for which these data are available are concentrated in Europe, Asia, and Oregon (USA), as shown in *Figure 6.2* above. The four GEBA polar sites included in the Assessment archive fall between 60° and 70° north. The BSRN collection of stations is more evenly distributed and includes four sites polewards of 70°, two in each hemisphere. Thus, GUOR data gives less weight to extreme and tropical latitudes. In addition, the quality of the GEBA flux data is less certain for the reasons described in Section 6.2.2. The procedures of the UOR SRML, however, are well established and documented, making these data more consistent and reliable. GUOR data submitted to the

assessment archive include only ASWDHEM values, or total hemispheric downward fluxes measured by a single pyranometer, rather than the direct and diffuse values provided by BSRN. Therefore, the comparisons between satellite shortwave fluxes and the GUOR data use these ASWDHEM values. No longwave data from GEBA or the University of Oregon was submitted to the RFA archive. The evaluation described below follows the same approach as the BSRN comparisons.

Solar downward fluxes from one satellite data set (GEWEX_SRBGSW) are compared to GUOR site data over the 1984 to 2004 time period in *Figure 6.14*. Although the spread of the scatter relative to GUOR in *Figure 6.14* appears worse than the spread against BSRN in *Figure 6.4*, it should be pointed out that comparisons to GUOR data involve three times as many data pairs and that there are many overlapping points near the 1:1 line in this case. This explains why the magnitudes of the bias and standard deviation relative to GUOR (4.6 and 19.5 Wm^{-2}, respectively) are smaller than the corresponding values relative to BSRN (-5.6 and 23.2 Wm^{-2}), although it should be kept in mind that time periods are not the same.

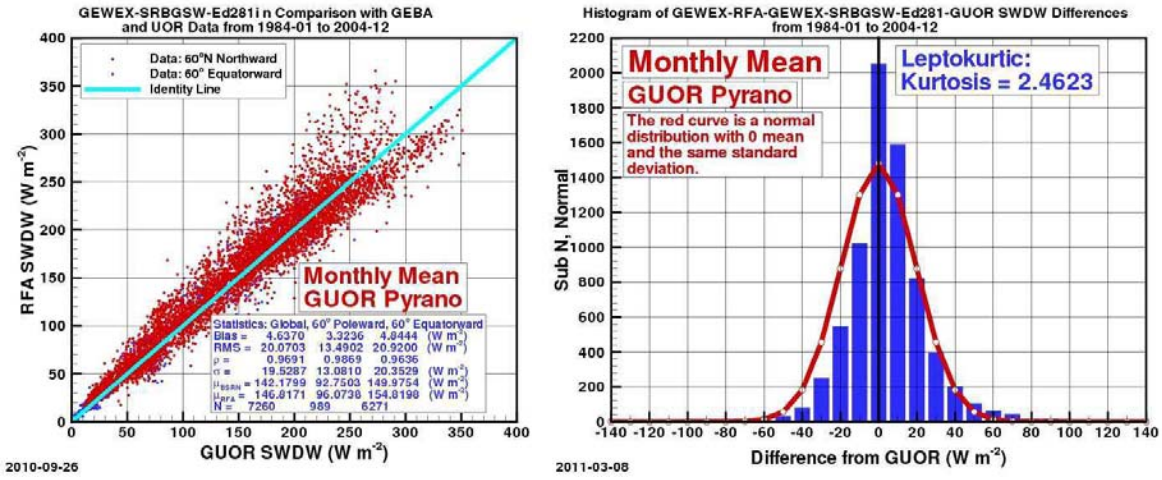

Figure 6.14: *Comparison between the GEWEX-SRBGSW-Ed281 and GUOR shortwave downward fluxes from 1984 to 2004. Format as in Figure 6.4*

Statistics relative to GUOR data for all satellite data sets (excluding CERES_SRBAVG) are summarized in *Table 6.11*. In all cases, the standard deviations are lower than in comparisons with BSRN data, while the correlation coefficients are not much changed. The biases have also become more positive, so that their magnitudes are larger for nearly all of the data sets, presumably because there is less cancellation between negative and positive values. The only exception is FORTH, for which the bias remains negative. However, the bias still became more positive, leading to a decrease in its magnitude.

In the BSRN comparison, the range of the bias magnitudes was 0.4 to 13.2 Wm^{-2} with only one value greater than 8 Wm^{-2}. In the GUOR comparison, the range of the bias magnitudes is 4 to 17 Wm^{-2}, with an average value of ~8.4 Wm^{-2}. It is not clear why the satellite values should tend to be higher than the GUOR values when they were not consistently so for the BSRN data. We speculate that loss of sensitivity for any pyranometers that were in use for long periods may be the cause of this difference. However, the biases computed for the CERES time period, shown in *Table 6.12,* are also nearly all positive (though somewhat smaller), despite the fact that most in situ radiometers would have been replaced between the early 1980s and 2000s. This suggests that the differences may be caused by sampling at less distributed sites rather than

instrumentation changes. The random component (1-σ standard deviation) for all satellite data sets with respect to the GUOR reference is about 20 Wm^{-2}. This is smaller than the 20-28 Wm^{-2} found relative to the BSRN solar reference.

Table 6.11: *Statistics from comparisons between the satellite and GUOR shortwave data from 1984 to 2004. Bias, RMS and standard deviation (σ) are all given in Wm^{-2}. The cross correlation is denoted by ρ and N is the number of samples used in the comparison.*

Data Set	Bias	RMS	ρ	σ	N
DLR_ISIS_Ed001	8.3	20.7	0.973	18.9	7260
FORTH_Ed01a	-4.0	20.4	0.966	20.0	7010
GEWEX_SRBGSW_Ed281	4.6	20.0	0.969	19.5	7260
GEWEX_SRBQSW_Ed025	8.2	22.2	0.966	20.7	7260
ISCCP_FD_Ed000_010	8.1	20.7	0.972	19.1	7260
UMD_SRB_Ed033	17.3	27.5	0.970	21.3	7260

Table 6.12 *Statistics from comparisons between satellite and GUOR shortwave data from March 2000 to February 2004 (CERES time period). Bias, root-mean-square difference (RMS) and standard deviation (σ) are all given in Wm^{-2}. The cross correlation is denoted by ρ and N is the number of samples used in the comparison.*

Data Set	Bias	RMS	ρ	σ	N
CERES_SRBAVG_Terra_GEO_MOD_Ed02d	14.6	24.3	0.972	19.4	1367
DLR_ISIS_Ed001	7.2	20.5	0.974	19.2	1375
FORTH_Ed01a	-5.2	20.4	0.968	19.7	1325
GEWEX_SRBGSW_Ed281	3.7	19.8	0.970	19.4	1375
GEWEX_SRBQSW_Ed025	7.3	21.4	0.969	20.2	1375
ISCCP_FD_Ed000_010	5.7	20.0	0.972	19.1	1375
UMD_SRB_Ed033	16.7	27.1	0.972	21.3	1375

Temporal variability of the biases and standard deviations for each satellite data set with respect to solar downward fluxes (ASWHEM) detected by GUOR radiometers are shown in *Figure 6.15*. Biases in the downward solar fluxes tend to spike low relative to the measurements during NH summers, especially for FORTH data. The highest values relative to the GUOR measurements often occur during NH spring or summer. Oddly, this pattern is opposite that found against the BSRN solar data. The exception to these trends is the UMD-SRB, whose biases are less variable and match the BSRN temporal pattern. Distinct offsets between the various data sets are obvious in the bias (left-hand) plot, with UMD-SRB having the greatest positive bias and FORTH having the largest negative bias, consistent with the statistics in *Table 6.11*. The standard deviation time series for the different satellite products overlie each other and have a distinct pattern of low values in the late fall in the NH and less clearly defined maxima in the early spring. Again, this differs from the BSRN pattern. No obvious reason for the differences between the BSRN and GUOR comparison seasonal cycles, although it may be related to the quite different spatial distribution of the two networks.

The bias and standard deviations computed for the individual GEBA stations over the CERES time period are plotted in *Figure 6.16*. In general, the satellite values exceed the station measurements. The exception is the FORTH product, which tends to be negatively biased, as noted above. Most biases fall in the range of -20 to + 35 Wm^{-2}; standard deviations over all the samples are mainly below 25 Wm^{-2}.

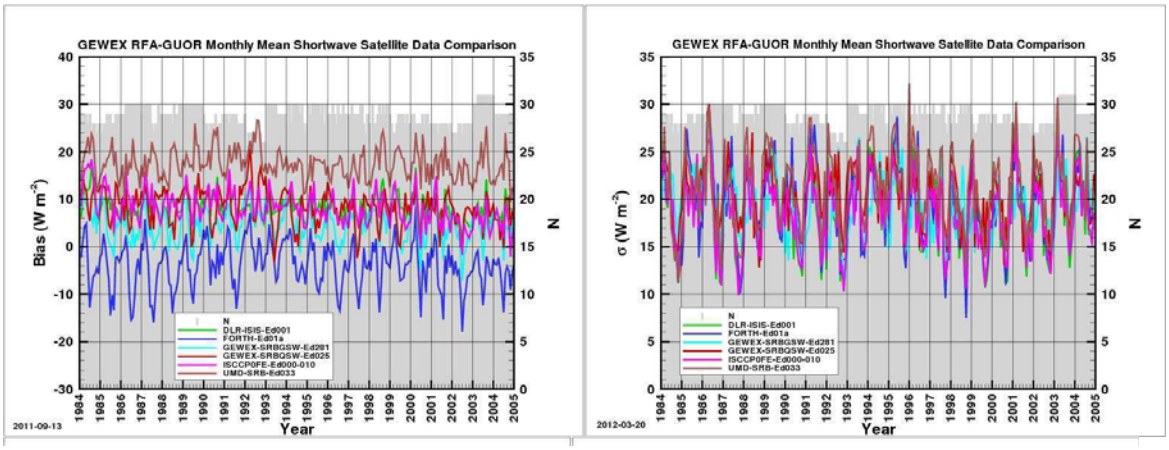

Figure 6.15: *Time series of bias and difference standard deviation for shortwave downward fluxes of each satellite data set relative to GUOR data from 1984 to 2004. "N" is the number of values available from GUOR (data pairs are slightly fewer for FORTH as in Table 6.10)*

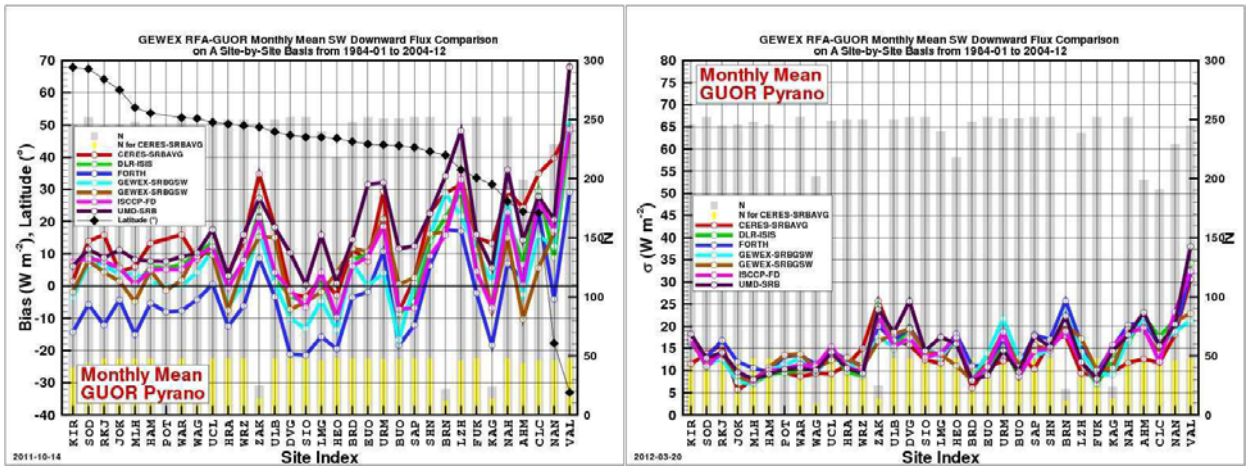

Figure 6.16: *Bias and difference standard deviation at individual GUOR sites for each set of satellite-based shortwave downward fluxes relative to measurements between March 2000 and February 2004. (CERES-SRBAVG and FORTH are missing some values in the polar regions, see Table 6.12)*

Unlike the BSRN, GEBA includes no sites in Antarctica and three of the four sites above the Arctic Circle are at least 80 km inland. (The exception is Reykjavik, Iceland, which is located on a small peninsula.) As a result, the extreme deviations observed in comparisons with the BSRN's coastal Antarctic sites do not occur in this case. Instead, the sites where larger biases occur are located in mountainous or coastal areas. By far the worst agreement occurs for Valparaiso (VAL) in Chile, which is on the Pacific coast and just slightly over 100 km from the Andes Mountains. At Valparaiso, biases for all the data sets exceed 20 Wm^{-2}, with a maximum

over 60 Wm^{-2} for the UMD-SRB product. Standard deviations are also excessive for this site, ranging from about 20 to 36 Wm^{-2}. While these large disagreements may indicate measurement errors at Valparaiso, other sites have consistent biases that are nearly as large. For example, the biases at Lanzhou (LZH) in China (1500 m elevation) and the Adriatic port city of Brindisi, Italy, run from about 16 to 35 Wm^{-2}, with one value of 48 Wm^{-2} at Lanzhou. Other sites with consistently larger biases include Zakopane (ZAK), Poland (857 m), at the foothills of the Tatra Mountains; Naha (NAH), Japan, on Okinawa Island; Calcutta (CAC), India, about 100 km from the Indian Ocean); and Urumqi (URM), China, at 918 m. These are all near coasts or mountains, where local samples are not expected to be representative of the larger spatial average of the satellite data sets, mainly in conjunction with locally generated clouds. Excess aerosols may also affect flux estimates at Calcutta and Urumqi.

An ensemble mean time series was created using GUOR data, as was done earlier for BSRN data. This time series includes data from 30 GUOR sites with few temporal gaps over the 1984 to 2004 time period. These stations are indicated in *Figure 6.2*. Analogous ensemble mean time series for the satellite data were computed. *Figure 6.17* illustrates the mean deseasonalized anomalies; comparison statistics are given in *Table 6.13*.

The satellite-based ensemble mean time series track the progression of the surface site ensemble mean data. As for the BSRN SW ensemble comparison, the magnitudes of the extreme anomalies are sometimes larger for the in-situ measurements than for the satellite data sets. The correlation coefficients (0.84-0.91) are much higher for GUOR comparisons than for BSRN comparisons. Part of this difference may be due to the fact that the GUOR ensemble anomaly time series contains some significant features (e.g., peaks greater than 20 Wm^{-2} in 1992 and 1994). Capturing peaks correctly yields higher correlation values. The anomaly difference time series appears to contain a number of linear segments, the longest being a downward segment from about 1998 until 2003 or possibly the end of the data record.

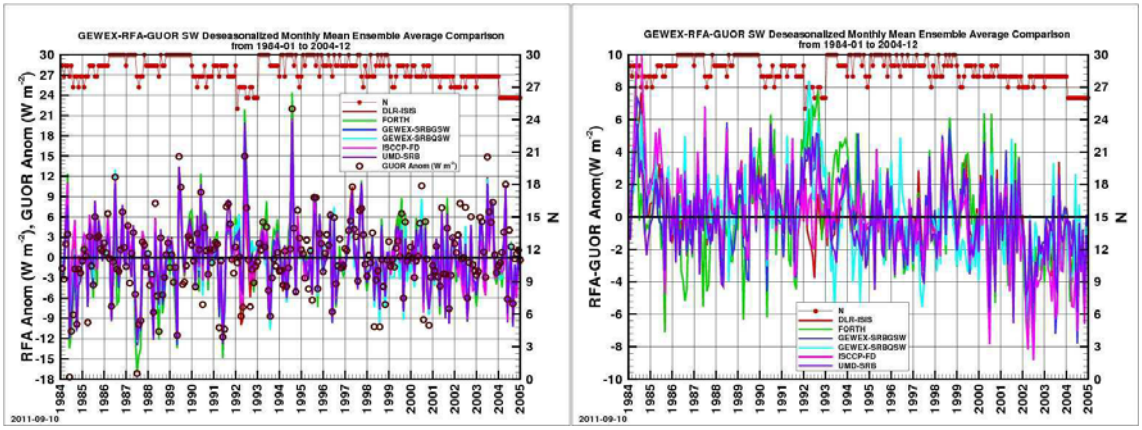

Figure 6.17: *Time series of the solar downward flux ensemble average over 30 GUOR sites with nearly continuous records. Shown here are the anomalies after the data from individual sites has been de-seasonalized by subtracting the mean annual cycle computed over the full time period shown and then averaged to create the ensemble mean.*

Table 6.13: *Statistics of comparisons between the satellite and GUOR 30-site shortwave ensemble averages from 1984 to 2004. Standard deviation (σ) is in Wm^{-2}. Cross correlation is denoted by ρ and N is the number of samples. The data are deseasonalized first on a site-by-site basis before the ensemble average is computed.*

Satellite Data Set	ρ	σ	N
DLR_ISIS_Ed001	0.905	2.3	7189
FORTH_Ed01a	0.856		6939
GEWEX_SRBGSW_Ed281	0.886	2.5	7189
GEWEX_SRBQSW_Ed025	0.880	2.6	7189
ISCCP_FD_Ed000_010	0.836	3.0	7189
UMD_SRB_Ed033	0.898	2.4	7189

An example anomaly time series plot for one satellite data set (DLR-ISIS) is shown in *Figure 6.18*. This figure illustrates the good agreement between time series from in-situ measurements and satellite-based data. The only obvious difference between the GUOR and BSRN data used for the ensemble average analyses is the overemphasis of European/northern mid-latitude sites in the GUOR data. Nevertheless, the large correlation coefficients suggest that the satellite data sets reproduce GUOR variability better than the variability detected by BSRN. Combining data from multiple sites and eliminating the influence of biases due to differences in the annual cycle reduced the standard deviations of the differences between the satellite based and surface measured fluxes from ~20 Wm^{-2} to between 2.3 and 3.0 Wm^{-2} compared to the 4.5-5.0 Wm^{-2} attained against the BSRN reference. However, the significance of this comparison is limited because the BSRN time series involved fewer (12) measurement sites and only covered about half the time period.

The extended record length of the GUOR reference data makes it possible to explore their temporal trends and compare them to trends of the satellite data sets with longer time records. GUOR trends of solar downward fluxes reaching the surface are analyzed for the time period from January 1984 to December 1999. (This time period was selected to match the corresponding analysis in Chapter 9.) First, the 12 GUOR sites (SOD, WAR, DVG, SIO, LMG, EUO, URM, BUO, SAP, SHN, FUK, and NAH; see *Figure 6.2*) with continuous records are selected, then the records are de-seasonalized and ensemble averaging is performed. Finally linear regression is used to determine the slope of each anomaly time series. Following a method described in Weatherhead *et al.* (1998), the data is treated as an autoregressive process of order 1, and the 95% confidence interval is computed as a function of the lag one autocorrelation coefficient, the standard deviation of the residual after the time series is deseasonalized and detrended, and the time span of the data. *Figure 6.18* shows the results for the satellite data set DLR-ISIS-Ed001 and the corresponding GUOR measurements. The estimated trends are shown as straight lines.

The trend estimates for all of the satellite and the surface measured data sets are shown in *Table 6.14*. The GUOR time series is found to have a trend of 0.32 $Wm^{-2}year^{-1}$ that is significant at the 95% level. On the other hand, the 95% confidence intervals for the fits to all satellite time series, except for ISCCP-FD, contain the value zero, meaning that the chosen ensemble average time series shows no significant trend. The ISCCP-FD exhibits a significant negative trend of -0.19 $Wm^{-2}year^{-1}$. This trend disagrees with the positive trend determined from the surface GUOR measurements. This inconsistency, along with the lack of significant trends derived from the other solar satellite data sets, makes it difficult to draw any substantive conclusions about the

change in the downwelling shortwave flux over the selected sites between January 1984 and December 1999.

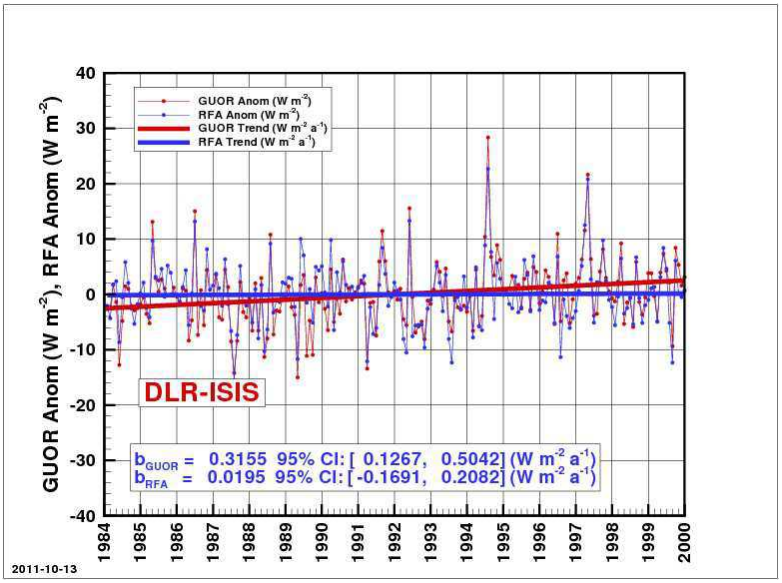

Figure 6.18: *Time series of the shortwave downward flux ensemble average over 30 GUOR sites with nearly continuous records and a matching time series from the DLR-ISIS data set for the time period 1984-2000. Shown here are the anomalies after the data from individual sites has been deseasonalized and then averaged to create the ensemble mean. Trends computed for these time series are also shown.*

Table 6.14: *Trends for the period January 1984 to December 1999, i.e., 192 months, for ensemble means of downwelling SW fluxes over 12 GUOR sites. Trends and confidence intervals (CI) are given in W m^{-2} a^{-1}.*

Data Set	Trend	95% CI
DLR-ISIS	0.0195	[-0.1691, 0.2082]
GEWEX-SRBGSW	0.0184	[-0.1605, 0.1974]
GEWEX-SRBQSW	-0.1559	[-0.3258, 0.0140]
ISCCP-FD	-0.1866	[-0.3603, -0.0128]
UMD-SRB	-0.0067	[-0.2019, 0.1885]
GUOR	**0.3155**	**[0.1267, 0.5042]**

6.7: Evaluation against ASRB data

The Alpine Surface Radiation Budget network is a regional network located in Switzerland. The six sites included in the RFA archive are located within a 3° x 1° area in or close to the Alps at elevations ranging from 370 to 3600 m. Although only one year (2004) of ASRB data has been submitted, this data allows examination of the performance of the satellite data sets in a mountainous area and how measurements at various points compare to satellite values averaged over a larger grid box, since all but one of the sites (Payerne) fall within the same 2.5° x 2.5°

satellite grid cell. The specific altitudes and locations of these sites are listed in *Appendix A.2.2.5*.

6.7.1: Shortwave Fluxes.

The ASRB SW data consist of the total hemispheric downward fluxes from pyranometers (ASWDHEM) and cover the year 2004. This temporal range allows CERES_SRBAVG data to be included in the comparisons. A comparison between the CERES_SRBAVG and ASRB fluxes is shown in *Figure 6.19*. The CERES_SRBAVG data fall within the range of the measured fluxes, with most differences being 30 Wm^{-2} or less and the match points falling on both sides of the 1:1 line. However, the overall bias is negative. The reason that the points in the scatter plot fall along horizontal lines is that a single CERES_SRBAVG value is compared to fluxes from five different ASRB stations, that is, the CERES_SRBAVG value remains the same while the ASRB values vary. Based on this plot, the fluxes can vary by as much as 60-80 W m^{-2} over the ASRB stations in a single 2.5° x 2.5° satellite grid cell. This implies that the apparent agreement could differ widely if the satellite flux was compared to a value from only one of the five ASRB measurement stations.

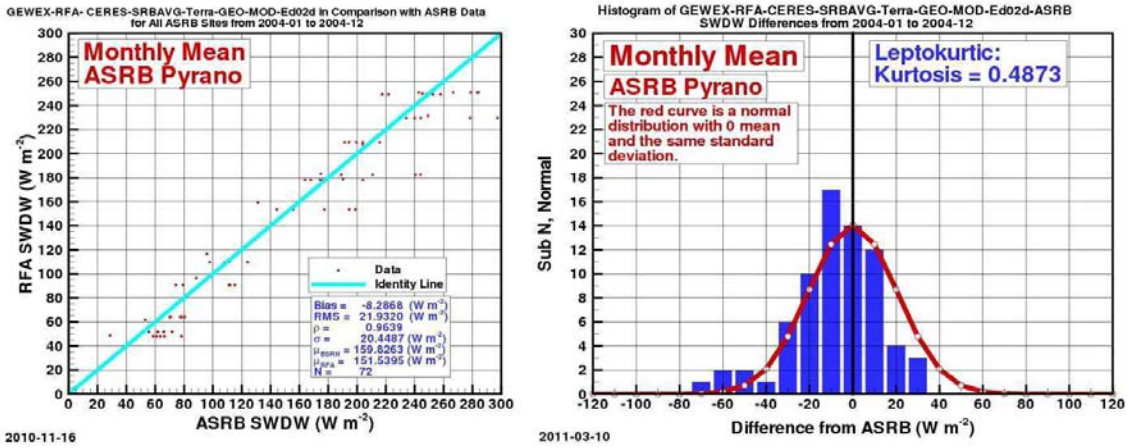

Figure 6.19: *Statistics from comparisons between satellite data set and ASRB shortwave data for the year 2004. The histogram for CERES-SRBAVG-minus-ASRB differences is shown in blue in the right-hand panel. The superimposed red curve is the best-fit zero-mean Gaussian curve. The y-axis label "Sub N" refers to the number of points in a bin.*

Comparison statistics for all of the satellite products are given in *Table 6.15*. In every case, the bias is negative, and, for all but the CERES_SRBAVG and UMD_SRB data sets, quite large (13-31 Wm^{-2}). Nevertheless, the standard deviations fall in the same range as in the earlier comparisons to BSRN and GEBA data (about 20-25 Wm^{-2}), which is a bit surprising given the range of fluxes occurring over the ASRB stations in a single grid box. The pattern of large biases and "typical" random error components suggests that the main problem is that the satellite algorithms do not accurately account for elevation but otherwise perform about as well in the mountains as in other areas.

Table 6.15: *Statistics of GEWEX RFA satellite shortwave data comparison with ASRB data for the year 2004. Bias, root-mean-square difference (RMS), and standard deviation (σ) are all given in Wm^{-2}. The cross correlation is denoted by ρ and N is the number of samples used in the comparison.*

Data Set	Bias	RMS	ρ	σ	N
CERES_SRBAVG_Terra_GEO_MOD_Ed02d	-8.2	21.9	0.964	20.4	72
DLR_ISIS_Ed0	-14.9	25.7	0.963	21.1	72
FORTH_Ed01a	-31.0	37.9	0.958	22.0	72
GEWEX_SRBGSW_Ed281	-20.7	29.0	0.965	20.4	72
GEWEX_SRBQSW_Ed025	-17.1	28.5	0.954	23.0	72
ISCCP_FD_Ed000_010	-13.2	23.1	0.969	19.1	72
UMD_SRB_Ed033	-2.6	24.8	0.954	24.8	72

6.7.2: Longwave Fluxes.

Longwave flux comparison results are presented in *Figure 6.20* and *Table 6.16*. The example plots are for the FORTH satellite data set. The satellite values again occur in discrete steps, but the corresponding ranges in the ASRB values are somewhat smaller than for the SW fluxes, reflecting the fact that downwelling LW surface fluxes vary less with location, altitude, and local topography than SW fluxes do. In addition, almost no bias is seen. These results can be generalized to the other satellite data sets, for which all of the biases (except for ISCCP_FD) are below 6 Wm^{-2}. The standard deviations (8-12 Wm^{-2}) are all lower than for the comparison to BSRN LW fluxes over the longer, but overlapping, CERES time period.

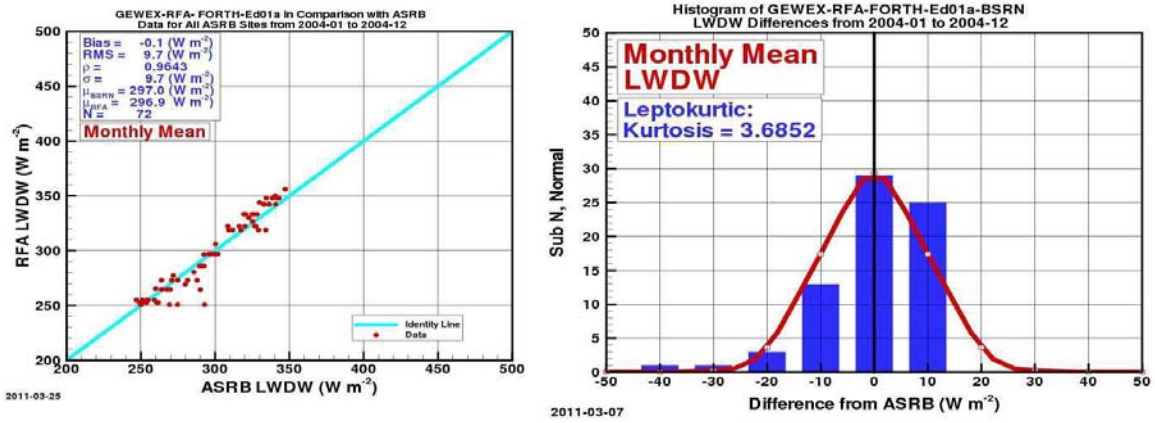

Figure 6.20: *Comparison between the FORTH-Ed01a and ASRB longwave downward fluxes from January 2004 to December 2004.*

Table 6.16: *Statistics from comparisons between the satellite and ASRB longwave data for the year 2004. Bias, root-mean-square difference (RMS), and standard deviation (σ) are all given in Wm^{-2}. The cross correlation is denoted by ρ and N is the number of samples used in the comparison.*

Data Set	Bias	RMS	ρ	σ	N
CERES_SRBAVG_Terra_GEO_MOD_Ed02d	5.5	9.9	0.964	8.3	72
FORTH_Ed01a	-0.1	9.7	0.964	9.7	72
GEWEX_SRBGLW_Ed025	-1.5	9.9	0.958	9.8	72
GEWEX_SRBQLW_Ed025	3.7	12.5	0.956	12.0	72
ISCCP_FD_Ed000_010	10.8	14.5	0.953	9.7	72

6.8: Summary

The satellite-based surface flux data sets in the RFA archive have been evaluated by comparison to direct measurements from around the world. These measurements are part of the Baseline Surface Radiation Network (BSRN), Global Energy Balance Archive (GEBA), University of Oregon Solar Radiation Monitoring Laboratory, and Alpine Surface Radiation Budget collections. It should be noted that, aside from a few BSRN sites and two of the GEBA sites, all of the surface measurements come from stations in the northern hemisphere. This means that the measurements are not globally representative, although they do include stations in a variety of geographic settings (coastal, continental, mountainous, island, polar, and desert locations.)

Comparisons were made between monthly mean surface measurements and the corresponding values from the 2.5° x 2.5° satellite grid cells in which the measurement sites are located. This means that the scales of the measured and satellite-derived fluxes are much different, which decreases the value of the comparisons. Nevertheless, surface measurements provide the best constraint for the satellite values available at this time. Using monthly mean values in the comparisons improves the equivalence of the data by averaging out intra-monthly variations. The data would compare much more poorly at shorter or instantaneous time scales.

1) For comparisons between individual monthly mean satellite-based and in situ observed all-sky shortwave downward fluxes, standard deviations were consistently in the range of 20-25 Wm^{-2} over all data set combinations. Biases, however, were less consistent. The magnitude of the biases between the satellite data and the BSRN and GUOR reference values were less than 10 Wm^{-2}. The exceptions (FORTH vs. BSRN, UMD_SRB and CERES_SRBAVG vs. GUOR) were all close to 15 Wm^{-2}. Nearly all solar flux biases relative to the GUOR reference were positive in sign (i.e., the satellite products suggest that greater solar downward fluxes reach the surface). In contrast, the bias direction was mixed relative to the BSRN reference. All satellite data sets show negative biases relative to the ASRB reference, with solar downward fluxes lower by as much as 30 Wm^{-2}. Nevertheless, the magnitude of the random differences (or standard deviations) relative to the ASRB data were similar to those computed relative to the BSRN or GUOR data. These values may be compared to the uncertainty estimates of 9 Wm^{-2} for the BSRN, 5% for GEBA, 10 Wm^{-2} for the University of Oregon and 3 Wm^{-2} (daily mean) for the ASRB. However, as discussed in more detail in Chapter 5, the meaningfulness of comparisons between temporal averages of point observations and instantaneous large-scale spatial averages from satellites is still a topic of active research.

2) Agreement between satellite-based data sets and surface-observed all-sky shortwave fluxes depended on the geographic setting of the surface stations. Both systematic and random differences were higher in the polar locations of the BSRN, while the biases for island sites were also poor. For the GUOR, which includes no polar sites, coastal and mountainous locations had the worst agreement. Some biases Alpine Surface Radiation Budget network were also large, but this data set only included a year of monthly values.

3) Very different seasonal patterns in agreement were observed for the BSRN and GUOR all-sky SW comparisons. Relative to the BSRN reference, satellite data set biases tended to be more positive during NH summer (more solar fluxes reaching the surface) and more negative during the NH winter (less solar fluxes reaching the surface). Relative to the GUOR reference,

satellite data sets have more negative biases during NH summer. There was no obvious explanation for these differences between the BSRN and GUOR comparisons. Standard deviations relative to both the BSRN and GUOR data were much larger during or towards the end of the NH winter. Seasonal comparisons were not made against the ASRB data because the length of the record provided to the Assessment is too short (2004 only).

4) Ensemble time series of deseasonalized all-sky downward solar flux data from 12 (BSRN) or 30 (GUOR) site locations both showed increasingly negative differences between the satellite and in situ data from 1998 to 2004. However, the anomalies themselves were largely stable. Using a 12-site GUOR ensemble, most of the satellite products did not yield meaningful (95% confidence) trends over the 1984-1999 time period. For GUOR solar fluxes, a statistically significant trend of 0.32 $Wm^{-2}year^{-1}$ was calculated, while for the ISCCP SW data, a trend of -0.19 $Wm^{-2}year^{-1}$ was found. Given the equivocal nature of these results, it is difficult to draw conclusions about the linear changes in downward solar fluxes over this time period.

5) Comparisons between clear-sky downward solar fluxes estimated from BSRN and satellite data yielded larger biases (-4.7 to -12.6 Wm^{-2}) and smaller standard deviations (11 to 14 Wm^{-2}) than the all-sky comparisons.

6) All-sky downward longwave flux comparisons of the satellite data sets were only possible with respect to BSRN and ASRB network data. Both biases and standard deviations were smaller than those for the solar downward fluxes, with biases less than 10 Wm^{-2} in magnitude and standard deviations in the range of 8 to 18 Wm^{-2}. The ISCCP-FD data was an outlier in these comparisons, with the largest biases as well as standard deviations greater than 20 Wm^{-2} relative to BSRN reference data. However, these discrepancies can be explained by changes in the temperature and water vapor profile data used as input to the ISCCP LW flux algorithms over time. These changes are evident in the large (~7 Wm^{-2}) increase in both bias and standard deviation for the ISCCP data relative to BSRN after 2000. Smaller changes are also evident in the other satellite products after 2000. However, all of the products stretching back beyond 2000 use cloud information produced by ISCCP, so are likely influenced by the same problem to varying degrees. The standard deviations for comparisons to the ASRB were consistently lower than for the BSRN data, generally less than 10 Wm^{-2}. The GEWEX-SRBQLW product had a slightly higher value of 12 Wm^{-2}. These statistics can be compared to the quoted uncertainties of 6 Wm^{-2} in the BRSN monthly mean downward longwave data and 3 Wm^{-2} (daily) for the ASRB measurements, again with caveats concerning the differences between the scales of the observations and satellite-based products.

7) Surface type played a less important role in the longwave comparisons. Disagreement was large (biases of 4-34 Wm^{-2}) at desert sites for the ISCCP and GEWEX-SRBGLW products but otherwise small or mixed for other conditions. Standard deviations were smallest for island and coastal sites.

8) All-sky longwave biases relative to the BSRN data tended to be more positive in the NH summer and more negative during the NH winter. This bias pattern is opposite that for the SW fluxes. Standard deviations were generally found to be largest during the NH winter, which is consistent with the SW fluxes.

9) The standard deviations between the all-sky longwave deseasonalized satellite-based and observed 12-site BSRN ensemble time series were below 3 Wm^{-2} for all products except ISCCP, for which the anomaly differences showed a distinct reversal from negative to positive in the middle of 1999. No trend estimation was performed for the LW data because the available record was only 13 years long.

10) The random and systematic differences between the BSRN and satellite-based clear-sky longwave downward fluxes fell in the same range as the all-sky values.

11) Comparisons between satellite products and measurements from the Alpine Surface Radiation Budget network illustrated that a range of fluxes can be measured over a small mountainous area, since in this case five measurement sites fell within a single satellite grid box. This implies that some of the observed differences between the satellite and observed fluxes are likely related to the location of the surface stations within the satellite grid cells.

Chapter 7:
Vertical Radiative Flux Divergence in the Atmosphere

E. Raschke, S. Kinne and Y.-C. Zhang

Abstract:

Differences between radiative net-fluxes (downward minus upward) at TOA and at surface allow estimates of the atmospheric radiative flux divergence, capturing the solar atmospheric absorption at solar wavelengths and the infrared atmospheric cooling at infrared wavelengths. These differences show regional patterns which are related to the location and mean height of cloud fields. In addition to all-sky properties, investigations at clear-sky conditions allow to stratify contributions from aerosol, trace-gases in the environmental framework of surface properties and atmospheric state, from contribution due to clouds. The solar absorption is primarily driven by the abundance of water vapor, aerosols but only weakly by clouds. The infrared divergence (or atmospheric cooling) is strongly influenced by trace-gases and surface properties. The (negative) infrared divergence is larger in magnitude than the (positive) solar divergence. Similarly, also the diversity among the three investigated data-sets of ISCCP, SRB and CERES much larger for the infrared diversity. When comparing contributions to the diversity from the representation of clouds and non-cloud ancillary data, the non-cloud ancillary data usually dominate the all-sky diversity. This indicates that the ancillary data in the investigated data-sets are in relatively poor shape. Estimates of the total flux divergence reveal large (up to 60 Wm^{-2}) differences between the three climate data sets and also to Median Model. More reliable estimates for both solar, infrared and total atmospheric divergence require more accurate and more consistent ancillary data.

7.1: Introduction

Gradients in net radiation fluxes within the atmosphere and at its boundaries force a manifold of dynamical processes. In that context, local differences between radiative net-fluxes as the difference between downward and upward hemispheric fluxes at the top of the atmosphere (TOA) and at the Earth's surface provide atmospheric column information on available radiative energy for atmospheric dynamics. However, these **divergences** (defined here with signs opposite to the use in classical mathematics), as difference [TOA minus surface] of differences [down minus up] (often similar in magnitude), are highly susceptive to already minor uncertainties introduced by ancillary data or by the representation of clouds. In this assessment we consider results on the column-integrated vertical divergence of solar (shortwave) and infrared (longwave or terrestrial) radiation, which were derived from the radiation products of the projects of ISCCP, SRB and CERES. The solar divergence is positive and describes an atmospheric energy gain to the system. Simply put, the solar divergence captures the solar absorption in the atmosphere. The terrestrial divergence is negative as it describes an atmospheric energy loss or cooling. The losses are reduced with an increasing greenhouse effect (e.g. by high clouds, see *Chapter 9.1*) and are increased by re-radiation to the surface (e.g. by low clouds). The term divergence is used here traditionally with opposite sign to the classical definition in mathematics.

We demonstrate that solar and infrared divergence data contain uncertainties which can be traced back in part to the existing diversity in ancillary data (which are already introduced in previous chapters). First multi-annual ISCCP global maps are introduced to illustrate amount, sign and global distribution and vertical distributions of solar and infrared divergence. Then

difference plots are applied to examine variations. Zonal anomalies in Hovmoeller diagrams reveal that actual trends and events are often contaminated by artifacts in ancillary data. To focus in on some of these artifacts annual global maps are used to identify regions with larger problems. Finally, maps of seasonal differences between ISCCP and CERES and between SRB and CERES identify regions of diversity in solar, infrared and total flux divergences and their sources are examined with the stratification into non-cloud and cloud contributions.

7.2: Current Understanding (on the Basis of ISCCP Data)

Our present knowledge on the radiative flux divergence within the atmosphere is primarily based on simulations with climate data and various numerical studies. *Webster and Stephens (1984)* illustrated in an impressive tutorial way the influence of atmospheric water vapor and of the vertical location of clouds on the shape of vertical radiative divergence profiles. Many other numerical studies and direct airborne measurements indicate that lower cloud bases might even be radiatively heated from below causing a destabilization. On the other side it also could be shown that high concentrations of absorbing aerosols can lead to a stabilization of the lower atmosphere. Data-products tied to satellite sensors allowed to examine diversity in long-term trends. For ISCCP-FD and GEWEX-SRB monthly data of more than 20 consecutive years (1984-2004) were analyzed, while the examined CERES (SRBAVG-GEO) monthly data covered only a period of 4 years (Mar.2000 to Feb.2004). The interaction of solar radiation with absorbing matter heats the atmosphere. Aside from trace-gases also clouds (and aerosol usually as well) absorb solar radiation. However, if clouds (or aerosol) add to the clear-sky columnar solar heating by trace-gases depends largely on their altitude placement (as the cloud reflection will reduce interactions or solar energy with trace-gases below the cloud). In the infrared the atmospheric composition acts as a heat sink and local contributions by clouds depends on cloud altitude and cloud optical thickness. Sample data by ISCCP for solar and infrared annual divergence maps and associated cloud radiative effects are illustrated in *Figures 7.2.1 and 7.2.2*. We use here the ISCCP data since at the time of writing they were apparently best documented.

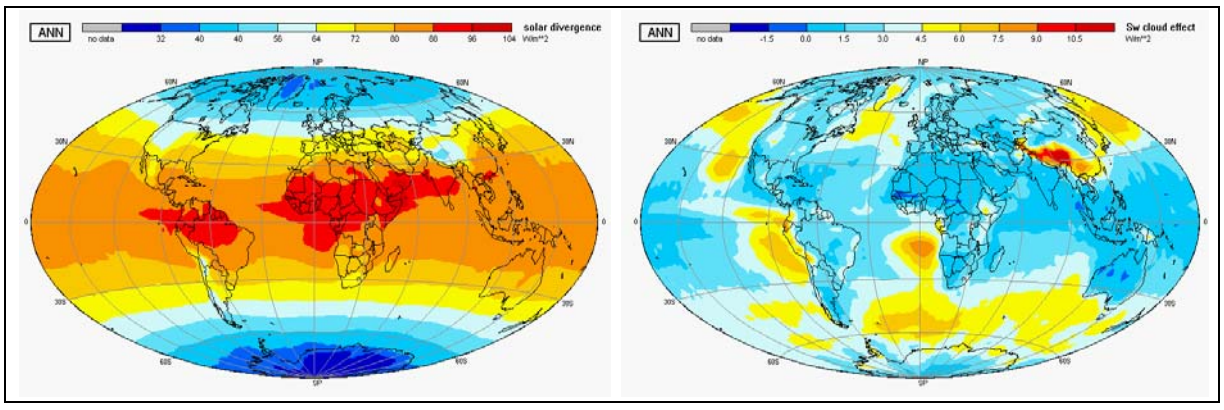

Figure 7.2.1: *Illustration for the atmospheric solar radiative net-flux divergence [atmospheric solar absorption] (left panel) and contributing cloud radiative effects (right) with the aid of annual averages of ISCCP-data for the period 1991 to 1995 (Raschke et al., 2005).*

All-sky values for the solar absorption are positive. All-sky annual solar absorption over the tropics reaches values of up to 90 Wm^{-2}. However, cloud effects are relatively small and display for ISCCP enhancements, except for a few regions with high convection.

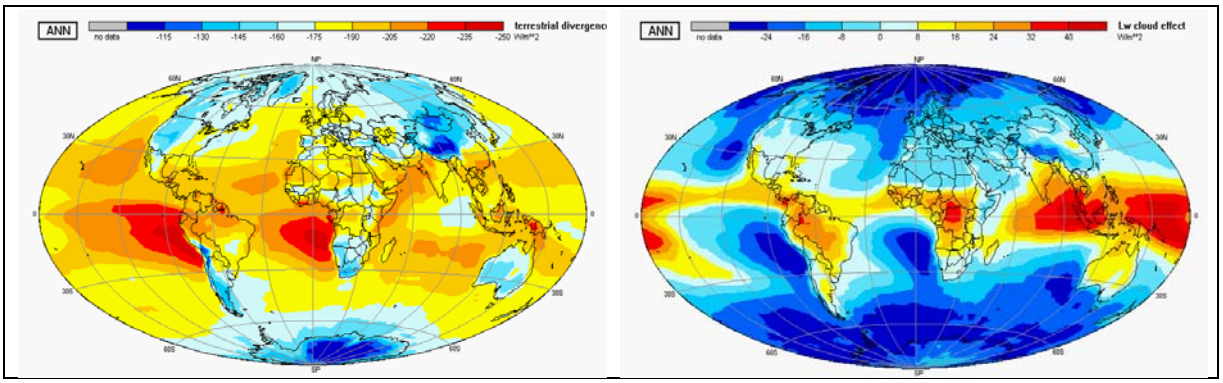

Figure 7.2.2: *Illustration for the atmospheric infrared (or terrestrial) radiative net-flux divergence [solar atmospheric cooling] (left panel) and contributing cloud radiative effects (right) with the aid of annual averages of ISCCP-data for the period 1991 to 1995 (Raschke et al., 2005). Note the infrared divergence is negative.*

All-sky values for the infrared flux divergence are negative as the atmosphere looses radiative energy to space and ground. Clouds reduce the negative infrared flux divergence over (yellow to red) regions with high (and cold) cloud tops and make the infrared flux divergence more negative over (dark blue) regions with low (and warm) cloud tops. Although impacts of clouds are relatively small, they are main-modulators. Hereby, the accuracy of cloud effects depends strongly on the altitude representation of clouds, which should be better constrained with new recent capabilities by active remote sensing from space by *Cloudsat* and *Calipso* (e.g. L'Ecuyer et al., 2008; Stephens et al., 2002). These new active radar and lidar sensors allow insights into vertical structures for aerosol and clouds and should constrain assumptions made in data-sets of passive sensors to yield more consistent are more accurate radiative flux data at the surface and in the atmosphere.

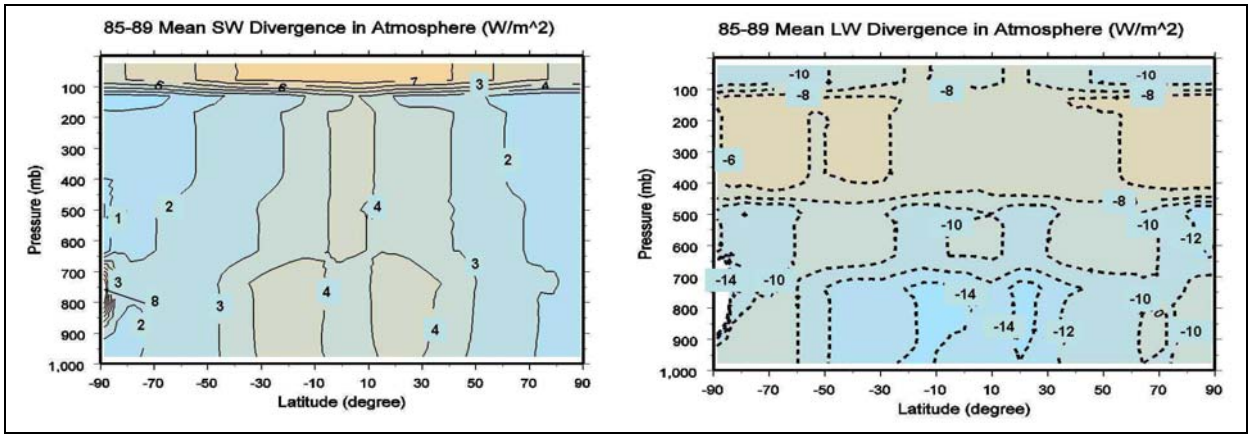

Figure 7.2.3: *Annual (1985-1989) zonal means of differential atmospheric divergence profiles for the solar (left) and infrared (right) divergence of ISCCP data in Wm^{-2}. For solar data blue areas are for < 2 Wm^{-2} and brown areas for > 4 Wm^{-2}. For the infrared blue areas are for < -14 Wm^{-2}, brown areas are for > - 6 Wm^{-2}. The values are based on 20 atmospheric layers. (Source: Y-C Zhang, 2009).*

Zhang et al. (2004, 2006) estimated "vertical profiles" of the net heating by solar and net cooling by infrared radiation, for the four altitude ranges (1000 to 680 hPa, 680 to 440 hPa, 440 to 100 hPa and 100 to 0 hPa) using the ISCCP cloud products and other ancillary data. *Figures*

7.2.3 show 5-year (1985-1989) means of zonally-averaged, differential atmospheric divergence profiles for solar and terrestrial radiation based on ISCCP data (Zhang et al., 2004).

The solar divergence (left panel) demonstrates that all atmospheric layers are heated by solar flux with a maximum in tropical upper troposphere and lower stratosphere, while minimum appearing in the polar regions through all tropospheric layers. By contrast, the infrared divergence (right panel) shows that all atmospheric layers are emitting infrared fluxes (negative values) with maximal heat loss (< -14 Wm^{-2}) at tropical lower troposphere and minimal heat loss of less than about 6 (≥ -6 in the figure) Wm^{-2} in the upper troposphere in Polar Regions. The corresponding cloud effects for atmospheric divergence profiles are presented in *Figure 7.2.4.*

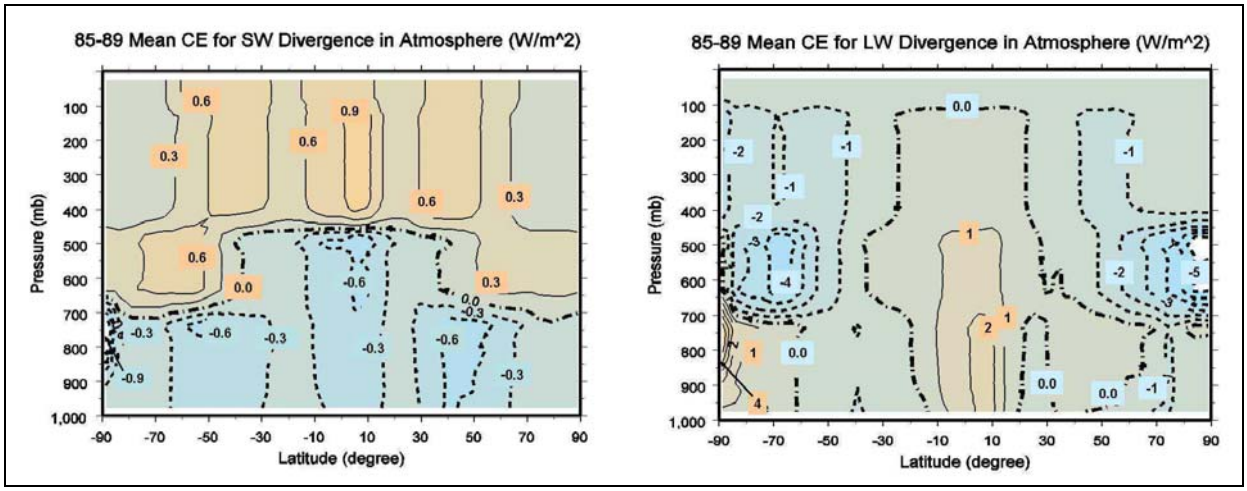

Figure 7.2.4: *Annual (1985-1989) zonal means of the cloud radiative effect (CRE or CE in figures) on the divergence of solar (left) and infrared (right) divergence of ISCCP data. (Source: Y-C Zhang, 2009). Brown areas describe an increase of absorption by clouds, while blue areas describe a decrease by clouds.*

The reflection of solar radiation at bright surfaces (e.g.: clouds or snow) increases the radiative heating above them. On the other hand clouds prevent significant fractions of solar radiation to reach altitudes below the cloud base where the potential for solar absorption is reduced. Thus, solar atmospheric heating above clouds should and is larger and solar atmospheric heating below clouds should and is lower. Largest reductions occur in mid-latitudes and tropics, where solar absorption is strongly driven by atmospheric aerosol. The sign of the integral vertical value depends on the cloud top altitude and is generally positive and especially so in regions with low cloud tops, as shown in *Figure 7.2.1*. Cloud altitudes, and here both cloud top and cloud base, influence the cloud impact on the infrared divergence. The largest positive values (or reductions to the clear-sky infrared divergence) appear in the lower tropical troposphere, whereas the largest negative values (or additions the clear-sky infrared divergence) occur in middle atmosphere in both polar regions. This horizontal cooling gradient suggests that clouds enhance the mean Hadley circulation. The feedback between these radiative effects on convection and the large scale circulation can produce more complicated responses (*Rind and Rossow, 1984*).

7.3: Influence of Uncertainties in Ancillary Data on Time Series

In *Chapters 3.4 and 4.5* we already identified several inconsistencies in ISCCP and SRB results which stem from inconsistencies in several "ancillary" data, describing the radiative transfer properties of the atmosphere (temperature, water vapor content, aerosols and clouds) and

of the surface (reflectance for solar radiation and skin temperature). These will also be visible in time series of the radiative flux divergence as demonstrated in this chapter. Further, the different Pinatubo aerosol data in ISCCP (e.g. Rossow and Schiffer, 1995) and SRB (Stackhouse et al., 2000) and the different handling of the El-Nino cloud anomaly during the year 1998 can be seen. Also some errors in the data handling may become visible in these radiation products. To demonstrate temporal changes in ISCCP and SRB 21-year data records (1984-2004) de-seasonalized zonal time series (in Hovmoeller diagrams) were chosen. The reference period in *Figures 7.3.1 to 7.3.3* covers four years (1985-1988).

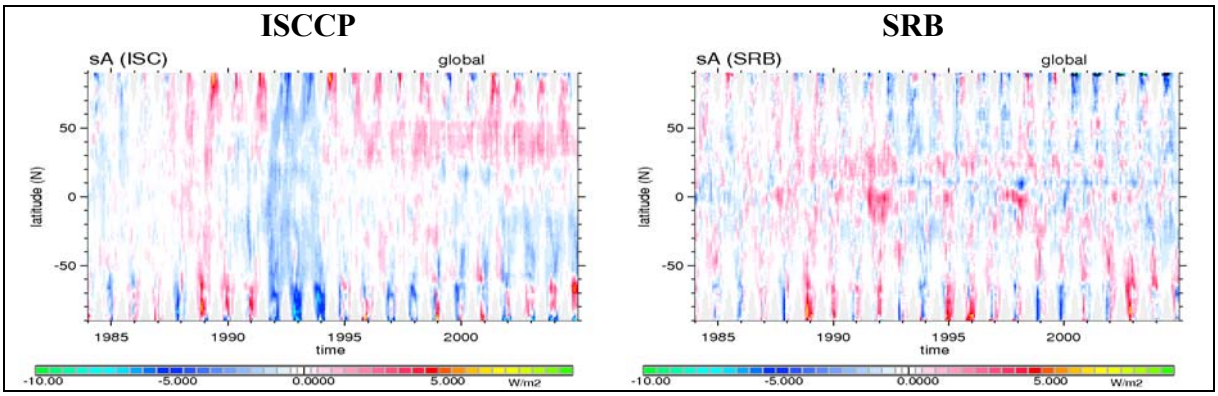

Figure 7.3.1: *Monthly de-seasonalized zonal anomalies of the vertically integrated solar divergence from January 1984 to December 2004 at all-sky conditions. The reference period covers 4 years: January 1985 to December 1988. Units are Wm^{-2}. Note the different signs with the occurrence of enhanced stratospheric aerosol following the Mt.Pinatubo in ISCCP and SRB results between 1992 and 1994. Results for clear skies are provided in the Appendix C.7.*

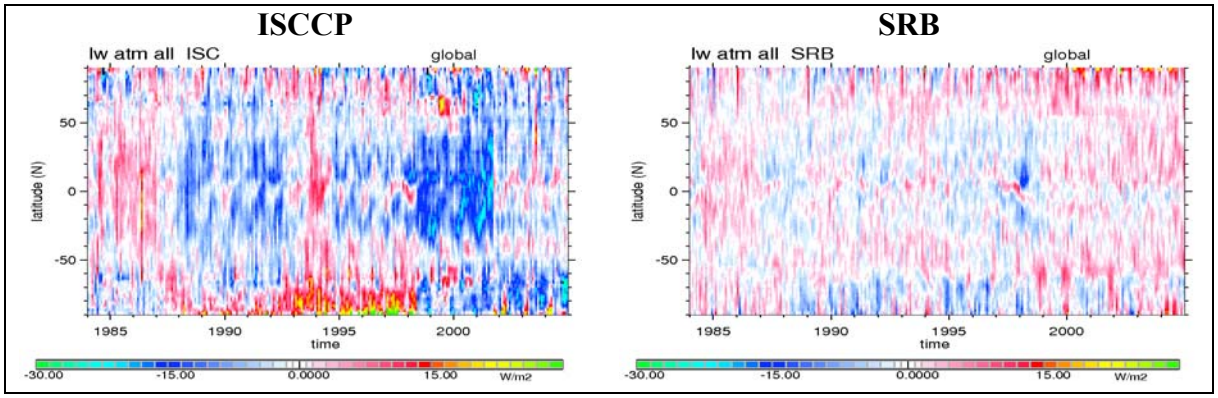

Figure 7.3.2: *Monthly de-seasonalised zonal anomalies of the vertically integrated infrared divergence from January 1984 to December 2004 at all-sky conditions. The reference period covers 4 years: January 1985 to December 1988. Units are Wm^{-2}. Since the terrestrial divergence is negative, blue colors indicate an increased divergence and red colors a decreased divergence. Results for clear skies are provided in the Appendix C.7.*

The patterns in these figures illustrate major "anomalies", associated with either natural events (e.g. response after the Mt.Pinatubo eruption in summer of 1991) or (even worse) with artifacts (e.g. a sudden increases of surface temperatures from September to October of 2001). Different Mt.Pinatubo responses for the two data-sets indirectly indicate the propagation of

ancillary data (e.g. representation of solar albedo, aerosol and cloud) into these atmospheric divergence data.

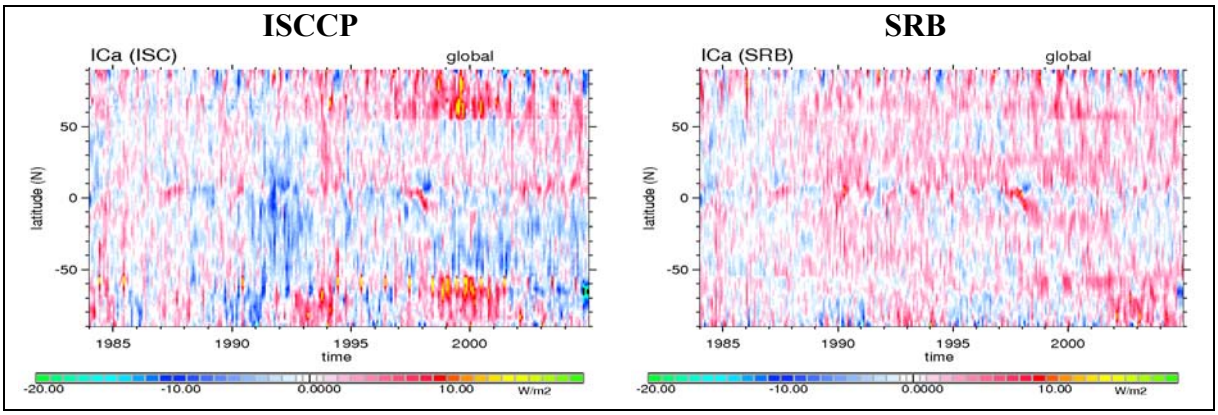

Figure 7.3.3: *Monthly zonal de-seasonalized anomalies of the cloud radiative effect (CRE) on the vertically integrated infrared divergence from January 1984 to December 2004. The reference period covers 4 years: January 1985 to December 1988. Since the terrestrial divergence is negative, blue colors indicate an increased divergence and red colors a decreased divergence.*

For the absorbed solar radiation (*Figure 7.3.1*) the monthly anomalies range between about ± (2.5 to 5) Wm^{-2}, often with opposite signs among the two data-sets (ISCCP negative; SRB: positive). The patterns for clear-sky *(see Appendix D.7)* and all-sky conditions are similar due to relatively weak modifications by clouds, because of their two opposing effects: Clouds shield lower tropospheric absorption by aerosol and water vapor, while on the other hand add absorption by clouds and increased absorption above clouds as a large fraction of solar radiation is reflected back to space. ISCCP-data consider solar reflection by Mt.Pinatubo volcanic aerosol, which resulted in the expected reduction of the solar absorption. In SRB-data the Mt.Pinatubo effect is poorly covered as impacts on solar absorption remain small.

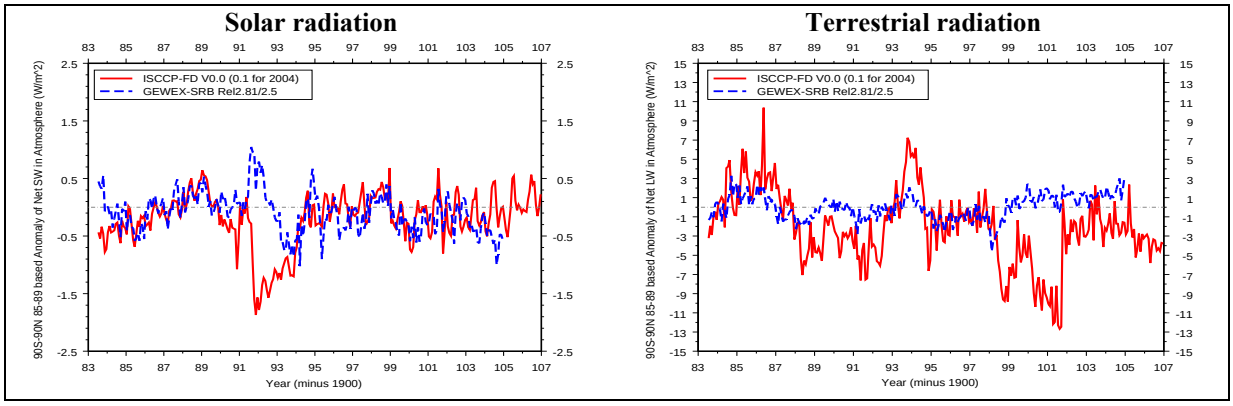

Figure 7.3.4: *Monthly global means of anomalies (1985-1989) of column-integrated solar (left) and infrared (right) divergence from 1983 to 2006 (left) for ISCCP (red) and SRB (blue) data.* ***(Source: Y-C Zhang, 2009).***

For the terrestrial divergence (*Figure 7.3.2*) ISCCP-data displays a lowering of the infrared divergence for the tropics over time, resulting in a minimum terrestrial divergence from 1998 to fall 2001, when the infrared divergence in the tropics suddenly increased by about 15 Wm^{-2} due to a sudden increase in surface temperature ancillary data. Even influence of this

inconsistency is so large that even the cloud effect anomaly (*Figure 7.3.3*) is influenced. Also, note that spatial pattern for ISCCP and SRB cloud effects are often opposite in sign and amplitudes are larger than for solar radiation.

Temporal anomalies for globally averaged, column-integrated atmospheric solar and infrared divergences are presented in *Figures 7.3.4*. For solar flux, although ISCCP and SRB have general agreement on trend for most of the time, they have substantial difference over Mt.Pinatubo effects. For the terrestrial radiation, they have wider discrepancies, particularly over 98-01 period that may be caused primarily by FD's input of TOVS temperature profiles (Zhang et al., 2006). Thus some trends in the ISCCP data are in reality apparent trends introduced by auxiliary data, which have been used when processing the sensor data.

7.4: Inter-Annual Variations of Regional Annual Anomalies

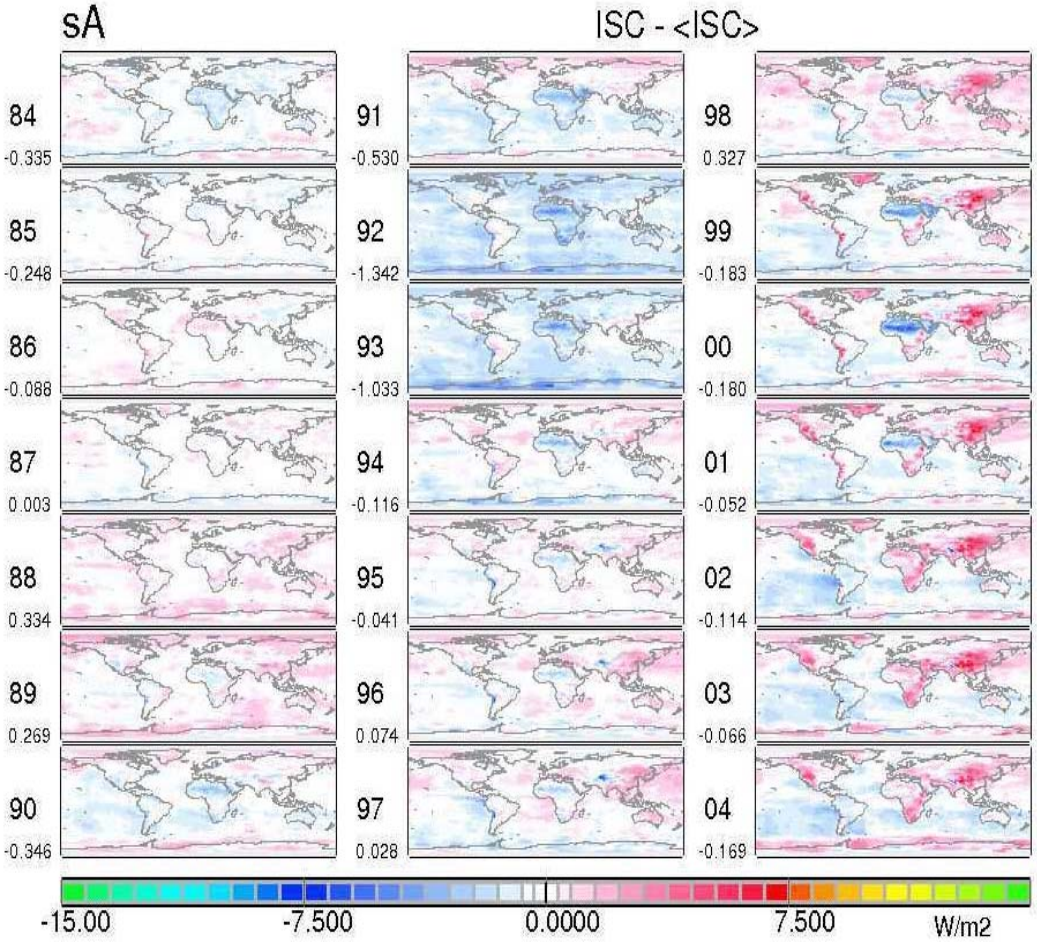

Figure 7.4.1a: *Inter-annual variation of anomalies of the integral* ***vertical divergence of solar radiation*** *(or atmospheric solar absorption) by* ***ISCCP*** *for all-sky conditions. Reference period: 1985-1988. Numbers left to the panels below the labels are global averages*

Maps of the inter-annual variation of annual averages for solar and infrared divergence are presented in *Figures 7.4.1a & b and Figures 7.4.2a & b* in terms of anomalies with respect to the 1985 to 1988 (four year) average. The anomaly presentation in these figures helps to identify regions strongly affected by inter-annual variations and trends.

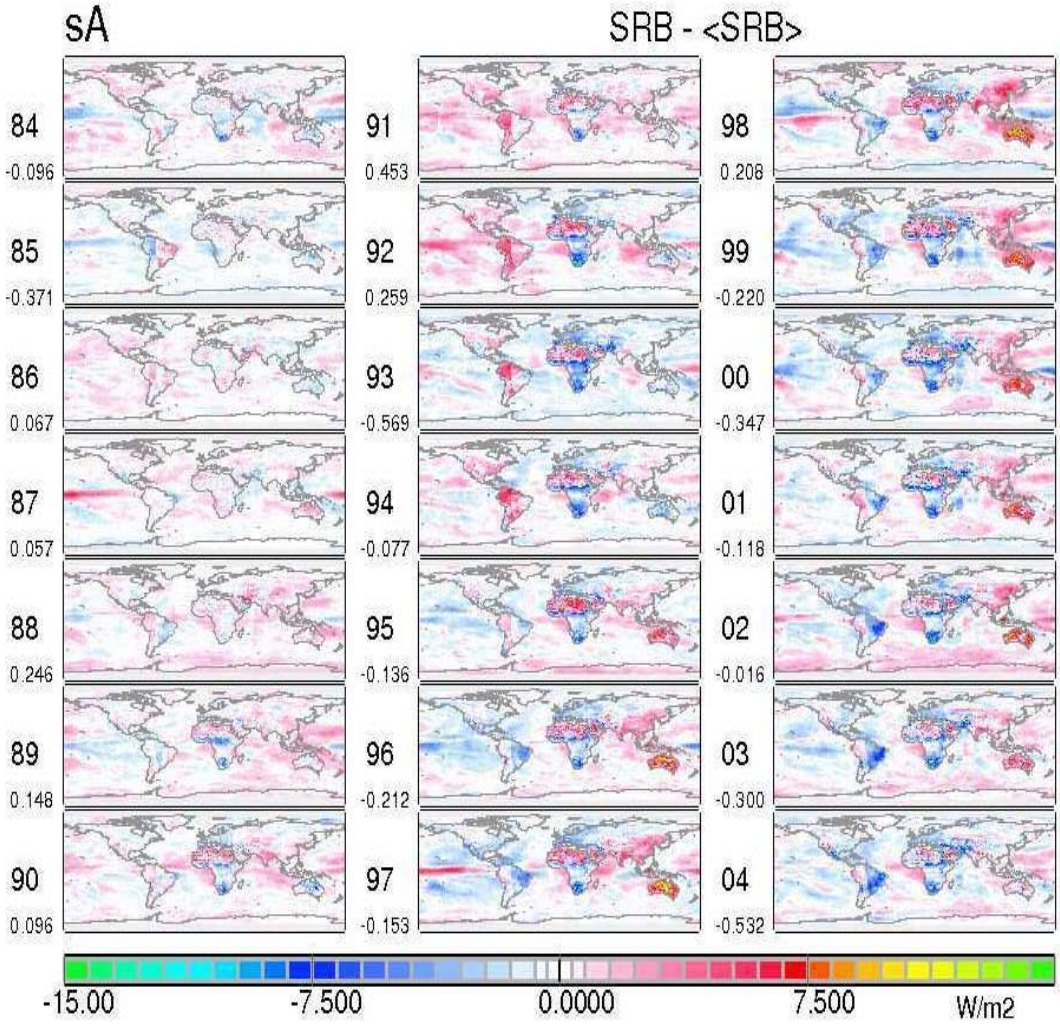

Figure 7.4.1b: *Inter-annual variation of anomalies of the integral vertical divergence of solar radiation (or atmospheric solar absorption) by* ***SRB*** *(dn) for all-sky conditions. Reference period: 1985-1988 Numbers left to the panels below the labels are global averages*

For the solar divergence *(Figure 7.4.1)* annual anomalies range between ±5 Wm^{-2} for both data sets (ISCCP and SRB). Again, Mt.Pinatubo stratospheric aerosol fails to reduce solar absorption in the SRB data. In the SRB data a persistent negative anomaly develops in 1989 over the southern tip of Africa and is later accompanied by another anomaly over eastern Brazil. Both, ISCCP and SRB, show a positive anomaly from 1995 to about 2003 over eastern Asia and Australia.

For the infrared divergence *(Figure 7.4.2)* anomalies are many times larger than for the solar divergence and especially for the ISCCP data strongly linked to temperature anomalies in the ancillary data (see *Chapter 3.4*, *and Figure 7.4.2*). The annual anomalies show that the lowering of the infrared divergence in the ISCCP data until 2001 mainly occurred over East-Asia and the western Pacific. SRB data display a weak tendency for a strengthening of the infrared divergence, with maxima developing after 2001 over African and Asian desert regions. In contrast, SRB-data display an intermittent (1995-2001) weakening of the infrared divergence over Australia.

Clearly, inter-annual variations can only be trusted if it can be assured that no (temporal varying) artifacts are introduced by in ancillary data, that is clouds, aerosol and surface properties as well as atmospheric state data. Thus, all input data time-series need to be carefully reviewed with respect to accuracy and consistency. The investigated divergence data-sets are strongly influenced by deficiencies in ancillary data, which at least complicates the identification of potential trends.

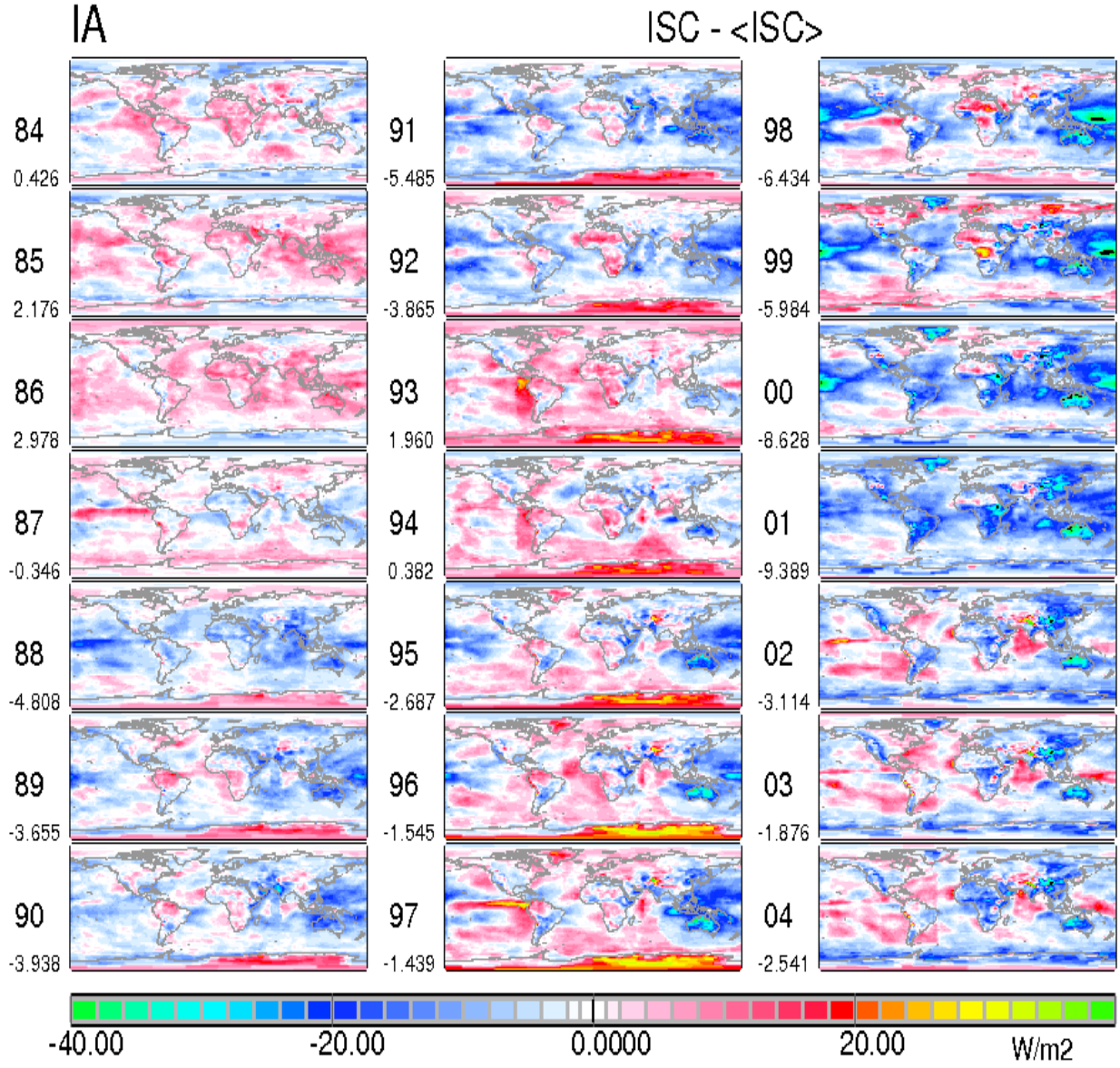

Figure 7.4.2a: *Interannual variation of anomalies of the integral vertical divergence of* ***terrestrial longwave radiation*** *by* ***ISCCP*** *for all-sky atmosphere. Reference period: 1985 to 1988. Since the terrestrial divergence is negative, bluish colors mean an increased divergence and red colors a decreased divergence. Numbers left to the panels below the labels are global averages.*

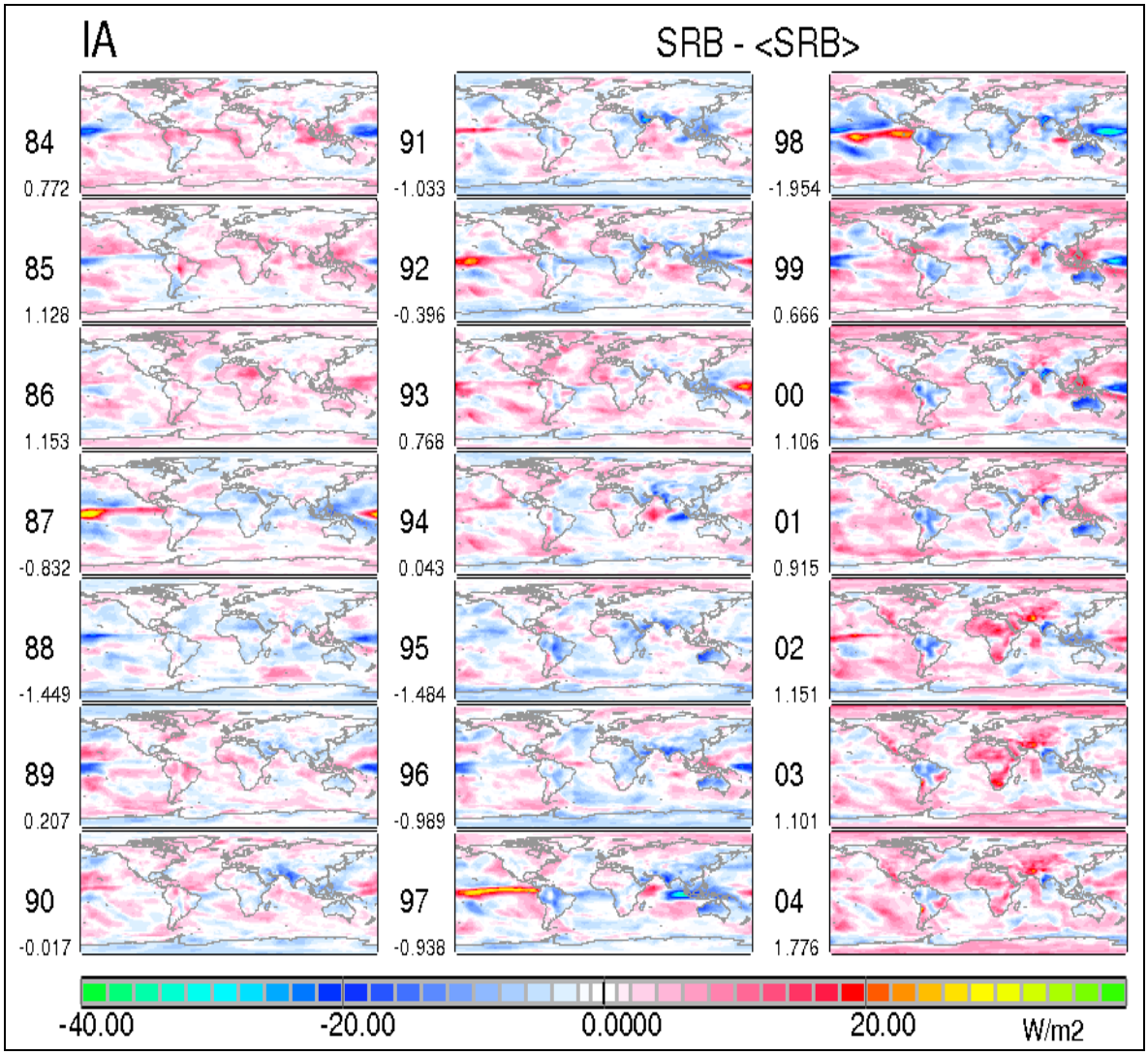

Figure 7.4.2b: *Interannual variation of anomalies of the integral vertical divergence of* ***terrestrial longwave radiation*** *by* ***SRB*** *for all-sky atmosphere. Reference period: 1985 to 1988. Since the terrestrial divergence is negative, bluish colors mean an increased divergence and red colors a decreased divergence. Numbers left to the panels below the labels are global averages.*

7.5: Seasonal Variations of Differences of ISCCP & SRB to CERES

In this section multi-annual seasonal averages for the solar and infrared (radiation flux) divergences are compared among three data-sets: ISCCP, SRB and CERES. The CERES-data refer to the 4-year period (March 2000 to February 2004), whereas ISCCP-data and SRB-data refer to the 1984-1995 period, to avoid complications introduced by inconsistencies in (ancillary) surface temperature. In order to separate impacts by different ancillary data, first clear-sky data are compared (to demonstrate the impact of aerosol and surface properties), then the cloud-effect are presented (to demonstrate the impact of clouds), before finally all-sky comparison are conducted. All subsequent plots in this chapter are prepared to show seasonal maps of absolute values for CERES and then seasonal difference maps of ISCCP with respect to (minus) CERES and of SRB with respect to (minus) CERES.

7.5.1: Solar Divergence (or: the solar atmospheric heating)

Multi-annual seasonal clear-sky solar divergence or solar atmospheric absorption maps and difference maps are presented in *Figure 7.5.1*.

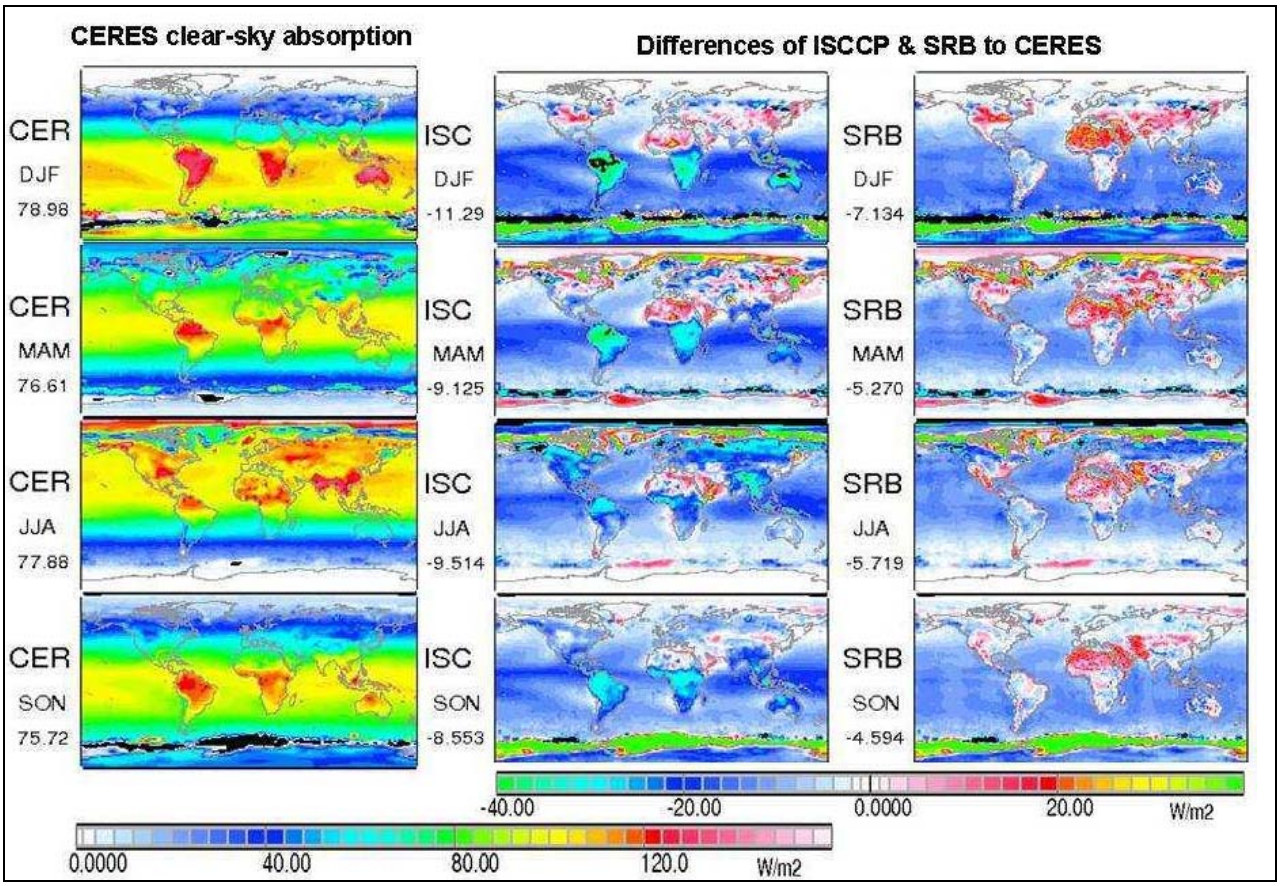

Figure 7.5.1: *Multi-annual seasonal* ***clear-sky solar absorption*** *by CERES data (left) and differences of ISCCP & SRB to CERES. Data of CERES are from the period March 2000 to February 2004, those of ISCCP and SRB are for 1985 to 1995 period. In the difference panels negative number (in blue) indicate regions where ISCCP or SRB absorb less solar radiation than CERES, with black colors indicating smaller absorption in excess of 30 Wm^{-2}. Positive numbers in the difference plots (in red and yellow) indicate regions where ISCCP or SRB absorb more solar radiation than CERES, with bright green colors indicating stronger absorption in excess of 30 Wm^{-2}. Numbers left to the panels below the labels are global averages.*

Clear-sky solar absorption is caused by aerosol and trace-gases, with the largest diversity coming from aerosol. CERES-data demonstrate solar absorptions between 0 and about 130 Wm^{-2} (black patches indicate errors, as negative values are impossible). The solar absorption is strongly related to the available sun-light, the presence of absorbing aerosol and the amount of column atmospheric water vapor. Difference plots indicate that ISCCP and SRB have weaker clear-sky solar absorption over (especially southern) oceans by about 15 Wm^{-2}. ISCCP-data have over southern hemispheric continental regions, especially during summers, much weaker solar absorption than both CERES and SRB. And both ISCCP and SRB have stronger solar

absorptions over continental tropics than CERES. Maximum local diversities among the different data-sets are about a quarter of the average.

Seasonal cloud-effects on solar absorption maps for CERES and data-set difference maps are presented in *Figure 7.5.2*.

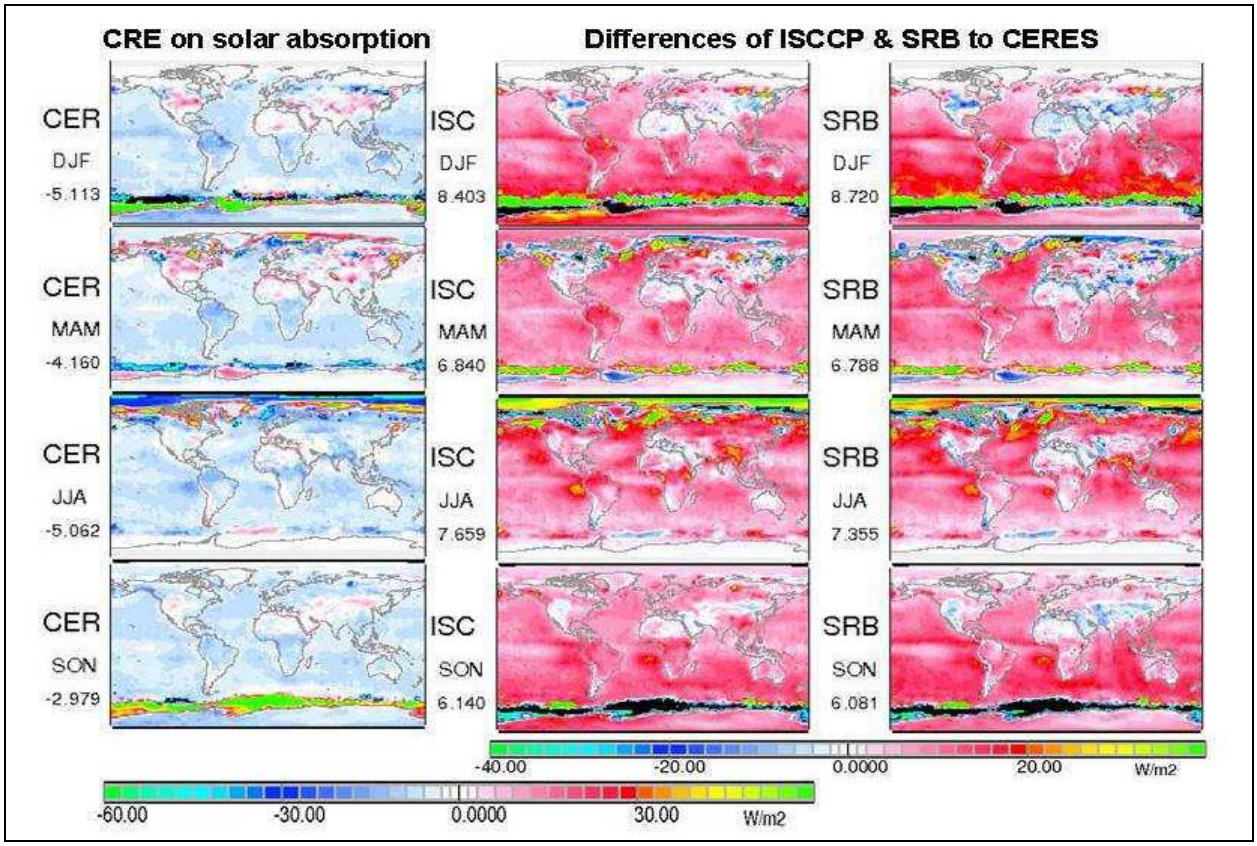

Figure 7.5.2: *Multi-annual seasonal* ***cloud radiative effects on the solar absorption*** *by CERES (left) and differences of ISCCP & SRB to CERES. Data of CERES are from March 2000 to February 2004 period, those of ISCCP and SRB are from 1985 to 1995. Note: CERES clouds reduce the solar absorption by about 5 Wm^{-2}. Numbers left to the panels below the labels are global averages.*

CERES cloud-effects do surprise with a solar absorption decrease (by about 5 Wm^{-2}). This is possibly due to higher altitude placement of clouds. In contrast, cloud-effects in ISCCP and SRB suggest a small increase in solar absorption, as does global modeling. CERES also displays a high solar absorption artifact over Antarctic oceans during summer to causes large deviations with respect to ISCCP and SRB. As this artifact does not appear in the all-sky data, it is believed that in those regions, due to persistent cloud cover, CERES is unable to provide any useful clear-sky data in those regions. Between ISCCP and SRB the strength and global distribution of seasonal cloud-effects is quite similar, as it should be as SRB applies the ISCCP cloud data. When comparing local variability among the data-sets, impacts from the diversity in the aerosol representation (clear-sky) are on average larger than impacts from the diversity in the cloud representation.

Adding clear-sky and cloud-effect maps yields the all-sky maps. The resulting multi-annual seasonal all-sky solar absorption maps and solar absorption difference maps are presented in *Figure 7.5.3*.

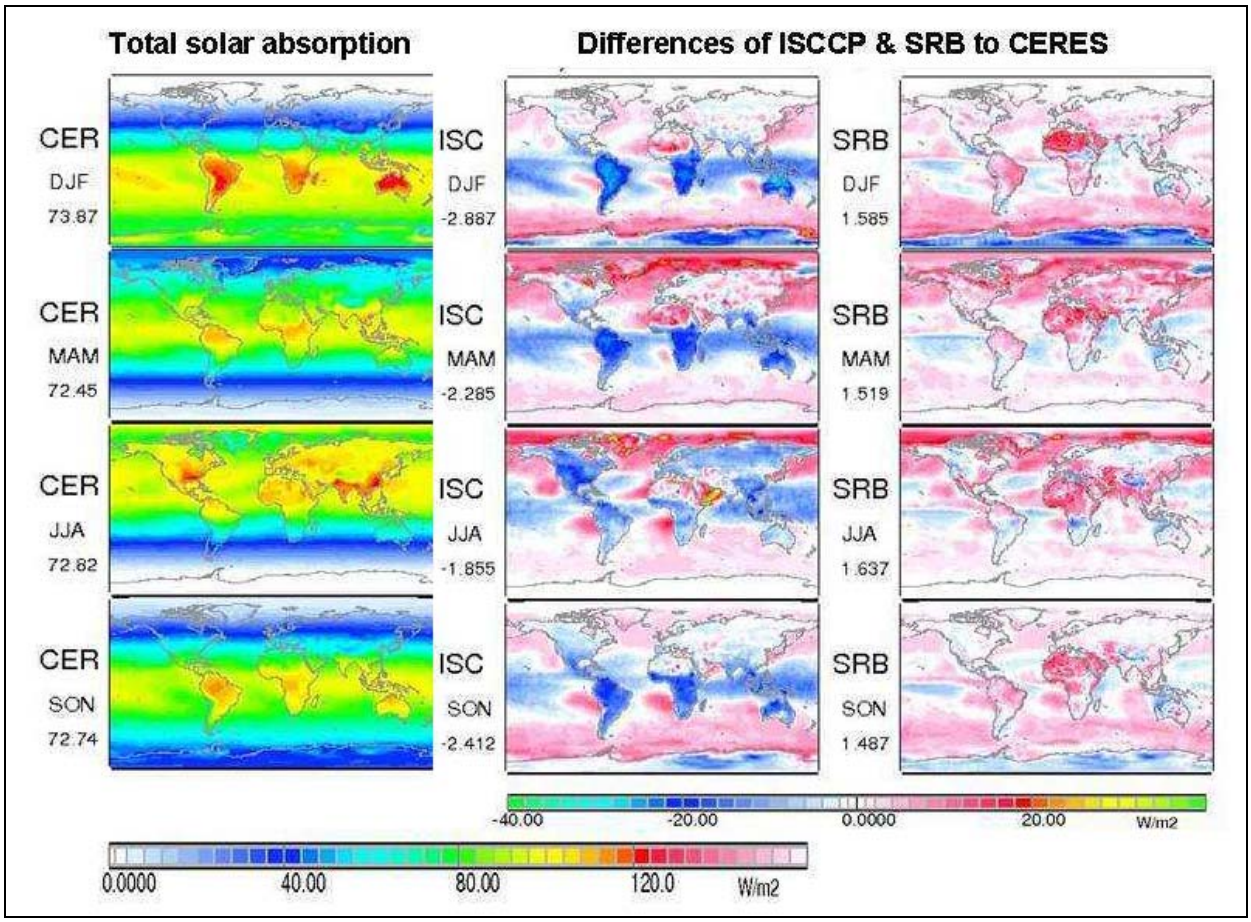

Figure 7.5.3: *Multi-annual seasonal* ***all-sky solar absorption*** *by CERES data (left) and differences of ISCCP & SRB to CERES. Data of CERES are from the period March 2000 to February 2004, those of ISCCP and SRB are for 1985 to 1995 period. In the difference plots smaller solar absorption compared to CERES occurs for negative (blue) values and stronger solar absorption for (red) values Relative differences can amount to 15 to 20% of the flux value. Here the CERES results are purposely used as reference, since hey are free of traces due to data from geostationary satellites. Numbers left to the panels below the labels are global averages.*

All-sky solar absorption ranges between about 0 and 120 Wm^{-2} and absorption is usually higher over continents (e.g. near aerosol sources) that over oceans for the same latitude. ISCCP have over the tropical continents lower values (although not anymore quite as low as for clear-sky condition) and larger values over the oceans. Continents dominate the solar values, which are higher for clear than for all-sky conditions.

The all-sky diversity for the solar absorption among the different data-sets usually amounts to about 15 of the total solar absorption, and interestingly it often smaller than the diversity for clear-sky solar absorption, as the clouds representation at times partially compensates. Since the aerosol and surface ancillary data are applied, when retrieving the cloud properties, it cannot be ruled out that the cloud-properties are chosen such as to compensate for (aerosol and surface) ancillary data, as validation usually occurs for all-sky conditions. ISCCP certainly provides an example since ISCCP all-sky deviations over tropical continents are smaller than at clear-sky conditions.

7.5.2: Infrared Divergence (or longwave cooling of the atmosphere)

Multi-annual seasonal clear-sky infrared divergence maps and infrared divergence difference maps are presented in *Figure 7.5.4*.

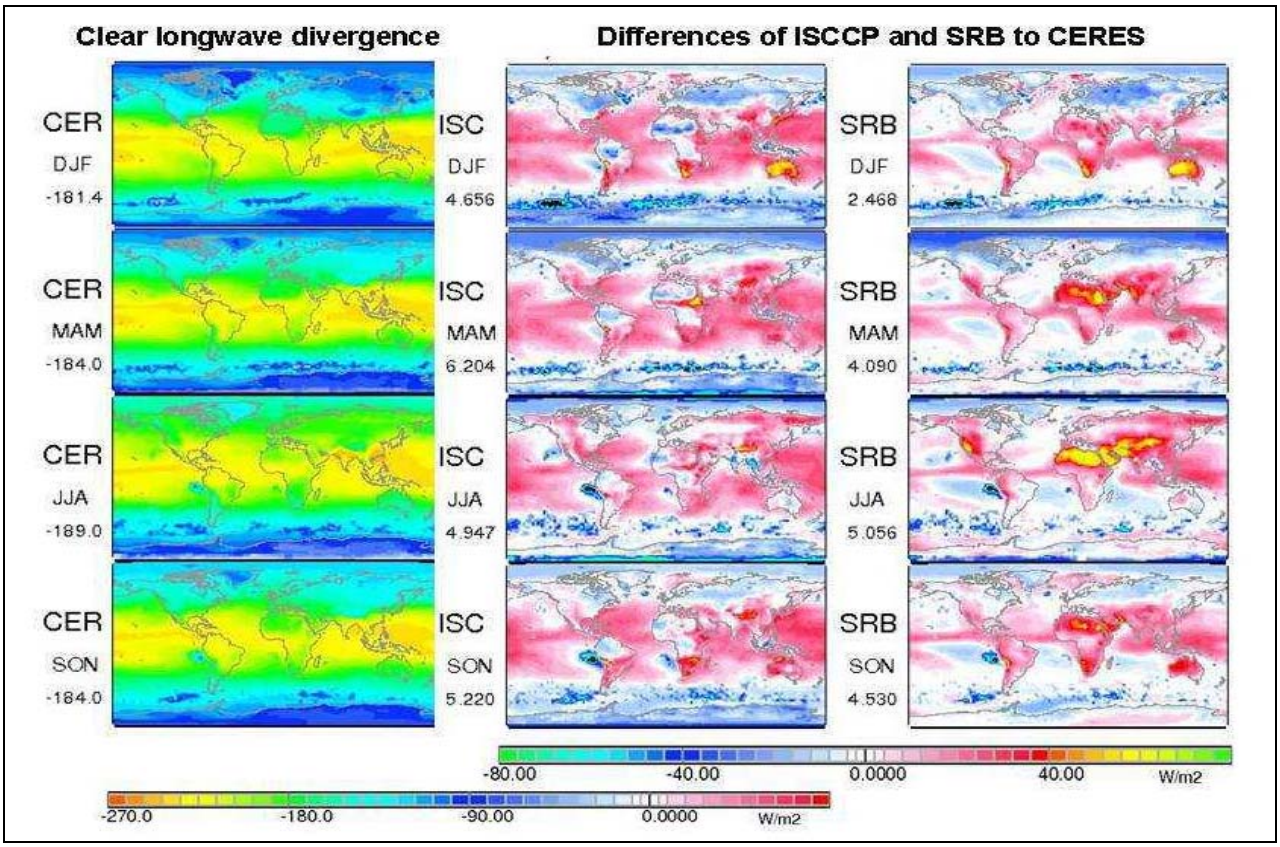

Figure 7.5.4: *Multi-annual seasonal* ***clear-sky infrared atmospheric divergence*** *by CERES and differences of ISCCP & SRB to CERES. Data of CERES are from the period March 2000 to February 2004, those of ISCCP and SRB for the 1985 to 1995 period. Since the terrestrial divergence is negative (blue), the negative values in the difference plots mean an increased divergence and positive (red) values a decreased divergence. Numbers left to the panels below the labels are global averages. Numbers left to the panels below the labels are global averages.*

CERES values for the clear-sky infrared divergence range from about – 80 Wm^{-2} over Antarctica to – 240 Wm^{-2} over the tropical Pacific. They are related to the (surface) temperature and the amount and vertical distribution of atmospheric trace gas concentrations. Strange patches in the near coastal areas of the Antarctic continent in CERES data are likely in error due to the lack in available clear-sky data. ISCCP and SRB suggest much stronger infrared divergences over off-coastal stratocumulus regions. ISCCP-data have over oceans smaller clear-sky infrared divergences than the other two data-sets and SRB-data have significantly weaker clear-sky infrared divergences over deserts than the other two data-sets (likely linked to lower infrared upward fluxes and lower sand emittances). The clear-sky infrared diversity in some areas is on the order of 30% of the average, which demonstrates the impact of non-cloud ancillary data.

Multi-annual seasonal cloud-effects on infrared divergence maps and infrared cloud-effect divergence difference maps are presented in *Figure 7.5.5*.

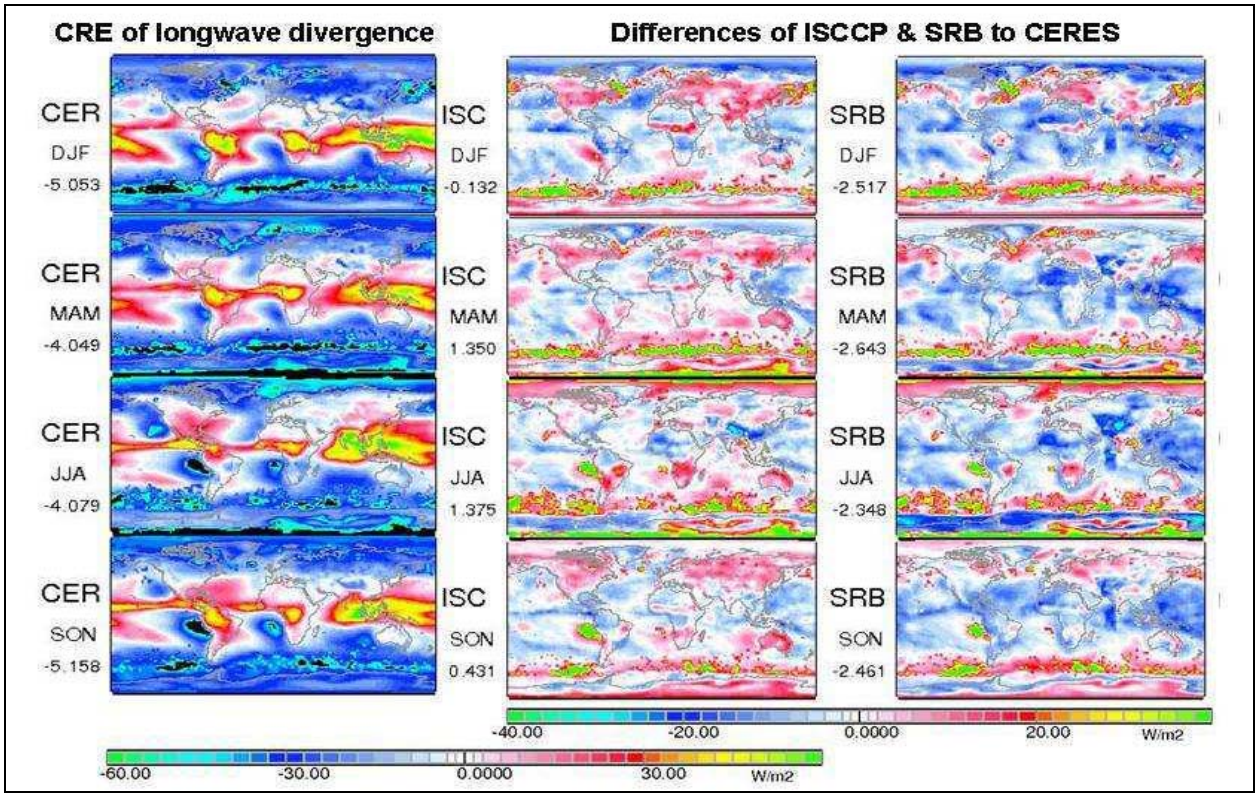

Figure 7.5.5: *Multi-annual seasonal* ***cloud effects on infrared atmospheric divergence*** *by CERES and differences of ISCCP & SRB to CERES. Data of CERES are from the period March 2000 to February 2004, those of ISCCP and SRB for the 1985 to 1995 period. Since the terrestrial divergence is negative (blue) values in the difference plots mean an increased divergence and positive (red) values a decreased divergence due to clouds. Numbers left to the panels below the labels are global averages.*

Clear-sky infrared divergences are negative and clouds an averages increase these values by an additional - 6 Wm^{-2}. Regionally, however, clouds can both reduce and increase infrared divergence, largely depending on temperature (contrast) and altitude distribution of clouds. Seasonal reductions can be as large as + 40 Wm^{-2} (mainly over warmer surfaces), while seasonal increases can an extra -60 Wm^{-2} (over stratocumulus regions). Compared to CERES ISCCP-data suggest a slightly weaker infrared cloud-effect on the infrared divergence whereas SRB-data indicate a slightly stronger cloud-effect on the infrared divergence.

Adding clear-sky and cloud-effect maps yield all-sky maps. The resulting multi-annual seasonal all-sky infrared divergence maps and infrared divergence difference maps are presented in *Figure 7.5.6*.

All-sky infrared divergences range from – 90 Wm^{-2} over Antarctica to values of -260 Wm^{-2} over off-coastal stratocumulus regions. ISCCP-data suggest weaker infrared diversities almost everywhere compared to CERES and SRB, with minima over Australia and Southern Africa. SRB display the strong reduced infrared divergence over the deserts. The similarity between all-sky difference patterns and clear-sky difference patterns for the infrared divergence suggest that the diversity in ancillary data (e.g. surface temperature, surface emissivity, trace-gas distribution and temperature profiles) may be more influential than the diversity in cloud properties. This should be a clear incentive to harmonize ancillary data-sets, and improve the "de-clouding"of the atmosphere.

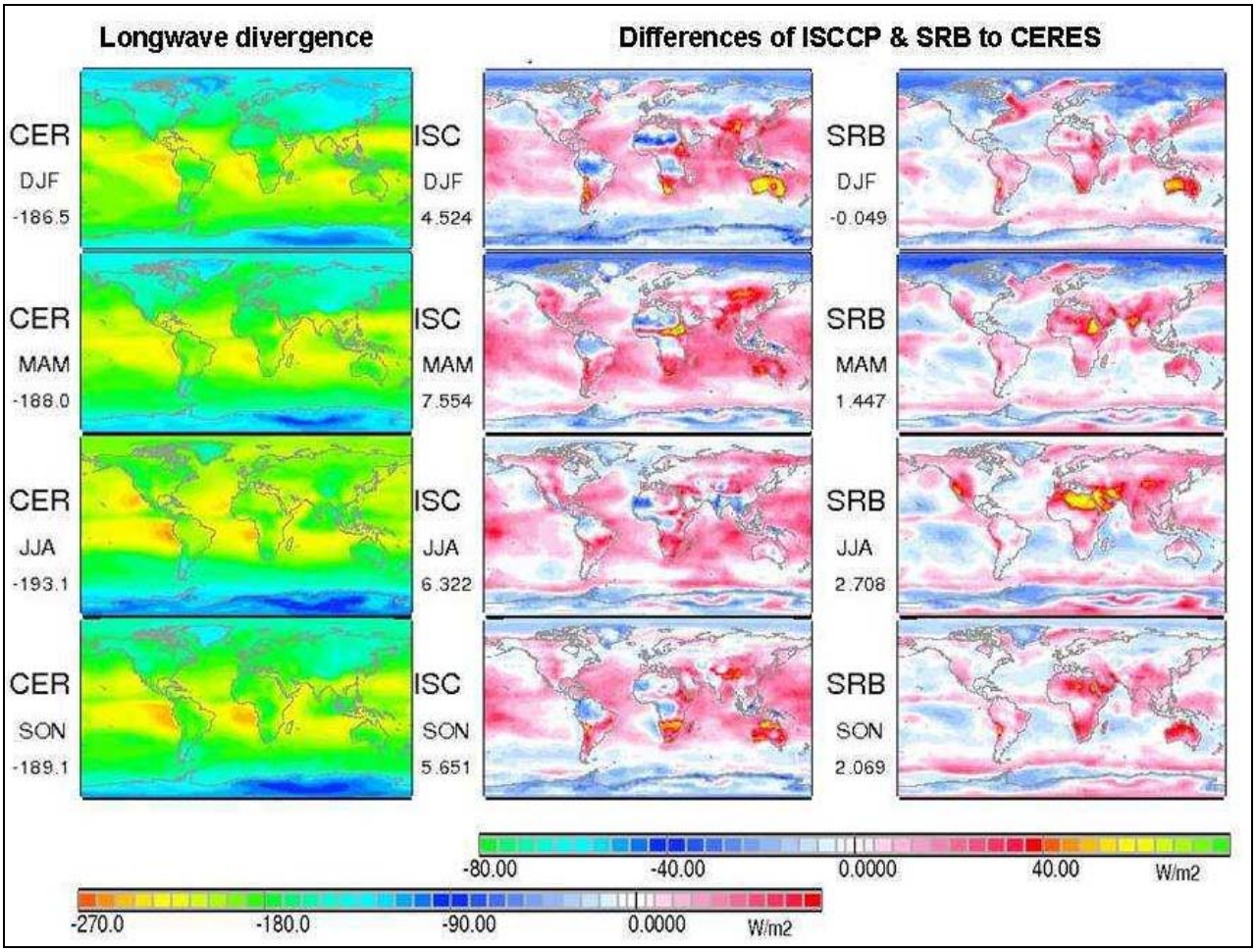

Figure 7.5.6: *Multi-annual seasonal* ***all-sky infrared divergence*** *by CERES data (left) and differences of ISCCP & SRB to CERES. Data of CERES are from the period March 2000 to February 2004, those of ISCCP and SRB are for 1985 to 1995 period. Since the terrestrial divergence is negative (blue) values in the difference plots mean an increased divergence and positive (red) values a decreased divergence. Numbers left to the panels below the labels are global averages.*

7.6: Total (solar + infrared) Vertical Flux Divergence

We finally complement the discussions on the vertical divergences for shortwave and longwave radiation with results of their sum: the total radiative flux divergence. The global averages of this quantity are a measure for the required influxes of sensible abd latent heat into the atmosphere from ground to maintain equilibrium. Seasonal averages as shown in *Figure 7.6.1* are negative in all four data sets (ISCCP, CERES, SRB and the IPCC Median Model) and during all seasons for all-sky (and clear-sky: not shown here) conditions.

That reflects the known facts, that the atmosphere is always a source for (longwave) radiative energy and its dynamics needs additionally be fed by sensible and latent heat from ground. Global averages, see *Table 7.6.1,* range between about -99 and -120 Wm^{-2} for all-sky, and -105 and -116 Wm^{-2} for clear-sky conditions. Differences between both values summarize the radiative influence of clouds (CRE); as shown in *Table 7.6.1.* In the climate datasets clouds seem to enhance the "radiative cooling" while they are reducing it in the model data.

Season	ISCCP	CERES	SRB	IPCC Median Model
	All / clear / CRE	All / clear / CRE	All / clear / CRE	All / clear / CRE
DJF	-111.0 / -109.1 / -1.9	-112.6 / -102.5 / -10.1	-111.1 / -107.1 / -4.0	- 98.9 / -105.1 / +6.2
MAM	-110.3 / -110.3 / -0	-115.5 / -107.4 / -8.1	-112.6 / -108.5 / -4.1	-100.2 / -107.3 / +7.1
JJA	--115.8 / -115.2 / -0.6	-120.3 / -111.1 / -9.2	-115.9 / -111.6 / -4.3	-104.0 / -111.1 / +7.1
SON	-113.2 / -111.6 / -1.6	-116.4 / -108.3 / -8.3	-112.8 / -108.3 / -4.5	-100.7 / -107.6 / +6.9

Table 7.6.1: *Seasonal* ***global*** *averages of the* ***total vertical radiative flux divergence*** *during the period March 2000 to February 2004. First value is for all-sky and second value is for clear-sky conditions, and the third is for the cloud radiative effect (CRE), where blue/red describe an increase or decrease of the total divergence by the presence of clouds.*

The maps in *Figure 7.6.1* for all-sky data show that highest (about -200 Wm^{-2}) cooling occurs over the southern subtropics, where low-level maritime strato-cumulus clouds dominate, and over the winter hemisphere, while smallest (about -50 Wm^{-2}) over continents and the Antarctics during their summer season. The geographic pattern is dominantly determined by continents and cloud heights. Similar patterns occur also in the maps for clear-sky data (see *Figure 7.7.2*), where apparently the sampling of really complete cloud-free areas was poorest in the infrared.

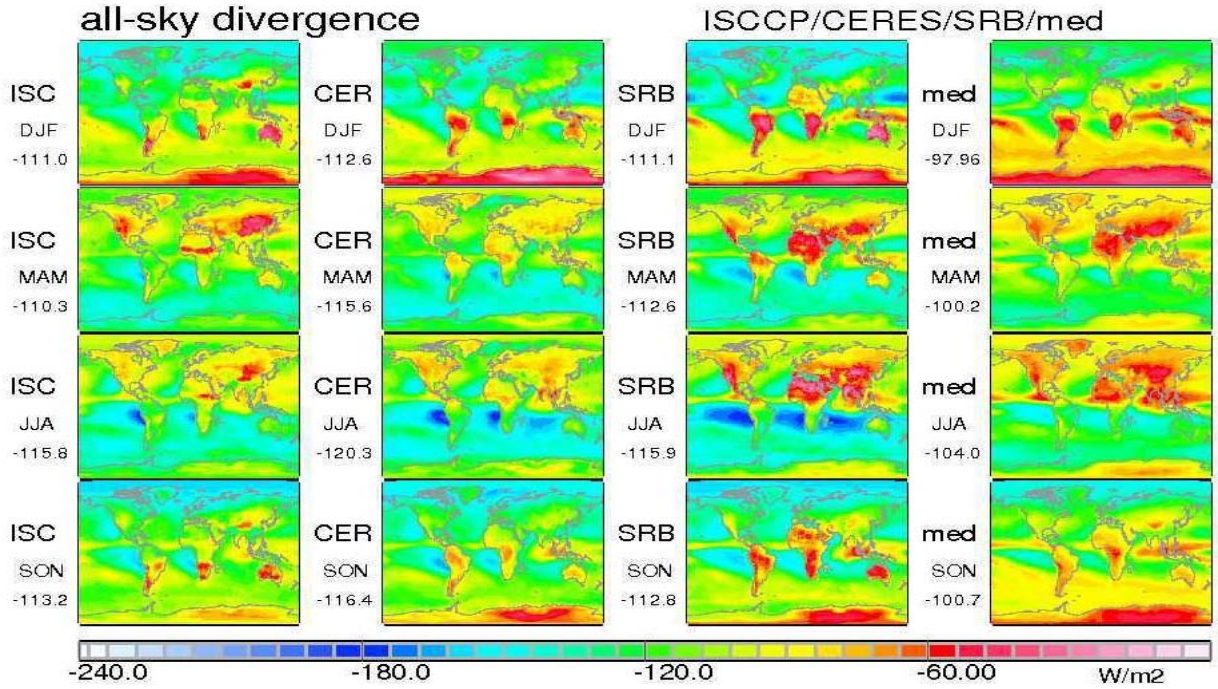

Figure 7.6.1: *Seasonal means of the* ***all-sky total (solar plus infrared) radiative flux divergence*** *within the atmosphere in data from ISCCP, CERES, SRB and the IPCC Median Model averaged over the period March 2000 to February 2004.*

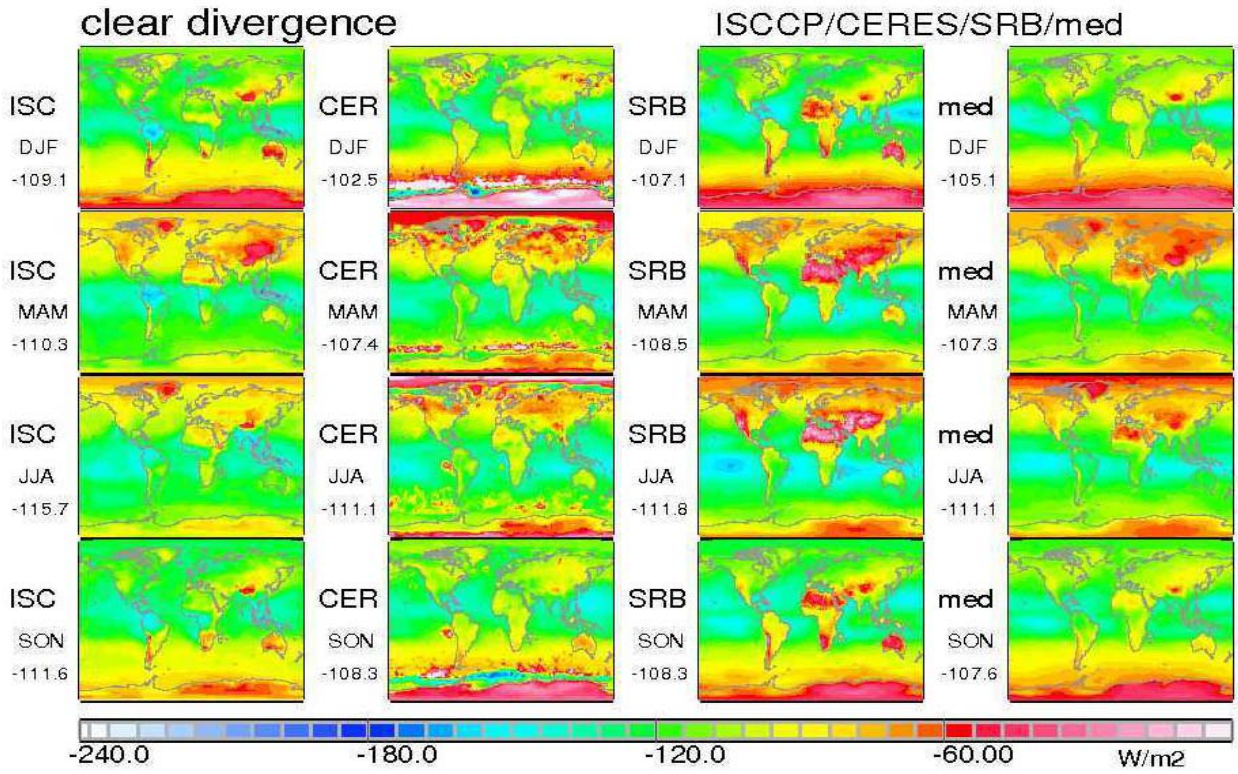

Figure 7.6.2: *Seasonal means of the* ***clear-sky the total (solar plus infrared) radiative flux divergence*** *within the atmosphere in data from ISCCP, CERES, SRB and the IPCC Median Model averaged over the period March 2000 to February 2004.*

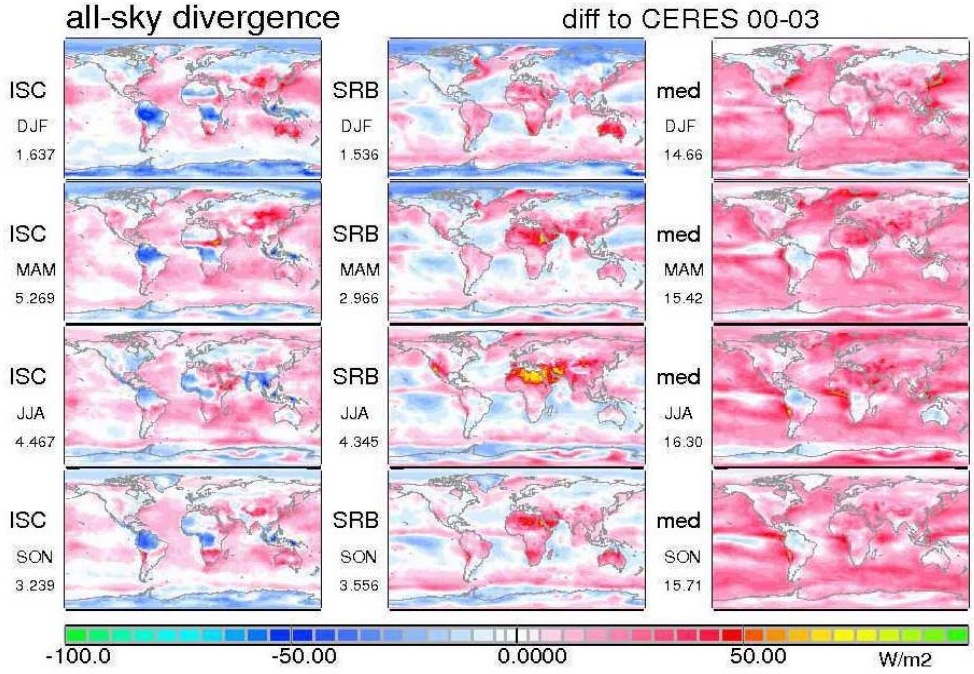

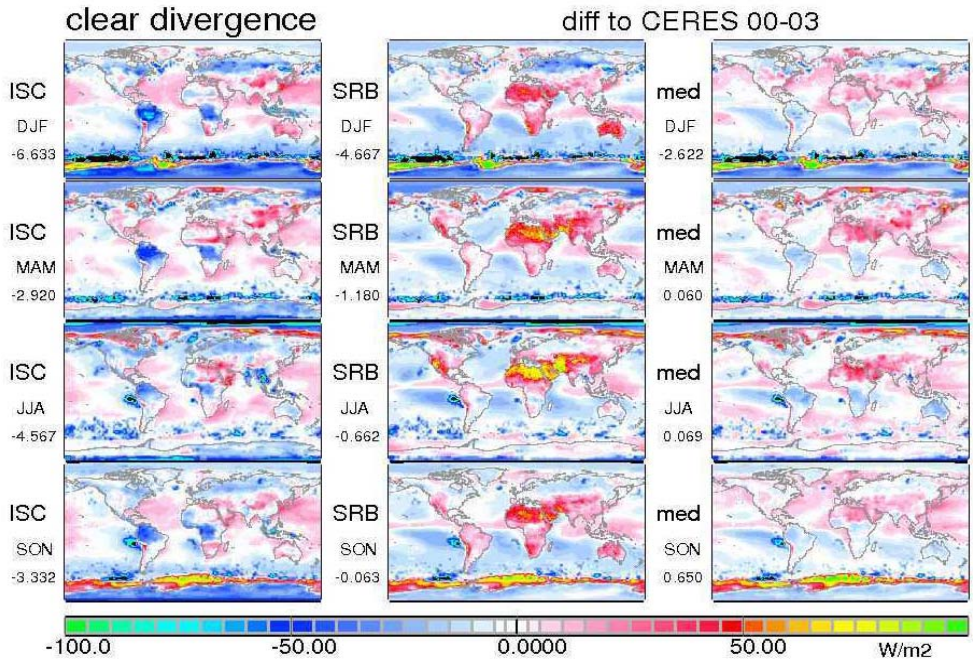

Figure 7.6.3: *Seasonal means of the all-sky (top and clear-sky (bottom)) **differences to CERES results** of **the total (solar plus infrared) radiative flux divergence** within the atmosphere in data from ISCCP, SRB and of the IPCC Median Model. **Reddish / bluish colors** indicate that the total loss of the atmosphere is in each data set **lower / higher** than in the CERES data. Note the positive maxima over the North African deserts and negative maxima over tropical rain forest areas. The anomalies near the Antarctic continent are due to errors in CERES data.*

The diversity between the three climate data sets and also those of the IPCC Median Model are quite large, as shown for the all-sky results in *Figure 7.6.3*. The models compute for all-sky conditions over all oceans and most continental areas mostly **less cooling** than obtained from the CERES data, while small reversed values are found over the Americas, southern Africa and Australia. Maximal differences can amount to about 70 Wm^{-2}. Larger positive differences to CERES data are found in the ISCCP and SRB data over the African and Asian deserts; on the other side negative anomalies (higher cooling than CERES) are found in ISCCP data over tropical rain forest regions and in SRB data over oceans.

The pattern in clear-sky difference maps (*Figure 7.6.3)* shows again many structures which are associated to cloud fields indicating that in one (CERES?) of both or in both data sets the clouds could not completely be removed.

7.7 Clear-Sky and All-Sky Water Vapor Biases

To separate all-sky data from clear-sky data (which by difference yields the cloud effect) the definition of clear-sky data matters. While CERES data in the comparison derive clear-sky data solely from observations at cloud-free conditions, these clear-sky data usually contain less atmospheric water vapor than their cloudy scenes. ISCCP and SRB determine clear-sky conditions simply by removing clouds and leaving the atmospheric water vapor unchanged. Thus, the CERES clear-sky solar divergence should be slightly weaker and the infrared divergence should be slightly larger. Regions with persistent cloud cover during the sampling period may

only vaguely determined with "clear-sky properties. Clear-sky calculations reveal that a 50% lower water vapor column amount yield a 5% weaker solar clear-sky absorptions and a 2% stronger clear-sky infrared divergence. Thus, the CERES solar absorption cloud effect should have a positive bias compared to ISCCP and CERES, yet the CERES cloud effect appears smaller.

7.8: Conclusions and Recommendations

In summary, the results shown in this *Chapter 7* demonstrate that useful estimates of the global fields of vertically integrated radiation flux divergences are possible. However the diversity between the 3 climate data sets and also between them and the IPCC Median Model is very large and in many cases due to uncertainties in ancillary data and also the treatment of cloud radiative properties. These maps help identify regions with major anomalies and to understand possible sources. However, errors in flux calculations, which primarily are due to uncertainties in some of the required ancillary data, penetrate into vertical flux divergence data, as divergence data are differences of differences of similar magnitude so that small uncertainty turn into large diversities.

A puzzling result is that unlike in ISCCP and SRB, where clouds increase the solar divergence (or atmospheric absorption) - a tendency was used from modeling - CERES clouds reduce the atmospheric solar absorption despite a positive water-vapor absorption bias (compared to ISCCP and SRB). A likely explanation is a higher placement of clouds in the CERES atmosphere but also the lower cloud optical thickness of CERES may be a contributing factor. Diversities in the altitude placement cloud can and should be reduced with recent available data from active space sensors of Cloudsat and CALIPSO. .

The stratification in diversity contribution for the solar and infrared flux divergence has demonstrated that all-sky diversity is largely driven by the clear-sky diversity. Thus, ancillary data other than clouds seem still the major problem, even more so as cloud properties are often retrieved in order to cover for other errors in ancillary data. Thus, there are strong arguments to review, assure accuracy and temporal consistency and to harmonize among different data-sets the needed ancillary data (more on ancillary data in *Appendices C.2 and D.7)* Once in careful analyses artifacts in all needed ancillary data have been removed, then (and only then) a complete reanalysis of all data sets is recommended.

The related maps for the clear-sky divergences and the CRE (see *Appendix D.7*) are smaller than ± 2.5 Wm^{-2} in the solar spectral range and ± 10 Wm^{-2} in the infrared; their spatial pattern is heavily influenced by traces from the insufficient inclusion of geostationary data into the cloud analyses. The pattern in ISCCP results is dominated by the "apparently smaller cooling" of the planet up to the year 2002, which preferably occurs over the Pacific Ocean. Both data sets show traces of the limb-darkening in geostationary measurements. In both panels the spatial pattern of CRE is dominated by the influence of incorrect corrections of the angular dependence of geostationary data. The pattern in ISCCP results is dominated by the "apparently smaller cooling" of the planet up to the year 2002, which preferably occurs over the Pacific Ocean. Both data sets show traces of the limb-darkening in geostationary measurements.

Chapter 8:

Global Mean Radiation Budget

N. Loeb and W. Su

Abstract:

This chapter presents an assessment of our current understanding of the global mean radiation budget at the top-of-atmosphere (TOA), within the atmosphere (ATM), and surface (SFC). It uses CERES and other datasets that participated in the GEWEX RFA. To place the results in proper context, we provide uncertainties in TOA and SFC fluxes based upon previously published results and perform a radiative perturbation analysis in order to illustrate how uncertainties in retrieved atmospheric, cloud, aerosol and surface properties influence radiative flux uncertainties. We find that agreement amongst GEWEX RFA datasets is better in the LW than in the SW at both the TOA and SFC. With the exception of SW TOA flux, differences amongst the GEWEX datasets lie within the one-standard deviation uncertainty estimates derived for CERES (Loeb et al., 2009) at the TOA, and from radiative perturbation analysis for SFC. Narrowing uncertainties in SFC fluxes requires improvements in ancillary data products, particularly surface temperature and atmospheric temperature and humidity.

8.1: Introduction

The exchange of radiant energy between the Earth and space and the flow of all forms of energy within the Earth-atmosphere system are fundamental to climate. To understand how climate is changing, our observing system must be able to track these energy flows with great precision and accuracy. A test of our understanding of climate is how accurately we can quantify the global annual mean Earth Radiation Budget (ERB).

Our interest in observing the ERB dates back to the mid-1880s (Hunt et al., 1986). The first serious attempt to provide observation-based estimates of the components of the ERB was made by Abbot and Fowle (1908a,b). Since the dawn of the space age there has been a series of experimental satellite instruments dedicated to measuring the ERB (House et al., 1986).

While the radiation community has made great strides improving both the instrumentation and algorithms required to quantify the components of the ERB (Trenberth et al., 2009), uncertainties remain, particularly at the surface, where radiative fluxes over much of the Earth are calculated using inputs from satellite cloud and aerosol retrievals, model-based assimilations of temperature and humidity profiles, and surface properties derived from satellite remote sensing or theoretical models. Errors in these ancillary datasets propagate into the radiation fields, as shown in Chapters 3.5 and 4.5 and 7.

Here we present results using only global mean radiative fluxes amongst the datasets in the GEWEX RFA database with both TOA and SFC values between March 2000 and February 2004.

8.2: The Global Annual Mean Radiation Budget

Figure 8.1 shows the global radiation budget at the TOA, surface and within the atmosphere based on CERES data. At the top-of-atmosphere (TOA), clear and all-sky fluxes are from the CERES Energy Balanced and Filled (EBAF) data product (Loeb et al., 2009) from March 2000 through

February 2004. As described in Loeb et al. (2009), CERES EBAF is derived by applying an objective constraint algorithm to adjust all-sky shortwave (SW) and longwave (LW) TOA fluxes in the CERES SRBAVG-GEO data product within their range of uncertainty to remove the inconsistency between average global net TOA flux and heat storage in the Earth-atmosphere system. The uncertainties used in this process are shown in Table 1 of *Section 3.8*. *Figure 8.1* uses TOA solar irradiance data from the Solar Radiation and Climate Experiment (SORCE) (Kopp and Lean, 2011) and accounts for the non-spherical shape of the earth (Loeb et al, 2009).

The surface radiative fluxes in *Figure 8.1* are based upon the CERES Radiative Fluxes and Clouds Monthly Regional (AVG) data product (Edition 2 Beta3). We assume no change in the CERES AVG within-atmosphere fluxes, surface albedo or upward LW flux, and slightly perturb the AVG downward and upward SW and downward LW fluxes to account for the difference between AVG and EBAF global mean SW and LW TOA fluxes. The global mean net radiation in the atmosphere of -105 Wm^{-2} is balanced by non-radiative terms in the energy budget associated with sensible and latent heat exchange between the surface and atmosphere. Assuming the 17 Wm^{-2} Trenberth et al. (2009) sensible heat estimate from reanalysis data is correct, this would imply that the global mean latent heat term is 88 Wm^{-2}, 8 Wm^{-2} greater than that of Trenberth et al. (2009) who based their estimate on subjective upward adjustment to Global Precipitation Climatology Project (GPCP) (Adler et al. 2003) and NOAA Climate Prediction Center (CPC) Merged Analysis of Precipitation (CMAP) (Xie and Arkin, 1997) data.

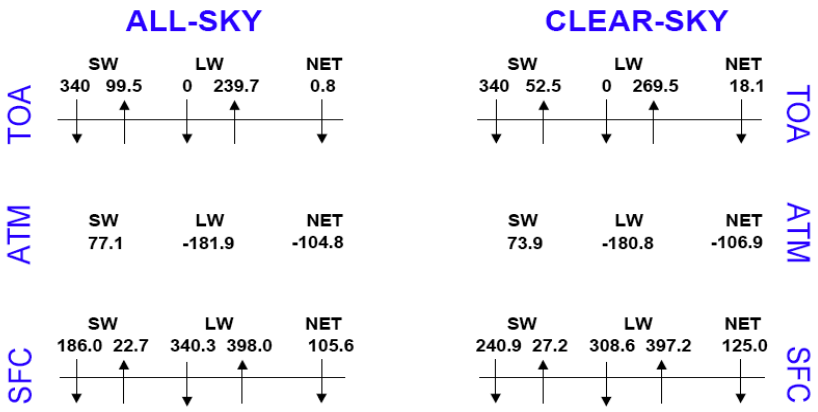

Figure 8.1: *Global mean radiation budget for clear-sky and all-sky conditions at the top-of-the-atmosphere (TOA), surface (SFC), and within the atmosphere (ATM). Results are based on CERES EBAF and CERES AVG(Tuned) Beta3 from Terra from March 2000 through February 2004 and a TSI of 1360 Wm^{-2}..*

Uncertainties in TOA fluxes are discussed in *Section 3.8.* At the surface, uncertainties are determined from an error propagation analysis using a modified version of the Fu and Liou radiative transfer code (Rose and Charlock 2002). *Table 8.1* provides the global mean and 1σ uncertainties of various atmospheric parameters considered for the surface flux uncertainty estimation. After computing radiative fluxes for the base state, each parameter is modified according to its 1σ uncertainty range and the model is run again, keeping all other parameters fixed. In order to avoid excessive radiative transfer calculations, we use a single solar zenith angle of 60° and adjust the global mean surface fluxes in *Figure 8.1* by the relative difference between the perturbed and based state computed fluxes. Separate calculations are performed for clear and all-sky conditions over ocean and land. Global uncertainties are determined by weighting the squares of the uncertainties for ocean and land by their fractional coverage over the globe.

Table 8.1: *Global means and their 1-sigma uncertainties of various atmospheric properties considered for the surface flux uncertainty estimation.*

Variables	Ocean	Land	Global	Reference
AOD	0.13±0.036	0.19±0.08		Remer et. al (2008)
Single Scattering Albedo (SSA)	0.97±0.02	0.95±0.04		Kinne (2008)
Cloud Optical Depth (COD)	3.9±0.5	3.9±0.5	3.9±0.5	ISCCP
Cloud Fraction (Fc), COD>0.1	0.73±0.05	0.59±0.05	0.68±0.03	Stubenrauch et al.(2012)
Fc Diurnal, COD>0.1	2%	3%	1%-2%	Stubenrauch et al.(2012
high-level out of all clouds	38%-48%	48%-58%	40%-50%	Stubenrauch et al.(2012
single-layer low-level out of all clouds	48%±5%	28%±5%	40%±3%	Stubenrauch et al.(2012
High Cloud Top Pres (hPa)	511±30	443±30	490±30	Wang (2000)
High Cloud Base Pres (hPa)	625±30	576±30	610±30	Wang (2000)
Low Cloud Top Pres (hPa)	866±30	811±30	850±30	Wang (2000)
Low Cloud Base Pres (hPa)	951±20	899±20	935±20	Wang (2000)
Effective Radius liquid (μm)	15±2	13±2	14±1	Stubenrauch et al.(2012
Effective Radius ice (μm)	26±5	25±5	25±2	Stubenrauch et al.(2012
Albedo	0.12±0.004	0.28±0.02	0.17±0.007	Zhang et al. (2007)
Skin Temp (*K*)	289.1±2.4	281.9±4.6	286.9±3.3	Zhang et al. (2007)
Near Surface Air Temp (K)	289.7±1.9	283.3±3.7	287.8±2.6	Zhang et al. (2006)
Precipitable Water (cm)	2.63 ± 0.34	1.86 ± 0.48	2.41 ± 0.39	Zhang et al. (2006)
Surface Emissivity	0.924±0.037	0.971±0.039	0.938±0.038	Zhang et al. (2007)
Solar Constant (Wm^{-2})	1365 or 1361	1365 or 1361	1365 or 1361	Kopp et al. (2011)

References:

Stubenrauch, C . J., W. B. Rossow, S. Kinne, S. Ackerman, G. Cesana, H. Chepfer, L. Di Girolamo, B. Getzewich, A. Guignard, A. Heidinger, B. Maddux, P. Menzel, P. Minnis, C. Pearl, S. Platnick, C. Poulsen, J. Riedi, S. Sun-Mack, A. Walther, D. Winker, S. Zeng, G. Zhao, 2012: Assessment of Global Cloud Datasets from Satellites: Project and Database initiated by the GEWEX Radiation Panel, *Bull. Amer. Meteor. Soc.*, in press (2013).

WCRP report 23/2012: Assessment of Global Cloud Datasets from Satellites: A Project of the World Climate Research Programme Global Energy and Water Cycle Experiment (GEWEX) Radiation Panel, (176 pp), Lead Authors: C. J. Stubenrauch, W. B. Rossow, S. Kinne.

Tables 8.2 and 8.3 provide a summary of the error propagation analysis showing how uncertainties in each variable influence the global mean surface radiation budget. The overall uncertainty in each table is calculated assuming the errors from every parameter are independent of one another. Relative uncertainties in global mean surface fluxes typically range from 3%-6% (1σ), much larger than TOA flux uncertainties, which are closer to 1% (1σ). Atmospheric state parameters (e.g., precipitable water, skin and air temperature) contribute the most uncertainty to the LW surface flux, while cloud properties, aerosols and surface albedo are the dominant error sources for SW surface fluxes. Our estimations of the uncertainties for clear-sky and all-sky down-welling SW fluxes are on the same magnitude (2% for clear-sky and 4% for all-sky) as those in Zhang et al. (2007).

***Table 8.2:**: Estimated uncertainty in global clear sky surface fluxes (1σ). (DN=downward flux at the surface; UP=upward flux at the surface).*

Variables	**SWDN**	**SWUP**	**LWDN**	**LWUP**	**Net**
Average State	240.9	27.2	308.6	397.2	125.0
AOD	3.1	0.3	0.7	0.1	2.5
SSA	0.9	0.1	0.9	0.1	1.4
Sfc albedo	0.2	1.3	0.0	0.0	1.1
Skin Temp. (K)	0.0	0.0	0.0	17.5	17.5
Air Temp. (K)	0.0	0.0	8.0	0.5	7.7
Precip. Water (cm)	3.0	0.4	9.2	0.5	6.7
Emissivity	0.0	0.0	0.0	2.1	2.1
Solar Const. (Wm^{-2})	-0.7	0.0	0.0	0.0	-0.7
Overall Uncertainty	**3.8**	**1.4**	**12.3**	**17.6**	**19.9**

***Table 8.3:** Estimated uncertainty in global all-sky surface fluxes (1σ).*

Variables	**SWDN**	**SWUP**	**LWDN**	**LWUP**	**Net**
Average State	186.0	22.7	340.3	398.0	105.6
AOD	2.0	0.2	0.3	0.0	1.7
SSA	0.8	0.1	0.4	0.1	1.0
Sfc albedo	0.4	1.1	0.0	0.0	0.7
Skin Temp. (K)	0.0	0.0	0.1	17.5	17.3
Air Temp. (K)	0.0	0.0	8.3	0.5	7.9
Precip. Water (cm)	2.1	0.2	5.2	0.4	3.4
Emissivity	0.0	0.0	0.0	1.0	1.0
High Cld Frac (%)	3.0	0.4	1.4	0.2	1.5
Low Cld Frac (%)	2.9	0.4	2.5	0.2	0.7
High COD	3.2	0.4	1.3	0.0	1.5
Low COD	5.4	0.6	3.1	0.3	2.4
High Cld Top Pres (hPa)	0.0	0.0	0.1	0.0	0.1
High Cld Base Pres (hPa)	0.0	0.0	0.2	0.0	0.2
Low Cld Top Pres (hPa)	0.0	0.0	0.2	0.0	0.2
Low Cld Base Pres (hPa)	0.0	0.0	0.2	0.0	0.2
High Cld diameter (μm)	0.1	0.0	0.1	0.0	0.1
Low Cld radius (μm)	0.1	0.0	0.2	0.0	0.1
Solar Const. (Wm^{-2})	-0.5	-0.1	0	0	-0.5
Overall Uncertainty	**7.7**	**1.4**	**10.8**	**17.5**	**19.3**

8.3: Consistency of Global Annual Mean Radiation Budget amongst GEWEX RFA Datasets

Figures 8.2 and 8.3 compare the global mean radiation budget at the TOA and SFC for those datasets in the GEWEX RFA database that provided both TOA and SFC values between March 2000 and February 2004. The all-sky global mean LW TOA flux is 238.5 Wm^{-2} with a 2 Wm^{-2} standard deviation amongst the four datasets. In the SW, the mean TOA flux is 100.4 Wm^{-2} with a 3 Wm^{-2} standard deviation. The LW differences are just within the 1σ uncertainty in CERES (*Table 8.2 Section 3.8),* while the SW differences fall well outside the 1 Wm^{-2} CERES 1σ uncertainty. The average net flux is 2.5 Wm^{-2} with a 3.5 Wm^{-2} 1σ range. The net flux ranges from -1.8 Wm^{-2} to 7.0 Wm^{-2}.

At the surface (*Figure 8.3*), SW flux differences amongst the datasets are just within the 1σ uncertainties from the error propagation analysis in *Table 8.3*. In the LW, the consistency amongst the datasets is much better than expected from the LW uncertainty analysis: 1σ-differences amongst the datasets is a factor of 6 smaller than the estimated LW uncertainty in *Table 8.3*. The large uncertainty estimate in LW upward flux at the surface is associated mainly with skin temperature uncertainty, while the uncertainty in LW downward flux at the surface is primarily from air temperature and precipitable water. Uncertainty estimates for all three of these variables are based on quoted values from Zhang et al., (2006, 2007) (see *Table 8.1*). Recently, Kato et al., (2011) compared surface flux calculations derived from MODIS cloud retrievals with those based upon combined MODIS, CALIPSO and Cloudsat cloud properties, with all other inputs (e.g., temperature and humidity) the same in both sets of calculations. They find that including the active sensors increases the global mean surface downward longwave flux by 3.4 Wm^{-2} due to an increase in cloud fraction and lower cloud base heights. They also find that surface downward shortwave fluxes increases by 1.6% (or approximately 3 Wm^{-2}), resulting in an increase in net surface flux when CALIOP and CPR derived cloud properties are used.

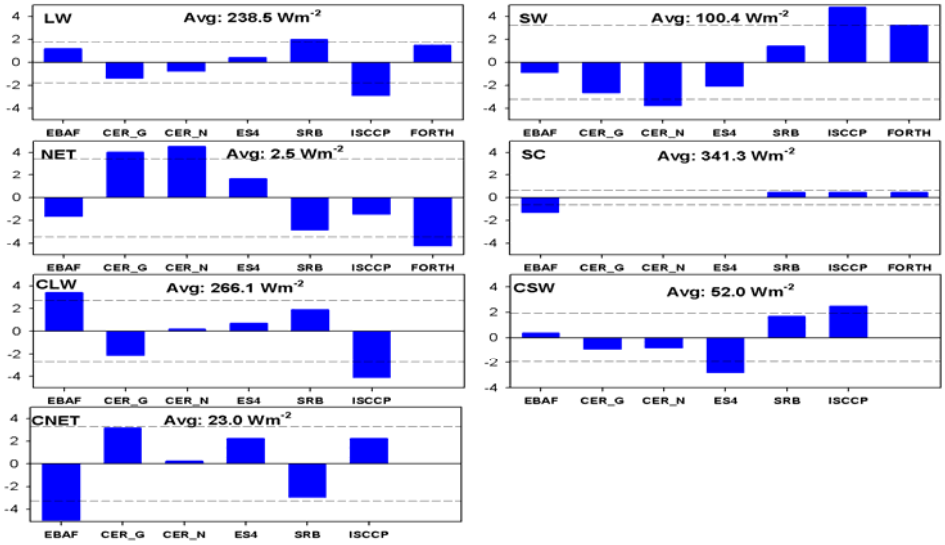

Figure 8.2*: Global mean TOA flux deviation from overall mean of seven datasets for CERES EBAF ("EBAF"), CERES_GEO ("CER_G"), CERES_NonGEO ("CER_N"), CERES ERBE-like ("ES4"), GEWEX SRB ("SRB"), ISCCP-FD ("ISCCP"), and FORTH for March 2000-February 2004. "SC" = Solar Constant; "CLW"=Clear Longwave; "CSW"=Clear SW; "CNET"=Clear net. Dashed lines represent one standard deviation.*

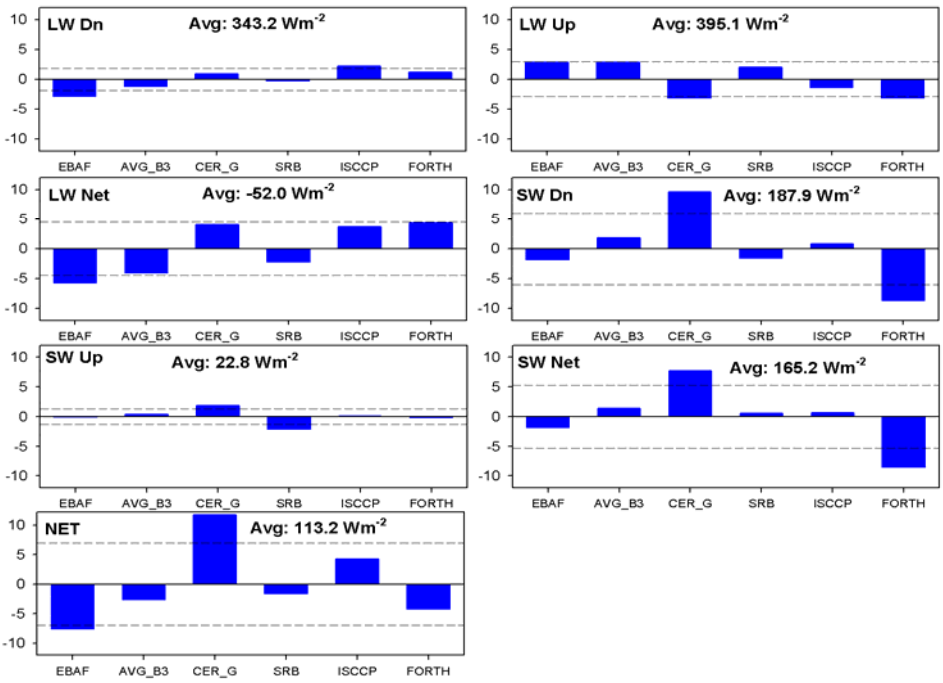

***Figure 8.3**: Global mean **surface flux** deviation from overall mean of seven datasets for CERES EBAF ("EBAF"), CERES_GEO ("CER_G"), CERES_NonGEO ("CER_N"), CERES ERBE-like ("ES4"), GEWEX SRB ("SRB"), ISCCP-FD ("ISCCP"), and FORTH for March 2000-February 2004.*

8.4: Summary and Conclusions

Further research is needed to reduce uncertainties in the Earth's radiation budget, particularly at the surface. The many new satellite data that have emerged in recent years provide exciting new opportunities to further refine our estimates of the components of the Earth's radiation budget. However, there is also a need to supplement the global radiation budget diagram with a consistent dataset at a higher temporal and spatial resolution (e.g., 0.25° or 1° monthly). While there are many surface and within-atmosphere flux products available to the research community, there presently is none that is consistent radiatively from top to bottom with the TOA net flux imbalance. Part of this problem was addressed at the TOA (e.g., EBAF), but even this should be updated as new in-situ ocean heat content data become available (ocean heating rates based upon "Argo" ocean heat content data is our most accurate constraint on the net TOA flux imbalance). The new satellite data such as AIRS, CALIPSO and Cloudsat together with surface radiation measurements and Argo ocean heat content data provide powerful constraints on TOA and surface flux components of the radiation budget and should be used to produce a monthly regional dataset that is consistent with the values in the global radiation budget diagram. Such a dataset, together with estimates of the uncertainties in each component, would be of great value in climate model evaluation efforts.

Chapter 9:

Radiative Fluxes in Global Modeling

S. Kinne and E. Raschke, S. Freidenreich, L. Hinkelman

9.1: Multi-Model Results *(S. Kinne and E. Raschke)*

Abstract:

Simulated radiative energy fluxes and cloud radiative effects by global modeling are investigated. To capture the characteristic behavior of different global models that contributed to the IPCC fourth assessment (IPCC-AR4), 1x1 lat/lon monthly median fields for a 12-year (1984-1995) base period are examined. The radiative flux maps of the "median model" are compared to flux data of four major radiation climatologies: ISCCP (1984-1995), SRB (1984-1995), ERBE (1985-1988) and CERES-SRBAVG (3/2000-2/2004).

The representation of global modeling by a single model, however, is an oversimplification, as there are significant differences among the twenty different IPCC-AR4 models. The inter-model diversity for radiative fluxes and cloud effects is about three times larger than the diversity among satellite sensor associated climatological flux products. Hereby, the radiative flux diversity is larger for the solar spectrum (compared to the IR) and larger for the surface budget (compared to the TOA budget). Thus, despite the sensor data diversity, (satellite data based) climatological TOA flux data do provide constraints to global modeling. However, to act as a stronger TOA constraint, the detected large diversity of influential ancillary data needs to be reduced. Efforts are strongly needed to obtain more consistency among the same ancillary data in different retrievals and to assure their consistency in time.

Regional differences for cloud radiative effects between modeling and satellite climatologies are generally larger over oceans as compared to land. Over tropical and northern hemispheric oceans simulated cloud effects are found to be too strong, possibly due to optical depth or cloud cover being too large, while they are too weak over stratocumulus regions off western continental coasts and SH storm tracks during summer. These differences demonstrate the need for an improved treatment of clouds (especially low altitude clouds) and cloud processes in global modeling.

9.1.1: Introduction

Global monthly fields of solar and infrared broadband radiative fluxes have been collected as part of the GEWEX Radiative Flux Assessment. All maps can be accessed via a website at NASA-Langley: http://eosweb.larc.nasa.gov/GEWEX-RFA/. The main focus is on radiative flux data associated with satellite sensors. However, with alternative radiative flux data sets offered by global modeling, there is a general interest, how these simulated data compare to satellite data. Such comparisons are investigated in this sub-chapter.

Model simulated radiative fluxes are represented by monthly averages of about twenty models, which were submitted by different climate research groups as their contribution to the IPCC 4th assessment report (IPCCAR4, *Forster et al., 2007*). *Table 9.1.1* lists the contributing IPCC models, their institution and the applied atmospheric model with its horizontal spectral (T…) resolution (e.g. T63 ca 2x2 lat/long, T42 ca 4x4 lat/long) and its number of vertical (L …)

levels. For a statistical summary of the different models, the monthly averages of all models were re-gridded at an identical horizontal (1x1 lat/long) resolution. This was done via linear interpolation using data of the four surrounding grid-points: first by longitude (at both the next higher and next lower latitude) and then by latitude (adopting at extreme latitudes the nearest (non-zero) lower latitude value at that longitude). This permitted the creation of characteristic values (average and median) and characteristic variability (standard deviation). In this chapter, primarily the IPCC model median is examined and compared to satellite data. To permit direct comparisons, the same horizontal re-gridding to a 1x1 (latitude/longitude) was also applied to all satellite sensor climatologies, including data sets considered as "reference" (e.g. CERES-SRBAVG or ERBE).

Table 9.1.1*: IPCC 4th assessment data sets: their origin, atmospheric model and 3-letter label*

label	institution	Location	atmospheric model
BCC	Bjerknes Center for Climate	Bergen, Norway	Arpege V3, T63/L31
CCc	Canadian Climate Center	Victoria, Canada	AGCM3, T63/L31
CCC	Canadian Climate Center	Victoria, Canada	AGCM3, T47/L31
CCs	Center for Climate Sys Res.	Tokyo, Japan	AGCM, T106/L56
CCS	Center for Climate Sys Res.	Tokyo, Japan	AGCM, T42/L20
CNR	CNRS Meteo-France	Toulouse, France	Arpege V3, T63/L45
CSI	CSIRO Atmospheric Research	Melbourne, Australia	CSIROmk3, T63/L18
DMN	Institute for Numerical Math	Moscow, Russia	INMcm3, 4x5/L21
GFD	NOAA, GFDL	Princeton, USA	GFDLcm2, T45/L24
GI1	Goddard Inst. for Space Studies	New York, USA	GISS-ER* 4x5/L20 run1
GI2	Goddard Inst. for Space Studies	New York, USA	GISS-ER* 4x5/L20 run2
GI3	Goddard Inst. for Space Studies	New York, USA	GISS-EH* 4x5/L20 run1
GIS	Goddard Inst. for Space Studies	New York, USA	GISS AOM, 4x3/L12
IAP	Inst. For Atmospheric Physics	Beijing, China	GAMIL, T42/L26
IPS	Inst. Pierre Simon Laplace	Paris, France	IPSL-CM4, 2.5x3.75/L19
MPI	Max-Planck-Institute	Hamburg, Germany	ECHAM5, T63L31
MRI	Meteorological Research Institute	Tsukuba, Japan	cGCM2.3.2, T42/L30
NCA	Nat. Center for Atmospheric Research	Boulder, USA	CAM3, T85/L26
PCM	Nat. Center for Atmospheric Research	Boulder, USA	CCM3.6.6, T42/L18
UBO	University of Bonn	Bonn, Germany	ECHAM4, T30/L19
UKM	UK Met Office	Exeter, England	HADcm3, 2.5x3.75/L19

** GISS ER uses a lower resolution **ocean** model (4x5/L13) than GISS EH (2x2/L16), note that spectral resolutions of T42 and T63 correspond to spatial resolutions of 2.8^ox2.8^o and 1.8^ox1.8^o, respectively*

The statistical value of choice for characterizing the IPCC model output average is the median, due to its being less sensitive than the mean to extreme outliers of individual models. The median is determined at each 1x1 point and combined to produce global maps on a monthly basis. The variability is captured in two ways: 1) by the standard deviation, and 2) by the relative standard deviation (ratio of the standard deviation to the median).

All global models that contributed with output to the 4th IPCC exercise provided monthly solar and infrared broadband radiative fluxes. These fluxes were given at the top of the atmosphere (TOA) and at the surface for 'all-sky' and 'clear-sky' (or cloud removed) conditions from pre-industrial times until the end of the year 1999. For comparisons to satellite sensor based data, only simulations for the last 20 years (1980-1999) are of interest here. In order to constrain the impact of inter-annual variations and avoid leap-year artifacts, the data are combined into 4 or

12 year multi-annual monthly averages. The 12 year average from Jan/1984 to Dec/1995 is mainly selected, because it falls into a time range also covered by SRB and ISCCP climatology products. Two satellite reference data sets are considered for the TOA: the ERBE SCANNER data from Jan/1985 to Dec/1988 and the CERES-SRBAVG data from Mar/2000 to Feb/2004.

Unfortunately, there is some ambiguity on what constitutes 'clear-sky' conditions, which affects CRE comparisons. Model simulations usually simplify this with artificial removal of clouds (e.g. via dual radiation calls). This ignores changes to the atmospheric environment, such as water vapor or aerosol. In contrast, actual observations at 'clear-sky' conditions (e.g. TOA fluxes by CERES) include also environmental change (e.g. usually at drier ambient conditions and also with different aerosol loadings). Thus, with more water vapor at cloudy conditions, observed CRE values tend to be stronger than modeled CRE.

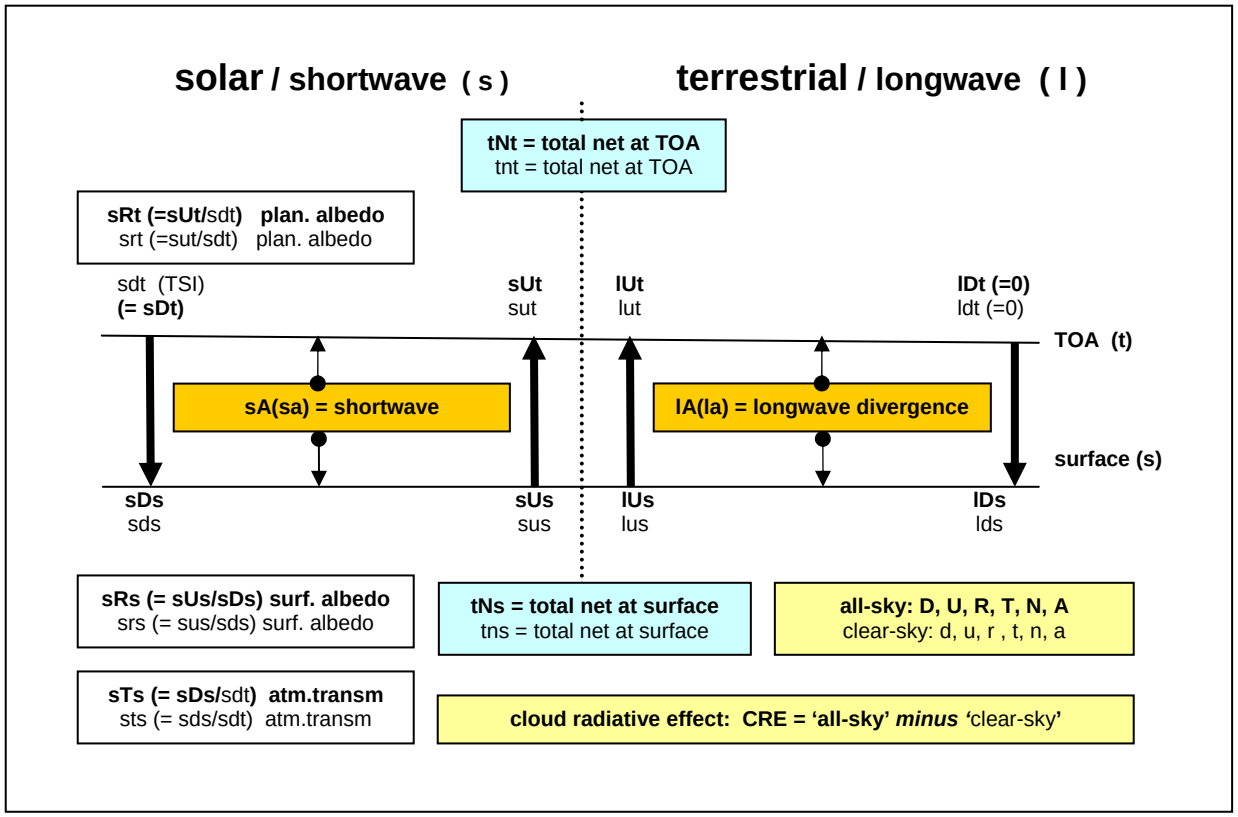

Figure 9.1.1: *Logic of symbols used to identify radiation products in subsequent diagrams of this chapter**.** First column letters indicate the associated spectral range (e.g.* ***'s' for shortwave****, 'l'* ***for longwave*** *(or IR) and 't' for the shortwave and longwave total). Second column letters refer to the* ***flux direction*** *(e.g. 'u' for upward, 'd' for downward, 'n' for net). Here, note that lower-case (second column) letters indicate 'clear-sky' conditions and that capital-case letters refer to 'all-sky' conditions. Third column letters indicate the* ***location*** *('t' for TOA' and 's' for surface). TSI is the total solar irradiance at TOA.*

9.1.2: The IPCC Median Model

The output of all contributing IPCC models (see *Table A.1.12* of the Appendix A to section 9.1 in Appendix C) for the same radiative flux quantity is represented by a median model, where local monthly median values are combined to generate global maps. Multi-annual monthly

means for the IPCC model median for twelve essential radiative flux quantities are displayed in *Figure 9.1.2*.

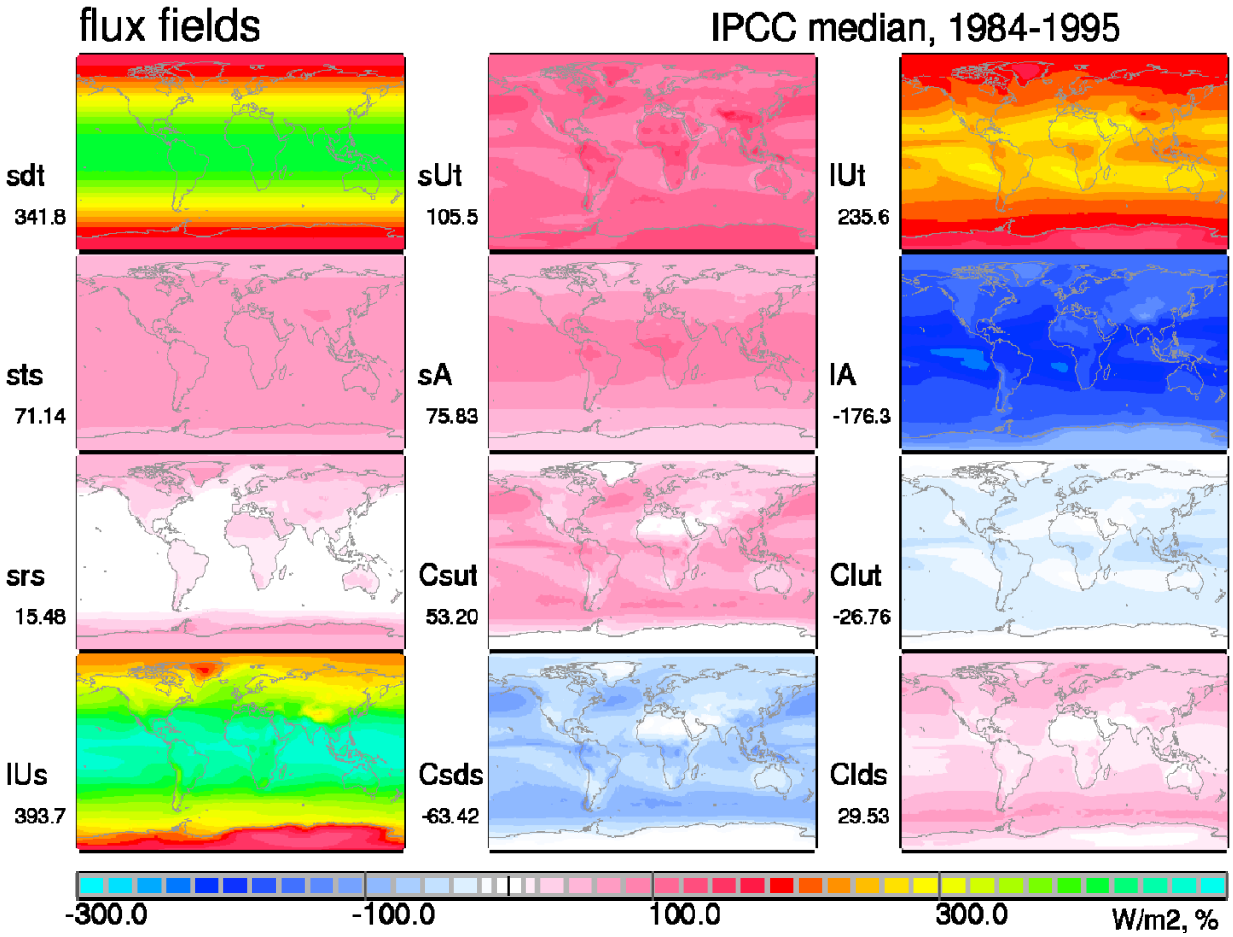

Figure 9.1.2: *Selected annual broadband flux fields and broadband cloud radiative effects (in W/m^2) of the IPCC-AR4 median model averaged over the 1984-1995 period. The labels are explained in Figure 9.1.1 and in Table 9.1.2. The center column displays solar fluxes and the right column displays IR fluxes, hereby including cloud radiative effects (as fluxes change from 'clear-sky' to 'all-sky') to upward fluxes at TOA and to downward fluxes at the surface. In addition, the left column presents ancillary data for TSI (sdt),'clear-sky' solar atmospheric transmittance (sts in %), solar surface reflectance (srs in %) and IR surface emission fluxes.*

The center and right columns *in Figure 9.1.2* illustrate fluxes or flux differences for the solar or shortwave region ('s..') and for the IR or longwave ('l..') region, respectively. The first row presents outgoing TOA fluxes (sUt, lUt) which on a global basis need to balance the incoming solar irradiance (sdt). The second row displays atmospheric divergence (sA, lA). The last two rows present (model-simulated) cloud radiative effects (CRE) for upward fluxes at TOA (Csut, Clut) and for downward fluxes at the surface (Csds, Clds).

These modeled fields are quite similar to those suggested by the climatological flux products of ISCCP, SRB and CERES-SRBAVG (see comparisons below and also in Appendix B to section 9.1 in APPENDIX S). However, the simulated radiative fluxes are also influenced by applied ancillary data. Thus, four important subsidiary data maps are added and presented in the

left column of *Figure 9.1.2*. These data were either provided directly for each model or were derived based on flux ratios (e.g. *Table 9.1.1*).

The examined subsidiary data are (1) the solar irradiation at the TOA (sdt), (2) the clear-sky solar atmospheric transmission (sts), (3) the clear-sky solar surface albedo (srs) and (4) the (all-sky) upward IR fluxes at the surface (lUs). Note that differences in these flux quantities are related to differences in the factors described below:

Solar irradiation at the TOA (sdt)
Differences are mainly caused by the prescription of the 'solar constant' value (TSI) as function of time and by the implementation of temporal (e.g. monthly) solar insolation variations as a function of latitude

Clear-sky solar atmospheric transmission (sts)
Differences are caused by the prescription of solar absorption by trace gases and more importantly by the representation of atmospheric aerosol.

Clear-sky solar surface albedo (srs)
Differences are strongly linked to the assumed vegetation type and snow cover over continents as well as sea-ice extent over oceans along with the assumed reflectance data or in its parameterization

All-sky **upward IR fluxes at the surface** (lUs).
Differences are caused by the surface (or skin) temperature and the surface emissivity of the soil, with larger diversity over desert regions.

9.1.3: Diversity in Modeling

The flux maps of the IPCC median (*Figure 9.1.2*), however, are associated with significant uncertainty. Local (IPCC-) model diversity is illustrated by associated maps for variability (standard deviation) in *Figure 9.1.3* and relative variability (standard deviation to median ratio) in *Figure 9.1.4*. Global averages for the IPCC standard deviations are placed in the context of the global averages for the IPCC median values for all 12 examined quantities in *Table 9.1.3*.

Table 9.1.3: *Global annual averages of broadband median fluxes, corresponding standard deviation and relative standard deviation (=standard deviation divided by median). Data follow the label convention of Table 9.1.2 and units are in W/m^2 unless noted otherwise.*

IPCC	sdt	sUt	lUt	sts %	sA	lA	sRs,%	lUs	Csut	Clut	Csds	Clds
Median	342	105.5	236	71.1	75.8	-176	15.5	394	53.2	-26.8	-63.4	29.5
std. dev	1.3	13	9.8	2.6	6.7	12	3.8	12	11	7.8	15	17
rel std %	0.4	13	4	4	9	7	24	3	20	29	23	40

These global annual values already provide initial information on model deficiencies. A spectral comparison of flux diversities for upward all-sky fluxes at TOA (sUt, lUt) indicate that model diversity is larger for the solar radiative transfer (with dominant scattering processes) than for the IR radiative transfer. About 80% of this diversity is associated with clouds (Csut, Clut). The variability for cloud effects on downward fluxes to the surface (Csds, Clds) is larger than the variability for cloud effects on upward fluxes to the TOA (Csut, Clut). This applies especially to IR fluxes, where, in addition to cloud cover and cloud optical depth, also cloud base altitude

differences add to the model diversity. The larger model diversity for surface fluxes is not completely surprising, because global modeling is usually forced to balance the TOA fluxes, which are much better constrained by satellite data.

The analysis of global patterns of model diversity often demonstrates the local diversity associated with the input ancillary data. The diversity for the solar clear-sky transmission is largely related to the treatment of aerosol; this is also evident in the diversity of the solar divergence (e.g. by differing absorbing dust amounts over the Sahara). The diversity for the solar surface reflectance in a relative sense is largest among all ancillary data and regionally larger at high latitudes due to differences in snow cover over land and the sea-ice extent over oceans. The diversity for solar cloud effects is strongest in the tropics, where solar irradiance is largest, whereas the diversity for IR cloud effect is strongly linked to issues regarding the altitude of the cloud placement, more specifically cloud tops in the tropics for TOA fluxes and cloud bases at mid-latitudes for surface fluxes.

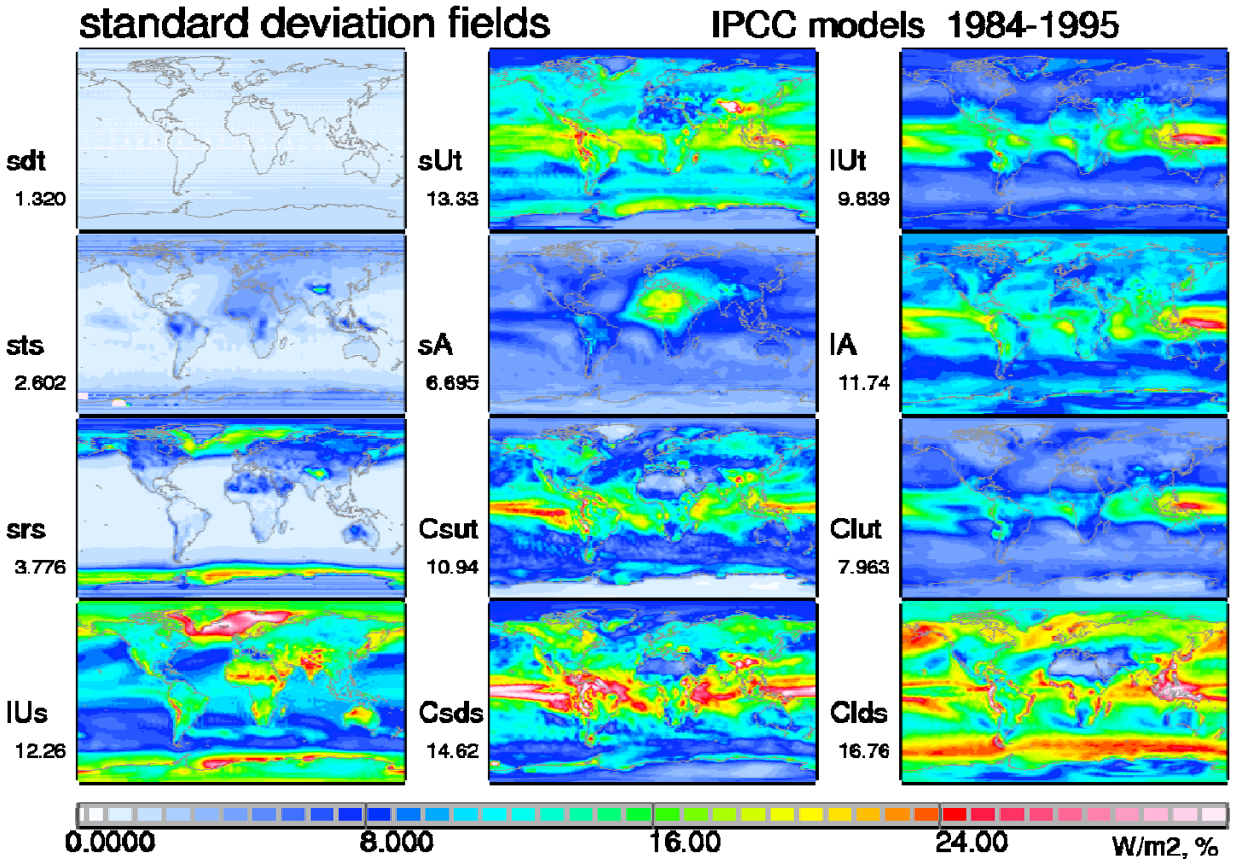

***Figure 9.1.3**: Multi-annual (1984-1995) local standard deviation in global IPCC modeling for selected radiative flux quantities, corresponding to maps presented in Figure 9.1.2*

Differences in (warmer) open water regions also explain the higher model diversities for upwelling IR fluxes from the surface at higher latitudes, while the diversity at lower latitudes occurs mainly over desert regions, probably due to surface emission. As ancillary data diversity propagates into simulated radiative flux products, a harmonization of these data in modeling is highly desirable. Assessments are required that examine and intercompare the different ancillary datasets and recommendations on their use are needed.

For cloud radiative effects, the diversity at solar wavelengths is mainly driven by cloud optical depth and/or cover, while the diversity at IR wavelengths is mainly driven by the altitude of the cloud placement. Clear issues in modeling are the representation of clouds in the tropics and over oceans, where differences to the assumed cloud base also cause diversity in the IR downward fluxes. Patterns of the relative diversity for cloud radiative effects are more difficult to interpret and also have to be understood in the context of the cloud cover (e.g. large relative errors in regions with low cloud cover such as deserts are less meaningful).

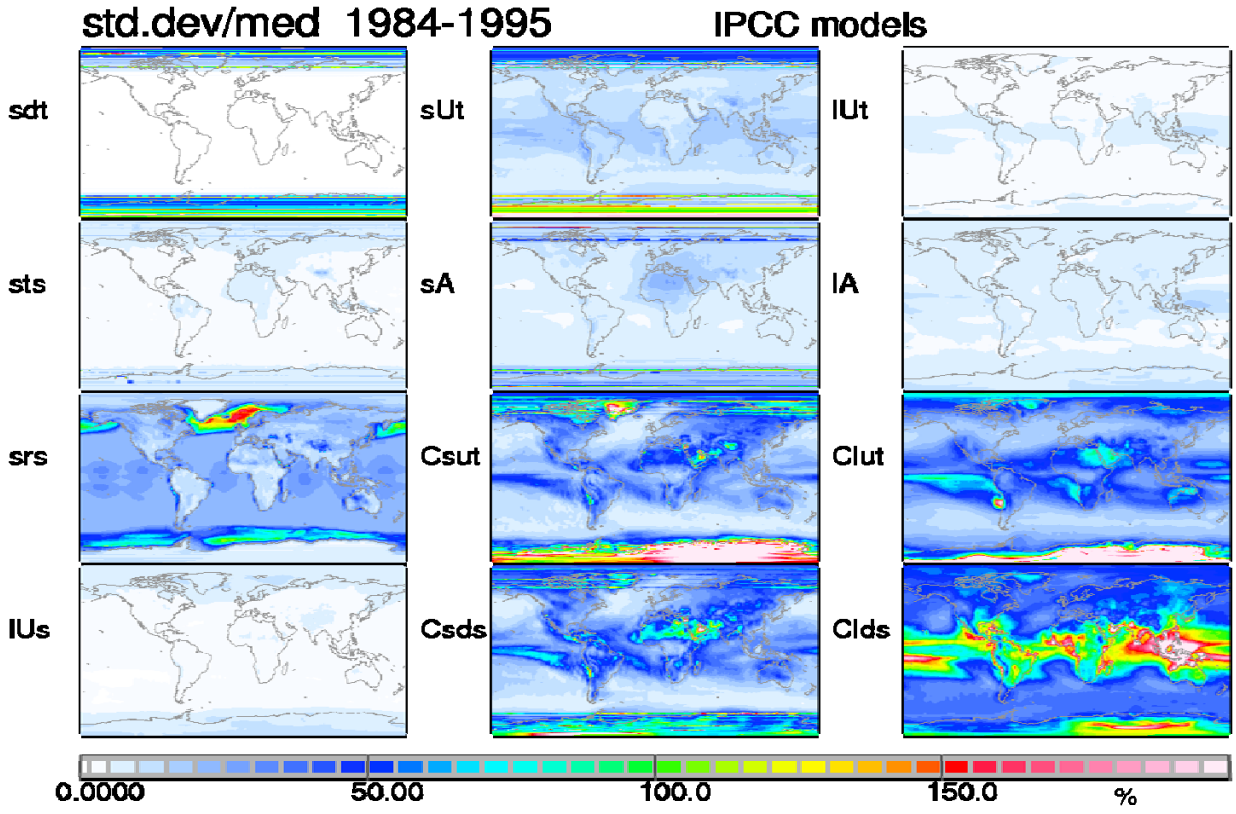

Figure 9.1.4*: Multi-annual (1984-1995) local relative variability (standard deviation / median) in global IPCC modeling for selected radiative fluxes, corresponding to maps presented in Figures 9.1.2 and 9.1.3.*

9.1.4: The CERES Data Reference

References for the simulated radiative fluxes by global modeling are provided by satellite sensor data. Hereby, the focus is on fluxes at the TOA. The selected reference data are lower latitude ERBE/ERBS data during the late 1980s and more recent CERES-SRBAVG data since the year 2000. For comparison purposes climatology products of ISCCP and SRB are also considered. CERES-SRBAVG, SRB and ISCCP provide, in addition to TOA fluxes, data products for surface fluxes based on complimentary sensor data for clouds and other ancillary data. Global radiative flux fields corresponding to those of *Figure 9.1.2* are presented for CERES-SRBAVG, as the primary satellite reference, in *Figure 9.1.5* (and for ISCCP and SRB for two different time-periods in the Appendix B to section 9.1 in APPENDIX S).

The general color patterns in *Figure 9.1.5* are quite similar to the IPCC median model of *Figure 9.1.2,* including those given for ISCCP and SRB. However, on closer inspection there are differences in magnitude; this is also seen from a comparison of global annual averages in *Table 9.1.4*. When comparing global averages in *Table 9.1.4* it becomes apparent that solar cloud effects in CERES-SRBAVG are relatively weak. Since satellite data-products are thought to establish a reference to modeling, their (regional) consistency (or diversity) is addressed next.

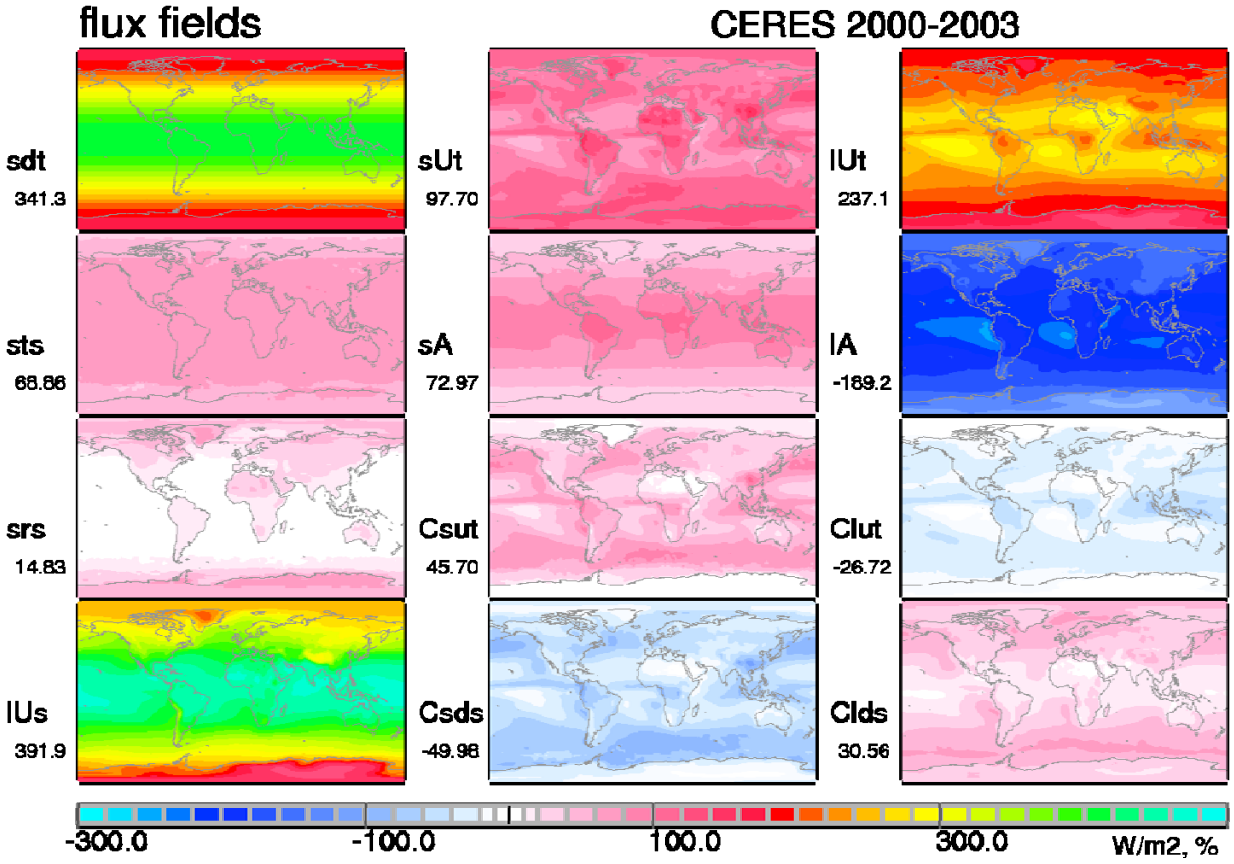

Figure 9.1.5*: Selected annual broadband flux fields and broadband cloud radiative effects (in W/m2) of the CERES-SRBAVG satellite product averaged over the 3/2000-2/2004 period. The labels are explained in Figure 9.1.1 and in Table 9.1.2. The center column displays solar fluxes and the right column displays IR fluxes, hereby including cloud radiative effects (as fluxes change from 'clear-sky' to 'all-sky') to upward fluxes at TOA and to downward fluxes at the surface. In addition, the left column presents ancillary data for TSI (sdt),'clear-sky' solar atmospheric transmittance (sts, in %), solar surface reflectance (srs, in %) and IR surface upward emission fluxes (lUs).*

Table 9.1.4 *Comparison of annual global averages for up fluxes and cloud effects (in Wm^{-2})*

		up-fluxes at top of atmosphere (TOA)					down-fluxes at surface		
data	*period*	*all, s*	*all, ir*	*CRE, s*	*CRE, ir*	*CRE*	*CRE, s*	*CRE, ir*	*CRE*
IPCC	**1984-95**	**105.5**	**235.6**	**53.2**	**-26.8**	**22.3***	**-63.4**	**29.5**	**32.5***
CERES	3/00-2/04	97.7	237.1	45.7	-26.7	19.9	-50.0	30.6	20.5
ISCCP	1984-95	105.7	233.3	49.7	-25.7	24.0	-58.3	31.0	27.3
ISCCP	2000-03	105.0	235.5	50.6	-26.3	24.3	-59.3	31.4	27.9
SRB	1984-95	102.1	240.1	46.9	-28.0	18.9	-56.2	35.7	20.5
SRB	2000-03	101.6	240.6	47.9	-27.4	20.5	-56.8	34.6	22.2

** Note that IPCC median model data are separately determined for solar, IR and net (solar+IR) fluxes with contributing data from different models so that IPCC median model global averages are not additive.*

9.1.5: Comparison of Satellite-Based Flux Products at TOA

The maps in *Figure 9.1.6* compare annual averages among satellite-based TOA upward solar and infrared (broadband) fluxes and their suggested modulations by clouds (CRE). These results complement the discussions in chapters 3.5 and 4.5.

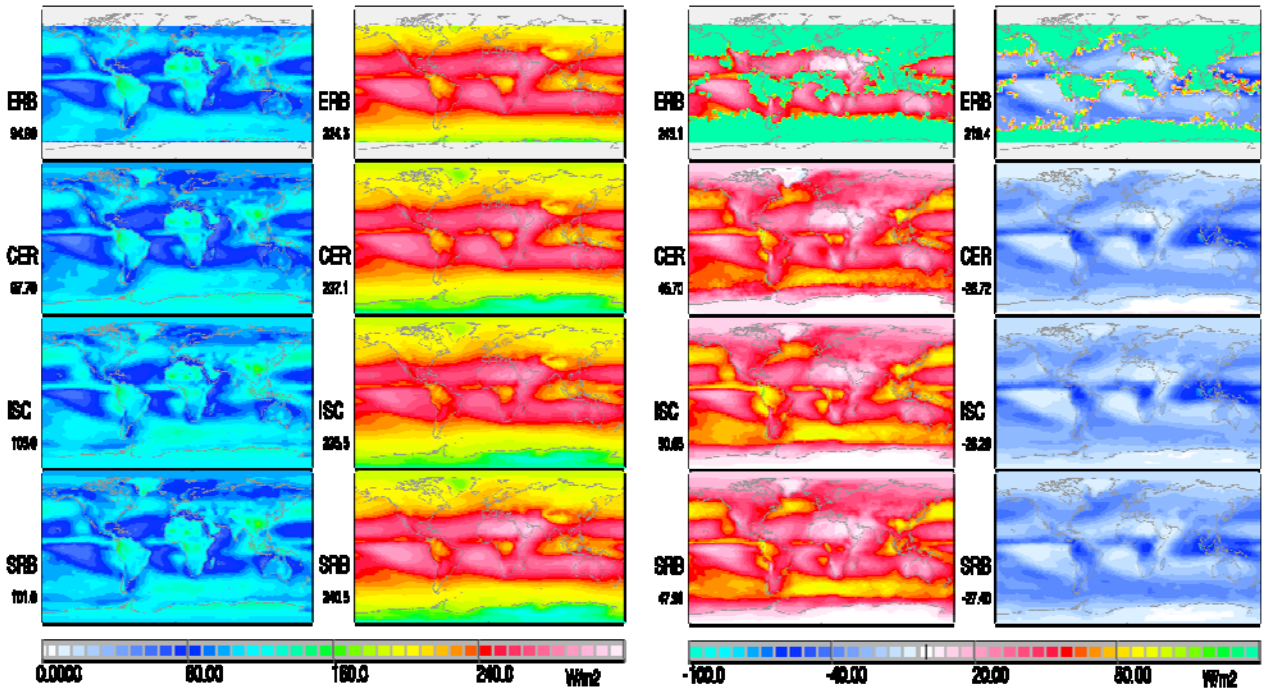

Figure 9.1.6: *Comparisons of multi-annual satellite sensor dependent TOA all-sky radiative fluxes and associated CRE. CERES-SRBAVG (CER), ISCCP (ISC) and SRB data are for the 2000-2003 period and ERBE (ERB) data (only available at lower latitudes) represent the 1985-1988 period. All-sky upward fluxes at TOA are displayed for the solar region in column 1 and for the IR region in column 2. Associated cloud impacts (CRE) are presented in column 3 for the solar and column 4 for the IR region.*

The TOA fluxes from satellite data were chosen, because they are strongly dependent on observations. Four different climatology products were compared in *Figure 9.1.6*: the CERES-SRBAVG reference data for the Mar/2000 to Feb/2004 period, the ISCCP and the SRB climatologies for the Jan/2000-Dec/2003 period and an older ERBE reference for the Jan/1985-Dec/1988 period. ERBE lacks high latitude data and spatial coverage for clear-sky conditions, thus CRE is limited. The comparison demonstrates good agreement in the spatial distribution patterns. Here, agreement for seasonal regional patterns appears better for the IR compared to solar fluxes. Larger solar differences are mainly related to the representation of clouds. CERES-SRBAVG solar cloud radiative effects (and solar all-sky upward fluxes) stand out as relatively weak compared to the other satellite climatologies. To better spot local disagreement, difference maps of multi-annual flux products are presented between ISCCP and CERES-SRBAVG in *Figure 9.1.7* and between SRB and CERES-SRBAVG in *Figure 9.1.8* (for the same 12 annual maps that were already presented in *Figures 9.1.2* and *9.1.5,* respectively). The differences also address subsidiary (or assumed ancillary) quantities.

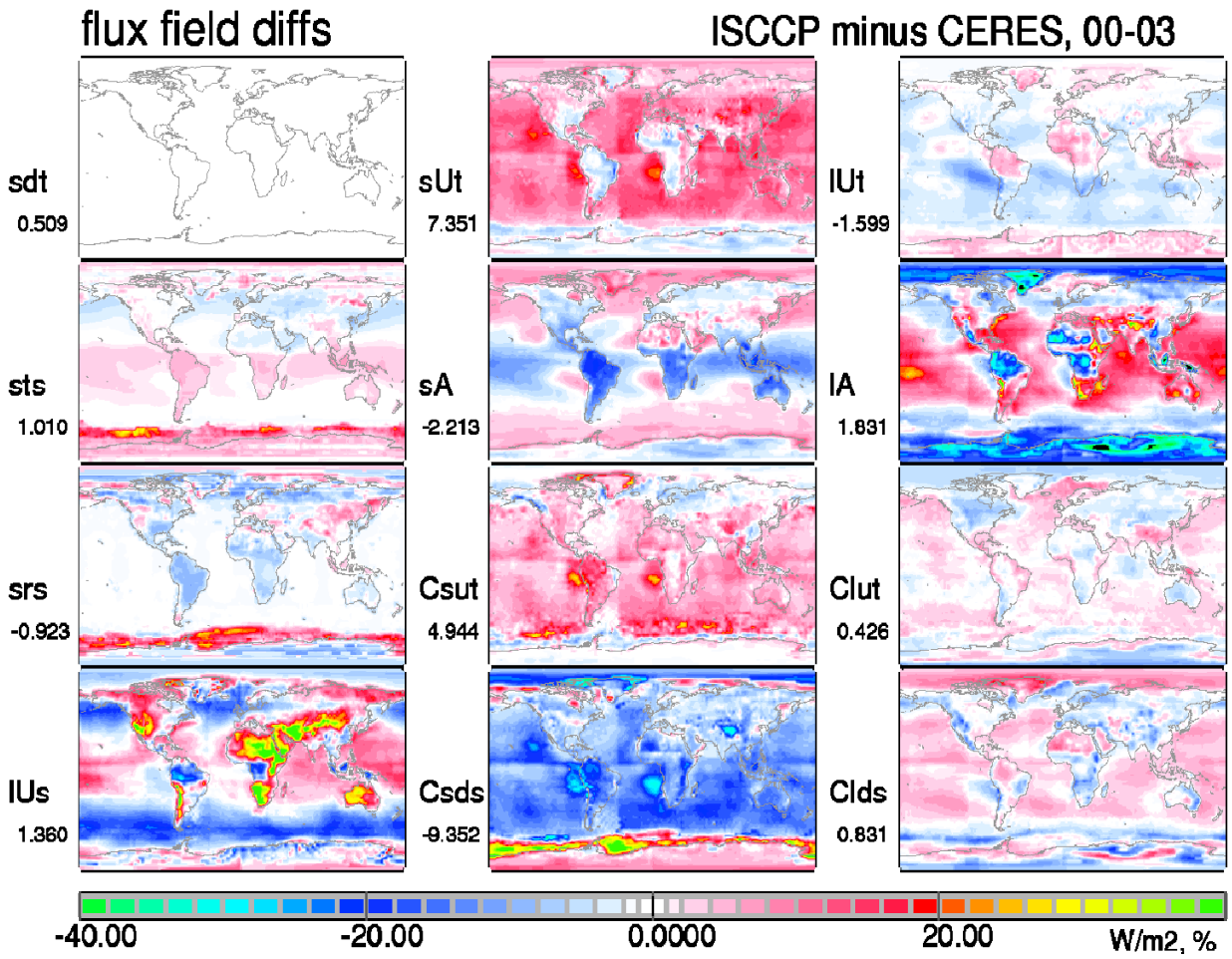

Figure 9.1.7: *Difference maps of multi-annual (2000-2003) flux and flux-ratio fields between ISCCP and CERES-SRBAVG. Differences are given for ancillary data in the left column and for solar (s…) and infrared (l…) broadband fluxes in the center and in the right column - including the cloud-effects (C…) on upward fluxes at TOA (C..ut) and downward fluxes at the surface (C..ds) sA is the "convergence" (negative divergence) of solar radiation and lA is the divergence of longwave radiation..*

The differences in the left column of *Figure 9.1.7* and *Figure 9.1.8* are intended to demonstrate impacts of external assumptions on the flux products.

Upward IR flux differences at the surface are particularly large. ISSCP and SRB have much larger upward IR fluxes than CERES-SRBAVG over desert regions where, aside from differences with the assumed surface temperature, the assumption about the surface emittance also matters. In ISCCP (on a global average sense) the positive bias over deserts is partially compensated by smaller emittances then CERES-SRBAVG over high latitude oceans and over tropical forests. CERES results did no show any traces caused by geostationary data.

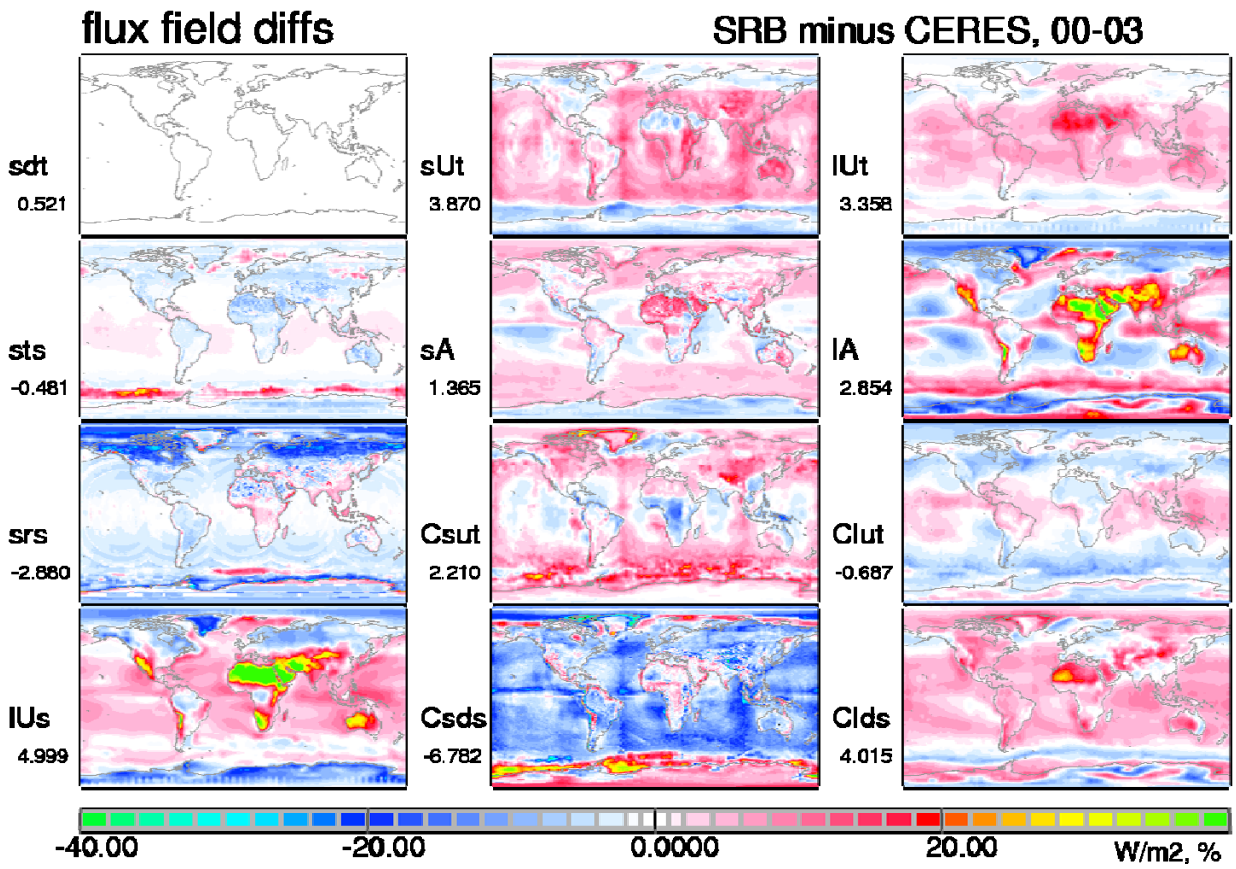

Figure 9.1.8: *Difference maps of multi-annual (2000-2003) flux and flux-ratio fields between SRB and CERES-SRBAVG. Differences are given for ancillary data in the left column and for solar (s…) and infrared (l…) broadband fluxes in the center and in the right column - including the cloud-effects (C…) on upward fluxes at TOA (C..ut) and downward fluxes at the surface (C..ds). Note the pattern in the maps with ISCCP and SRB results*

Clear-sky solar transmission differences provide insight on the representation of aerosol amount and, to a lesser degree, on the treatment of solar absorption by trace gases. Associating larger clear-sky fluxes with less aerosol (and vice versa), ISCCP appears to assume more aerosol amount than CERES-SRBAVG over the Northern, but less over the Southern Hemisphere. The lower solar transmission for CERES-SRBAVG over the Southern Hemisphere is currently an unresolved data issue. Similarly, SRB has more aerosol amount over land and less over oceans than CERES-SRBAVG.

Solar surface albedo differences indicate that ISCCP assumes a slightly lower reflection than CERES-SRBAVG over land. The biggest differences involve SRB data at continental high latitudes in the Northern Hemisphere. There SRB surface reflections are much lower than both CERES-SRBAVG and ISCCP, pointing to snow reflectance not properly being accounted for.

Also shown in *Figures 9.1.7* and *9.1.8*, in the four lower right panels, are differences for cloud radiative effects (CRE). Here, it should be noted that downward solar cloud effects at the surface (Csds) and TOA upward longwave cloud effect (Clut) are both negative, which should be kept in mind when interpreting differences between data sets.

For solar fluxes, cloud effect differences between ISCCP and CERES-SRBAVG are contaminated by rectangular hemispheric zonal sectional patterns, whereas differences between

SRB and CERES-SRBAVG display circular patterns. These artificial cloud effect patterns also show up in the differences for the upward solar flux at the TOA, displayed in the top center panels of *Figure 9.1.7*. Similarly, the strongest CRE by ISCCP over the stratocumulus regions make their mark on the upward solar fluxes at the TOA. However, cloud effects can only explain in part the relatively strong ISSCP solar upward TOA fluxes over oceans.

For the IR, the outgoing fluxes at the TOA (or OLR) of ISCCP, SRB and CERES-SRBAVG are not identical, as displayed in the upper right panels of *Figure 9.1.7*. If CERES-SRBAVG is considered as the reference, then ISCCP locally underestimates OLR over the Southern Hemispheric sub-tropics, while SRB strongly overestimates the OLR over the Sahara, and globally overall. These large differences over the Sahara are not so much influenced by clouds (as contributing CRE differences are relatively small), but rather by a much larger longwave divergence (second-row/right-column panel in *Figure 9.1.7*) for the SRB data. Differences for the downward IR re-radiation to the surface by clouds are displayed in the lower right panels of *Figure 9.1.7*. Larger values by ISCCP or SRB compared to CERES-SRBAVG are expected, as their solar reflectance data for clouds indicate larger cloud optical depths than CERES-SRBAVG. The positive biases of SRB are much larger than those of ISCCP. This suggests that base heights of low clouds in SRB are assumed to be at lower altitudes than in ISCCP or CERES-SRBAVG.

Solar divergence (sA) and IR divergence (lA) differences are presented in the second row of *Figure 9.1.7*. The divergence captures atmospheric warming (positive values) and atmospheric cooling (negative values). The difference in solar heating can be largely attributed to the assumptions for amount and absorption of tropospheric aerosol. Infrared atmospheric divergence is larger than for the solar and occurs in tandem with differences to IR upward fluxes from the surface, which is displayed in the lower left panels of *Figure 9.1.7*.

Finally, a note of caution is given, regarding limitations when comparing cloud effects. Cloud radiative effects depend on the definition of clear-sky. Measurements limited to clear-sky regions, as is for the CERES-SRBAVG data, include in addition to the cloud effect, also a water vapor effect, since water vapor concentrations are usually higher in and around clouds. In contrast, model simulations of clear-sky conditions simply remove clouds in an otherwise identical simulation. Such cloud effects are provided by ISCCP, SRB and global modeling. Also, these cloud effects do not consider changes in atmospheric water vapor. Thus, observational cloud effects should be stronger than simulated ones, as they contain this additional water vapor effect. More extensive investigations among satellite flux climatologies are presented in chapters 3 and 4.

9.1.6: Comparison of IPCC Median with Satellite Reference Data at TOA

This section focuses on highlighting major differences in radiative flux patterns between global modeling and satellite data at the TOA. We consider as most reliable satellite flux products those for the TOA, because CERES-SRBAVG and ERBE provide direct measurements. Thus, solar and IR TOA upward all-sky fluxes and the associated cloud radiative effects of CERES-SRBAVG and ERBE are applied as reference data for comparison with global modeling results, represented here by the IPCC median model (*Figure 9.1.2*). Flux differences with respect to the four satellite data (IPCC-ERBE, IPCC-CERES, IPCC-ISCCP, IPCC-SRB) are presented *in Figure 9.1.9*.

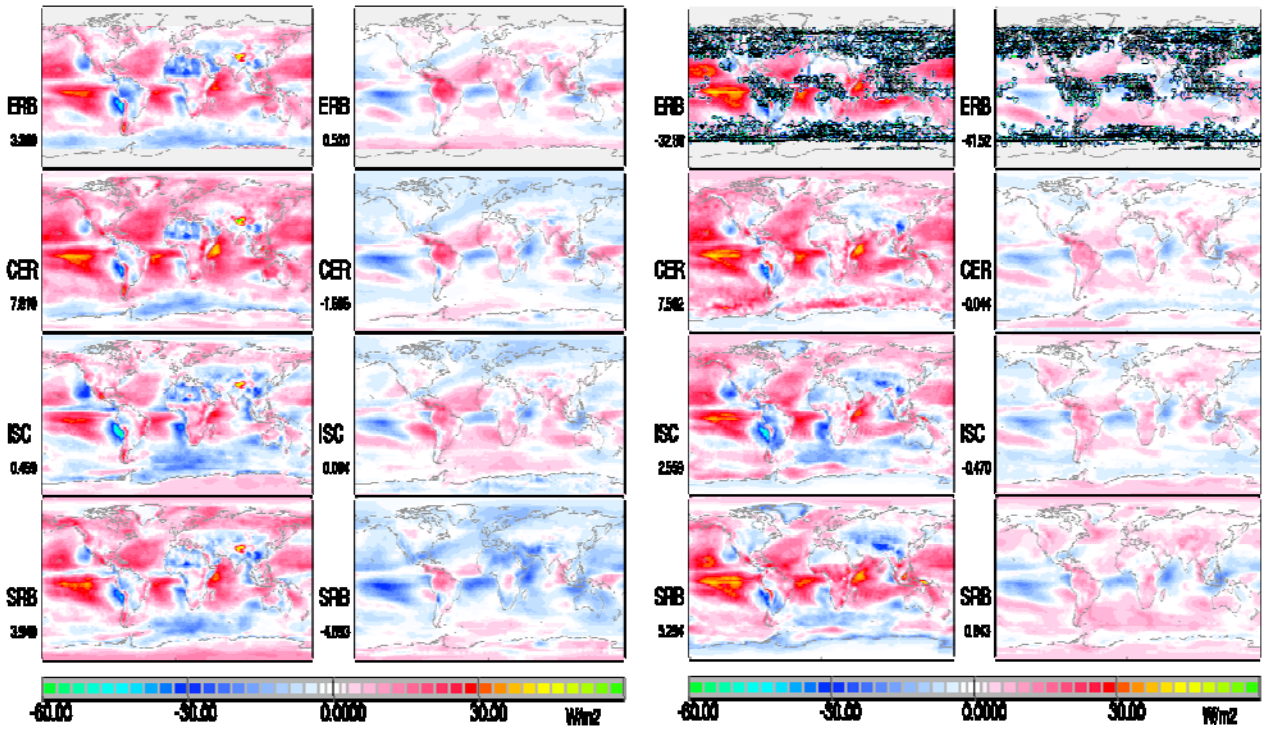

Figure 9.1.9*: Annual difference maps for solar upward fluxes at the TOA (left, colunm1) and infrared upward fluxes at the TOA (left, column2) and for cloud effects on solar upward fluxes at the TOA (right, column1) and on infrared upward fluxes at the TOA (right, column2) between the multi-annual (1984-1995) IPCC median model and four different satellite climatologies: ERBE (1985-1988), CERES-SRBAVG (2000-2003), ISCCP (2000-2003) and SRB (2000-2003). ERBE data for CRE are spatially limited due to data gaps for 'clear-sky' conditions, also causing global averages (below labels) to be in error.*

It is quite interesting to see that, despite varying global annual differences, the difference patterns are quite similar. This demonstrates that the flux diversity in satellite products is smaller than that between satellite data and the model median. Differences for all-sky upward fluxes are more or less mirrored by the differences in the cloud radiative effects at the TOA. This mirroring is even quantitatively quite similar for the solar radiative transfer. Cloud effect mirroring is not so strong in the IR, which suggests that other factors contribute towards OLR differences, such a water vapor. Cloud effect differences indicate strong model underestimates (40 Wm^{-2} or greater) over stratocumulus fields off continental west coasts with compensating overestimates over tropical oceans. For more detail, seasonal differences are examined again in *Figure 9.1.10*.

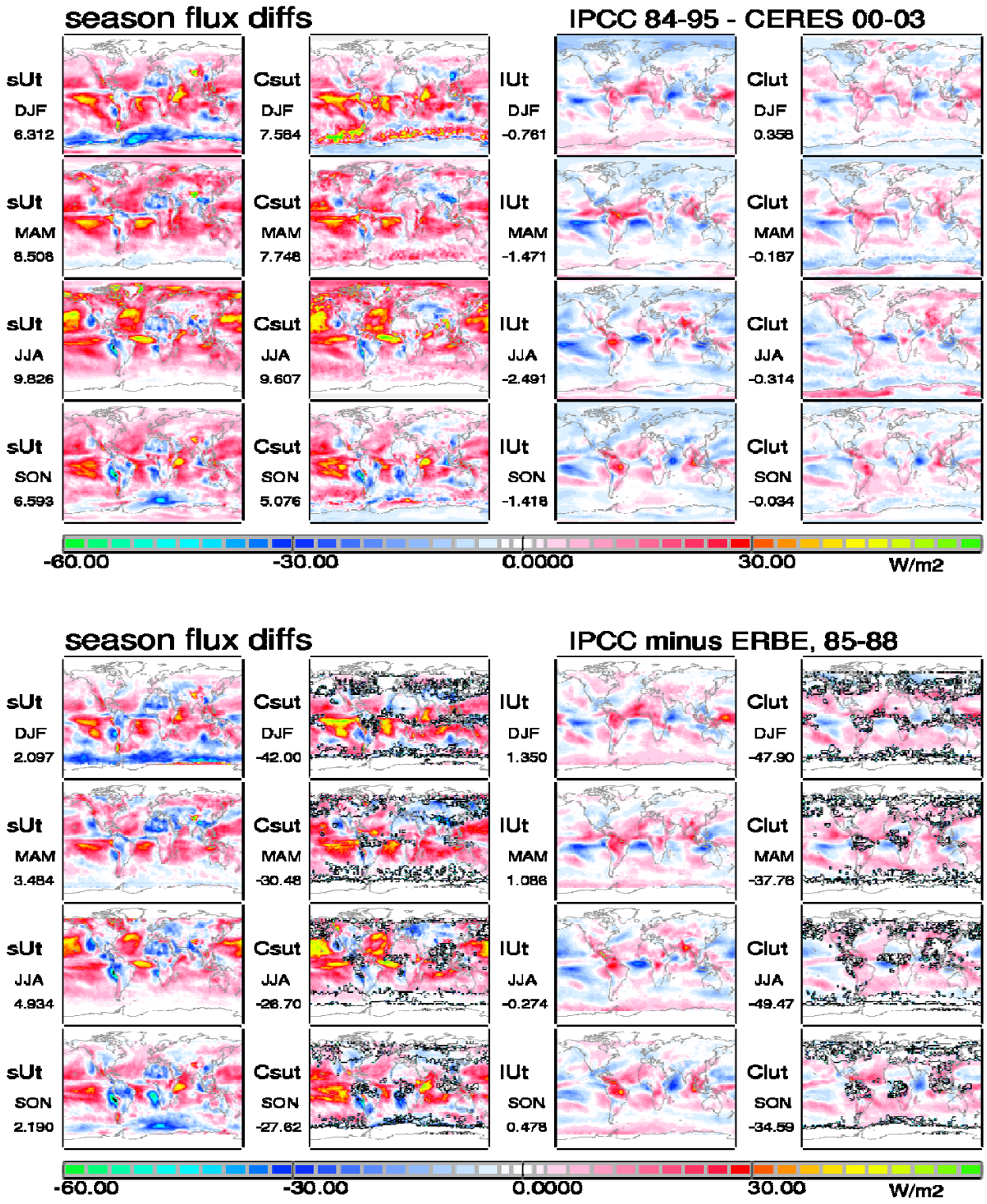

Figure 9.1.10: *Seasonal difference maps for upward 'all-sky' fluxes at the TOA and for contributing cloud effects on these fluxes. Solar values are presented in the two left columns and IR values in the two right columns. The upper set of panels displays differences between the multi-annual (1984-1995) IPCC median and CERES-SRBAVG (2000-2003) satellite data, whereas the lower set of panels compare the IPCC median with ERBE for the same (1985-1988) time-period. ERBE data on the CRE are biased in the global average due to gaps in those for the cloud-free atmosphere.*

9.1.7: Comparison of IPCC Median with Satellite Data at the Surface

Complimentary to the TOA flux differences, those at the surface are examined next. CERES-SRBAVG data at the surface, although tuned to be consistent with TOA observations, should not be considered a reference but as another data set, since it is simulated based on many assumptions (along with the use of ancillary data). Nonetheless, comparisons of IPCC model median data to CERES-SRBAVG can demonstrate characteristic biases in global modeling. Seasonal differences between IPCC modeling and CERES for surface fluxes (complimenting TOA comparisons of *Figure 9.1.10*) are presented in *Figure 9.1.11*.

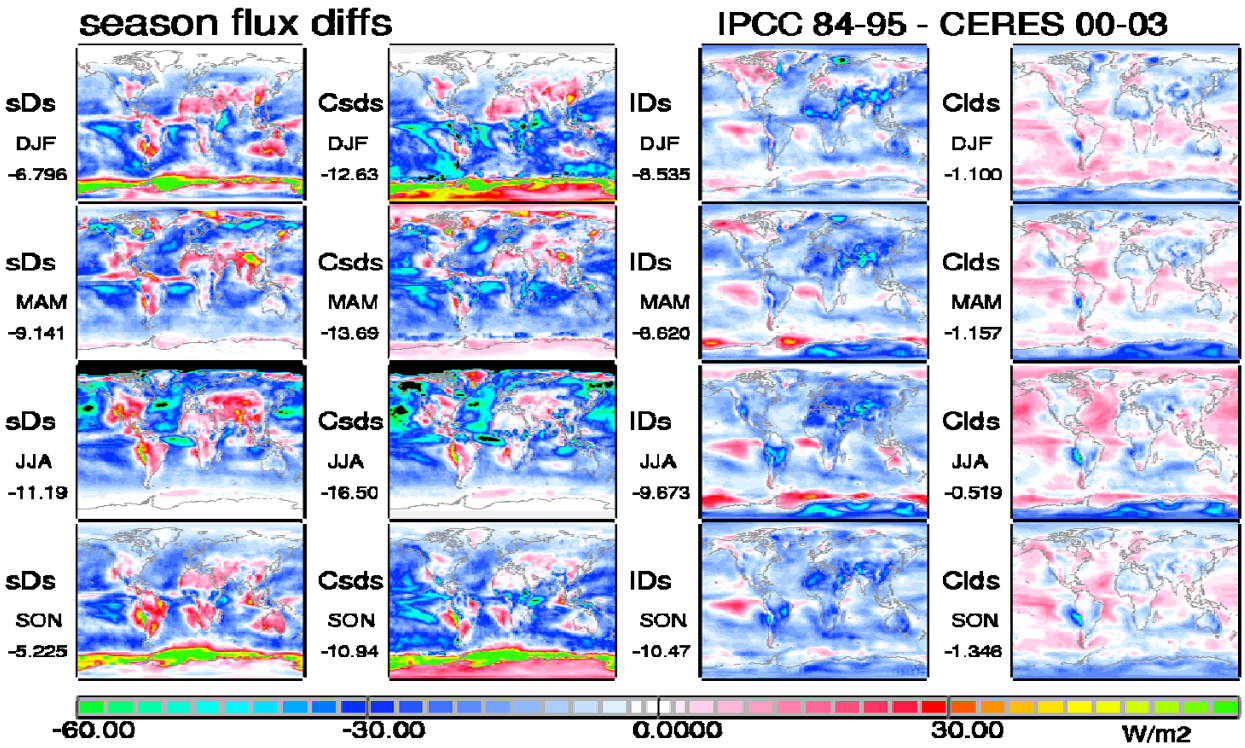

Figure 9.1.11: *Seasonal difference maps for downward 'all-sky' fluxes at the surface and for contributing cloud effects on these fluxes. Solar values are presented in the two left columns and IR values in the two right columns. Differences are displayed between the multi-annual (1984-1995) IPCC median and CERES climatological (2000-2003) data. A black color indicates biases more negative than -60 Wm^{-2}, whereas a green color indicates biases in excess of +60 Wm^{-2}.*

Interestingly, for all-sky conditions, global differences between IPCC and CERES-SRBAVG for the solar upward TOA fluxes (left column *Figure 9.1.10*) are smaller than their differences for the downward solar fluxes at the surface (left column *Figure 9.1.11*). This suggests that assumed cloud particle sizes in IPCC modeling are smaller.

For comparisons of cloud effects on downward radiative fluxes to the surface, the regional deviations between IPCC and CERES-SRBAVG are much larger than the water vapor bias, which should give CERES-SRBAVG data slightly stronger effects. Differences are larger for the solar spectral region than for the IR. Both solar and IR deviations have clear regional biases. Solar cloud effects in IPCC modeling are much stronger (e.g. indicating more cloud cover or cloud

optical depth in IPCC models) over most oceans and here especially in SH high latitudes during summer. In contrast, solar cloud effects in IPCC modeling are too weak over continents and in association with attached marine stratocumulus over upwelling colder ocean waters. Globally averaged, the cloud effects on solar surface fluxes are stronger in IPCC global modeling (although based on the CERES-SRBAVG water vapor bias, expectations were opposite).

The overall IPCC to CERES-SRBAVG difference for the cloud effect on the solar downward fluxes is larger than the corresponding difference for the solar downward flux alone at all-sky conditions. This indicates higher clear-sky solar transmissions in IPCC modeling, as confirmed in *Figure 9.1.12*, where flux differences between *Figure 9.1.2* and *Figure 9.1.5* are presented.

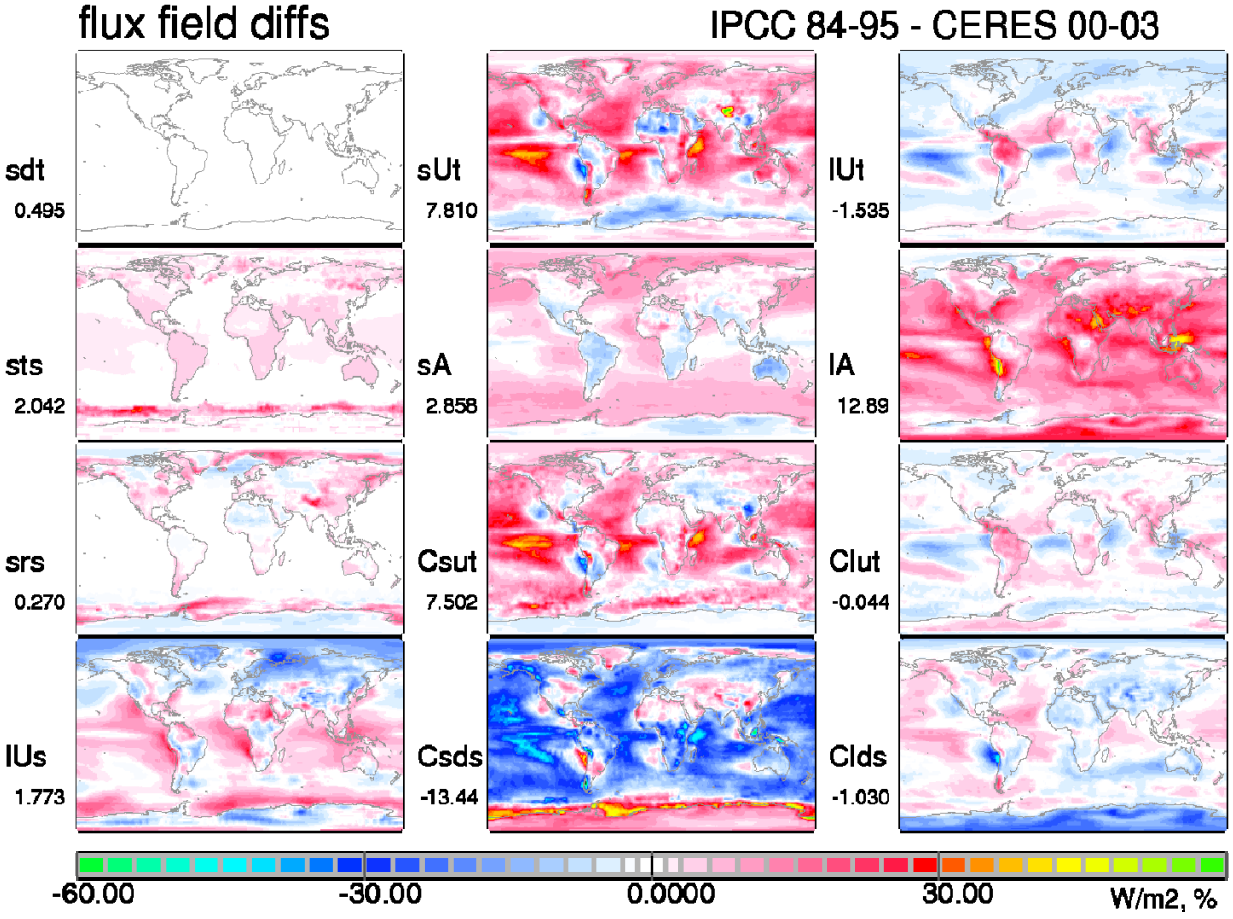

Figure 9.1.12: *Difference maps between multi-annual (1984-1995) flux and flux-ratio fields of the IPCC median model and CERES-SRBAVG multi-annual (2000-2003) fluxes. Differences are given for ancillary data in the left column and for solar (s…) and infrared (l…) broadband fluxes in the center and in the right column - including the cloud-effects (C…) on upward fluxes at TOA (C..ut) and downward fluxes at the surface (C..ds).*

The cloud effect difference patterns on IR downward fluxes (Clds) are consistent with the solar patterns. Still, on a global average basis, a strong positive IPCC bias that would be expected from the solar cloud effect differences is missing. A likely explanation is that simulated low cloud base altitudes in IPCC modeling are much higher than for CERES-SRBAVG. Also globally averaged, differences for the cloud effects on the IR downward flux are small in comparison to

all-sky flux differences, implying near surface trace-gas absorption in CERES-SRBAVG is much stronger.

CERES-SRBAVG solar and IR all-sky broadband surface fluxes are on a global annual average basis about 10 Wm^{-2} larger (each) than those for the IPCC model median (see columns 1 and 3 in *Figure 9.1.11*) . Thus, in CERES-SRBAVG a surplus of about 20 Wm^{-2} in the downward radiative flux need to be balanced by that escaping from the surface into space, in order to maintain the expected energy balance on a global annual average basis. There are indications that latent heat estimates are too low in global modeling (as sub-grid and weak precipitation or precipitation at high latitudes is often missed) but only by about 10 Wm^{-2}. The remaining 10 Wm^{-2} difference is more difficult to explain.

These comparisons demonstrate differences in the radiative flux data between the IPCC median model and CERES-SRBAVG, especially when examined on a regional and seasonal basis. More effort is needed to better quantify the uncertainties of both products. Only TOA satellite flux products have some (observational) credibility which is demonstrated by their general consistency in global patterns. Many issues in global modeling, however, go unnoticed when describing differences by one (IPCC median) model, rather than exploring the entire range of model diversity (see *Figures 9.1.3* and *9.1.4*). To illustrate this range in IPCC global modeling, including the extreme behavior of individual models, comparisons for selected flux data, including differences to CERES-SRBAVG, are presented for individual global models in Appendix C to section 9.1 in APPENDIX S. In this Appendix flux fields of individual IPCC-AR4 models are compared for the all-sky net fluxes at TOA and surface, and - stratified into solar and IR portions – for all-sky downward fluxes to the surface and for the atmospheric forcing (or divergence as explored in subchapter 7). In addition in this Appendix, individual model behavior is explored with respect to ancillary data for aerosol and solar trace-gas absorption (via the clear-sky solar transmission), for solar surface albedo and for IR surface temperature and/or emittance (via the upward IR fluxes from the surface).

The comparison of flux data along with their associated ancillary data (for individual models as well as for satellite data) demonstrates that a poor representation of aerosol (and trace-gas absorption) propagate into the clear-sky solar flux products. These clear-sky errors are often compensated by errors in the modeling of cloud effects in the all-sky solar flux. An even larger ancillary data impact is created by differences in surface property assumptions. In particular, different assumptions for ice and snow cover (at higher latitudes) have strong impacts as they propagate from (solar and IR) upward surface fluxes into many other flux products.

The net flux comparisons reveal, to what degree the energy is balanced at the TOA and how much energy is expected to be taken up by the latent and sensible heat at the surface. At the TOA the outgoing solar and IR fluxes to space should balance the incoming solar radiation. This is actually a required constraint in global modeling and demonstrated in a Table in the Appendix C to section 9.1 in APPENDIX S (where global annual average flux properties of satellite data and individual models are compared). However, the way this TOA balance is spatially accomplished in most models strongly suggests that the regional representation of clouds in modeling, and in particular that of low-level clouds over oceans, has strong deficiencies. Another issue is the radiative energy balance at the surface, where overall differences between solar and IR net-fluxes are balanced by sensible and latent heat. Compared to suggestions by the IPCC-model median, this difference is larger in simulations associated with satellite data (and particularly when compared to CERES-SRBAVG values). This suggests that precipitation is strongly (by about 20%) underestimated in global modeling. However, when looking at individual models and in the solar and IR detail, there is on a global annual basis often quite good agreement between a few models and satellite data and even CERES-SRBAVG. This demonstrates the large

diversity in modeling and that an assessment via a model median may has a limited value, particularly if most models produce poor simulations, so that the better ones might be removed as outliers. This stresses the need for quality assessments in modeling, in order to ensure that model ensembles are determined from the best quality set of simulations.

9.1.8: Atmospheric Greenhouse Effect

The "greenhouse effect" is another useful diagnostic variable used in climate modeling. It is defined as the difference between emitted longwave upward flux at the surface (controlled by surface temperature and surface emissivity) and the outgoing longwave flux at the TOA (e.g.: Lacis et al. 2010). For instance, assuming a global mean surface temperature of +15°C and 100% emissivity (producing an emitted upward surface flux of about 390 Wm^{-2}) and a space-borne observation of -18°C (producing an emitted upward TOA flux of about 240 Wm^{-2}), then the associated greenhouse effect is about 150 Wm^{-2}. Seasonal greenhouse effects at all-sky conditions, for cloud effect and clear-sky conditions are compared among the satellite data sets and the IPCC median model in *Figures 9.1.13* to *9.1.15*.

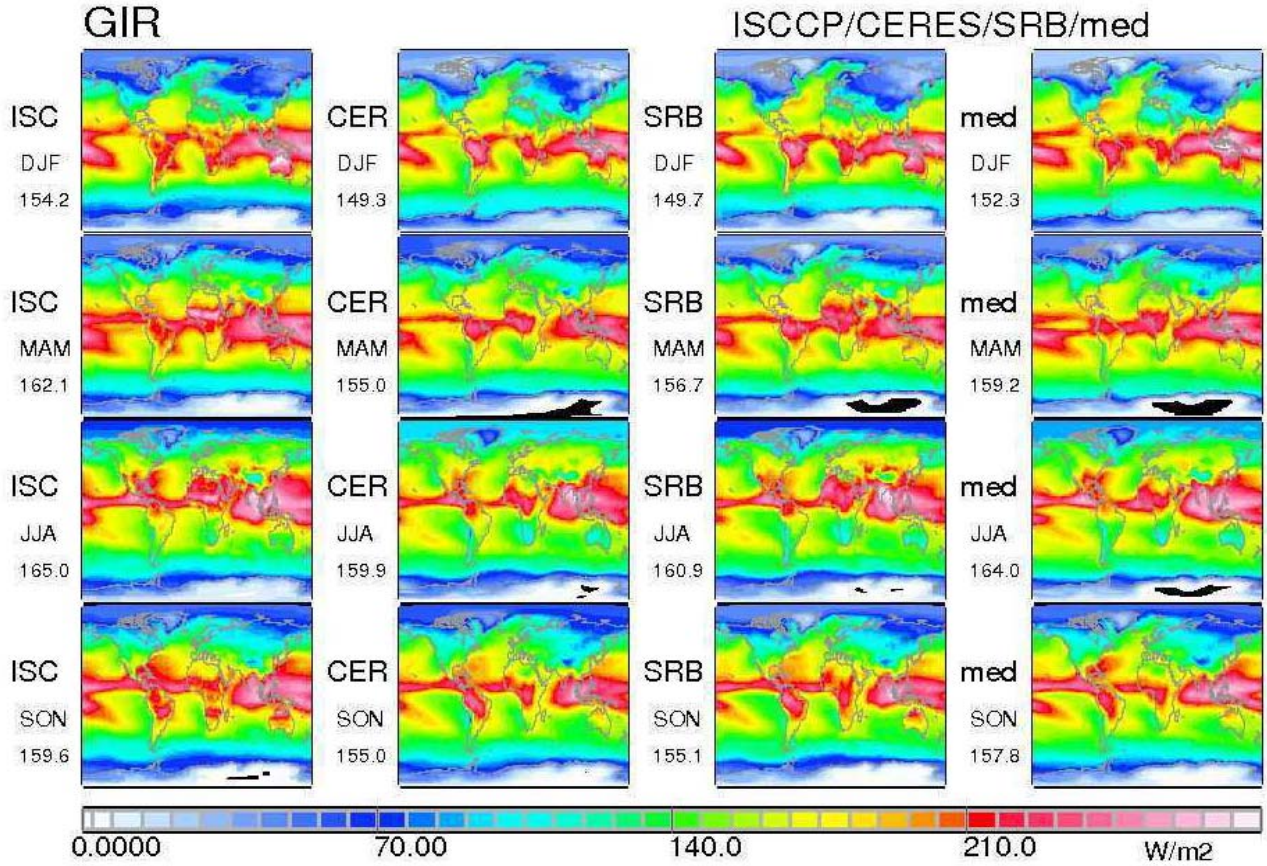

Figure 9.1.13: *Seasonal multi-year means of the greenhouse effect at all-sky conditions from ISSCP, CERES-SRBAVG, SRB and the IPCC median model. Regions with larger high cloud cover show the strongest greenhouse effects*

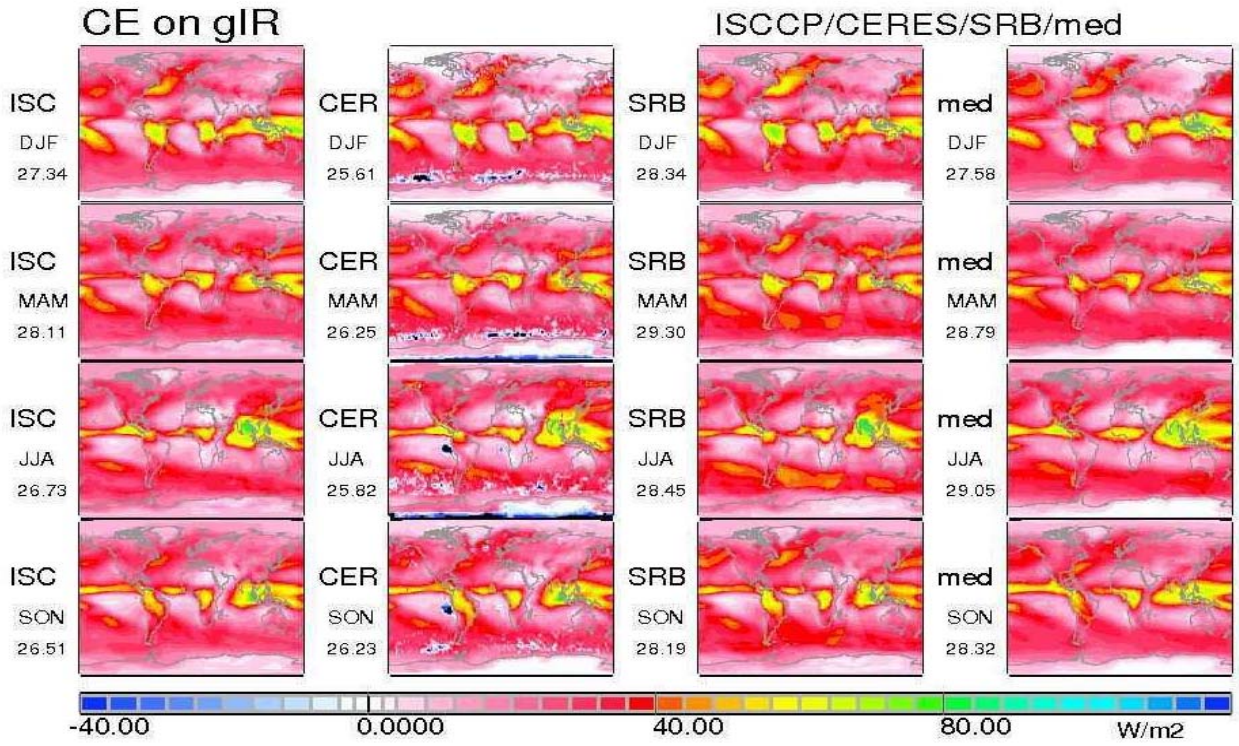

Figure 9.1.14: *Seasonal multi-year means of the* ***CRE*** *on the greenhouse effect from ISSCP, CERES-SRBAVG, SRB and the IPCC-median model.*

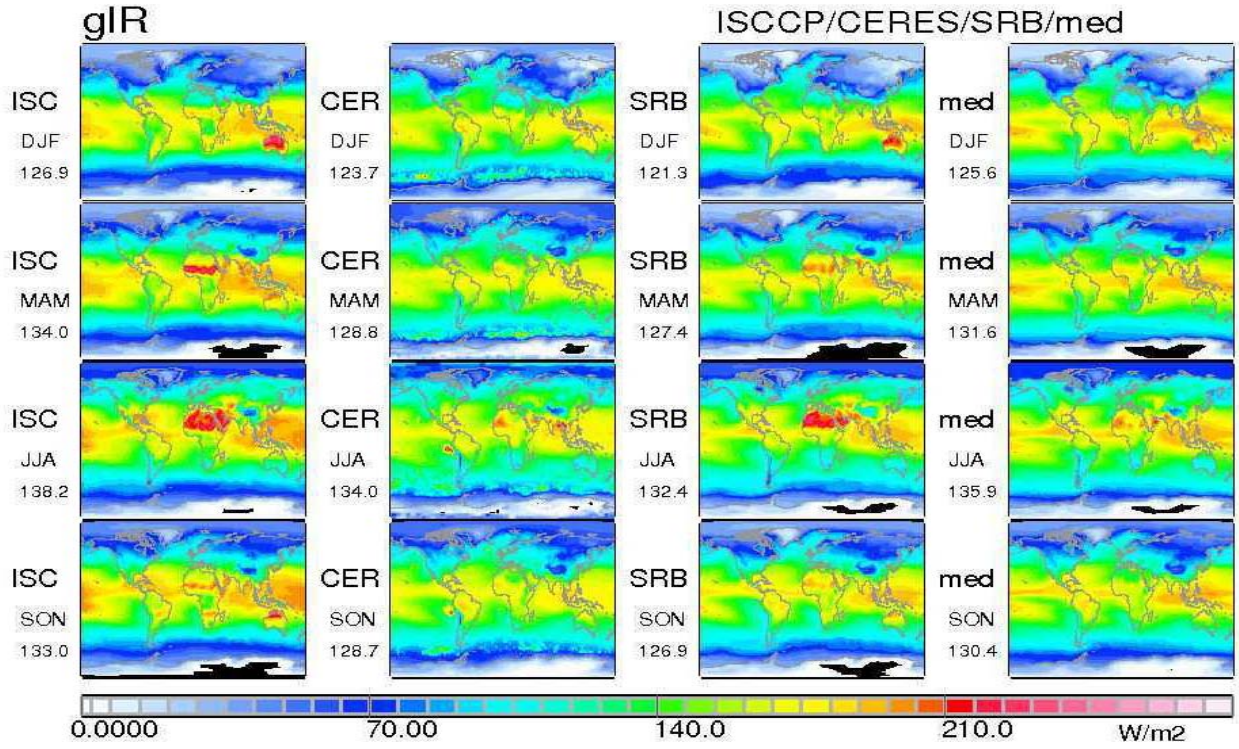

Figure 9.1.15: *Seasonal multi-year means of the greenhouse effect at clear-sky conditions from ISSCP, CERES-SRBAVG, SRB and the IPCC median model.*

The clear-sky greenhouse effect is mainly a function of atmospheric water vapor content and the surface temperature, and increases with increases in both of these factors. Thus, clear-sky greenhouse effects are usually larger at lower latitudes. Clouds generally increase the greenhouse effect, especially in regions with high cloud tops, thus mainly over lower latitude continental regions. There is a resultant increase in latitudinal gradients and zonal variability. On a global seasonal basis, cloud contributions to the greenhouse effect range between 25 and 30 Wm^{-2} and corresponds to about 20% of the clear-sky greenhouse effect, as illustrated in *Table 9.1.5*.

Table 9.1.5: *Global seasonal averages for the greenhouse effect at all-sky/ clear sky conditions and for the cloud effect in the data sets of CERES, ISCCP, SRB and the IPCC median model. Units are* Wm^{-2}.

season	CERES	ISCCP	SRB	IPCC median model
DJF	149/124 26	154/127 27	150/121 28	152/126 28
MAM	155/129 26	162/134 28	157/127 29	159/132 29
JJA	160/134 26	165/138 27	161/132 28	164/136 29
SON	155/129 26	160/133 27	155/127 28	158/130 28

The greenhouse effect determined from all data sets show a small seasonal variation with the highest values during the Northern summer (JJA) and lowest during the Northern winter (DJF). This is in part related to stronger summer heating and stronger winter cooling over northern hemispheric continental areas. Of particular interest within the frame of this assessment are greenhouse effect differences among the four investigated data sets.

Seasonal differences of the ISCCP, SRB and IPCC median model data with respect to the CERES data are presented in *Figures 9.1.16 to 9.1.18*.

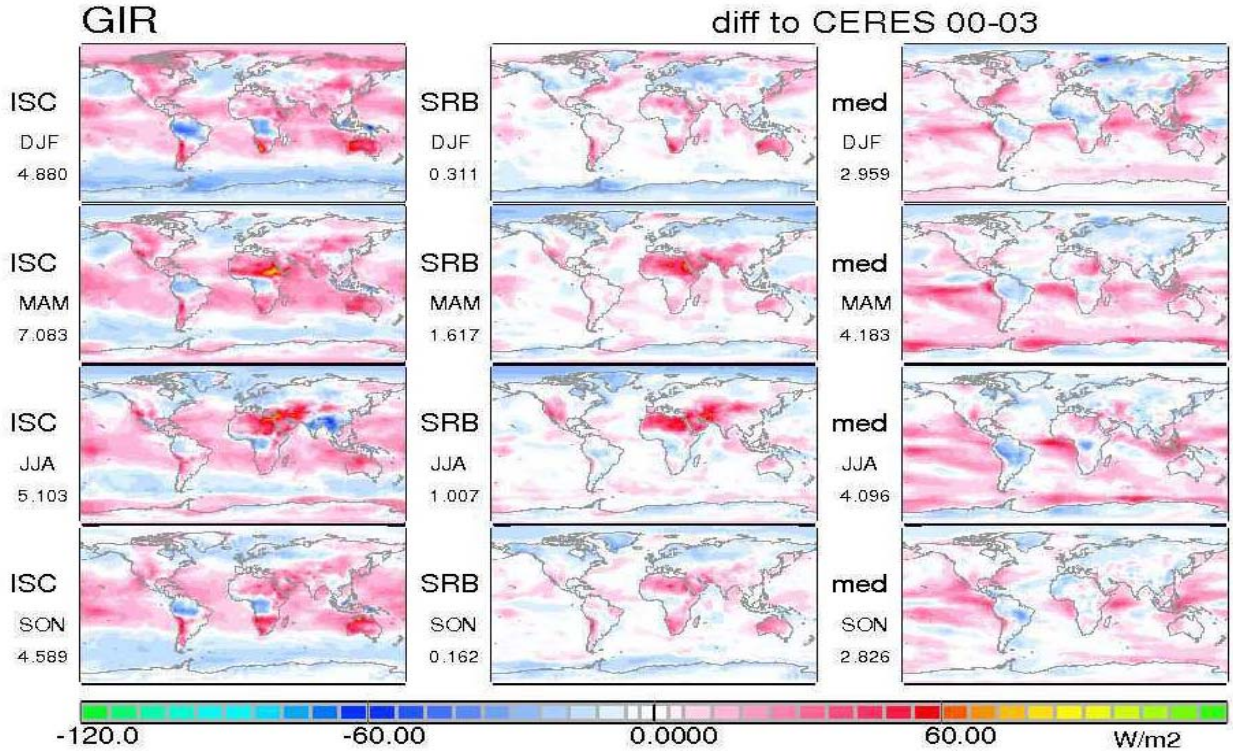

Figure 9.1.16 *Seasonal multi-annual mean differences in greenhouse effects under all-sky conditions of 1984-1995 ISCCP, SRB and the IPCC median data with respect to a CERES 2000-2003 reference*

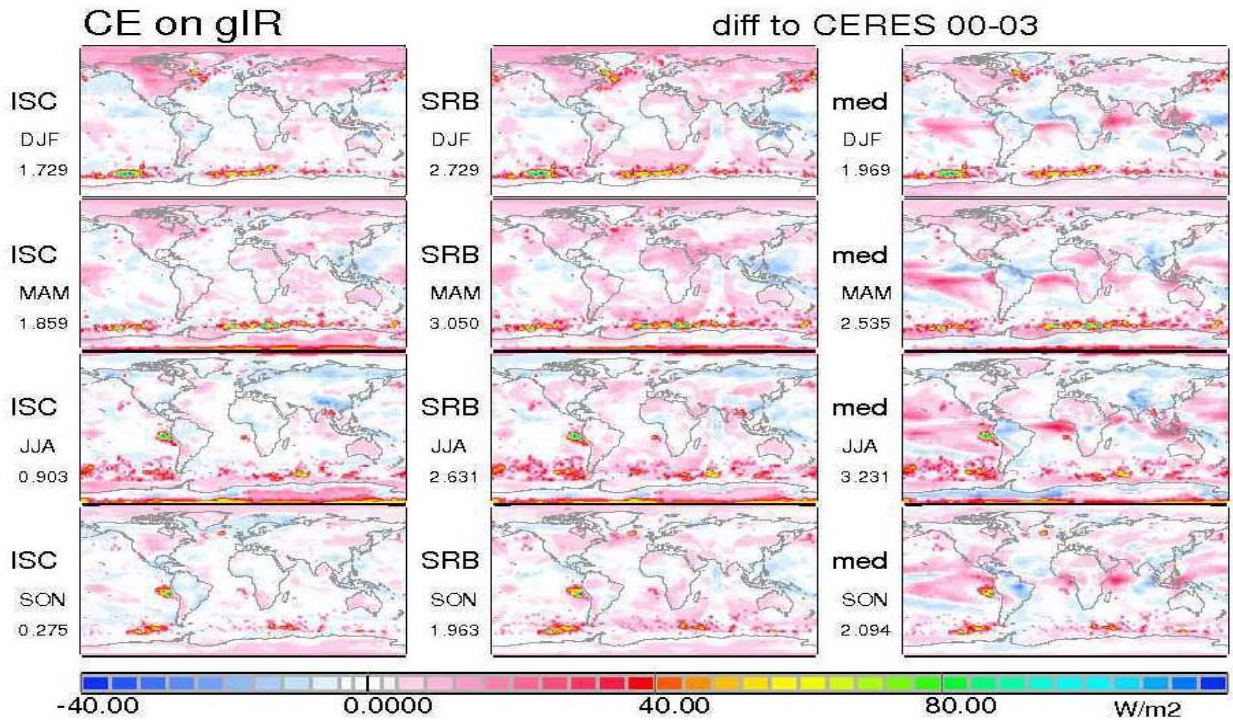

Figure 9.1.17 *Seasonal multi-annual mean differences of the CRE in greenhouse effects of 1984-1995 ISCCP, SRB and the IPCC median data with respect to a CERES 2000-2003 reference*

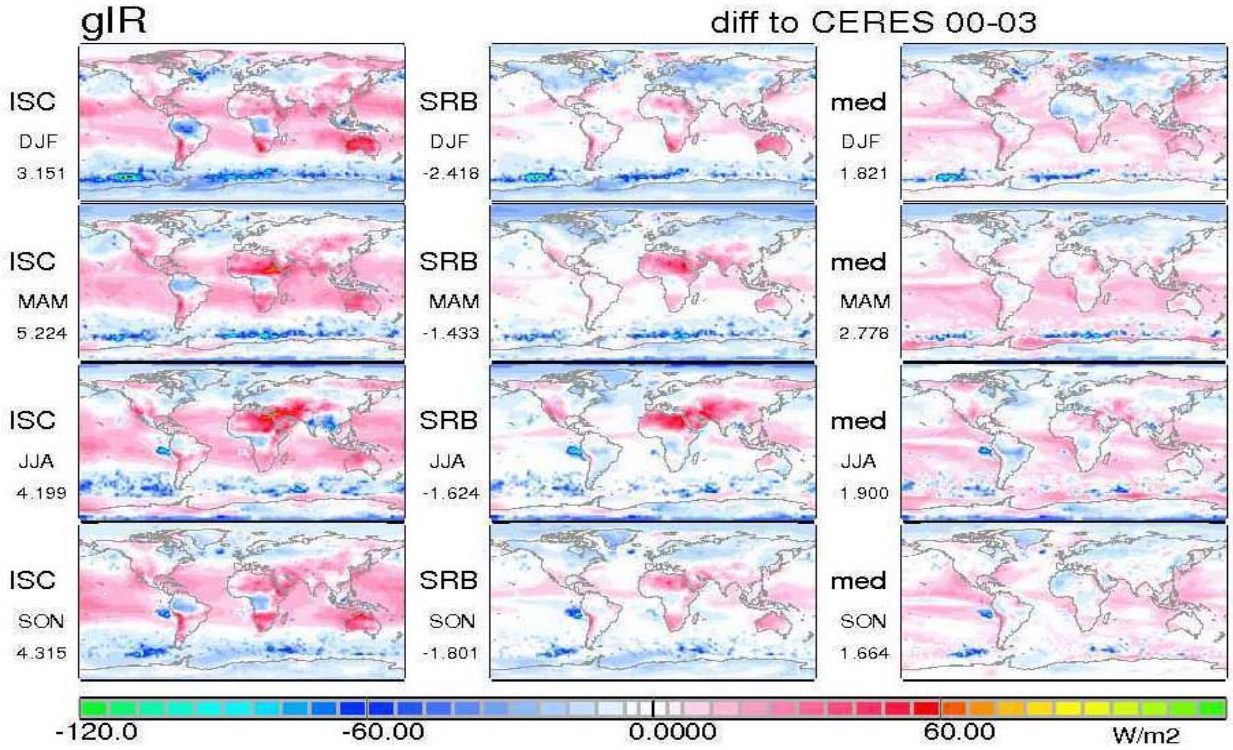

Figure 9.1.18 *Seasonal multi-year mean differences in greenhouse effects under clear-sky conditions for 1984-1995 from ISCCP, SRB and the IPCC median data with respect to a CERES 2000-2003 reference*

Greenhouse effect differences among each of the three data sets to CERES-SRBAVG products can be large, with underestimates reaching values of about 30 Wm^{-2} and overestimates reaching values of about 60 Wm^{-2} on a regional basis. The patterns reflect uncertainties or inconsistencies in the specified radiative characteristics of surfaces and atmospheric properties (especially due to clouds) over continents. The temporal evolution of greenhouse effects at all-sky conditions for ISCCP and SRB are shown in *Figures 9.1.19* as de-seasonalized anomalies of zonal monthly averages. The reference period ranges from January 1985 to December 1988.

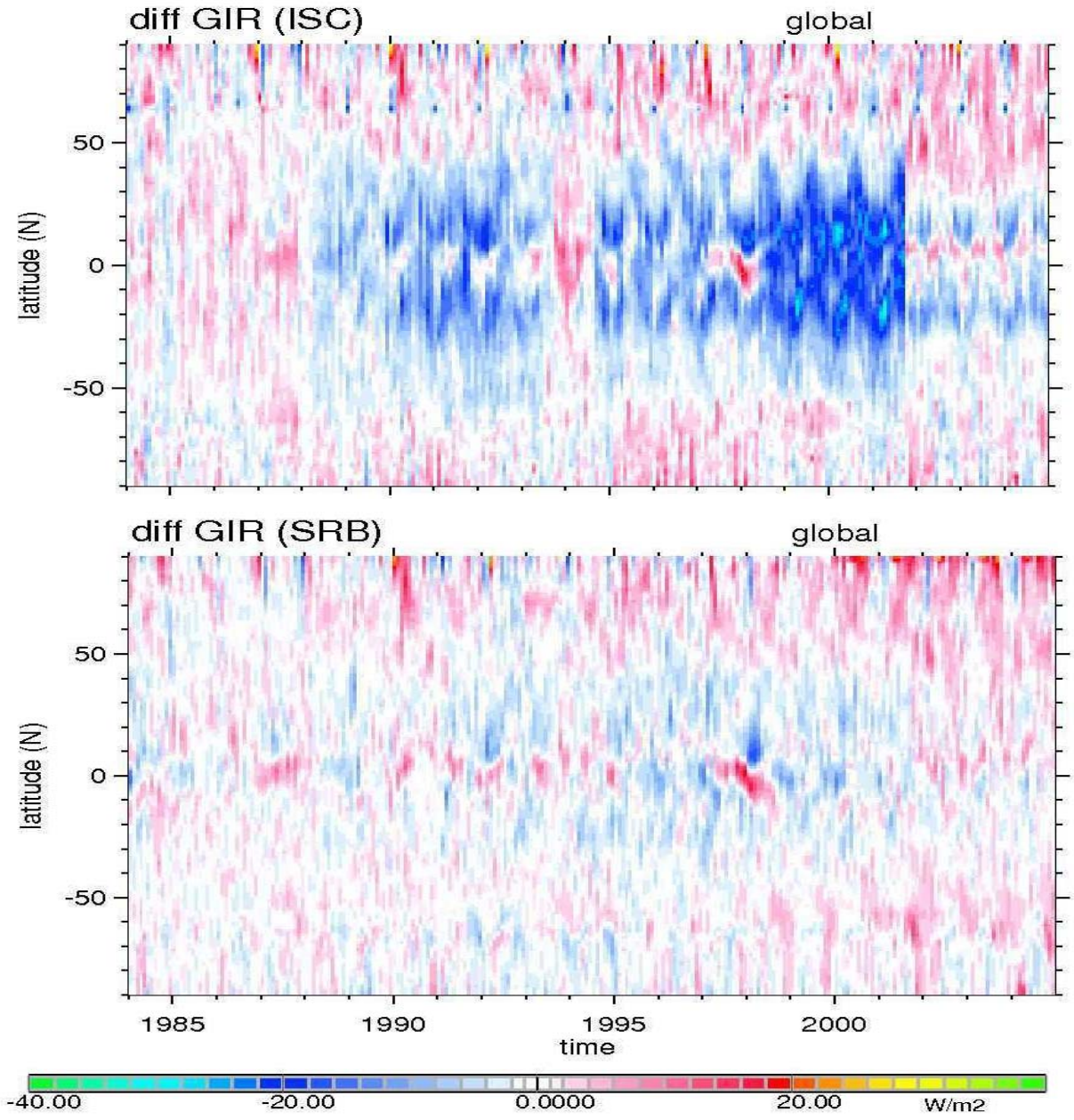

Figure 9.1.19: *Temporal evolution of the de-seasonalized anomaly of zonal average greenhouse effect by ISCCP and SRB for all-sky conditions, using January 1985 to December 1988 as reference period.*

The patterns that occur in ISCCP and SRB data are not only due to natural variability (e.g, in tropical cloud fields during the 1997 El Nino) but also due to errors in various ancillary data assumed in their derivation (see also discussions in *Chapters 3, 4 and 7*).

The corresponding greenhouse effect temporal evolution of the IPCC median model is displayed in *Figure 9.1.20*, distinguishing between clear-sky and all-sky conditions.

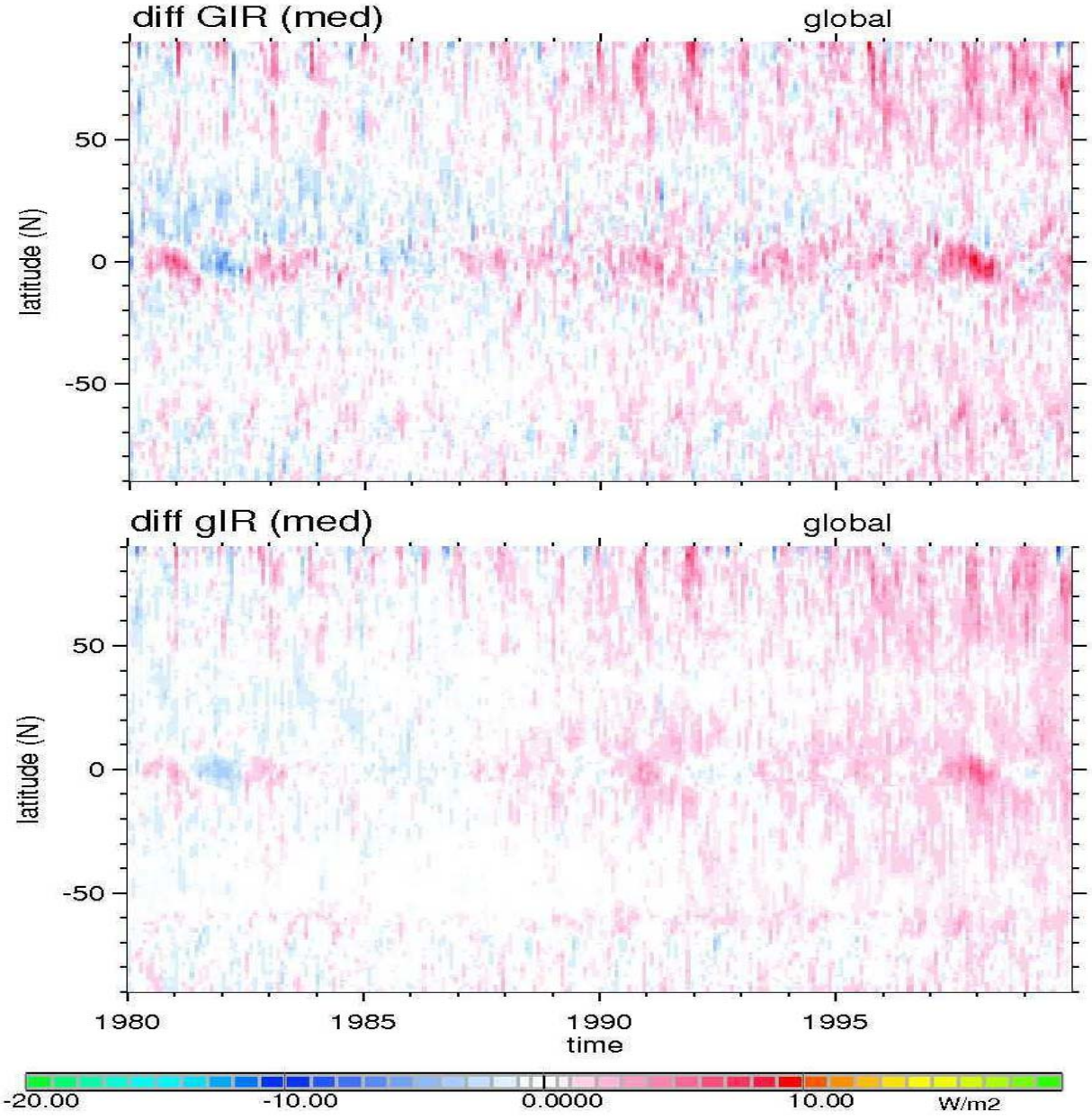

Figure 9.1.20: *Temporal evolution of the de-seasonalized anomaly of zonal average greenhouse effect of the IPCC model median for all-sky (upper panel) and clear-sky conditions (lower panel), using January 1985 to December 1988 as reference period.*

The IPCC median model vaguely indicates a very small increase of the greenhouse effect. The zonal average increase amounts to about 4 to 6 Wm^{-2} in the extra-tropics over both hemispheres between 1980 and 1999. It can be speculated that this increase is a consequence of the increasing carbon dioxide content within the atmosphere. The El-Nino anomalies are well reproduced in the model data and impact the expected trend.

Major error sources in greenhouse effect trends include uncertainties contained in the various ancillary data required in the computational procedures. Of particular importance here is the surface temperature over all continents, which is only estimated from the temperature of the atmosphere at its lowest layer. An important consideration is the accuracy of its specified monthly average. The patterns in *Figure 9.1.16* demonstrate that their regional diversity is quite large, and this causes deviations of up to 40% of the mean greenhouse effect. The other dominant quantity to consider is the accuracy of the specified mean height and temperature of cloud tops.

9.1.9: Summary of Major Findings

Global solar (or shortwave) and IR (or longwave) radiative (broadband) fluxes are key elements in assessing the performance of climate models and in understanding processes of the climate system. The global energy balance serves as diagnostic tool for radiative forcings (due to changes in external, atmospheric or surface properties), for the energy exchange at the surface and the heat capacity of the atmosphere-ocean system.

The comparisons among climate data sets and among model results identified significant diversity arising from inconsistencies and limited accuracies in the applied ancillary data. These deficiencies restrict the interpretation of sensor data (e.g. trend analysis) and also limit assessments of process representations (e.g. cloud properties) in global modeling. Thus, currently applied ancillary data (of all satellite sensor products and also those applied in modeling) should be carefully evaluated for accuracy and consistency and should be replaced with higher quality data, if available.

The uncertainties introduced by errors and inconsistencies in ancillary data currently limit the application of satellite sensor dependent TOA radiative fluxes as reference for global modeling. Still, the diversity among global models themselves is much larger. Thus, even in their current condition the TOA fluxes of satellite sensors do already provide useful constraints to global modeling. On a global annual basis, modeling needs to assure near-balance for the radiative energy at the TOA. However, the way this balance is achieved differs among models and differs as to choice of satellite data, which itself displays some (reassuring) consistency. Especially revealing are flux data differences on spatial and temporal sub-scales, as overall agreement often has become the result of offsetting errors.

Radiative fluxes, associated with satellite sensor TOA measurements, are also offered for the atmosphere and at the surface. But with differences in cloud treatment and other uncertainties in applied ancillary data, increased diversity occurs among flux data derived from different satellite sensors, as expected. Nonetheless, a limited reference value remains through the association to TOA data, especially since surface radiative fluxes in modeling display much larger diversities at the surface than at the TOA.

To strengthen observational reference data requires not only a consistent use of ancillary data and consistent assumptions but also smartly chosen combinations of strength exhibited by different satellite sensors. This involves understanding of issues such as sampling, temporal coverage, spatial coverage and accuracy, and therefore will be challenging.

Selected conclusions of this sub-chapter are:

- strong diversity exists for radiative flux distributions in modeling
- (modeling) diversity is larger for the solar region than for the IR
- (modeling) diversity is larger at the surface than at the TOA
- ancillary data are an issue for modeling, not just for satellite retrievals
- the representation of clouds is a main cause for diversity in flux data
- satellite data provide relatively solid reference for spatial pattern at the TOA
- surface fluxes of satellite data are as good as the model used and no real reference
- comparisons to satellite TOA data identify limited skill of models in representing clouds
- some agreement to satellite data is often achieved by (partially) off-setting errors
- efforts are needed to continuously improve (satellite, ground) data references to modeling

9.2: Comparisons to GFDL Model Simulation *(Stuart Freidenreich)*

Abstract:

A coupled ocean-atmosphere GCM developed at the Geophysical Fluid Dynamics Laboratory (GFDL) has been used to derive global datasets of shortwave and longwave flux at the TOA and surface. Results from simulations utilizing the GFDL CM2.1 GCM are compared with the ISCCP-FD and SRB estimated flux climatologies, to assess the differences between them in both the mean state and the variability. This analysis is done for various regional and for global spatial scales. An assessment is made on how these flux differences relate to model biases in the aerosol optical depth and cloud amount. For greater simplicity, only the downward surface components are considered here.

9.2.1: Introduction

One of the important goals of this report is to assess the flux differences among various global datasets, including GCM's, in both the temporal mean and the variability. At the surface, an examination of these differences can reveal deficiencies in the determination of various factors (particularly aerosol optical depth and cloud amounts) that affect its computation, thus providing a means by which the GCM simulations can be further improved. Such a comparison can also point out deficiencies in the assumptions considered in determining the estimated climatologies as well.

In line with this, results derived from simulations utilizing the GFDL CM2.1 GCM (contained in the RFA archive) are compared with the ISCCP-FD and SRB estimated flux climatologies. For greater simplicity, only the downward surface components are considered here. Both the shortwave and longwave flux differences are presented, for the clear-sky and all-sky cases, although explanations for these differences are mainly limited to the shortwave results. The time period covered is 1984-2003, for which the ISCCP-FD and SRB data availability for full year periods overlap with the model integration. The spatial scales considered range from regional to global. For the global geographical analysis, CM2.1 comparisons are made only with ISCCP-FD, due to its more realistic prescription of aerosol and cloud climatologies. For spatial averages, comparisons with SRB are also made. Note that the ISCCP-FD product effectively incorporates aerosol optical depth values that are too large by a factor of 2. Thus, its shortwave flux estimates are biased lower (Zhang et al., 2010), and this may affect the interpretations here, more so for the clear-sky case.

9.2.2: Differences between CM2.1 and CM2.0 Historical Means

The results utilized in previous sections of this chapter are based on an earlier version of the GFDL coupled model (referred to as "CM2_0" there and CM2.0 here), while the results utilized in this subsection are based on the updated CM2.1 version of the model. An explanation of the important updates is given in the accompanying data set description summary (see Appendix A). Before comparing the flux differences between CM2.1 and the estimated climatologies, it is useful to illustrate the corresponding differences that exist between these two versions of the model. *Figure 9.2.1* shows the difference between the historical (1984 to 2003) means of the **downward** clear-sky and all-sky fluxes of shortwave and longwave radiation between CM2.1 and CM2.0. The global averages of the differences are +0.17, +5.05 Wm^{-2} for the shortwave and longwave clear-sky, and +3.01 and +6.46 Wm^{-2} for the shortwave and longwave all-sky, respectively. Notable increases in the clear-sky shortwave flux occur over the

Sahara, while notable decreases occur over equatorial Africa and Indonesia. The global increase in the all-sky shortwave flux is largely attributed to a reduction of low level cloudiness in the Northern Hemisphere middle latitudes. For the longwave flux, improvements to the land model aid in a reduction of a cold bias over the Northern Hemisphere land regions, contributing to an overall increase. Delworth et al. (2006) further discusses some of the resulting climatological differences between these two versions of the model.

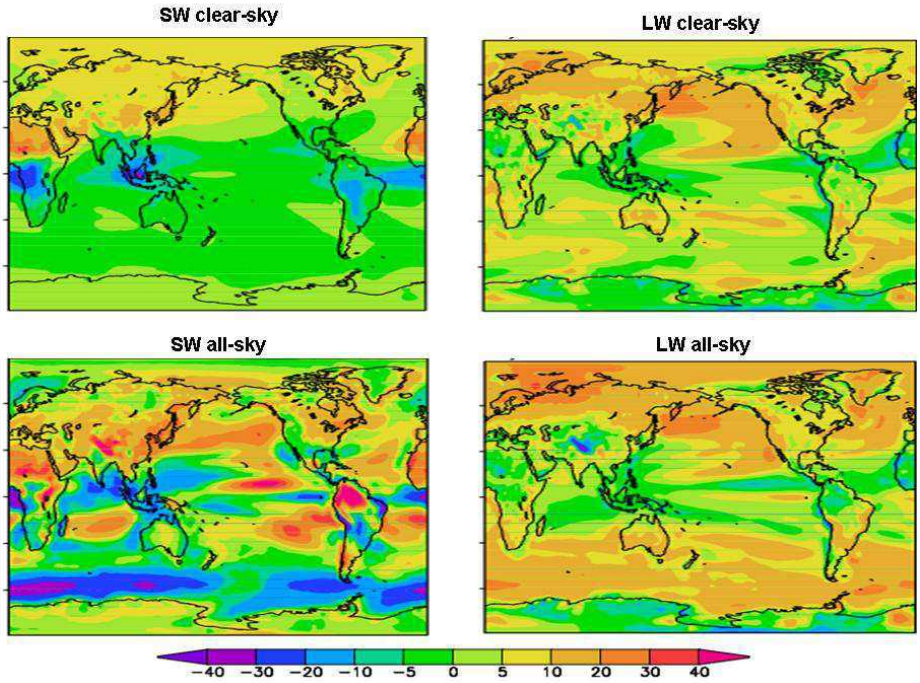

Figure 9.2.1: *Differences (CM2.1 – CM2.0) between historical (1984 to 2003) means of the downward clear-sky and all-sky fluxes (W/m^2) of shortwave and longwave radiation at the* ***surface*** *for the two versions of the GFDL CM2 model considered in this chapter.*

9.2.3: Differences in Historical Means of Radiation Fluxes

Figures 9.9.2a and b (top panels) present the global differences in the shortwave and longwave historical time mean clear-sky fluxes, respectively, between CM2.1 and the ISCCP-FD values.

To aid in assessing the possible role of aerosols in these, the difference between CM2.1 and AERONET (Holben et al., 2001) climatological values of the aerosol optical depth are shown in *Figure 9.9.3***.** Notable shortwave flux underestimates occur over North America, Europe and eastern Asia. There is an accompanying overestimate of the aerosol optical depth. This is due to the sulfate optical depth being too large in CM2.1, and is a result of the assumption of hygroscopic growth of aerosols for relative humidities up to 100% in conjunction with the nature of the parameterization expression for very high relative humidities (Freidenreich and Ramaswamy, 2011; hereinafter FR11).

Similarly, flux underestimates occur over the Saharan region and the eastern tropical Atlantic. These are due to the overestimate of dust aerosol optical depth, and this anomaly is transported westward (Ginoux et al., 2006). Also noteworthy are the positive shortwave biases

over Australia and over Arabia and southern Asia. An underestimate of the aerosol optical depth appears also to contribute towards these.

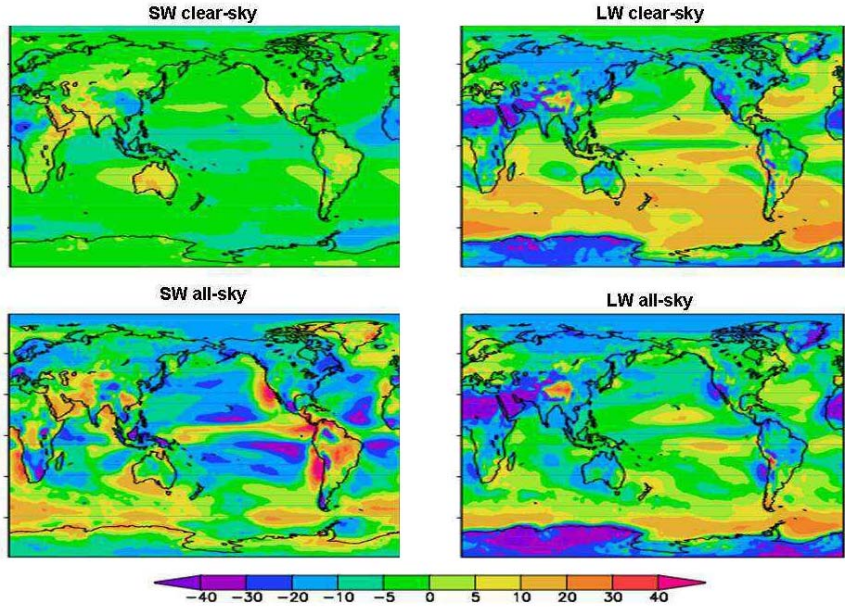

Figure 9.2.2: *Difference in historical mean (1984-2003) for: a) shortwave clear-sky, b) longwave clear-sky, c) shortwave all-sky and d) longwave all-sky, for the downward flux (W/m^2) at the surface between CM2.1 and ISCCP-FD.*

To delineate the global biases in CM2.1 arising in the presence of clouds, the all-sky case is next examined in *Figure 9.2.2c and d* (lower panels). The linkages between CM2.1's downward flux biases to those occurring in cloud amount, with respect to the ISCCP-FD values (Rossow and Schiffer, 1999) (see *Figure 9.2.4*) are examined; again the focus here is for the shortwave. In FR11, several comparisons are done that give a measure of certainty in using the ISCCP-FD cloud amounts as a comparative reference for this type of analysis; further, the regional pattern of this relationship is quantified there. The relationship in the annual mean differences is briefly summarized here; the seasonal dependencies are also investigated in FR11.

For land regions, over Europe, northern and eastern Asia and North America, *Figure 9.2.2c* shows that the model produces large shortwave underestimate biases, with differences of more than 10 Wm^{-2} encompassing most of these regions. In association with these flux biases, cloud amount overestimates of more than 10% occur for these areas, a further indication of an overall moist bias in CM2.1 noted in Delworth et al. (2006). For Southern Africa, and interior of Australia, underestimates also are present. These are associated with cloud amount overestimates, and are an indication that the model can also be too moist for drier regions**.** For India, underestimates (which are especially strong during summer; see FR11) are an indication that the Asian summer monsoon is too strong in CM2.1.

Flux underestimates in the Arctic occur with cloud amount overestimates. Flux overestimates exceed 10 Wm^{-2} for equatorial Africa and for the Amazon region, and are also associated with significant cloud amount underestimates. This is indicative of the fact that CM2.1 does not account well for the seasonal shift in the ITCZ, also producing too little precipitation for these regions (Delworth et al., 2006).

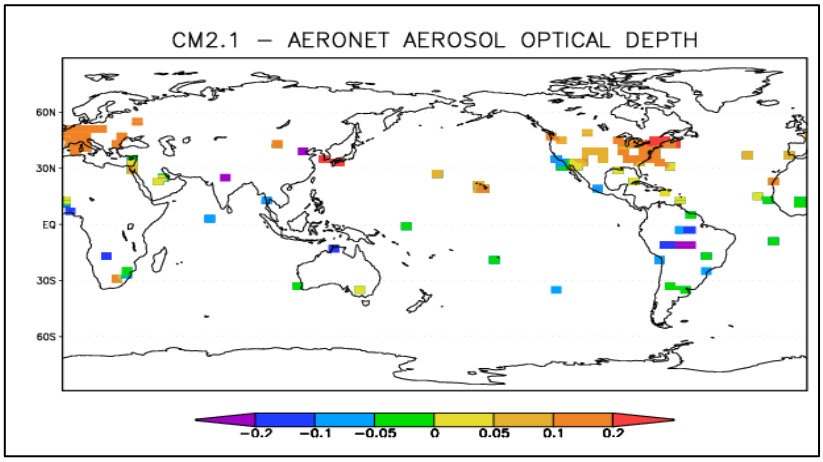

Figure 9.2.3: *Absolute difference in the aerosol optical depth between CM2.1 and AERONET data.*

For oceanic regions, the pattern of shortwave flux underestimates in the subtropical Pacific and Atlantic, and overestimates near and along the equator bear a linkage to cloud amount for these regions. The large biases just south of the equator are again indicative of a double ITCZ produced by CM2.1 (Delworth et al., 2006). The flux overestimates off the west coast of the Americas occur due to a lack of marine stratocumulus. Overestimates occur across the southern ocean from around 60°S southward to coastal Antarctica occur mostly in conjunction with cloudiness overestimates.

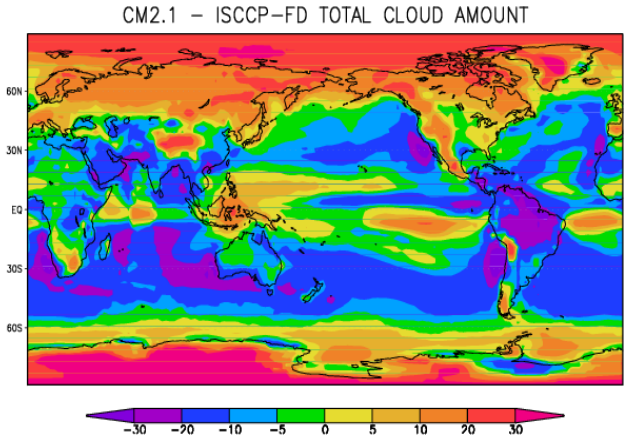

Figure 9.2.4: *Difference in the historical mean (1984-2003) total cloud amount (%) between CM2.1 and ISCCP-FD.*

Table 9.2.1 *(at the end of this contribution)* summarizes the temporal mean flux values for CM2.1 ISCCP-FD and the SRB datasets, averaged globally, zonally, and over land and oceanic regions separately. Except for the clear-sky longwave, CM2.1 underestimates the ISCCP-FD in the global, land-only and ocean-only averages for the various flux components. CM2.1 also underestimates ISCCP-FD across most of the zonal sectors.

a)

	CLEAR-SKY			ALL-SKY		
	CM2.1	ISCCP-FD	SRB	CM2.1	ISCCP-FD	SRB
GLOBAL	244.5	247.7	242.5	185.4	189.3	183.5
LAND	252.1	252.9	245.4	196.5	200.5	199.4
OCEAN	244.6	248.6	244.7	181.6	186.5	179.6
20S-20N	294.1	298.7	287.1	235.8	241.7	235.4
20N-40N	258.9	260.4	255.1	203.7	208.3	205.9
20S-40S	268.6	269.9	268.8	205.7	209.0	208.2
40N-60N	197.4	199.3	200.5	129.2	136.6	134.3
40S-60S	206.9	211.3	209.7	131.5	127.7	115.8
60N-75N	142.7	145.6	145.6	95.6	102.7	96.7
60S-75S	156.1	161.5	157.8	114.5	111.2	91.9
75N-90N	121.5	125.3	126.7	81.9	87.5	85.7
75S-90S	144.4	146.9	144.2	127.1	128.6	115.0

b)

	CLEAR-SKY			ALL-SKY		
	CM2.1	ISCCP-FD	SRB	CM2.1	ISCCP-FD	SRB
GLOBAL	312.9	312.8	314.4	338.1	343.7	348.7
LAND	300.5	310.3	309.4	322.6	334.0	337.0
OCEAN	323.3	319.1	321.9	350.5	353.0	358.8
20S-20N	386.3	386.6	389.0	399.1	405.0	411.1
20N-40N	324.9	330.8	333.0	346.3	357.2	364.0
20S-40S	330.1	323.0	327.5	352.0	355.3	365.3
40N-60N	252.8	259.3	259.8	293.0	298.7	302.0
40S-60S	262.8	251.0	256.7	303.8	301.7	309.5
60N-75N	205.1	214.2	208.4	246.6	255.7	251.8
60S-75S	188.9	185.6	180.2	231.9	232.2	229.0
75N-90N	180.8	186.2	180.1	217.9	231.0	222.9
75S-90S	115.6	127.4	109.3	138.2	159.8	139.5

Table 9.2.1: *The mean (1984-2003) clear-sky and all-sky surface flux (W/m^2) values from the CM2.1, ISSCP-FD and SRB datasets for a) the downward shortwave, and b) the downward longwave radiation.*

There is a notably large negative longwave flux bias over Antarctica, and this is correlated with the land temperature being too cold there. For the clear-sky shortwave, CM2.1's better agreement with ISCCP-FD than with SRB is mainly in the land-only contribution, and is probably a manifestation of the similarities in the aerosol climatology. Hence, from this brief consideration, it is evident that aerosol optical depth (mainly for clear-skies) and cloud amount (for all-skies) are notable factors affecting the degree of agreement between the GCM and reliable estimations of the temporal mean shortwave downward flux at the surface. For a more detailed analysis of CM2.1's differences with both observed and estimated downward shortwave surface flux, its relationship with aerosol optical depth and cloud amount, and the uncertainties associated with these analyses, see FR11.

9.2.4: Differences in the Variability of the Radiation Fluxes

The variability in the radiation fluxes is assessed, using the standard deviation in the deseasonalized monthly time series. *Figure 9.2.5* displays the global difference in the standard deviation in the monthly values between CM2.1 and ISCCP-FD for the various flux quantities. The overall variability is considerably less in CM2.1, and this is explained by the fact that ISCCP-FD more realistically captures the randomness in the temporal variations of atmospheric parameters that affect surface flux variability. Some regional differences are noteworthy. For the shortwave, the clear-sky variability is larger in CM2.1 over East Asia. There, the large sulfate burden in the presence of high relative humidities cause the aerosol optical depth to vary more significantly. The all-sky variability is considerably less over the western Pacific and larger over Indonesia, due to the ENSO related variability in cloudiness being both less in magnitude and shifted westward. This is also in line with the corresponding precipitation patterns pointed out previously (Wittenberg et al, 2005). The bias around 60^{o}S, evident in both the clear-sky and all-sky cases, is due to underestimation of variability in moisture and cloudiness.

For the longwave, the underestimate over the high mountainous terrain are due in part to uncertainty in the temperature used in deriving the observed flux estimate. Other notable underestimation biases in the longwave occur over Africa, Antarctica and Greenland.

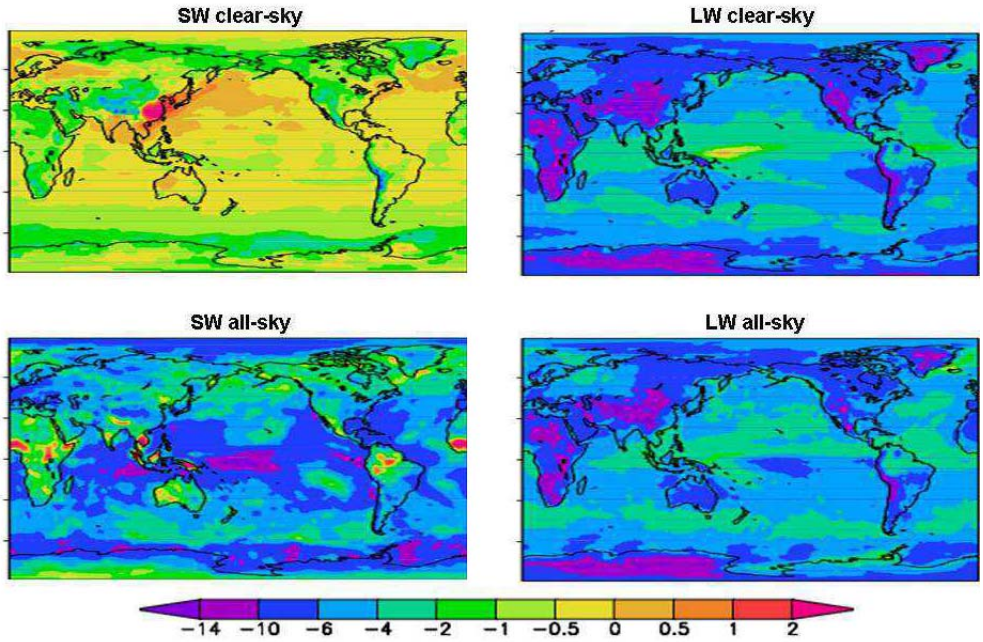

Figure 9.2.5: *The global difference in the standard deviation of the deseasonalized monthly time series for the downward flux (W/m^2) at the surface, between CM2.1 and ISCCP-FD (1984-2003) for a) shortwave clear-sky, b) longwave clear-sky, c) shortwave all-sky and d) longwave all-sky.*

Tables 9.2.2 summarize the corresponding standard deviation in the deseasonlized time series of spatial-mean flux values. These means are obtained for global, zonal, and land-only and ocean-only spatial scales, for CM2.1, ISCCP-FD and SRB. Also included are the results of a CM2.1 control experiment that uses aerosol and trace gas concentrations, insolation, and distribution of land-cover types representative of 1990 conditions. Comparing CM2.1 with ISCCP-FD further highlights the underestimate of the variability discussed previously. This same bias is also noted in comparing CM2.1 with SRB, except for the clear-sky shortwave case. There, the absence of inter-annual variations in the aerosol burden assumed in the SRB calculations results in a lesser variability than in CM2.1. Also the control experiment, which similarly lacks this characteristic, produces values more in agreement with SRB.

a)

	CLEAR−SKY				ALL−SKY			
	MODEL		OBS		MODEL		OBS	
	1990	CM2.1	ISCCP−FD	SRB	1990	CM2.1	ISCCP−FD	SRB
GLOBAL	0.255	1.163	1.403	0.227	1.043	0.860	1.727	1.230
LAND	0.450	1.095	1.378	0.390	2.680	1.529	2.165	1.544
OCEAN	0.256	1.201	1.510	0.236	1.323	0.900	2.093	1.551
20S−20N	0.450	1.519	1.932	0.458	1.976	1.460	2.770	1.681
20N−40N	0.497	1.123	1.376	0.465	2.623	1.313	2.551	2.023
20S−40S	0.342	1.040	1.380	0.458	2.744	1.426	2.524	2.515
40N−60N	0.490	1.114	1.342	0.568	2.546	1.038	2.439	2.661
40S−60S	0.237	1.320	1.903	0.501	2.280	1.123	3.008	4.806
60N−75N	0.589	1.094	1.405	0.720	3.451	1.659	4.008	6.129
60S−75S	0.566	1.479	2.039	0.678	3.187	1.565	6.470	7.365
75N−90N	0.779	1.079	1.481	0.907	4.477	2.240	7.117	6.734
75S−90S	0.669	1.693	1.884	1.015	3.049	1.597	6.106	5.862

b)

	CLEAR−SKY				ALL−SKY			
	MODEL		OBS		MODEL		OBS	
	1990	CM2.1	ISCCP−FD	SRB	1990	CM2.1	ISCCP−FD	SRB
GLOBAL	1.618	1.518	1.956	1.398	1.625	1.449	2.185	1.371
LAND	2.504	1.984	5.857	1.857	2.519	1.862	5.390	1.997
OCEAN	1.537	1.422	2.314	1.430	1.504	1.342	2.151	1.267
20S−20N	3.174	2.373	3.153	2.542	2.975	2.176	3.006	2.226
20N−40N	2.042	1.849	3.048	2.027	2.110	1.750	2.960	1.936
20S−40S	1.239	1.098	3.192	1.320	1.401	1.090	2.866	1.484
40N−60N	2.900	1.840	3.932	2.539	2.963	1.720	4.085	2.448
40S−60S	1.217	0.690	2.665	1.129	1.493	0.876	2.925	1.195
60N−75N	3.595	2.187	5.077	2.936	4.571	2.603	5.348	3.382
60S−75S	2.672	0.960	5.185	2.465	3.244	1.151	5.798	2.946
75N−90N	4.900	2.775	6.847	4.613	6.865	3.927	7.629	5.801
75S−90S	3.288	1.310	7.244	3.522	4.842	1.975	8.097	5.012

Table 9.2.2: *The standard deviation in the de-seasonalized time series of spatial-mean flux (W/m^2) values, obtained for global, zonal, and land-only and ocean-only spatial scales, from the CM2.1, ISSCP-FD and SRB datasets for a) the downward shortwave, and b) the downward longwave radiation. Also shown are the corresponding values from a control experiment for 1990 conditions.*

9.2.5: Summary and Conclusion

The comparisons done here between the GFDL CM2.1 GCM and the estimated satellite-based shortwave surface flux climatologies show that these type of analyses can provide additional metrics for delineating where and to what extent aerosol optical depth and cloud amount determination can be improved upon in the model simulation, both for the mean state and for temporal variations. Although the corresponding longwave flux results are also presented here, further investigation is needed to properly assess the factors (such as temperature and moisture biases) behind those differences. Overall, improvements in simulating these effects will play a key role in the improved fidelity of models for long-term climate prediction.

9.3: Comparison of Reanalysis and Model Surface Radiative Fluxes to in-situ Surface Measurements

(Laura Hinkelman and Taiping Zhang)

9.3.1: Introduction

This chapter focuses on evaluating the shortwave (SW) and longwave (LW) **downward fluxes** of the five reanalysis and model data sets in the GEWEX-RFA archive against ground-based measurements. The in situ measurements come from the Baseline Surface Radiation Network (BSRN), Global Energy Balance Archive (GEBA), and University of Oregon (UOR) Solar Radiation Monitoring Laboratory. The GEBA and UOR data are combined to form the "GUOR" data set. The analysis including the BSRN data covers the period of January 1992 to December 1999 because the first BSRN stations became operational in 1992 and the models were only run through December 1999. The reanalysis and model datasets are evaluated against the GUOR over the ERBE period, i.e., January 1985 to December 1989, and the full period of overlap, namely January 1984 to December 1999.

The structure of this section and the types of analysis performed are essentially the same as in Chapter 6 (Satellite-Based Surface vs. in-situ Surface Measurement Comparisons). Therefore the reader is directed to Chapter 6 for details regarding the surface measurements and the computations.

9.3.2: Ground-Based Data Description

The in situ measurements from the Baseline Surface Radiation Network (BSRN), Global Energy Balance Archive (GEBA), and University of Oregon (UOR) Solar Radiation Monitoring Laboratory are described in detail in Chapter 5 and in Appendix A.2.

9.3.3: Reanalysis and Model Data Sets

Table 9.3.1: *Temporal availability of reanalysis, model, and ground-based data sets.* ASWDN = sum of all-sky direct and diffuse downwelling SW flux measurements; ASWDHEM = all-sky single-instrument measurement of total SW hemispheric downwelling flux; ALWDN =measured all-sky longwave downwelling flux.*

Data Set	Time Span
Reanalysis and Model Data	
ECMWF-ERA40_Ed001	1983-07 / 2002-08
GFDLCM2.1_Ed001	1983-01 / 2003-12
IPCC-AVERAGE_EdAR4	1980-01 / 1999-12
IPCC-MEDIAN_EdAR4	1980-01 / 1999-12
NCEP-DOE-R2_Ed002*	1983-07 / 2006-06
Common Time Span	**1983-07 / 1999-12**
Ground-Based Data	
BSRN (ASWDN, ASWDHEM, ALWDN)	1992-01 / 2006-04
GEBA+UOR (ASWDHEM)	1979-04 / 2008-12

***** Note: Some of the NCEP-DOE-R2 reanalysis grid boxes are missing SW flux values.

The reanalysis and model data sets discussed in this section are listed in *Table 9.3.1*. There are two reanalysis products and three data sets based on global climate model (GCM) output. All of the data sets either have a native 2.5°x2.5° grid or have been converted to this grid system. Each data set includes both SW and LW surface fluxes. The common time span of these data sets is from July 1983 to December 1999, however only full years are analyzed, starting with January 1984. For the purpose of our comparisons, we generally use the longest available time period but include a few analyses over the ERBE period (January 1985 to December 1989) to facilitate comparisons to the satellite product assessment results presented in earlier chapters.

9.3.4: Evaluation Methods

The method of evaluation is described in Section 6.4 and summarized here in brief. Monthly mean in situ measurements are compared to monthly mean reanalysis and model fluxes from the 2.5°x2.5° grid box in which the measurement site falls. The sign of the bias is defined using the convention model minus in-situ value. The comparison to BSRN data covers the period from January 1992, when the first BSRN stations became operational, to December 1999 the end of the model period. The reanalysis and model datasets are evaluated against the GUOR data over the ERBE period, i.e., January 1985 to December 1989, and the full years in the period of overlap, namely January 1984 to December 1999.

9.3.5: Comparisons to BSRN Data

9.3.5.1: Shortwave Fluxes

The shortwave fluxes from the model and reanalysis datasets are first compared with the BSRN ASWDN fluxes over the common overlap period of January 1992 to December 1999. Missing values do occur in the time series from the measurement sites, but, since model outputs generally do not have spatial or temporal gaps, every comparison includes the same number of data points.

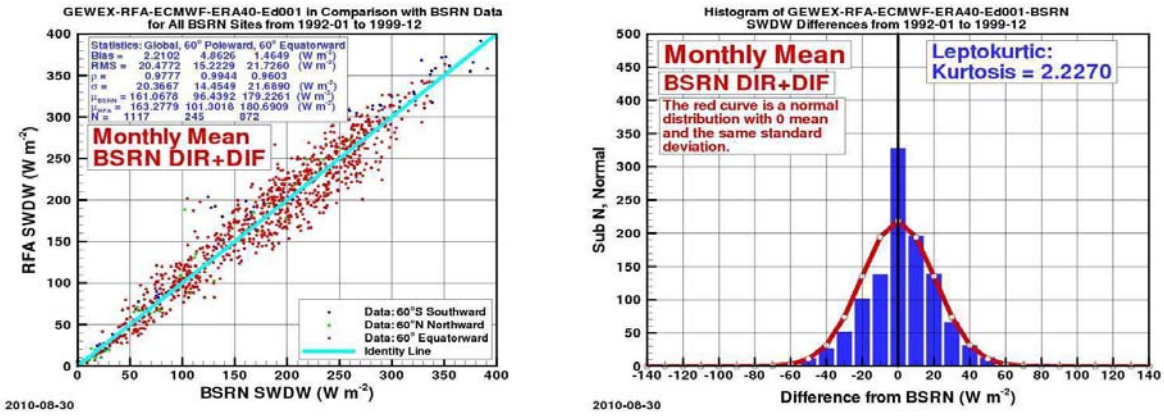

Figure 9.3.1: *Comparison between the ECMWF-ERA40-Ed001 and BSRN shortwave downward fluxes from January 1992 to December 1999. A histogram for the ECMWF-ERA40-Ed001-BSRN differences is shown in blue in the right-hand panel, and the superimposed red curve is the best fit zero-mean Gaussian curve. "Sub N" refers to the number of points in a given bin.*

A sample result from this comparison is shown in *Figure 9.3.1*. The left panel is a scatter plot of the ECMWF ERA-40 reanalysis data vs. all available BSRN data, and the right panel is a histogram of the ECMWF-BSRN differences with a normal curve having the same standard deviation but zero mean plotted as a reference. The flux values available for the comparison are more or less normally distributed (not shown). As expected, the absolute values of the differences increase with the magnitude of the fluxes: the correlations between the magnitudes of the differences and the BSRN and model fluxes are 0.32 and 0.35, respectively, which may explain why the distribution of the bias is leptokurtic. Note that the unusually high bar at the center of the bar chart includes 53 site-months of complete polar night, which renders the corresponding flux differences exactly 0 Wm^{-2}, contributing to the positive kurtosis. In fact, all of the model-BSRN difference populations are leptokurtic distributions, meaning that they are more concentrated around the mean than the corresponding Gaussian distribution.

Table 9.3.2 lists the comparison statistics for all of the model and reanalysis data sets. The values shown in black are derived for the entire collection of BSRN stations. Like the satellite data sets, the biases for the model fluxes are generally below 10 Wm^{-2}, typical standard deviations are about 20 to 25 Wm^{-2}, and correlations fall between 0.95 and 0.98. The NCEP-DOE-R2 reanalysis product is the exception to these statements with a bias of 25 Wm^{-2} and a standard deviation close to 30 Wm^{-2}. (The correlation falls in the same range as the others.) The latter result is not surprising – the presence of a high bias in the surface downwelling SW fluxes from the NCEP Reanalysis was already identified in 1996 (Betts et al.) and quantified as 25-50 Wm^{-2} in 1999 (Berbery et al.) In a more recent evaluation of this product, Schroeder et al. (2009) found a continuing bias of about 35 Wm^{-2}. This bias is greatest under cloudy conditions and is generally attributable to insufficient absorption by water vapor and aerosols and poor representation of clouds in the model underlying the reanalysis (Hinkelman et al., 1999).

The high bias of the NCEP-DOE-R2 data is clearly evident in the bias time series in *Figure 9.3.2,* in which every NCEP bias value is positive. The biases from the ECMWF-ERA40 and IPCC-median data sets are small and of both signs, while the GFDLCM2.1 and IPCC-average biases are generally larger and negative. Once the number of station samples has increased enough for the annual patterns to become clear, the largest RMS differences are seen to occur during the NH summer. Consistent with the bias values, the RMS differences for the NCEP-DOE-R2 product are by far the largest.

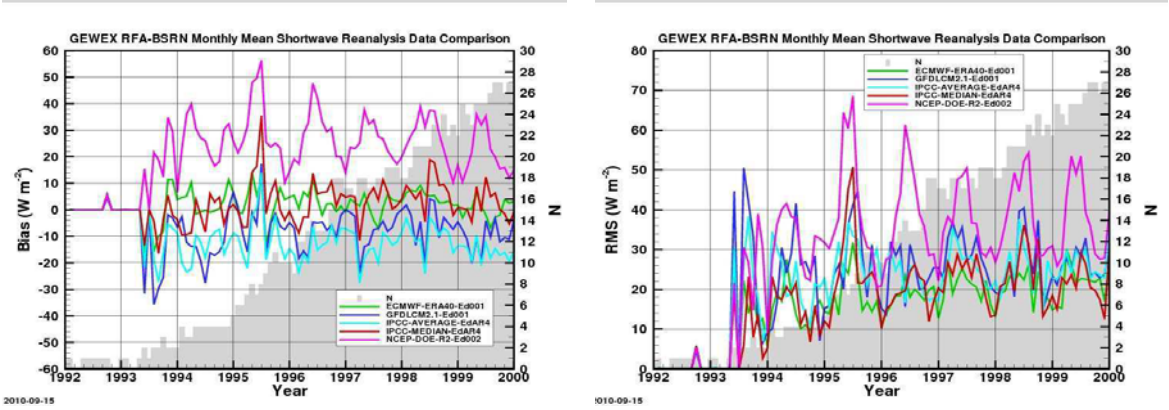

Figure 9.3.2: *Time series of bias and RMS difference for shortwave downward fluxes from each reanalysis or model product relative to BSRN data from January 1992 to December 1999.*

Figure 9.3.3 and Table 9.3.2 allow us to determine the surface types for which the agreement between the surface measured and model derived SW irradiances is best and worst. Note that in *Figure 9.3.3*, the sites are arranged in order of decreasing latitude on the horizontal axis (i.e., north to south.) The left panel of *Figure 3* shows the site latitudes in a curve with black diamonds. The pattern of agreement is quite different here than it was for the satellite-BSRN comparisons. Most notably, the models are in much better agreement with the data from the coastal Antarctic sites, with biases around 20-25 Wm^{-2} and RMS differences of 35 Wm^{-2} or less (vs. 20-70 Wm^{-2} and 30-90 Wm^{-2}, respectively, for the satellite products.) For the models, the consistently worst agreement is found at Iloren, Nigeria, and Florianopolis, Brazil. However, very few data points are available for these comparisons. Payern, Switzerland, which is near the Swiss Alps, is another problematic location.

Table 9.3.2: *Comparison between reanalysis/model and BSRN shortwave data from January 1992 to December 1999. Bias, root-mean-square difference (RMS), and standard deviation (σ) are all given in Wm^{-2}. For each data set, the first line (black) is for the entire globe; the second line (red) is for the tropics from 20°S to 20°N; the third line (green) is for the mid-latitudes from 20° to 60° in both hemispheres; the fourth line (blue) is for the polar latitudes (60° polewards) in both hemispheres.*

Data Set	Bias	RMS	ρ	σ	N
ECMWF-ERA40	2.2	20.5	0.9777	20.4	1117
	-21.3	30.6	0.8563	22.1	95
	4.2	20.4	0.9686	19.9	777
	4.9	15.2	0.9944	14.5	245
GFDLCM2.1	-7.8	27.2	0.9628	26.0	1117
	11.0	31.5	0.5953	29.7	95
	-13.2	29.0	0.9459	25.9	777
	2.1	17.5	0.9905	17.4	245
IPCC-AVERAGE	-12.9	25.5	0.9744	22.0	1117
	-14.1	29.8	0.7325	26.4	95
	-13.4	25.9	0.9594	22.2	777
	-10.7	22.0	0.9945	19.2	245
IPCC-MEDIAN	3.6	22.7	0.9740	22.4	1117
	9.3	26.2	0.7662	24.6	95
	4.3	24.6	0.9576	24.2	777
	-0.8	13.1	0.9944	13.1	245
NCEP-DOE-R2	24.9	38.5	0.9594	29.5	1117
	3.4	31.8	0.6592	31.8	95
	29.3	40.2	0.9439	27.5	777
	19.0	35.4	0.9823	29.9	245

The NCEP-DOE-R2 reanalysis data has larger biases (20-50 Wm^{-2}) and RMS differences (30-55 Wm^{-2}) than the other data sets at many of the BSRN locations. As a percentage of the incoming SW flux, by far the worst agreement occurs for NCEP-DOE-R2 at the Arctic sites (Ny Ålesund, Spitsbergen, and Barrow, Alaska), but the largest differences in terms of magnitude occur at midlatitude sites. There is no obvious pattern in the surface types for which the NCEP-DOE-R2 RMS deviations are large: they occur at mountain (Boulder (BOS)), island (Tateno (TAT) and Bermuda (BER)), open grassland (Bondville (BON), Rock Springs (PSU), Billings (BIL), Lindenberg (LIN), and Goodwin Creek (GCR)), desert (Saudi Solar Village (SOV)), and polar (Ny Ålesund (NYA) and Barrow (BAR)) locations.

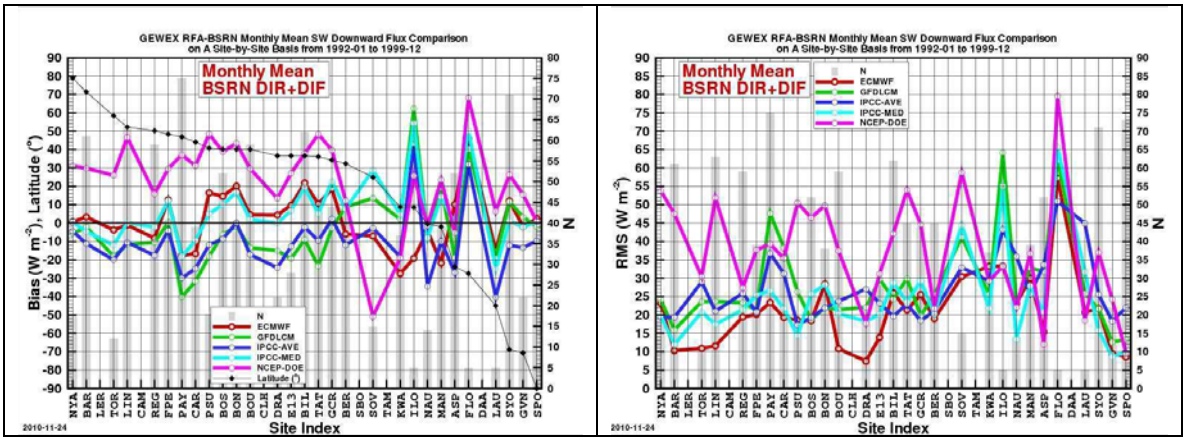

Figure 9.3.3: *Bias and RMS difference at individual BSRN sites for each set of reanalysis shortwave downward fluxes relative to measurements between January 1992 and December 1999. Note that direct and diffuse shortwave flux measurements from Lerwick, Camborne, Chesapeake Lighthouse, Sede Boqer, Tamanrasset, or De Aar are available in the GEWEX RFA archive during this time period.*

Table 9.3.2 summarizes the results as a function of latitude band: global, tropical, midlatitude, and polar. Note that there are different numbers of stations in each category, so that the statistics are not entirely comparable. However, some trends are evident. Interestingly, for each model the largest RMS differences occur in the tropics, where the satellite data sets had good agreement. The reverse is true in the Polar Regions, where the satellites perform poorly and the models well. The large overall bias for the NCEP-DOE-R2 data set clearly originates in the midlatitudes and Polar Regions. The high bias of 29 Wm^{-2} in the midlatitudes is notable, being by far the largest bias in this area for any of the satellite or model data sets, for which the range is otherwise 0 to 13 Wm^{-2}.

9.3.5.2: Long-wave Radiative Fluxes

Comparisons between the modeled and BSRN longwave fluxes were performed using the same methods as the shortwave comparisons. The results are shown in *Figures 9.3.4* to *9.3.6* and *Table 9.3.3*. *Figure 9.3.4* shows a typical comparison result. For the IPCC-MEDIAN data set, there is a consistent negative bias for the range of fluxes, leading to an overall bias of -8.0 Wm^{-2}. The standard deviation is about 15 Wm^{-2}. The LW irradiance difference distribution in this case is nearly Gaussian.

Comparison statistics for all of the model LW data sets are given in *Table 9.3.3*. As was the case for the satellite-based products, the standard deviations for the LW comparisons are smaller than they were for the SW data, running between 10 and 20 Wm^{-2} versus 20 to 25 Wm^{-2} for the SW. The correlations are also better. However, the biases are not much different than they were for the SW, with magnitudes of 2.5-9.0 Wm^{-2}. It is notable that the LW biases are all negative for the model data while they were positive for the satellite products. The bias for the NCEP-DOE-R2 data set is larger than the others (about -16 Wm^{-2}), although its standard deviation falls within the range of the other data sets. This bias is smaller than that found for the SW data and opposite in sign, partly offsetting the net radiative energy budget error introduced by the SW bias. Again, this is expected from a previous report regarding the Eta model, which incorporates the same LW flux algorithm as the NCEP reanalysis (Hinkelman et al., 1999).

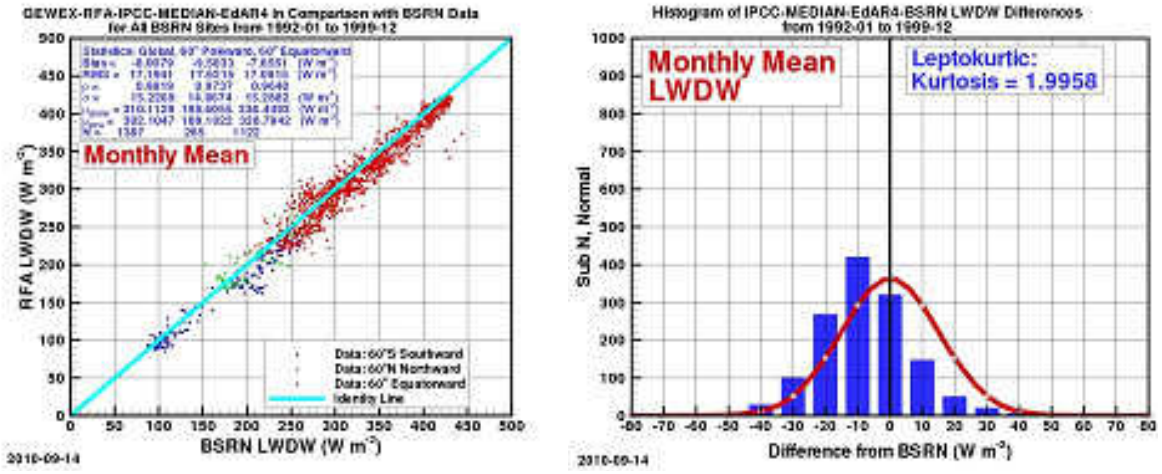

Figure 9.3.4: *Comparison between the IPCC-MEDIAN and BSRN longwave downward fluxes from January 1992 to December 1999.*

Table 9.3.3: *Statistics of comparisons between reanalysis/model and BSRN longwave data from January 1992 to December 1999. Bias, root-mean-square difference (RMS), and standard deviation (σ) are all given in W m^{-2}.*

Data Set	Bias	RMS	ρ	σ	N
ECMWF_ERA40_Ed001	-2.6	13.8	0.990	13.5	1387
GFDLCM2.1_Ed001	-2.6	17.2	0.978	17.0	1387
IPCC_AVERAGE_EdAR4	-8.8	17.2	0.983	14.8	1387
IPCC_MEDIAN_EdAR4	-8.0	17.2	0.982	15.2	1387
NCEP_DOE_R2_Ed002	-15.6	23.1	0.986	17.1	1387

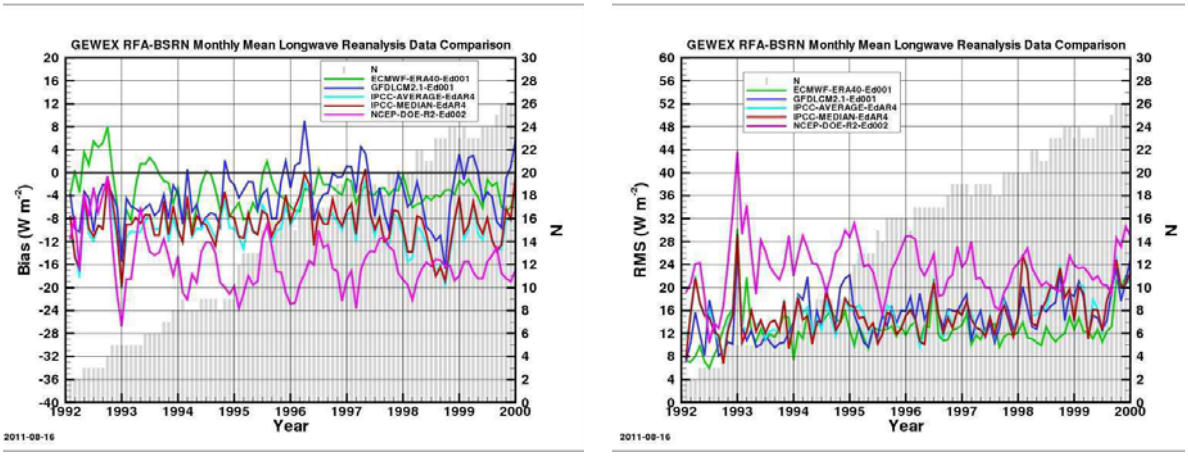

Figure 9.3.5: *Time series of bias and RMS difference for longwave downward fluxes from each reanalysis or model product relative to BSRN data from January 1992 to December 1999.*

Agreement between the modeled and BSRN measured LW fluxes is plotted as a function of time in *Figure 9.3.5.* The large negative differences between the NCEP-DOE-R2 product and the site measurements are immediately obvious. The worst agreement for this data set occurs during the Northern Hemisphere winter. Both the ECMWF-ERA40, and GFDLCM2.1 data sets include some positive biases, mainly in the NH summer for the ECMWF-ERA40 and NH spring

and fall for the GFDLCM2.1. The biases for the IPCC mean and media data roughly parallel those of the GFDLCM2.1 model but are larger in magnitude. The RMS differences are strikingly large for the NCEP-DOE-R2 while those from the other reanalysis and model data sets are clumped together, the result of the larger biases in the NCEP-DOE-R2 data.

Results of site-by-site comparisons are presented in *Figure 9.3.6.* As for the satellite-based LW products, the worst agreement occurs at Florianopolis, Brazil, but fewer than 10 data points are available at this location. The models have large biases at two other sites with very few data points – Lauder, New Zealand (LAU), and Desert Rock, Nevada (DRA).

Otherwise, the most consistent features of these plots are the larger biases at the four sites around 40° N, and somewhat higher biases and RMS differences at the Antarctic sites – South Pole (SPO), Syowa (SYO), and Georg-von-Neumeyer (GVN). Interestingly, these are mainly different sites than those with large discrepancies in the LW for the satellite-based products, although several were problematic for the SW satellite products (LAU, SYO, and GVN). (see Section 6.1.5.2.) Somewhat larger biases occur at Payerne and Carpentras for all but the NCEP-DOE-R2 data, however, the RMS differences for these sites do not stand out.

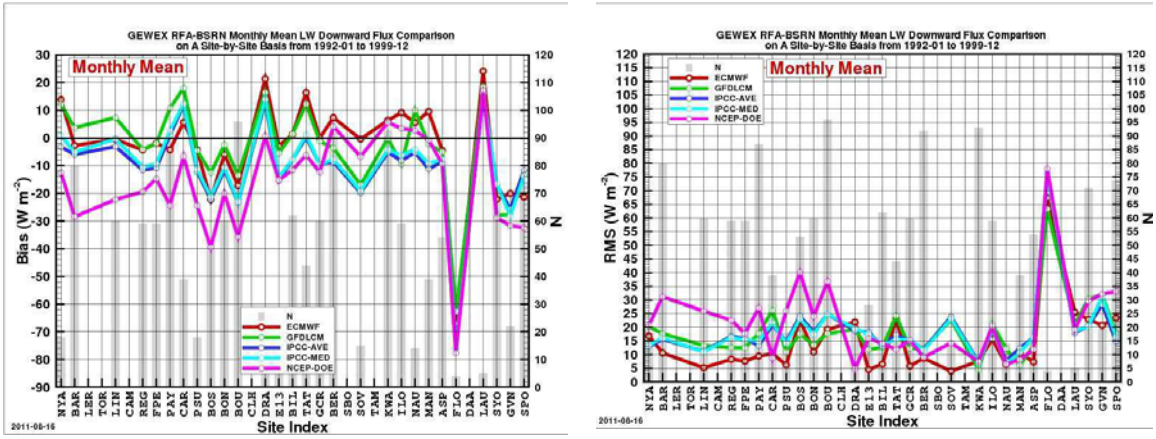

Figure 9.3.6: *Bias and RMS difference at individual BSRN sites for each set of reanalysis longwave downward fluxes relative to measurements between January 1992 and December 1999. Note that no longwave flux measurements from Lerwick, Toravere, Camborne, Chesapeake Lighthouse, Sede Boqer, Tamanrasset, or De Aar are available in the GEWEX RFA archive during this time period.*

9.3.6: Comparison to GUOR (GEBA and UOR) Data

9.3.6.1: Short-wave Radiative Fluxes

The Global Energy Balance Archive (GEBA) and University of Oregon (UOR) data sets are extremely useful for the evaluation of irradiances from models because of their long records: GEBA data extends back to the early 1900s, while the UOR record begins in 1979. This permits an evaluation to be made for all of the entire years during common time period of the model/analysis data sets, namely January 1984 through December 1999, which includes over 5000 data points. However, it should be noted that the geographical distribution of these sites is more limited, with the GEBA sites mainly falling in Europe, with a few in Asia

We first show a typical comparison result (*Figure 9.3.7*). Over the full period of January 1984 through December 1999, the GFDLCM2.1 has a bias of - 1.2 Wm^{-2} and standard deviation of 31.2 Wm^{-2} relative to the GUOR SW data, with a correlation of 0.924. This means that the

GFDLCM2.1 SW data agrees more poorly with the GUOR than with the BSRN data (std. dev. 26.0, correlation 0.963) except for the improved bias (-7.8 for BSRN).

Statistics for the same comparison for all of the reanalysis and model products are listed in *Table 9.3.4.* Bias magnitudes are mainly less than 10 Wm^{-2} with standard deviations of 26-31 Wm^{-2}. Correlation coefficients range from 0.92-0.95. Interestingly, while the NCEP-DOE-R2 SW product has a very large bias relative to the GUOR values (39 Wm^{-2}), its standard deviation and correlation coefficient are in line with the other data sets. A large bias was also found between the NCEP-DOE-R2 and BSRN SW data, although in that case the standard deviation and correlation coefficients were also worse than those of the other reanalysis/model products. For the other products, the biases relative to BSRN were about the same as here, but the standard deviations and correlations showed closer agreement. This was also the case for the satellite data. A possible reason for this is the improved accuracy of the BSRN instruments, although other explanations are possible, particularly since the comparisons covered different time periods.

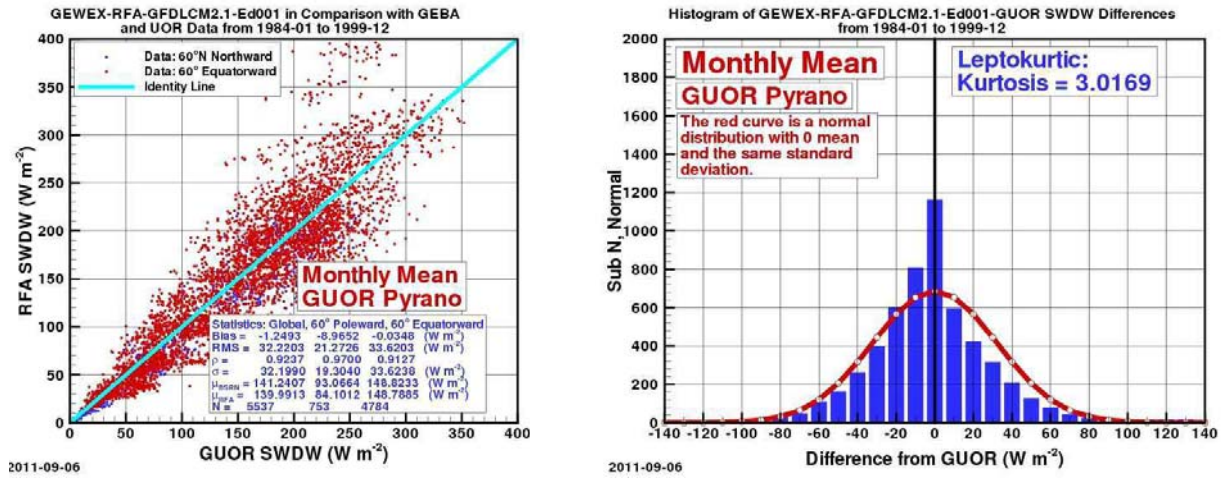

Figure 9.3.7: *Comparison between the GFDLCM2.1-Ed001 and GUOR shortwave downward fluxes from January 1984 to December 1999.*

Table 9.3.4: *Statistics of comparisons between reanalysis/model and GUOR shortwave data from January 1984 to December 1999; Bias, root-mean-square difference (RMS), and standard deviation (σ) are all given in W m^{-2}.*

Data Set	Bias	RMS	ρ	σ	N
ECMWF_ERA40_Ed001	7.6	29.7	0.943	28.7	5537
GFDLCM2.1_Ed001	-1.2	32.2	0.924	31.2	5537
IPCC_AVERAGE_EdAR4	-7.1	27.1	0.944	26.1	5537
IPCC_MEDIAN_EdAR4	6.7	29.9	0.942	29.1	5537
NCEP_DOE_R2_Ed002	39.2	49.6	0.950	30.3	5537

Relative to the satellite products, which were compared to the GUOR SW data over a somewhat longer time period (January 1984-December 2004), the biases are about the same while the standard deviations are larger (about 20 Wm^{-2} for the satellite products). The correlations are also worse (about 0.97 for the satellite products). This suggests that the satellite products are more accurate than the model and reanalysis products. However, the two data types showed similar performance against the BSRN SW measurements.

Statistics for the ERBE time period (January 1985 to December 1989) are listed in *Table 9.3.5*. The comparison over this shorter time period yield results similar to those for the full time period: typical biases are below 10 Wm^{-2}, the standard deviations range between 25 and 32 Wm^{-2}, and the correlations range from 0.92 to 0.95. The exception to these results is again the large bias (~38 Wm^{-2}) determined for the NCEP-DOE-R2 SW product. The correlation and standard deviation for this data set fall in the range typical of the model data sets

Table 9.3.5: *Statistics of comparisons between the model/reanalysis and GUOR shortwave data from January 1985 to December 1989 (ERBE period). Bias, root-mean-square difference (RMS), and standard deviation (σ) are all given in W m^{-2}.*

Data Set	Bias	RMS	ρ	σ	N
ECMWF_ERA40_Ed001	7.9	30.7	0.940	29.7	1758
GFDLCM2.1_Ed001	-0.3	31.2	0.928	31.3	1758
IPCC_AVERAGE_EdAR4	-6.9	27.1	0.944	26.2	1758
IPCC_MEDIAN_EdAR4	6.9	29.7	0.943	28.9	1758
NCEP_DOE_R2_Ed002	38.3	49.7	0.941	31.6	1758

The bias and RMS time series for the model and reanalysis products relative to the GUOR shortwave data (*Figure 9.3.8*) reveal differences from the BSRN comparisons. Although the NCEP-DOE-R2 biases are still by far the largest and always positive, the positive biases are also evident in the ECMWF-ERA40 and IPCC-MEDIAN data, while the IPCC-AVERAGE data have a clear negative bias. Only the GFDLCM2.1 time series has nearly equal positive and negative deviations. The largest biases occur during the Northern Hemisphere summer, although the sign of these biases depends on the overall bias of the individual data set. The RMS difference time series corroborate that the model and analysis products agree worst with the station data in the NH summer.

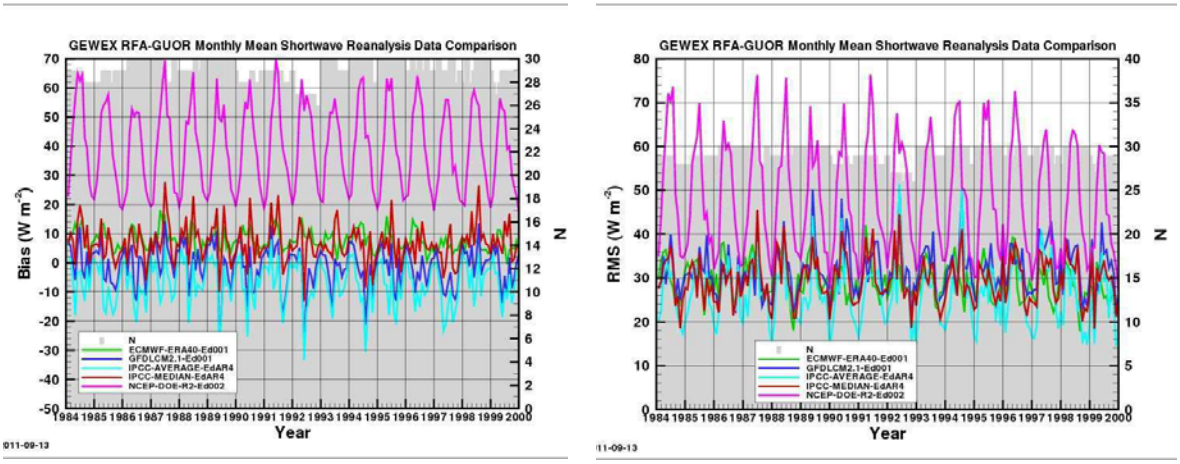

Figure 9.3.8: *Time series of bias and RMS difference for shortwave downward fluxes from each reanalysis or model product relative to GUOR data from January 1984 to December 1999.*

The bias and RMS deviations computed at the individual GEBA stations are plotted in *Figure 9.3.9.* Except for some locations for which there is no data during this time period, the geographic pattern of biases exhibited by the model SW data are surprisingly similar to those computed for the satellite data sets and shown in Section 6.1.6.1. While some of the biases here

are larger than for the satellite data (particularly for the NCEP-DOE-R2 reanalysis), the worst agreement is still at Valparaiso, Chile, where biases for all the data sets exceed 40 W m^{-2}, with a maximum of about 100 Wm^{-2} for NCEP-DOE-R2. Root-mean-square differences are also excessive for this site, ranging from about 50 to 100 Wm^{-2}.

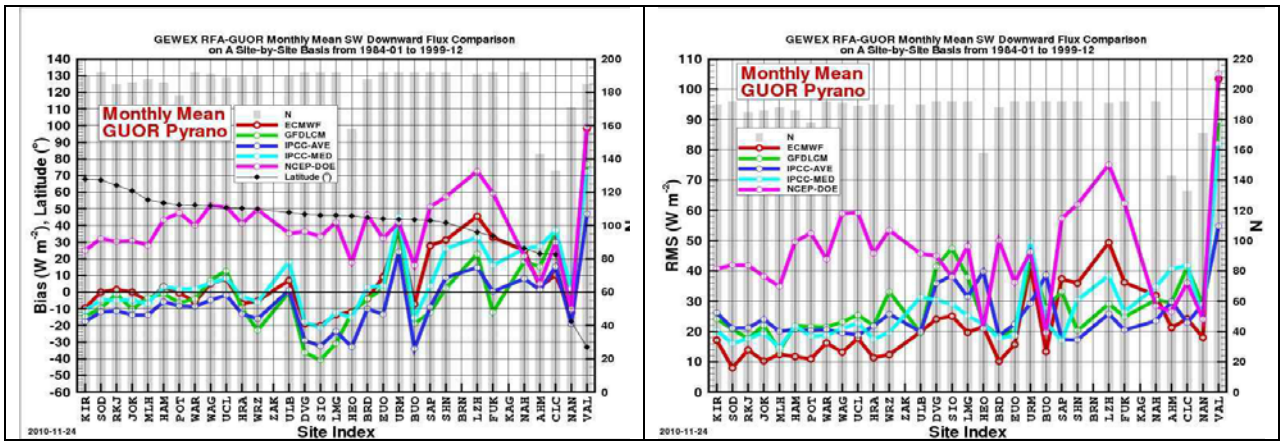

Figure 9.3.9: *Bias and RMS difference at individual GUOR sites for each set of reanalysis shortwave downward fluxes relative to measurements between January 1984 and December 1999. Note that no shortwave flux measurements from Zakopane, Brindisi, or Kagoshima are available in the GEWEX RFA archive during this time period.*

Other sites with consistently large biases include Calcutta, India (~100 km from the Indian Ocean), Lanzhou, China (1517 m elevation), Sapporo, Japan (Hokkaido Island), and Burns, Oregon, USA (above 1250 m). Large-bias sites that did not appear on the list for the satellite data include Shenyang and Urumqi, China, and Ulan-Bator, Mongolia, of which Urumqi and Ulan-Bator are at high elevation (918 and 1264 m, respectively). High RMS values (frequently greater than 30 W m^{-2}) are found for Calcutta, Lanzhou, and Urumqi, as well as Davos, Sion, and Locarno-Monti, Switzerland, of which all but Calcutta are located at elevations of about 400 m or more. This suggests that the models have difficulty handling mountainous areas. The excessive biases and RMS differences occurring at Valparaiso (here RMS values of about 100-210 Wm^{-2}) in comparison to both the models and the satellites cast doubt on the accuracy of the measurements made at this station.

The GUOR data set contains 30 stations (indicated in *Figure 6.1.2*) with very few temporal gaps in their records over the full common time period (January 1984 to December 1999.) An ensemble average time series including the data from each of these sites was created for both the GUOR and model data sets by de-seasonalizing the time series for each site and then averaging the results over all of the sites. De-seasonalization consisted of subtracting the monthly means computed over the entire time period for each individual location. Comparisons of these anomaly time series are shown in *Figure 9.3.10*. Here the left panel shows the time series themselves while the right panel shows the differences between the anomalies computed for models and those for the observational data. Corresponding statistics are listed in *Table 9.3.5*.

The model time series do tend to rise and fall in parallel with the observational anomalies, but the magnitudes of the anomalies are very different, with differences greater than 5 Wm^{-2} quite common. The correlations are much lower than for any other comparison of observational and model or satellite data in this report, with maximum values around 0.7 and minimums around 0.1. The standard deviations are between 4 and 7 Wm^{-2}, which is about twice the values of 2-3 Wm^{-2}

found for the satellite data in an analogous comparison. In any event, the models are able to capture the month-to-month variability of the GUOR ensemble to about 7 Wm^{-2} at the one standard deviation level. For a similar analysis using an ensemble over the 12 sites with completely continuous records (SOD, WAR, DVG, SIO, LMG, EUO, URM, BUO, SAP, SHN, FUK, and NAH, shown as triangles in *Figure 6.1.2*), the correlations increase to 0.3-0.9 and the standard deviations fall to below 5.5 Wm^{-2}, on average. (see *Table 9.3.6.*)

Table 9.3.6*: Statistics of comparisons between a 30-site ensemble average of GUOR and model shortwave data from January 1984 to December 1999. The data for each site was deseasonalized by subtracting the mean annual cycle over the same period before the ensemble average was computed. "S-M" = site months.*

Data Set	μ	σ	ρ	Months	S-M
ECMWF_ERA40_Ed001	0	2.7	0.87	192	5536
GFDLCM2.1_Ed001	0.02	5.9	-0.025	192	5536
IPCC_AVERAGE_EdAR4	0.01	5.3	0.218	192	5536
IPCC_MEDIAN_EdAR4	0.02	5.4	0.203	192	5536
NCEP_DOE_R2_Ed002	0.01	3.7	0.736	192	5536

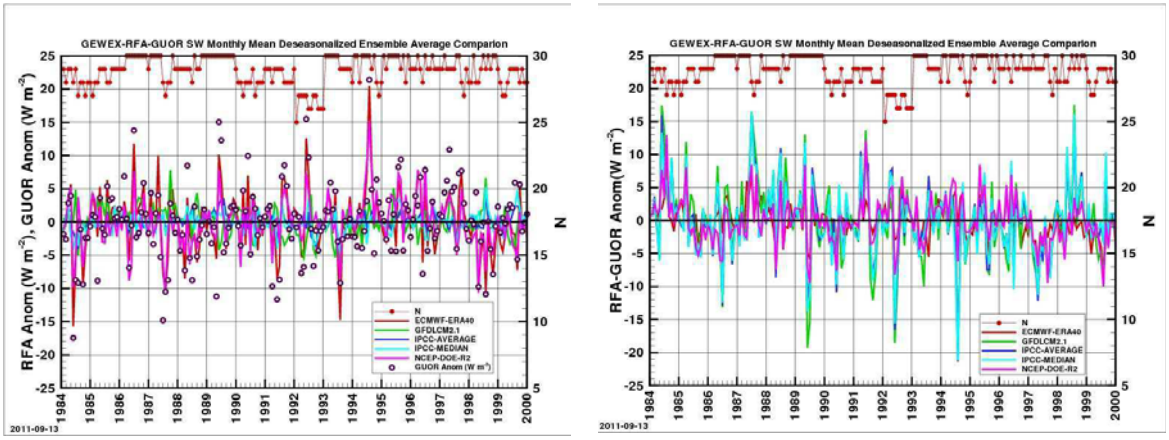

Figure 9.3.10*: Time series of the shortwave downward flux ensemble average over the 30 GUOR sites with nearly continuous records. Shown here are the anomalies after the data have been deseasonalized. Deseasonalization was performed on the time series from each individual site before the ensemble average was computed.*

Table 9.3.7: *Statistics of a comparison between a 12-site ensemble average of GUOR and model shortwave data from January 1984 to December 1999. The data for each site was deseasonalized by subtracting the mean annual cycle over the same period before the ensemble average was computed. "S-M" = site months.*

Data Set	μ	σ	ρ	Months	S-M
ECMWF_ERA40_Ed001	0	4.0	0.738	192	2304
GFDLCM2.1_Ed001	0	6.7	0.108	192	2304
IPCC_AVERAGE_EdAR4	0	5.9	0.504	192	2304
IPCC_MEDIAN_EdAR4	0	6.0	0.085	192	2304
NCEP_DOE_R2_Ed002	0	4.1	0.706	192	2304

9.3.6.2: Trend Analysis

Recently, great interest has been shown in long-term trends in the downwelling solar flux at the surface of the earth. (See Section 5.3, this report). Here we evaluate the trend in down-welling SW flux that each reanalysis dataset and the GUOR data exhibits over the 16-year common time period. This is done by performing a linear regression is performed on each of the 12-site ensemble mean anomaly time series described above to obtain the slope of each set. Following the procedure described in Weatherhead *et al.* (1998), the data is treated as following an autoregressive model of order 1. The 95% confidence interval for each slope is then computed as a function of the lag one autocorrelation coefficient, the standard deviation of the residual after the time series is deseasonalized and detrended, and the time span of the data.

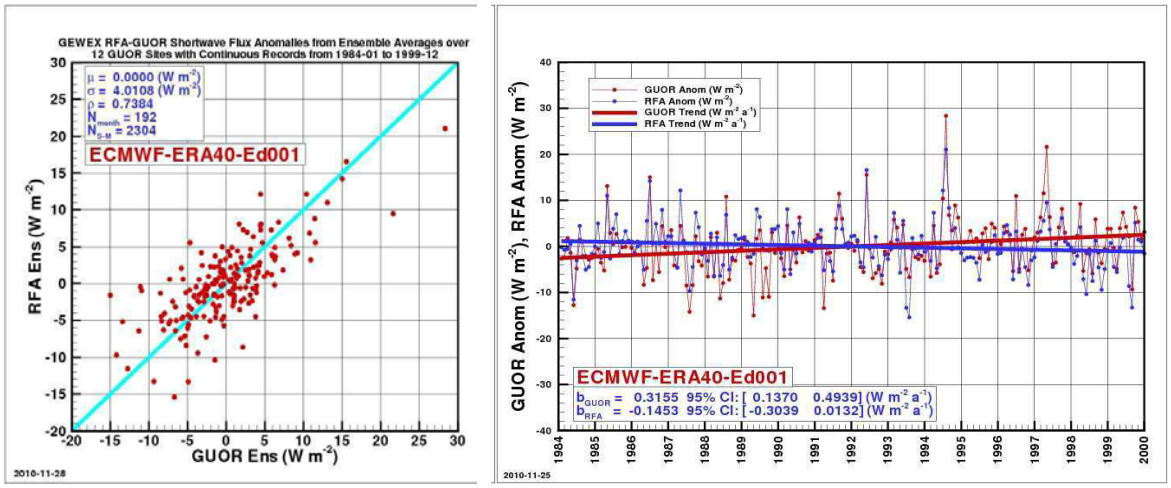

Figure 9.3.11*: Comparison of GUOR and ECMWF-ERA40-Ed001 shortwave anomalies averaged over 12 sites with continuous records. The data for each site was deseasonalized by subtracting the mean annual cycle over the same period before the ensemble average was computed. Best fit lines to the historic anomaly time series are also shown.*

Figure 9.3.11 shows the results for the reanalysis dataset ECMWF-ERA40-Ed001. The left panel shows a scatter plot of the reanalysis ensemble average anomalies vs. their GUOR counterparts and indicates that the agreement between the two is quite good; in the right panel are the anomaly time series overlaid by the estimated trends, shown as straight lines. The trend estimates and the corresponding confidence intervals of the reanalysis and observational datasets are given in *Table 9.3.7*.

The results show that the 95% confidence intervals for all the models except GFDLCM2.1-Ed001 contain the value 0, which means that it is not possible to establish with 95% certainty whether the computed trend is positive or negative. This indicates that trend analysis for these models over the given time period is not meaningful. This result might be expected from the plots in *Figure 9.3.10*, in which most of the anomaly time series exhibit multiple periods with upward or downward trends. For its part, the GFDLCM2.1-Ed001 shows a negative trend at the 95% confidence level, in contrast to the statistically significant positive trend obtained from the observational data.

Table 9.3.7: *Trends and 95% confidence intervals computed for the deseasonalized 12-site ensemble average time series of GUOR and model shortwave irradiance data. The period covered is January 1984 to December 1999, a time-span of 16 years or 192 months. The total number of site-months in each case is thus 2304 (192 months x 12 sites).*

Satellite Data Set	Trend (W m^{-2} a^{-1})	95% CI (W m^{-2} a^{-1})
ECMWF_ERA40_Ed001	-0.145	(-0.320, 0.029)
GFDLCM2.1_Ed001	-0.205	(-0.303, -0.107)
IPCC_AVERAGE_EdAR4	0.026	(-0.033, 0.085)
IPCC_MEDIAN_EdAR4	0.030	(-0.038, 0.097)
NCEP_DOE_R2_Ed002	-0.083	(-0.2311, 0.065)
GUOR	**0.316**	**(0.127, 0.504)**

9.3.7: Summary and Conclusions

The model and reanalysis surface flux data sets in the RFA archive have been assessed by comparison to direct measurements from around the world. These measurements are part of the Baseline Surface Radiometer Network (BSRN), Global Energy Balance Archive (GEBA), and University of Oregon Solar Radiation Monitoring Laboratory data sets. It should be noted that, aside from a few BSRN sites and two of the GEBA sites, all of the surface measurements come from stations in the northern hemisphere. This means that the measurements are not globally representative, although they do include stations in a variety of geographic settings (coastal, continental, mountainous, island, polar, and desert locations).

Comparisons were made between monthly mean surface measurements and the same values from the 2.5° x 2.5° model grid cell in which they are located. This means that the spatial scales of the measured and modeled fluxes are much different, which decreases the comparability of the two types of data. (See Section 6.2 for an extensive discussion of the difficulties introduced by these differences). Nevertheless, surface measurements provide the best constraint for modeled surface irradiance available at this time. Using monthly mean values in the comparisons improves the equivalence of the data by averaging out the variations present in each of set of fluxes. The data would compare much more poorly at shorter or instantaneous time scales.

It is not possible to state categorically whether the agreement between the two sets of values is within the uncertainty of the in situ data. This is not only due to the spatial and temporal mismatch between the model and in situ radiative flux data, but also because the accuracy of the surface measurements is not always well know. This accuracy depends not only on the type of instrument used, but also its calibration and maintenance history. Monthly means are also affected by the way in which temporal averaging accounts for missing data points. Therefore, we do not attempt to make absolute claims regarding the accuracy of the model or reanalysis data relative to the surface measurements. Further discussion about the difficulties inherent to establishing the uncertainty of in situ radiative flux measurements is provided in Chapter 5.

We can conclude that:

1) Comparisons between individual monthly mean values of downwelling shortwave fluxes from the model/reanalysis data sets and both the BSRN and GUOR data over the longest possible comparison time periods generally yielded biases less than 10 Wm^{-2}. Significant exceptions were the large biases of 25 and 38 Wm^{-2} found between NCEP-DOE-R2 and the BSRN and GUOR values, respectively. The standard deviations for all the model SW irradiances

relative to the in situ data fell within a range of about 20-30 Wm^{-2}. However, standard deviations with respect to the GUOR measurements were about 5 Wm^{-2} higher than relative to the BSRN values.

2) Based on comparisons to both BSRN and GUOR SW data, the models did not perform well in mountainous areas. Except for the NCEP-DOE-R2 reanalysis, all of the models performed better in the polar areas than the satellite-based products did. In general, the models showed the worst agreement in the tropics. However, NCEP-DOE-R2 performed worst in the midlatitudes. The largest biases relative to the BSRN SW irradiances occurred during the northern hemisphere summer.

3) Comparisons between monthly mean SW flux anomaly time series over a 30 GUOR site ensemble showed that the models reproduced the overall variability to 4-7 Wm^{-2} (one-sigma agreement). This is larger than the range of 2-3 Wm^{-2} found for the satellite data products. The agreement between the models and GUOR data improved when an ensemble limited to the twelve GUOR stations with completely continuous records was used instead. This may imply that stations with continuous records are better maintained than those with missing values.

4) Trend analysis was performed for deseasonalized SW fluxes for ensemble data time series consisting of averages over 12 GUOR station locations over the period of January 1984 to December 1999. Only two of the data sets were found to have trends significant at the 95% level: GUOR with a trend of 0.316 Wm^{-2} a^{-1} and GFDLCM2.1 with a trend of -0.205 Wm^{-2} a^{-1}. No firm conclusions about trends in surface down-welling shortwave fluxes over the January 1984 to December 1999 can be drawn from these results.

5) Biases computed between the modeled and BSRN monthly mean longwave irradiances over the period January 1992 to December 1999 were similar to the SW biases (less than 10 W m^{-2}) but the standard deviations were smaller (10-20 Wm^{-2} vs. 20-30 Wm^{-2}) than their SW counterparts. Interestingly, all of the biases between the model and in situ LW flux values were negative, i.e., the models fluxes were smaller.

Chapter 10:

References

(From chapters 1 to 9)

Abakumova, G.M., E.M. Feigelson, V. Russak, and V.V. Stadnik (1996), Evaluation of long-term changes in radiation, cloudiness and surface temperature on the territory of the Former Soviet Union, *J. Climate,* **9***,* 1319–1327.

Abbot, C. G., and F. E. Fowle, 1908a: Determination of the intensity of the solar radiation outside the earth's atmosphere, otherwise termed "the Solar Constant of Radiation," in Annals of the Astrophysical Observatory of the Smithsonian Institution, vol. 2, Chapter 1 , Smithsonian Institution, Washington, D.C..

Abbot, C. G., and F. E. Fowle, 1908b: Radiation and terrestrial temperature, in Annals of the Astrophysical Observatory of the Smithsonian Institution, vol. 2, chap.2, Smithsonian Institution, Washington, D .C..

Ackerman, T. P., and G. M. Stokes (2003): The Atmospheric Radiation Measurement Program, *Physics Today,* **56***,* 38–44.

Adler, R. F. and co-authors, 2003: The version-2 global precipitation climatology project (GPCP) monthly precipitation analysis (1979-present), *J Hydrometeor***. 4**, 1147-1167.

Alpert, P., P. Kishcha, Y. J. Kaufman, and R. Schwarzbard, 2005: Global dimming or local dimming?: Effect of urbanization on sunlight availability, *Geophys. Res. Lett.,* **32***,* L17802, doi:10.1029/2005GL023320.

Augustine, J. A., J. J. DeLuisi, and C. N. Long, 2000: SURFRAD -- A national surface radiation budget network for atmospheric research, *Bull. Amer. Met. Soc., 81*, 2341-2358.

Barnard, J. C., and C. N. Long, (2004): A Simple Empirical Equation to Calculate Cloud Optical Thickness Using Shortwave Broadband Measurement, JAM, **43**, 1057-1066.

Barnard, J. C., C. N. Long, E. I. Kassianov, S. A. McFarlane, J. M. Comstock, M. Freer, and G. M. McFarquhar, 2008: Development and Evaluation of a Simple Algorithm to Find Cloud Optical Depth with Emphasis on Thin Ice Clouds, *OASJ,* **2**, 46-55, doi: 10.2174/1874282300802010046.

Barkstrom, B. R., 1984: The Earth Radiation Budget Experiment (ERBE). Bull. Amer. Meteor. Soc., **65**, 1170-1185.

Barnett, T.P., J. Ritchie, J. Foat, and G. Stokes, 1998: On the space-time scales of the surface solar radiation field *J. Clim.* **11**. 88-96.

Bush B.C, and FPJ Valero, 1999: Comparison of ARESE celear sky surface radiation measurements. *J. Quant. Spectro. Radiative Trans.,* **61**, 249-264.

Berbery, E. H., K. E. Mitchell, S. Benjamin, T. Smirnova, H. Ritchie, R. Hogue, and E. Radeva (1999), Assessment of land surface energy budgets from regional and global models, *J. Geophys. Res.*, **104(D16),** 19,329 – 19,348..

Berger, A., 1978: Long-Term Variations of Daily Insolation and Quarternary Climate Changes. *J. Atmos. Sci.,* **35,** 2362 - 2367.

Bess, T.D., G.L. Smith, R.N. Green, D.A. Rutan, R.S. Kandel, P. Raberanto, and M. Viollier, 1997: : Intercomparison of Scanning Radiometer for Radiation Budget (ScaRaB) and Earth Radiation Budget Experiment (ERBE) results, Proc. 9th Conf. Atmos. Radiation, Long Beach, California.

Betts, A. K., S. Y. Hong, and H. L. Pan, 1996: Comparison of NCEP-NCAR reanalysis with 1987 FIFE data, *Mon. Wea. Rev.*, **124(7):**1480-1498

Bretagnon, P. and G. Francou, 1988: Planetary theories in rectangular and spherical variables. VSOP87 solutions. *Astron. Astrophys*. **202**, 309-315.

Butler, J.J., Johnson, B.C., Rice, J.P., Shirley, E.L., and Barnes R.A., 2008: "Sources of differences in on-orbital total solar irradiance measurements and description of a proposed laboratory intercomparison," *Journal of Research of the National Institute of Standards and Technology*, July 1, 2008.

Brooks, D.R., E. H. Harrison, P. Minnis, J. T. Suttles, and R. Kandel, 1986: Development of Algorithms for Understanding the Temporal and Spatial Variability of the Earth's Radiation Balance, *Rev. Geophys*., **24**, 2, 422-438.

Capderou, M., 1998: Determination of the shortwave anisotropic function for clear-sky desert scenes from ScaRaB data. Comparison with models issued from other satellites. *Journal of Applied Meteorology,* **37** 1398-1411

Chang F.-L., Li Z. and A.P. Trishchenko, 2000: The dependence of TOA Reflectance Anisotropy on Cloud Properties Inferred from ScaRaB Satellite Data. *J. Appl. Meteor.,* 39, 2480-2493.

Clerbaux, N., and co-authors. 2009. Comparison of GERB instantaneous radiance and flux products with CERES Edition-2 data. *Remote Sens. of Environ*. **112:** 102-114.

Comer, R. E., A. Slingo, R. P. Allen, 2007: Observations of the diurnal cycle of outgoing longwave radiation from the Geostationary Earth Radiation Budget instrument, *Geophys. Res. Lett*., **34**, L02823, doi:10.1029/2006GL028229.

Desbois, M., M. Capderou, L. Eymard, R. Roca, N. Viltard, M. Viollier et N. Karouche (**2007**), Megha-Tropiques : un satellite hydrométéorologique franco-indien, *La Météorologie, pp 19-27, n° 57*.

Delworth, T.L., and Coauthors, 2006: GFDL's CM2 global coupled climate models. Part I: Formulation and simulation of characteristics, *J. Climate*, **19**, 643-674.

Deneke, H., A. Feijt, A. van Lammeren and C. Simmer, 2005: Validation of a physical retrieval scheme of solar surface irradiances from narrowband satellite radiances. *J. Appl. Meteor*., **44**, 1453-1466.

Domingo, V., Ermolli, I., Foukal, P., Fox, P., Fröhlich, C., Haberreiter, M., Krivova, N., Kopp, G., Schmutz, W., Solanki, S.K., Spruit, H.C., Unruh, Y., Vögler, A., 2009: "Solar Magnetism and Irradiance: Understanding the Influence of Magnetic Field on Solar Irradiance," *Space Science Reviews*, **145**: 337–380, 2009, DOI 10.1007/s11214-009-9562-1

Dupont J.C., M. Haeffelin, and C.N. Long (2008): Evaluation of cloudless-sky periods detected by shortwave and longwave algorithms using lidar measurements, *GRL* **35(10),** doi:10.1029/2008GL033658.

Durr B. and R. Philipona, 2004: Automatic cloud amount detection by surface longwave downward radiation measurements, *JGR*, **109**, D05201, doi:10.1029/2003JD004182.

Dutton, E.G., R.S. Stone, D.W. Nelson, and B.G. Mendonca (1991), Recent interannual variations in solar radiation cloudiness, and surface temperature at the South Pole, *J. Clim., 4*, 848-858.

Dutton, E.G., 1993: An Extended Comparison Between Lowtran7-Computed and Observed Broadband Thermal Irradiances: Global Extreme and Intermediate Surface Conditions. *J. Atmos. Ocean. Tech.* **10***,* 326-336.

Dutton, E.G., J.J. Michalsky, T. Stoffel, B.W. Forgan, J. Hickey, D.W. Nelson, T.L. Alberta, and I. Reda, 2001: Measurement of broadband diffuse solar irradiance using current commercial instrumentation with a correction for thermal offset errors. *J. Atmos. Oceanic Tech*., **18**, 297-314.

Dutton, E. G., A. Farhadi, R. S. Stone, C. N. Long, and D. W. Nelson, 2004: Long-term variations in the occurrence and effective solar transmission of clouds as determined from surface-based total irradiance observations, *J. Geophys. Res.*, **109**, D03204, doi:10.1029/2003JD003568.

Dutton E.G., D. W. Nelson, R. S. Stone, D. U. Longenecker, G. Carbaugh, J. M. Harris, and J. Wendell, 2006: Decadal Variations in Surface Solar Irradiance as Observed in a Globally Remote Network. 2006: *J. Geophys. Res.,* **111**, D19101, doi:10.1029/2005JD006901.

Duvel, J.-Ph., and P. Raberanto, 2000 : A geophysical cross-calibration approach for broadband channels: Application to the ScaRaB experiment, *J. Atmos. Oceanic Technol.* **17**, 1609-1717

Duvel, J. P., S. Bouffiès-Cloché, and M. Viollier, 2000: Determination of shortwave Earth reflectances from visible radiance measurements: Error estimate using ScaRaB data, *J. Appl. Meteorol.*, **39**, 957– 970.

Duvel, J. P., M. Viollier, P. Raberanto, R. Kandel, M. Haeffelin, L.A. Pakhomov, V.A. Golovko, J. Mueller, R. Stuhlmann, and the International ScaRaB Scientific Working Group (ISSWG), 2001: The ScaRaB-Resurs Earth Radiation Budget Dataset and first results, *Bull. Am. Metereol. Soc.,* **82,** 1397-1408.

Evan, A. T., A. K. Heidinger, and D. J. Vimont, 2007: Arguments against a physical long-term trend in global ISCCP cloud amounts, *Geophys. Res. Lett.*, **34**, L04701, doi:10.1029/2006GL028083.

Fasullo, J. T., and K. E. Trenberth, 2008: The annual cycle of the energy budget. Part II: Meridional structures and pole-ward transport. *J. Climate,* **21,** 2313–2325.

Fontenla, J., O.R. White, P. Fox, E. Avrett, R. Kurucz, 1999: Calculation of Solar Irradiances. I-Synthesis of the Solar Spectrum. *Astrophysical. J.*, **518**, 480-499.

Foukal P. and P. Bernasconi, 2008: "Do Photospheric Brightness Structures Outside Magnetic Flux Tubes Contribute to Solar Luminosity Variation?" *Solar Physics*, **248**, #1, March 2008, 1-15, DOI: 10.1007/s11207-008-9134-7

Freidenreich, S.M., and V. Ramaswamy, 2011: Analysis of the biases in the downward shortwave surface flux in the GFDL CM2.1 General Circulation Model, *J. Geophys. Res.* (in press).

Fröhlich, C., and J. London, 1986: Revised Instruction Manual on Radiation Instruments and Measurements. WCRP Publ. Ser. No. 7, WMO/TD-NO. 149, WMO, Geneva, 140 pp.

Fröhlich, C., and J. Lean, "Total Solar Irradiance Variations: The Construction of a Composite and its Comparison with Models," ESA SP 415, Dec. 1997, 1997ESASP.415..227F

Fröhlich, C. and J. Lean, 2002: Solar irradiance variability and climate. *Astron. Nach.,* **323,** 203 – 212**.**

Futyan, J. M. and J. E. Russell, 2005: Developing clear sky flux products for the Geostationary Earth Radiation Budget (GERB) experiment. *J. Appl. Meteorol*., **44**, 13611374.

Gates WL, Boyle JS, Covey C, Dease CG, Doutriaux CM, Drach RS, Fiorino M, Gleckler PJ, Hnilo JJ, Marlais SM, Phillips TJ, Potter GL, Santer BD, Sperber KR, Taylor KE, Williams DN. 1999. An overview of the results of the Atmospheric Model Intercomparison Project (AMIP). *Bull. Am. Meteor. Soc.* **80**: 29–55.

Gilgen, H., M. Wild, and A. Ohmura, 1998: Means and trends of shortwave irradiance at the surface estimated from GEBA, *J. Clim.*, **11**, 2042-2061.

Gilgen, H., and A. Ohmura (1999): The Global Energy Balance Archive, *Bull. Amer. Meteorol. Soc.,* **80**, 831-850.

Gilgen, H., A. Roesch, M. Wild, and A. Ohmura: 2009: Decadal changes of shortwave irradiance at the surface in the period 1960 to 2000 estimated from Global Energy Balance Archive, *J. Geophys. Res*., **114***,* D00D08, doi:10.1029/2008JD011383.

Ginoux, P., L. W. Horowitz, V. Ramaswamy, I. V. Geogdzhayev, B. N. Holben, G. Stenchikov, and X. Tie, 2006: Evaluation of aerosol distribution and optical depth in the Geophysical Fluid

Dynamics Laboratory coupled model CM2.1 for present climate. *J. Geophys. Res.*, **111**, D22210, doi:10.1029/2005JD006707.

Golovko, V.A., L.A. Pakhomov, and A.B. Uspensky, 2003: Исследование поля уходящего излучения Земли с помощью сканирующего радиометра радиационного баланса на российских спутниках серии «Метеор» и «Ресурс» (Earth radiation budget investigations from "Meteor" and "Resurs" satellites.) Электронный журнал «ИССЛЕДОВАНО В РОССИИ» (Electronic journal "Investigated in Russia"), 106, 1280-1299. http://zhurnal.ape.relarn.ru/articles/2003/106.pdf

Gray, L.J., J. Beer, M. Geller, J. D. Haigh, M. Lockwood, K. Matthes, U. Cubasch, D. Fleitmann, G. Harrison, L. Hood, J. Luterbacher, G. A. Meehl, D. Shindell, B. van Geel, and W. White, 2010: "Solar Influences on Climate," *Reviews of Geophysics*, **48**, RG4001, doi:10.1029/2009RG000282.

Gueymard, C.A. and D. R. Myers, 2009: Evaluation of conventional and high-performance routine solar radiation measurements for improved solar resource, climatological trends, and radiative modeling. *Solar Energy*, **83**, 171-185.

Gueymard, C.A. and D.R. Myers, 2008: Solar radiation measurement: Progress in radiometry for improved modeling, in Modeling Solar Radiation at the Earth Surface, V. Badescu ed., Springer.

Gupta, S. K., D. P. Kratz, P. W. Stackhouse, Jr., A. C. Wilber, T. Zhang, and V. E. Sothcott, 2010: Improvement of surface longwave flux algorithms used in CERES processing, *J. Applied Meteorol. Climatol.*, **49,** 1579-1589.

Haeffelin, M., B. Wielicki, J.-Ph. Duvel, K. Priestley, and M. Viollier, 2001 : Intercalibration of CERES and ScaRaB Earth radiation budget datasets using temporally and spatially collocated radiance measurements. *Geophys. Res. Let.* **28(1)**, 167-170

Haigh, J. D., 1994: The role of stratospheric ozone in modulating the solar radiative forcing of climate, *Nature*, **370**, 544.

Haigh, J.D., Winning, A.R., Toumi, R., and Harder, J.W., 2010: An influence of solar spectral variations on radiative forcing of climate, *Nature* **467**, 696–699 , doi:10.1038/nature09426

Hansen, J., R. Ruedy, M. Sato, and K. Lo, 2010: Global surface temperature change, *Rev. Geophys.,* **48**, RG4004, doi:10.1029/2010RG000345.

Harries, JE, and coauthors,, 2005: The geostationary Earth Radiation Budget Project, *Bull. Am. Met. Soc.,* **86 (7):** 945 JUL 2005.

Harrison, E. F., D. R. Brooks, P. Minnis, B. A. Wielicki, W. F. Staylor, G. G. Gibson, D. F. Young, and F. M. Denn, 1988: First estimates of the diurnal variation of longwave radiation from the multiple-satellite Earth Radiation Budget Experiment (ERBE). *Bull. Amer. Met. Soc*., **69**, 1144-1151.

Harrison, E. F., P Minnis, and G. G. Gibson, 1983: Orbital and cloud cover sampling analyses for multi-satellite Earth radiation budget experiments, *J. Spacecraft and Rockets*, **20**, 491-495.

Hatzianastassiou, N., et al. (2005), Global distribution of Earth's surface shortwave radiation budget, *Atmos. Chem. Phys., 5,* 2847– 2867.

Hay, J. E., 1983: Solar energy system design: The impact of mesoscale variations in solar radiation, *Atmos.-Ocean*, **21(2),** 138-157.

Hinkelman, L. M., T. P. Ackerman, and R. T. Marchand, 1999: An evaluation of NCEP Eta model predictions of surface energy budget and cloud properties by comparison with measured ARM data, *J. Geophys. Res*., **104(D16)**:19,535-19,549.

Hinkelman, L. M., P. W. Stackhouse, Jr., B. A. Wielicki, T. Zhang, and S. R. Wilson, 2009: Surface insolation trends from satellite and ground measurements: Comparisons and challenges, *J. Geophys. Res*., **114**, D00D20, doi:10.1029/2008JD011004.

Holben, B.N, and Coauthors, 2001: An emerging ground-based aerosol climatology: Aerosol optical depth from AERONET. *J. Geophys. Res.*, **106,** 12067-12097.

Hood, L. L., 2003: Thermal response of the tropical tropopause region to solar ultraviolet variations, *Geophys. Res. Lett*., **30(23),** 2215, doi:10.1029/2003GL018364.

House, F.B., A. Gruber, G.E. Hunt, and A.T. Mecherikunnel, 1986: History of satellite missions and measurements of the Earth radiation budget (1957-1984). *Rev. Geophys.,* **24**, 357-377.

Hoyt, D.V. and Schatten, K.H., 1993: A Discussion of Plausible Solar Irradiance Variations, 1700-1992, *JGR*, **98**, pp: 18,895-18,906.

Hunt, G.E., R. Kandel, and A.T. Mecherikunnel, 1986: A history of presatellite investigations of the Earth's radiation budget. *Rev. Geophys*., **24**, 351-356.

IPCC 2007: Climate Change 2007: The Physical Science Basis. Contribution of the Working Group I to the Fourth Assessment Report of the Intergovernmental Panel on Climate Change. Cambridge University Press, Cambridge, United Kungdom and New York, NY, USA, 996.

Kanamitsu, M., W. Ebisuzaki, J. Woollen, S-K, Yang, J.J. Hnilo, M. Fiorino, and G. L. Potter, 2002: NCEP-DEO AMIP-II Reanalysis (R-2), *Bull. Am. Meteorol. Soc*., **83**, No. 11, 1631-1643, Nov 2002.

Kandel, R., M. Viollier, P. Raberanto, J. P. Duvel, L. A. Pakhomov, V. A. Golovko, A. P. Trishchenko, J. Mueller, E. Raschke, R. Stuhlmann, and the International ScaRaB Scientific Working Group (ISSWG), 1998: The ScaRaB Earth Radiation Budget Dataset, *Bull. Am. Meteorol. Soc.,* **79**, 765-783.

Kandel, R., and M. Viollier, 2010: Observation of the Earth's radiation budget from space. C. R. *Geoscience*, doi:10.1016/j.crte.2010.01.005

Kato, S., F. G. Rose, S. Sun-Mack, W. F. Miller, Y. Chen, D. A. Rutan, G. L. Stephens, N. G. Loeb, P. Minnis, B. A. Wielicki, D. M. Winker, T. P. Charlock, P. W. Stackhouse, K.-M. Xu, and W. Collins, 2011: Computation of top-of-atmosphere and surface irradiances with CALIPSO, CloudSat, and MODIS derived cloud and aerosol properties, *J. Geophys. Res.* (in press).

Kato S, N. G. Loeb, 2003. Twilight irradiance reflected by the Earth estimated from clouds and the Earth's Radiant Energy System (CERES) measurement. *J. Climate*, **16**, 26

Kim, D. and V. Ramanathan. Solar radiation budget and radiative forcing due to aerosols and clouds. *J. Geophys. Res*., **113(D02203),** 2008.

Kopp, G. and Lean, J.L., 2011: "A New, Lower Value of Total Solar Irradiance: Evidence and Climate Significance," *Geophys. Res. Letters*, **38**, L01706, doi:10.1029/2010GL045777.

Kopp, G. and Lawrence, G., 2005: "The Total Irradiance Monitor (TIM): Instrument Design," *Solar Physics*, **230**, 1, Aug. 2005, pp. 91-109.

Kopp, G., Lawrence, G., and Rottman, G., 2005: "The Total Irradiance Monitor (TIM): Science Results," *Solar Physics*, **230**, 1, Aug. 2005, 129-140.

Kopp, G., Harder, J., and Richard, E. 2006: "Correlations Between Total Solar Irradiance and Spectral Irradiances Using SORCE Measurements," AGU Fall Meeting, 11-15 Dec. 2006

Kopp, G., Heuerman, K., Harber, D., and Drake, V. 2007: "The TSI Radiometer Facility - Absolute Calibrations for Total Solar Irradiance Instruments", *SPIE Proc*. **6677-09**, 26-28 Aug. 2007.

Kopp, G. and Lean, J.L., 2011: "A New, Lower Value of Total Solar Irradiance: Evidence and Climate Significance," *Geophys. Res. Letters* Frontier article, **38**, L01706, doi:10.1029/2010GL045777.

Krivova, N. A., S. K. Solanki , M. Fligge , and Y. C. Unruh, "Reconstruction of solar irradiance variations in cycle 23: is solar surface magnetism the cause?" *Astronomy & Astrophysics*, **399**, L1-L4 (2003), DOI 10.1051/0004-6361:20030029

Lacis, A. A., G. A. Schmidt, D. Rind, R. A. Ruedy, 2010: "Atmospheric CO2: Principal Control Knob Governing Earth's Temperature", *Science,* **330,** 356-359.

Lean, J., "Evolution of the Sun's Spectral Irradiance Since the Maunder Minimum," *Geoph. Res. Lett.,* **27**, #16, pp. 2425-2428, Aug. 15, 2000.

Lean, J.L. and Rind, D.H., "How natural and anthropogenic influences alter global and regional surface temperatures: 1889 to 2006," GRL, **35**, L18701, doi:10.1029/2008GL034864, 2008.

Lean, J.L. and Woods, T.N., 2010: Solar Total and Spectral Irradiance Measurements and Models: A Users Guide, in *Heliophysics: Evolving Solar Activity and the Climates of Space and Earth*, eds. Schrijver & Siscoe, ISBN-13: 9780521112949.

L'Ecuyer, T., N. B. Wood, T. Haladay, G. L. Stephens, and P. W. Stackhouse Jr. (2008), Impact of clouds on atmospheric heating based on the R04 CloudSat fluxes and heating rates data set, *J. Geophys. Res., **113,*** D00A15, doi:10.1029/2008JD009951.

Liepert, B.G., P. Fabian, and H. Grassl (1994), Solar radiation in Germany- observed trends and assessment of their causes; Part I: regional approach, *Beitr. Phys. Atmos., **67,*** 15-29.

Liepert, B.G. (2002), Observed reductions of surface solar radiation at sites in the United States and worldwide from 1961 to 1990, *Geophy. Res. Lett., **29***, doi:10.1029/2002GL014910.

Li, Z., C.H. Whitlock, and T.P. Charlock, 1995: Assessment of the Global Monthly Mean Surface Insolation Estimated from Satellite Measurements Using Global Energy Balance Archive Data. *J. Clim.,* **8,** 315-328.

Li, Z., M. C. Cribb, F-L. Chang, A. Trishchenko, and Y. Luo, 2005: Natural variability and sampling errors in solar radiation measurements for model validation over the Atmospheric Radiation Measurement Southern Great Plains region, *J. Geophys. Res., 110,* D15S19, doi:10.1029/2004JD005028.

Li, Z., and A. Trishchenko, 1999: A study towards an improved understanding of the relation between visible and SW albedo measurements, *J. Atmos. Oceanic Technol.,* **17**, 347– 360.

Liley, B. (2009), New Zealand dimming and brightening, *J. Geophys. Res., **114,*** D00D10, doi:10.1029/2008JD011401.

Loeb, N. G., S. Kato, K. Loukachine, and Manalo-Smith N., 2005: Angular Distribution Models for Top-of-Atmosphere Radiative Flux Estimation from the Clouds and the Earth's Radiant Energy System Instrument on the Terra Satellite. Part I: Methodology, *J. Atm. Ocean. Techn.,* **22,** 338-351, doi:.10.1175/JTECH1712.1.

Loeb, N. G., B. A. Wielicki, F. G. Rose, and D. R. Doelling, 2007: Variability in global top-of-atmosphere shortwave radiation between 2000 and 2005, *Geophys. Res. Lett., **34,*** L03704, doi:10.1029/2006GL028196.

Loeb, N. G., S. Kato, K. Loukachine, N. Manalo-Smith, D. R. Doelling, 2007: Angular Distribution Models for Top-of-Atmosphere Radiative Flux Estimation from the Clouds and the Earth's Radiant Energy System Instrument on the Terra Satellite. Part II: Validation. *J. Atmos. Oceanic Technol.*, **24**, 564–584.

Loeb, N. G., B. A. Wielicki, D. R. Doelling, G. L. Smith, D. F. Keyes, S. Kato, N. Manalo-Smith, and T. Wong, 2009: Towards Optimal Closure of the Earth's Top-of-Atmosphere Radiation Budget. *J. Climate*, **22**, 748-766.

Loeb, N. G., B. A. Wielicki, D. R. Doelling, G. L. Smith, D. F. Keyes, S. Kato, N. Manalo−Smith, and T. Wong, 2009, "Toward optimal closure of the Earth's top-of-atmosphere radiation budget," *J. Clim.*, **22**, 748–766, doi:10.1175/2008JCLI2637.1

Lohmann, S., C. Schillings, B. Mayer and R. Meyer, 2006: Long-term variability of solar direct and global irradiance derived from ISCCP data and comparison with re-analysis data. Solar Energy, **80**, doi:10.1016/j.solener.2006.03.004.

Lohmann, S., L. Riihimaki, F. Vignola, R. Meyer (2007): Trends in direct normal irradiance in Oregon: comparison of surface irradiance and ISCCP-derived irradiance. *Geophys. Res. Lett.,* **34,** L02705, doi:10.1029/2006GL027322.

Long, C.N. and T.P. Ackerman, 1995: Surface measurements of solar irradiance – A study of the spatial correlation between simultaneous measurements at separated sites. *J. Appl. Meteor.* **34,** 1039-1046.

Long, C. N. and T. P. Ackerman, (2000): Identification of Clear Skies from Broadband Pyranometer Measurements and Calculation of Downwelling Shortwave Cloud Effects, *JGR*, ***105*,** No. D12, 15609-15626.

Long CN, TP Ackerman, and JE Christy. 2002. "Variability Across the ARM SGP Area by Temporal and Spatial Scale." 12th ARM Science Team Meeting Proceedings, April 8-12, 2000, St. Petersburg, Florida.

Long, C. N., 2004: The Next Generation Flux Analysis: Adding Clear-sky LW and LW Cloud Effects, Cloud Optical Depths, and Improved Sky Cover Estimates, 14th ARM Science Team Meeting Proceedings, Albuquerque, New Mexico, March 22-26, 2004.

Long, C. N., 2005: On the Estimation of Clear-Sky Upwelling SW and LW, 15th ARM Science Team Meeting Proceedings, Daytona Beach, Florida, March 14-18, 2005.

Long, C. N., T. P. Ackerman, K. L. Gaustad, and J. N. S. Cole, 2006: Estimation of fractional sky cover from broadband shortwave radiometer measurements, *JGR*, **111,** D11204, doi:10.1029/2005JD006475.

Long, C. N., and Y. Shi, 2008: An Automated Quality Assessment and Control Algorithm for Surface Radiation Measurements, *OASJ*, **2**, 23-37, doi: 10.2174/1874282300802010023.

Long, C. N., and D. D. Turner, 2008: A Method for Continuous Estimation of Clear-Sky Downwelling Longwave Radiative Flux Developed Using ARM Surface Measurements, *JGR*, **113**, D18206, doi:10.1029/2008JD009936.

Long, C.N., E.G. Dutton, J.A. Augustine, W. Wiscombe, M. Wild, S.A. McFarlane, and C.J. Flynn, 2009: Significant decadal brightening of downwelling Shortwave in the Continental US, *J. Geophys. Res.,* **114**, D00D06, doi:10.1029/2008JD011263.

McArthur, L.J.B. 2005: BSRN Operations Manual Ver 2.1. WMO-TD-No 1274, WCRP-121, http://www.bsrn.awi.de/fileadmin/user_upload/Home/Publications/McArthur.pdf

McClintock, W.E., Rottman, G.J., and Woods, T.N., "Solar-Stellar Irradiance Comparison Experiment II (SOLSTICE II): Instrument Concept and Design," *Solar Physics*, **230**, 1, Aug. 2005, pp. 225-258.

Merkel, A.W.; Harder, J.W.; Marsh, D.R.; Smith, A.K.; Fontenla, J.M.; Woods, T.N., "The impact of solar spectral irradiance variability on middle atmospheric ozone," Geophys. Res. Lett., **38**, #13, doi: 10.1029/2011GL047561.

Minnis, P. and Harrison, E. F., 1984: Diurnal variability of regional cloud and clear-sky radiative parameters derived from GOES data; Part III: November 1978 Radiative Parameters. *J. Climate Appl. Meteorol*., **23**, 1032-1051.

Monge, J.L., R.S. Kandel, L.A. Pakhomov, and V.I. Adasko, 1991: ScaRaB Earth radiation budget scanning radiometer, *Metrologia,* **28**, 261-284.

Myers, D. R. (1989). Uncertainty Analysis for Thermopile and Pyranometer and Pyrheliometer Calibrations Performed by SERI. SERI/TR 215-3294. Golden, CO, , Solar Energy Research Institute.

Mueller, J., R. Stuhlmann, R. Becker, E. Raschke, H. Rinck, P. Burkert, J.L. Monge, F. Sirou, R. Kandel, T. Trémas, and L.A. Pakhomov, 1997 : Ground Characterization of the Scanner for Radiation Budget (ScaRaB) Flight Model 1, *J. Atmos. Oc. Technol.*, **14**, 802-813

Neckel, H. and D. Labs, 1984: The Solar Radiation between 3300 and 12500 Å. *Solar Physics,* **90**, 205 – 258

Norris, J. R., and M. Wild (2007), Trends in aerosol radiative effects over Europe inferred from observed cloud cover, solar ‘‘dimming,’’ and solar ‘‘brightening’’, *J. Geophys. Res.,* **112***,* D08214, doi:10.1029/2006JD007794.

Norris, J. R., and M. Wild (2009), Trends in aerosol radiative effects over China and Japan inferred from observed cloud cover, solar ‘‘dimming,’’ and solar ‘‘brightening’’, *J. Geophys. Res.,* **114***,* D00D15, doi:10.1029/2008JD011378.

Ohmura, A., and H. Lang (1989), Secular variation of global radiation over Europe, in *Current problems in Atmospheric Radiation*, J. Lenoble, J.F. Geleyn, Eds. (Deepak, Hampton, VA), 98-301.

Ohmura, A., H. Gilgen, and M. Wild, 1989: Global Energy Balance Archive GEBA, World Climate Program - Water Project A7, *Zuercher Geografische Schriften*, **34**, Verlag der Fachvereine, Zürich, 62 pp.

Ohmura, A., and 9 co-authors; 1998: Baseline Surface Radiation Network, a new precision radiometry for climate research, *Bull. Am. Meteorol. Soc.*, **79,** 2115-2136.

Ohmura, A., 2006: Observed long-term variations of solar irradiances at the Earth’s surface, *Space Sci. Rev.,* **125**, 111–128, doi:10.1007/s11214- 006-9050-9.

Ohmura, A., 2009: Observed decadal variations in surface solar radiation and their causes, *J. Geophys. Res.*, **114**, D00D05, doi:10.1029/2008JD011290.

Ohring, G., et al., 2005: Satellite Instrument Calibration for Measuring Global Climate Change. *Bull. Am. Met. Soc. **86, 9,*** 1303-1313.

Ohring, G., B. Emery, B.A. Wielicki, J. Butler, L.E. Flynn, F. Weng, K. St. Germain, C. Cao, M. Goldberg, J. Xiong, G.T. Fraser, D. Kunkee, G. Kopp, D. Winker, L. Miller, S.G. Ungar, D. Tobin, Anderson, D. Pollock, T. Stone, S. Shipley, P.E. Ardanuy, 2007: “Achieving Satellite Instrument Calibration for Climate Change,” *EOS*, **88**, No. 11.

Ohvril, H., and 16 co-authors, 2009: Global dimming/brightening vs. atmospheric column transparency and volcanic activity, *J. Geophys. Res.*, **114,** D00D12, doi:10.1029/2008JD010644.

Padma Kumari, B., A. L. Londhe, S. Daniel, and D. B. Jadhav, 2007: Observational evidence of solar dimming: Offsetting surface warming over India, *Geophys. Res. Lett.,* **34,** L21810, doi:10.1029/2007GL031133.

Pavlakis, K.G., D. Hatzidimitriou, C. Matsoukas, E. Drakakis, N. Hatzianastassiou, and I. Vardavas (2003), Ten-year global distribution of downwelling longwave radiation, *Atmos. Chem. Phys. Discuss.,* **3**, 5099-5137, 2003.

Philipona, R., B. Dürr, C. Marty, A. Ohmura, and M. Wild, 2004: Radiative forcing -measured at Earth’s surface - corroborate the increasing greenhouse effect, *Geophys. Res. Lett.,* **31***,* L03202, doi:10.1029/2003GL018765.

Pinker, R. T. and I. Laszlo, 1992: Modeling of surface solar irradiance for satellite applications on a global scale. *J. Appl. Meteor.,* **31,** *194-211*.

Pinker, R. T., B. Zhang, and E. G. Dutton, 2005: Do satellites detect trends in surface solar radiation?, *Science,* **308,** 850–854.

Prata, F., 2008: The climatological record of clear-sky longwave radiation at the Earth’s surface: evidence for water vapor feedback?, *Int. J. Remote Sens.,* doi:10.1080/01431160802036508.

Ramanathan, V., C. Chung, D. Kim, T. Bettge, L. Buja, J. T. Kiehl, W. M. Washington, Q. Fu, D. R. Sikka, and M. Wild (2005), Atmospheric brown clouds: Impacts on South Asian climate and hydrological cycle, *Proc. Natl. Acad. Sci. U.S.A.,* **102***,* 5326–5333.

Raschke, E., M. A. Giorgetta, S. Kinne, and M. Wild (2005), How accurate did GCMs compute the insolation at TOA for AMIP-2? *Geophys. Res. Lett*., **32**, L23707, doi:10.1029/2005GL024411.

Raschke E., T. H. Vonder Haar, W. R. Bandeen, M. Pasternak, 1973: The Annual Radiation Budget of the Earth-Atmosphere System During 1969-70 from Nimbus 3 Measurements. *J. Atmos. Sci.,* **30,** 341-364.

Raschke, E., A. Ohmura, W. B. Rossow, B. E. Carlson, Y.-C. Zhang, C, Stubenrauch, M. Kottek, M, Wild, 2005: Cloud effects on the radiation budget based on ISCCP data, *Int. J. Climatology,* **25,** 1103-1142.

Riihimaki, L., F. E. Vignola, and C. N. Long (2009): Analyzing the contribution of aerosols to an observed increase in direct normal irradiance in Oregon, *J. Geophys. Res*., **114,** D00D02, doi:10.1029/2008JD010970.

Rind, D., and W.B. Rossow, 1984: The effects of physical processes on the Hadley circulation, *J. Atmos. Sci.,* **41**, 479-507

Roesch, A., M. Wild, A. Ohmura, E. Dutton, C.N. Long, and T. Zhang (2011), Assessment of the completeness of BSRN radiation records and the consequence for the computation of monthly means, Atmos. Meas. Tech., **4**, 339–354 .

Rose, F. G. and T. P. Charlock, 2002: New Fu-Liou code tested with ARM Raman Lidar and CERES in pre-CALIPSO exercise. Extended Abstract for 11th Conference on Atmospheric Radiation, AMS.

Rossow, W.B, and R. Schiffer, 1999: Advances in understanding clouds from ISCCP. *Bull. Amer. Meteor. Soc*., **80**, 2261-2287..

Rottman, G. 2005: The SORCE Mission, *Solar Phys.,* **230,** 7-25.

Ruckstuhl, C., and J. R. Norris (2009), How do aerosol histories affect solar ‘‘dimming’’ and ‘‘brightening’’ over Europe?: IPCC-AR4 models versus observations, *J. Geophys. Res.,* **114***,* D00D04, doi:10.1029/2008JD011066.

Russak, V., 1990: Trends of solar radiation, cloudiness and atmospheric transparency during recent decades in Estonia, *Tellus,* **42B**, 206–210.

Russak, V., 2009: Changes in solar radiation and their influence on temperature trend in Estonia (1955-2007), *J. Geophys. Res.,* **114***,* D00D01, doi:10.1029/2008JD010613.

Rutan, D. A. and G. L. Smith, 1998: Diurnal variations of albedo, *Proc. 14th Conference on Probability and Statistics in the Atmospheric Science*, American Meteorological Society.

Saha, S., et al., 2010: The NCEP Climate Forecast System Reanalysis. *Bull. Am. Met. Soc.* ***91, 8,*** 1015-1057.

Sanchez-Lorenzo, A., M. Brunetti, J. Calbo, and J. Martin-Vide, 2007: Recent spatial and temporal variability and trends of sunshine duration over the Iberian Peninsula from a homogenized data set, *J. Geophys. Res.,* **112***,* D20115, doi:10.1029/2007JD008677

Schrijver, C. J., Livingston, W. C., Woods, T. N., and Mewaldt, R. A., 2011: The minimal solar activity in 2008–2009 and its implications for long-term climate modeling, *GRL*, **38**, L06701, doi:10.1029/2011GL046658.

Schroeder, T. A., R. Hember, N. C. Coops, and S. L. Liang, 2009: Validation of solar radiation surfaces from MODIS and reanalysis data over topographically complex terrain. *J. Appl. Meteorol. Clim.*, **48(12):**2441-1458.

Sellers, W.D., Physical Climatology, Univ. of Chicago Press, 1965.

Shapiro, A. I., Schmutz, W., Rozanov, E., Schoell, M., Haberreiter, M., Shapiro, A.V, and Nyeki, S., 2011: A new approach to long-term reconstruction of the solar irradiance leads to large historical solar forcing, *Astron. &Astro.,*. **??**

Shi, Y. and C. N. Long, 2002: Best Estimate Radiation Flux Value Added Product: Algorithm Operational Details and Explanations, Atmospheric Radiation Measurement Program Technical Report, ARM TR-008, 58 pp., Available via http://www.arm.gov.

Shi, G.-Y., T. Hayasaka, A. Ohmura, Z.-H. Chen, B. Wang, J.-Q. Zhao, H.-Z. Che, and L. Xu, 2008: Data quality assessment and the long-term trend of ground solar radiation in China, *J. Appl. Met. Climatol.*, **47,** 1006-1016.

Sirou F., Dinguirard M., and T. Tremas, 2000 : Ultimate determination of ScaRaB flight model 2 channel gains, *Metrologia,* **37** : 469-472.

Smith, G.L., R.N. Green, E. Raschke, L.M. Avis, J.T. Suttles, B.A. Wielicki, and R. Davies, 1986: Inversion methods for satellite studies of the earth's radiation budget : Development of algorithms for the ERBE mission. *Rev. Geophys*., **24**, 407-421.

Smith, G. L. and D. A. Rutan, 2003: The diurnal cycle of outgoing longwave radiation from Earth Radiation Budget Experiment measurements, *J. Atmos. Sci*., **60**, 1529-1542.

Smith, G. L., Z. P. Szewczyk, D. A. Rutan, and R. B. Lee, 2006: Comparison of measurements from satellite radiation budget instruments. *J. Geophys. Res.,* **111**, D04101, doi:10.1029/2005JD006307.

Stackhouse, P.W. and co-authors, 1999: The WCRP/GEWEX Surface Radiation Budget Project release 2: first results at 1 degree resolution, *10th Conference on Atmospheric Radiation: A Symposium with tributes to the works of Verner E. Suomi. American Meteorological Society, Madison, Wisconsin, 28 June-2 July,* 1999.

Standfuss C., Viollier M., Kandel R.S and J. Ph. Duvel, 2001: Regional Diurnal Albedo Climatology and Diurnal Time Extrapolation of Reflected Solar Flux Observations. Application to the ScaRaB record*, Journal of Climate*, **14**, 1129-1146.

Stanhill, G., and S. Moreshet. 1992: Global radiation climate changes: the world radiation network, *Climatic Change,* **21***,* 51-75.

Stanhill, G., and S. Moreshet, 1994): Global radiation climate change at seven sites remote from surface sources of pollution, *Climatic Change,* **26***,* 89–103.

Stanhill, G., and S. Cohen, 2001: Global dimming: a review of the evidence for a widespread and significant reduction in global radiation, *Agricultural and Forest Meteorology*, **107,** 255-278.

Steinhilber F., J. Beer, C. Fröhlich, 2009: "Total solar irradiance during the Holocene," *Geoph. Res. Lett.,* **36,** L19704, doi:10.1029/2009GL040142.

Stephens, G. L. and co-authors, 2002: The CloudSat Mission and the A-Train: A new dimension of space-based observations of clouds and precipitation. *Bull. Amer. Meteor. Soc.*, **83(12),** 1771-1790, 2002.

Stokes, G.M., and S.E. Schwartz, 1994: The atmospheric radiation – measurement (ARM) program – programmatic background and design of the cloud and radiation test-bed, *Bull. Am. Meteorol. Soc.*, **75,** 1201-1221.

Streets, D.G., Y. Wu, and M. Chin, 2006: Two-decadal aerosol trends as a likely explanation of the global dimming/brightening transition, *Geophys. Res. Lett*., ***33,*** doi:10.1029/2006GL026471.

Stubenrauch, C., J.-P. Duvel, and R.S. Kandel, 1993: Determination of longwave anisotropic emission factors from combined broad- and narrow-band radiance measurements, *J. Appl. Meteo.,* **32**, 848-856.

Stubenrauch, C. J., V. Briand and W. B. Rossow, 2002: The role of clear sky identification in the study of cloud radiative effects: Combined analysis from ISCCP and the Scanner of Radiation Budget (ScaRab). *J. Appl. Meteor*., **41**, 396-412.

Suttles, J.T. and G. Ohring, 1986: Surface Radiation Budget for Climate Applications. NASA Reference Publication 1169.

Tapping, K.F., D. Boteler, P. Charbonneau, A. Crouch, A. Manson, H. Paquette, 2007: "Solar Magnetic Activity and Total Irradiance Since the Maunder Minimum," *Solar Phys*, **246**, 309–326 DOI 10.1007/s11207-007-9047

Thekaekara, M. P., 1976: Solar irradiance: total and spectral and its possible variations, Apl. Opt. **15,** 915 – 925.

Tremas T. and M. Dinguirard, 1997: Calibration of ScaRaB FM1 : Methods and first results. *Adv. Space Res.* **19***,* 1335-1343.

Trenberth, K.E. and Fasullo, J.T., 2010, "Tracking Earth's Energy," *Science*, **328**, 316-317.

Trenberth, K. E., J. T. Fasullo, and J. Kiehl, 2009: Earth's Global Energy Budget, *Bull. Am. Meteor. Soc.*, **90(3),** 311-+, doi:10.1175/2008bams2634.1.

Trishchenko, A., and Z. Li, 1998: Use of ScaRaB measurements for validating a GOES-based TOA radiation product. *J. Appl. Meteor.,***37***,* 591-605*.*

Tsuchima, Y. & 8 co-authors, 2008: Some Key Parameters to Explain Inconsistencies in Fields of the Incoming Solar Radiation at the TOA. Proceedings of the International Radiation Symposium (IRS).

Usoskin, I., S. Solanki, M. Schussler, K. Mursula, and K. Alanko, 2003: Millennium-Scale Sunspot Number Reconstruction: Evidence for an Unusually Active Sun Since the 1940s, *Physical Review Letters*, **91**, 21.

Viollier, M., R. Kandel, and P. Raberanto, 1995: Inversion and space-time averaging algorithms for ScaRaB (Scanner for Earth Radiation Budget) - Comparison with ERBE. *Annales Geophysicae*, **13**, 959-968.

Viollier, M., C. Standfuss, O. Chomette and A. Quesney, **2009**: Top-of-Atmosphere Radiance-to-Flux conversion in the SW domain for the ScaRaB-3 instrument on Megha-Tropiques. *J. Atmos. Oceanic Technol.*, **26**, 2161-2171.

Wang, Y.-M., Lean, J. L., and Sheeley, N. R., 2005: Modeling the Sun's Magnetic Field and Irradiance Since 1713, *Ap. J.*, **625**:522–538,

Wang, H., and R. T. Pinker, 2009: Shortwave radiative fluxes from MODIS: Model development and implementation, *J. Geophys. Res.*, **114,** D20201. doi:10.1109/LGRS.2008.923209.

Weatherhead, E., and 12 co-authors, 1998: Factors affecting the detection of trends: Statistical considerations and applications to environmental data., *J. Geophys. Res*., **103** (D14), 17,149 – 17,161.

Webster P. & G. Stephens, 1984: Cloud-radiation interaction and the climate problem. In J.T. Houghton (ed.), The Global Climate, Cambridge University Press, pp 63-77.

Wielicki, B. W., and R. N. Green, 1989: Cloud identification for ERBE radiative flux retrieval. *J.Appl. Meteor.,* **28**, 1133–1146.

Wielicki, B.W., R. D. Cess, M.D. King, D.A. Randall and E.F. Harrison, 1995: Mission to Planet Earth: Role of Clouds and Radiation in Climate. *Bull. of Amer. Met. Soc*., **76**, *11, 2125-2153.*

Wielicki, B. A., and co-authors, 1996: Clouds and the Earth's Radiant Energy System (CERES): An Earth Observing System experiment. *Bull. Amer. Meteor. Soc*., **77,** 853-868

Wielicki, Bruce A., Edwin F. Harrison, Robert D. Cess, Michael D. King, David A. Randall, 1995: Mission to Planet Earth: Role of Clouds and Radiation in Climate. *Bull. Amer. Meteor. Soc.*, **76**, 2125–2153.

Wild, M., A. Ohmura, and U. Cubasch, 1997: GCM simulated surface energy fluxes in climate change experiments, *J. Clim.,* **10***,* 3093– 3110.

Wild, M., and 9 co-authors, 2005: From dimming to brightening: decadal changes in surface solar radiation, *Science,* **308**, 847-850.

Wild, M., J. Grieser, and C. Schär, 2008: Combined surface solar brightening and increasing greenhouse effect support recent intensification of the global land-based hydrological cycle,

Geophys. Res. Lett., **35***,* L17706, doi:10.1029/2008GL034842.

Wild, M., B. Trüssel, A. Ohmura, C.N. Long, E.G. Dutton, G. König-Langlo, and A. Tsvetkov (2009), Global Dimming and brightening: an update beyond 2000, *J. Geophys. Res*., **114**, D00D13, doi:10.1029/2008JD011382.

Wild, M., 2009a: Global dimming and brightening: A Review, *J. Geophys. Res.,* **114***,* D00D16, doi:10.1029/2008JD011470.

Wild, M..,2009b: How well do IPCC-AR4/CMIP3 climate models simulate global dimming / brightening and 20th century day- and night-time warming? *J. Geophys. Res*. **114,** D00D11, doi:10.1029/2008JD011372.

Wild, M., and E. Schmucki (2011) Assessment of global dimming and brightening in IPCC-AR4/CMIP3 models and ERA40 based on surface observations. *Clim. Dyn*. (in press), DOI: 10.1007/s00382-010-0939-3

Wittenberg, A. T., A. Rosati, N-C. Lau, and J. J. Ploshay, 2006: GFDL's CM2 Global Coupled Climate Models. Part III: Tropical Pacific climate and ENSO. *J. Climate*, **19,** 698-722.

WMO, 1981: Meteorological Aspects of the Utilization of Solar Radiation as an Energy Source. WMO Technical Note No. 172, WMO-No. 557, WMO, Geneva, 298 pp.

Woods, T., F. Eparvier, S. Bailey, S. C. Solomon, G. Rottman, G. Lawrence, R. Roble, O. R. White, J. Lean, and W. K. Tobiska, 1998: "TIMED Solar EUV Experiment," *SPIE Proceedings*, **3442**, 180.

Xie, P., and P. A. Arkin, 1997: Global precipitation: A 17-year monthly analysis based on gauge observations, satellite estimates and numerical model outputs. *Bull. Amer. Meteor. Soc.,* **78,** 2539–2558.

Zhang, Y.-C., W.B. Rossow and A. A. Lacis, 1995, Calculation of surface and top of atmosphere radiative fluxes from physical quantities based on ISCCP data sets, 1. Method and sensitivity to input data uncertainties, *J. Geophys. Res.,* **100,** 1149-1165.

Zhang, Y.-C., and W. B. Rossow, 1997: Estimating meridional energy transports by the atmospheric and oceanic general circulation using boundary flux data, *J. Climate.,* **10***,* 2358-2373.

Zhang, Y., W. B. Rossow, A. A. Lacis, V. Oinas, and M. I. Mishchenko, 2004: Calculation of radiative fluxes from the surface to top of atmosphere based on ISCCP and other global data sets: Refinements of the radiative transfer model and the input data., *J. Geophys. Res.*, **109**, D19105, doi:10.1029/2003JD004457.

Zhang, Y., W. B. Rossow, and P. W. Stackhouse Jr., 2006: Comparison of different global information sources used in surface radiative flux calculation: Radiative properties of the near-surface atmosphere, *J. Geophys. Res.,* **111***,* D13106, doi:10.1029/2005JD006873.

Zhang, Y-C, W. B. Rossow, and P. W. J. Stackhouse 2007. Comparison of different global information sources used in surface radiative flux calculation: radiative properties of the surface. *J. Geophys. Res*., **112**(D01102).

Zhang, Y., C. N. Long, W. B. Rossow, and E.G Dutton, 2010: Exploiting diurnal variations to evaluate the ISCCP-FD flux calculations and Radiative-Flux-Analysis-Processed surface observations from BSRN, ARM and SURFRAD. *Journal Geophys. Res.,* **115,** D15105, doi:10.1029/2009JD012743

References for Historical TSI Values; see Chapter 2

Foitzik, L., H. Hinzpeter, 1958: Sonnenstrahlung und Lufttrübung. *Akademische Verlagsgesellschaft Geest & Portig K.-G., Leipzig,* 309 pp.

Crommelynck, D.A., Brusa, R.W., and Domingo, V., 1986: Results of the solar constant experiment onboard Spacelab 1. *Solar Physics*, **107**, 1-9.

Drummond, A.J., Hickey, J.R., Laue, E.G., and Scholes, W.J., 1967: *Multichannel radiometer measurement of solar irradiance*. American Institute of Aeronautics, Aerospace Meeting, 5th, New York, N.Y., United States, 23-26 Jan. 1967, 12 pp.

Fröhlich, C. and Lean, J., 1998: The sun's total irradiance: Cycles, trends and related climate uncertainties since 1976. *Geophys. Res.Lett*., **25**, 4377-4380.

Fröhlich, C., Ed., 2000: Jahresbericht PMOD/WRC 1999. Publication No. 841, Physikalisch-Meteorologisches Observatorium Davos. 31 pp.

Hickey, J.R., Alton, B.M., Griffin, F.J., Jacobowitz, H., Pellegrino, P., Maschhoff, R.H., Smith, E.A., and Vonder Haar, T.H., 1982: Extraterrestrial solar irradiance variability - Two and one-half years of measurements from NIMBUS 7. *Solar Energy*, **29**, 125-127.

Johnson, F. S.: 1954: The solar constant. *J. Meteorol*., **11**, 6, 431-439. 888-891.

Kondratyev, K.Ya and Nikolskii, G.A. 1980: *Solnechnaya postoyannaya (Solar constant)*, Obzornaya informatsiya, Ser. Meteorologiya, Obninsk, No.4, 53 pp.

Murcray; D.G., 1969: *Balloon borne measurement of the solar constant*. Final Report, 15 May 64-15 Dec 68. AD0691061.

Willson, R.C., 1973: New radiometric techniques and solar constant measurements. *Solar Energy*, **14**, 203-211.

Willson, R.C., Gulkis, S., Janssen, M., Hudson, H.S., and Chapman, G.A.1981: Observations of solar irradiance variability. *Science*, **211**, 700-702.